



Optimising nutrient use efficiency in crop production

Holly Jean Butler

B.Sc. (Hons) Biological Sciences with Biomedicine

This thesis submitted in partial fulfilment of the requirements for the degree of Doctor of Philosophy at Lancaster University

September 2016



**This project was supported by the Centre for
Global Eco-Innovation and is part financed by the
European Regional Development Fund.**

Centre for Global Eco-Innovation



EUROPEAN UNION
Investing in Your Future
European Regional
Development Fund 2007-13

www.cgeinnovation.org

Declaration

I declare that the contents in this thesis are my own work and have not been submitted in the same form for the award of higher degree at any other institution. Chapters 2-4 have been peer reviewed and published as a consequence of this project, whilst Chapters 5-7 have been submitted for publication.

Holly J. Butler

Lancaster, UK, September 2016

Contents

Title Page	i	
Centre for Global Eco-Innovation	ii	
Declaration	iii	
Contents	iv	
Acknowledgements	viii	
Abstract	ix	
List of Abbreviations	xi	
List of Figures	xiv	
List of Tables	xix	
Chapter 1	General Introduction	1
Chapter 2	Using Fourier transform IR spectroscopy to analyze biological materials	56
	Matthew J. Baker, Júlio Trevisan, Paul Bassan, Rohit Bhargava, Holly J. Butler , Konrad M Dorling, Peter R. Fielden, Simon W. Fogarty, Nigel J. Fullwood, Kelly Heys, Caryn Hughes, Peter Lasch, Pierre L. Martin-Hirsch, Blessing Obinaju, Ganesh D. Sockalingum, Josep Sulé-Suso, Rebecca J. Strong, Michael J. Walsh, Bayden R. Wood, Peter Gardner and Francis L Martin	
	Nature Protocols 9(8): 1771-1791 (2014)	
Chapter 3	Using Raman spectroscopy to characterise biological materials	95
	Holly J. Butler , Lorna Ashton, Benjamin Bird, Gianfelice Cinque, Kelly Curtis, Jennifer Dorney, Karen Esmonde-White, Nigel J. Fullwood, Benjamin Gardner,	

Pierre L. Martin-Hirsch, Michael J. Walsh, Martin R. McAinsh, Nicholas Stone, and Francis L. Martin

Nature Protocols 11(4): 664-687 (2016)

Chapter 4	Application of vibrational spectroscopy techniques to non-destructively monitor plant health and development	120
	Holly J. Butler, Martin R. McAinsh, Steven Adams, and Francis L. Martin	

Analytical Methods 7(10): 4015-4378 (2015)

Chapter 5	Observation and quantification of Calcium uptake at the adaxial surface of leaves of tomato (<i>Solanum lycopersicum</i>) using Raman spectroscopy	143
	Holly J. Butler, Steve Adams, Martin R. McAinsh, and Francis L. Martin	

Submitted for publication: Analyst August 2016

Chapter 6	Detecting nutrient deficiency in plant systems using synchrotron FTIR microspectroscopy	177
	Holly J. Butler, Steve Adams, Martin R. McAinsh, and Francis L. Martin	

Submitted for publication: Vibrational Spectroscopy

Invite for special issue 'Prominent Young Spectroscopists'

Chapter 7	Pre-symptomatic detection of Ca stress in tomato using vibrational spectroscopy and next generation sequencing	207
------------------	---	------------

Holly J. Butler, Steve Adams, Martin R. McAinsh, and Francis L. Martin

Prepared for publication: Nature Communications

Chapter 8	General Discussion	246
------------------	---------------------------	------------

References		252
-------------------	--	------------

Appendix I	Other Publications	281
-------------------	---------------------------	------------

Application of IR spectroscopy to environmental health monitoring using sycamore (*Acer pseudoplatanus*) as a sentinel species

J. Ord, **Holly J. Butler**, Martin R. McAinsh, Francis L. Martin

Analyst (2016) **141**: 2896-2903

Gold nanoparticles as a substrate in bioanalytical near-infrared surface-enhanced Raman spectroscopy	292
---	------------

Holly J. Butler, Simon W. Fogarty, Jemma G. Kerns, Pierre L. Martin-Hirsch, Nigel J. Fullwood, Francis L. Martin

Analyst (2015) **140**: 3090-3097

Aluminium foil as a potential substrate for ATR-, transflection FTIR and Raman spectrochemical analysis of biomedical specimens	304	
Li Cui, <u>Holly J. Butler</u> , Pierre L. Martin-Hirsch, Francis L. Martin		
<i>Analytical Methods</i> (2016) 8(3) : 481-487		
Appendix II	Conference Abstracts	312
Appendix III	Conference Posters	316

Acknowledgements

This project would not have been possible without the invaluable expertise, assistance and encouragement of my supervisors Professor Frank L. Martin and Dr Martin McAinsh. They showed faith in a wide-eyed undergraduate and I'm forever thankful for the fantastic supervision they have imparted with me. Thanks to the Centre for Global Eco-Innovation (CGE) and to Dr. Steven Adams at Plant Impact Plc for supporting and encouraging this research.

Endless thanks go to the Centre for Biophotonics and its members, specifically my two brothers Kelly Heys and Rebecca Strong, my spirit animal Maria Paraskevaidi, as well as Blessing Obinaju, Junyi Li, Georgios Theophilou, Alana Mitchell and the other wonderful people I've met and worked with along the way. Special thanks go to Dennis Touliatos, Richard Boyle, Dr Geoff Holroyd and Dr Dawn Worrall in the Plant Physiology and Molecular Biology lab groups for their help and guidance. I would also like to thank the Faculty of Science and Technology, UKEMS, the Royal Society of Chemistry, and the SPEC 2016 organising committee for awarding me with travel grants. A special mention must be given to the Clinical Infrared and Raman Spectroscopy (CLIRSPEC) network for welcoming me so warmly into the field of 'spectrophilia'.

Ultimately, I have to thank those closest to me who have provided me with unsurmountable personal support and inspiration. To Mom and Dad – thank you for everything. From the experiences I've had, to my outlook on life, I owe it all to you both. My motivation in life has always been to make you proud and I hope I have succeeded so far. To Hayley and Louis; thanks for instilling that competitive edge in me from an early age. Further thanks go to you both, as well as Ben and Pam, for providing me with the most welcome distractions in the world: Madison, Fynley, Lucy, Charley, Carter and Lilly. All my love to my grandparents for putting up with me over all those weekends, and to the rest of my extended family who've always been so supportive. Thanks to Glasgow, for motivating me; and football, for keeping me sane. I must mention my fellow LUWFC alumni who have become a second family to me; the Duck family in fact. Good friends are hard to come by – I know this because I am still looking!

Abstract

Food security for a growing population presents a significant challenge for crop production, with increasing pressures upon agricultural productivity. There is a vast need to improve crop yield and quality using an efficient approach that does not present negative environmental impacts. A novel interrogation technique that is able to provide information of the overall health of a plant, would be extremely beneficial in an agricultural, as well as research, setting. This information could be utilised to better understand the mechanisms of plant functions, including stress responses.

Vibrational spectroscopy encompasses a range of techniques that are able to derive chemically specific information from a biological sample in a rapid, non-destructive and cost-effective manner. Fourier-transform infrared (FTIR) spectroscopy and Raman spectroscopy are two such approaches and have been readily implemented across biological samples. However, their applications in the field of plant science have been relatively underexploited. This is largely associated with the presence of water and fluorescent metabolites found in plant tissues.

The application of attenuated total reflectance (ATR)-FTIR and spontaneous Raman spectroscopy for *in vivo* plant monitoring to elucidate spectral alterations indicative of healthy plant growth in a non-destructive manner. These approaches are able to characterise the biochemical signature of leaves at distinct developmental stages, and correspond to known biological processes within the leaf such as cell wall expansion. This information is useful prior to monitoring studies as normal leaf growth could be considered background variance. No significant local or systemic effects manifest as a consequence of interrogation with these techniques, establishing this as a non-destructive approach for plant system investigations.

Raman microspectroscopy as a tool for monitoring nutrient uptake at the leaf surface is also considered, alongside complementary ion probe and elemental analysis. Such a technique is useful in the agrochemical production of foliar fertilisers, where the efficiency of specific formulae can be rapidly compared. This can also further the current understanding of nutrient transport into plant tissues, as well as translocation. Agriculturally relevant levels of calcium were applied to the leaf surface and uptake was

successfully illustrated at concentrations as low as 15 mM using Raman microspectroscopy. Ion probe analysis also complemented these findings, with elemental analysis unable to detect this subtle uptake of nutrients. This assay is now being implemented in agrochemical practise as a fertiliser screening method.

Deficiencies in essential nutrients such as calcium are detrimental to crop yield and thus are a potential target for improving crop production. A range of spectroscopic methods, including the use of synchrotron radiation, were utilised to presymptomatically detect these deficiencies prior to their onset in live samples. Coupled with multivariate analysis, these techniques discriminate between deficient and control samples with high sensitivity and specificity, without extensive sample preparation that traditional analytical techniques require. These results suggest that Raman and ATR-FTIR spectroscopic approaches could highly valuable in the field, where plant health and nutrient status could be assessed rapidly *in situ*.

Here it is shown that these issues can be overcome and that qualitative spectral measurements can be obtained from plant samples. Due to the non-destructive nature of these approaches, they can be applied for a wider range of crop screening investigations, including the efficiency of nutrient uptake, as well as distinguishing nutrient deficiencies presymptomatically. As such, these spectroscopic methods may be implemented to unearth further details regarding nutrient use efficiency during crop production.

List of Abbreviations

λ	Wavelength
AES	Atomic emission spectroscopy
ANN	Artificial neural network
ANOVA	Analysis of variance
ATR	Attenuated total reflectance
AU	Arbitrary units
BER	Blossom end rot
Ca	Calcium
CARS	Coherent anti-Stokes Raman scattering
CCD	Charge coupled device
CE	Carbon equivalents
CGE	Centre for Global Eco-Innovation
CLIRSPEC	Clinical Infrared and Raman Spectroscopy network
CV	Cluster vector
DBM	Difference between mean
D_P	Penetration depth
DTGS	Deuterated triglycine sulphate
E	Energy
EC	Epidermal cell
EDTA	Ethylenediaminetetraacetic acid
EMCCD	Electron-multiplying charge coupled device
f	Frequency
FAAS	Flame atomic absorption spectroscopy
FAO	Food and Agriculture Organization
FE	Feature extraction

FFPE	Formalin-fixed, paraffin-embedded
FFS	Forward feature selection
FTIR	Fourier-transform infrared
FPA	Focal plane array
GHG	Greenhouse gas
GC	Guard cell
GM	Genetically modified
HCA	Hierarchical cluster analysis
ICP	Inductively coupled
IR	Infrared
IRE	Internal reflection element
InGaAs	Indium gallium arsenide
Linac	Linear accelerator
LD	Linear discriminant
LDA	Linear discriminant analysis
LDC	Linear discriminant classifier
low-E	Low emission
MCT	Mercury cadmium telluride
MIR	Mid-infrared
MIRIAM	Multimode infrared IR imaging and microspectroscopy beamline
MS	Mass spectrometry
NA	Numerical aperture
NE	Newly expanded
NIR	Near-infrared
OES	Optical emission spectrometry
PC	Principal components

PC-DFA	Principal component – discriminant function analysis
PCA	Principal component analysis
QCL	Quantum cascade lasers
RF	Random forest
RNA	Ribonucleic acid
SERS	Surface-enhanced Raman spectroscopy
SFL	Spectrometer focal length
SORS	Spatially offset Raman spectroscopy
SG	Savitzky-Golay
SNR	Signal-to-noise ratio
SR	Synchrotron radiation
SRS	Stimulated Raman scattering
SVM	Support vector machine
TERS	Tip-enhanced Raman spectroscopy
TGAC	The Genome Analysis Centre
UN	United Nations
UV	Ultraviolet
WDN	Wavelet denoise

List of Figures

	Title	Page
Figure 1.1	Population growth since 1950 to 2015	6
Figure 1.2	The prevalence of undernourishment around the globe between 2014-2016	8
Figure 1.3	Liebig's law of the minimum	10
Figure 1.4	The relationship between nutrient availability and optimal growth	14
Figure 1.5	Worldwide food wastage in 2007	16
Figure 1.6	The electromagnetic spectrum of light	20
Figure 1.7	Jablonski energy level diagram displaying the energy transition processes in infrared, Raman (Stokes and anti-Stokes) scattering and fluorescence.	21
Figure 1.8	Common vibrational modes of chemical bonds characterised by the CH ₂ group of CH ₂ X ₂ compounds.	22
Figure 1.9	The interaction of light with a sample	23
Figure 1.10	A Michelson interferometer	25
Figure 1.11	Schematic overview of the Diamond Light Source, at the Rutherford Appleton Laboratory	26
Figure 1.12	Schematic of the three primary sampling modes in FTIR spectroscopy; (A) Transmission FTIR; (B) Transflection FTIR and (C) attenuated total reflectance (ATR)-FTIR.	28
Figure 1.13	Typical infrared and Raman spectra of live plant leaf of the <i>Solanum lycopersicum</i>	31

Figure 1.14	Generalised overview of a spontaneous Raman microspectrometer.	32
Figure 1.15	Examples of unprocessed IR and Raman spectra displaying discrepant baselines.	34
Figure 1.16	The application of baseline corrections on Raman and IR spectra	35
Figure 1.17	The effects of normalisation on baseline correction IR spectra derived from three plants species	36
Figure 1.18	An overview of principal component analysis observing the data transformation and the corresponding visual outputs	38
Figure 1.19	A comparison between PCA and PCA-LDA scatterplots.	39
<hr/>		
Figure 2.1	Typical biological spectrum showing biomolecular peak assignments	58
Figure 2.2	The instrumentation underlying the main forms of IR spectroscopic sampling	58
Figure 2.3	FTIR spectroscopy work flow for imaging and diagnosis	59
Figure 2.4	Visual effect of different pre-processing steps on a set of FTIR spectra	60
Figure 2.5	Classification rates of all possible combinations between three pre-processing, three feature extraction and two supervised classifier options	74
Figure 2.6	IR image reconstruction of a human colon mucosa	74
<hr/>		
Figure 3.1	Schematic identifying light scattering after laser exposure on a sample surface.	97
Figure 3.2	Raman microspectroscopy work flow diagram highlighting key aspects of experimental design	98

Figure 3.3	Generalised overview of instrumentation options within a typical spontaneous Raman spectroscopic microscope system	99
Figure 3.4	Simplified overview of the effect of laser excitation wavelength on the fluorescence background	102
Figure 3.5	Raman spectra derived from blood serum containing 150 and 40 nm gold nanospheres	104
Figure 3.6	Examples of common troubleshooting issues during spectral acquisition	113
Figure 3.7	A brief overview of pre-processing options in Raman spectral analysis	114
Figure 3.8	Raman map of fixed endometrial tissue	115
<hr/>		
Figure 4	Front cover of <i>Analytical Methods</i> 2015 7(10)	121
Figure 4.1	An overview of experimental principles and procedure	123
Figure 4.2	Visible effect of ATR-FTIR spectroscopy on leaf tissue	126
Figure 4.3	Cross-validated PCA-LDA 1D scores plot of ATR-FTIR spectra to determine spectral effects of the technique	126
Figure 4.4	Cross-validated PCA-LDA 1D scores plots of Raman spectra to determine spectral effects of the technique	127
Figure 4.5	Spectral data derived from ATR-FTIR and Raman spectroscopy to identify alterations indicative of healthy growth	127
Figure 4.6	Spectra derived from ATR-FTIR and Raman with grouped time points to depict spectral differences symptomatic of leaf development	128

Figure 4.7	Three biomarker extraction approaches to establish spectral biomarkers indicative of plant development	129
Figure 4.8	Linear regression analysis at key biomarker wavenumbers	131
<hr/>		
Figure 5.1	A schematic overview of experimental procedure	149
Figure 5.2	Example of the effects of surfactant use in Ca solution dispersal	155
Figure 5.3	Proof of concept study observing $\text{Ca}(\text{NO}_3)_2$ solution upon the leaf surface	156
Figure 5.4	First derivative spectra of aqueous $\text{Ca}(\text{NO}_3)_2$ with and without EDTA	158
Figure 5.5	Raman intensity at 1050 cm^{-1} at different time points to observe increased $\text{Ca}(\text{NO}_3)_2$ treatments	159
Figure 5.6	Raman intensity at 1050 cm^{-1} to observe uptake over 72-hours	160
Figure 5.7	Raman intensity at 743 cm^{-1} at different time points to observe increased $\text{Ca}(\text{NO}_3)_2$ treatments	161
Figure 5.8	Raman intensity at 743 cm^{-1} to observe uptake over 72-hours	163
Figure 5.9	Ca^{2+} ion concentration on the adaxial leaf surface in comparison to plastic and a glass surface	165
Figure 5.10	NO_3^- ion concentration on the adaxial leaf surface in comparison to plastic and a glass surface	165
Figure 5.11	% Ca content within the ‘banded area’ and ‘remaining’ area of leaflet using FAAS	168
<hr/>		
Figure 6.1	Unprocessed spectra from benchtop FTIR with a globar source in comparison to FTIR with SR	188

Figure 6.2	Microscope images from unfixed and fixed abaxial epidermis from <i>C. communis</i>	189
Figure 6.3	A comparison of pre-processed spectra from unfixed isolated abaxial epidermis and FFPE tissue from <i>C. communis</i> .	190
Figure 6.4	SR-FTIR spectral analysis of unfixed abaxial epidermis from <i>C. communis</i>	193
Figure 6.5	Pre-processed spectra comparing the effects of varying Ca availabilities in GCs and ECs	194
Figure 6.6	Leave-one-out cross validated PCA-LDA analysis of both fixed and unfixed <i>C. communis</i> samples.	196
<hr/>		
Figure 7.1	Fresh and dry weights of <i>S. lycopersicum</i> plants grown in modified Hoagland's solution to mimic Ca deficiency	219
Figure 7.2	Ca content (%) as determined by FAAS of Ca deficient samples	221
Figure 7.3	Processed Raman mean spectra and corresponding 1D PCA-LDA scatterplots for full Ca treatment	223
Figure 7.4	Processed Raman mean spectra and corresponding 1D PCA-LDA scatterplots for Ca remediation	225
Figure 7.5	Processed ATR-FTIR mean spectra and corresponding 1D PCA-LDA scatterplots for full Ca treatment	227
Figure 7.6	Processed ATR-FTIR mean spectra and corresponding 1D PCA-LDA scatterplots for Ca remediation	228
Figure 7.7	Separation of Ca treatments replicates based upon gene expression values derived from RNA-sequencing analysis.	230
Figure 7.8	Hierarchical cluster map of gene probes displaying intensity differences in expression between Ca treatments	231

List of Tables

	Title	Page
Table 1.1	The average concentration of essential macro- and micro-nutrients in dried plant matter, their function within plant growth and the common symptoms of deficiency	12
Table 2.1	FTIR spectroscopy modes used for the interrogation of cellular materials	61
Table 2.2	Sample types and preparation	63
Table 2.3	Typical conditions of the main variables affecting SNR in spectroscopy instruments	65
Table 2.4	Some existing FTIR spectroscopy data analysis software	66
Table 2.5	Instruments and corresponding data acquisition software	68
Table 3.1	Raman microspectroscopy method derivatives and the respective experiment benefits and limitations	99
Table 3.2	Data analysis software for Raman spectral datasets	106
Table 3.3	Commercially available instruments and corresponding operational software	109
Table 3.4	Sensitivity and specificity rates of control and endometrial cancer patients from blood serum and plasma	115
Table 4.1	Average CO ₂ assimilation for equivalent leaflets to determine detrimental effects of ATR-FTIR spectroscopy	126
Table 4.2	Key wavenumber features determined by DBM, CV and FFS feature extraction methods	128
Table 4.3	Top discriminating biomarkers as derived from feature extraction techniques with tentative wavenumber assignments	130

Table 5.1	The rate of ion uptake at the adaxial leaf surface using ion probe measurements	166
Table 6.1	Discriminating spectral regions derived from Figure 6.3, 4 and 5 with tentative molecular assignments	191
Table 6.2	Discriminating biomarkers of Ca deficiency from PCA-LDA analysis of SR-FTIR spectra of unfixed and fixed <i>C. communis</i> samples	197
Table 6.3	Classification rates of each tissue sample and Ca treatment (%) using a PCA-LDC	199
Table 7.1	Sensitivity and specificity values of binary SVM classifiers for distinguishing Ca treatments	224
Table 7.2	Standard deviation of sensitivity and specificity values of binary SVM classifiers for distinguishing Ca treatments	224
Table 7.3	Functional overview of genes identified within each cluster identified using HCA between Ca treatments	232
Table 7.4	Top 5 differentially expressed genes with known function from each hierarchical cluster between Ca treatments	233

Chapter 1

General Introduction

General Introduction

Contents	Page
Chapter Title Page	1
Contents	2
1.1 Aims & Objectives	4
1.2 Introduction	6
1.3 Food Security	8
1.4 Nutrient Use Efficiency	9
1.4.1 Nutrient Deficiencies	11
1.4.2 Fertilisers	14
1.4.3 Environment Impacts of Inefficient Crop Production	15
1.5 Calcium in Plants	17
1.5.1 Calcium Deficiencies	17
1.5.2 Calcium Signalling	18
1.5.3 Measuring Cytosolic Free Ca^{2+}	19
1.6 Vibrational Spectroscopy	20
1.6.1 Fundamentals of Fourier Transform Infrared Spectroscopy	23
1.6.1.1 Instrumentation	24
1.6.1.2 Light Sources	24
1.6.1.3 Sampling Modes	27
1.6.1.4 Detector	29
1.6.2 Fundamentals of Raman Spectroscopy	29
1.6.2.1 Instrumentation	32
1.6.3 Spectral Pre-processing	33

1.6.3.1	Baseline Correction	33
1.6.3.2	Normalisation	36
1.6.4	Multivariate Analysis	37
1.6.4.1	Principal Component Analysis	37
1.6.4.2	Linear Discriminant Analysis	39
1.6.4.3	Classification Algorithms	40
1.6.5	Vibrational Spectroscopy in Plant Research	41
1.6.5.1	Applications of FTIR Spectroscopy	41
1.6.5.2	Applications of Raman spectroscopy	42
1.7	References	43

1.1 Aims & Objectives

This project has the fundamental aim of developing vibrational spectroscopic techniques for plant based research, with a focus upon agricultural applications. Specifically, the suitability of IR and Raman spectroscopies are evaluated as rapid, non-destructive, *in vivo* analytical techniques that are able to deduce molecular information without the need of extensive sample preparation steps. Known barriers to translation of biospectroscopy in plant research, such as water interference in IR and fluorescence in Raman, are investigated and the viability is determined.

Additional to this initial aim, the non-destructive nature of these approaches will be addressed; by monitoring any detrimental side effect of *in vivo* spectral acquisition on plant tissue. The spectral information derived from this study would then be correlated with known biological changes within these tissue, to determine the viability of the information extracted.

Once the suitability of these approaches has been determined, Raman spectroscopy as a novel method to analyse the fertiliser efficiencies will be investigated. By using these techniques to observe and quantify Ca^{2+} uptake at the adaxial leaf surface, the addition of key fertiliser components can be examined. With industrial collaboration, this approach would be fed directly into a fertiliser product production pipeline, where compositions could be compared readily.

Nutrient deficiencies have a significant impact on crop yield in agricultural settings, and thus a range of spectroscopic measurements will be implemented to describe the biochemical alterations indicative of nutrient deficiency. Due to the importance of Ca as a plant nutrient, Ca stress will be the focus of these investigations. Initially, the analysis of fixed tissue using FTIR spectroscopy coupled to SR will be investigated and compared against traditional benchtop instruments. SR will also be used to derive FTIR measurements from fresh tissues with high water content, to overcome limitations of FTIR in plant research.

Subsequent to this investigation, blossom-end rot in *S. lycopersicum*, the common tomato plant, is highlighted as a model system to investigate presymptomatic detection of deficiency using spectroscopic analysis. Ca deficiency is induced using a hydroponic nutrient supply system providing defined levels of Ca. Raman spectroscopy

will be used for rapid, non-destructive *in vivo* measurements additional to ATR-FTIR of fixed samples for complementary analysis.

1.2 Introduction

The total world population has been on a steep rise since the early 1950s and currently stands at 7.3 billion people; and this figure is expected to increase. By 2050, the population is projected to reach 9 billion people and will likely surpass 11 billion by 2100 (**Figure 1.1**)¹. With increasing population size, there is an equivalent increase in pressure upon crop production due to the demand for sustainable food sources ^{2,3}. In order to provide a sufficient food supply for the growing population, it is imperative to improve agricultural productivity ⁴. It is estimated that as much as 70 – 100% more food will be required to feed our population by 2050 ⁵. There are a number of significant barriers to this process namely; the availability of water, nutrients, and arable land, as well the effects of abiotic and biotic stresses upon crops and of course, climate change ⁶. All of these factors contribute to reduced agricultural productivity and thus the concept of food security is established.

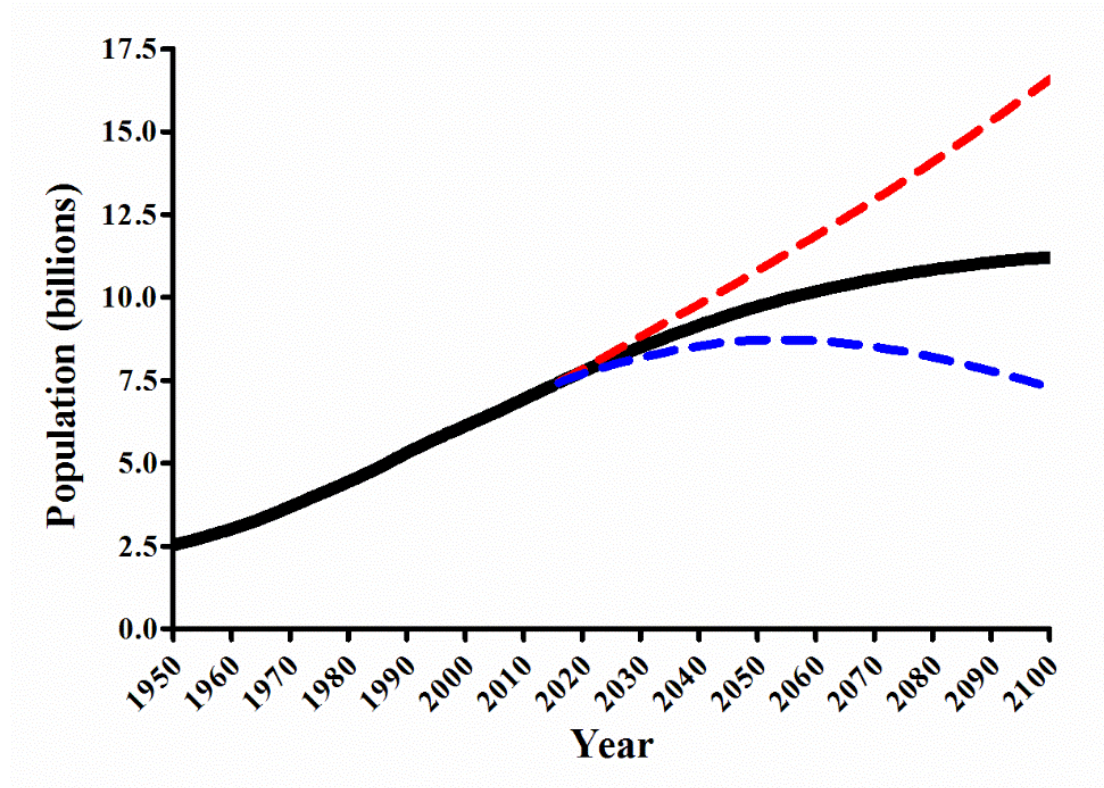


Figure 1.1. Population growth since 1950 to 2015, with high (red), median (black) and low (blue) variant estimates for population growth until 2100. Data provided by the United Nations Department of Economic and Social Affairs ¹.

Fundamental plant research remains the key to optimising crop production and has spearheaded the ‘Green Revolution’^{7,8}. The diverse field of plant science has contributed to improved crop efficiency, ultimately resulting in increased crop yield and quality⁹. There have been huge advances made in the field of genetically manipulated (GM) crops, creating more resilient crop species that are resistant to environmental stresses including disease, pathogens and herbicides¹⁰⁻¹². Although the development of GM crops provides a powerful approach to improving agricultural productivity, there is a substantial ethical obstruction to real-world applications¹³.

The selective breeding of organisms naturally resistant to stresses such as water scarcity, is one favourable alternative that has been particularly well exploited in plant research¹⁴. The complementary use of pesticides has also contributed to overall improvements in crop yield, although these present negative connotations with regards to unnecessary chemical use in the environment and food chain^{15,16}. Movement away from traditional soil based growth protocols, such as using hydroponic systems, has also contributed to improved agricultural efficiency, as both water and nutrient supply are optimised for the specific crop¹⁷.

Nutrient availability can be considered one of the most significant factors impacting crop yield and consequently fertiliser use is a primary resource for improving productivity. Maintaining an optimum level of soil fertility is paramount to an effective agricultural environment and can significantly increase crop yield. However, the use of fertilisers is a relatively inefficient process, with the vast majority of current nutrient supplementation protocols focused upon a few specific nutrients, namely nitrogen (N), phosphorous (P) and potassium (K).

In order to optimise crop production by improving nutrient use efficiency, there is a need for a novel crop screening technology that will allow rapid determination of crop nutrient status, as well as to monitor the effects of nutrient supplementation. Generally speaking, plant monitoring and interrogation tools are often limited to technical approaches that require specialist users, or are often constrained to applications in model species such as *Arabidopsis thaliana* which have been thoroughly characterised for molecular studies¹⁸. Currently, the determination of nutrient content is reliant upon

invasive, destructive, and time-consuming analytical processes that are not suitable for *in situ* investigation in field environments ¹⁹.

A technique that was able to derive nutrient specific biochemical information rapidly, non-invasively, with the potential of analysis in the field would be hugely beneficial to the field on plant biology. Specifically, the nutrient status of crops could be determined, allowing the exact nutrient requirements to be established. This is a movement towards a precision farming approach where fertilisers are only applied at the levels to which are necessary, leading to more efficient resource use as well as increase crop yield and quality ²⁰.

1.3 Food Security

Since first being coined at the first World Food Conference held by the United Nations (UN) Food and Agriculture Organization (FAO), the term ‘Food Security’ has evolved ²¹. Today the phrase encompasses the concept that everybody throughout the world has continual access to safe and nutritious food that they require for a healthy and active lifestyle ²². It is evident that, even at this point in time, there is a significant shortfall in achieving this aim, with up to 795 million people currently experiencing food poverty ²³.

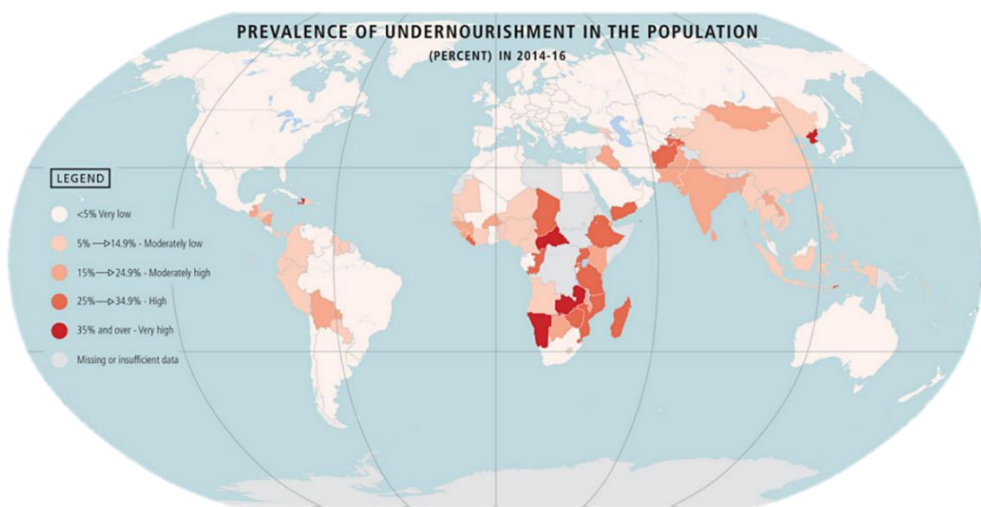


Figure 1.2. The prevalence of undernourishment around the globe between 2014-2016 showing areas most susceptible to the impacts of food insecurity.

The effects of insufficient food security are predicted to worsen, with the primary pressures of a growing population, land availability and climate change. This will likely be felt initially in rural areas of developing countries, where more than 70% of the world of the world's starving population reside (**Figure 1.2**)²⁴. However, there is predicted to be a significant effect throughout the world as the gravity of the problem increases ²⁵. The reader is directed to the following reviews for further information regarding the topic of food security which provide in-depth analyses of pressures and challenges surrounding this issue ^{2,26-28}.

Crucial to achieving widespread food security is the ability to produce food in an adequate quantity and quality in the most efficient way possible ²⁹. There have been many advancements for optimised crop production such as the use of light emitting diode (LEDs) lighting systems in agricultural settings for providing optimal light and temperature conditions, as well as the use of vertical farming apparatus for space efficiency in urban environments ^{30,31}. Both of these approaches present increased energy efficiencies during crop production and thus simultaneously tackle the issues of greenhouse gas (GHG) emissions associated with food production. However, one of the most significant factors in crop production is adequate supply of the essential nutrients to the crop and as such is the primary target for increased crop production efficiency ³².

1.4 Nutrient Use Efficiency

The availability of nutrients during crop development is crucial to optimum crop yield and quality ³³. Plants require six essential macro-nutrients; nitrogen (N), potassium (K), phosphorous (P), calcium (Ca), sulphur (S) and magnesium (Mg), and eight micro-nutrients; boron (B), chlorine (Cl), copper (Cu), iron (Fe), manganese (Mn), molybdenum (Mo), nickel (Ni) and zinc (Zn) ³⁴. These nutrients are indispensable due to their pivotal role in biochemical processes downstream of photosynthesis and all have specific roles in plant growth and development ³². Their transport is primarily in ionic form through the soil and their uptake is dependent upon the root parameters, shoot-root and root-to-soil relationships; all of which are affected by environmental conditions ³⁵.

Due to the central role that these nutrients have in crop growth, crop yield is directly related to the nutrient supply available to the crop and the efficiency at which it

can absorb and utilise those nutrients, defined as the nutrient use efficiency ³⁶. The relationship between nutrient availability and crop growth was well characterised by the work of Justus von Liebig, who established that crop growth was limited due to the least available nutrient rather than a generic availability of all nutrients ³⁷. Referred to as Liebig's Law of the Minimum, this theory is best described by Liebig's Barrel, where the shortest stave is responsible for water (yield) loss (**Figure 1.3**).

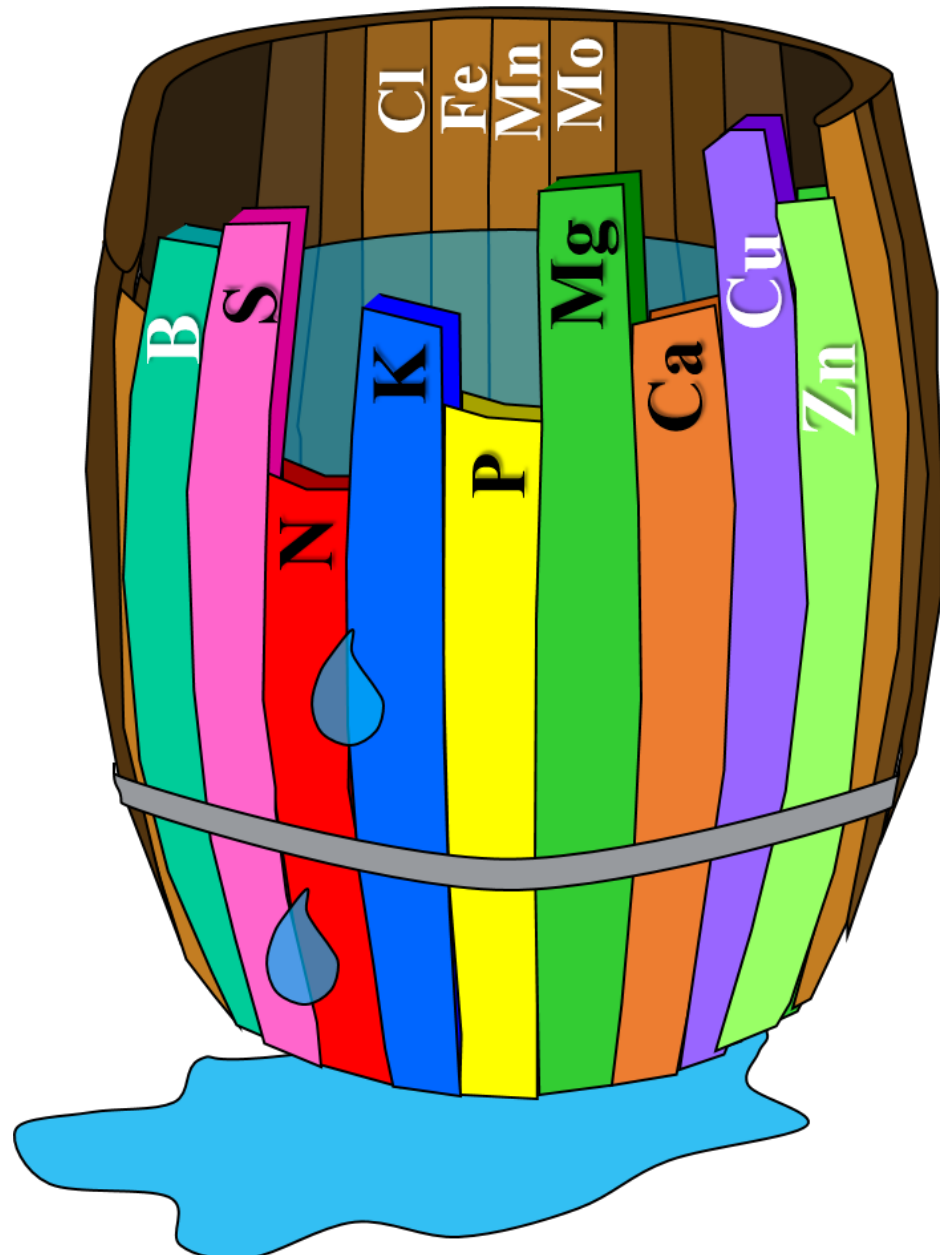


Figure 1.3. Liebig's Law of the Minimum. Crop yield is dependent upon the most limiting nutrient, with N, P, K. ³⁷

1.4.1 Nutrient Deficiencies

Although nutrient deficiencies, particularly those of micro-nutrients, are relatively rare in nature, they are commonplace in agricultural systems due to intensive farming practises³⁸. Insufficient availability of essential crop nutrients has a detrimental impact on crop growth and thus can significantly reduce crop yield (**Figure 1.4**). The theoretical yield, compared to the actual obtained yield of a given area is referred to as the yield gap³⁹. Nutrient availability is the main limiting factor in reducing this yield gap, but is difficult to quantify due to the diversity of arable lands, crop species and also the relationships of nutrients themselves⁴⁰. Nutrient uptake and deficiency are not independent of other nutrients and synergistic, antagonistic and additive relationships have been identified in nutrient stressed organisms⁴¹.

Nutrient deficiencies can therefore manifest across a range of crop species, with a variety of species specific symptoms (**Table 1.1**). The tissues in which these symptoms manifest are often indicative of the mobility of the limiting nutrient. A mobile element can be readily translocated from one tissue to another and thus many symptoms are presented in mature tissues, where nutrients such as Mg and P are transported to younger tissues in deficient conditions⁴². In contrast, a deficiency in immobile elements such as Ca and Cl, results in insufficient nutrient supply to younger tissues from the soil, but also from older tissues⁴³.

However, the detection of nutrient deficiency of crops via visual symptoms is restricted; initially, due to non-specific symptoms and also due to delayed onset of deficiency¹⁹. As **Table 1.1** begins to illustrate, visual symptoms are analogous between different elemental deficiencies, and can vary significantly between crop species. Furthermore, the interpretation of visual symptoms suggests that a nutrient deficiency has fully developed within an organism and by this stage remediation may already be impossible⁴⁴.

Table 1.1. The average concentration of essential macro- and micro-nutrients in dried plant matter (adapted from ³⁴, their function within plant growth and the common symptoms of deficiency (adapted from ³³).

Nutrient	Conc.	Function	Symptoms of deficiency
		(mg kg⁻¹)	
N	15,000	<ul style="list-style-type: none"> • Chlorophyll production • Protein component • Leaf development • Yield formation 	<ul style="list-style-type: none"> • Reduced growth rate • Chlorosis of older leaves
K	10,000	<ul style="list-style-type: none"> • Water economy • Signalling and transport • Stress resistance 	<ul style="list-style-type: none"> • Stunted growth • Chlorosis at leaf boundary • Browning at tips of old leaves
Ca	5,000	<ul style="list-style-type: none"> • Cell wall component • Signalling component • Cell division and growth 	<ul style="list-style-type: none"> • Cell wall necrosis of developing tissues, fruits and young leaves.
P	2,000	<ul style="list-style-type: none"> • Root development • Seed and fruit development • Amino acid component 	<ul style="list-style-type: none"> • Reduced growth rate • Red tint on older leaves
Mg	2,000	<ul style="list-style-type: none"> • Chlorophyll component • Metabolic roles 	<ul style="list-style-type: none"> • Chlorosis of older leaves • Generic symptoms of senescence
S	1,000	<ul style="list-style-type: none"> • Amino acid component • Formation of chlorophyll and essential oils 	<ul style="list-style-type: none"> • Chlorosis of young leaves • Reduced growth rate • Fruit do not mature

Cl	100	<ul style="list-style-type: none"> • Oxygen production in photosynthesis • Maintaining osmotic pressure 	<ul style="list-style-type: none"> • Chlorosis of young leaves • Wilting
Fe	100	<ul style="list-style-type: none"> • Chlorophyll synthesis • N assimilation • Carbohydrate metabolism 	<ul style="list-style-type: none"> • Chlorosis of vascular tissues • Leaf chlorosis leading to white leaves
Mn	50	<ul style="list-style-type: none"> • Water electrolysis in photosynthesis 	<ul style="list-style-type: none"> • Chlorosis of vascular tissues • Chlorosis of young leaves
B	20	<ul style="list-style-type: none"> • Membrane integrity • Cell wall growth 	<ul style="list-style-type: none"> • Deformity of young tissues • Cracking of stalks and fruit
Zn	20	<ul style="list-style-type: none"> • Enzyme systems • Protein synthesis 	<ul style="list-style-type: none"> • Stunted plant growth • Variable between species
Cu	6	<ul style="list-style-type: none"> • Chlorophyll component • Lignin, protein and carbohydrate metabolism 	<ul style="list-style-type: none"> • Twisted leaves • Pale white shoot tips • Variable between species
Mo	0.1	<ul style="list-style-type: none"> • Enzyme systems • Protein synthesis 	<ul style="list-style-type: none"> • Chlorosis of leaf margins • Rolling of leaves
Ni	0.1	<ul style="list-style-type: none"> • Enzyme systems 	<ul style="list-style-type: none"> • Reduced growth • Chlorosis and necrosis of leaves

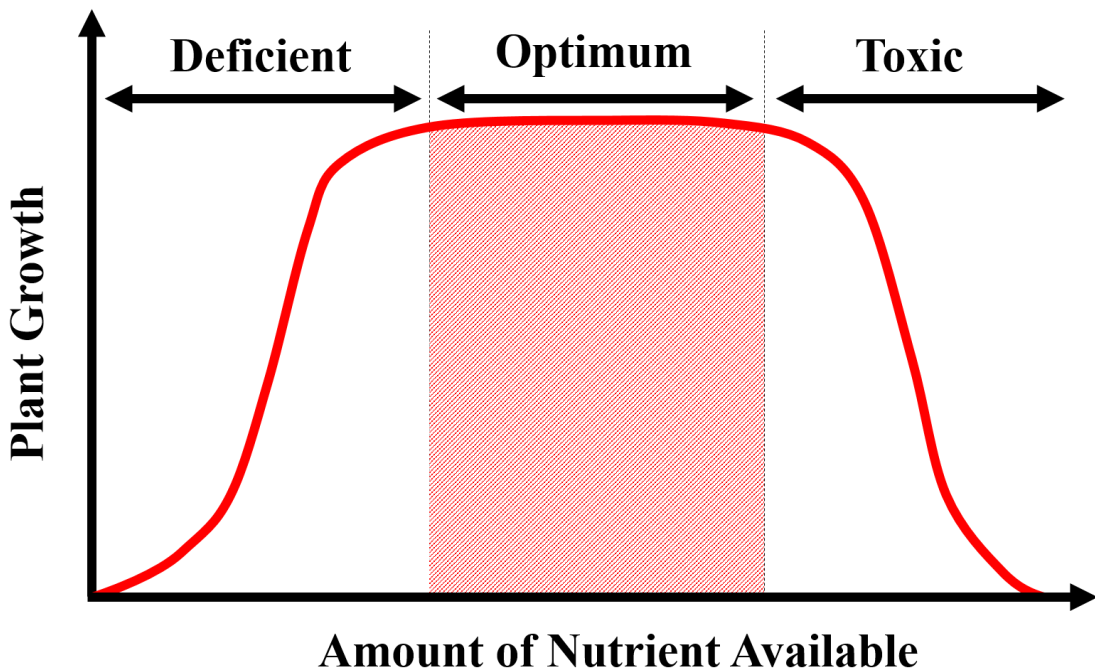


Figure 1.4. The relationship between nutrient availability and optimal growth. Adapted from 38

Alternatively, nutrient stress can be identified using plant or soil analysis approaches, where the exact elemental content of these tissues is determined using an analytical approach such as inductively coupled plasma (ICP)-mass spectroscopy (MS), ICP- atomic emission spectroscopy (AES), ICP- optical emission spectrometry (OES), flame atomic absorption spectroscopy (FAAS), and flame photometry ^{32,45,46}. The result of tissue specific sampling is that an exact nutrient profile can be established and consequently remediation can be targeted. However, such approaches often require extensive sample preparation steps that are not easily implemented in agricultural environments.

1.4.2 Fertilisers

The application of nutrient fertilisers to provide supplementary minerals to growing media has been a regular practice for up to 2000 years ³⁴. N, P and K are considered the most limiting of the essential minerals and consequently have the largest incidence of nutrient deficiency in both temperate and tropical growth environments ³². Consequently,

the vast majority of fertilisers applied contain at least one of these essential nutrients. It is estimated that in 2016 alone, over 194.1 million tonnes of N, P and K containing fertiliser will be applied worldwide in order to improve soil fertility⁴⁷. Whilst this approach is effective when a reduction in these nutrients is present, this is not efficient when another essential mineral is the limiting factor; a deficiency can only be remediated by supplementation of that exact nutrient, based upon the Law of the Minimum^{33,37}. Aside from being inefficient in regards to crop yield and agricultural productivity, this is extremely costly to the grower and presents a host of negative environmental impacts⁴⁸.

Furthermore, a plentiful supply of nutrients in the growth medium is not always a precursor to active absorption of these nutrients and thus nutrient stress can still occur³³. Nutrient uptake from the soil is dependent upon a number of root and soil parameters; a potential outcome of this is that some nutrients are not accessible from the soil, despite their abundance³⁵. As such, foliar fertilisers have been suggested as an alternative approach to nutrient supply, particularly as a short term aid to nutrient stress⁴⁹. There are a number of associated benefits of foliar rather than soil based fertiliser applications; largely centred upon the reduced volume requirement as well as potential improvement in nutrient recovery rate⁵⁰. Additionally, foliar nutrient applications can be combined with other crop treatments such as herbicides, for increased productivity⁴⁹.

1.4.3 Environmental Impacts of Inefficient Crop Production

There are a number of undesirable side effects of inefficient crop production, supplementary to the shortcomings in crop yield that are damaging to global food security. Broadly speaking these can be economical, social and also environmental; it is the latter of which is of interest in this instance.

The traditional approach to fertiliser application is a relatively inefficient process, due to generic application of N, P and K containing fertilisers regardless of specific nutrient requirements of the crop. This, in itself, is highly inefficient, and there is also a significant carbon footprint associated with this process. Of the cumulative total of worldwide GHG emissions, N fertiliser production is responsible for 1.2% of this total value. This equates to nearly 700 kg of CO₂ and carbon equivalents (CE) per hectare of

farmland each year, as 90% of total emissions from farm operations are attributed to fertiliser use ⁵¹. The extensive effects of fertiliser use on GHG emissions are excellently addressed by Snyder et al., and the reader is directed to this review for additional information ⁵².

N-based fertilisers also present other significant environmental issues that occur when they are leached from agricultural land. The loss of N into the surrounding ecosystem has been shown to have negative impacts on human health, biodiversity and contamination of water supplies ⁵³. Eutrophication is one such example of the detrimental effects of fertiliser run off and can cause devastating loss of marine life ⁵⁴.

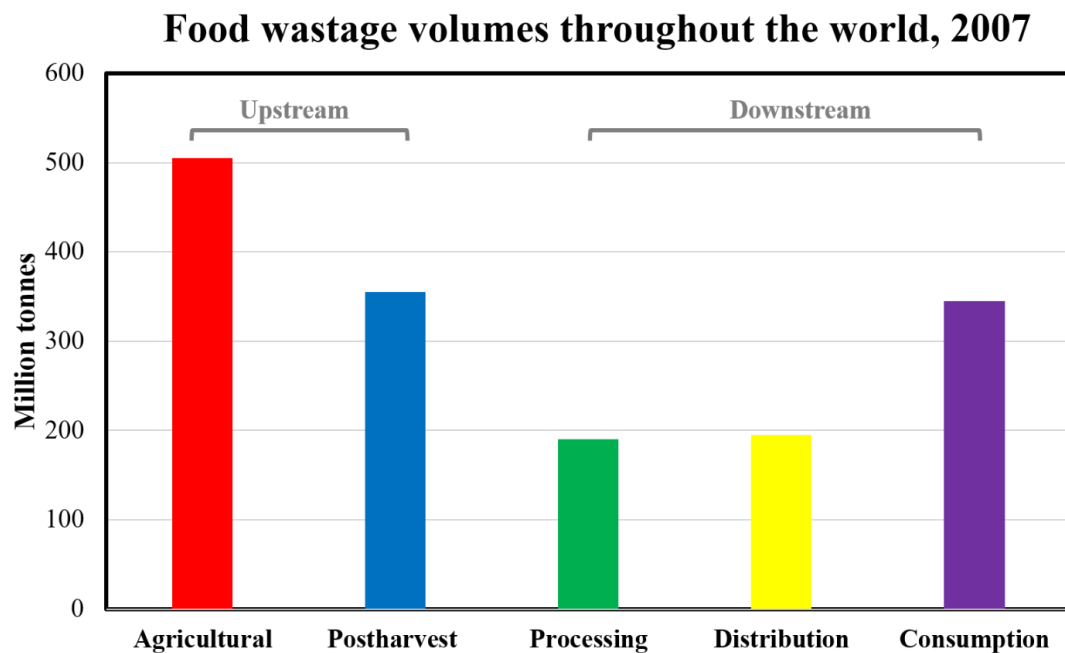


Figure 1.5. Worldwide food wastage in 2007, regarding the relative areas of the food production chain. Adapted from ⁵⁵.

Aside from the impacts of fertiliser use in crop production, there is also the issue of food quality. Nutrient availability has a direct effect on crop yield, but also on crop quality, and thus inadequate growing conditions are transferred to the quality of the food. Up to 1.3 Gtonnes of edible produce was wasted worldwide in 2007 ⁵⁵. During agricultural production, also referred to as upstream of the food supply chain, 46% of

produce is discarded purely based on appearance and shelf life, which is likely as a consequence of the nutrient status of the crop during growth⁵⁵. Downstream of this chain, specifically at retailers and in homes, an almost equivalent amount of food is wasted, with UK alone discarding 7 million tonnes of food every year (Figure 1.5)⁵⁶.

1.5 Calcium in Plants

Ca is an essential macronutrient in all living organisms that has a conserved function in many biological processes. Ca has a vital role in coordinating cellular responses and signalling and acts as an important counter-cation in aiding anionic exchange across the plasma membrane in its divalent cation form (Ca^{2+}). Ca^{2+} is cytotoxic to a cell at high concentrations as it has an affinity for biological molecules, causing precipitation of phosphate, aggregation of proteins and nucleic acids, and damage to the lipid membrane⁵⁷. As a consequence, controlling the concentration of Ca^{2+} has been a priority to a cell since the early evolution of cellular life⁵⁸. It is thought that the energy expenditure of cells to maintain this homeostasis has been coupled through evolution to signal transduction in both eukaryotic and prokaryotic cells⁵⁹.

1.5.1 Calcium Deficiencies

Ca has a number of structural and functional roles in plants, particularly in binding strands of pectin together in the cell wall⁶⁰. A plant's source of Ca is derived from the soil and is distributed through the plant via the apoplastic and symplastic pathways^{61,62}. Ca is relatively immobile in the phloem and consequently Ca distribution is largely reliant on xylem flow and therefore transpiration in particular tissues⁶³.

As a consequence of this, there are a number of Ca related deficiencies that can arise, which are commonly found in horticulture and agriculture⁶⁴. Ca deficiencies occur when the element is unavailable in developing tissues, enclosed tissues and tissues that are supplied predominantly by the phloem⁶⁵. Insufficient Ca has been shown to cause up to 50% loss of yield in crop production and has a distinctly negative impact on agricultural productivity^{66,67}. Deficiencies such as 'tipburn' in expanding leaves of leafy vegetables, 'blackheart' in the enclosed tissues of celery and 'blossom end rot' and

‘bitter pit’ affecting the fruit of tomatoes and apples respectively^{68,69}. Due to the detrimental effect of these disorder, as well as the role that Ca^{2+} plays in fruit ripening, maintaining fruit firmness and reducing postharvest decay, Ca^{2+} supplementation in agriculture is becoming an emerging section of the crop enhancement market^{60,70}.

1.5.2 Calcium Signalling

Ca^{2+} is a fundamental signalling component of plant responses to environmental and developmental stimuli, which are crucial to a number of plant functions such as regulation of stomatal aperture⁷¹. Due to the cytotoxic nature of Ca^{2+} , the cytosolic calcium concentration ($[\text{Ca}^{2+}]_{\text{cyt}}$) must be kept at a tolerable level. $[\text{Ca}^{2+}]_{\text{cyt}}$ is maintained at a resting level of 100nM which can be up to a 20,000-fold difference from the extracellular Ca^{2+} concentration in the apoplast, a gradient that requires a substantial amount of energy to maintain⁵⁹.

This resting level is maintained by pumps and exchangers found on the cell plasma membrane, regulating efflux to the apoplast, and on endomembranes, regulating efflux to intracellular stores such as the vacuole and endoplasmic reticulum. These can be described as ‘off mechanisms’, an aspect of the Ca^{2+} signalling toolkit described by MJ Berridge and colleagues in 2000 in mammalian cells⁷². The mechanisms in which $[\text{Ca}^{2+}]_{\text{cyt}}$ are elevated in response to a stimulus can similarly be referred to as the ‘on mechanisms’. To generate a transient Ca^{2+} signal, there is a passive movement of Ca^{2+} into the cytosol, which is mediated by a collection of channels that allow rapid influx of Ca^{2+} ions. Ca^{2+} floods the cytosol from both the apoplast via the plasma membrane and from intracellular stores via various endomembranes such as the tonoplast⁷³.

A role for calcium has been found to be ubiquitous with an array of plant functions, from stress signalling, to pollen tube growth, circadian clock regulation, pathogen interactions, and the highly researched area of regulation of stomatal aperture⁷⁴. A prevalent question is how such a simple ion can encode specificity in so many plant functions. The issue of specificity is best described by the response of a plant cell to the plant hormones auxin and abscisic acid (ABA), which both induce an elevation of $[\text{Ca}^{2+}]_{\text{cyt}}$ although with opposite effects, as auxin stimulates stomatal opening whereas ABA reduces stomatal aperture^{75,76}. From the vast number of channels that have so far

been found to be involved with the elevation of $[Ca^{2+}]_{cyt}$, it is evident that there is the ability within a plant cell to generate complex calcium signatures. The comprehensive review by McAinsh & Pittman discusses several mechanisms that may contribute to encrypting specificity ⁷⁷.

1.5.3 Measuring Cytosolic Free Ca^{2+}

Many Ca related studies have been facilitated by the ability to measure intracellular free Ca^{2+} in living cells. These basic, non-destructive methods have enabled the visualisation Ca^{2+} influx in guard cells in response to ABA, Ca^{2+} localisation pollen tubes and root hair cells as well a host of other key studies that have helped shape the current knowledge of Ca^{2+} functionality ⁷⁸. Current widely implemented methods include the application of Ca^{2+} -sensitive fluorescent dyes, the calcium-sensitive luminescent protein aequorin, cameleon sensing proteins and Ca^{2+} -sensitive microelectrodes ⁷⁹. These dyes work on the basis that the sensor dye and its loading, in no way compromises normal cellular function ⁷⁸.

A key aspect of imaging cytosolic free Ca^{2+} and Ca monitoring is that all of these approaches are limited to certain model species such as *Arabidopsis thialana* and *Commelina communis* ⁷⁹. As a consequence, current restrictions in methods of imaging free Ca^{2+} in plant cells may be inhibiting the progress of research in plant related Ca^{2+} studies.

1.6 Vibrational Spectroscopy

The principle of spectroscopy is the interaction between radiation and matter. Radiation is provided in the form of a wave that has both electric and magnetic field components. The electromagnetic spectrum describes the photon energy (E), wavelength (λ) and frequency (f) of these waves (Figure 1.6). λ is inversely proportional to the f of the wave, whilst the f is proportional to the E . Photons are fundamental particles possess properties of both waves and particles, and can be described as having wave-particle duality. Max Planck pioneered mathematical modelling of photon energy as a function of f and Planck's constant describes the inverse proportionality of E to λ ⁸⁰.

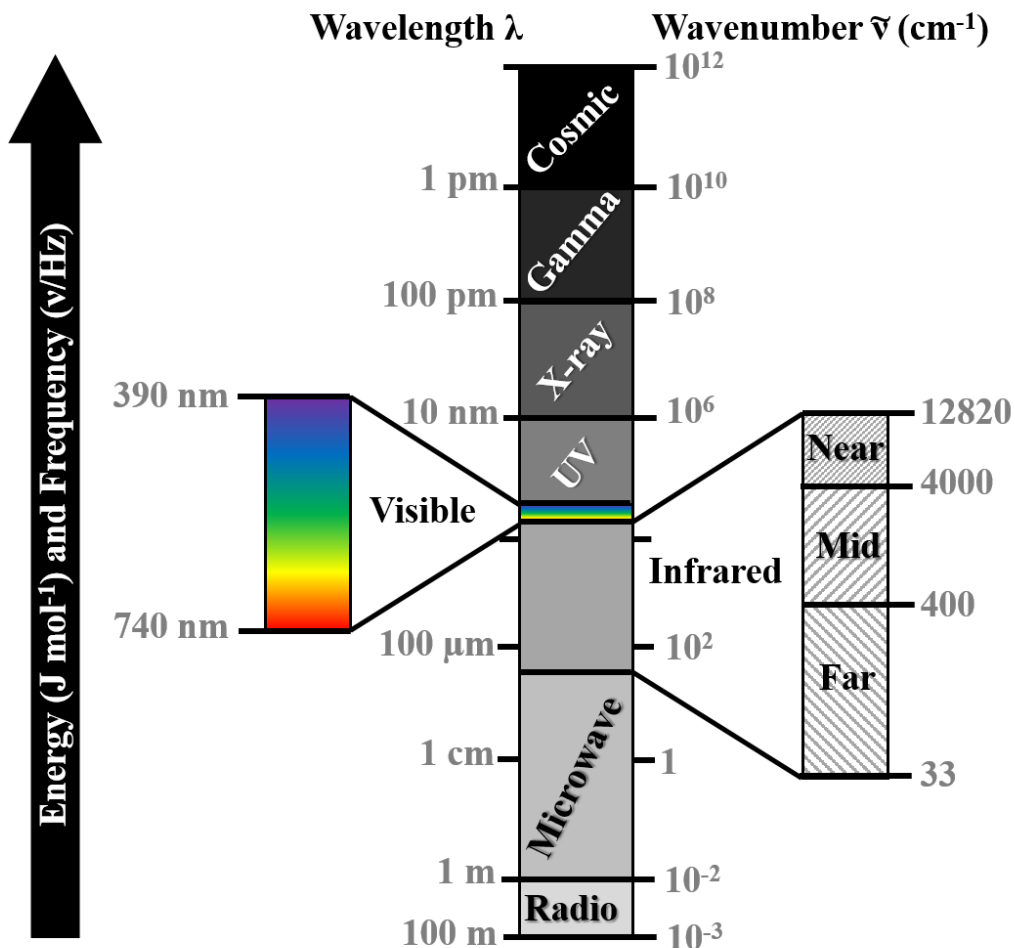


Figure 1.6. The electromagnetic spectrum of light with the visible and infrared regions expanded. Adapted from⁸¹ and⁸².

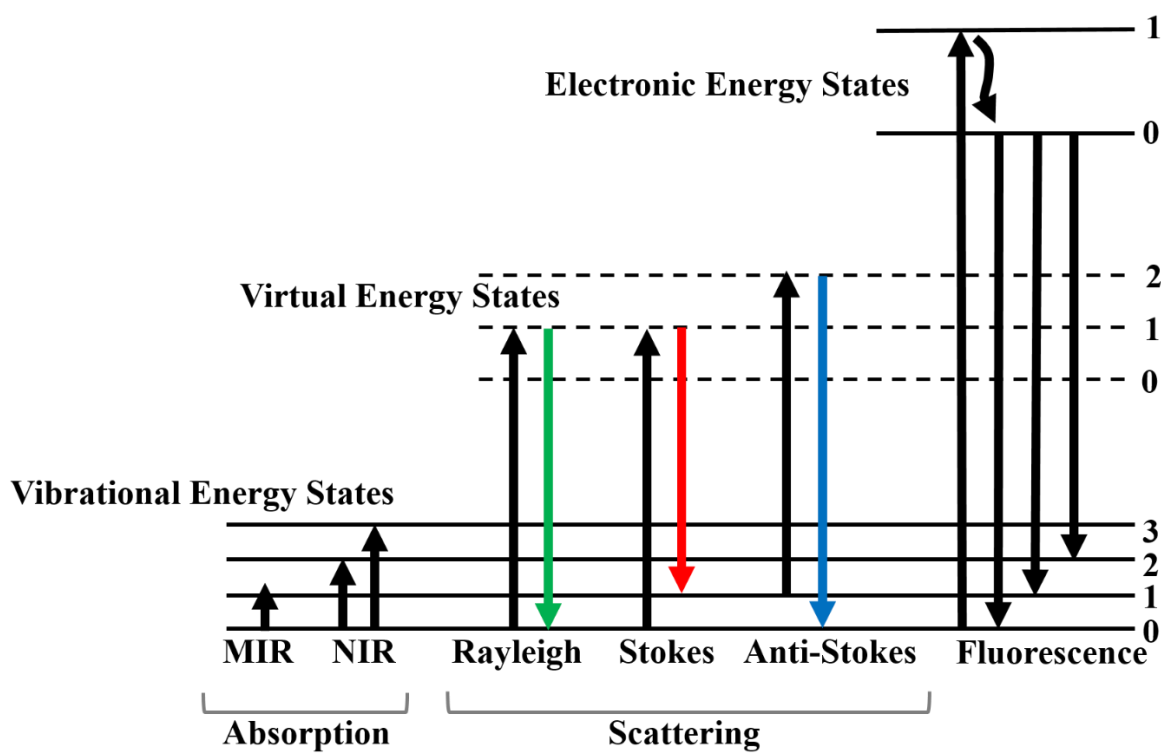


Figure 1.7. A schematic overview of a Jablonski energy level diagram displaying the energy transition processes in infrared, Raman (Stokes and anti-Stokes) scattering and fluorescence. Adapted from ⁸³ and ⁸⁴.

Vibrational spectroscopy is based on the principle that electromagnetic radiation causes chemical bonds to vibrate at energy levels higher than the zero-point energy ^{85, 86}. The molecules can only accept a photon that has the exact energy value required to elevate to a higher vibrational or electronic energy level. For many molecules, including biomolecules, this is in the mid-infrared (MIR) region, where fundamental bond vibrations are excited to higher energy levels ⁸⁴. An overview of energy transitions in vibrational spectroscopy is provided in **Figure 1.7**.

A given molecule will have a discrete number of vibrational modes dependent upon its chemical structure. A linear molecule will exhibit $3N - 5$ modes, where N is the number of atoms in the molecule, and a non-linear molecule will have $3N - 6$ vibrational modes ⁸⁷. The disparity between the two is due to linear molecules being unable to rotate upon their axis. Water, for example, has three distinct vibrational modes; the symmetric

and asymmetric O-H stretch [$\nu_s(\text{O-H})$ and $\nu_{\text{sym}}(\text{O-H})$ respectively] and the scissoring mode [$\delta(\text{H-O-H})$] ⁸⁸. A methylene group (-CH₂) of a CH₂X₂ compound, where X can be any other atom, is often an example used to show the variety of vibrational modes and is overviewed in **Figure 1.8**.

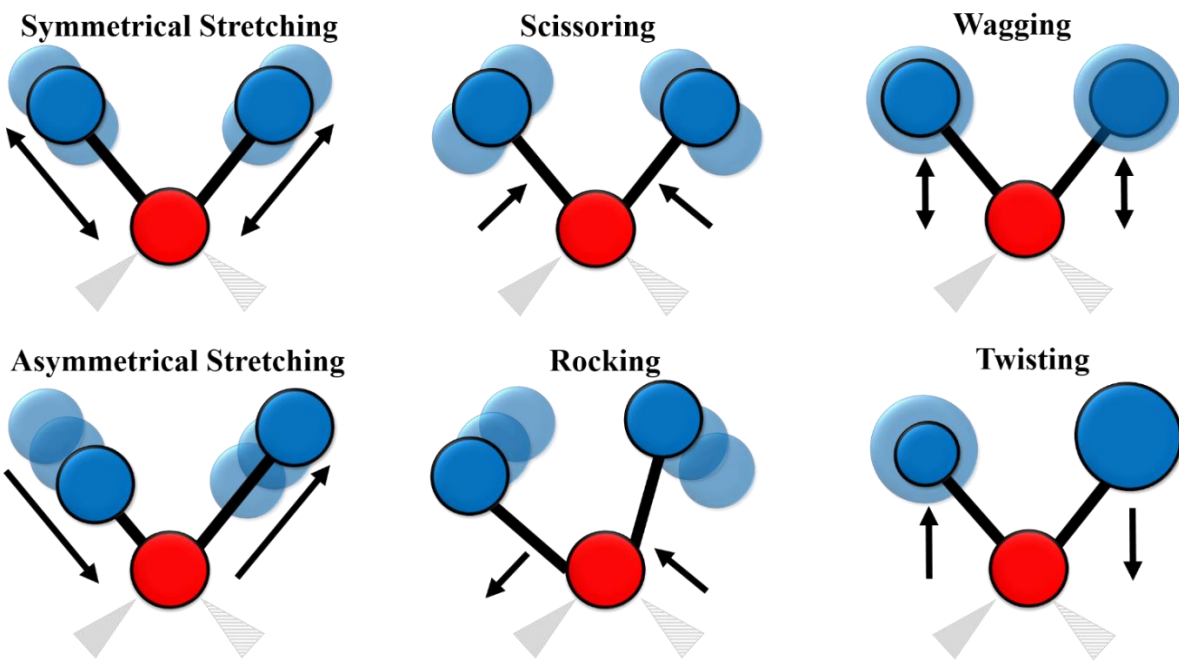


Figure 1.8. Common vibrational modes of chemical bonds characterised by the CH₂ group of CH₂X₂ compounds.

These molecular bond vibrations may occur in the ground energy state; however, when a sample is irradiated with light this can occur at higher energy levels, and consequently an alteration to the energy of the incidence photon occurs. This energy alteration can occur due to several distinct interactions with the sample, as portrayed in **Figure 1.9**. The incident light, at a defined energy intensity (I_0), is partially absorbed (I_A), reflected (I_R), and or transmitted (I_T) through the sample ⁸⁹. The absorption of energy is fundamental to IR spectroscopy and is further discussed in the next section of this chapter. The incident light can also be scattered; both elastically (I_S) at the same

energy level, or inelastically (I_{IS}) at an altered energy level. It is the latter of these interactions that is the principle of Raman spectroscopy and is also discussed here. It is important to note that energy conservation is applicable in this instance and thus $I_0 = I_A + I_R + I_T + (I_S + I_{IS})$.

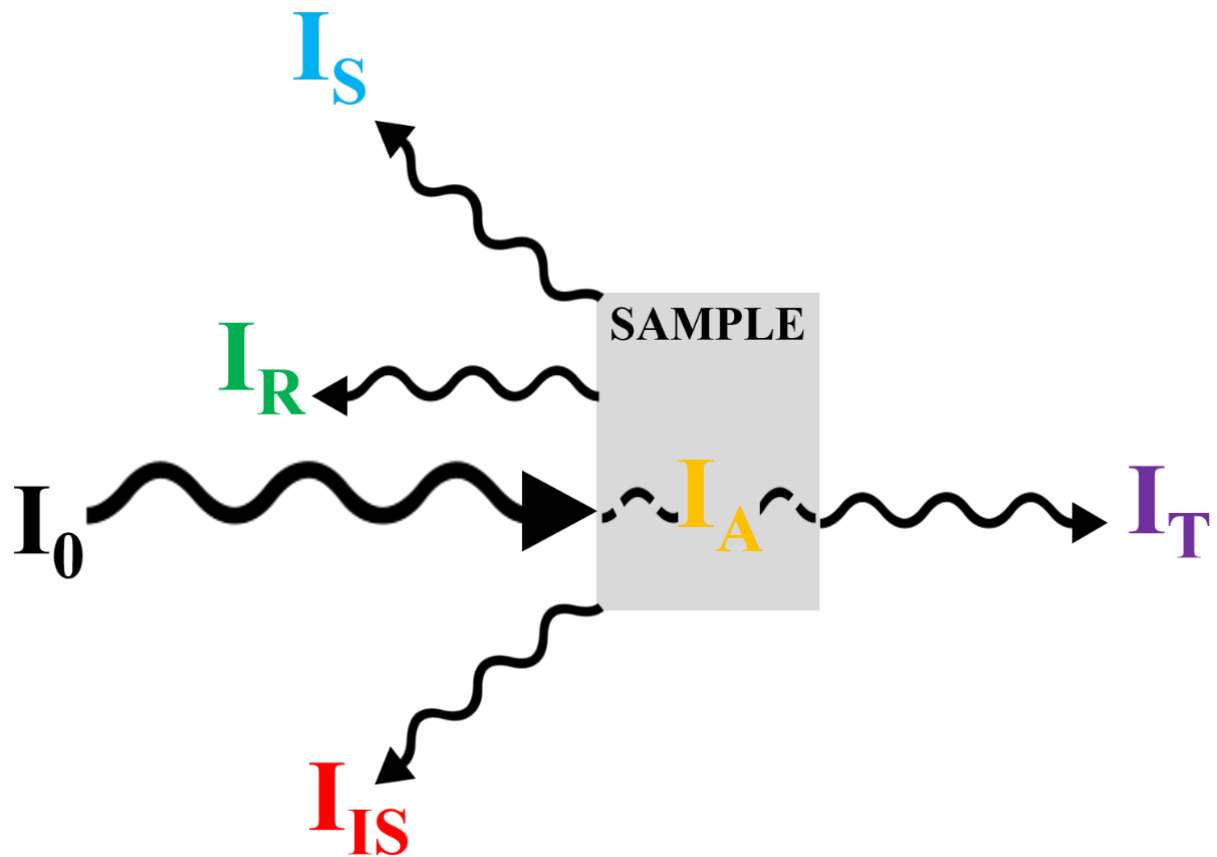


Figure 1.9. The interaction of light with a sample results in absorption (I_A), reflectance (I_R), transmission (I_T), elastic scattering (I_S), and inelastic scattering (I_{IS}) of the incident photon beam (I_0).

1.6.1 Fundamentals of Fourier Transform Infrared Spectroscopy

Infrared (IR) spectroscopy measures the energy absorbed by a given sample, and is dependent upon the chemical bond vibrations resulting in a change in the dipole moment of the molecule and absorption of a photon ⁹⁰. Consequently, some molecules that do not possess molecular dipoles will not be IR active, which is often the case in molecules that exhibit symmetry. The absorbance of energy by a given chemical bond can be proportional to its concentration and follows the principle of the Beer-Lambert Law, thus allowing quantitative measurements using this approach ^{91,92}. Instrumentation

developments such as the Michelson interferometer and transformation algorithms have allowed rapid acquisition of IR spectra. In the following section, the principles of Fourier Transform (FT) IR spectroscopy are discussed; however, an in-depth review is presented in Chapter 2 that covers this topic in greater detail ³.

1.6.1.1 Instrumentation

A standard benchtop FTIR spectrometer is composed of several key components: an IR light source, a Michelson interferometer, and a detector. The FT approach to acquiring IR spectra is key to modern advancements in IR spectroscopy that allows the sampling of multiple light wavelengths in one measurement. This process is reliant upon the Michelson interferometer, a schematic of which is shown in **Figure 1.10**. In overview, an interferometer is comprised of two mirrors, one fixed and one adjustable, as well as a beam splitter. IR light is passed through this beamsplitter and focused upon both the fixed and adjustable mirror. When these two waves reflect back towards the beamsplitter, they interact, effectively cancelling each other out when at equivalent pathlengths. As the adjustable mirror moves, the different pathlength results in two waves of different phases that consequently interfere when recombined. This measurement of intensity as a function of distance (of the adjustable mirror) and time (mirror speed) is known as an interferogram ⁹³. FT of this produces a typical IR spectrum that is plotted as a function of frequency in wavenumbers against spectral absorbance intensity ⁹⁴.

1.6.1.2 Light Sources

For FTIR spectroscopy, polychromatic light in the MIR region ($4000 - 400 \text{ cm}^{-1}$) is used, where biological samples are known to vibrate ³. For traditional benchtop instruments, this IR source is often based upon electrical heating of a silicon carbide rod, known as globar IR sources. There are, however, alternatives that provide light of greater intensity than seen in the use of globar sources, such as the use of quantum cascade lasers (QCLs), that are able to rapidly acquire spectra of superior noise quality by sampling over discrete frequencies ^{95,96}.

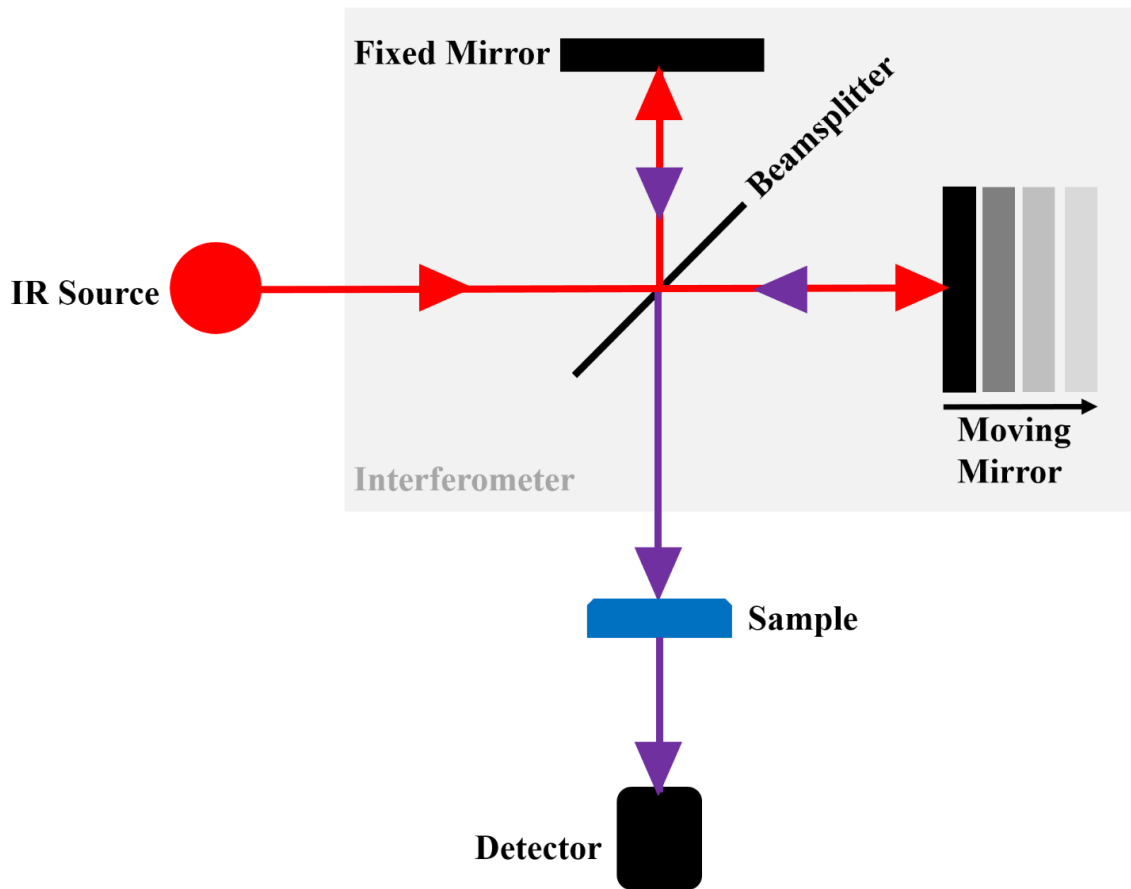


Figure 1.10. A Michelson interferometer consisting of a fixed mirror, an adjustable mirror and a beamsplitter, that work to focus IR light at different wavelengths onto the sample under interrogation. Adapted from ⁹⁷.

Synchrotron radiation (SR) is an alternative radiation source that is able to produce light up to 1000 brighter than conventional IR sources ⁹⁸. Due to the superior collimation of the IR light, it is possible to interrogate smaller area using apertures below the standard 10 μm spatial resolution achieved with globar sources ^{99,100}. As with traditional spectrometers, the minimum sampling area is still limited by the diffraction of light; however, SR is able to obtain spectra with increased spectral quality and intensity allowing increased sensitivity to subtle biochemical changes ¹⁰¹.

Put simply, a synchrotron is a circular particle accelerator, specifically in the case of FTIR spectroscopy, an electron accelerator. National synchrotron facilities such as the

Diamond Light Source at the Rutherford Appleton Laboratory are available on a proposal based process ¹⁰². An overview of this facility is provided in **Figure 1.11**.

Initially, electrons are released from an electron gun via thermoionic emission and then accelerated using a linear accelerator (linac) which focuses the electron beam to high fluxes ¹⁰³. These electrons are then further accelerated in the booster synchrotron using a series of electromagnets that direct the beam until it approaches the speed of light, at which point electrons are then released into the storage ring where light is emitted ¹⁰⁴. This light is emitted at a range of wavelengths across the electromagnetic spectrum and is thus applicable in IR studies.

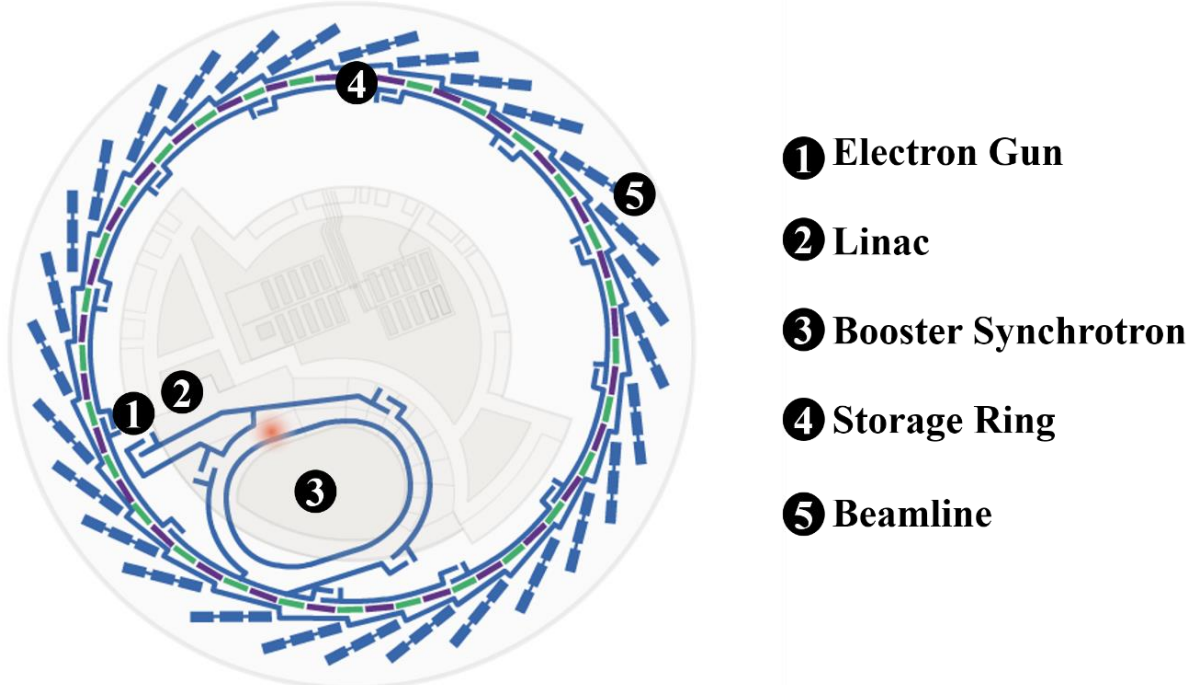


Figure 1.11. Schematic overview of the Diamond Light Source, at the Rutherford Appleton Laboratory, Oxfordshire, UK. Electrons are emitted from the electron gun and accelerated in the linear accelerator (Linac) and booster synchrotron until the particles are travelling to around 3GeV. At this point they are released into the storage ring where light is then emitted and directed to radiation specific beamlines and end stations. Obtained from the Diamond Light Source Ltd.

1.6.1.3 Sampling Modes

Commonly, FTIR spectrometers are coupled to microscope attachments that allow sampling from defined microscopic areas of a sample at high resolution. In this FTIR microspectroscopy approach, spectra can be obtained in two distinct sampling modes: transmission and transflection¹⁰⁵.

In transmission mode, the IR beam is passed through the sample and collected on the other side by a condenser and passed onto the detector, which is able to monitor alterations in the beam (**Figure 1.12.A**)¹⁰⁶. For this approach to be efficient, the sample needs to be supported by a IR transparent substrate such as barium fluoride (BaF₂) or calcium fluoride (CaF₂)¹⁰⁷. For transflection measurements, the IR beam is again passed through the sample; however, the addition of an IR reflective slide is used to return the beam to the objective, where it is then collected by the detector (**Figure 1.12.B**). One benefit of this approach in comparison to transmission FTIR microspectroscopy is that reflective slides such as low-E have significantly lower cost implications, compared to high grade substrates required for transmission measurements. On the other hand, there is controversy in the field regarding the reproducibility of spectra obtained in transflection mode, due to the presence of the electric field standing wave (EFSW) artefacts¹⁰⁸⁻¹¹⁰. Ultimately with both transmission and transflection measurements, sample thickness plays a substantial role in the resultant IR spectra, with a maximum thickness limit applicable for both modes as well as a minimum required thickness for transflection measurements due to the effects of the EFSW³.

Due to the strong dipole present in the water molecule, H₂O is highly IR active; for this reason, samples that contain water are often swamped by absorption of this fundamental molecule. Consequently, samples obtained in transmission and transreflectance measurements are largely limited to fixed tissues that have been dehydrated¹¹¹. Chemical fixative techniques such as formalin or ethanol fixation are known to have significant impacts on IR spectra and thus limit spectral interpretation¹¹².

Attenuated total reflectance (ATR)-FTIR is one approach that has been shown to minimise the presence of water absorbance within IR spectra^{113,114}. Due to the reduced pathlength of the interrogative beam, the issues of water interference are reduced, which minimises sample preparation times¹¹⁴. Rather than reliant upon a microscope optics, ATR-FTIR uses an internal reflection element (IRE) of a highly refractive material such

as diamond, zinc selenide, or germanium. Total internal reflectance (TIR) can occur within these prisms when IR is shone above a defined angle, known as the critical angle¹¹⁵. The consequence of this is either a single, or multiple reflections, at the sample side of the crystal, where an evanescent wave is produced. Thus when a sample is placed into contact with this IRE, it is interrogated with the evanescent wave⁸⁴. As with the basic principles of IR spectroscopy, alterations to the energy of this beam as a consequence of vibrational of chemical bonds are detected using this approach.

One important consideration is the penetration depth (D_p) of the evanescent wave, which is dependent upon the angle of incidence (Θ), and the diffractive index of the IRE and the sample¹¹⁶. Consequently, the optical thickness of the sample must be considered, or a reflective substrate should be used.

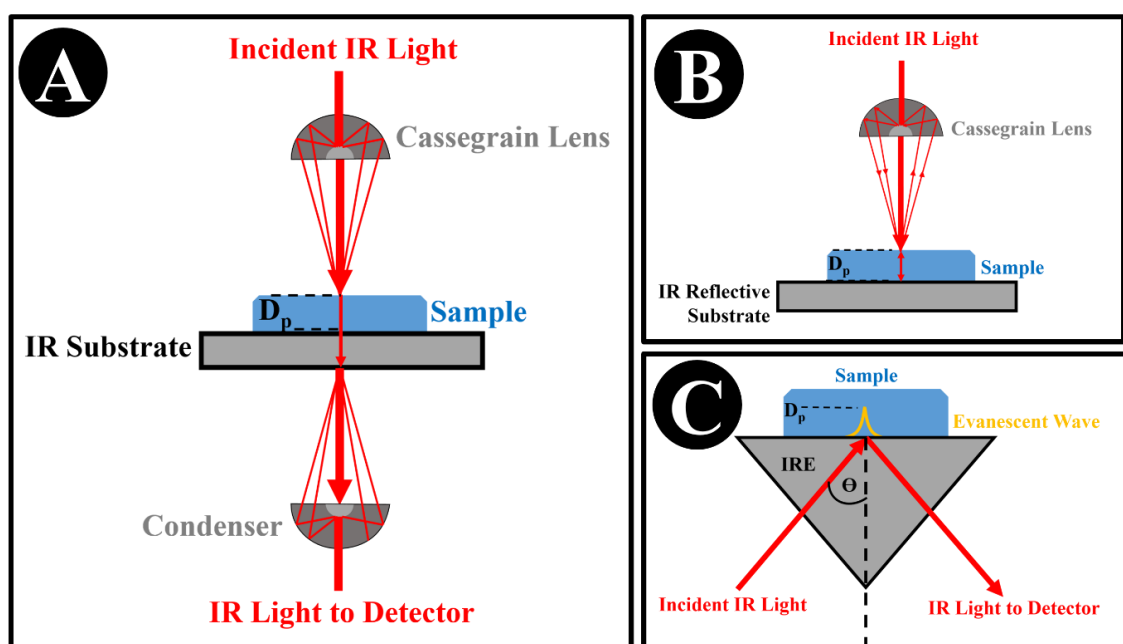


Figure 1.12. Schematic of the three primary sampling modes in FTIR spectroscopy; (A) Transmission FTIR; (B) Transflection FTIR and (C) attenuated total reflectance (ATR)-FTIR. The net direction of the IR light is shown in each example as a thickened red line, although it is important to note that light will be shone from a variety of angles in the case of A and B. The angle of incidence in in ATR (Θ), is fixed and is dependent upon the internal reflection element (IRE) of use. The depth of penetration (D_p) is shown in each approach. These images are based upon the works of^{3,109,116}

1.6.1.4 Detector

Traditional benchtop FTIR spectrometers utilise single element detectors that obtain spectral information on a point-by-point basis⁹⁷. At ambient temperatures, deuterated triglycine sulphate (DTGS) detectors are often used due to their ease of use and respectable spectral signal and sensitivity. However, liquid N cooled mercury cadmium telluride (MCT) detectors are more favourable for obtaining superior spectral quality, as using this photovoltaic approach yields is more sensitive to incident photons¹⁰⁶.

In regards to spectral acquisition, the use of these detectors enables spectral measurements to be obtained from a single area, referred to as point spectra approach, but also allows for spectral mapping, where spectra are obtained in a point-by-point manner across a sample to then produce an image map¹¹⁷. Using a point mapping approach, a spectral data cube is produced where the absorbance of a sample can be mapped with regards to its spectral information. Although highly informative and well implemented in the field of spectral histopathology, this approach is limited by acquisition times due to the limitations of the detector^{118,119}.

The development of array detectors, such a focal plane array (FPA), have improved these acquisition times by allowing simultaneous measurements of spectra from defined points across a sample¹²⁰. An array is split into individual pixel areas which can be as low as $0.54 \times 0.54 \mu\text{m}$, providing extremely high spatial resolution by oversampling³. This enhanced spatial resolution can often come at the price of reduced signal to noise ratio (SNR) in comparison to point approaches.

1.6.2 Fundamentals of Raman Spectroscopy

For an in-depth overview of Raman spectroscopy of biological samples, please see **Chapter 3** in which a recently published article will encompass instrumental, sample and acquisition parameters of this technique. A brief overview of the technique will be provided here, also comparing Raman with the IR technique.

First described by C. V. Raman and K. S. Krishnan in 1928, inelastic or Raman scattering, occurs when the scattered light is returned at an altered energy to the original beam¹²¹. In comparison to its counterpart elastic (or Rayleigh) scattering, the Raman effect has a markedly lower incidence rate, with as few as 1 in 10^8 photons undergoing Raman scattering.

Figure 1.7 illustrates the Raman scattering effect and its two forms: Stokes and Anti-Stokes scattering. Stokes scattering occurs when the material exposed to radiation is in the ground energy state, and upon interaction with a chemical bond, is promoted to a higher energy level ¹²². The opposite is true for Anti-Stokes Raman scattering, as the material is already at an elevated energy level and returns to a lower energy level. The probability of Anti-Stokes shift is decidedly lower than its counterpart due to the increased likelihood that a material will be in its ground state at room temperature ¹²³. For this reason, the majority of benchtop Raman spectrometers measure Stokes scattering, although coherent Anti-Stokes Raman spectroscopy (CARS) adaptations have resulted in increased signal strength and sensitivity ¹²⁴.

Due to the inherently low probability of the Raman effect, Raman spectroscopy is a relatively weak signal and can be often enveloped by fluorescence contributions ¹²⁵. A number of additional developments in the field of Raman spectroscopy have helped to overcome such issues, such as surface-enhanced Raman spectroscopy (SERS) and stimulated Raman spectroscopy (SRS) ^{126,127}.

In the case of vibrational spectroscopy, Raman scattering occurs as a consequence of interaction with chemical bonds which have inherent polarisability ¹²⁸. For a molecule to be considered polarisable, the electron cloud surrounding a molecule can be distorted. Thus, a Raman active molecule will exhibit a change in the polarisability during a molecular vibration ¹²⁹. Molecules with a strong dipole are often more difficult to polarise and so Raman spectroscopy can be considered complementary to IR spectroscopy, as not all polarisable molecules display changes in their dipole moment and *vice versa* ¹³⁰.

An example of this in water; this is a highly polar molecule and consequently demonstrates strong absorption in the IR ⁸⁸. In contrast, the strong polarity of this molecule means that an incoming photon is unable to alter the electron field of these bonds, and subsequently Raman spectroscopy is relatively insensitive to water contributions ¹²³.

The complementary nature of IR and Raman spectroscopy is depicted in **Figure 1.13** where spectra obtained from the same sample are compared. Processed spectra obtained from a *Solanum lycopersicum* leaf are displayed and clear differences in the relative spectra can be seen. The spectra are visibly distinct, with IR portraying broader

spectral features in comparison to the Raman spectrum. The broad peak between 3600 – 3000 cm^{-1} in the IR, is indicative of the ν_{sym} (O-H) bond of water, which is not apparent in Raman spectra. This particular IR spectrum was obtained using ATR-FTIR spectroscopy and thus signal from a water containing sample was possible.

Similarly to IR spectroscopy, Raman spectra can be obtained in a point spectrum, point mapping and global imaging scale and thus allows imaging of samples to a high spectral resolution (diffraction limited). Furthermore, considerations to substrate choice must be made prior to spectral acquisition, as Raman active substrates will affect the spectral output of the approach. CaF_2 , quartz and metal-coated slides are considered optimum, although the use of novel substrates such as aluminium foil has been shown 131-133.

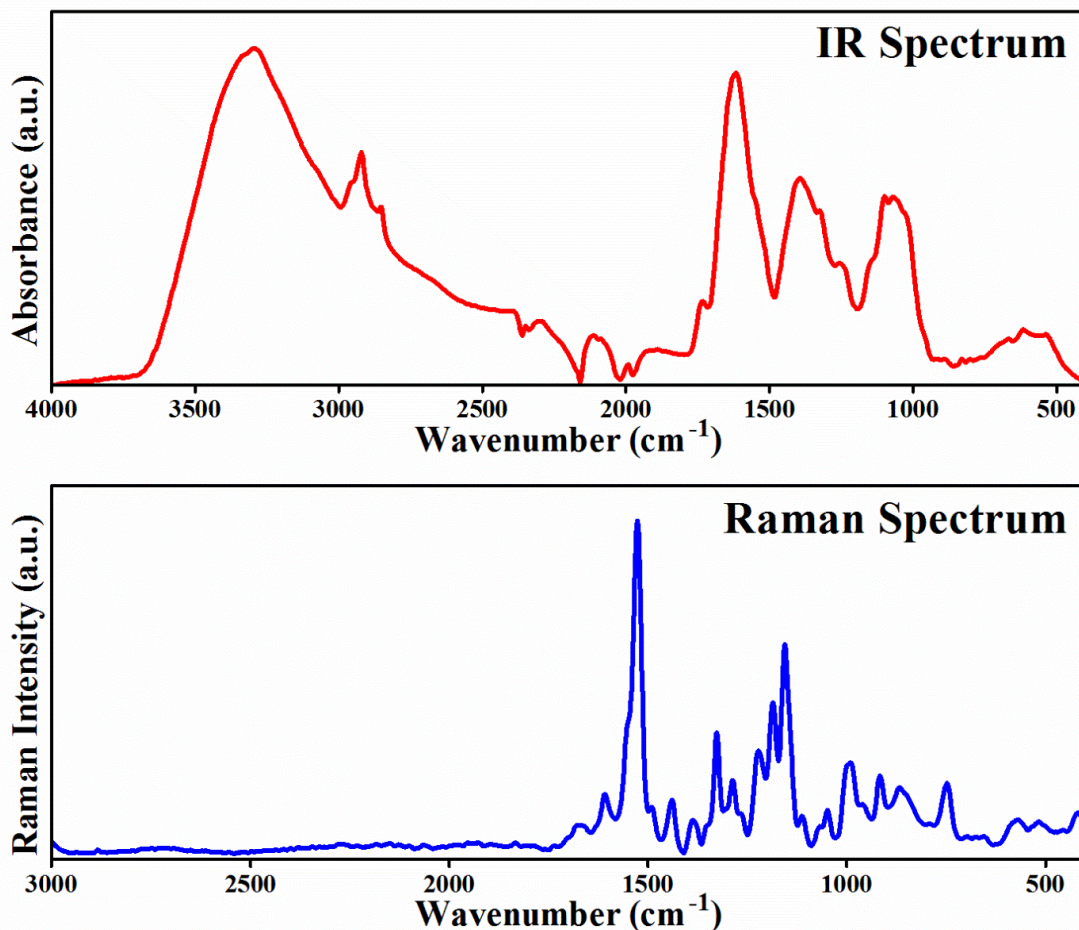


Figure 1.13. Typical infrared and Raman spectra of live plant leaf of the *Solanum lycopersicum*, common tomato plant.

1.6.2.1 Instrumentation

There are a number of instrumentation options in a typical Raman spectrometer, the majority of which are covered in detail in **Chapter 3**. As in IR spectroscopy, Raman can be coupled to a microscope for spatial spectral measurements. A schematic overview of a standard Raman microspectrometer can be seen in **Figure 1.14**. Unless otherwise stated, spontaneous Raman microspectrometry will be discussed rather than alternative spectrometer approaches.

A typical Raman microspectrometer is composed of an excitation source, a microscope with corresponding objectives, Rayleigh filters, a monochromator and a detector. Initially light of a defined light wavelength is focused upon the sample where vibration of polarisable bonds occurs which induces Raman scattering. In contrast to IR spectroscopy, Raman spectroscopy employs monochromatic light to interrogate samples and a range of wavelength frequencies can be used. Lasers are often in the visible region (wavelengths between 390 – 740 nm), although lasers from across the mid ultraviolet (UV; 200 nm) to the NIR (1084 nm) can be used. In this thesis, Raman spectroscopy will be described in regards to NIR Raman analysis using a 785 nm laser. The laser excitation wavelength has a direct effect on spectral dispersion and spatial resolution of the system as well as the overall spectral quality from a given sample ^{126,134}.

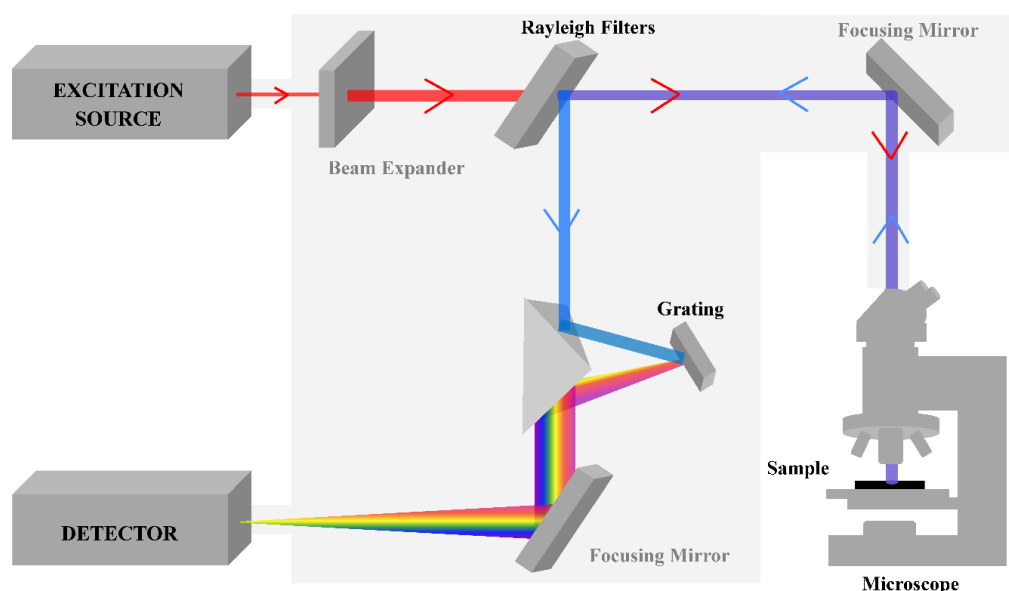


Figure 1.14. Generalised overview of a spontaneous Raman microspectrometer. Obtained from ³

Upon interaction with the sample, both elastic and inelastically scattered light is passed through the spectrometer. As elastic scattering is a high probability event, this would overpower the underlying Raman scattering of interest and is therefore removed by Rayleigh filters. From this point, only Raman scattered light is passed through a monochromator (or spectrometer), where light is separated into its different wavelengths and focused upon the detector¹³⁵. A number of detector options are available, although charge coupled device (CCD) detectors are commonly used in benchtop applications¹²⁷.

1.6.3 Spectral Pre-processing

The spectra obtained from vibrational spectroscopic measurements can infer a wealth of biochemical information from a biological sample and thus allows comparative studies between sample classes. However, this spectrum not only contains the biological information of interest, but also contains information about the biological replicates, substrate and background interferences, as well as instrument and environment differences¹³⁶. These confounding factors in IR and Raman spectra should be minimised through optimum sample preparation, spectral acquisition as well as during pre-processing.

The following sections will provide a brief insight into the core pre-processing steps, with given examples. However, the reader is directed to the following articles for more in-depth discussion¹³⁷⁻¹³⁹.

1.6.3.1 Baseline Correction

Figure 1.15 shows raw IR and Raman spectra that have been cut to their relative fingerprint regions. This region is where the majority of biological molecules are known to vibrate and thus are often the target for spectroscopic studies¹⁴⁰. In IR studies, the region between 1800 – 900 cm⁻¹ is often used, due to detector limitations, whereas the Raman spectral fingerprint region is slightly more variable, but falls within the 1800 – 400 cm⁻¹ region due to more sensitive detectors¹⁴¹⁻¹⁴³.

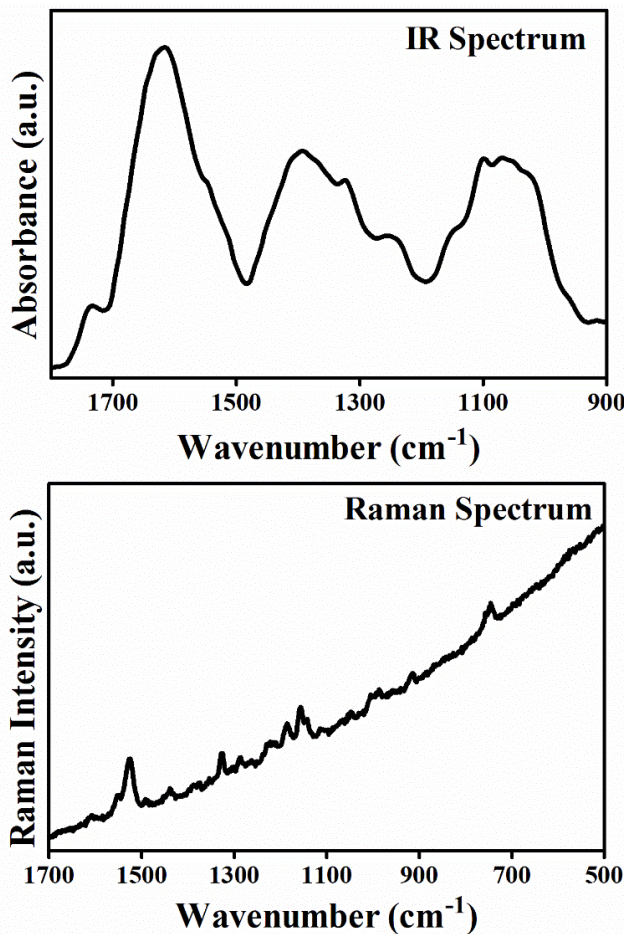


Figure 1.15. Examples of unprocessed IR (top) and Raman spectra in their relative fingerprint regions displaying discrepant baselines.

For IR spectra, the main concern with raw spectral information is the oscillating baseline that occurs due to the effects of light scattering¹⁴⁴. Rayleigh or Mie scattering is observed when light of a given intensity interacts with a sample, a relationship that was previously shown in **Figure 1.9**. As IR spectroscopy is concerned with I_A , the absorption of photons at the sample, this scattering effect is detrimental to the overall IR spectra, and can be visualised as alterations to the spectral baseline. In this particular case, the start and end point of the spectrum are on different baselines and therefore values of absorbance are not comparable across the spectrum.

Raman spectra can also be affected by variable baselines, largely

associated with substrate interaction and autofluorescence within the sample; the latter of which is typified in **Figure 1.15**. In this example, the extremely sloped baseline is indicative of intrinsic fluorescence within plant tissue, as well as background scattering¹⁴⁵. As a consequence, spectral features are difficult to determine and are again incomparable.

For this reason, baseline corrections are routinely applied to spectra to account for these spectral artefacts. A number of correction algorithms are available, such as polynomial, rubberband, and differentiation, applications of which are shown in **Figure 1.16**. In the case of Raman spectra, polynomial baseline correction is favourable as the baseline is often highly variable¹³⁸. This approach assumes the mathematical equation of the baseline by selecting n points along the spectrum a fitted with a spline, that is then subtracted from the original spectrum¹⁴⁶. The rubberband baseline correction works by

determining convex areas of spectral features, indicative of the baseline¹⁴⁷. As Raman spectra of biological samples often contain more Raman bands, this baseline approximation is often inappropriate and is therefore principally implemented in IR spectral processing.

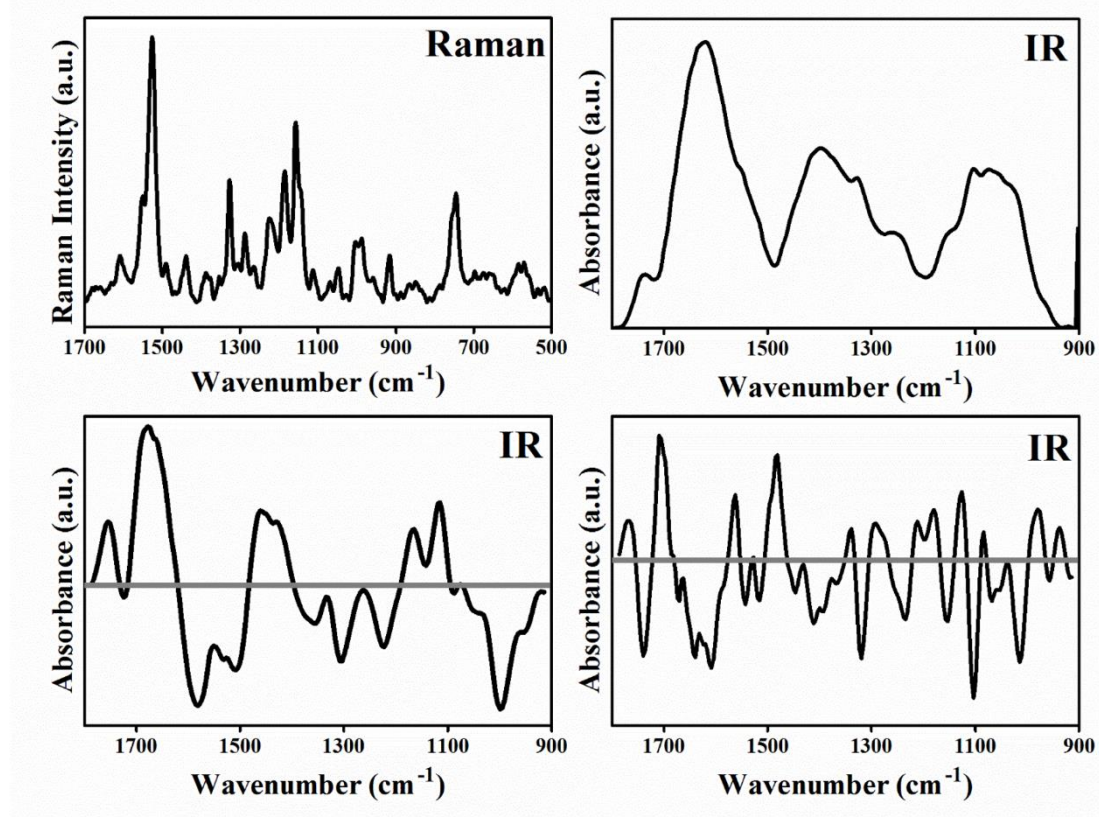


Figure 1.16. The application of baseline corrections on Raman (**A**) and IR (**B, C, and D**) spectra. **(A)** Shows a polynomial correction; **(B)** a rubberband correction; **(C)** first order differentiation and **(D)** a second order differentiation.

Derivative spectra exhibit flattened baselines in both IR and Raman spectra, although at the cost of SNR (**Figure 1.17**). For first-order derivatives, the spectral intensity at each wavenumber is differentiated so that the peak centroid becomes zero, essentially splitting the original spectral features. A second-order derivative, is a repeat of the aforementioned process, with the subsequent spectral regions relating back to the original spectrum ¹⁴⁸. The resultant derivative spectra often contain more spectral features due to the deconvolution of the original bands, as shown in **Figure 1.16 C and D**. This is useful for interpretation of IR data where the biological spectrum is often composed of a handful of IR bands; however, can often over complicate a Raman spectrum where deconvolution is not necessary. Band-specific deconvolution is often more appropriate for Raman spectra, if deconvolution and not baseline correction is the ultimate goal ¹⁴⁹.

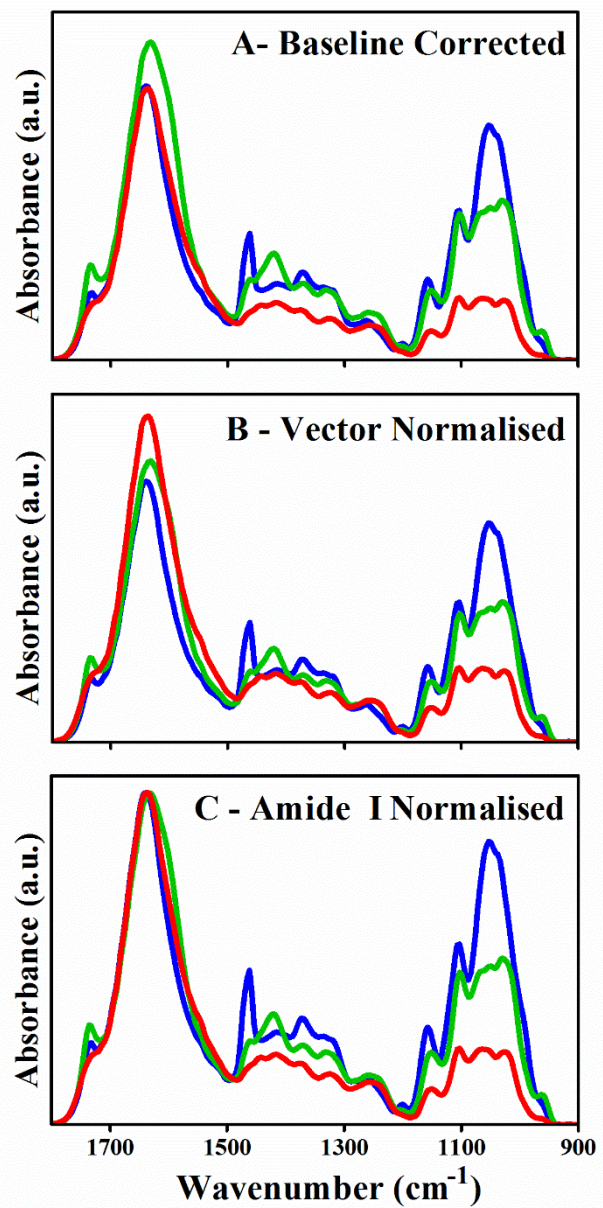


Figure 1.17. The effects of normalisation on baseline correction IR spectra derived from three plant species; tomato (red), barley (blue) and *Commelina* (green).

1.6.3.2 Normalisation

To account for differences in sample thickness, a normalisation step is usually conducted during pre-processing. The most widely implemented is that of vector normalisation, that is best shown comparatively between classes (**Figure 1.17 B**). In this example, leaves from three plant species, *S. lycopersicum* (tomato; red), *Hordeum vulgare* (barley; blue) and *Commelina communis* (Commelina; green) are compared. Vector normalisation works by calculating the average absorbance (or scattering) intensities, by

first finding the sum of all the square values and then finding the square root of this value. By scaling the spectra to this value, the sum of the squared standard deviation is equivalent to one and thus all spectra are normalised against one another. In comparison to other approaches, such as normalisation to the amide I peak, spectra are normalised across the whole wavenumber region, preventing exaggerated differences at other parts of the spectrum (**Figure 1.17 C**).

1.6.4 Multivariate Analysis

Extracting biological information from spectral datasets can be challenging due to the sheer size and complexity of the data. Dependent upon the parameters of the spectrometer such as spectral resolution, a single spectrum can be composed of thousands of individual intensity values relating to individual wavenumbers ¹⁴⁵. As the size of the sample set increases, it is clear to see how rapidly the computational burden can augment. For simple observations between spectra, such as comparisons of peak intensities and shifts, this is a relatively unchallenging. Approaches such as this are referred to as univariate, as they only take into consideration one variable, such as wavenumber. However, by taking into consideration the whole spectral range and the relationship between all points on the spectrum, greater detail can often be revealed and this the basis of multivariate analysis ¹⁵⁰.

1.6.4.1 Principal Component Analysis

One of the most robust multivariate techniques in spectral processing is principal component analysis (PCA). The output of this approach, is a dataset with reduced dimensionality whilst retaining the valuable variance within the dataset ¹⁵¹. In theory, in order to distinguish variance in a spectral dataset the correlation between each spectrum at each specific wavenumber would need to be observed. However, due to the large dimensionality of this dataset, this is not possible.

PCA extracts variance from the dataset by orthogonal transformation of the dataset, meaning that the data is viewed on an axis that best describes the variance in correlation to the wavenumbers ¹⁵². Specifically, this is referred to as covariance, as it is

the comparison of multiple dimensions within the spectral dataset. The covariance matrix produced from the original dataset can be split into eigenvalues (the score matrix) and eigenvectors (or principal components [PCs]). An eigenvector is a vector or view through the original data, projected in multidimensional space. Eigenvalues correspond to the exact variance explained by a given eigenvector. The first PC (PC1) explains the most amount of variance in the dataset, determined from eigenvectors and its corresponding eigenvalue; followed by PC2, which is orthogonal to the previous eigenvector¹⁵³. As such, each PC accounts for less variance compared to the previous.

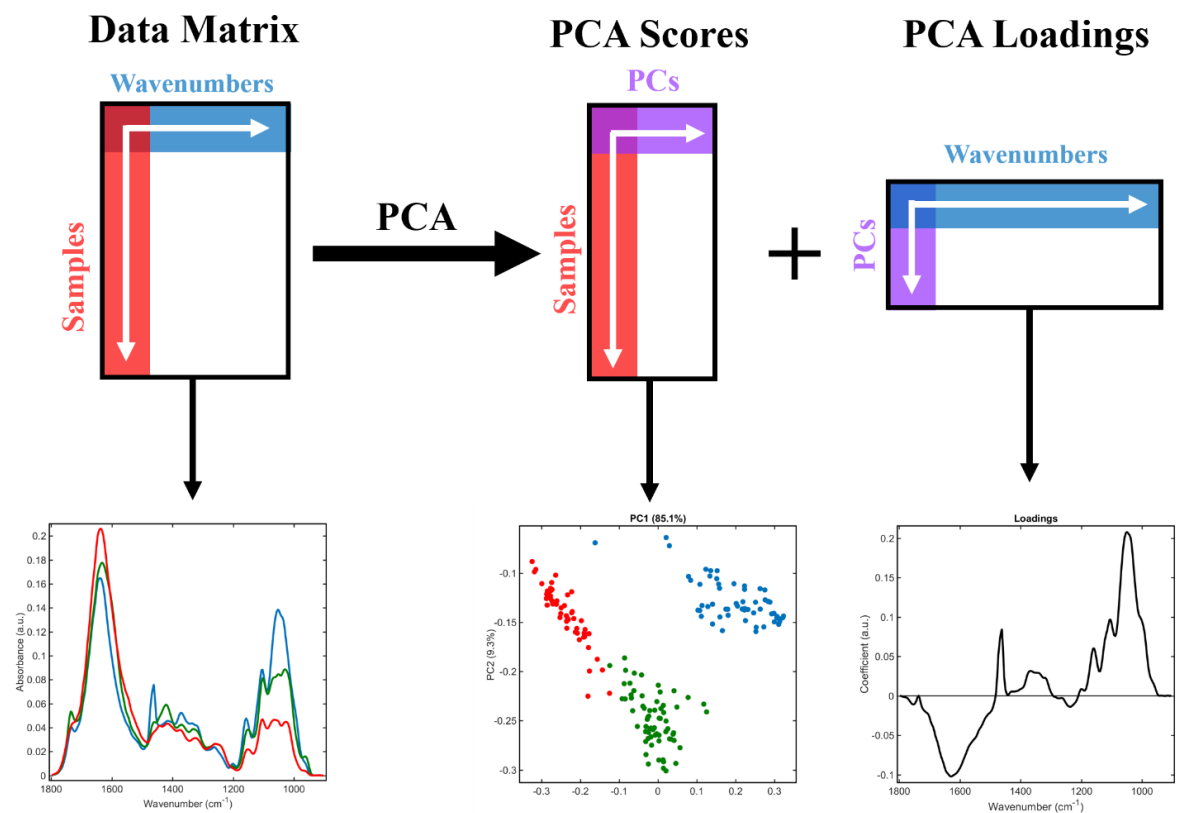


Figure 1.18. An overview of principal component analysis observing the data transformation (top panel) and the corresponding visual outputs. A comparison between tomato, barley and Commelina is used to visualise the original data matrix, the PC1 vs PC2 scatterplot and the loadings plot of PC1 accounting for wavenumber specific information regarding covariance in the dataset. Adapted from¹⁵³

The importance of this approach is that the dataset is now reduced and is representative of purely the variance in the dataset. As each spectrum is now composed of a set number of PCs that account for a defined amount of variance within the dataset, there are less data to handle in subsequent computational approaches. Usually around 10

PCs is considered enough to encompass ~99% of the variance in the dataset; however, this is highly dependent upon the dataset and should be explored thoroughly before additional analysis¹⁴⁷.

PCA allows the variance within the dataset to be visualised in the form of either scatter or loadings plots. By plotting PC values in 2- or 3-dimensions, the relationship between samples can be deduced, with separation inferring samples heterogeneity and clustering inferring sample homogeneity. **Figure 1.18** depicts the same spectral dataset presented in **Figure 1.17** following PCA. In this example 99% of the variance in the dataset is encompassed by the first 7 PCs, with PC1 accounting for a significant proportion of the variance. By plotting PC1 and PC2 values against each other separation between the three plant species is clear. The subsequent loadings plot refers back to the original wavenumber dimensions of the dataset and thus separation in the PC plot can be associated with distinct spectral regions.

1.6.4.2 Linear Discriminant Analysis

PCA can be considered an unsupervised analysis technique and thus derives variance from a dataset regardless of class information. In instances where variance between spectral classes is not immediately evident, a supervised technique may be necessary to help tease out underlying differences.

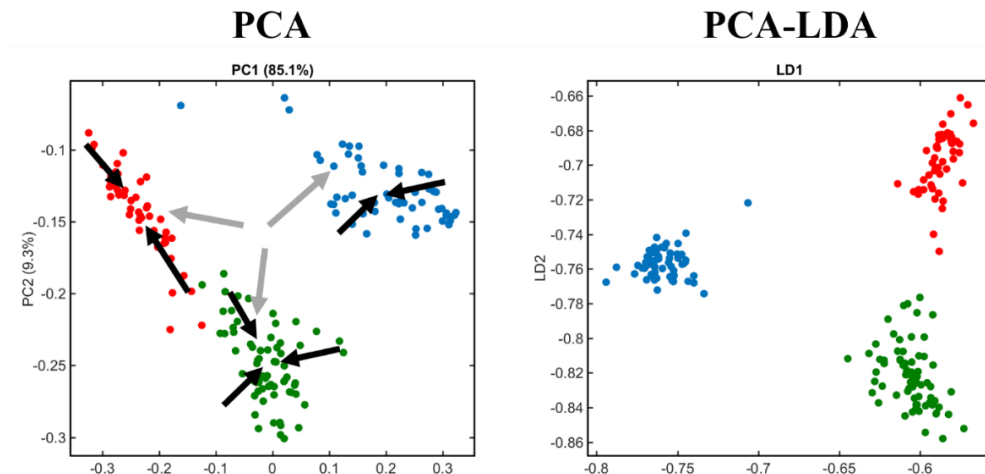


Figure 1.19. A comparison between PCA and PCA-LDA scatterplots. Black arrows on the PCA plot are indicative of the reduction in intra-class variance, whereas grey arrows depict the maximisation of inter-class differences. Tomato (red), barley (blue) and Commelina (green) are shown to separate more readily following PCA-LDA.

Linear discriminant analysis (LDA) is one such technique that takes into account class labels and can enhance separation between classes. This supervised technique minimises the intra-class differences, but maximises the inter-class differences, resulting in a more separated dataset ¹⁵⁴. When coupled to the covariance matrix derived from PCA, this linear transformation improves the ability to distinguish between spectral datasets is enhanced, allowing for better classification ¹⁵⁴. As all PCs are fed into LDA, it is important to observe the data explained by each PC, as introduction of too few PCs can result in the loss of significant spectral variance, whereas the addition of too many PCs can result in noise introduction and overfitting. **Figure 1.19** portrays the differences between PCA and PCA-LDA scatterplots from the three plant species.

1.6.4.3 Classification Algorithms

Dependent upon the aim of spectral investigation, the use of classification algorithms may be required to derive numerical values to define the diagnostic capabilities of the approach to a given scenario ¹⁵⁵. This is particularly important for biomedical application of IR and Raman spectroscopy, where often disease status is determined by spectral analysis of a sample ¹⁵⁶. In the case of cancer diagnostics using tissues or biofluids, it is often necessary to obtain sensitivity and specificity values to assess the performance of the approach ^{157,158}.

There are a numerous classification approaches available some of which are well characterised in the following articles ^{147,159,160}. Commonly implemented chemometric approaches include Bayesian modelling, artificial neural network (ANN), random forest (RF), hierarchical cluster analysis (HCA), and PC-discriminant function analysis (PC-DFA). Key considerations in chemometric modelling, are the efficient training, testing and validation of a model, as well as the sample size ^{136,155,161}.

A linear discriminant classifier (LDC) is a relatively simple approach to classification of spectra, that fits a classification model to the dataset to be trained, without the need for optimisation of parameters within the model ³. This chemometric approach is directly related to the outputs of PCA-LDA and thus can be considered complementary. One caveat of this approach is that validation is essential to avoid overfitting.

A support vector machine (SVM) is a particularly well implemented chemometric model applied to spectral datasets. In brief, an SVM uses a small section of the dataset, termed support vectors, and searches for the optimal dimension for separation between them, defined as the hyperplane. This approach is applicable to both linear and non-linear datasets and is less prone to overfitting comparative to other methods, although can present a computational burden through parameter optimisation¹⁶².

1.6.5 Vibrational Spectroscopy in Plant Research

The application of vibrational spectroscopy in biological materials has undoubtedly been extended to include investigations using Plant^a from single compound quantification, to *in vivo* applications^{126,163}. However, it is a just statement that application in this field has not been exploited to the extent of biomedical applications, which are already being implemented in real-world environments and clinical translation^{164,165}.

1.6.5.1 Applications of FTIR Spectroscopy

Between the two techniques, FTIR spectroscopy has been more widely implemented in plant research in comparison to Raman spectroscopy. Despite the issues associated with water interference in IR absorption, the technique has still been able to infer valuable molecular information from fixed tissues and plant specific substances^{166,167}. The latter of these applications is where FTIR of plant matter has been particularly prevalent, with a number of applications for quantification of isolated plant metabolites¹⁶⁸⁻¹⁷⁰. Specific tissues have also been investigated using this technique including the cell wall, the cuticle layer of leaves and fruit¹⁷¹⁻¹⁷⁴. Discriminatory investigations have also been conducted on fixed samples, such as for mutant screening, as well a wide range of applications in the field of food analysis and adulteration¹⁷⁵⁻¹⁷⁷.

The imaging capabilities of FTIR spectroscopy have also been utilised in plant research, particularly in conjunction with SR. These studies have described the molecular structure of plant tissues and allowed the visualisation of chemical distributions¹⁷⁸⁻¹⁸³,

The development of ATR-FTIR has significantly benefitted plant research as spectra can be acquired from aqueous samples, allowing a wider range of applications. Similarly to traditional FTIR applications, ATR-FTIR has been used to interrogate fixed samples, particularly to characterise cell wall structure and content¹⁸⁴⁻¹⁸⁶.

However, it is movement towards *in vivo* measurements of plant systems using ATR-FTIR that fully-exploits the attributes of ATR-FTIR. *In situ* measurements have been readily obtained from leaves and petals, reflecting the capability to sample from water containing, fresh samples whilst still being able to derive biological information¹⁸⁷. Recently, ATR-FTIR imaging has also been exploited to image plant tissue *in situ* presenting a significant advancement in the field¹⁸⁸⁻¹⁹⁰. It is clear from the literature that there remains a shortfall of *in vivo* spectral investigations using FTIR spectroscopy and its derivatives.

1.6.5.2 Applications of Raman Spectroscopy

Unlike IR that is limited by water interference, Raman is subject to competition with fluorescence, which is intrinsically high in the majority of plant tissues¹⁹¹. As such the application of Raman spectroscopy in plant research has been almost solely limited to isolated plant materials and tissues that do not possess fluorophore components¹⁴⁵.

Similarly to FTIR spectroscopy, Raman has also been used to investigate valuable plant substances and cell wall architecture¹⁶⁸. The imaging or mapping capabilities of Raman have also been well implemented, with a number of wood based studies having been presented¹⁹². The work of Gierlinger has particularly revealed the potential applications of Raman-based imaging investigations^{191,193-195}.

A number of instrumental adaptations to the conventional spontaneous Raman approach have allowed spectra to be derived without contributions from fluorescence. With FT-Raman spectroscopy, SRS and SERS the influence of fluorescence is minimised and thus spectral measurements can be derived¹⁹⁶⁻¹⁹⁹. However, the application of Raman spectroscopy for *in vivo* plant measurements are again not fully exploited, highlighting the need for further development in this area.

References

- 1 FAO. World Population Prospects: The 2015 Revision - Key Findings and Advance Tables. (United Nations, 2015).
- 2 Godfray, H. C. J. *et al.* Food security: the challenge of feeding 9 billion people. *science* **327**, 812-818 (2010).
- 3 Baker, M. J. *et al.* Using Fourier transform IR spectroscopy to analyze biological materials. *Nature protocols* **9**, 1771-1791 (2014).
- 4 Tilman, D., Balzer, C., Hill, J. & Befort, B. L. Global food demand and the sustainable intensification of agriculture. *Proceedings of the National Academy of Sciences* **108**, 20260-20264 (2011).
- 5 Tscharntke, T. *et al.* Global food security, biodiversity conservation and the future of agricultural intensification. *Biological conservation* **151**, 53-59 (2012).
- 6 Khush, G. S. Challenges for meeting the global food and nutrient needs in the new millennium. *Proceedings of the Nutrition Society* **60**, 15-26 (2001).
- 7 Evenson, R. E. & Gollin, D. Assessing the impact of the Green Revolution, 1960 to 2000. *Science* **300**, 758-762 (2003).
- 8 Beddington, J. Food security: contributions from science to a new and greener revolution. *Philosophical Transactions of the Royal Society of London B: Biological Sciences* **365**, 61-71 (2010).
- 9 Premanandh, J. Factors affecting food security and contribution of modern technologies in food sustainability. *Journal of the Science of Food and Agriculture* **91**, 2707-2714 (2011).
- 10 Delmer, D. P. Agriculture in the developing world: connecting innovations in plant research to downstream applications. *Proceedings of the National Academy of Sciences of the United States of America* **102**, 15739-15746 (2005).
- 11 Dibden, J., Gibbs, D. & Cocklin, C. Framing GM crops as a food security solution. *Journal of Rural Studies* **29**, 59-70 (2013).
- 12 Qaim, M. & Kouser, S. Genetically modified crops and food security. *PloS one* **8**, e64879 (2013).
- 13 Wynne, B. Creating public alienation: expert cultures of risk and ethics on GMOs. *Science as culture* **10**, 445-481 (2001).
- 14 Jacobsen, S.-E., Sørensen, M., Pedersen, S. M. & Weiner, J. Feeding the world: genetically modified crops versus agricultural biodiversity. *Agronomy for sustainable development* **33**, 651-662 (2013).
- 15 Popp, J., Pető, K. & Nagy, J. Pesticide productivity and food security. A review. *Agronomy for sustainable development* **33**, 243-255 (2013).

16 Birch, A. N. E., Begg, G. S. & Squire, G. R. How agro-ecological research helps to address food security issues under new IPM and pesticide reduction policies for global crop production systems. *Journal of Experimental Botany* **62**, 3251-3261 (2011).

17 Bradley, P. & Marulanda, C. in *World Congress on Soilless Culture: Agriculture in the Coming Millennium* 554. 289-296.

18 Meinke, D. W., Cherry, J. M., Dean, C., Rounsley, S. D. & Koornneef, M. *Arabidopsis thaliana*: a model plant for genome analysis. *Science* **282**, 662-682 (1998).

19 Reuter, D. *Plant analysis: an interpretation manual*. (CSIRO publishing, 1997).

20 Schnitkey, G., Hopkins, J. & Tweeten, L. An economic evaluation of precision fertilizer applications on corn-soybean fields. *Precision Agriculture*, 977-987 (1996).

21 Pinstrup-Andersen, P. Food security: definition and measurement. *Food security* **1**, 5-7 (2009).

22 FAO. in *World Food Summit*. (FAO).

23 McGuire, S. FAO, IFAD, and WFP. The State of Food Insecurity in the World 2015: Meeting the 2015 International Hunger Targets: Taking Stock of Uneven Progress. Rome: FAO, 2015. *Advances in Nutrition: An International Review Journal* **6**, 623-624 (2015).

24 FAO. The FAO Hunger Map 2015. (The State of Food Security in the World 2015, 2015).

25 FAO. How to feed the world in 2050. (2009).

26 Schmidhuber, J. & Tubiello, F. N. Global food security under climate change. *Proceedings of the National Academy of Sciences* **104**, 19703-19708 (2007).

27 Smith, P. Delivering food security without increasing pressure on land. *Global Food Security* **2**, 18-23 (2013).

28 Rosegrant, M. W. & Cline, S. A. Global food security: challenges and policies. *Science* **302**, 1917-1919 (2003).

29 Baulcombe, D. *et al. Reaping the benefits: science and the sustainable intensification of global agriculture*. (The Royal Society, 2009).

30 Despommier, D. The vertical farm: controlled environment agriculture carried out in tall buildings would create greater food safety and security for large urban populations. *Journal für Verbraucherschutz und Lebensmittelsicherheit* **6**, 233-236 (2011).

31 Bula, R. *et al.* Light-emitting diodes as a radiation source for plants. *HortScience* **26**, 203-205 (1991).

32 Fageria, N. K., Baligar, V. C. & Jones, C. A. *Growth and mineral nutrition of field crops*. (CRC Press, 2010).

33 Roy, R., Finck, A., Blair, G. & Tandon, H. Plant nutrition for food security. *A guide for integrated nutrient management. FAO Fertilizer and Plant Nutrition Bulletin* **16**, 368 (2006).

34 Marschner, H. *Marschner's mineral nutrition of higher plants*. (Academic press, 2011).

35 Sauerbeck, D. & Helal, H. in *Genetic aspects of plant mineral nutrition* 11-17 (Springer, 1990).

36 Craswell, E. & Godwin, D. The efficiency of nitrogen fertilizers applied to cereals grown in different climates. (1984).

37 van der Ploeg, R. R. & Kirkham, M. On the origin of the theory of mineral nutrition of plants and the law of the minimum. (1999).

38 Alloway, B. J. *Micronutrient deficiencies in global crop production*. (Springer Science & Business Media, 2008).

39 FAO. Yield gap analysis of field crops: methods and case studies. (UN, Rome, 2015).

40 Mueller, N. D. *et al.* Closing yield gaps through nutrient and water management. *Nature* **490**, 254-257 (2012).

41 Krupa, Z., Siedlecka, A., Skorzynska-Polit, E. & Maksymiec, W. in *Physiology and biochemistry of metal toxicity and tolerance in plants* 287-301 (Springer, 2002).

42 Loneragan, J., Snowball, K., Robson, A. & Wardlaw, I. Remobilization of nutrients and its significance in plant nutrition. *Transport and transfer processes in plants*, 463-469 (1976).

43 Hill, J. The remobilization of nutrients from leaves. *Journal of Plant Nutrition* **2**, 407-444 (1980).

44 Lucena, J. in *III International Symposium on Mineral Nutrition of Deciduous Fruit Trees* 448. 179-192.

45 Oliveira, S. R., Neto, J. A. G., Nobrega, J. A. & Jones, B. T. Determination of macro- and micronutrients in plant leaves by high-resolution continuum source flame atomic absorption spectrometry combining instrumental and sample preparation strategies. *Spectrochimica Acta Part B: Atomic Spectroscopy* **65**, 316-320 (2010).

46 Fried, M. & Dean, L. A concept concerning the measurement of available soil nutrients. *Soil Science* **73**, 263-272 (1952).

47 FAO. Current world fertilizer trends and outlook to 2016. (Rome, 2012).

48 Baligar, V., Fageria, N. & He, Z. Nutrient use efficiency in plants. *Communications in Soil Science and Plant Analysis* **32**, 921-950 (2001).

49 Brown, P. H. in *IV International Symposium on Mineral Nutrition of Deciduous Fruit Crops* 564. 217-223.

50 Dixon, R. C. Foliar fertilization improves nutrient use efficiency. *Fluid Journal* **11**, 22-23 (2003).

51 Hillier, J. *et al.* The carbon footprints of food crop production. *International Journal of Agricultural Sustainability* **7**, 107-118 (2009).

52 Snyder, C., Bruulsema, T., Jensen, T. & Fixen, P. Review of greenhouse gas emissions from crop production systems and fertilizer management effects. *Agriculture, Ecosystems & Environment* **133**, 247-266 (2009).

53 Skinner, J. *et al.* An overview of the environmental impact of agriculture in the UK. *Journal of environmental Management* **50**, 111-128 (1997).

54 Smith, V. H., Tilman, G. D. & Nekola, J. C. Eutrophication: impacts of excess nutrient inputs on freshwater, marine, and terrestrial ecosystems. *Environmental pollution* **100**, 179-196 (1999).

55 FAO. Food Wastage Footprint: Impacts on natural resources. (FAO Regional Conference for Europe 2014).

56 Waste, L. F. H., (2016).

57 Jaiswal, J. Calcium—how and why? *Journal of biosciences* **26**, 357-363 (2001).

58 Case, R. M. *et al.* Evolution of calcium homeostasis: From birth of the first cell to an omnipresent signalling system. *Cell Calcium* **42**, 345-350 (2007).

59 Clapham, D. E. Calcium signaling. *Cell* **131**, 1047-1058 (2007).

60 Aghdam, M. S., Hassanpouraghdam, M. B., Paliyath, G. & Farmani, B. The language of calcium in postharvest life of fruits, vegetables and flowers. *Scientia Horticulturae* **144**, 102-115 (2012).

61 Clarkson, D. T. Calcium transport between tissues and its distribution in the plant. *Plant, Cell & Environment* **7**, 449-456 (1984).

62 White, P. J. The pathways of calcium movement to the xylem. *Journal of experimental botany* **52**, 891-899 (2001).

63 Gillham, M. *et al.* Calcium delivery and storage in plant leaves: exploring the link with water flow. *Journal of experimental botany* **62**, 2233-2250 (2011).

64 Kirkby, E. & Pilbeam, D. Calcium as a plant nutrient. *Plant, Cell & Environment* **7**, 397-405 (1984).

65 White, P. J. & Broadley, M. R. Calcium in Plants. *Annals of Botany* **92**, 487-511 (2003).

66 Taylor, M. D. & Locascio, S. J. Blossom-end rot: A calcium deficiency. *Journal of plant nutrition* **27**, 123-139 (2004).

67 Carter, M. & Cutcliffe, J. Effects of gypsum on growth and mineral content of Brussels sprouts, and soil properties of Orthic Podzols. *Fertilizer research* **24**, 77-84 (1990).

68 Saure, M. Causes of the tipburn disorder in leaves of vegetables. *Scientia Horticulturae* **76**, 131-147 (1998).

69 Simon, E. W. The symptoms of calcium deficiency in plants. *New Phytologist* **80**, 1-15 (1978).

70 Raese, J. T. & Drake, S. R. Effects of preharvest calcium sprays on apple and pear quality. *Journal of plant nutrition* **16**, 1807-1819 (1993).

71 Ng, C. K. Y. *et al.* Calcium-based signalling systems in guard cells. *New Phytologist* **151**, 109-120 (2001).

72 Berridge, M. J., Lipp, P. & Bootman, M. D. The versatility and universality of calcium signalling. *Nature Reviews Molecular Cell Biology* **1**, 11-21 (2000).

73 Demidchik, V. & Maathuis, F. J. M. Physiological roles of nonselective cation channels in plants: from salt stress to signalling and development. *New Phytologist* **175**, 387-404 (2007).

74 Dodd, A. N., Kudla, J. & Sanders, D. The language of calcium signaling. *Annual review of plant biology* **61**, 593-620 (2010).

75 Schroeder, J. I., Allen, G. J., Hugouvieux, V., Kwak, J. M. & Waner, D. Guard cell signal transduction. *Annual review of plant biology* **52**, 627-658 (2001).

76 Sanders, D., Pelloux, J., Brownlee, C. & Harper, J. F. Calcium at the crossroads of signaling. *The Plant Cell Online* **14**, S401-S417 (2002).

77 McAinsh, M. R. & Pittman, J. K. Shaping the calcium signature. *New Phytologist* **181**, 275-294 (2009).

78 Rudd, J. J. & Franklin-Tong, V. E. Calcium signaling in plants. *CMLS, Cell. Mol. Life Sci.* **55**, 214-232 (1999).

79 McAinsh, M. R. & Ng, C. K.-Y. Vol. 312 289-302 (2005).

80 Planck, M. Ueber das gesetz der energieverteilung im normalspectrum. *Annalen der physik* **309**, 553-563 (1901).

81 Pitts, D. G. & Kleinstein, R. The electromagnetic spectrum. *Environmental Vision. Boston, Butterworth-Heinemann*, 87-135 (1993).

82 L'Annunziata, M. F. *Handbook of radioactivity analysis*. (Academic Press, 2012).

83 Baker, M. J., Hughes, C. S. & Hollywood, K. A. in *Biophotonics: Vibrational Spectroscopic Diagnostics* 3-1-3-13 (Morgan & Claypool Publishers, 2016).

84 García-González, D. L., Baeten, V., Pierna, J. A. F. & Tena, N. in *Handbook of Olive Oil* 335-393 (Springer, 2013).

85 Sheppard, N. in *Handbook of Vibrational Spectroscopy* (John Wiley & Sons, Ltd, 2006).

86 Baker, M. J., Hughes, C. S. & Hollywood, K. A. in *Biophotonics: Vibrational Spectroscopic Diagnostics* 2-1-2-14 (Morgan & Claypool Publishers, 2016).

87 Siebert, F. & Hildebrandt, P. *Vibrational spectroscopy in life science*. (John Wiley & Sons, 2008).

88 Du, Q., Superfine, R., Freysz, E. & Shen, Y. Vibrational spectroscopy of water at the vapor/water interface. *Physical Review Letters* **70**, 2313 (1993).

89 Martens, H., Nielsen, J. P. & Engelsen, S. B. Light scattering and light absorbance separated by extended multiplicative signal correction. Application to near-infrared transmission analysis of powder mixtures. *Analytical Chemistry* **75**, 394-404 (2003).

90 Colthup, N. *Introduction to infrared and Raman spectroscopy*. (Elsevier, 2012).

91 Beer, A. Bestimmung der Absorption des rothen Lichts in farbigen Flüssigkeiten. *Annalen der Physik* **162**, 78-88 (1852).

92 Davis, W., Erickson, C., Johnston, C., Delfino, J. & Porter, J. Quantitative Fourier Transform Infrared spectroscopic investigation humic substance functional group composition. *Chemosphere* **38**, 2913-2928 (1999).

93 Michelson, A. A. & Morley, E. W. On the Relative Motion of the Earth and of the Luminiferous Ether. *Sidereal Messenger*, vol. 6, pp. 306-310 **6**, 306-310 (1887).

94 Van De Weert, M., Hering, J. A. & Haris, P. I. Fourier Transform Infrared. *Methods for structural analysis of protein pharmaceuticals* **3**, 131 (2005).

95 Clemens, G., Bird, B., Weida, M., Rowlette, J. & Baker, M. J. Quantum cascade laser-based mid-infrared spectrochemical imaging of tissue and biofluids. *Spectroscopy Europe* **26**, 14-19 (2014).

96 Yeh, K., Kenkel, S., Liu, J.-N. & Bhargava, R. Fast infrared chemical imaging with a quantum cascade laser. *Analytical chemistry* **87**, 485-493 (2014).

97 Griffiths, P. R. & De Haseth, J. A. *Fourier transform infrared spectrometry*. Vol. 171 (John Wiley & Sons, 2007).

98 Miller, L. M. & Smith, R. J. Synchrotrons versus globars, point-detectors versus focal plane arrays: Selecting the best source and detector for specific infrared microspectroscopy and imaging applications. *Vibrational spectroscopy* **38**, 237-240 (2005).

99 Nasse, M. J. *et al.* High-resolution Fourier-transform infrared chemical imaging with multiple synchrotron beams. *Nature methods* **8**, 413-416 (2011).

100 Carr, G. Resolution limits for infrared microspectroscopy explored with synchrotron radiation. *Review of Scientific Instruments* **72**, 1613-1619 (2001).

101 Hirschmugl, C. J. & Gough, K. M. Fourier transform infrared spectrochemical imaging: review of design and applications with a focal plane array and multiple beam synchrotron radiation source. *Applied spectroscopy* **66**, 475-491 (2012).

102 Martin, F. L. Shining a new light into molecular workings. *Nature methods* **8**, 385-387 (2011).

103 Chasman, R., Green, G. K. & Rowe, E. Preliminary design of a dedicated synchrotron radiation facility. *IEEE Transactions on Nuclear Science* **22**, 1765-1767 (1975).

104 Duncan, W. & Williams, G. P. Infrared synchrotron radiation from electron storage rings. *Applied optics* **22**, 2914-2923 (1983).

105 Smith, B. C. *Fundamentals of Fourier transform infrared spectroscopy*. (CRC press, 2011).

106 Stuart, B. *Infrared spectroscopy*. (Wiley Online Library, 2005).

107 Wehbe, K., Filik, J., Frogley, M. D. & Cinque, G. The effect of optical substrates on micro-FTIR analysis of single mammalian cells. *Analytical and Bioanalytical Chemistry* **405**, 1311-1324 (2013).

108 Filik, J., Frogley, M. D., Pijanka, J. K., Wehbe, K. & Cinque, G. Electric field standing wave artefacts in FTIR micro-spectroscopy of biological materials. *Analyst* **137**, 853-861 (2012).

109 Bassan, P. *et al.* The inherent problem of transfection-mode infrared spectroscopic microscopy and the ramifications for biomedical single point and imaging applications. *Analyst* **138**, 144-157 (2013).

110 Wrobel, T. P., Wajnchold, B., Byrne, H. J. & Baranska, M. Electric field standing wave effects in FT-IR transfection spectra of biological tissue sections: Simulated models of experimental variability. *Vibrational Spectroscopy* **69**, 84-92 (2013).

111 Gazi, E. *et al.* Fixation protocols for subcellular imaging by synchrotron-based Fourier transform infrared microspectroscopy. *Biopolymers* **77**, 18-30 (2005).

112 Faolain, E. O. *et al.* A study examining the effects of tissue processing on human tissue sections using vibrational spectroscopy. *Vibrational Spectroscopy* **38**, 121-127 (2005).

113 Kazarian, S. & Chan, K. Applications of ATR-FTIR spectroscopic imaging to biomedical samples. *Biochimica et Biophysica Acta (BBA)-Biomembranes* **1758**, 858-867 (2006).

114 Kazarian, S. G. & Chan, K. A. ATR-FTIR spectroscopic imaging: recent advances and applications to biological systems. *Analyst* **138**, 1940-1951 (2013).

115 Glassford, S. E., Byrne, B. & Kazarian, S. G. Recent applications of ATR FTIR spectroscopy and imaging to proteins. *Biochimica et Biophysica Acta (BBA)-Proteins and Proteomics* **1834**, 2849-2858 (2013).

116 Barth, A. Infrared spectroscopy of proteins. *Biochimica et Biophysica Acta (BBA) - Bioenergetics* **1767**, 1073-1101 (2007).

117 Lasch, P., Haensch, W., Naumann, D. & Diem, M. Imaging of colorectal adenocarcinoma using FT-IR microspectroscopy and cluster analysis. *Biochimica et Biophysica Acta (BBA) - Molecular Basis of Disease* **1688**, 176-186 (2004).

118 Fernandez, D. C., Bhargava, R., Hewitt, S. M. & Levin, I. W. Infrared spectroscopic imaging for histopathologic recognition. *Nature biotechnology* **23**, 469-474 (2005).

119 Petibois, C. & Deleris, G. Chemical mapping of tumor progression by FT-IR imaging: towards molecular histopathology. *Trends in biotechnology* **24**, 455-462 (2006).

120 Lewis, E. N. *et al.* Fourier transform spectroscopic imaging using an infrared focal-plane array detector. *Analytical chemistry* **67**, 3377-3381 (1995).

121 Raman, C. V. & Krishnan, K. S. A new type of secondary radiation. *Nature* **121**, 501-502 (1928).

122 Kereszty, G. Raman spectroscopy: theory. *Handbook of vibrational spectroscopy* (2002).

123 Reichenbächer, M. & Popp, J. *Challenges in molecular structure determination*. (Springer Science & Business Media, 2012).

124 Cheng, J.-X. & Xie, X. S. Coherent anti-Stokes Raman scattering microscopy: instrumentation, theory, and applications. *The Journal of Physical Chemistry B* **108**, 827-840 (2004).

125 Zhao, J., Lui, H., McLean, D. I. & Zeng, H. Automated autofluorescence background subtraction algorithm for biomedical Raman spectroscopy. *Applied spectroscopy* **61**, 1225-1232 (2007).

126 Butler, H. J. *et al.* Using Raman spectroscopy to characterize biological materials. *Nature protocols* **11**, 664-687 (2016).

127 Long, D. A. Raman spectroscopy. *New York*, 1-12 (1977).

128 Heller, E. J., Sundberg, R. & Tannor, D. Simple aspects of Raman scattering. *The Journal of Physical Chemistry* **86**, 1822-1833 (1982).

129 Byrne, H., Sockalingum, G. & Stone, N. Raman microscopy: complement or competitor. (2011).

130 Gremlich, H. U. The use of optical spectroscopy in combinatorial chemistry. *Biotechnology and bioengineering* **61**, 179-187 (1999).

131 Cui, L., Butler, H. J., Martin-Hirsch, P. L. & Martin, F. L. Aluminium foil as a potential substrate for ATR-FTIR, transfection FTIR or Raman spectrochemical analysis of biological specimens. *Analytical Methods* **8**, 481-487 (2016).

132 Lewis, A. T. *et al.* Mirrored stainless steel substrate provides improved signal for Raman spectroscopy of tissue and cells. *Journal of Raman Spectroscopy* (2016).

133 Kerr, L. T., Byrne, H. J. & Hennelly, B. M. Optimal choice of sample substrate and laser wavelength for Raman spectroscopic analysis of biological specimen. *Analytical Methods* **7**, 5041-5052 (2015).

134 Leeds, S., Davis, T., May, P., Pickard, C. & Ashfold, M. Use of different excitation wavelengths for the analysis of CVD diamond by laser Raman spectroscopy. *Diamond and Related Materials* **7**, 233-237 (1998).

135 Smith, E. & Dent, G. *Modern Raman spectroscopy: a practical approach*. (John Wiley & Sons, 2013).

136 Beleites, C., Neugebauer, U., Bocklitz, T., Krafft, C. & Popp, J. Sample size planning for classification models. *Analytica chimica acta* **760**, 25-33 (2013).

137 Lasch, P. Spectral pre-processing for biomedical vibrational spectroscopy and microspectroscopic imaging. *Chemometrics and Intelligent Laboratory Systems* **117**, 100-114 (2012).

138 Bocklitz, T., Walter, A., Hartmann, K., Rösch, P. & Popp, J. How to pre-process Raman spectra for reliable and stable models? *Analytica chimica acta* **704**, 47-56 (2011).

139 Jarvis, R. M. & Goodacre, R. Genetic algorithm optimization for pre-processing and variable selection of spectroscopic data. *Bioinformatics* **21**, 860-868 (2005).

140 Martin, F. L. *et al.* Distinguishing cell types or populations based on the computational analysis of their infrared spectra. *Nature protocols* **5**, 1748-1760 (2010).

141 Socrates, G. *Infrared and Raman characteristic group frequencies: tables and charts*. (John Wiley & Sons, 2004).

142 Movasaghi, Z., Rehman, S. & Rehman, I. U. Raman spectroscopy of biological tissues. *Applied Spectroscopy Reviews* **42**, 493-541 (2007).

143 Movasaghi, Z., Rehman, S. & ur Rehman, D. I. Fourier transform infrared (FTIR) spectroscopy of biological tissues. *Applied Spectroscopy Reviews* **43**, 134-179 (2008).

144 Kohler, A. *et al.* Estimating and correcting Mie scattering in synchrotron-based microscopic Fourier transform infrared spectra by extended multiplicative signal correction. *Applied spectroscopy* **62**, 259-266 (2008).

145 Butler, H. J., McAinsh, M. R., Adams, S. & Martin, F. L. Application of vibrational spectroscopy techniques to non-destructively monitor plant health and development. *Analytical Methods* **7**, 4059-4070 (2015).

146 Leger, M. N. & Ryder, A. G. Comparison of derivative preprocessing and automated polynomial baseline correction method for classification and quantification of narcotics in solid mixtures. *Applied spectroscopy* **60**, 182-193 (2006).

147 Trevisan, J., Angelov, P. P., Carmichael, P. L., Scott, A. D. & Martin, F. L. Extracting biological information with computational analysis of Fourier-transform infrared (FTIR) biospectroscopy datasets: current practices to future perspectives. *Analyst* **137**, 3202-3215 (2012).

148 Dong, A., Huang, P. & Caughey, W. S. Protein secondary structures in water from second-derivative amide I infrared spectra. *Biochemistry* **29**, 3303-3308 (1990).

149 Kumar, S. *et al.* Raman and infra-red microspectroscopy: towards quantitative evaluation for clinical research by ratiometric analysis. *Chemical Society Reviews* **45**, 1879-1900 (2016).

150 Lasch, P. & Kneipp, J. *Biomedical vibrational spectroscopy*. (John Wiley & Sons, 2008).

151 Jolliffe, I. in *Wiley StatsRef: Statistics Reference Online* (John Wiley & Sons, Ltd, 2014).

152 Cowe, I. A. & McNicol, J. W. The Use of Principal Components in the Analysis of Near-Infrared Spectra. *Applied Spectroscopy* **39**, 257-266 (1985).

153 Kelly, J. G. *et al.* Biospectroscopy to metabolically profile biomolecular structure: a multistage approach linking computational analysis with biomarkers. *Journal of proteome research* **10**, 1437-1448 (2011).

154 Harvey, T. *et al.* Factors influencing the discrimination and classification of prostate cancer cell lines by FTIR microspectroscopy. *Analyst* **134**, 1083-1091 (2009).

155 Trevisan, J. *et al.* Measuring similarity and improving stability in biomarker identification methods applied to Fourier-transform infrared (FTIR) spectroscopy. *Journal of biophotonics* **7**, 254-265 (2014).

156 Krafft, C., Steiner, G., Beleites, C. & Salzer, R. Disease recognition by infrared and Raman spectroscopy. *Journal of biophotonics* **2**, 13-28 (2009).

157 Gajjar, K. *et al.* Fourier-transform infrared spectroscopy coupled with a classification machine for the analysis of blood plasma or serum: a novel diagnostic approach for ovarian cancer. *Analyst* **138**, 3917-3926 (2013).

158 Stone, N., Kendall, C., Smith, J., Crow, P. & Barr, H. Raman spectroscopy for identification of epithelial cancers. *Faraday discussions* **126**, 141-157 (2004).

159 Bhargava, R., Fernandez, D. C., Hewitt, S. M. & Levin, I. W. High throughput assessment of cells and tissues: Bayesian classification of spectral metrics from infrared vibrational spectroscopic imaging data. *Biochimica et Biophysica Acta (BBA)-Biomembranes* **1758**, 830-845 (2006).

160 Goodacre, R. Explanatory analysis of spectroscopic data using machine learning of simple, interpretable rules. *Vibrational Spectroscopy* **32**, 33-45 (2003).

161 Beleites, C. & Salzer, R. Assessing and improving the stability of chemometric models in small sample size situations. *Analytical and bioanalytical chemistry* **390**, 1261-1271 (2008).

162 Gromski, P. S. *et al.* A tutorial review: Metabolomics and partial least squares-discriminant analysis--a marriage of convenience or a shotgun wedding. *Anal Chim Acta* **879**, 10-23 (2015).

163 Shaw, R. A. & Mantsch, H. H. Vibrational biospectroscopy: from plants to animals to humans. A historical perspective. *Journal of Molecular Structure* **480-481**, 1-13 (1999).

164 Byrne, H. J. *et al.* Spectropathology for the next generation: Quo vadis? *Analyst* **140**, 2066-2073 (2015).

165 Baker, M. J. *et al.* Developing and understanding biofluid vibrational spectroscopy: a critical review. *Chemical Society Reviews* **45**, 1803-1818 (2016).

166 Heredia-Guerrero, J. A. *et al.* Infrared and Raman spectroscopic features of plant cuticles: a review. *Frontiers in plant science* **5**, 305 (2014).

167 Stewart, D. Fourier transform infrared microspectroscopy of plant tissues. *Applied Spectroscopy* **50**, 357-365 (1996).

168 Schulz, H. & Baranska, M. Identification and quantification of valuable plant substances by IR and Raman spectroscopy. *Vibrational Spectroscopy* **43**, 13-25 (2007).

169 Kumar, J. K. & Prasad, A. D. Identification and comparison of biomolecules in medicinal plants of *Tephrosia tinctoria* and *Atylosia albicans* by using FTIR. *Romanian J Biophys* **21**, 63-71 (2011).

170 Li, Y.-q., Kong, D.-x. & Wu, H. Analysis and evaluation of essential oil components of cinnamon barks using GC-MS and FTIR spectroscopy. *Industrial Crops and Products* **41**, 269-278 (2013).

171 Stewart, D., McDougall, G. J. & Baty, A. Fourier-transform infrared microspectroscopy of anatomically different cells of flax (*Linum usitatissimum*) stems during development. *Journal of agricultural and food chemistry* **43**, 1853-1858 (1995).

172 Merk, S., Blume, A. & Riederer, M. Phase behaviour and crystallinity of plant cuticular waxes studied by Fourier transform infrared spectroscopy. *Planta* **204**, 44-53 (1997).

173 Fernández, V. *et al.* New insights into the properties of pubescent surfaces: Peach fruit as a model. *Plant Physiology* **156**, 2098-2108 (2011).

174 Ramirez, F., Luque, P., Heredia, A. & Bukovac, M. Fourier transform IR study of enzymatically isolated tomato fruit cuticular membrane. *Biopolymers* **32**, 1425-1429 (1992).

175 Chen, L. *et al.* A rapid method to screen for cell-wall mutants using discriminant analysis of Fourier transform infrared spectra. *The Plant Journal* **16**, 385-392 (1998).

176 Tapp, H. S., Defernez, M. & Kemsley, E. K. FTIR spectroscopy and multivariate analysis can distinguish the geographic origin of extra virgin olive oils. *Journal of agricultural and food chemistry* **51**, 6110-6115 (2003).

177 Rodriguez-Saona, L. & Allendorf, M. Use of FTIR for rapid authentication and detection of adulteration of food. *Annual review of food science and technology* **2**, 467-483 (2011).

178 Yu, P. Molecular chemistry imaging to reveal structural features of various plant feed tissues. *Journal of Structural Biology* **150**, 81-89 (2005).

179 Yu, P. *et al.* Use of synchrotron FTIR microspectroscopy to identify chemical differences in barley endosperm tissue in relation to rumen degradation characteristics. *Canadian journal of animal science* **84**, 523-527 (2004).

180 Yu, P., McKinnon, J. J., Christensen, C. R. & Christensen, D. A. Using synchrotron transmission FTIR microspectroscopy as a rapid, direct, and nondestructive analytical

technique to reveal molecular microstructural-chemical features within tissue in grain barley. *Journal of agricultural and food chemistry* **52**, 1484-1494 (2004).

181 Yu, P., Mckinnon, J. J., Christensen, C. R. & Christensen, D. A. Using synchrotron-based FTIR microspectroscopy to reveal chemical features of feather protein secondary structure: comparison with other feed protein sources. *Journal of agricultural and food chemistry* **52**, 7353-7361 (2004).

182 Yu, P. *et al.* Chemical imaging of microstructures of plant tissues within cellular dimension using synchrotron infrared microspectroscopy. *Journal of agricultural and food chemistry* **51**, 6062-6067 (2003).

183 Heraud, P. *et al.* Focal plane array infrared imaging: a new way to analyse leaf tissue. *New Phytologist* **173**, 216-225 (2007).

184 Kristensen, J. B., Thygesen, L. G., Felby, C., Jørgensen, H. & Elder, T. Cell-wall structural changes in wheat straw pretreated for bioethanol production. *Biotechnology for biofuels* **1**, 1 (2008).

185 Abidi, N., Cabrales, L. & Haigler, C. H. Changes in the cell wall and cellulose content of developing cotton fibers investigated by FTIR spectroscopy. *Carbohydrate Polymers* **100**, 9-16 (2014).

186 Ricci, A., Olejar, K. J., Parpinello, G. P., Kilmartin, P. A. & Versari, A. Application of Fourier Transform Infrared (FTIR) Spectroscopy in the Characterization of Tannins. *Applied Spectroscopy Reviews* **50**, 407-442 (2015).

187 Monti, F. *et al.* A multivariate statistical analysis approach to highlight molecular processes in plant cell walls through ATR FT-IR microspectroscopy: The role of the α -expansin PhEXPA1 in Petunia hybrida. *Vibrational Spectroscopy* **65**, 36-43 (2013).

188 Warren, F. J. *et al.* Infrared microspectroscopic imaging of plant tissues: spectral visualization of Triticum aestivum kernel and Arabidopsis leaf microstructure. *The Plant Journal* **84**, 634-646 (2015).

189 Ribeiro da Luz, B. Attenuated total reflectance spectroscopy of plant leaves: a tool for ecological and botanical studies. *New Phytologist* **172**, 305-318 (2006).

190 Ivanova, D. G. & Singh, B. R. Nondestructive FTIR monitoring of leaf senescence and elicitor-induced changes in plant leaves. *Biopolymers* **72**, 79-85 (2003).

191 Gierlinger, N. & Schwanninger, M. The potential of Raman microscopy and Raman imaging in plant research. *Spectroscopy* **21**, 69-89 (2007).

192 Agarwal, U. P. Raman imaging to investigate ultrastructure and composition of plant cell walls: distribution of lignin and cellulose in black spruce wood (*Picea mariana*). *Planta* **224**, 1141-1153 (2006).

193 Gierlinger, N., Keplinger, T. & Harrington, M. Imaging of plant cell walls by confocal Raman microscopy. *Nature protocols* **7**, 1694-1708 (2012).

194 Gierlinger, N. *et al.* Cellulose microfibril orientation of *Picea abies* and its variability at the micron-level determined by Raman imaging. *Journal of experimental botany* **61**, 587-595 (2010).

195 Gierlinger, N. & Schwanninger, M. Chemical imaging of poplar wood cell walls by confocal Raman microscopy. *Plant Physiology* **140**, 1246-1254 (2006).

196 Sene, C. F., McCann, M. C., Wilson, R. H. & Grinter, R. Fourier-transform Raman and Fourier-transform infrared spectroscopy (an investigation of five higher plant cell walls and their components). *Plant Physiology* **106**, 1623-1631 (1994).

197 Edwards, H., Farwell, D. & Webster, D. FT Raman microscopy of untreated natural plant fibres. *Spectrochimica Acta Part A: Molecular and Biomolecular Spectroscopy* **53**, 2383-2392 (1997).

198 Rösch, P., Popp, J. & Kiefer, W. Raman and surface enhanced Raman spectroscopic investigation on Lamiaceae plants. *Journal of molecular structure* **480**, 121-124 (1999).

199 Zeiri, L. SERS of plant material. *Journal of Raman Spectroscopy* **38**, 950-955 (2007).

Chapter 2

Using Fourier transform IR spectroscopy to analyze biological materials

Matthew J. Baker, Júlio Trevisan, Paul Bassan, Rohit Bhargava, **Holly J. Butler**, Konrad M Dorling, Peter R. Fielden, Simon W. Fogarty, Nigel J. Fullwood, Kelly Heys, Caryn Hughes, Peter Lasch, Pierre L. Martin-Hirsch, Blessing Obinaju, Ganesh D. Sockalingum, Josep Sulé-Suso, Rebecca J. Strong, Michael J. Walsh, Bayden R. Wood, Peter Gardner and Francis L Martin

Nature Protocols 9(8): 1771-1791 (2014)

Contribution:

I wrote the ‘Instrumentation’ and ‘Spectral Acquisition’ sections

I produced figures 1 and 3, and table 3

Júlio Trevisan and I, compiled manuscript feedback from other authors and prepared manuscript for publication

Professor F. L Martin

Dr. Martin. R. McAinsh

H. J. Butler

Using Fourier transform IR spectroscopy to analyze biological materials

Matthew J Baker^{1,13}, Júlio Trevisan^{2,3}, Paul Bassan⁴, Rohit Bhargava⁵, Holly J Butler², Konrad M Dorling¹, Peter R Fielden⁶, Simon W Fogarty^{2,7}, Nigel J Fullwood⁷, Kelly A Heys², Caryn Hughes⁴, Peter Lasch⁸, Pierre L Martin-Hirsch², Blessing Obinaju², Ganesh D Sockalingum⁹, Josep Sulé-Suso¹⁰, Rebecca J Strong², Michael J Walsh¹¹, Bayden R Wood¹², Peter Gardner⁴ & Francis L Martin²

¹Centre for Materials Science, Division of Chemistry, University of Central Lancashire, Preston, UK. ²Centre for Biophotonics, Lancaster Environment Centre, Lancaster University, Lancaster, UK. ³School of Computing and Communications, Lancaster University, Lancaster, UK. ⁴Manchester Institute of Biotechnology (MIB), University of Manchester, Manchester, UK. ⁵Department of Bioengineering, University of Illinois at Urbana-Champaign, Urbana, Illinois, USA. ⁶Department of Chemistry, Lancaster University, Lancaster, UK. ⁷Division of Biomedical and Life Sciences, School of Health and Medicine, Lancaster University, Lancaster, UK. ⁸Proteomics and Spectroscopy (ZBS 6), Robert-Koch-Institut, Berlin, Germany. ⁹Equipe MéDIAN-Biophotonique et Technologies pour la Santé, Université de Reims Champagne-Ardenne, UnitéMÉDyC, CNRS UMR7369, UFR Pharmacie, SFR CAP-Santé FED4231, Reims, France. ¹⁰Institute for Science and Technology in Medicine, School of Medicine, Keele University, Stoke-on-Trent, UK. ¹¹Department of Pathology, College of Medicine Research Building (COMRB), University of Illinois at Chicago, Chicago, Illinois, USA. ¹²Centre for Biopspectroscopy and School of Chemistry, Monash University, Clayton, Victoria, Australia. ¹³Present address: WestCHEM, Department of Pure and Applied Chemistry, University of Strathclyde, Glasgow, UK. Correspondence should be addressed to F.L.M. (f.martin@lancaster.ac.uk).

Published online 3 July 2014; doi:10.1038/nprot.2014.110

IR spectroscopy is an excellent method for biological analyses. It enables the nonperturbative, label-free extraction of biochemical information and images toward diagnosis and the assessment of cell functionality. Although not strictly microscopy in the conventional sense, it allows the construction of images of tissue or cell architecture by the passing of spectral data through a variety of computational algorithms. Because such images are constructed from fingerprint spectra, the notion is that they can be an objective reflection of the underlying health status of the analyzed sample. One of the major difficulties in the field has been determining a consensus on spectral pre-processing and data analysis. This manuscript brings together as coauthors some of the leaders in this field to allow the standardization of methods and procedures for adapting a multistage approach to a methodology that can be applied to a variety of cell biological questions or used within a clinical setting for disease screening or diagnosis. We describe a protocol for collecting IR spectra and images from biological samples (e.g., fixed cytology and tissue sections, live cells or biofluids) that assesses the instrumental options available, appropriate sample preparation, different sampling modes as well as important advances in spectral data acquisition. After acquisition, data processing consists of a sequence of steps including quality control, spectral pre-processing, feature extraction and classification of the supervised or unsupervised type. A typical experiment can be completed and analyzed within hours. Example results are presented on the use of IR spectra combined with multivariate data processing.

INTRODUCTION

The use of Fourier transform IR (FTIR) spectroscopic techniques for the nondestructive analysis of biological specimens is a rapidly expanding research area, with much focus on its utility in cytological and histological diagnosis through the generation of spectral images^{1,2}. Molecular bonds with an electric dipole moment that can change by atomic displacement owing to natural vibrations are IR active. These vibrational modes are quantitatively measurable by IR spectroscopy³, providing a unique, label-free tool for studying molecular composition and dynamics without perturbing the sample. For interrogating biological materials, the most important spectral regions measured are typically the fingerprint region ($600\text{--}1,450\text{ cm}^{-1}$) and the amide I and amide II (amide I/II) region ($1,500\text{--}1,700\text{ cm}^{-1}$). The higher-wavenumber region ($2,550\text{--}3,500\text{ cm}^{-1}$) is associated with stretching vibrations such as S-H, C-H, N-H and O-H, whereas the lower-wavenumber regions typically correspond to bending and carbon skeleton fingerprint vibrations⁴. Together, these regions comprise a biochemical fingerprint of the structure and function of interrogated cellular specimens. A typical biological IR spectrum with molecular assignments is shown in **Figure 1**.

IR microspectroscopy

Although the spectral domain allows chemical identification, the combination with microscopy (microspectroscopy) permits

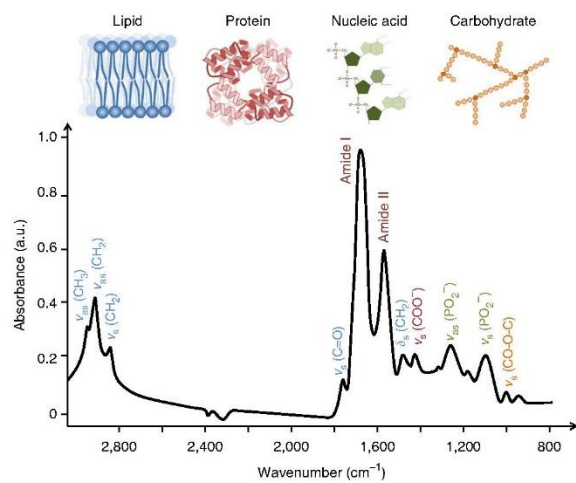
the examination of complex tissues and heterogeneous samples⁵. Detection by microscopy (see schematic of instrumentation in **Fig. 2**) may be accomplished by raster-scanning a point illuminated on the sample or by using wide-field illumination and focal plane array (FPA) or linear array detectors⁶. At present, wide-field scanning of a sample is possible in seconds, providing tens of thousands of spectra. A variety of choices are available for the IR source, including globar⁷, synchrotron^{8–12} and quantum-cascade lasers (QCLs)¹³, as well as for the detector (2D FPA, linear array or single element)¹⁴. The three major IR-spectroscopic sampling modes (**Fig. 2b**) are transmission, transfection and attenuated total reflection (ATR). Each mode offers convenience for some samples and challenges for others. In transfection mode, for illustration, the sample is placed on an inexpensive IR-reflecting surface (such as that found on low-emissivity (Low-E) slides) and measurements are generated by a beam passing through the sample and reflecting back from the substrate (i.e., the reflective surface) through the sample. As is clear from both theoretical and experimental studies^{15,16}, the recorded spectral intensities depend on both sample morphology and chemistry. Hence, care should be taken on substrate choice^{17,18}. Recently, topographical features of the sample and its effects have been shown to be minimized by inputting second derivative spectra in the classification model; better segregation of normal versus various

PROTOCOL

Figure 1 | Typical biological spectrum showing biomolecular peak assignments from 3,000–800 cm⁻¹, where ν = stretching vibrations, δ = bending vibrations, s = symmetric vibrations and as = asymmetric vibrations. The spectrum is a transmission-type micro-spectrum from a human breast carcinoma (ductal carcinoma *in situ*). The sample was cryosectioned (8 μ m thick) and mounted on BaF₂ slides (1 mm thick) before IR microspectroscopy. Equipment: Bruker IR scope II, circular diameter of aperture ~60 μ m; a.u., arbitrary units.

disease categories facilitates potential spectral histopathological diagnosis¹⁹. Research by Cao *et al.*²⁰ has demonstrated that if this pre-processing data analysis approach is performed (e.g., after both transfection and transmission measurements on dried cellular monolayers), the resulting classification is the same. This example suggests that irrespective of sampling geometry, mathematical tools can be applied to minimize confounding effects and to interpret their influence. As such, spectral processing may determine the diagnostic efficacy of spectral processing, not only from a biological perspective but also from the ability to control optical or distorting influences.

FTIR imaging provides spatially resolved information based on chemically specific IR spectra in the form of an information-rich image of the tissue or cell type being interrogated^{21–23}. Further multivariate data analysis allows potential diagnostic markers to be elucidated, thus providing a fast and label-free technology to be used alongside conventional techniques such as histology^{2,22}. At present²⁴, rapid imaging permits imaging in hours for a whole-organ cross-section, such as that from the prostate; this not only allows one to objectively visualize pathology *in situ* but the aforementioned classification models could also allow one to grade disease on the basis of the categories into which spectra might be



aligned. One excellent interpretation application of IR imaging data is to consider it as a metabolomic tool that allows the *in situ*, nondestructive analysis of biological specimens, (e.g., determining the glycogen levels in cervical cytology)²⁵.

Data can be recorded from a variety of samples, ranging from live cells to formalin-fixed, paraffin-embedded (FFPE) archival tissue typical of a pathology specimen. IR spectra representing distinguishing fingerprints of specific cell types (e.g., stem cells versus transit-amplifying cells versus terminally differentiated cells) within a defined tissue architecture (e.g., crypts of the gastrointestinal tract and cornea)^{9,26} are now easily recorded. Consequently, spectral analyses delineate cellular hierarchy on the basis of protein, lipid and carbohydrate composition and/or DNA conformational changes²⁷. For biomedical analyses, the major goal today is to derive an image of tissue architecture expressing the underlying biochemistry in a label-free fashion²⁸, a development that can considerably extend our diagnostic potential beyond present capabilities. For example, to distinguish cells committed toward a pathological process (e.g., transformation) that conventional methods (e.g., visual scoring) might identify as normal. The screening of cervical cytology specimens to distinguish normal versus low-grade versus high-grade cells^{4,29}, to grade primary neoplasia³⁰, or to determine whether tissue margins and potential metastatic sites are tumor free^{31,32} are examples of this concept across many types of tissues. It is this bridge from the technology and potential of IR spectroscopy and imaging to biological, mainly clinical, applications that is the subject of this protocol (Fig. 3).

IR spectroscopy in cancer classification and imaging

By using IR spectroscopy either as an imaging tool or by classifying spectral categories, it has been possible to distinguish

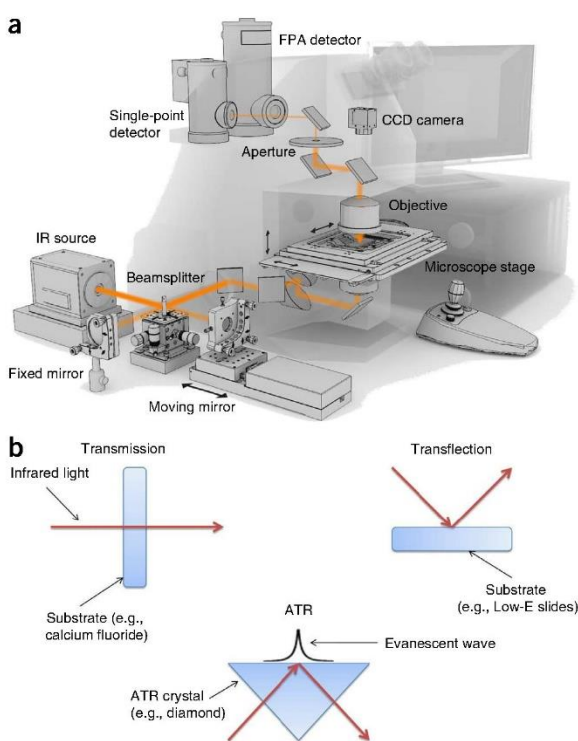


Figure 2 | The instrumentation underlying the main forms of IR spectroscopic sampling. (a) Schematic of modern FTIR-imaging spectrometer. Reproduced with permission from ref. 6. (b) Schematic representation of the three main sampling modes for FTIR spectroscopy. Reprinted from *Trends Biotechnol.*, 31, Dorling, K.M. and M.J. Baker, Highlighting attenuated total reflection Fourier transform infrared spectroscopy for rapid serum analysis, 327–328, Copyright 2013 with permission from Elsevier (ref. 132).

Figure 3 | FTIR spectroscopy work flow for imaging and diagnosis. The three major steps are sample preparation, FTIR spectral acquisition and data analysis. Sample preparation may differ depending on the sample format, requiring different materials and procedures. At FTIR spectral acquisition, several options have to be considered for light source and sampling mode. Data analysis presents different paths depending on the analysis goal (i.e., imaging or diagnosis). The framework for diagnosis is somewhat more complex, involving training of classification systems and validation of these systems using test data sets. Although not illustrated, the data sets used for testing are also obtained through sample preparation followed by FTIR spectral acquisition.

between benign and malignant tumors in tissue samples of breast^{32–35}, colon^{22,23,36}, lung³⁷ and prostate^{8,30,38,39} along with cervical cytology or biopsies^{4,28,40}. IR spectroscopic analysis is also an ideal tool for the study of biofluids such as urine, saliva, serum or whole blood; the use of biofluids is desirable in a clinical setting as samples are obtained rapidly and relatively noninvasively, and minimal sample preparation is required. By using such methods, a spectral fingerprint of the biofluid can be obtained, which allows the subsequent classification of spectra from different categories with computational methods and possibly the identification of biomarkers^{41–44}.

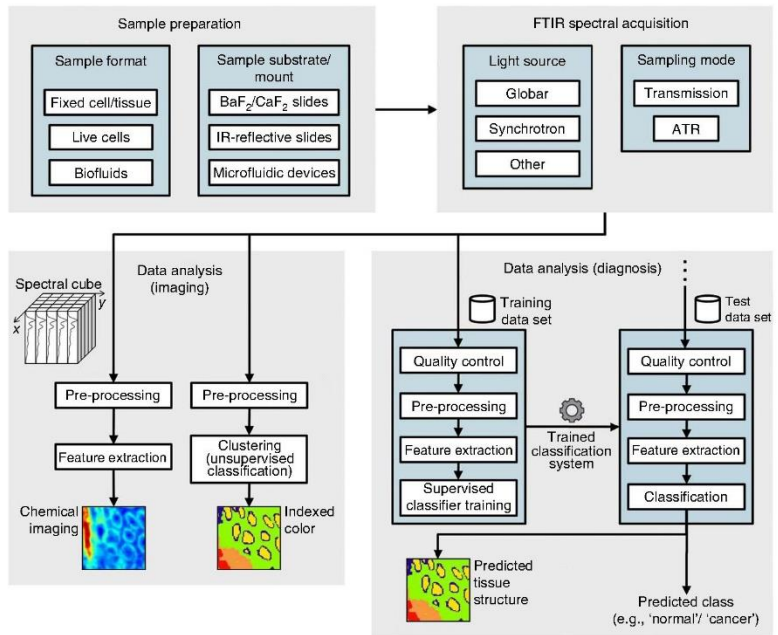
FTIR imaging of tissue and cells

Imaging of live cells is possible using both globar and synchrotron-based light sources, with the latter permitting greater lateral spatial resolution and data quality owing to higher flux^{21,45–47}. Diffraction-limited resolution with ATR-FTIR imaging can also be advantageous as it allows analysis of live cells in aqueous systems^{21,48}. In addition, the spatial resolution of the image can be increased by incorporating optics with a high refractive index^{21,34}.

We describe a protocol that has three components: (i) specimen preparation and removal of possible sample contaminants; (ii) acquisition of spectra with a sufficiently high signal-to-noise ratio (SNR); and (iii) data processing for classification and imaging. As the precise steps in acquisition of spectra and data processing are, respectively, dependent on the instrument and software available, this protocol covers (ii) and (iii) to deliver a general understanding of the steps involved. **Supplementary Methods 1–4** correspond to four different examples of standard operating procedures (with troubleshooting) specific to common instruments and acquisition/analysis software. Together, this protocol and the material contained in **Supplementary Methods 1–4** are designed to build researchers' confidence in conducting their studies using their own instrumentation and computational settings.

Application of this protocol to other research areas

The application of this protocol is not limited to the biomedical field. IR spectroscopy has previously been used in the fields of



environmental toxicology^{49–52}, consumer safety^{53,54}, taxonomy^{55–57}, and in the food industry⁵⁸; a non-instrument- and non-software-specific protocol for imaging and classification could be of considerable use to these areas of research.

Experimental design: instrumental options

The main steps required to analyze a sample of interest are sample preparation, instrumental setting, acquisition of spectra and data processing (Fig. 4). Before instrumental options are chosen, it is important for the user to understand the expectations from the intended experiment. These include the desired spectral and spatial resolution and type of study (e.g., diagnostic versus exploratory). In addition, proper consideration must be given to potential sample restrictions such as acquiring appropriate sample thickness for respective modes.

Sampling modes. Figure 2b shows a schematic representation of each sampling mode and details of each can be seen in Table 1; however, it is important to note that different manufacturer systems may vary slightly in some parameters, such as sampling apertures. Transmission and transfection sampling modes have been applied to a variety of biological specimens that can be sectioned into a thin layer allowing for accurate spectral data acquisition⁵⁹. ATR-FTIR mode differs in that the IR beam is directed through an internal reflection element (IRE) with a high refractive index (e.g., diamond, zinc selenide, germanium or silicon)⁶⁰. The evanescent wave extends beyond the IRE surface penetrating the sample, which must be in direct contact with the IRE. The penetration depth of this wave typically ranges from 1 to 2 μm within the 1,800–900 cm^{-1} region, but it should be remembered that there is still ~5% intensity at a depth of 3 μm (refs. 18,61,62). It has been shown that samples with thicknesses of <2 μm may give rise to spectral artifacts with IR-reflective substrates such as MirrIR Low-E slides (Kevley Technologies); therefore, when these

PROTOCOL

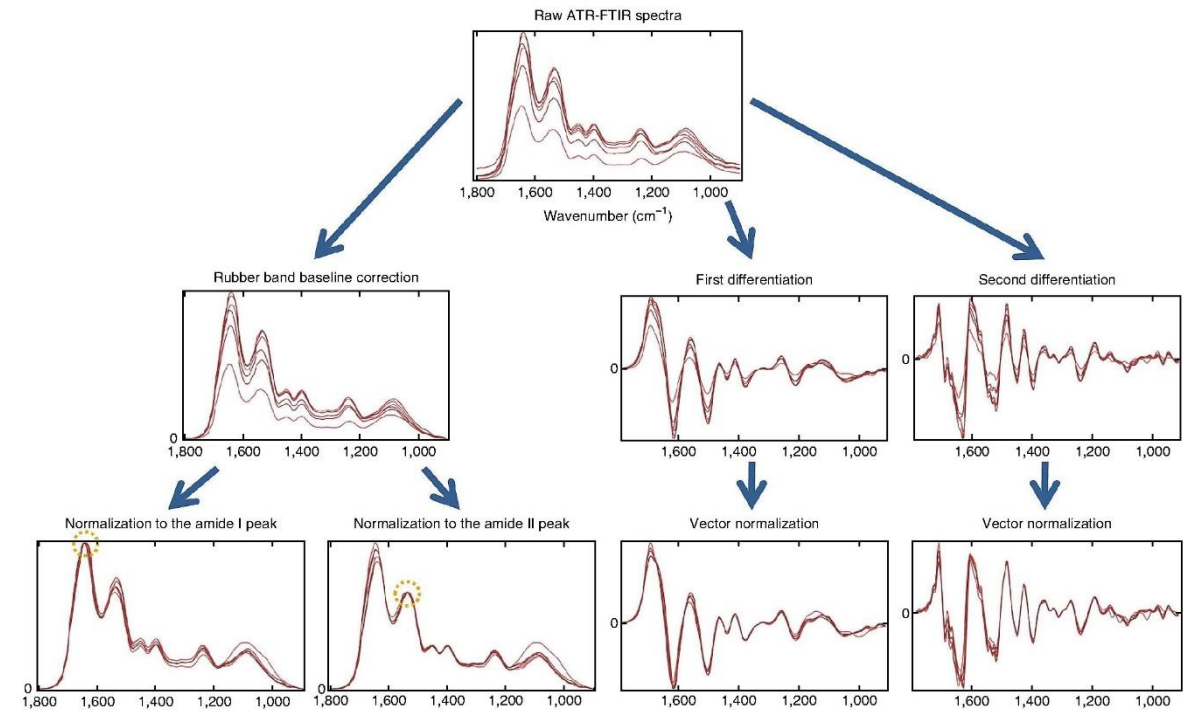


Figure 4 | Visual effect of different pre-processing steps on a set of FTIR spectra. Two common pre-processing sequences are rubber band baseline correction followed by normalization to the amide I/II peak and first or second differentiation followed by vector normalization. Rubber band baseline correction subtracts a rubber band, which is stretched 'bottom-up' at each spectrum, eliminating slopes. Amide I/II normalization forces all spectra to have the same absorbance intensity at the amide I/II peak. Differentiation (Savitzki-Golay (SG) method) has the advantage of eliminating slopes while also resolving overlapped bands, but has the drawback of altering the shape of the spectra (the y axis unit is no longer a.u. (arbitrary units), but 'a.u. per wavenumber' (first differentiation) or 'a.u. per wavenumber squared' (second differentiation)) and enhancing noise (note how second-differentiated spectra are visibly more noisy). Vector normalization is typically applied after differentiation. This normalization technique does not require a reference peak as amide I/II normalization does.

© 2014 Nature America, Inc. All rights reserved.



substrates are used with ATR-FTIR spectroscopy, a thicker sample is recommended¹⁸.

A magnification-limited digital camera may be used for visualization in order to guide manual navigation across a given sample so as to locate a region of interest and help identify basic microscopic features such as separation between cancer cells and stromal elements. An alternative setup for ATR involves placing the sample directly onto the IRE aperture of the ATR accessory. This is particularly useful for biofluid analysis as it bypasses any potential contributions from any slide substrate that the sample could be placed on (**Supplementary Method 1**). This methodology may also help to reduce experimentation time owing to reduced sample preparation.

Light sources. In IR microspectroscopy, the user has the option of several light sources: a conventional thermal (globar) or synchrotron radiation source for FTIR interferometric measurements or alternative sources such as QCLs⁶³ and filters⁶⁴, which obviate the use of interferometers. The majority of benchtop instruments use conventional thermal light sources often in conjunction with single-element detectors. A globar source is composed of a silicon carbide rod that generates IR radiation, and can typically generate a collimated beam of

~1,000 μm in diameter, providing a uniformly illuminated aperture of 20–100 μm of the diameter at the sample⁶⁵. It has been shown that single-cell investigations can be conducted using standard globar IR sources to derive subcellular information⁶⁶.

A synchrotron radiation light source is ~100–1,000-fold brighter than current benchtop thermal ones, but it illuminates a much smaller area. Thus, a synchrotron source has a natural sampling aperture of 10–20 μm in diameter with a high SNR⁶⁷. It is therefore possible to achieve single-cell and large organelle (e.g., nucleus) lateral spatial resolution with these modern sources, allowing subcellular molecular distribution analysis^{68,69}. There are ~50 synchrotron facilities worldwide, all easily accessible for routine use as they operate on a call-for-projects basis⁷⁰. Alternatively, other available sources that may be advantageous to individual studies include optic parametric oscillator (OPO) lasers, QCLs and free-electron lasers (FELs); traditionally they have been primarily used for gas sensing because of intrinsically narrow linewidths^{71,72}; however, modern QCLs can cover much broader wavelength regions (hundreds of cm⁻¹).

Mapping versus imaging. Broadly speaking, detectors can be separated into single-element, linear array and FPA detectors; the detector choice will be influenced by the requirement being

TABLE 1 | FTIR spectroscopy modes used for the interrogation of cellular materials.

Mode	Suitable samples	Substrate	Typical interrogation area (μm)	Pros	Cons
ATR	Tissues, cells and biofluids	Calcium or barium fluoride, zinc selenide, MirrIR Low-E-coated glass	250 × 250	High SNR Reduced scattering Analysis of large target area Better for aqueous samples with appropriate substrate Highest spatial resolution (because of the refractive index n , which is 3.5 or even 4 in case of Si or Ge)	Can be destructive because of pressure Air between sample and IRE will affect spectra Minimum sample thickness is required (~2.3 μm) Interactions of samples with the IRE leading to structural alterations (e.g., secondary protein structure)
Transmission	Tissues, individual cells, cellular components and biofluids	Calcium or barium fluoride and zinc selenide	5 × 5 to 150 × 150	High spatial resolution Nondestructive of prepared sample Automated stage allows for spectral acquisition at several different locations of choice with little user interaction	Lower SNR than ATR Maximum sample thickness is required Sample thickness should be twice as large as for transfection to achieve the same absorbance Longer sample and machine preparation is required
Transfection	Tissues, individual cells, cellular components and biofluids	Calcium or barium fluoride and zinc selenide	5 × 5 to 150 × 150	High spatial resolution Nondestructive of prepared sample Automated stage allows for spectral acquisition at several different locations of choice with little user interaction Approximate sample thickness can be 1–4 μm, whereas for transmission it needs to be 2–8 μm	May give rise to standing wave artifacts Lower SNR than ATR Maximum sample thickness is required Longer sample and machine preparation is required Scattering effects such as RMieSc will be much more intense in transfection type measurements

imaging (i.e., FPA) or point spectra with high SNR (i.e., single element). The use of a single-element detector allows for individual point spectra to be obtained across a whole sample (for instance, useful when analyzing biofluids); a particular application has been to derive single-cell-specific fingerprint spectra across a heterogeneous tissue section. Acquiring large data sets containing point spectra is a method regularly used in biomedical and environmental studies coupled with multivariate data analysis^{40,73}. Although time consuming, point spectra often have a high SNR, resulting in high-quality spectra, as spatial resolution is limited by IR apertures⁷⁴. Maps can be generated when point spectra are collected in a stepwise manner in a grid from a target area, which is useful for comparing the different cell types from that particular area, e.g., gastrointestinal crypt²³. Spectral maps take a much longer time than individual point spectra and, thus, in order to make large maps feasible to run, the acquisition time for each point can be reduced leading to a lower SNR. The absorbance intensity at each spectral point within the map becomes an individual pixel in the resultant pseudocolor images, which can give details of how different biomolecules vary across the target area.

In contrast to aperture-based systems, non-aperture-based instruments such as FPA and linear array detectors provide imaging using spatially arranged detectors. Multielement detectors allow for simultaneous spectral acquisition, which, combined with suitable optics, produce spectral images with good SNR and lateral spatial resolution close to the diffraction limit⁷⁵. Measurements using an FPA detector (typically 32 × 32, 64 × 64 or 128 × 128) are rapid as such detectors allow for the acquisition of thousands of spectra simultaneously⁷⁶; for a typical methodology see **Supplementary Method 2**. The acquired spectral data can be used to generate pseudocolor images of the target area such as shown in the characterization of prostate tissue⁷⁷ and cervical biopsy samples²⁸. The benefits of using a synchrotron radiation light source with FPAs also mean that much smaller pixel sizes can be used (e.g., 0.54 μm × 0.54 μm at some synchrotron facilities) resulting in higher spatial-resolution images of the target area⁷⁶.

ATR-FTIR spectroscopy coupled to an array detector can allow for sample imaging down to diffraction-limited resolution for the spectral range of interest⁷⁸. The spatial resolution of

PROTOCOL

non-aperture-based techniques is determined by the optics chosen, and it has been shown that a germanium optic is preferential, although ZnSe and diamond crystals can also be used³⁴. Although transmission and transfection imaging have been widely implemented in biological tissues, imaging in ATR mode is a versatile option, because little sample preparation is required owing to minimal sample-thickness restrictions, which thus means that it has been implemented in biological fields such as pharmacology and subcellular interrogation^{59,78,79}.

Experimental design: sample preparation

Sample formats. The main sample formats for clinical IR spectroscopy are fixed cell and tissue samples, biofluids and live cells. Spectroscopic approaches can be used to examine tissues of human extraction (all require the appropriate ethical approval before their use). The type of sample used greatly determines which type of IR spectroscopy is appropriate and how it should be prepared for analysis. **Table 2** shows the main types of samples and how they should be prepared for analysis.

Sample thickness. Sufficient thickness of material needs to be placed onto the support matrix to allow a sufficiently large absorbance intensity to be recorded. In transmission and transfection modes, the specimen thickness needs to be adjusted appropriately: if it is too thick, the detector response function will be nonlinear so that Beer-Lambert's law cannot be applied anymore. This has serious consequences for subsequent quantitative and classification analyses. In contrast, to achieve an adequate SNR and to avoid interactions of the evanescent wave with the underlying substrate, samples must also not be too thin. For example, when using ATR-FTIR spectroscopy, it is ideal if the specimen is three- or fourfold thicker than the penetration depth (that said, there is no maximum thickness for ATR-FTIR, and samples that are even a millimeter thick can be analyzed). This is pertinent for internal reflection measurements, which are commonly used for the disease diagnosis of biofluids; such samples can be naturally thinner in composition (especially with regard to cerebrospinal fluid (CSF), although this is not so much the case with blood or serum/plasma; serum, for example, is a solution containing a high protein concentration, $\sim 80 \text{ mg ml}^{-1}$). The effect of substrate interference on spectra, especially in reference to transfection measurements, has now been shown independently in the last year by several groups^{17,18,80}. Given this, we would urge extreme caution regarding the use of Low-E slides with transfection measurements; with ATR-FTIR, it is unlikely that there will be optical effects associated with substrate.

Substrate choice. Proper consideration of the substrate (the slide or matrix) upon which the sample will be placed and any preparation steps associated with this are essential in order to acquire the best and most-reproducible spectra. For transmission measurements, this needs to be an IR-transparent material such as BaF₂ or CaF₂ (the latter, in particular, for live-cell IR spectroscopy), whereas for reflection or transfection measurements an IR-reflective substrate (e.g., Low-E slides) is required because glass alone absorbs the radiation and has a spectral signature in the mid-IR region^{81,82}. Previously, it had been recommended that biological materials be placed on IR-reflective substrates. However, there now appears to be a shift in the general consensus that suggests

that transmission or ATR spectroscopy measurements are more applicable to interrogation of biological material.

Microfluidic devices. Traditionally, aqueous sampling environments were unsuitable for IR spectroscopy because of the contribution of water. Development of microfluidic devices and processing to remove the water contribution has made it possible to achieve real-time, live-cell monitoring with IR spectroscopy. Nondestructive to cells, it better replicates physiological conditions; no labeling is required and the resolution is such that single cells can be studied⁸³. The nondestructive nature of these methods has allowed studies to look at samples over time (e.g., stem cells *in situ* as they differentiate and chemical reactions in flow systems have been monitored^{84,85}.

The key challenge of IR spectroscopy using microfluidics is associated with the materials' transparency over the spectral range to be studied, and especially when live-cell monitoring is desirable. Many potential window materials are unsuitable on the basis of their water solubility (e.g., KBr and NaCl), toxicity toward the cells under observation (e.g., CdTe) or spectral dispersion (e.g., ZnS and BaF₂)⁸⁶. A flow chamber is used that combines IR transparency and robustness of diamond as window material. Although manufacture is complicated, the windows must be sufficiently thin (0.4–0.8 μm) to avoid multiple internal reflections⁸⁶. CaF₂ is extensively used as a window material, and a simple flow cell with inlet and outlet flow is constructed by clamping two CaF₂ plates together. One of the plates is etched to form a 10- μm well, designed for the IR observation of live cells in aqueous media⁸⁵. A similar device has been used for synchrotron IR spectroscopy of living cells using a surface micro-etched silicon substrate⁸⁷. Further advances in the field have led to the development of sandwich devices and entirely polymeric devices.

Experimental design: spectral acquisition

Instrumental and operational settings to maximize spectral quality. When acquiring spectra, it is important to maximize as best as possible the SNR in order to produce high-quality spectral data (**Table 3**). There are a number of noise-related and signal-related parameters, with an effect on SNR, which can be altered depending on the instrument mode being used (e.g., point mode versus imaging)^{88–91}. The instrumental and operational settings will be specific to the user experimental setup; **Table 1** compares properties of different sampling modes for optimized spectral acquisition. An initial noise-related parameter that can be altered is the sampling aperture in point or mapping mode; this will reduce the SNR when the aperture size is reduced⁹². However, in imaging mode there is no aperture. The interferometer mirror velocity may also have an effect on SNR³. Weighting the interferogram with an apodization function will also contribute to a reduction in SNR, as this smoothing effect can incorporate spectral artifacts while one is attempting to optimize the information contained⁹³. In general, the square root of the number of co-additions is proportional to the SNR, and therefore an increased number will enhance the SNR⁹⁴.

IR spectroscopy has a spatial resolution that is limited by the diffraction limit; hence, as the resolution approaches this value, the SNR is reduced to a point where there is no further gain in image quality⁹⁵. A synchrotron radiation source (e.g., at the IR

TABLE 2 | Sample types and preparation.

Sample type	Preparation	Removal of contaminants	Sample mount	Considerations
Biofluids	Biofluids such as blood, urine, saliva and synovial fluid should be collected as per hospital SOPs Samples that are not immediately used should be frozen and stored at -80°C Samples should be thawed fully before use	When using blood-based biofluids such as serum and plasma, spectra from erythrocytes may mask that of other biomolecules, so they should be removed if not being directly investigated ⁴¹	Biofluids may be placed onto slides and dried, or dried directly onto the IRE ⁴⁴	Dry film analysis (where the fluid is dried onto the slide) often results in large signals compared with the wet biofluid, but measurements may be impeded by uneven distribution Only small sample volumes are needed, normally in the region of a few nanoliters ¹³⁶
FFPE tissue samples	FFPE tissue should be de-waxed for a minimum of 5 min in xylene and three washes should be performed Sample thickness should not exceed 8–12 μm (transmission, less for transfection; see Table 1) in order to avoid a nonlinear detector response (at absorbance values >1.2 (for MCT) or >1.5 (for deuterated triglycine sulfate)), to even total absorption	Samples must be de-waxed in order to probe the full wavenumber range, as paraffin is known to have significant peaks at $\sim 2,954\text{ cm}^{-1}$, $2,920\text{ cm}^{-1}$, $2,846\text{ cm}^{-1}$, $1,462\text{ cm}^{-1}$ and $1,373\text{ cm}^{-1}$, which may mask solvent-resistant methylene components of native tissue ^{128,129} Samples are then cleared with acetone to remove any final xylene contamination Another recent and emerging alternative is to model the paraffin contribution and numerically de-paraffinize the sample ³⁶ . In this way, the sample is not affected by chemical de-paraffinization, and intact tissue biochemical information is used for spectral histology	De-waxed tissue should be floated onto slides	If using tissue for imaging and extraction of tissue cell type, sample thickness is not just an SNR issue. The thicker the tissue, the greater the chance of probing heterogeneous layers and possibly multiple cell types, rendering cell type signal less pure
Cryosectioned tissue samples	Tissue must be thoroughly thawed before IR analysis Once a sample is thawed, components may start to degrade, so we suggest imaging sections as soon as possible after thawing and drying, in a dark environment ¹³⁰ However, under dry conditions, cryosections can be stored for months without major problems other than lipid oxidation, as seen by the decrease of the ester carbonyl bands (degrades within 2 weeks; this can be avoided when samples are stored in a N_2 atmosphere)	Serial sections should be carefully isolated from the cryoblock to prevent OCT compound contamination of the final tissue slice	Snap-frozen tissue should be cut and placed onto slides	Although snap-freezing negates the use of fixatives such as formalin or the use of paraffin, it may damage the structural integrity of the tissue

(continued)

PROTOCOL

TABLE 2 | Sample types and preparation (continued).

Sample type	Preparation	Removal of contaminants	Sample mount	Considerations
Fixed cells	<p>Medium contaminants must be removed before cells are placed in fixative such as ethanol or formalin</p> <p>For formalin fixation, cells should be washed twice in PBS before suspension in formalin for at least 30 min</p> <p>Slides should be dipped three times in double-distilled water (this should not be extended beyond quick dips) as formalin fixation can be reversed in the presence of water⁹²</p> <p>For ethanol fixation, cells should be washed three times in ethanol (min. 70% (vol/vol)) before being left to stand in ethanol for at least 1 h</p>	<p>After formalin fixation, cells should be washed in HBSS before IR analysis to remove residual phosphate ions</p> <p>After ethanol fixation, slides should be left to dry for 24 h on the benchtop and 24 h in a desiccator so that all residual ethanol evaporates</p>	<p>Cells can be grown onto IR substrates that have been first sterilized in 70% (vol/vol) ethanol, as growing directly onto the slides can preserve cell morphology</p> <p>They can also be grown in a 3D culture matrix, which can then be fixed or frozen and sectioned; this may provide the most realistic environment in which cells can be studied</p>	<p>If grown on slides, cells will typically be thin, as they grow and stretch over a 2D surface</p> <p>Cells fixed and then placed onto slides may be uneven in thickness, which may be resolved using cytopinning, which allows cells to be proportionally dispersed over the substrate</p>
Live cells	<p>Cells that are to be analyzed in suspension should be detached from the growth substrate using trypsin and then stored at 4 °C to prevent autolysis¹³⁷</p> <p>For ATR-FTIR measurements, cells can be seeded and grown directly onto the ATR IRE using a cell chamber⁵⁹</p>	<p>Cells in suspension must be washed with PBS to remove residual medium or trypsin</p>	<p>Spectra recorded in an aqueous environment show minimal dispersion because the refractive index of aqueous medium for the background single-beam spectrum closely matches that of the cell for the sample spectrum⁴⁷</p> <p>Therefore, cell suspension can be placed onto the IR slides as microdroplets</p> <p>Cells can be grown directly onto a detachable IRE such as diamond for ATR-FTIR analysis</p> <p>Live cells can also be analyzed <i>in situ</i> by the use of microfluidic devices²¹</p>	<p>The critical β-DNA conformational marker bands are enhanced in the hydrated state², and thus can be used to determine the concentration of DNA in simple cells^{138,139}</p> <p>Single-cell micro-spectroscopy is inherently difficult because of the strong absorptivity of the water molecule, which can swamp the spectrum especially when the sample path length is > 10 μm (ref. 140)</p> <p>A bright source of IR photons is required to achieve a good SNR because the IR beam must usually pass through two IR transparent windows, cell medium and the hydrated cell, causing attenuation of the IR signal</p> <p>Thus, most measurements performed on single living cells with an FTIR microscope configuration use a synchrotron light source</p>

Environmental Imaging Facility (IRENI) at the Synchrotron Radiation Centre (SRC)) in the mid-IR region is 1,000 times brighter than a thermal globar source and thus may generate

enhanced SNR spectra when using apertures approaching the diffraction limit; however, when using an FPA detector, this cannot be exploited as the brightness is applied over a larger area. By

TABLE 3 | Typical conditions of the main variables affecting SNR in spectroscopy instruments.

Variable	Instrument options					
	FTIR			ATR-FTIR		
	Single-element detector		FPA	Single-element detector		FPA
Light source	Globar ^a	Synchrotron ^b	Globar ^c	Synchrotron ^d	Globar ^e	Globar ^f
Sampling aperture	15 × 15 to 150 × 150 μm	5 × 5 to 20 × 20 μm	700 × 700 μm FOV	50 × 50 to 175 × 175 μm	250–250 μm	60 × 60 to 700 × 700 μm
No. of co-additions	512	256	64 or 128	128	32	32
Spectral resolution	4 or 8 cm^{-1}	4 or 8 cm^{-1}	4 or 8 cm^{-1}	4 or 8 cm^{-1}	8 cm^{-1}	4 or 8 cm^{-1}

^aRef. 141. ^bRefs. 119,142. ^cRefs. 142,143. ^dRefs. 76,144. ^eRefs. 145,146. ^fPatented by Agilent Technologies¹⁴⁹.

using multiple beams, such as at IRENI, the single-beam disadvantage when using an FPA may be overcome.

It is important to consider that an optimized and well-aligned benchtop instrument is not considered to be inferior with regard to SNR or image quality to a general synchrotron-based machine⁶³. A number of options regarding the detector can also have an effect on the SNR, such as the choice between a thermal detector versus a quantum detector. A mercury cadmium telluride (MCT) quantum detector usually provides a superior SNR than, for example, a thermal detector such as a deuterated triglycine sulfate detector⁹⁶. An optimized cooling system in the detector, such as thermoelectrical cooling, will also reduce the dark current produced by the detector, which has been shown to have a detrimental effect on SNR^{97,98}. In addition, signal-related parameters can affect the SNR; for instance, an increase in the optical path length can reduce spectral quality, which has been particularly important in the analysis of aqueous samples such as biofluids³³. When producing spectral images with the help of multielement detectors, such as an FPA, one must consider optimizing the SNR. The authors point readers to the authoritative reference on FTIR spectroscopy by Griffiths and De Haseth³ for theoretical and instrumental discussions; this book has supported the authors since their undergraduate studies and continues to support them today³.

Water vapor and instrument purging. The presence of water vapor in the instrumentation and sample area can result in reduced transmission of IR light, potentially obscuring important spectral details even at low spectral resolutions often used in biomedical IR spectroscopy. Water vapor interference can be minimized by computational subtraction of a pure water vapor spectrum from the sample spectrum⁹⁹. The efficacy of this compensation is limited and it is therefore considered crucial before spectral acquisition to purge the instrumentation with dry air or nitrogen and/or desiccants to remove any water vapor that may contaminate spectra between 1,350 and 1,950 cm^{-1} , and between 3,600 and 3,900 cm^{-1} (ref. 100). By doing so, ambient CO_2 is also purged, thereby reducing its contribution to the spectra.

Acquisition of sample and background. Measurements of an FTIR absorption spectrum involve collecting a ‘single-beam’ spectrum.

A background single-beam spectrum provides the source intensity, as modified by the instrument; placing a sample in the beam path and measuring the single beam again, theoretically, provides just the additional effect of the sample absorbance. A logarithm (to the base 10) of the ratio of these quantities provides the absorbance, which is directly related to concentration by Beer’s law. With point spectra, a background spectrum is typically retained for recording 5–10 sample spectra and with each different sample to reduce the effects of constantly changing atmospheric conditions. As spectral maps are composed of a large number of point spectra acquired in a stepwise manner, it is necessary to set up background scans to be taken at set intervals (e.g., at the end of every row) to account for the atmospheric variation over the extended acquisition time⁶⁶. When acquiring spectral images, background spectra should be acquired over a defined time period, depending on the sample acquisition time.

Experimental design: data processing

Data processing is carried out in a sequence of steps (Fig. 3) and the most important factor determining its workflow is the analysis goal; typical spectroscopy software programs used are shown in Table 4. Here we describe two analysis goals: imaging and diagnosis. Other goals not covered here include pattern finding and biomarker identification^{101,102}.

Imaging is defined as data analysis that uses an unsupervised data processing method to reveal tissue structure on a ‘spectral cube’ acquired by a mapping or imaging technique. Imaging allows for the study of shape and penetration of important histopathological features on the basis of the underlying chemistry²⁸.

In contrast, a diagnosis using IR spectroscopy requires a more complex framework that uses supervised classification methods. A supervised data processing method is one that uses classes assigned *a priori* to each IR spectrum as teaching information to build models that are used later to predict the classes of a data set that does not have classes associated with its spectra^{103,104}. The modeling process for diagnosis requires separate training and testing stages and respective training and test data sets. The optimal size of a training data set (i.e., one that will maximize classification accuracy at a reasonable cost of data set generation) has been underinvestigated to date, but it has been suggested that it may be problem dependent¹⁰⁵. For example, in a study, one could

PROTOCOL

TABLE 4 | Some existing FTIR spectroscopy data analysis software.

Software	Website	Description	License
Cytospec	http://www.cytospec.com	Software for hyperspectral imaging (IR and Raman)	Commercial; free demo available
IRootLab	https://code.google.com/p/irootlab/	MATLAB toolbox for biospectroscopy data analysis	Open source
OPUS	http://www.bruker.com	Spectral acquisition software with data processing capabilities	Commercial
Pirouette	http://www.infometrix.com	Chemometrics modeling software	Commercial
Unscrambler X	http://www.camo.com	Multivariate data analysis and design of experiments	Commercial
PLS, MIA, EMSC toolboxes	http://www.eigenvector.com	MATLAB toolboxes for spectroscopy data analysis	Commercial
OMNIC	http://www.thermoscientific.com	Spectral acquisition software with data processing capabilities	Commercial
PyChem	http://pychem.sourceforge.net/	Package for univariate and multivariate data analysis	Open source
ENVI, IDL	http://www.exelisvis.com	Integrated development, data analysis and image processing suite	Commercial
MCR-ALS toolbox	http://www.cid.csic.es/homes/rtaqam/tmp/WEB_MCR/welcome.htm	MATLAB Toolbox implementing the MCR-ALS algorithm	Open source

start with ten samples (acquiring 5–10 spectra from each sample), creating a trained model with eight samples and testing the model using the remaining two samples; one could then repeat this procedure four more times, each time using two different samples for testing and the remaining eight samples for training (this is called five-fold cross-validation). The number of times that the classifier correctly guessed the class of the testing sample would be counted to calculate a classification rate (i.e., the number of correct guesses divided by the total number of guesses). Next, one could acquire spectra from an additional five samples and repeat the cross-validation process, comparing the new classification rate with the old one (it is expected to improve). The process of adding samples and repeating cross-validation could continue until the classification rate stops improving.

It is important to note that a diagnostic framework may be set to use either point spectra or image maps; in the latter case, the trained classification system can be used to predict tissue structure.

We describe the following data analysis steps: pre-processing, feature extraction (FE), clustering (unsupervised classification) and supervised classification, and we exemplify some visualization options in the ANTICIPATED RESULTS section. Quality control is another step that is not covered in this protocol, but there are guidelines on this available in the literature^{105,106}.

Pre-processing. Pre-processing essentially aims to improve the robustness and accuracy of subsequent multivariate analyses and to increase the interpretability of the data by correcting issues associated with spectral data acquisition¹⁰⁷. Pre-processing

methods may be divided into de-noising, spectral correction, normalization and other manipulations; two or three methods are often combined (e.g., de-noising followed by spectral correction and normalization). The choices of pre-processing methods may depend on the analysis goal, the physical state of the sample, and the time and computing power available.

De-noising of IR spectra may be carried out with Savitzki-Golay (SG) smoothing, minimum noise fraction¹⁰⁸ or wavelet de-noising (WDN)¹⁰¹. The latter is known to be the best method for eliminating high-frequency noise while still keeping intact high sharp peaks (this is essential in Raman spectra processing, but WDN works well on IR spectra too). Another option is to decompose the spectra by principal component analysis (PCA), and then reconstruct them from only a few of their principal components (PCs), thus discarding those PCs that represent mostly noise^{85,109}.

Measurement characteristics that may require spectral correction include:

- *Sloped or oscillatory baselines that result from scattering, with resonant Mie scattering in biological materials being the most pronounced effect.* The effects of sample (scattering centers, edges and substrates) have often been lumped together and the effects of the same on spectra are termed ‘artifacts’. Although this terminology was initially acceptable, it is now clear that there is a rational explanation for these effects and they arise merely from the coupling of morphology and optics. Hence, we will refer to these as morphological effects on spectra. There are two major efforts in understanding and resolving these effects to recover absorption spectra free from the effects of morphology. The first group

of methods is termed ‘physics based’. In this approach, explicit optical image-formation modeling from first principles is used to predict and correct data. Here each sample effect (boundary scattering, scattering centers in the sample and substrate) needs to be explicitly accounted for. The theory has been shown to be generally valid and there are methods now for correcting the same for films, spheres and fibers^{16,110,111}. Extension to more complex samples is still the subject of ongoing research. A second group of methods may be termed ‘model based’. In these methods, a model is assumed to explain all sample effects, typically, Mie scattering. Subsequently, rigorous theory is used to recover spectra, e.g., including extended multiplicative scattering correction (EMSC)¹¹², resonant Mie scattering correction (RMi-SC)^{113–115} and rubber band baseline correction¹¹⁶. An indirect way to deal with baseline slope is to apply first or second derivative to spectra using the SG algorithm. This alters the shape of the spectra, but may also resolve overlapped bands. Model-based methods will generally be faster than explicit modeling methods and may prove to be broadly useful but need to be validated in each case. A third approach, which was traditionally used but is now recognized to be of limited value, is to simply correct baselines with a piecewise linear approach. Obviously, this method is the fastest, as it requires the least effort to apply and no modeling. It is as yet unclear which of these methods works best.

- *Spectral contributions may arise from atmospheric water vapor, carbon dioxide, paraffin or other interfering compounds.* Although these artifacts may be compensated mathematically through EMSC¹¹⁷ or other least-squares-based technique¹¹⁸, the most common actions are to remove contaminated spectral bands from the data set, improve the control of atmospheric conditions or take background spectra more often. In this aspect, before pre-processing, it is often useful to implement quality tests to verify SNR and minimize water vapor contribution. By following this approach, ‘bad quality’ spectra are discarded as they can influence subsequent analysis. The threshold values for defining ‘bad’ and ‘good’ spectra can be adjusted according to the biological application.
- *It is vital to normalize IR spectra to account for confounding factors such as varying thickness of sample.* Common normalization methods are amide I/II peak normalization and vector normalization. Amide I/II normalization is often used after baseline correction, whereas vector normalization is often used after differentiation of spectra (after correction by differentiation, there is no longer a consistent amide I/II peak in the spectra to allow for amide I/II peak normalization). For imaging, leaving spectra non-normalized for chemical imaging or unsupervised clustering will reveal tissue structures primarily based on absorbance intensity, whereas normalization will highlight differences in biochemical structure. For diagnosis, some form of spectral normalization is conducted.

The optimal pre-processing method or sequence to apply is a subject of discussion and no universal best approach exists for all samples. Often the choices are based on the problems visually spotted in the spectra; a more objective criterion is to optimize the pre-processing method (e.g., through a genetic algorithm)¹¹⁹. In this protocol, we offer several alternatives based on cues identified by visual expression of raw (non-pre-processed) spectra, although objective validation will probably become more common in the future.

FE. FE methods process the IR spectra to form new variables based on the original variables (which are absorbance intensities).

FE has an important or even essential role in both imaging and diagnosis. For imaging, FE is responsible for generating a single value based on the whole of an input IR spectrum. This value can subsequently be used to set the color of a pixel in the image; FE is repeated for all spectra, thus forming the pseudocolor image. Popular FE methods for imaging include calculating the ratios between wavenumber absorbance intensities, area under a subregion of the spectrum, selecting a single wavenumber or an ensemble of wavenumbers, or performing PCA. PCA may be applied to the spectral data set, followed by selection of a single PCA factor for the color gradient.

For diagnosis, FE constitutes an important data reduction step in order to match the complexity of the subsequent supervised classifier with the amount of data available so as to avoid overfitting or undertraining. PCA is one particular popular form of unsupervised FE that is used for this purpose¹⁰³. The number of PCA factors to retain may be subject to optimization. One way out is to order the PCA factors from the most to the least discriminant on the basis of their *P* values as determined by a statistical test. The percentage of explained variance can also be taken into account. Within FE, the subgroup of feature selection (FS) methods is particularly interesting because it can confer biological interpretability (i.e., identify the wavenumbers most important for classification) to the classification system. Popular FS methods include forward FS¹²⁰ and COVAR¹²¹. Variance analyses may also be used to select spectral variables for elimination¹²². Another approach to FS is to use spectral features that are obtained from a biochemical understanding of the problem¹²³. These cases in which direct spectral interpretation is possible are termed metrics for measures of biochemical activity in the samples. It is important to note that not all metrics may be useful biomarkers. Thus, even FE may be a multistep process, (i.e., one in which metrics are converted to statistically relevant biomarkers).

Clustering (unsupervised classification). Clustering aims at sorting different objects (i.e., spectra) into categories or clusters on the basis of a so-called distance measure¹²⁴. Clustering methods such as hierarchical cluster analysis (HCA) and *k*-means clustering (KMC) are frequently used in IR-imaging studies to identify tissue morphology^{23,125}. HCA groups spectra into mutually exclusive clusters; in IR-imaging studies, HCA-based segmentation is achieved by assigning a distinct color to the spectra in one cluster. Because each spectrum of an IR-imaging experiment has a unique spatial (*x,y*) position, pseudocolor segmentation maps can be easily generated by plotting specifically colored pixels as a function of the spatial coordinates.

Supervised classification. Supervised or concept-driven classification techniques are machine-learning techniques for creating a classification function from training data. These methods involve a supervised learning procedure in which models are created that map input objects (spectra) to desired outputs (class assignments). Popular supervised techniques are artificial neural networks, support vector machines (**Supplementary Method 3**), linear discriminant classifier^{11,103,126} and Bayesian inference-base methods⁷⁷. Among the many criteria guiding the choice of classifier, the most important is probably the accuracy (related to sensitivity and specificity) when tested on an independent test data set. Other criteria include ease to train, computational time, spatial resolution considerations¹²⁷ and software availability.

PROTOCOL

Classifiers such as artificial neural networks and support vector machines may require a two-stage training, where the first stage is dedicated to finding optimal tuning parameters or architecture and the second stage fits the classifier model to the training data. Linear discriminant classifier (LDC) is a parameterless classifier

that requires only the fitting stage. A general rule of thumb is that if two different classifiers are equally well performing on an independent test data set, the simplest one should be preferred over the more complex one, as simpler classifiers are more likely to be better generalizers¹⁰³.

MATERIALS

REAGENTS

▲ **CRITICAL** For sample preparation and analysis, please refer to **Tables 1** and **2** and the INTRODUCTION for further information.

- FFPE blocks: see Reagent Setup for further information
- Sample preparation: advice regarding collection of biofluids, cryosectioned tissue samples, fixed cells and live cells can be found in the Reagent Setup section ! **CAUTION** Human tissues (including biofluids, cytology or FFPE blocks) should be obtained with appropriate local institutional review board (e.g., in the UK, this is a Local Research Ethics Committee (LREC)) approval; generally, ethical permission will be granted for a carefully designed study in which patient participants sign a consent form. Worldwide, studies using human tissues should adhere to the principles of the Declaration of Helsinki. Similarly, for research using animals, appropriate approvals are required; The Animals (Scientific Procedures) Act of 1986 is the legislation that regulates the use of animals in scientific procedures in the United Kingdom and this is enforced by the Home Office, which issues the licenses required.

Other reagents

- ThinPrep (PreservCyt Solution, Cytac)
- SurePath (TriPath Care Technologies)
- Formalin, 10% (vol/vol), neutral buffered (Sigma-Aldrich, cat. no. HT501128)
- **! CAUTION** It is a potential carcinogen, an irritant and an allergenic. Always work in a fume hood while handling it.
- Acetone (Fisher Scientific, cat. no. A/0600/17) ! **CAUTION** Its vapors may cause dizziness. Always work in a fume hood while handling it.
- Ethanol, 2.5 liters (Fisher Scientific, cat. no. E/0600DF/17)
- Virkon (Antec, DuPont, cat. no. A00960632) ! **CAUTION** It is an irritant.
- Paraplast Plus paraffin wax (Thermo Fisher Scientific, cat. no. SKU502004)
- Xylene (Sigma-Aldrich, cat. no. 534056) ! **CAUTION** It is a potential carcinogen, an irritant and an allergenic. Always work in fume hood while handling it.
- Histoclear (Fisher Scientific, cat. no. HIS-010-010S) ! **CAUTION** It is an irritant.
- Isopentane (Fisher Scientific, cat. no. P/1030/08) ! **CAUTION** It is an extremely flammable, irritant, aspiration hazard and toxic reagent. Always work in fume hood while handling it.
- Optimal cutting temperature (OCT) compound (Agar Scientific, cat. no. AGR1180)
- Liquid nitrogen (BOC, CAS no. 7727-37-9) ! **CAUTION** May cause asphyxiation and contact with skin will cause burns. Wear cryoprotective clothing and use it in a fume hood.

EQUIPMENT

Electronic equipment

For a list of commercial instruments available, please refer to **Table 5**

Substrate

- Low-E slides (Kevley Technologies, CFR)
- BaF₂ slides (Photox Optical Systems)
- Silicon multi-well plate (Bruker Optics)
- Superfrost slides: these can be obtained from various manufacturers, e.g., Menzel Glazer Superfrost slides (Menzel-Glaser, cat. no. AA00008132E); Thermo Scientific SuperFrost slides (Thermo Fisher Scientific); or Fisherbrand Superfrost slides (Fisher Scientific)

Accessories

- Coverslips (Thermo Fisher Scientific, cat. no. 102440)
- Specac Golden Gate single-reflection diamond ATR accessory (Specac)
- Microtomes: these can be obtained from various manufacturers, e.g., Microtome (Surgipath Medical Industries); Leica rotary microtomes (Leica Microsystems, Davy Avenue Knowlhill); or Bright Cryostat (Bright Instruments)
- Microtome blades: these can be obtained from various manufacturers, e.g., Feather disposable microtome blades S35 (VWR, cat. no. SURG08315E), Edge-Rite disposable microtome blades (Thermo Fisher Scientific);

or Leica Surgipath DB80 blade (Leica Microsystems) ! **CAUTION** Blades are extremely sharp; handle and dispose of them with care.

- Paraffin section mounting bath (40–75 °C; Electrothermal, cat. no. MH8515)
- Desiccator: these can be obtained from various manufacturers, e.g., desiccator (Duran Group) or WHEATON Dry-Seal vacuum desiccators (Wheaton Industries)
- Labofuge 400e (Heraeus Instruments)

REAGENT SETUP

FFPE blocks These are prepared according to the standard methods used routinely in all pathology laboratories; the overall steps are: immerse fresh

TABLE 5 | Instruments and corresponding data acquisition software.

Manufacturer	Instruments	Software
Agilent Technologies	Agilent 670-IR spectrometer	Resolutions Pro
	Cary 600 series FTIR spectrometers	
	Agilent 600 series FTIR microscope	
Bruker Optics	Bruker Tensor 27 spectrometer	OPUS
	ALPHA FT-IR spectrometer	
	HYPERION series FT-IR microscope	
	LUMOS FT-IR microscope	
JASCO UK	JASCO FTIR-4100 series	Spectra Manager
	JASCO FTIR-6000 series	
	IRT-5000 FTIR microscope	
PerkinElmer	PerkinElmer Frontier	Spectrum 10
	Spectrum Two	
	Spotlight FTIR microscope system	
Thermo Fisher Scientific	Thermo Nicolet iS50 spectrometer system	OMNIC 8
	Thermo Nicolet Scientific FTIR 5700 spectrometer with continuum microscope	
Shimadzu	IRTracer-100 spectrometer	Lab Solutions IR
	IRAffinity-1S spectrometer	

tissue in formalin solution that acts as a chemical fixative; dehydrate the tissue in sequential washes of xylene and ethanol; and embed the tissue in paraffin wax, which creates an airtight barrier. Tissue blocks can then be stored indefinitely at room temperature (20–22 °C).

Biofluids These are primarily blood plasma or serum, but can also potentially include cerebrospinal fluid, saliva or urine. Typically, after acquisition, such samples should be stored in appropriate tubes at –85 °C until they are thawed before analysis.

Cryosectioned tissue samples Tissue samples can be snap-frozen and stored at –80 °C before use. Tissue should be coated with optimal cutting temperature (OCT) compound before freezing, and it should be frozen with isopentane cooled with liquid nitrogen.

Fixed cells Typically, these would originate from cytology specimens placed in a fixative buffer; an ideal example of this is cervical cytology. However, it could be extended to any cell type isolated in the form of a suspension in a preservative buffer solution.

Live cells This is an emerging area within the field whereby viable cells can be spectrochemically analyzed, primarily in a constructed microfluidic platform (for a typical method, see **Supplementary Method 4**).

EQUIPMENT SETUP

Software Two types of software are required: spectral acquisition and data analysis. Spectral acquisition software is normally provided by the instrument manufacturer. Most instrumentation software also provides a number of preprocessing and sometimes more advanced data analysis options. Various data analysis software programs and packages exist, ranging from those for general purpose use to those targeting specific data analysis tasks (e.g., multiplicative curve resolution—alternating least squares (MCR-ALS)). A popular development environment and programming language is MATLAB (<http://www.mathworks.com>) in which customized software can be written for specific tasks. Python (<http://www.python.org>) is another programming language that is becoming increasingly popular in the FTIR spectroscopy field, and it has the advantage of being open source. For a list of commonly used software and packages, please refer to **Table 4**.

PROCEDURE

Sample preparation

1 Prepare the samples by following the steps listed in one of the options given below. Perform the steps in option A for FFPE tissue samples; option B for cryosectioned tissue samples; option C for cytological specimens; and option D for biofluids.

Live cells may be prepared in three main ways for IR-transmission studies: grown directly onto IR substrates; grown in a 3D culture matrix (and then processed as described in options A and B); or fixed in suspension, e.g., as cervical cytological specimens in fixative obtained from hospital pathology laboratories. Cells that are fixed in suspension should be processed by following the steps in option C.

To grow cells on IR substrates, sterilize the IR substrate for 1 h in 70% (vol/vol) ethanol before growing cells directly onto the chosen IR substrate.

Cells grown onto IR substrates	Sterilize the IR substrate for 1 h in 70% (vol/vol) ethanol before growing cells directly onto the chosen IR substrate. Generally, cellular materials are then fixed in order to preserve their architectural integrity, and the samples are stored in a desiccator prior to spectral acquisition (Step 2).
Cells grown in 3D culture matrix	Cells may be grown on 3D culture matrices (a tissue culture environment or device in which live cells can grow or interact with their surroundings in three dimensions), and subsequently fixed or snap-frozen and sectioned as described for tissue samples in Step 1A and Step 1B

(A) FFPE tissue • TIMING 50 min

- (i) Obtain FFPE tissue blocks of interest from a pathology laboratory.
- (ii) Place a FFPE block onto an ice block for 10 min. Use a microtome to trim into the block to expose the entire tissue sample to the face of the block. This will ensure that a full tissue section is cut for analysis. Place trimmed blocks back on ice for 10 min.

▲ CRITICAL STEP Make sure that the blocks are cold before cutting sections. This hardens the wax, reducing the friction between the block surface and blade allowing a much smoother cut.

- (iii) Cut a ribbon of 10-µm sections and float it onto a heated water bath (40–44 °C). Separate the individual sections with forceps.

▲ CRITICAL STEP Optimal tissue thickness for the maximum SNR should be determined in-house by applying variable thicknesses of sections (depending on the tissue type) to slides for IR interrogation, e.g., ~3 µm (e.g., for bone), 5 or 10 µm (e.g., for prostate tissue), and 15-µm serial sections to BaF₂, CaF₂ or Low-E slides. SNR is judged on the quality of the raw spectra; in particular, the presence of many narrow, sharp peaks indicates high noise. If using tissue for imaging and extraction of tissue cell type, sample thickness is not just an SNR issue. The thicker the tissue, the greater the chance of probing heterogeneous layers and perhaps multiple cell types, rendering the cell type signal less pure.

▲ CRITICAL STEP Depending on the melting point of the paraffin wax used for embedding tissue samples, the temperature of the water bath will need to be adjusted to prevent melting of the wax.

PROTOCOL

(iv) Prepare tissue slides by re-floating a single 10- μm -thick tissue section onto a BaF₂, CaF₂ or Low-E slide for FTIR microspectroscopy or ATR-FTIR spectroscopy. In our experience, a 5–10- μm section is the optimal thickness for maximum SNR.

▲ **Critical Step** As BaF₂ slides can be 1 cm \times 1 cm in size to fit common slide holders, a H&E-stained parallel section may be required to identify an area of interest for analysis. Once a section is floated onto the water bath, sections can be picked up on normal microscope slides, dissected using a scalpel for the area of interest and floated back onto water for application to BaF₂ slide.

(v) Place the tissue slide in a 60 °C oven for 10 min.

(vi) De-wax the tissue slide by immersing it in xylene for 5 min at room temperature. Repeat this step twice with fresh xylene. For small, round slides that are difficult to handle during solvent immersion, slides can be encased into plastic histology cassettes that can be threaded round a large metal clip. The same procedure can be conducted using hexane.

▲ **Critical Step** For IR analysis, it is necessary to de-wax the tissue in order to probe unhindered the full wavenumber range. This is paramount as paraffin is known to have significant peaks at \sim 2,954, 2,920, 2,846, 1,462 and 1,373 cm⁻¹. If there is uncertainty about paraffin removal, these regions of the spectrum can be removed from subsequent analysis. However, this comes at the cost of probing many solvent-resistant methylene components of the native tissue^{128,129}.

(vii) Sequentially, wash and clear the tissue slide by immersing it in acetone or 100% ethanol for 5 min at room temperature.

(viii) Allow the tissue slide to air-dry before placing it into an adequate-sized Petri dish for storage in a desiccator.

■ **Pause Point** Slides can be stored in a desiccator before IR interrogation; in our experience, storage should be <1 year.

(B) Snap-frozen and cryosectioned tissue samples ● **TIMING** 120 min + drying time (3 h)

! **Caution** Snap-freezing should be carried out in a fume hood while you are wearing cryoprotective gloves, clothing and a facemask.

(i) The fresh tissue should be no more than 2 cm in any one dimension; gently blot away any fluids from the surface, place a cryomold and fill the mold with OCT compound.

(ii) Fill a plastic cryobucket with 3–4 cm of liquid nitrogen. Pour isopentane into the stainless steel beaker until it is about 1–2 cm deep. Place the stainless steel beaker into the liquid nitrogen and allow temperatures to equilibrate (3–5 min).

(iii) Take the cryomold containing the tissue sample in OCT compound and use long forceps to lower it into the isopentane; hold until the OCT compound freezes (60–90 s).

(iv) Remove the cryomold and transfer it to the bucket of dry ice. Wrap snap-frozen tissue in aluminum foil and label it before storing it in –80 °C freezer.

■ **Pause Point** Snap-frozen tissue can be stored in a –80 °C freezer for several months.

(v) Retrieve previously prepared snap-frozen tissue blocks from the –80 °C freezer and transfer them to the cryostat in dry ice to prevent thawing.

(vi) Unwrap the frozen block from its protective foil covering and mount it into the cryostat. Allow the block to equilibrate to the cryostat temperature for 30 min. The optimum cryostat cutting temperature will depend on the sample, but –20 °C will be suitable for most tissues.

(vii) Cut sections with a cryostat until the region of interest is reached. Next, take serial sections of the tissue sample at the desired thickness for your study.

(viii) Carefully mount the sections onto the substrate window. Immediately upon acquiring the cryosection, transfer the slides to a slide box on dry ice, wrap them in foil and store them at –80 °C to preserve the biochemical content.

(ix) Before imaging, bring slides to room temperature in a dark slide box with desiccant for several hours (minimum 3 h) until they are dry.

▲ **Critical Step** The tissue needs to be adequately thawed before IR analysis (freezing and thawing may also damage the structural integrity of the tissue). During the thawing process, store the sample under dark, dry conditions at room temperature. Light exposure is only advised during the short time required for the instrumental setup; this maintains the stability of spectral acquisition. Room lights and bright-field microscope illumination should be switched off during measurement collection¹³⁰.

(C) Cytological specimens ● **TIMING** 30 min + desiccation time (24 h)

(i) For formalin fixation, cellular pellets should be washed twice in PBS to remove culture medium before resuspension in formalin solution (in which they should remain for at least 30 min). Before IR analysis, cells should be washed with HBSS to wash out the residual phosphate ions.

▲ **Critical Step** SurePath and ThinPrep fixative solutions, used in hospital pathology laboratories, have IR signatures in the biochemical cell-fingerprint region and should therefore be removed from the sample by sequential washes before analysis. Alcohol-based fixatives may remove some lipids from the sample.

- (ii) Resuspend the remaining cell pellet in 0.5 ml of distilled water, transfer the cells to the appropriate IR slide and allow them to air-dry before storing in a desiccator. Cells may be transferred to a slide as microdroplets, or they can be cytospun.
- (iii) For cytopinning, take a maximum volume of 200 μ l of cells in suspension (spin-fixed cells at 800g (g force = $0.0000118 \times$ radius of rotation (mm) \times r.p.m. 2) for 5 min). After spinning, leave the slide to air-dry for 24 h; the centrifugal force will have squashed the cells onto the slide, but if you try to wash the slides with water straight away you might lose them. After this time, wash the slide with 1-ml aliquots of deionized water three times (at around 5–10 s per wash, more water can be used if found necessary and cells stick adequately). The cells will remain on the slide and can always be washed further if traces of salts remain.

▲ **Critical Step** When transferring the cellular material to the slide, ensure that an even deposit of cells is placed on the slide. Cytospinning allows the cells to be proportionally dispersed over the substrate. If the cells are particularly small, they may ‘bounce’ off the slide during the spinning instead of getting stuck down. In this case, do a 5-min spin at 400g, then another 5-min spin at 800g to ensure firm plating.

(D) Biofluids ● **TIMING 10 min**

- (i) Biofluids (i.e., urine, serum, plasma and saliva) should be immediately stored at -80°C in cryovials after collection from pathology laboratories and thawed at room temperature before use.
- (ii) Samples of biofluids are painted directly onto the aperture (e.g., for ATR analysis) or a standard amount is pipetted onto suitable IR substrates (50–250 μ l would be typical, but depending on the biofluid, preliminary analysis would be needed).
- (iii) Samples are allowed to dry before analysis.

▲ **Critical Step** Contact of the sample with the crystal is a very important parameter for ATR-FTIR analysis. If you are using an aperture ATR-FTIR accessory, 1 μ l of sample has been shown to be dry within 8 min⁴⁴.

Acquisition of spectra

2| Acquire spectra by ATR-FTIR spectroscopy (option A) or transmission FTIR microspectroscopy (option B) or FPA. A standard operating procedure for direct-drop ATR-FTIR for biofluid analysis is included in **Supplementary Method 1**; this would primarily be used when very small aliquots of the sample are available. A standard operating procedure for FTIR-FPA imaging with an Agilent 670-IR spectrometer coupled with an Agilent 620-IR microscope and FPA detector is included in **Supplementary Method 2** (this file also contains a troubleshooting section).

(A) ATR-FTIR spectroscopy ● **TIMING 20 min (10 spectra)**

- (i) Open the instrument-operating software.
- (ii) Apply instrumental settings (guidelines are described in ‘Experimental design: spectral acquisition’).
- (iii) Check the path where files are to be saved; set the file name according to a previously devised file-naming convention.
- (iv) Visualize the sample through the instrument digital camera to locate the region of interest from which you wish to acquire the spectrum.
- ▲ **Critical Step** If the instrument has been switched off, make sure you check the interferogram signal for the correct location and amplitude. The system may need to be re-aligned if it has been moved or if components have been changed.
- (v) Clean the ATR IRE with distilled water and dry it with tissue.
- ▲ **Critical Step** Make sure that the crystal is thoroughly cleaned and dried before a background acquisition.
- (vi) To acquire a background spectrum, the IRE should not be in contact with the sample or slide, and it should be open to the surrounding environment. Record a background spectrum.
- ▲ **Critical Step** It is very important that a background spectrum is taken before every sample. Also, a background spectrum should be taken if atmospheric changes occur (e.g., if a door has been suddenly opened).
- (vii) Place the slide in contact with the IRE.
- ▲ **Critical Step** Ensure that the ATR IRE is completely covered by the sample and that the minimum sample thickness is 3–4 times the depth of penetration to ensure that there is no interference from the substrate.
- (viii) Acquire a spectrum.

(B) FTIR microspectroscopy ● **TIMING 1 h per sample (~12 spectra) or 6 h per sample (image map, ~72 spectra)**

- (i) Switch on the microscope and instrument.
- (ii) Fill the detector with liquid N_2 .
- ▲ **Critical Step** If you are using a MCT detector, filling it with liquid N_2 is essential; allow the detector (and therefore the signal) to stabilize (~10 min) to an optimal peak-to-peak value. Top up with N_2 every 9 h (depending on the instrument).
- (iii) Open the instrument-operating software.
- (iv) Apply settings.

PROTOCOL

- (v) Use the software to get a view of the slide as seen through the microscope.
- (vi) Load the sample onto the stage and focus the microscope.
- (vii) To check the signal quality, move to a sample-free area of the slide and adjust the position to bring the surface of the blank area of the substrate into focus.
- (viii) In our experience, the optimal sample aperture for a benchtop FTIR spectrometer with a globar source is $20\text{ }\mu\text{m} \times 20\text{--}100\text{ }\mu\text{m} \times 100\text{ }\mu\text{m}$ (dependent on sample quality and instrumental limitations). Apply the aperture size.

▲ **CRITICAL STEP** Optimization of the aperture size should be performed to confirm the smallest possible aperture that can be used to acquire spectra with a high SNR.

TROUBLESHOOTING

- (ix) Use the joystick to move the sample around the microscope stage to identify points or areas to interrogate.
- (x) Select a clean, sample-free point on the slide and acquire a background spectrum according to your device.

▲ **CRITICAL STEP** Acquire a background spectrum each time the detector is filled with liquid N_2 and at regular intervals (or before each sample) to account for atmospheric changes.

- (xi) Acquire a sample measurement either as a point map or as an image map.

A point map Select a number and location of points of interest

Image map Use automatic allocation of adjacent points in a grid

▲ **CRITICAL STEP** Be sure to define a number of points (or map size) that does not exceed the scheduled time frame of the liquid N_2 top-up.

▲ **CRITICAL STEP** The integration time is essentially a measure of the time for which the shutter is open to collect the incoming photons. The aim is to optimize the SNR without saturating the detector. If the integration time is too high, the user will observe saturation effects in the FTIR images; if it is too low, the data quality and SNR will be reduced as the FPA has not been fully illuminated. This calibration is a nonuniformity correction, and results are shown with measures of high and low flux (in counts) and the number of out-of-range pixels.

- (xii) Acquire spectra.

■ **PAUSE POINT** Once the spectra are saved they can be stored in a database until data processing.

Data pre-processing ● **TIMING** 15 min–4 h (depending on the size of the data set)

▲ **CRITICAL** Steps 3–7 below all contain different options at each step; however, there are combinations of these steps that may be more or less appropriate than others, depending on the sample type, instrumentation setup, noise level, need for visualization of spectra, personal preference and classification performance among other factors (Table 4). Although they are usually carried out in the sequence presented, none of the steps from 3 to 7 are mandatory. For guidelines on choosing specific preprocessing steps and options, please refer to the ‘Experimental design data processing’ section. The reader may also refer to the **Supplementary Method 3** for an illustrated example of a pre-processing sequence applied to a real-world data set using specific software.

3| De-noise the spectra (optional, depending on the SNR of the spectra). Consider using one of the following de-noising algorithms: Savitzky-Golay de-noising, WDN (not commonly used, but is a nonlinear method with its own advantages), PCA noise reduction or minimum noise fraction.

4| Perform spectral correction, which can be carried out using physical theory-based methods such as RMieSC or rubber band baseline correction^{49,53,113–115}.

5| Perform SG differentiation (first differentiation is most used; second differentiation is also common).

6| Perform data normalization. This can be done using min-max normalization (e.g., normalization to the amide I/II peak) or vector normalization.

7| Scale the variables: this could be done by standardization (normalization of variables to zero mean and unit s.d.) or by normalization to a 0–1 range.

Data analysis ● **TIMING** 1 h–2 d (depending on file size)

8| Choose a data analysis procedure appropriate to your analysis goal; here we cover diagnosis (supervised classification; option A below) and imaging (options B–D). For option A, data sets obtained with a single-element IR detector are normally

used and the physical location of one spectrum within its sample is used in the data analysis. The procedures for creating an image use a data set acquired by point or array mapping, or an FPA detector. Each spectrum has its Cartesian (x, y) location. There are three different options for achieving this step (options B–D). Options B and C are suitable for chemical imaging using the FE method and unsupervised classification, respectively. Option D (supervised classification) is suitable for spatial diagnosis of tissues. It uses a training set of images to build a model to subsequently apply this model to unknown images. After performing options B, C or D, follow the instructions in option E.

(A) Diagnosis (supervised classification)

▲ **CRITICAL** Training and test data sets are required. In rare cases, one single training and test data set pair could be enough to obtain a meaningful estimation of real-world classification; however, most of the time such estimation is obtained through cross-validation, in which the procedure below (training and testing) is repeated multiple times to get an average performance (or error) estimation.

- (i) *FE training.* Input pre-processed training data set into the FE algorithm of your choice (see 'Experimental design: data processing') in training mode. Generate a model that will be able to subsequently extract features from a test data set.
- (ii) *Classifier training.* Apply the FE model obtained in a previous step to the training data set. Next, input the FE-processed data set to the classification algorithm of your choice (see 'Experimental design: data processing') in training mode. Generate a model to be subsequently applied to test data set.
- (iii) *Testing.* Apply the trained FE model to the test data set to obtain an FE-processed output data set; input the FE-processed data set into classification model to obtain one-class estimation per spectrum. If there are several spectra per sample, conduct a 'majority vote' procedure to obtain one class estimation per sample.

▲ **CRITICAL STEP** Training and testing should be repeated through a cross-validation procedure, depending on the sample size.

(B) Chemical imaging using an FE method

- (i) *Map each spectrum into a single scalar value.* Choose an FE technique to obtain a scalar value for each spectrum (this value will be subsequently used to address a particular color within a gradient color map). Refer to 'Experimental design: data processing' for guidelines on choosing the FE method.
- (ii) Continue to Step 8E.

(C) Clustering (unsupervised classification)

- (i) Apply a clustering algorithm (e.g., HCA or k -means) to organize the spectra into clusters.
- (ii) Assign a different integer number to each cluster and continue to Step 8E.

(D) Supervised classification for imaging

- (i) Conduct histological assessment of the training set to identify different regions within the training set images; this will be used as teaching information for the supervised learning algorithms.
- (ii) Apply Step 8A(i,ii), using the training data set obtained in the previous step to obtain a classification model.
- (iii) Apply the model to the test data to obtain one class estimation per spectrum in the image.
- (iv) Assign a different integer number to each class and continue to Step 8E.

(E) Mapping different scalar values to different color tones

- (i) Map different scalar values obtained in previous steps into different color tones. For chemical imaging (Step 8B), a gradient color map is used (e.g., red to yellow, rainbow and so on), whereas for Step 8C and Step 8D, an indexed color map in which each cluster or class is represented by a color of choice is suitable. Although the idea is presented here for understanding, this step is normally carried out by imaging software.

?

TROUBLESHOOTING

Optimizing the sample aperture

To overcome the problem of over- and undersampling for fine imaging, the spatial sampling area should be at least two times larger than the (spatial) frequency of the feature under study. The step size should be equal or smaller than the aperture size divided by 2.

For Troubleshooting for FTIR imaging with an Agilent 620 IR microscope coupled with an Agilent 670/680 IR spectrometer, see **Supplementary Method 2**.

● TIMING

Step 1A, FFPE tissue: 50 min

Step 1B, snap-frozen and cryosectioned tissue samples: 120 min + drying time (3 h)

Step 1C, cytological specimens: 30 min + desiccation time (24 h)

Step 1D, biofluids: 10 min

Step 2A, ATR-FTIR spectroscopy: 20 min (10 spectra)

Step 2B, FTIR microspectroscopy: 1 h per sample (~12 spectra) or 6 h per sample (Image map, ~72 spectra)

PROTOCOL

Figure 5 | Classification rates (% classification \pm s.d.) of all possible combinations between three different pre-processing, three different feature extraction and two different supervised classifier options. Pre-processing options: rubber band baseline correction followed by normalization to the amide I peak; first Savitzky-Golay (SG) differentiation (7 points; second order) followed by vector normalization; and second SG differentiation followed by vector normalization. FE options: PCA (optimization of number of PCs); forward feature selection (FFS) using multivariate analysis of variance (MANOVA) *P* values as a criterion to including the next variable (this is similar to the COVAR method for optimization of number of selected features); and 'Identity' (FE skipped). Supervised classifier options: linear discriminant classifier (LDC); and support vector machine (SVM; using Gaussian kernel; optimization of the *C* and γ parameters^{133,134}). The figure's cells are gradient-colored according to their respective classification rate inside (yellow to red). RBBC, rubber band baseline correction.

Pre-processing	Feature extraction	Classifier	
		LDC	SVM
RBBC \rightarrow Amide I norm	PCA	83.25 \pm 11.50	79.75 \pm 10.88
	FFS(MANOVA)	82.00 \pm 11.50	76.42 \pm 19.42
	Identity	75.42 \pm 12.66	77.25 \pm 13.28
1st diff \rightarrow Vector norm	PCA	77.58 \pm 15.77	80.75 \pm 12.29
	FFS(MANOVA)	78.83 \pm 13.71	84.25 \pm 16.15
	Identity	81.08 \pm 09.98	77.75 \pm 19.02
2nd diff \rightarrow Vector norm	PCA	78.17 \pm 15.12	72.50 \pm 17.23
	FFS(MANOVA)	82.67 \pm 11.78	76.83 \pm 14.69
	Identity	77.42 \pm 17.05	76.42 \pm 11.35

Steps 3–7, data pre-processing: 15 min–4 h (depending on the size of the data set)
Step 8, data analysis: 1 h–2 d (depending on the file size)

ANTICIPATED RESULTS

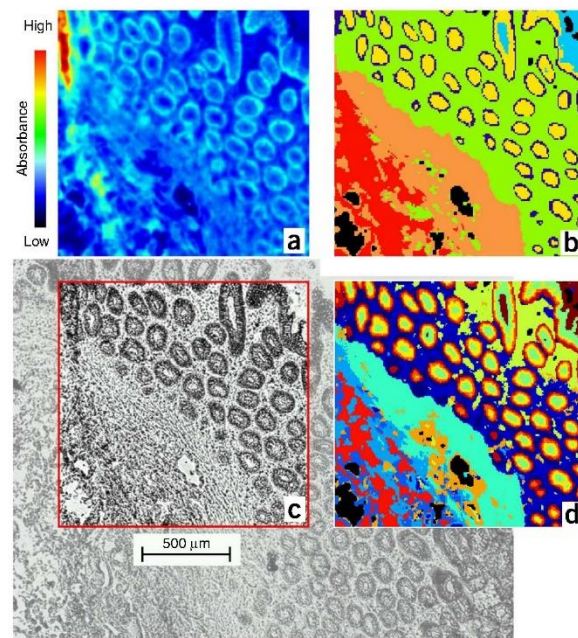
Preprocessing options

Figure 4 is a basic example that shows a set of ATR-FTIR raw spectra (cut to the 1,800–900 cm⁻¹ region) and their appearance after being pre-processed by different methods. Rubber band baseline correction is one of the options to remove sloped baselines. Normalization to the amide I/II peak shifts and scales all the spectra so that their vertical minimum is at zero and the amide I/II peak of all spectra match at the same height. To resolve overlapping bands, mathematical derivatives are used to narrow their full width at half height value (FWHH). Narrower bandwidths (i.e., higher resolution of differential spectra) potentially allow for subtle differences between spectra to be more easily resolved. However, each differentiation amplifies noise and therefore the SG differentiation algorithm (with implicit de-noising) is often used. Vector normalization is applied after differentiation to normalize the Euclidean norm of each spectrum to unity.

Classification of blood plasma

This example shows a comparison of supervised classification performance between different combinations of pre-processing, FE and supervised classification methodologies (**Fig. 5**). This data set consisted of blood serum and plasma samples of patients with ovarian cancer or endometrial cancer (*n* = 30 for both) and control patients without ovarian cancer (*n* = 30) analyzed with ATR-FTIR spectroscopy (7 spectra per sample)^{41,131}. The classification rate, defined as the average between sensitivity and specificity, was used as a classification performance measure to class patients on the basis of their disease

status (i.e., 'normal' versus 'cancer'). The example illustrates that no single pre-processing, FE or supervised classification methodology is the absolute best, but a combination of these may be the best solution to the problem posed. The counterpoint to this is that different data sets may require different pre-processing, FE and/or supervised classifier methodologies, as pointed to in the machine-learning literature¹⁰³. This is evidence that different combinations of methodologies should be attempted and compared in any diagnostic study.



Imaging of human colon mucosa in Cytospec using agglomerative HC and KMC

An example of imaging of human colon mucosa sections by using agglomerative hierarchical clustering and KMC is shown in **Figure 6**. The image was produced using the Cytospec software. **Figure 6c** shows the original histological image from which FTIR spectra were recorded at a spatial

Figure 6 | IR image reconstruction of a section of human colon mucosa. (a) Chemical map based on the integrated absorbance of the amide I band (1,620–1,680 cm⁻¹). (b) IR imaging using agglomerative HCA (six clusters). (c) Standard histological preparation of the colonic mucosa. (d) IR map generated on the basis of *k*-means clustering (15 clusters). Adapted with permission from ref. 135.

resolution of 232×233 pixels. Some images (Fig. 6b,d) have been reconstructed using the multivariate methods of agglomerative hierarchical clustering (AHC) and KMC, respectively, with both demonstrating clear differentiation of the histological structures of the sample analyzed.

Note: Any Supplementary Information and Source Data files are available in the online version of the paper.

ACKNOWLEDGMENTS Over several years, work in F.L.M.'s laboratories has been funded by the UK Engineering and Physical Sciences Research Council (EPSRC), the Rosemere Cancer Foundation and the UK Biotechnology and Biological Sciences Research Council (BBSRC). Work in R.B.'s laboratories has been funded by the US National Institutes of Health (grants R01CA138882 and R01EB009745). M.J.W. acknowledges the Department of Pathology, University of Illinois at Chicago for funding. P.R.F. and P.G. acknowledge the EPSRC. M.J.B. acknowledges the Rosemere Cancer Foundation, the EPSRC, Brain Tumour North West, the Sydney Driscoll Neuroscience Foundation and the Defence Science and Technology (Dstl).

AUTHOR CONTRIBUTIONS F.L.M. is the principal investigator who conceived the idea for the manuscript; M.J.B. and K.M.D. provided information regarding FTIR FPA imaging; and P.R.F. provided information regarding microfluidic devices; J.T. wrote sections regarding Data processing, ANTICIPATED RESULTS and Figures, as well as maintaining a working manuscript; H.J.B. wrote the Instrumentation and Spectral acquisition sections; K.A.H. and B.O. wrote the Sample preparation and MATERIALS sections; R.J.S. wrote the INTRODUCTION and PROCEDURE, and contributed to the ANTICIPATED RESULTS section; C.H. provided material for Sample preparation, PCA-k-means clustering and cross-validation; P.L. provided figure suggestions and information regarding water vapor; B.R.W. provided information regarding live-cell imaging; R.B. provided significant revisions to the final manuscript; M.J.B., P.B., K.M.D., N.J.F., C.H., P.L., P.L.M.-H., G.D.S., J.S.-S., M.J.W., S.W.F., B.R.W. and P.G. all provided feedback on the manuscript; and F.L.M. brought together the text and finalized the manuscript.

COMPETING FINANCIAL INTERESTS The authors declare competing financial interests: details are available in the online version of the paper.

Reprints and permissions information is available online at <http://www.nature.com/reprints/index.html>.

1. Bellisola, G. & Sorio, C. Infrared spectroscopy and microscopy in cancer research and diagnosis. *Am. J. Cancer Res.* **2**, 1–21 (2012).
2. Diem, M., Romeo, M., Boydston-White, S., Mijikovic, M. & Matthaus, C. A decade of vibrational micro-spectroscopy of human cells and tissue (1994–2004). *Analyst* **129**, 880–885 (2004).
3. Griffiths, P. & De Haseth, J.A. *Fourier Transform Infrared Spectrometry* 2nd edn. (John Wiley & Sons, 2007).
4. Walsh, M.J. *et al.* FTIR microspectroscopy coupled with two-class discrimination segregates markers responsible for inter-and intra-category variance in exfoliative cervical cytology. *Biomark. Insights* **3**, 179–189 (2008).
5. Bhargava, R., Wall, B.G. & Koenig, J.L. Comparison of the FT-IR mapping and imaging techniques applied to polymeric systems. *Appl. Spectrosc.* **54**, 470–479 (2000).
6. Bhargava, R. Infrared spectroscopic imaging: the next generation. *Appl. Spectrosc.* **66**, 1091–1120 (2012).
7. Colarusso, P. *et al.* Infrared spectroscopic imaging: from planetary to cellular systems. *Appl. Spectrosc.* **52**, 106–120 (1998).
8. German, M.J. *et al.* Infrared spectroscopy with multivariate analysis potentially facilitates the segregation of different types of prostate cell. *Biophys. J.* **90**, 3783–3795 (2006).
9. Walsh, M.J. *et al.* Fourier transform infrared microspectroscopy identifies symmetric PO_2^- modifications as a marker of the putative stem cell region of human intestinal crypts. *Stem Cells* **26**, 108–118 (2008).
10. Kelly, J.G. *et al.* Derivation of a subtype-specific biochemical signature of endometrial carcinoma using synchrotron-based Fourier-transform infrared microspectroscopy. *Cancer Lett.* **274**, 208–217 (2009).
11. Romeo, M.J. *et al.* In Vibrational Spectroscopy for Medical Diagnosis (eds. Diem, M., Lasch, P., & Chalmers, J.) (John Wiley & Sons, 2008).
12. Diem, M. *et al.* Comparison of Fourier transform infrared (FTIR) spectra of individual cells acquired using synchrotron and conventional sources. *Infrared Phys. Technol.* **45**, 331–338 (2004).
13. Kole, M.R., Reddy, R.K., Schulmerich, M.V., Gelber, M.K. & Bhargava, R. Discrete frequency infrared microspectroscopy and imaging with a tunable quantum cascade laser. *Anal. Chem.* **84**, 10366–10372 (2012).
14. Bhargava, R. & Levin, I.W. *Spectrochemical Analysis Using Infrared Multichannel Detectors* (Wiley-Blackwell, 2005).
15. Davis, B.J., Carney, P.S. & Bhargava, R. Theory of mid-infrared absorption microspectroscopy: II. Heterogeneous samples. *Anal. Chem.* **82**, 3487–3499 (2010).
16. Davis, B.J., Carney, P.S. & Bhargava, R. Theory of mid-infrared absorption microspectroscopy: I. Homogeneous samples. *Anal. Chem.* **82**, 3474–3486 (2010).
17. Filik, J., Frogley, M.D., Pijanka, J.K., Wehbe, K. & Cinque, G. Electric field standing wave artefacts in FTIR micro-spectroscopy of biological materials. *Analyst* **137**, 853–861 (2012).
18. Bassan, P., Sachdeva, A., Lee, J. & Gardner, P. Substrate contributions in micro ATR of thin samples: Implications for analysis of cells, tissue and biological fluids. *Analyst* **38**, 4139–4146 (2013).
19. Miljković, M., Bird, B., Lenau, K., Mazur, A.I. & Diem, M. Spectral cytopathology: new aspects of data collection, manipulation and confounding effects. *Analyst* **138**, 3975–3982 (2013).
20. Cao, J. *et al.* Fourier transform infrared microspectroscopy reveals that tissue culture conditions affect the macromolecular phenotype of human embryonic stem cells. *Analyst* **38**, 4147–4160 (2013).
21. Chan, K.L.A. & Kazarian, S.G. Aberration-free FTIR spectroscopic imaging of live cells in microfluidic devices. *Analyst* **138**, 4040–4047 (2013).
22. Kallenbach-Thielges, A. *et al.* Immunohistochemistry, histopathology and infrared spectral histopathology of colon cancer tissue sections. *J. Biophotonics* **6**, 88–100 (2013).
23. Lasch, P., Haensch, W., Naumann, D. & Diem, M. Imaging of colorectal adenocarcinoma using FT-IR microspectroscopy and cluster analysis. *Biochim. Biophys. Acta* **1688**, 176–186 (2004).
24. Bassan, P. *et al.* Whole organ cross-section chemical imaging using label-free mega-mosaic FTIR microscopy. *Analyst* **138**, 7066–7069 (2013).
25. Nakamura, T. *et al.* Microspectroscopy of spectral biomarkers associated with human corneal stem cells. *Mol. Vis.* **16**, 359–368 (2010).
26. Hammiche, A., German, M.J., Hewitt, R., Pollock, H.M. & Martin, F.L. Monitoring cell cycle distributions in MCF-7 cells using near-field photothermal microspectroscopy. *Biophys. J.* **88**, 3699–3706 (2005).
27. Walsh, M.J. *et al.* Tracking the cell hierarchy in the human intestine using biochemical signatures derived by mid-infrared microspectroscopy. *Stem Cell Res.* **3**, 15–27 (2009).
28. Wood, B.R., Bamberg, K.R., Evans, C.J., Quinn, M.A. & McNaughton, D. A three-dimensional multivariate image processing technique for the analysis of FTIR spectroscopic images of multiple tissue sections. *BMC Med. Imaging* **6**, 12 (2006).
29. Bird, B. *et al.* Cytology by infrared micro-spectroscopy: Automatic distinction of cell types in urinary cytology. *Vib. Spectrosc.* **48**, 101–106 (2008).
30. Baker, M.J. *et al.* FTIR-based spectroscopic analysis in the identification of clinically aggressive prostate cancer. *Br. J. Cancer* **99**, 1859–1866 (2008).
31. Bird, B. *et al.* Infrared micro-spectral imaging: distinction of tissue types in axillary lymph node histology. *BMC Clin. Pathol.* **8**, 8 (2008).
32. Bird, B. *et al.* Detection of breast micro-metastases in axillary lymph nodes by infrared micro-spectral imaging. *Analyst* **134**, 1067–1076 (2009).
33. Naumann, D. *et al.* Cells and biofluids analyzed in aqueous environment by infrared spectroscopy. *Biomed. Opt.* **10**, 609301 (2005).
34. Walsh, M.J., Holton, S.E., Kajdacsy-Balla, A. & Bhargava, R. Attenuated total reflectance Fourier-transform infrared spectroscopic imaging for breast histopathology. *Vib. Spectrosc.* **60**, 23–28 (2012).
35. Ooi, G.J. *et al.* Fourier transform infrared imaging and small angle X-ray scattering as a combined biomolecular approach to diagnosis of breast cancer. *Med. Phys.* **35**, 2151–2161 (2008).
36. Nallala, J. *et al.* Infrared imaging as a cancer diagnostic tool: Introducing a new concept of spectral barcodes for identifying molecular changes in colon tumors. *Cytometry Part A* **83**, 294–300 (2013).
37. Bird, B. *et al.* Infrared spectral histopathology (SHP): a novel diagnostic tool for the accurate classification of lung cancer. *Lab. Invest.* **92**, 1358–1373 (2012).

PROTOCOL

38. Baker, M.J. *et al.* Investigating FTIR-based histopathology for the diagnosis of prostate cancer. *J. Biophotonics* **2**, 104–113 (2009).
39. Gazi, E. *et al.* A correlation of FTIR spectra derived from prostate cancer biopsies with Gleason grade and tumour stage. *Eur. Urol.* **50**, 750–761 (2006).
40. Walsh, M.J. *et al.* IR microspectroscopy: potential applications in cervical cancer screening. *Cancer Lett.* **246**, 1–11 (2007).
41. Gajjar, K. *et al.* Fourier-transform infrared spectroscopy coupled with a classification machine for the analysis of blood plasma or serum: a novel diagnostic approach for ovarian cancer. *Analyst* **138**, 3917–3926 (2013).
42. Ollesch, J. *et al.* FTIR spectroscopy of biofluids revisited: an automated approach to spectral biomarker identification. *Analyst* **138**, 4092–4102 (2013).
43. Scaglia, E. *et al.* Noninvasive assessment of hepatic fibrosis in patients with chronic hepatitis C using serum Fourier transform infrared spectroscopy. *Anal. Bioanal. Chem.* **401**, 2919–2925 (2011).
44. Hands, J. *et al.* Investigating the rapid diagnosis of gliomas from serum samples using infrared spectroscopy and cytokine and angiogenesis factors. *Anal. Bioanal. Chem.* **405**, 7347–7355 (2013).
45. Munro, K.L. *et al.* Synchrotron radiation infrared microspectroscopy of arsenic-induced changes to intracellular biomolecules in live leukemia cells. *Vib. Spectrosc.* **53**, 39–44 (2010).
46. Tobin, M.J. *et al.* FTIR spectroscopy of single live cells in aqueous media by synchrotron IR microscopy using microfabricated sample holders. *Vib. Spectrosc.* **53**, 34–38 (2010).
47. Whelan, D.R., Bamberg, K.R., Puskar, L., McNaughton, D. & Wood, B.R. Synchrotron Fourier transform infrared (FTIR) analysis of single living cells progressing through the cell cycle. *Analyst* **138**, 3891–3899 (2013).
48. Kuimova, M.K., Chan, K.L.A. & Kazarian, S.G. Chemical imaging of live cancer cells in the natural aqueous environment. *Appl. Spectrosc.* **63**, 164–171 (2009).
49. Llabjani, V. *et al.* Polybrominated diphenyl ether-associated alterations in cell biochemistry as determined by attenuated total reflection Fourier-transform infrared spectroscopy: a comparison with DNA-reactive and/or endocrine-disrupting agents. *Environ. Sci. Technol.* **43**, 3356–3364 (2009).
50. Malins, D.C. *et al.* Biomarkers signal contaminant effects on the organs of English sole (*Parophrys vetulus*) from Puget Sound. *Environ. Health Perspect.* **114**, 823–829 (2006).
51. Cakmak, G., Togan, I. & Sevencan, F. 17 β -Estradiol induced compositional, structural and functional changes in rainbow trout liver, revealed by FT-IR spectroscopy: a comparative study with nonylphenol. *Aquat. Toxicol.* **77**, 53–63 (2006).
52. Llabjani, V. *et al.* Alterations in the infrared spectral signature of avian feathers reflect potential chemical exposure: A pilot study comparing two sites in Pakistan. *Environ. Int.* **48**, 39–46 (2012).
53. Trevisan, J. *et al.* Syrian hamster embryo (SHE) assay (pH 6.7) coupled with infrared spectroscopy and chemometrics towards toxicological assessment. *Analyst* **135**, 3266–3272 (2010).
54. Ahmadzai, A.A. *et al.* The Syrian hamster embryo (SHE) assay (pH 6.7): mechanisms of cell transformation and application of vibrational spectroscopy to objectively score endpoint alterations. *Mutagenesis* **27**, 257–266 (2012).
55. Ami, D., Natalello, A., Zullini, A. & Doglia, S.M. Fourier transform infrared microspectroscopy as a new tool for nematode studies. *FEBS Lett.* **576**, 297–300 (2004).
56. Hobro, A.J. & Lendl, B. Fourier-transform mid-infrared FPA imaging of a complex multicellular nematode. *Vib. Spectrosc.* **57**, 213–219 (2011).
57. Mariéy, L., Signolle, J.P., Amiel, C. & Travert, J. Discrimination, classification, identification of microorganisms using FTIR spectroscopy and chemometrics. *Vib. Spectrosc.* **26**, 151–159 (2001).
58. Gómez-De-Anda, F. *et al.* Determination of *Trichinella spiralis* in pig muscles using mid-Fourier transform infrared spectroscopy (MID-FTIR) with attenuated total reflectance (ATR) and soft independent modeling of class analogy (SIMCA). *Meat Sci.* **91**, 240–246 (2012).
59. Kazarian, S.G. & Chan, K.A. ATR-FTIR spectroscopic imaging: recent advances and applications to biological systems. *Analyst* **138**, 1940–1951 (2013).
60. Glassford, S.E., Byrne, B. & Kazarian, S.G. Recent applications of ATR FTIR spectroscopy and imaging to proteins. *Biochim. Biophys. Acta* **1834**, 2849–2858 (2013).
61. Stuart, B. *Infrared Spectroscopy: Fundamentals and Applications*. John Wiley and Sons (2005).
62. Mantsch, H.H. & Chapman, D. *Infrared Spectroscopy of Biomolecules* (Wiley-Liss, 1996).
63. Miller, L.M. & Dumas, P. Chemical imaging of biological tissue with synchrotron infrared light. *Biochim. Biophys. Acta* **1758**, 846–857 (2006).
64. Liu, J.-N., Schulmerich, M.V., Bhargava, R. & Cunningham, B.T. Optimally designed narrowband guided-mode resonance reflectance filters for mid-infrared spectroscopy. *Opt. Express* **19**, 24182–24197 (2011).
65. Miller, L.M. & Smith, R.J. Synchrotron versus globars, point-detectors versus focal plane arrays: Selecting the best source and detector for specific infrared microspectroscopy and imaging applications. *Vib. Spectrosc.* **38**, 237–240 (2005).
66. Lasch, P., Boese, M., Pacifico, A. & Diem, M. FT-IR spectroscopic investigations of single cells on the subcellular level. *Vib. Spectrosc.* **28**, 147–157 (2002).
67. Duncan, W. & Williams, G.P. Infrared synchrotron radiation from electron storage rings. *Appl. Optics* **22**, 2914–2923 (1983).
68. Pijanka, J.K. *et al.* Spectroscopic signatures of single, isolated cancer cell nuclei using synchrotron infrared microscopy. *Analyst* **134**, 1176–1181 (2009).
69. Dumas, P., Sockalingum, G.D. & Sule-Suso, J. Adding synchrotron radiation to infrared microspectroscopy: what's new in biomedical applications? *Trends Biotechnol.* **25**, 40–44 (2007).
70. Martin, F.L. Shining a new light into molecular workings. *Nat. Methods* **8**, 385–387 (2011).
71. Menzel, L. *et al.* Spectroscopic detection of biological NO with a quantum cascade laser. *Appl. Phys. B* **72**, 859–863 (2001).
72. Valle, J.J. *et al.* Free electron laser-Fourier transform ion cyclotron resonance mass spectrometry for obtaining infrared multiphoton dissociation spectra of gaseous ions. *Rev. Sci. Instrum.* **76**, 023103 (2005).
73. Llabjani, V. *et al.* Differential effects in mammalian cells induced by chemical mixtures in environmental biota as profiled using infrared spectroscopy. *Environ. Sci. Technol.* **45**, 10706–10712 (2011).
74. Schubert, J.M., Mazur, A.I., Bird, B., Miljković, M. & Diem, M. Single point vs. mapping approach for spectral cytopathology (SCP). *J. Biophotonics* **3**, 588–596 (2010).
75. Carter, E.A., Tam, K.K., Armstrong, R.S. & Lay, P.A. Vibrational spectroscopic mapping and imaging of tissues and cells. *Biophys. Rev.* **1**, 95–103 (2009).
76. Nasse, M.J. *et al.* High-resolution Fourier-transform infrared chemical imaging with multiple synchrotron beams. *Nat. Methods* **8**, 413–416 (2011).
77. Fernandez, D.C., Bhargava, R., Hewitt, S.M. & Levin, I.W. Infrared spectroscopic imaging for histopathologic recognition. *Nat. Biotechnol.* **23**, 469–474 (2005).
78. Chan, K. & Kazarian, S. New opportunities in micro-and macro-attenuated total reflection infrared spectroscopic imaging: spatial resolution and sampling versatility. *Appl. Spectrosc.* **57**, 381–389 (2003).
79. Holton, S.E., Walsh, M.J. & Bhargava, R. Subcellular localization of early biochemical transformations in cancer-activated fibroblasts using infrared spectroscopic imaging. *Analyst* **136**, 2953–2958 (2011).
80. Bassan, P. *et al.* The inherent problem of transfection-mode infrared spectroscopic microscopy and the ramifications for biomedical single point and imaging applications. *Analyst* **138**, 144–157 (2013).
81. Goormaghtigh, E., Raussens, V. & Ryckaert, J.M. Attenuated total reflection infrared spectroscopy of proteins and lipids in biological membranes. *Biochim. Biophys. Acta* **1422**, 105–185 (1999).
82. Wehbe, K., Filik, J., Frogley, M.D. & Cinque, G. The effect of optical substrates on micro-FTIR analysis of single mammalian cells. *Anal. Bioanal. Chem.* **405**, 1311–1324 (2013).
83. Vaccari, L. *et al.* Synchrotron radiation infrared microspectroscopy of single living cells in microfluidic devices: advantages, disadvantages and future perspectives. *J. Phys.: Conf. Ser.* **359**, 012007 (2012).
84. Chan, K.L.A. & Kazarian, S.G. FT-IR spectroscopic imaging of reactions in multiphase flow in microfluidic channels. *Anal. Chem.* **84**, 4052–4056 (2012).
85. Marcsis, E.J., Uttero, C.M., Miljkovic, M. & Diem, M. Infrared microspectroscopy of live cells in aqueous media. *Analyst* **135**, 3227–3232 (2010).
86. Nasse, M., Ratti, S., Giordano, M. & Hirschmugl, C. Demountable liquid/flow cell for *in vivo* infrared microspectroscopy of biological specimens. *Appl. Spectrosc.* **63**, 1181–1186 (2009).
87. Holman, H.-Y.N., Bechtel, H.A., Hao, Z. & Martin, M.C. Synchrotron IR spectromicroscopy: chemistry of living cells. *Anal. Chem.* **82**, 8757–8765 (2010).
88. Bhargava, R. & Levin, I.W. Fourier transform infrared imaging: theory and practice. *Anal. Chem.* **73**, 5157–5167 (2001).
89. Bhargava, R. & Levin, I.W. Effective time averaging of multiplexed measurements: A critical analysis. *Anal. Chem.* **74**, 1429–1435 (2002).
90. Bhargava, R., Ribar, T. & Koenig, J.L. Towards faster FT-IR imaging by reducing noise. *Appl. Spectrosc.* **53**, 1313–1322 (1999).

91. Bhargava, R., Schaeberle, M.D., Fernandez, D.C. & Levin, I.W. Novel route to faster Fourier transform infrared spectroscopic imaging. *Appl. Spectrosc.* **55**, 1079–1084 (2001).

92. Gazi, E. *et al.* Fixation protocols for subcellular imaging by synchrotron-based Fourier transform infrared microspectroscopy. *Biopolymers* **77**, 18–30 (2005).

93. Bretzloff, R. & Bahder, T. Apodization effects in Fourier transform infrared difference spectra. *Rev. Phys. Appl.* **21**, 833–844 (1986).

94. Tahtouh, M., Despland, P., Shimmon, R., Kalman, J.R. & Reedy, B.J. The application of infrared chemical imaging to the detection and enhancement of latent fingerprints: method optimization and further findings. *J. Forensic Sci.* **52**, 1089–1096 (2007).

95. Lasch, P. & Naumann, D. Spatial resolution in infrared microspectroscopic imaging of tissues. *Biochim. Biophys. Acta* **1758**, 814–829 (2006).

96. Sun, D.-W. *Infrared Spectroscopy for Food Quality Analysis and Control* (Academic Press, 2009).

97. Snook, R.D., Harvey, T.J., Faria, E.C. & Gardner, P. Raman tweezers and their application to the study of singly trapped eukaryotic cells. *Integr. Biol.* **1**, 43–52 (2009).

98. Bhargava, R., Fernandez, D.C., Schaeberle, M.D. & Levin, I.W. Effect of focal plane array cold shield aperture size on Fourier transform infrared micro-imaging spectrometer performance. *Appl. Spectrosc.* **54**, 1743–1750 (2000).

99. Bruun, S.W. *et al.* Correcting attenuated total reflection-Fourier transform infrared spectra for water vapor and carbon dioxide. *Appl. Spectrosc.* **60**, 1029–1039 (2006).

100. Lasch, P. & Petrich, W. Data acquisition and analysis in biomedical vibrational spectroscopy. *Biomed. Appl. Sync. Infrared Microscop.* **11**, 192–225 (2011).

101. Trevisan, J., Angelov, P.P., Carmichael, P.L., Scott, A.D. & Martin, F.L. Extracting biological information with computational analysis of Fourier-transform infrared (FTIR) biopspectroscopy datasets: current practices to future perspectives. *Analyst* **137**, 3202–3215 (2012).

102. Martin, F.L. *et al.* Distinguishing cell types or populations based on the computational analysis of their infrared spectra. *Nat. Protoc.* **5**, 1748–1760 (2010).

103. Duda, R.O., Hart, P.E. & Stork, D.G. *Pattern Classification* 2nd edn. (Wiley Interscience, 2001).

104. Goodacre, R. Explanatory analysis of spectroscopic data using machine learning of simple, interpretable rules. *Vib. Spectrosc.* **32**, 33–45 (2003).

105. Naumann, D. FTIR spectroscopy of microorganisms at the Robert Koch Institute: experiences gained during successful project. *Proc. SPIE* 6853, Biomedical Optical Spectroscopy 68530G (2008).

106. Lasch, P. & Petrich, W. in *Biomedical Applications of Synchrotron Infrared Microspectroscopy: Practical Approach*, RSC Analytical Spectroscopy Series Vol. 11, (ed. D. Moss), 192–225 (RSC Analytical Spectroscopy Series, 2011).

107. Lasch, P. Spectral pre-processing for biomedical vibrational spectroscopy and microspectroscopic imaging. *Chemom. Intell. Lab. Syst.* **117**, 100–114 (2013).

108. Bhargava, R., Wang, S.-Q. & Koenig, J.L. Route to higher fidelity FT-IR imaging. *Appl. Spectrosc.* **54**, 486–495 (2000).

109. Reddy, R.K. & Bhargava, R. Accurate histopathology from low signal-to-noise ratio spectroscopic imaging data. *Analyst* **135**, 2818–2825 (2010).

110. van Dijk, T., Mayerich, D., Bhargava, R. & Carney, P.S. Rapid spectral-domain localization. *Opt. Express* **21**, 12822–12830 (2013).

111. van Dijk, T., Mayerich, D., Carney, P.S. & Bhargava, R. Recovery of absorption spectra from Fourier transform infrared (FT-IR) microspectroscopic measurements of intact spheres. *Appl. Spectrosc.* **67**, 546–552 (2013).

112. Martens, H. & Stark, E. Extended multiplicative signal correction and spectral interference subtraction – new pre-processing methods for near-infrared spectroscopy. *J. Pharmaceut. Biomed.* **9**, 625–635 (1991).

113. Bassan, P. *et al.* Resonant Mie scattering in infrared spectroscopy of biological materials – understanding the ‘dispersion artefact’. *Analyst* **134**, 1586–1593 (2009).

114. Bassan, P. *et al.* Resonant Mie scattering (RMieS) correction of infrared spectra from highly scattering biological samples. *Analyst* **135**, 268–277 (2010).

115. Bassan, P. *et al.* RMieS-EMSC correction for infrared spectra of biological cells: extension using full Mie theory and GPU computing. *J. Biophotonics* **3**, 609–620 (2010).

116. *Opus 5 Reference Manual* (Bruker Optik, 2004).

117. Ly, E. *et al.* Combination of FTIR spectral imaging and chemometrics for tumour detection from paraffin-embedded biopsies. *Analyst* **133**, 197–205 (2008).

118. Beier, B.D. & Berger, A.J. Method for automated background subtraction from Raman spectra containing known contaminants. *Analyst* **134**, 1198–1202 (2009).

119. Baker, M. *et al.* An investigation of the RWPE prostate derived family of cell lines using FTIR spectroscopy. *Analyst* **135**, 887–894 (2010).

120. Guyon, I., Gunn, S., Nikravesh, M. & Zadeh, L. *Feature Extraction, Foundations and Applications* (Springer, 2006).

121. Udelhoven, T., Novozhilov, M. & Schmitt, J. The NeuroDeveloper (R): a tool for modular neural classification of spectroscopic data. *Chemometr. Intell. Lab.* **66**, 219–226 (2003).

122. Kwak, J.T., Reddy, R., Sinha, S. & Bhargava, R. Analysis of variance in spectroscopic imaging data from human tissues. *Anal. Chem.* **84**, 1063–1069 (2011).

123. Bhargava, R., Fernandez, D.C., Hewitt, S.M. & Levin, I.W. High throughput assessment of cells and tissues: Bayesian classification of spectral metrics from infrared vibrational spectroscopic imaging data. *Biochim. Biophys. Acta* **1758**, 830–845 (2006).

124. Naumann, D. in *Encyclopedia of Analytical Chemistry* (John Wiley & Sons, 2000).

125. Hughes, C. *et al.* FTIR microspectroscopy of selected rare diverse sub-variants of carcinoma of the urinary bladder. *J. Biophotonics* **6**, 73–87 (2013).

126. Hastie, T., Tibshirani, R. & Friedman, J. *The Elements of Statistical Learning: Data Mining, Inference and Prediction* 2nd edn. (Springer, 2009).

127. Bhargava, R. Towards a practical Fourier transform infrared chemical imaging protocol for cancer histopathology. *Anal. Bioanal. Chem.* **389**, 1155–1169 (2007).

128. Berenbaum, M.C. The histochemistry of bound lipids. *Q. J. Microsc. Sci.* **53–99**, 231–242 (1958).

129. Wigglesworth, V.B. Bound lipid in the tissues of mammal and insect: a new histochemical method. *J. Cell Sci.* **8**, 709–725 (1971).

130. Stitt, D.M. *et al.* Tissue acquisition and storage associated oxidation considerations for FTIR microspectroscopic imaging of polyunsaturated fatty acids. *Vib. Spectrosc.* **60**, 16–22 (2012).

131. Owens, G.L. *et al.* Vibrational biopspectroscopy coupled with multivariate analysis extracts potentially diagnostic features in blood plasma/serum of ovarian cancer patients. *J. Biophotonics* **7**, 200–209 (2014).

132. Dorling, K.M. & Baker, M.J. Highlighting attenuated total reflection Fourier transform infrared spectroscopy for rapid serum analysis. *Trends Biotechnol.* **31**, 327–328 (2013).

133. Chang, C.-C. & Lin, C.-J. LIBSVM: a library for support vector machines. *ACM TIST* **2**, 27 (2011).

134. Trevisan, J. *et al.* Measuring similarity and improving stability in biomarker identification methods applied to Fourier-transform infrared (FTIR) spectroscopy. *J. Biophotonics* **7**, 254–265 (2014).

135. Lasch, P., Fabian, H., Thi, N.A.N. & Naumann, D. Infrarot-bildgebung für die pathohistologische Diagnostik. *Laborwelt* **2**, 8–12 (2004).

136. Lasch, P. & Kneipp, J. *Biomedical Vibrational Spectroscopy*. (Wiley-Blackwell, 2008).

137. Lyng, F., Gazi, E. & Gardner, P. in *Preparation of Tissues and Cells for Infrared and Raman Spectroscopy* (RSC Analytical Spectroscopy Monographs, No. 11, ed. Moss, D.) 147–185 (Royal Society of Chemistry, 2011).

138. Whelan, D.R., Bamberg, K.R., Puskar, L., McNaughton, D. & Wood, B.R. Quantification of DNA in simple eukaryotic cells using Fourier transform infrared spectroscopy. *J. Biophotonics* **6**, 775–784 (2013).

139. Whelan, D.R. *et al.* Monitoring the reversible B- to A-like transition of DNA in eukaryotic cells using Fourier transform infrared spectroscopy. *Nucleic Acids Res.* **39**, 5439–5448 (2011).

140. Rahmelow, K. & Hubner, W. Phase correction in Fourier transform spectroscopy: subsequent displacement correction and error limit. *Appl. Optics* **36**, 6678–6686 (1997).

141. Gazi, E. *et al.* The combined application of FTIR microspectroscopy and ToF-SIMS imaging in the study of prostate cancer. *Faraday Discuss.* **126**, 41–59 (2004).

142. Patel, I.I. *et al.* Isolating stem cells in the inter-follicular epidermis employing synchrotron radiation-based Fourier-transform infrared microspectroscopy and focal plane array imaging. *Anal. Bioanal. Chem.* **404**, 1745–1758 (2012).

143. Bassan, P. *et al.* FTIR microscopy of biological cells and tissue: data analysis using resonant Mie scattering (RMieS) EMSC algorithm. *Analyst* **137**, 1370–1377 (2012).

144. Kastyak-Ibrahim, M. *et al.* Biochemical label-free tissue imaging with subcellular-resolution synchrotron FTIR with focal plane array detector. *NeuroImage* **60**, 376–383 (2012).

145. Gajjar, K. *et al.* Diagnostic segregation of human brain tumours using Fourier-transform infrared and/or Raman spectroscopy coupled with discriminant analysis. *Anal. Methods* **5**, 89–102 (2013).

146. Kelly, J.G., Martin-Hirsch, P.L. & Martin, F.L. Discrimination of base differences in oligonucleotides using mid-infrared spectroscopy and multivariate analysis. *Anal. Chem.* **81**, 5314–5319 (2009).

PROTOCOL

Supplementary Method 1

Direct drop ATR-FTIR spectroscopy biofluid analysis

Materials

- Ethanol 2.5 L (Fisher Scientific, UK; E/0600DF/17)
- Virkon (Antec International, a DuPont Company, UK; A00960632) !CAUTION Irritant

Equipment

- JASCO FTIR-4100 (JASCO UK Ltd, UK)
- SpecacGolden Gate™ single reflection diamond ATR Accessory(Specac, UK)
- Microcentrifuge
- Filters

Software

- JASCO Spectra Manager Software
- Matlab

Procedure

- Ensure that the ATR-FTIR crystal is clean and dry prior to use, if required it can be washed with Virkon solution and Ethanol or distilled water

▲CRITICAL STEP Make sure the crystal is thoroughly cleaned and dried before background acquisition

- Collect background spectrum with a resolution of 4 cm^{-1} and using 32 co-added scans

▲CRITICAL STEP It is very important that the background spectrum is collected. It should be re-collected at least every hour and upon changes in the environmental conditions. Background collection between each sample is recommended

- Place 1 μl of the biofluid on the crystal and allow to dry

▲CRITICAL STEP Intimate contact of the sample with the crystal is a very important parameter for ATR-FTIR analysis. One μl of sample has been shown to be dry by 8 minutes by Hands JR *et al.* *Analytical and Bioanalytical Chemistry* 405: 7347-7355 (2013); doi:10.1007/s00216-013-7163-z

- Acquire sample spectrum with a resolution of 4 cm^{-1} and 32 co-added scans. It is common to collect multiple technical replicate samples. For biofluid analysis it is also recommended to have multiple biological replicates. 3 biological replicates (biofluid aliquots on the crystal) and 3 technical replicates (spectra collected from each aliquot) is recommended.
- After sample spectral acquisition wash the crystal with Virkon and Ethanol and ensure the crystal is dry.

S1

Supplementary Method 2

FTIR FPA Imaging using Agilent 670-IR spectrometer coupled with Agilent 620-IR microscope and FPA detector

• TIMING 4 min per sample image (16,384 spectra for 128 × 128; 8,192 spectra for 64 × 64)

- i. Switch on the Agilent 670-IR, Agilent 620-IR spectrometer and microscope, and connected PC.
- ii. Fill the focal plane array (FPA) detector with liquid N₂.

▲CRITICAL STEP Filling the FPA detector with liquid N₂ is essential; allow the detector (and therefore the signal) to stabilize (approximately 10 min) to an optimal peak-to-peak. Top-up with N₂ every 4-6 h to maintain temperature.

- iii. Place sample under the microscope, and bring the surface of a blank area of the substrate into focus.
- iv. Open Resolutions Pro. Agilent Resolutions Pro is Agilent Technologies software, which comes with the instruments from this company. Other devices come with their own interface software; however, the steps will be similar or for the same purpose.
- v. Go to '*Collect*', '*Imaging*', '*Rapid scan*'. This brings up a window displaying all the modifiable parameters for the experiment. Click on the '*Optics*' tab.
- vi. Select the internal DTGS detector within the spectrometer. Normally, three parameters need to be modified: change '*Beam*' to '*Internal*', '*Detector*' to '*DLaTGS*', and '*Aperture source*' to ' 0.1 cm^{-1} ' at 4000 cm^{-1} '. The correct parameters for this step are shown in **Figure S1**. Click on '*Setup*' to view the interferogram of the internal DTGS detector. Click '*Find Centreburst*' and press '*OK*' to go back to the set-up window.

▲CRITICAL STEP A centreburst must be used to transform and process FTIR spectral data. The FPA is connected to the PC directly and not through an electronics board like conventional detectors and does

S1

not have its own interferogram. This is why the centreburst must be obtained from another detector, such as the internal DTGS detector.

- vii. Select the FPA detector in the ‘*Optics*’ tab. The same three parameters need to be modified: change ‘*Beam*’ to ‘Left’ (if the attached microscope is on the left of the spectrometer), ‘*Detector*’ to ‘Ground’, and ‘*Aperture source*’ to ‘Open’. The ‘*Optics mode*’ should be changed relative to the experiment; ‘*Transmittance*’ for transmission experiments and ‘*Reflectance*’ for transfection experiments. The correct parameters for this step are shown in **Figure S2**. Click on ‘*Setup*’ and bring up the Lancer Control window.
- viii. Click on ‘*Show Raw data*’ to observe the live illumination of the face of the FPA detector. Ensure that a clean (sample-free) area of the slide is in focus, and that the manually modifiable microscope aperture is fully open. For transfection experiments, move the ‘*Signal Intensity*’ slider to change the integration time and the intensity distribution curve until a smooth, rounded curve appears. The integration time should equate to about 0.024 ms but can vary between instruments. An example of a good illumination and intensity distribution is shown in **Figure S3**. For transmission experiments, the position of the condenser lens must also be adjusted to allow as much light to the sample as possible. The intensity distribution curve should resemble a very shallow, straight curve. The integration time should equate to about 0.032 ms but can vary between instruments. Click ‘*Calibrate*’ and ensure the number of out-of-range (OOR) pixels is low (<6). Click ‘*OK*’ and ‘*OK*’ again in Resolutions Pro to return to the Imaging Setup window.
▲CRITICAL STEP The integration time is essentially a measure of the time that the shutter is open to collect the incoming photons. The aim is to optimise the SNR without saturating the detector. If the integration time is too high, the user will observe saturation effects in the FTIR images; too low and the data quality and SNR will be reduced as the FPA has not been fully illuminated. This calibration is a non-uniformity correction, and results are shown with measures of high and low flux (in counts), and the number of out-of-range (OOR) pixels.

- ix. Click on the '*Electronics*' tab (**Figure S4**). This tab shows a number of parameters that can be changed by the user. The wavenumber range can be modified by the user, but is limited by the band-gap of the FPA detector, and the optical filters in use. The optimal usable wavenumber range for the system is around 900 cm^{-1} - 3800 cm^{-1} . The number of co-added scans can be varied, but is subjective to the experiment. Usually, 16 to 128 scans give an acceptable SNR for most experiments. The spectral resolution can also be subjectively modified, although resolutions of 4 cm^{-1} or 8 cm^{-1} are most common. It is recommended that all other parameters are left at the default values for novice users. Standard FTIR imaging parameters are shown in Figure S1.
- x. Click on the '*Background*' tab. Set the number of co-added scans to be collected for the background image. This value should not be below the value set for the number of sample scans. Click '*Collect into new file*'. Browse a location and filename for each new background that is taken.
- xi. Click '*Collect Background*'. Save the background if prompted. Click on the resulting FTIR image and check the uniformity of the spectra across the whole sample area.

▲CRITICAL STEP Acquire a background image each time the detector is filled with N_2 and at regular intervals (or before each sample) to account for atmospheric changes.

- xii. Move the stage until the desired sample area is in the field of view, and ensure the sample surface is in full focus. Go to '*Collect*', '*Imaging*' and '*Rapid Scan*' once more. Now click '*Scan*'. When prompted to save, browse to a desired location and name the file. Check the spectra from the resulting sample image to ensure acceptable and even levels of noise and atmospheric contributions.
- xiii. Repeat step xii for multiple images from the same sample. After changing the sample, bring a clean (sample-free) area of the slide is in focus once again and repeat from step xi. If longer periods of time are left in between measurements, or the FPA detector is refilled with liquid N_2 , repeat procedure from step v.

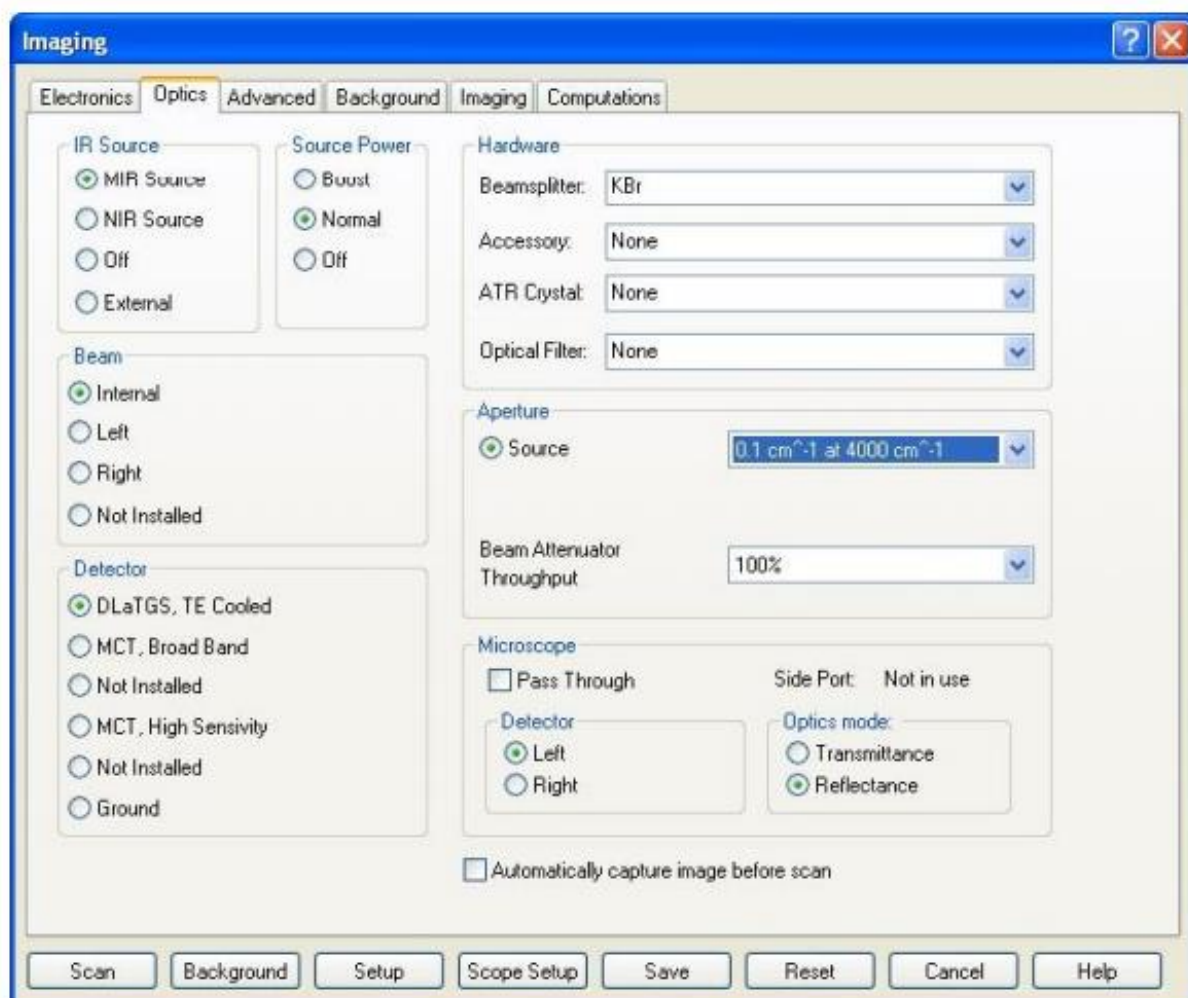


Figure S1 Screenshot associated with Step vi.

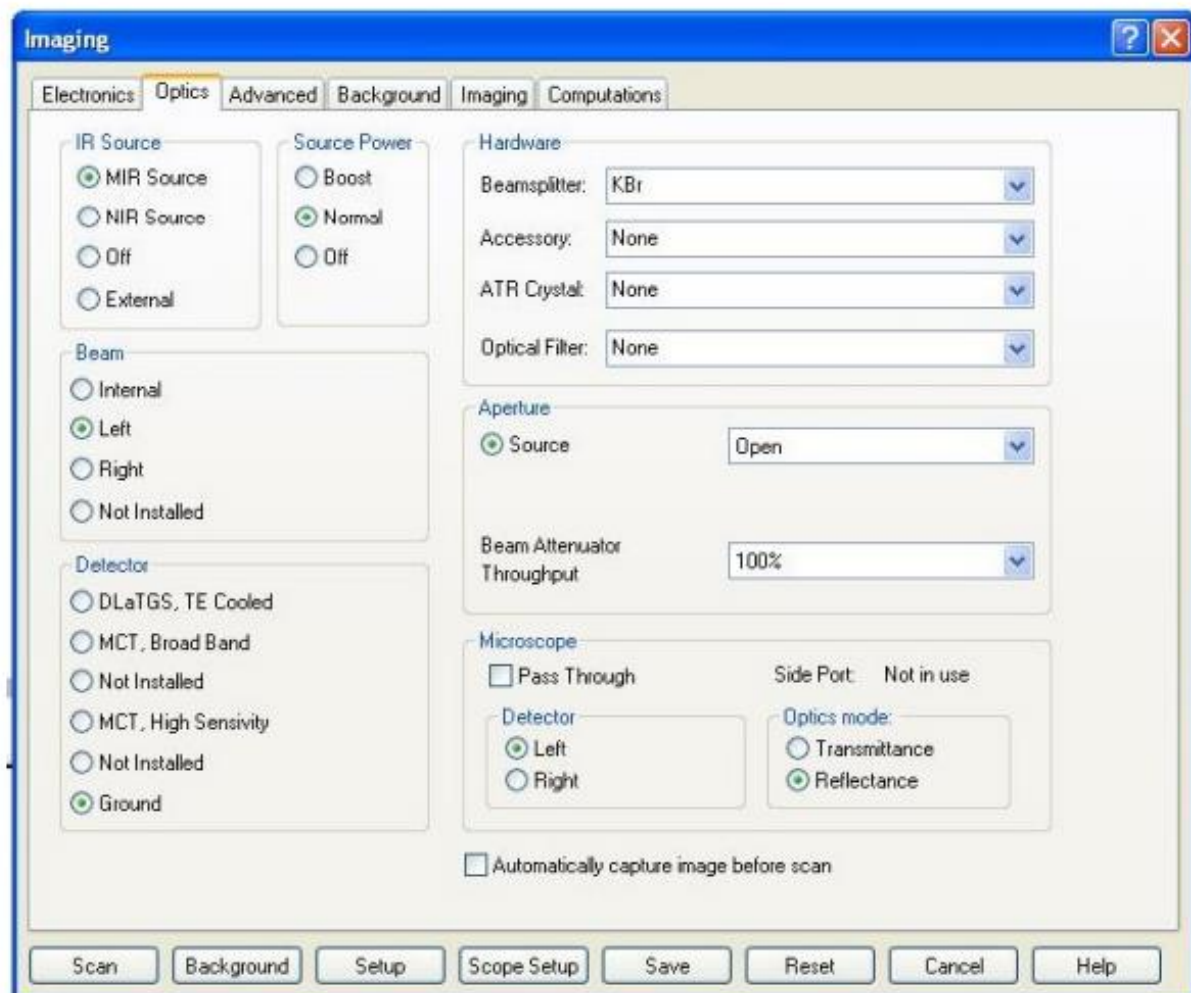


Figure S2 Screenshot associated with **Step vii**.

S5

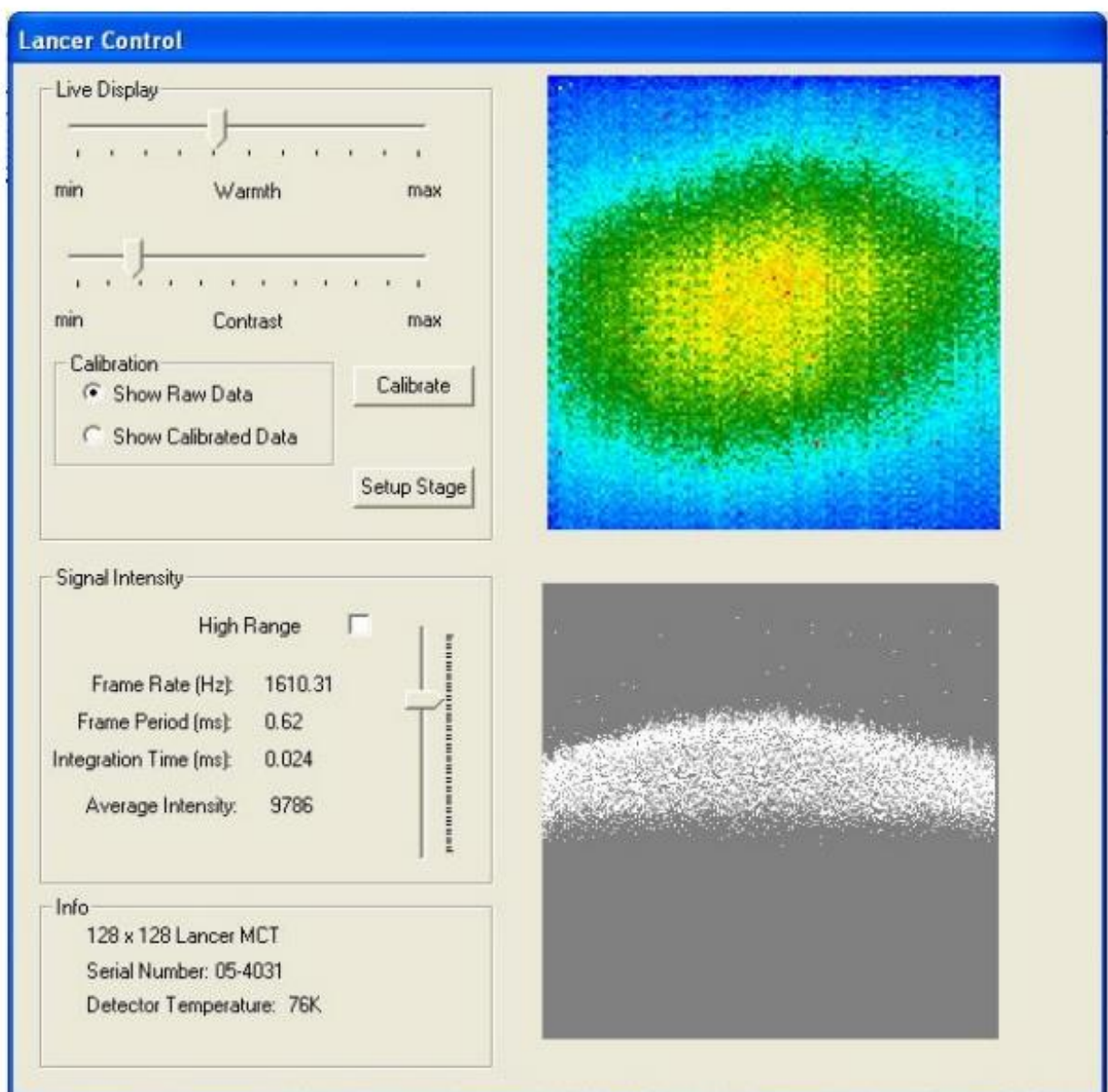


Figure S3 Screenshot associated with **Step viii**.

S6

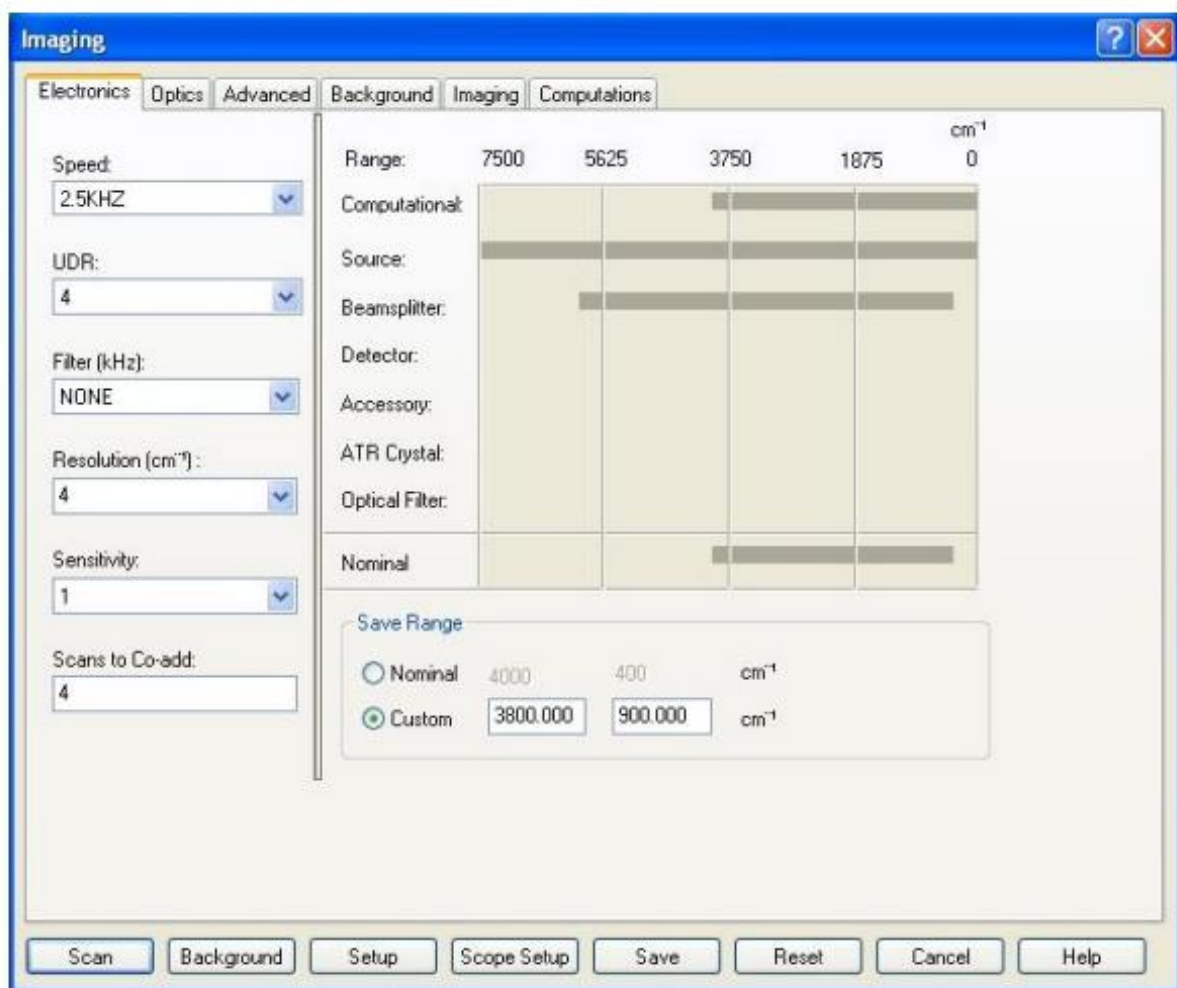


Figure S4 Screenshot associated with **Step ix**.

S7

Troubleshooting for FTIR Imaging using an Agilent 620-IR microscope coupled with an Agilent 670/680-IR spectrometer

If the user experiences problems with calibration or with data collection:

- Check that all parts of the instrument are turned on and operational (green light on spectrometer).
- Check all physical flaps and sliders are in the correct (open) positions.
- Check that the sampling mode is set correctly to your sample and substrate (e.g., transmission, reflection).
- Check that the microscope aperture is fully open.
- Check that the air is flowing properly through all incoming purge lines.
- Check that the protocol has been followed correctly.
- Restart the PC and software. Sometimes drivers need to be reloaded and memory refreshed. If problems persist, contact an Agilent customer support representative for advanced troubleshooting tips.

If the user experiences problems with the quality of data:

- Check that the FPA has been fully filled with liquid N₂, and has a temperature of ~76K. If the detector is not cool, it will not work properly.
- The incoming IR radiation may be saturating the FPA detector. Make sure the integration time and intensity set in the calibration step are not too high. If saturation is occurring, this is noticeable in the resulting FTIR images in the form of cloud-like spots originating in the centre of the images.
- If spectral data quality is inconsistent across the image, there may be an issue with the consistency of the purge. Make sure again, that all air flowing through incoming purge lines, and there are no regular variations in the environment surrounding the sample (e.g., people breathing, open door/window. For best results, take measurements inside a closed purge box).
- Check that the microscope objective in use is locked in place.
- Check that both the substrate surface and sample are fully in visual focus when taking background and sample images respectively.
- If spectra are very noisy, the user can try increasing the number of co-added scans or decrease the wavenumber resolution to improve the signal to noise ratio.
- Spectral data can also often be improved through pre-processing methods.

Supplementary Method 3

SVM Classification in MATLAB using the IRootLab toolbox

Loading dataset.

1. Start MATLAB and IRootLab as indicated in IRootLab manual.
2. In MATLAB command prompt, type “objtool”.
3. Click on “Load...” and select dataset.

Pre-processing: cut to the 1800 - 900 cm⁻¹; 1st differentiation (Savitzki-Golay); vector normalization (spectrum-wise); normalization to the [0, 1] range (variable-wise).

4. Locate and double-click “Feature Selection” in the right panel.
5. Click on “OK”.
6. Select “ds01_fsel01” in the middle panel.
7. Locate and double-click on “SG Differentiation->Vector normalization” in the right panel.
8. Click on “OK”.
9. Locate and double-click on “Normalization” in the right panel.
10. Select “[0, 1] range” from the “Type of normalization” pop-up box.
11. Click on “OK”.

Optimization of SVM classifier.

12. Click on “Sub-dataset Generation Specs” in left panel.
13. Click on “New...” in middle panel.
14. Locate and double-click on “K-fold Cross-Validation”.
15. Enter “5” in the “K-Fold’s ‘K’” box.
16. Optionally type any number (e.g., 12345) in the “Random seed” box (recommended)
17. Click on “OK”.
18. Click on “Classifier” in left panel.
19. Click on “New...” in middle panel.
20. Locate and double-click on “Support Vector Machine”.
21. Click “OK” (the values in the boxes will not be used anyway).
22. Click on “Dataset” in left panel.
23. Click on dataset named “ds01_fsel01_diffvn01_norm01” in middle panel.
24. Locate and double-click “Grid Search” in right panel.
25. In the “SGS” drop-down box, select “sgs_crossval01”.
26. In the “Classifier” drop-down box, select “clssr_svm01”. You may optionally change the search space of *c* and *gamma* or accept the default values.
27. Click on “OK”. **Warning:** grid search is potentially time-consuming.
28. Watch MATLAB command window for progress indicator.

Visualization of optimization progress.

29. Click on “Log” in left panel.
30. Select “log_gridsearch_gridsearch01” in middle panel.
31. Double-click on “Grid Search Log Report” in right panel. This will show the best classification rate. found at each iteration, with respective parameters (see Figure below)

Estimation and visualization of confusion matrix for best parameters.

32. Click on “Log” in the left panel.
33. Click on “log_gridsearch_gridsearch01” in the middle panel.
34. Double-click on “extract_block” in the right panel.

S1

35. Click on “Dataset” in the left panel.
36. Click on “ds01_fsel01_diffvn01_norm01” in the middle panel.
37. Double-click on “Rater” in the right panel.
38. In the “Classifier” box, select “clssr_svm_gridsearch01” (this is the block that was created from the block extraction action above).
39. In the SGS box, select “sgs_crossval01”. This will cause the cross-validated estimation to use the same dataset splits as the grid search optimization before.
40. Click on “OK”.
41. Click on “Log” in the left panel.
42. Click on “estlog_classxclass_rater01” in the middle panel.
43. Double-click on “Confusion matrices” in the right panel.
44. Click on “OK” (generates report).

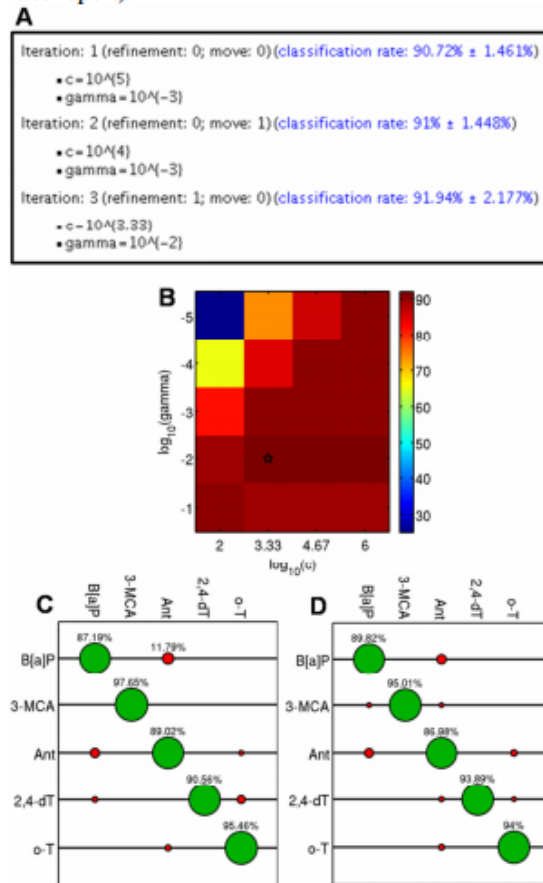


Figure - SVM classifier design and classification using SVM and LDC. (A) Iterations of Grid search optimization to find optimal C and γ for the SVM classifier. (B) Classification rate as a function of C and γ (3rd iteration of (A)). (C) Confusion matrix for classification using the optimal classifier found through Grid search (5-fold cross-validation). (D) Confusion matrix using the LDC classifier (5-fold cross-validation using the same train and test sets of (C)).

S2

Supplementary Method 4

Protocol for FTIR spectroscopy of single living cells using a synchrotron source

S1

Supplementary Method 4

Protocol for FTIR spectroscopy of single living cells using a synchrotron source

S1

Deposition of cells

- 10 μL of a cells suspended in isotonic saline are placed on the bottom window of the sample holder with the mylar spacer in place
- The second window is placed on top of the cell suspension and the clamping plate fixed into position
- With the aid of a stereomicroscope the clamping plate is tightened so that the top plate just makes contact with the cells
- The sample holder is then placed onto the microscope stage

S3

Instrumentation

- The beamline on the Australian Synchrotron uses a novel beam extraction technique to produce two synchrotron IR beams derived from edge radiation and bending radiation that are split apart in an optical chamber and directed to two separate instruments.
- For the microspectroscopy beamline the beam is directed to a Bruker Hyperion 2000 IR confocal microscope (Bruker Optics GmbH., Ettlingen, Germany) equipped with a liquid-nitrogen-cooled mercury-cadmium-telluride (MCT) detector with a 36x IR objective (NA.0.5).
- **The Hyperion** 2000 microscope is coupled to a Bruker Vertex 80v spectrometer and data collection is carried out using Bruker's OPUS version 6.5 software, with an additional 3D package (Bruker Optics GmbH., Ettlingen, Germany).
- The Hyperion microscope and the sample are purged with dry nitrogen gas to minimize water vapour contributions in the spectra.

S4

FTIR measurements

- Once the cells are in focus select a group of cells in the field of view and a background position
- It is important that the background spectrum is recorded through the media and in close proximity to the group of cells to be analysed
- It is also important that a background is recorded before every cell measurement
- For synchrotron measurements using the condenser Cassegrain is adjusted so that the signal is optimized in the 1600-1000 cm⁻¹ region

85

FTIR instrumental parameters

- The knife edge aperture is set to the same size as the cell
- For each spectrum 128 interferograms are co-added with a spectral resolution of 4 cm^{-1}
- To assign DNA bands spectra are recorded in both the hydrated state and dehydrated state as the DNA bands shift in response to hydration whereas the RNA bands remain at the same wavenumber values.

S6

Chapter 3

Using Raman spectroscopy to characterise biological materials

Holly J. Butler, Lorna Ashton, Benjamin Bird, Gianfelice Cinque, Kelly Curtis, Jennifer Dorney, Karen Esmonde-White, Nigel J. Fullwood, Benjamin Gardner, Pierre L. Martin-Hirsch, Michael J. Walsh, Martin R. McAinsh, Nicholas Stone, and Francis L. Martin

Nature Protocols 11(4): 664-687 (2016)

Contribution:

I wrote and prepared the manuscript for publication

I acquired all data used throughout

I prepared all figures

I coordinated feedback from external authors and compiled the final manuscript

Professor F. L Martin

Dr. Martin. R. McAinsh

H. J. Butler

PROTOCOL

Using Raman spectroscopy to characterize biological materials

Holly J Butler^{1,2}, Lorna Ashton³, Benjamin Bird⁴, Gianfelice Cinque⁵, Kelly Curtis⁶, Jennifer Dorney⁶, Karen Esmonde-White⁷, Nigel J Fullwood⁸, Benjamin Gardner⁶, Pierre L Martin-Hirsch^{1,9}, Michael J Walsh^{10,11}, Martin R McCain¹, Nicholas Stone^{6,12} & Francis L Martin¹

¹Lancaster Environment Centre, Lancaster University, Lancaster, UK. ²Centre for Global Eco-Innovation, Lancaster Environment Centre, Lancaster University, Lancaster, UK.

³Department of Chemistry, Lancaster University, Lancaster, UK. ⁴Daylight Solutions, San Diego, California, USA. ⁵Diamond Light Source, Harwell Science and Innovation Campus, Chilton, Oxfordshire, UK. ⁶Department of Biomedical Physics, Physics and Astronomy, University of Exeter, Exeter, UK. ⁷Department of Internal Medicine, University of Michigan Medical School, Ann Arbor, Michigan, USA. ⁸Department of Biomedical and Life Sciences, School of Health and Medicine, Lancaster University, Lancaster, UK.

⁹School of Pharmacy and Biomedical Sciences, University of Central Lancashire, Preston, UK. ¹⁰Department of Pathology, University of Illinois at Chicago, Chicago, Illinois, USA.

¹¹Department of Bioengineering, University of Illinois at Chicago, Chicago, Illinois, USA. ¹²Biophotonics Research Unit, Gloucestershire Hospitals NHS Foundation Trust, Gloucester, UK. Correspondence should be addressed to M.R.M. (m.mccainsh@lancaster.ac.uk), N.S. (n.stone@exeter.ac.uk) or F.L.M. (f.martin@lancaster.ac.uk).

Published online 10 March 2016; doi:10.1038/nprot.2016.036



Raman spectroscopy can be used to measure the chemical composition of a sample, which can in turn be used to extract biological information. Many materials have characteristic Raman spectra, which means that Raman spectroscopy has proven to be an effective analytical approach in geology, semiconductor, materials and polymer science fields. The application of Raman spectroscopy and microscopy within biology is rapidly increasing because it can provide chemical and compositional information, but it does not typically suffer from interference from water molecules. Analysis does not conventionally require extensive sample preparation; biochemical and structural information can usually be obtained without labeling. In this protocol, we aim to standardize and bring together multiple experimental approaches from key leaders in the field for obtaining Raman spectra using a microspectrometer. As examples of the range of biological samples that can be analyzed, we provide instructions for acquiring Raman spectra, maps and images for fresh plant tissue, formalin-fixed and fresh frozen mammalian tissue, fixed cells and biofluids. We explore a robust approach for sample preparation, instrumentation, acquisition parameters and data processing. By using this approach, we expect that a typical Raman experiment can be performed by a nonspecialist user to generate high-quality data for biological materials analysis.

INTRODUCTION

Raman microspectroscopy has been shown to be a powerful analytical technique in the study of biological materials, and it allows rapid, noninvasive and high spatial resolution acquisition of biochemical and structural information through the generation of point spectra or spectral images. Although it has been traditionally used for analytical chemistry applications, there has been a notable rise in the use of this technique within biological studies, particularly in the field of biomedicine^{1–4}.

Raman spectroscopy

Raman spectroscopy uses monochromatic light, often in the near-IR (NIR), visible or UV range, to exploit the phenomena of inelastic scattering, or Raman effect, that describes the excitation of photons to virtual energy states and the resultant loss (Stokes) or gain (anti-Stokes) of energy that occurs because of the interaction of light with vibrational modes associated with chemical bonds within the sample. This shift in energy is indicative of discrete vibrational modes of polarizable molecules, and thus a qualitative measurement of biochemical composition can be obtained. Raman spectra can infer quantitative information, provided that the instrument response function is adequately corrected. Typically, the significant regions of the Raman spectrum that are observed within biological specimens fall within 400–2,000 cm^{−1} wavenumbers, associated with bond vibrations of proteins (1,500–1,700 cm^{−1}), carbohydrates (470–1,200 cm^{−1}), phosphate groups of DNA (980, 1,080 and 1,240 cm^{−1}) and additional cellular biomolecules^{1,5}. Higher-frequency bond vibrations associated with CH, NH and OH stretching in lipids and proteins can also be observed at higher wavenumbers (2,700–3,500 cm^{−1})⁵.

Consequently, a distinctive biological 'fingerprint' is derived from the biological sample under investigation, and it can contribute to our understanding of the specimen. Figure 1 illustrates the principle of elastic (Rayleigh) and inelastic scattering when analyzing biological specimens.

Raman spectroscopy has a high molecular specificity, making it an excellent technique for materials analysis. However, Raman scattering is a rare phenomenon with an exceptionally low probability of occurrence (~ 1 in 10^8) in comparison with its counterpart Rayleigh scattering, and thus it is typically described as an insensitive technique. Its increased applicability is largely attributed to the technological advancement of highly efficient laser sources, low-noise detectors, effective Rayleigh filters and high-throughput optics⁶. The development of microspectrometers, which combine the power of optical magnification and direct visualization of the sample, has also contributed to further exploitation in biological fields. Because of this, it is possible to not only derive single point spectra but also to produce highly informative Raman images of the sampling area with improved interpretability⁷. The ability to acquire high-quality spectra at subcellular resolution coupled with the capability to obtain valuable information noninvasively, label-free and without interference from water, makes Raman spectroscopy an ideal approach for *in vivo* biological investigations.

There are many factors that influence spectral resolution, which are outlined in detail in this protocol. The spatial resolution of optical Raman microspectroscopy is governed mainly by the diffraction limit of light, and therefore it is dependent on the laser wavelength (λ) in use, as well as on the numerical aperture (NA)

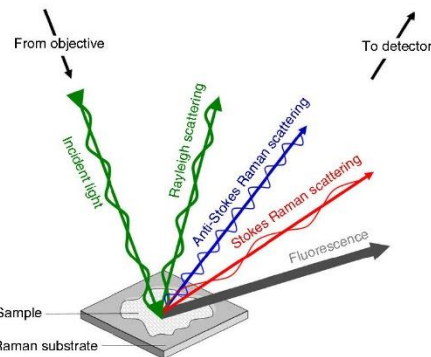


Figure 1 | Schematic identifying light scattering after laser exposure on a sample surface. Photons of light are focused on the sample through the microscope objective at a defined magnification. When they interact with chemical bonds within the biological specimen, electrons are excited to virtual energy levels. These biological molecules return to the original energy level by emitting a photon of light, known as elastic or Rayleigh scattering, or it can undergo an energy shift and return at lower (Stokes) or higher (anti-Stokes) energy levels, known as Raman scattering. Raman scattering is a low-probability process with around 1 in 10^8 photons inelastically scattered (arrow widths are not representative); Stokes Raman scattering is more intense than anti-Stokes scattering because of the increased probability of a molecule being in the ground vibrational state. Fluorescence can occur when electrons are excited to electronic energy levels and return to the ground energy level by emitting a photon of light at a longer wavelength.



of the objective. Theoretically, for a confocal microscope, the diffraction limit for visible (488 nm) to NIR ($\sim 1,033$ nm) light, using long-working-distance to water- or oil-immersion objectives with NA values from 0.5 to 1.2, would be in the range of 0.2–1 μm . In practice, it is rarely possible to achieve the diffraction limit, owing to both imperfect optics and beam scattering at the interface of the sample. However, alternative sampling modes such as surface-enhanced Raman scattering (SERS) and tip-enhanced Raman spectroscopy (TERS) have been shown to provide spatial resolution below the diffraction limit, as targeted single-molecule detection is possible^{8,9}. This is due to the interaction of biomolecules with roughened surfaces, such as metallic nanoparticles, that effectively enhance the electric field by a factor of up to 10^{14} . This is associated with the excitation of localized surface plasmons, which significantly enhance the local electric field of the light incident on the molecules adsorbed onto the metal surface. Furthermore, some small enhancement can originate from the charge transfer between the two materials.

A typical Raman study can rapidly accumulate a large, information-rich spectral data set. However, as this data set expands, the extraction of biological information becomes increasingly challenging. For this reason, multivariate analysis approaches are often used in order to effectively extricate the underlying chemical and structural information¹⁰. Spectral data sets often present a substantial computational burden, and thus analysis usually includes a data-reduction step, particularly as there are many covariant features in the spectra. This information can then be fed into unsupervised (clustering) or supervised classifications to differentiate individual spectra, which can then infer biological information¹¹. Raman imaging (global illumination) and mapping (stepwise) have particularly benefited from these classification

capabilities, as spectral discrimination is indicative of the underlying biological architecture, which has proved to be valuable in the field of cancer diagnosis, in which this approach has complemented conventional histopathological techniques¹².

Applications

Raman spectroscopy presents a method of sample examination with a high degree of flexibility, enabling data to be recorded from a diverse array of sample types including fixed, fresh or live tissues and cells. The application of Raman microspectroscopy to the characterization of biological materials is a rapidly expanding field, and it has been used in the fields of pharmacology^{13–15}, microbiology^{16–20}, toxicology^{21,22}, plant science^{23–25} and human biology. Considerable advances have been made, particularly in regard to cancer diagnosis and prognosis²⁶. Clinical implementation is firmly on the horizon²⁷, as spearheaded by recently formed networks such as 'Raman4Clinics' (<http://www.raman4clinics.eu/>) and Clinical Infrared and Raman Spectroscopy for Medical Diagnosis (CLIRSPEC; <http://clirspec.org/>). Raman spectroscopy and its derivatives, coupled with multivariate analysis, can classify neoplasia in brain^{28–31}, breast³², bladder³³, colorectal^{34,35}, larynx³⁶, lung³⁷, lymph node^{38,39}, esophageal^{40–42}, prostate^{43–46}, and uterine and cervical^{47–50} tissues using both point spectra and imaging approaches. These examples have used a range of sample formats, including fixed cells and tissues, *in vivo* measurements with advances in fiber optic attachments and spatially offset Raman spectroscopy (SORS), as well as noninvasive biofluid measurements⁵¹. In addition to cancer studies, the technique has been used to shed light on infectious diseases such as malaria^{52–55}. Owing to the relatively fast sampling time and mapping ability of Raman microspectroscopy in aqueous environments, the 2D and 3D analysis of *in vitro* cell models is possible^{56–59}, which has been particularly useful in toxicology and therapeutic studies^{60,61}.

The application of SERS has been shown to vastly improve the spectral intensity obtained from typically weak Raman scatterers, such as dilute biofluids⁶². SERS has been used across a wide range of biomedical studies, including DNA and drug detection^{63–66}. This approach has also been shown to overcome autofluorescence, which has often limited research capabilities in samples with intrinsic fluorescence, such as chlorophyll in plants, as this strong signal can often engulf the relatively rare Raman event²⁴. Reduced Raman performance in plant research has markedly restricted its application in this area, with previous research focused on the quantification and identification of plant constituents^{67–72}, as well as the imaging of nonfluorescent tissues^{25,73–75}. As fluorescence has a defined wavelength profile, it is also possible to overcome fluorescence by using alternative radiation sources using lasers at wavelengths that are outside typical biological matrix absorbance, e.g., in the NIR (1,064 nm) region⁷⁶. Water has also been found to be a significant fluorescence quencher, which has benefited *in vivo* studies, as was recently demonstrated in fundamental plant monitoring^{77,78}.

Limitations

The molecular specificity of Raman spectroscopy is powerful for the study of biological materials. However, there are a number of disadvantages associated with the technique. As Raman scattering is a relatively low-probability event, low sensitivity can be an issue, which is exacerbated by interference from fluorescence¹³. Because of the intense laser powers typically used, local thermal decomposition of the sample may be encountered, especially

PROTOCOL

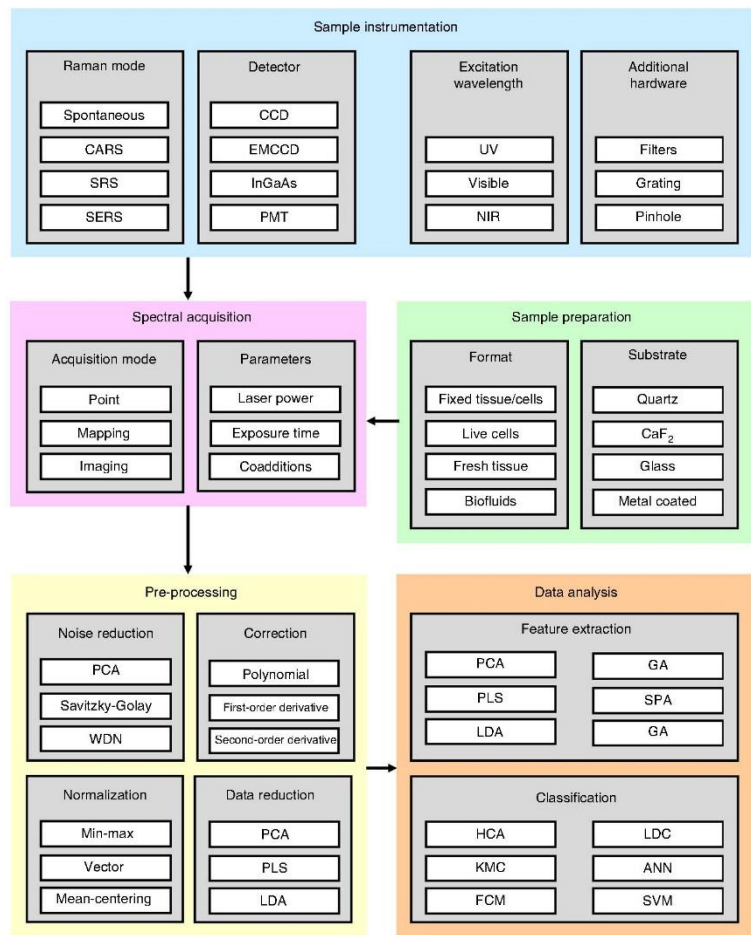
Figure 2 | Raman microspectroscopy workflow diagram highlighting the key aspects of experimental design including instrumentation, sample preparation, spectral acquisition and data processing with representative examples. It is not possible to conduct some options in combination, such as an InGaAs detector with UV wavelengths, and thus experimental design requires thorough planning before experimentation. Options provided are not exhaustive, and other alternatives are available. LDA, linear discriminant analysis; GA, genetic algorithm; SPA, sequential progression algorithm; HCA, hierarchical cluster analysis; KMC, *k*-means clustering; ANN, artificial neural networks.

when using UV or visible wavelengths. Sample burning (or photoablation) may be observed visibly by dark areas on the sample and spectroscopically by the presence of amorphous carbon bands ($C=C$, $\sim 1,500\text{ cm}^{-1}$) in the spectra, or saturation of the detector. The protocol described here will provide troubleshooting advice to avoid these particular issues. Fourier-transform IR (FTIR) spectroscopy is an alternative vibrational spectroscopy technique that is also suitable for the analysis of biological materials (for a recent protocol, see Baker *et al.*⁷⁹). Although it is based on fundamentally different physical excitation processes, FTIR retains both molecular specificity and sensitivity, and thus it has been used to derive spectral data and elucidate biological information, complementary to Raman spectroscopy^{80–82}.

The aim of this article is to describe a specific protocol for Raman microspectroscopy that can be applied to a variety of biological samples independent of a specific manufacturer's instrumentation and software. The protocol will address (i) sample preparation, (ii) spectral acquisition and (iii) data analysis of spectral data sets, with anticipated results derived from a range of biological studies (Fig. 2). It is important to note that this technique can also be applied to nonbiological materials, providing insights into the steps involved in Raman studies. In this protocol, we approach principal aspects of planning and implementing Raman investigations that can be applied to a variety of biological samples. We direct the reader to additional protocols that approach specific biological applications^{75,83–86}. It is our aim that by unifying protocols from leading researchers in the field, spectroscopists and biologists can build new interdisciplinary studies into biological samples incorporating Raman microspectroscopy into the suite of molecular biology tools.

Experimental design

In the PROCEDURE, we focus on four experimental examples: (i) *in vivo* spectral exploration of live plant samples (suitable for fresh tissue analysis); (ii) imaging of fixed human tissue;



(iii) SERS classification of endometrial cancer using biofluids; and (iv) analysis of cultured mammalian cells. These examples encompass both point and image mapping acquisition approaches, while exploring a range of pre-processing and analysis steps including exploratory image processing and spectral classification. This section of the INTRODUCTION provides background on these steps and more detailed guidance on how to decide which of these approaches to take.

Experimental design: instrument options

Figure 3 presents an overview of a typical Raman system and identifies key instrumental components. There are numerous Raman spectroscopic variations available, as described in Table 1. This protocol will focus primarily on spontaneous Raman microspectroscopy, which is a standard approach that does not require additional instrumentation, unless otherwise stated.

Before setting up the instrument and starting the analysis (Step 3), you need to consider what scientific questions you are trying to answer and what types of samples you are going to be analyzing. In this protocol, we refer to two types of investigative aims: exploratory (where you are trying to find out



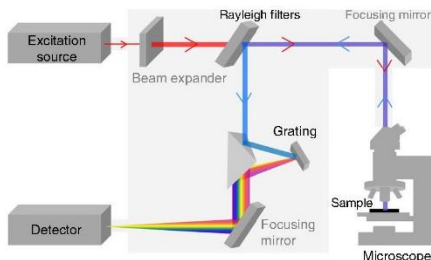


Figure 3 | Generalized overview of instrumentation options within a typical spontaneous Raman spectroscopic microscope system. The beam path will vary slightly between manufacturers, and thus it may contain additional optical components.

what compounds are present in your sample) and diagnostic (where you are using the presence of a compound or a molecular fingerprint to draw conclusions about the sample; see Step 17 of the PROCEDURE). Within these aims, you will have analytical goals or expectations that may be one of the following types: pattern finding, biomarker identification, or spectral classification for diagnostics or imaging^{79,87}.

Raman microspectroscopy can be used to analyze a wide variety of sample types including fresh plant material (Step 1A), fixed mammalian tissue (Step 1B), biofluids (Step 1C) and cultured mammalian cells (Step 1D). The constraints of the sample under investigation need to be considered (e.g., format, impurities) along with the investigative aims and analytical goals when deciding what equipment to use and how it should be set up. The first decision to make is what excitation source to use.

Excitation source. It is possible to use a variety of excitation sources to irradiate samples, depending on the suitability of the specimen to increased photon energies, as well as on the sensitivity and resolution required in the study. Broadly speaking, there are three main parameters to consider when choosing a laser system: (i) the type of laser source, (ii) the desired wavelength and (iii) the desired spot size.

There are several laser source options available within Raman systems, of which diode lasers are increasingly commonplace, particularly within biological investigations. Diode lasers are based on solid or semiconductor technology, and consequently they provide greater energy efficiency than their popular noble gas-based counterparts^{88,89}. Although gas-based lasers have been frequently used in laser-based technologies, they are restricted by a finite lifetime. A helium neon (HeNe) laser has a relatively low power output in comparison with diode lasers, and more powerful alternatives, such as the argon-ion laser, discharge large amounts of heat that require a cooling system to counteract, which is energy inefficient and also reduces portability⁸⁸. The introduction of diode-based lasers has contributed to the development of portable Raman systems because of their durability and compactness^{90,91}.

When choosing a laser source, it is also important to consider whether the experiment requires the use of pulsed rather than continuous-wave lasers. For example, a pulsed laser would be required in a stimulated Raman spectroscopy system, as the more intense electric field strength of the laser pulse energy can contribute to the increased frequency of Raman scattering events.

The line width of the laser is also an important consideration, as it has a direct influence on the spectral resolution, regardless of spectrometer configuration. Generally, gas-based and solid-state

TABLE 1 | Raman microspectroscopy method derivatives and the respective experimental benefits and limitations.

Technique	Adaption	Benefits	Limitations	Applications/references
Coherent anti-Stokes Raman scattering (CARS)	Nonlinear approach that uses multiple laser frequencies; a pump (ω_p) and Stokes (ω_s) field that combine, tuned to a frequency equivalent to a specific molecular vibration, thus generating a strong anti-Stokes signal ($\omega_{as} = 2\omega_p - \omega_s$) that detects vibrational coherence	10^3 – 10^6 increased signal ¹⁵³ High sensitivity 3D imaging	Nonresonant background can dominate weak resonance signals	Cell imaging ^{154,155} Tissue imaging ^{156,157} Cancer diagnosis ^{158,159} Pharmaceuticals ^{160,161}
Confocal Raman microscopy	Addition of a confocal microscope that allows depth measurements within a tissue. A pinhole is used within the spectrometer to reject stray light, effectively reducing the collimation of the beam and information to be derived from an alternative focal plane	High sensitivity High lateral and depth resolution 3D imaging Rapid acquisition	Diffraction-limited resolution	Cell imaging ^{162,163} Tissue imaging ¹⁶⁴ Cancer diagnosis ^{165–167} Pharmaceuticals ^{168,169} Plant cell imaging ^{74,75}
Drop-coating deposition Raman spectroscopy	Sample preparation for fluid analysis that drops a small volume of sample onto a flat substrate and allows it to dry	Accurate preparation of biofluids Small volumes of fluid are required (2–10 μ l)	Not completely free from the 'coffee ring' effect	Biofluid analysis ¹¹⁹ Protein quantification ^{117,120}

(continued)

NATURE PROTOCOLS | VOL.11 NO.4 | 2016 | 667

PROTOCOL

TABLE 1 | Raman microspectroscopy method derivatives and the respective experimental benefits and limitations (continued).

Technique	Adaption	Benefits	Limitations	Applications/references
FT-Raman	Nondispersive system that uses FT using a Michelson interferometer	High throughput High resolution Free from fluorescence	Low scattering intensity Limited to IR measurements Detector noise limited	Pharmaceuticals ^{13,170} Plant materials ^{71,171}
Kerr-gated Raman spectroscopy	A linear technique that uses repeated laser pulses and a Kerr gate that capture Raman light temporally (up to 3 picoseconds)	Depth measurements up to several millimeters Fluorescence rejection High sensitivity	Not completely free from fluorescence Better performance when in conjunction with shifted excitation Raman difference spectroscopy (SERDS)	Depth profiling in human tissue ^{172–174}
Polarized Raman spectroscopy (PRS)	Polarized light with a specific electric field vector will only obtain spectral information from specific vibrational modes, depending on their orientation in relation to the incident beam	Information regarding molecular structure and orientation	Not applicable to most samples Loss of spectral information Time consuming	Collagen orientation ¹⁷⁵ Plant photosystems ¹⁷⁶
Raman optical activity (ROA)	By using right- and left-circularly polarized incident light, the small changes in Raman scattering can be indicative of optical activity of discrete molecular vibrations	Structural information from specific conformations of chiral molecules	Circular intensity differences are very small Vibrational coupling in ROA signals can prevent accurate band assignment	Biopolymer analysis ^{177–179} Pharmaceuticals ^{180,181}
Resonance Raman spectroscopy (RRS)	Exploits the ‘resonance effect’ observed when the laser frequency matches (or approaches) that of an electronic transition of the sample or compound in question	Up to six orders of magnitude increase in signal ¹⁸²	Susceptible to fluorescence interference	Plant photosystems ¹⁸² Human biology ^{54,55,183,184}
SERDS	Nonlinear approach that obtains two spectra at marginally different laser frequencies and creates a difference spectrum by subtracting the two, thus removing background fluorescence	Fluorescence rejection Increased sensitivity	Difference spectra are reconstructed using peak fitting Prone to error	Live cells ¹⁸⁵ Animal tissue ¹⁸⁶ Human tissue ¹⁸⁷
SORS	Continuous, low-intensity laser beams are used to illuminate the surface of the sample, and Raman spectra are then derived at distinct distances away from this point. A scaled subtraction between these spectra reveals alterations indicative of the underlying subsurface layers	Depth measurements up to several millimeters	Relatively weak signal	Cancer diagnosis ^{32,188,189} Chemical analysis beneath physical obstructions ^{190,191}
Surface-enhanced SORS (SESRORS)	A combination of SERS and SORS approaches, able to detect SERS nanoparticles introduced into turbid samples	Detects SERS signals up to 50 mm beneath the sample surface ¹⁹²	Requires nanoparticle introduction	Depth measurements ^{193–196}

(continued)

TABLE 1 | Raman microspectroscopy method derivatives and the respective experimental benefits and limitations (continued).

Technique	Adaption	Benefits	Limitations	Applications/references
SRS	Nonlinear approach using a pump (ω_p) and Stokes (ω_s) field that are tuned to a defined frequency representative of molecular vibrations ($\omega_p - \omega_s$). When this occurs, ω_p observes a stimulated Raman loss in energy, and ω_s observes a stimulated Raman gain. The transferred intensity is proportional to the biochemical constituents	Not affected by fluorescence and non-resonant background High sensitivity (1 in 10^6 photons) High spatial resolution	Prone to interference from strong Raman scatterers Limited to measurement of one Raman peak per acquisition	Cell imaging ⁵⁸ Plant imaging ^{23,197,198}
SERS	Because of surface plasmon resonance, a metal surface with nanoscale roughness can substantially increase the electric field when excited by a laser. Thus, when adsorbed to a biomolecule, these nanoparticles result in greatly enhanced Raman scattering	10^3 – 10^{10} enhancement Below diffraction limit resolution Quenches fluorescence Low detection limit Molecular labeling	Lack of reproducibility Can reduce band intensity of high-frequency modes Molecular selectivity to nanoparticle adherence	Single-molecule detection ^{199,200} Tumor targeting ²⁰¹ Live-cell analysis ²⁰² Pharmaceuticals ²⁰³ Cancer diagnosis ^{62,204,205} Bacterial identification ^{16,206} Plant materials ²⁰⁷
Surface-enhanced resonance Raman scattering	Combination of RRS and SERS approaches, using a laser frequency in resonance with a biomolecule of interest and the addition of a SERS active substrate	Up to 10^{15} enhancement ²⁰⁸ Cumulative benefits of both SERS and RRS	Increased experimental complexity	Biomolecule detection ²⁰⁹ Protein analysis ^{210,211}
TERS	Based on the same electromagnetic and chemical theory as SERS, TERS uses an atomic force microscope tip coated with SERS active metal. When placed in close proximity to the sample, it results in enhanced scattering	Tip-dependent spatial resolution Low detection limit Quenches fluorescence Below diffraction-limit resolution	Increased experimental complexity Sample heating at tip apex	Microbiology ¹⁸ Biochemical imaging ²¹²
Total internal reflection Raman spectroscopy	The sample is placed in contact with a reflective prism, through which a laser beam is reflected, producing an evanescent wave that penetrates the sample below	Defined penetration depth	Reduced surface sensitivity	Plant materials ⁶⁸
Transmission Raman	Raman scattered light is captured on the opposite side of laser illumination	Depth measurements up to 30 mm Suitable for opaque materials	Interference from surface molecules	Cancer diagnosis ²¹³ Pharmaceuticals ^{214,215}

lasers have narrow bandwidths and thus higher spectral resolution, whereas some multimode diode lasers can have wide bandwidths with broad spontaneous emission.

The wavelength of the laser is critical to the experimental design (Fig. 4). The wavelengths available are laser-specific, yet they generally fall between the mid-UV (>200 nm) and the NIR (<1.1 μ m) regions. Fluorescence contribution (shown in black in Fig. 4) to a Raman spectrum can be avoided if you are exciting the sample with a wavelength that falls outside its profile. Therefore, by using NIR wavelengths, the resulting Raman spectrum (shown in red in Fig. 4) is free of any fluorescent contribution. Similarly, UV

wavelengths can be used, as the fluorescence resulting from light of these wavelengths is red-shifted beyond the fingerprint region of the Raman spectrum; therefore, the spectrum is comparatively free from fluorescence, despite the fact that higher-energy wavelengths are used⁷⁶.

Because of the effects of phototoxicity, a key constraint to consider is the interaction between the laser wavelength and the sample. Exposure to high-energy radiation, especially over prolonged periods of exposure, can have a destructive effect on samples. This is particularly important when conducting *in vivo* studies and interrogation of sensitive samples such as single cells.

PROTOCOL

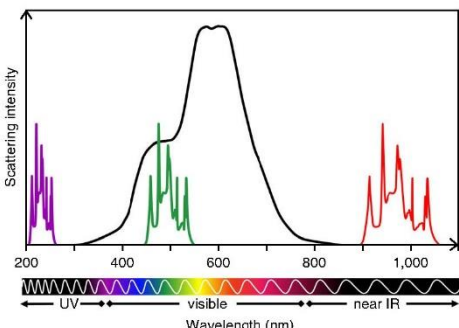


Figure 4 | Simplified overview of the effect of laser excitation wavelength on the fluorescence background. Visible lasers, such as the 532-nm (green) laser, are largely susceptible to background because of the defined wavelength profile of fluorescence (black), whereas high-energy UV (purple) and lower-energy IR (red) wavelengths, such as those at 244 and 1,064 nm, respectively, are relatively free of fluorescence.

Although reducing the laser power at the sample can decrease photodamage and the effects of phototoxicity, not all laser wavelengths are suitable for a given sample, and this should be considered beforehand; for example, cellulose is rapidly damaged at UV wavelengths. It is advised to reduce exposure times wherever possible and to conduct controls to determine the toxic effects of the laser wavelength in use.

In addition, the effect that laser wavelength has on other key experimental parameters such as resolution and sensitivity must also be considered. The spatial resolution is dependent on the spot size of the illuminating beam, which is dependent on the optics and the wavelength of the laser. Sensitivity is also dependent on the excitation wavelength, as the Raman scattering intensity is proportional to $1/\lambda^4$, resulting in substantially reduced sensitivity at lower laser photon energies, such as at the 1,064-nm laser wavelength.

NIR lasers, most commonly those at 785 and 830 nm, have been extensively applied in biological studies, particularly in fixed and live cells, as these lasers have relatively low photon energy and generally do not cause substantial photodamage^{92–95}. Tissue Raman microspectroscopy is also typically performed in the NIR region, because it is within the diagnostic window of low melanin and water absorption⁹⁶. For some molecules such as DNA, it makes more sense to perform excitation in the UV region, because the laser frequency and the electronic transition of the molecule under investigation are similar^{97,98}. This would provide a molecule-specific enhancement of the scattering, termed resonance Raman scattering.

Practically speaking, it is better to have >30 mW laser power at the source for the shorter visible wavelengths and >100 mW for the longer ones, and then to use a series of attenuators to optimize the illumination power delivered at the specimen. The total laser intensity (power/area) illuminating the sample is a central factor when aiming to acquire high-quality results from biological samples, given that they are generally low-scattering materials that suffer from radiation damage. It is important to consider this last point, as the laser intensity is dependent on laser spot size (sampling area) and magnification; therefore, these factors can have a major impact on the laser exposure of the sample.

It is possible to alter the profile of the laser spot in some Raman systems. By focusing the laser in a line (rather than a spot), a larger

surface area is illuminated, which results in more Raman scattered light. Thus, spectral information is obtained from a larger surface area, and photodamage is reduced⁹⁹. Raman maps can be obtained by raster-scanning the line-focused laser across the sample. Line mapping can be achieved in shorter acquisition times compared with point mapping, without compromising image quality^{83,100–102}. However, the intensity across the laser line is variable, and therefore this approach leads to spectra with variable signal-to-noise ratios (SNRs) across the laser line, unless corrections are applied to compensate for this. An alternative is to globally illuminate the sample area, often via a fiber-optic array probe, resulting in high-quality spectral imaging with enhanced power distribution across the sample^{103,104}. Specialized filters (e.g., liquid-crystal tunable, dielectric acousto-optic filters) are used to actively select specific wavelengths from the sample, which along with a 2D detector allows the production of true Raman images from relatively flat samples¹⁰¹. Although global illumination allows for the production of high-quality images, this often comes at a cost of the underlying spectral quality due to the reduced laser intensities across the sampling area.

After considering how best to illuminate the sample, we need to turn our attention to the choice of detector.

Detector. To detect the weak intensity of scattering, the detector included in the Raman system needs to be extremely sensitive. Greater levels of sensitivity may be necessary in some studies in which scattering is especially weak, or in which noise is particularly high, and thus the challenge of detection is increased. Charge-coupled devices (CCDs) are commonly integrated in Raman systems, because they exhibit high quantum efficiencies and low SNRs, compared with early alternative detectors such as photomultiplier tubes (PMTs) and photodiode arrays (PDAs)¹⁰⁵. CCDs are multichannel arrays made up of thousands of pixels, each of which can collect charge from scattered photons¹⁰⁶. This charge is directly proportional to the Raman scattering intensity. The CCD detector then reads out this charge by translating it from one pixel to the next until it reaches the edge of the detector chip and can be read out by the readout electronics. There are a range of CCD choices available, including intensified CCDs (ICCDs) and electron-multiplying CCDs (EMCCDs). At extremely low scattering intensities, EMCCDs can provide superior sensitivity than conventional CCDs by creating further electrons and therefore providing a signal relatively higher than the readout noise. However, if spectra are shot noise- or Poisson noise-limited, as is usually the case with biological tissues and cells, the use of an EMCCD will not improve SNRs¹⁰⁷. Dark, or thermal, noise can be markedly improved by detector cooling, often by using liquid nitrogen cryogenic or thermoelectric Peltier cooling, with deep cooling toward -80 to -100 °C providing up to one order of magnitude improved noise reduction¹⁰⁸.

The quantum efficiency of the silicon-based CCD detectors is wavelength-dependent, and it drops off rapidly in the NIR region. In this spectral region, back-illuminated CCDs could suffer from fringing effects, as the detector thickness effectively behaves as a wavelength resonator. Thus, longer wavelengths of light may not be effectively absorbed and can result in signal modulation and artifacts that could appear in the spectra, with detrimental effects on spectral quality. The use of deep-depletion CCDs can reduce fringing effects, as a thicker photosensitive region is used so that reflection of NIR light is reduced. For NIR studies beyond 950 nm,

in which the photon energy is less than the silicon bandgap, multichannel array detectors such as indium gallium arsenide (InGaAs) detectors are advantageous in order to overcome thermally generated noise in the higher-wavelength region¹⁰⁹.

There are a number of additional hardware options and parameters that can affect experimental output. These include the choice of filters and monochromators, the sampling aperture and the microscope objective.

Filters and monochromators. Rayleigh scattering is more intense than Raman scattering and can easily overpower the more informative signal, so it must be optically filtered. Dispersive Raman spectrometers use specialized Rayleigh filters or a multistage monochromator, whereas nondispersive spectrometers often use Fourier transformation (FT) based on a Michelson interferometer¹⁰⁹. There are a range of manufacturer-specific Rayleigh filters available¹¹⁰; however, holographic notch and dielectric edge filters are most commonly used. Edge filters only transmit light wavelengths above that of the laser in use, whereas notch filters will effectively filter only the laser wavelength, allowing both Stokes and anti-Stokes measurements¹¹¹. Metal oxide edge filters have been shown to have much longer lifetimes than notch filters.

Rayleigh filters must be selected to be specific to the laser wavelength. Multistage monochromators with variable laser wavelengths can be used, but there is a major throughput disadvantage to using multistage monochromators⁶. Single monochromators comprise a diffraction grating, which is used to disperse the Raman scattered light, and they are universally used in conjunction with Rayleigh filters. Gratings differ with respect to the number of grooves (per mm) or lines (per mm) on the surface, which can be anywhere in the range of 150–4,000 per mm, corresponding to the diffraction or angular dispersion capabilities of the grating. Higher groove frequency can improve the spectral resolution at the cost of reduced spectral intensity and range.

Sampling aperture. The sampling aperture of the system determines how much light, and therefore Raman scatter, is passed through the spectrometer. Slits and pinholes range from 10 to 100 μm , with a larger aperture allowing more light through the system and thus increasing sensitivity, but at the expense of spectral and depth resolution. For thin samples such as fixed cells, the use of pinhole and optimal in-depth focus of the laser illumination is crucial to maximizing the Raman signal from the sample volume.

Microscope objective. The choice of microscope objective is crucial in Raman microspectroscopy. The objective's throughput depends on its magnification and solid angle of light collection—i.e., NA. A high-magnification/high-NA objective provides higher axial spatial resolution, but it has a shorter working distance and may be better suited for thin samples. Low-magnification/moderate-NA objectives provide lower axial spatial resolution, but they have a longer working distance and may be better suited for bulky specimens to avoid the specimen touching the objective. Low magnification may be more appropriate for samples that do not require high spatial resolution, such as liquids and homogeneous samples. Conversely, high magnification is beneficial in studies that require high spatial resolution so that specific biological architecture can be examined.

Importantly, microscope objectives can be specially coated in anti-reflective materials or wavelength filter coatings for optimal performance in a specific wavelength region, and those coatings can produce significant background signals if another wavelength is used. We encourage careful consideration of the microscope objective and additional preliminary tests with the sample under investigation.

Experimental design: sample preparation

One of the major advantages of Raman microspectroscopy in biological studies is the ability to derive label-free and non-destructive spectral information with minimal sample preparation. However, it is important to appreciate sample constraints, as well as substrate options, that can have a substantial effect on experimental procedures. Sample stabilization and relative flatness are also important sample preparation considerations, because the technique relies on maintaining optical focus.

Sample format. Although it is possible to analyze fresh tissues directly, fixation can be an important step in preparing mammalian tissue samples or samples of cultured cells. Advantages are that it is a standard method for sample archiving, that it is easy to obtain thin sections from fixed and embedded tissue, and that fixation isolates a sample at a distinct experimental time point.

Formalin-fixed, paraffin-embedded (FFPE) tissues have been historically archived in pathological settings, and these specimens have been widely analyzed using microspectroscopy. A problem for Raman analysis of these samples is that formalin modifies proteins by cross-linking, and it can thus alter spectral peaks associated with proteins between 1,500 and 1,700 cm^{-1} . Furthermore, paraffin has strong signals in the fingerprint and higher-wavenumber regions of the spectrum. These signals can be found at 892, 1,065, 1,135, 1,174, 1,298, 1,421, 1,443 and 1,464 cm^{-1} , and thus they have substantial overlap with the underlying sample biology¹¹². The contributions of paraffin in the Raman spectrum can be removed by either de-waxing the sample or by digital de-waxing, which can remove the strong paraffin peaks from the spectrum¹¹³. De-waxing, as well as the fixation process itself, has been shown to have a marked effect on lipid content in samples, and it should therefore be used cautiously when drawing conclusions based on lipid alterations¹¹⁴. Digital de-waxing avoids modifying the sample molecularly, yet it can limit the number of viable spectral regions that can be interpreted. In the PROCEDURE, we describe sample de-waxing using xylene (Step 1A).

Analysis of fresh or snap-frozen tissues may overcome these substantial drawbacks, although sample acquisition becomes more difficult, sectioning is encumbered and sample degradation must be controlled. Live-cell analysis is a rapidly expanding field that allows the user to interrogate cells *in situ* in aqueous environments and 3D cell cultures while maintaining key growth parameters, including temperature and gas availability⁵⁶. In these studies, it is important that the cells adhere sufficiently to a growth substrate before analysis. In addition, the background signal from the cell medium should also be considered beforehand, as it may provide unwanted background interference.

Liquid samples can be easily examined by Raman microspectrometry. This can be achieved using either an immersion

PROTOCOL

objective or a microfluidic device to overcome spectral artifacts due to the presence of bubbles and surface tension. This has permitted the analysis of biofluids, such as blood plasma, sputum, saliva and urine, in diagnostic studies⁵¹. Another approach for biofluid analysis is a combined drop coating deposition Raman spectroscopy (DCDRS), which is also known as drop deposition/Raman spectroscopy; this is covered in Step 1C. Small biofluid volumes are deposited onto a flat substrate and allowed to dry on the basis of sessile drop formation principles¹¹⁵. Sessile drop formation has many benefits for Raman spectroscopy, with pre-concentration of proteins, coarse separation of impurities and reproducible prediction of protein solution concentrations^{116,117}. The resultant 'coffee ring' dried drop can be examined by Raman microspectroscopy, with the knowledge that a variable coffee ring thickness affects spectral intensities and the distribution of macromolecules within the ring deposit^{118–120}.

Raman substrates. Substrate choice is a critical factor in experimental design, and it is dependent on the experimental outputs and sample characteristics. The matrix on which a sample is supported contributes to physical stability, and therefore it directly affects the spectral quality by keeping the sample in focus for the duration of the experiment. The most important properties of the substrate to consider are the spectral background signals, as well as the substrate cost, availability and composition. Care should be taken in choosing a substrate and appropriate preliminary experiments should be performed, because contaminants can produce unwanted background signals. The glass slides typically used in optical microscopy are exceptionally cost effective, but they have a strong background fluorescence at most wavelengths except 532 nm (ref. 121). One approach is to use metal-coated glass slides, such as aluminum- or gold-coated glass, which effectively eliminate the glass signal. Gold-coated slides with roughened surfaces have also been shown to be good SERS substrates¹²². Calcium fluoride (CaF_2), quartz or fused silica slides are used as Raman substrates, because they show minimal background interference. Barium fluoride (BaF_2) slides have also been used as Raman (and IR) substrates, but their partial solubility in water makes them unsuitable for *in vivo* and aqueous studies¹²³. Although these specialty substrates are more expensive than glass, they are often reusable in a laboratory setting. In a clinical setting, these costs may be prohibitive, particularly for large-scale screening programs. The development of low-cost, single-use sterilized Raman substrates is an ongoing process in which there have been a number of recent developments, including the use of aluminum foil¹²⁴.

SERS. To acquire enhanced spectra using the SERS technique, a greater degree of sample preparation is required than in traditional approaches. As mentioned previously, SERS relies on the interaction of materials with nanoscale roughness with biomolecules within the sample, and the user must first decide on an appropriate SERS substrate. Gold and silver nanoparticles are considered ideal SERS substrates for biological studies using radiation in the visible and NIR regions, as their plasmon resonance frequencies are within this range, although other noble metals such as platinum can be used. The enhancement capabilities of metallic nanoparticle solutions are highly dependent on nanoparticle size, shape and aggregation^{125,126}. Theoretically,

as nanoparticles increase in size, the resonance will red shift; however, at diameters >100 nm, this comes at a cost of increased resonance linewidth and therefore specificity. Metallic nanospheres have been commonly used in SERS studies, although novel nanostructures such as nanorods and nanostars have exhibited optimized enhancement of the Raman signal¹²⁷.

Label-free detection of analytes is a relatively simple SERS approach, which does not require substantial sample preparation. Colloidal nanoparticles can be mixed at a user-defined ratio with other liquids or applied directly onto a sample and allowed to dry. Provided that substantial adsorption occurs between the nanoparticles and the sample, it is possible to acquire consistent, enhanced spectra from homogeneous samples. Conversely, the enhancement effect and resultant spectra become more variable in complex samples, as nonspecific enhancement of each biomolecule within the sample can occur (Fig. 5). This issue can be overcome by using SERS labels to specifically target molecules of interest, and it has proven to be a valuable tool in analytical studies^{64,65}.

Experimental design: spectral acquisition

The desired spectral output must be considered when approaching spectral acquisition, as the experimental parameters for simple point spectra and image construction are different (Steps 7A and 7B). A point-mapping approach allows the user to actively, or randomly, select specific areas of the sample to interrogate with the laser spot. In contrast, an image-mapping approach will derive spectra in a stepwise manner across a larger sample area, thus allowing image generation. In general, superior spectral quality can be obtained using a point-mapping approach, as data sets can benefit from longer acquisition times. In comparison, hyperspectral data cubes generated from mapping and imaging techniques can provide user-friendly data interpretation, although a balance between extensive acquisition times and spectral and image quality is required¹⁰¹. For example, a map spanning a biological feature $10 \times 10 \mu\text{m}$ in size would be made up of 100 spectra when using a step size of $1 \mu\text{m}$ (with oversampling). This map could be acquired

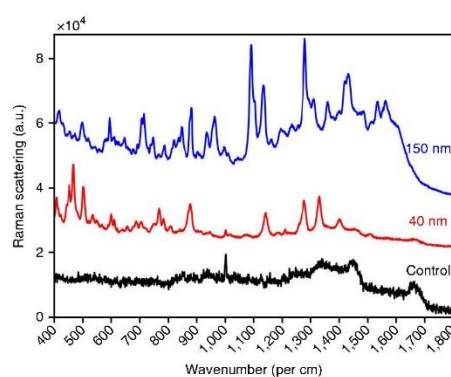


Figure 5 | Raman spectra derived from blood serum containing 150- and 40-nm diameter gold nanospheres, and a control sample containing no SERS substrates. An enhancement effect can be seen in comparison with the control sample, with a 10- and a 30-fold increase in scattering intensity with 40- and 150-nm nanoparticles, respectively (not to scale). However, clear spectral differences are evident because of the complex nature of the sample and the distinctive effects of nanoparticle diameter. a.u., arbitrary units.

relatively quickly when using acquisition times <10 s, although some samples may require longer laser exposures because the sample volume is small or because the sample has weak scattering tendencies (as the latter is relevant for single-cell studies, for example). However, it is important to note that huge numbers of poor-quality spectra can still provide exquisite detail if multivariate approaches are used to analyze the data.

Resolution. The desired spectral and spatial resolution of the experiment, and hence the required sensitivity, must be decided before spectral acquisition. As mentioned with regard to instrumentation options, spatial resolution is ultimately diffraction limited and therefore linearly dependent on the laser wavelength, and it is inversely proportional to the NA of the objective. Accordingly, high spatial resolutions can be achieved with lasers at shorter wavelengths and high-magnification optics.

In contrast, spectral resolution is greater at higher excitation wavelengths, provided that the Raman optical configuration remains constant. An increased number of smaller-sized pixels within the detector and lower levels of cross talk between pixels can also contribute to higher spectral resolution¹²⁸. Spectrometer focal length (SFL) is the distance between the diffraction grating and the detector. This distance is typically 200–800 mm, with greater distances generally providing improved spectral resolution¹²⁹. A larger SFL requires a larger entrance slit, in order to allow the maximum passage of light, which can also influence spectral resolution¹³⁰. However, it is often impractical to alter these parameters within a single Raman system. Gratings with higher groove frequencies can improve spectral resolution at a cost to sensitivity and spectral range, and they can be relatively easy to change on a single Raman instrument.

It is evident that when choosing a laser excitation wavelength there is a potential trade-off between desired spectral and spatial resolution. High spectral resolution (up to 0.5 cm^{-1}) may be required in studies in which specific molecular information is required and thus adjacent Raman bands need to be differentiated, such as in pharmaceutical studies monitoring drug uptake at the cellular level. Increased spatial resolution (up to $1\text{ }\mu\text{m}$) is required when specific localized information is required, which is particularly important when interrogating tissue features to extract biological information. This is particularly valuable in mapping and imaging approaches, as specific architecture can be imaged, such as when identifying cancer progression in tissue samples^{42,45}.

Although they are not exhaustive, these factors determine the spectral output and must be considered before analysis. Once these parameters have been chosen, there are steps that can be taken to optimize the experimental conditions. These include instrument calibration (Step 4), adjustment of experimental parameters to optimize for spectral quality and determination of the levels of spectral contamination, which are discussed below.

Calibration. Commercially available instruments produce the Raman spectrum as given wavelengths of light strike the detector at defined pixel values. The process of calibrating the spectrum from pixels to Raman shift, typically reported in wavenumbers, is a multistep process. We recommend daily calibration of the instrument (according to the numbered guidelines below), as even subtle shifts in the instrument optics may produce an observable change in the Raman shift.

- (1) It is important that the user ensure that the laser spot corresponds to the visual and spectrometer sampling point before sample acquisition. If necessary, beam alignment can be performed using manual or computerized beam-steers, and it should be checked regularly to optimize spectral acquisition.
- (2) Depending on the instrument manufacturer, there are manual and/or automatic calibration options. The first calibration step is conversion of pixels to wavelength. This is achieved by measuring the light emissions of a calibration lamp (such as neon or argon) that has multiple atomic emission lines, and using a nonlinear model to fit the spectral peaks to the CCD pixel.
- (3) The second and third steps are converting wavelength to wavenumber units by forming the inverse of the wavelength and correction of the laser wavelength using reference materials with defined Raman signatures. The easiest reference material to use is silicon, which has a sharp peak at 520.5 cm^{-1} , and any band shifts can be easily offset¹³¹. Other Raman reference materials include cyclohexane, acetaminophen or Teflon. Luminescent or broadband emission standards can be used to derive a system response function measure to correct for filter, detector etaloning and quantum efficiency effects¹³². Further performance validation tests can include the measurement of a well-characterized protein in order to check SNR and calibration consistency between measurements. National Institute of Standards and Technology (NIST) standards are also routinely used as calibration references.

Spectral quality. Optimizing experimental parameters is an iterative process, requiring an element of trial-and-error to obtain a method for optimum spectral quality and high SNR. Spectral quality is governed by instrumentation, sample suitability and, ultimately, time constraints. Within these constraints, the following steps can be followed to improve spectral quality:

- (1) Depending on the sample type, it is possible to attenuate the laser power so that higher power is used for weak scatterers to get the highest possible Raman signal, and lower power is used for intense scatterers in order to prevent detector saturation¹²⁸.
- (2) After power adjustments, the exposure time of the laser on the sample can be increased, thus multiplying the intensity of scattered photons and therefore the spectral quality.
- (3) The user also has the option to accumulate multiple spectra, increasing the signal intensity and reducing baseline interference. Longer exposure times and acquiring multiple spectra, commonly referred to as coadditions, can substantially affect sampling times, thus resulting in a potential trade-off between spectral range, quality and time availability.

Spectral contamination. There are a variety of common contaminants that can be observed in Raman spectra, some of which can be sample or instrument dependent. As previously described, fringing effects from the detector and unwanted background from sample substrates are examples of potential spectral contamination. Others include:

- (1) Cosmic rays are sporadic background artifacts recognized by sensitive detectors, which manifest in Raman spectra

PROTOCOL

as narrow-bandwidth spikes¹³³. Most of the instrument software packages contain cosmic ray removal algorithms that allow the user to selectively eliminate cosmic rays, as well as algorithms in processing packages for automated cosmic ray removal¹³⁴.

- (2) Peaks from known contaminants, such as paraffin in FFPE tissues, can be removed using wavenumber exclusion techniques or computational algorithms, which are widely available on instrumentation software, as well as analysis programs¹¹².
- (3) For samples that contain extrinsic fluorescence, photo-bleaching could be used to suppress interference from contaminants. Exposing samples to the incident light source for a few seconds before acquiring spectra on the detector, effectively 'bleaching' the fluorescent contaminants, has been shown to reduce oscillating baselines¹³⁵.

Experimental design: data processing

Spectroscopic studies can rapidly generate large data sets that require computational processing in order to derive biochemical

information. Depending on the specific spectral acquisition and experimental objectives, it is possible to extract informative images, spectral biomarkers and patterns, and also to classify samples on the basis of their spectral fingerprint. As a rule, data processing can be divided into three distinct steps: (i) data set pre-processing, (ii) feature extraction and (iii) classification⁷⁹. **Table 2** provides a list of available analysis software. There is also a strong relationship between Raman and IR spectral analysis (for reviews of this technique, see Baker *et al.*⁷⁹, Martin *et al.*⁸⁷, Lasch¹³⁴ and Trevisan *et al.*¹³⁶).

Pre-processing. Immediately after acquiring the spectra, the quality of the spectral data sets should be assessed, and pre-processing should be applied to improve the accuracy of the study by minimizing insignificant variability¹³⁴ (Steps 11–16). At this point, spectra should be corrected for cosmic rays, and the quality of the spectra can be visually assessed. There are some circumstances in which visual inspection of spectra shows clear outliers, including substantial spectral contamination, fluorescence or very poor SNR¹³⁷. In those cases, obvious outliers can be removed from the data set. Other spectra that are outliers in

TABLE 2 | Data analysis software for Raman spectral data sets.

Software	Website	License
CytoSpec	http://www.cytospec.com/ftir.php	Commercial
ImageLab	http://www.imagelab.at/en_home.html	Commercial
MATLAB		Commercial
Biodata Toolbox	http://www.mathworks.com/matlabcentral/fileexchange/22068-biodata-toolbox	Open source
Extended Multiplicative Signal Correction (EMSC) Toolbox	http://www.models.life.ku.dk/emsctoolbox	
IRootLab	https://code.google.com/p/irootlab/	Open source
Multivariate Image Analysis (MIA) Toolbox	http://www.eigenvector.com/software/mia_toolbox.htm	Open source
Multivariate Curve Resolution-Alternating Least Squares (MCR-ALS) Toolbox	http://www.cid.csic.es/homes/rtaqam/tmp/WEB_MCR/welcome.htm	Commercial
PLS Toolbox	http://www.eigenvector.com/software/pls_toolbox.htm	Open source
Raman Processing Program	http://cares.wayne.edu/rp/	Commercial Open source
Origin for Spectroscopy	http://www.originlab.com/index.aspx?go=Solutions/Applications/Spectroscopy	Commercial
PeakFit	https://systatsoftware.com/products/peakfit/	Commercial
Python		Open source
PyChem	http://pychem.sourceforge.net/	Open source
PyVib2	http://pyvib2.sourceforge.net/	Open source
R		
HyperSpec	http://hyperspec.r-forge.r-project.org/	Open source
The Unscrambler X	http://www.camo.com/	Commercial



the data set could be identified using a Q-test or another outlier-detecting algorithm; to reduce user bias, this could be done in addition to or even instead of visual inspection. We recommend sagacious and limited removal of spectra from a data set, particularly with respect to hyperspectral images and small data sets.

Raman spectra are particularly prone to noise, and data may require noise reduction to enhance spectral quality. The first approach to improve the quality of the Raman signal would be to alter spectral acquisition settings, such as by using increased integration times and higher laser power. Sample preparation may also be adjusted by preconcentrating or photobleaching the sample. If these approaches are inadequate, then spectra can be computationally manipulated after acquisition to improve the SNR. Principal component analysis (PCA) is a powerful technique in Raman pre-processing that can effectively reduce the spectra into a defined number of principal components (PCs) that account for significant spectral variance¹³⁸. This technique can be used to reconstruct spectra using only significant PCs, thus retaining important spectral data while removing background noise¹³⁹. Other noise-reduction approaches include Savitzky-Golay (SG) smoothing, minimum noise fraction transform and wavelet denoising (WDN) techniques that can filter high-frequency noise¹³⁶. Although smoothing spectra does reduce the apparent noise, we note that these processes also degrade spectral features, and we recommend limited and cautious use of smoothing.

Sample and background fluorescence, as well as thermal fluctuations of the CCD, can markedly affect the spectral baseline, and therefore baseline correction is necessary. Polynomial baseline fitting attempts to estimate the unknown background. This is often dependent on user-defined polynomial points, and it can effectively abolish sloped or oscillatory baselines^{140,141}. Care should always be taken with any baseline subtraction routines, as they can introduce unintended artifacts. Alternatively, first- or second-order differentiation, coupled with SG smoothing, can be applied to mathematically remove contributions from scalar offsets or baseline slopes, while simultaneously resolving overlapped peaks¹⁴². Unlike polynomial fitting, which yields spectra with conventional morphologies, derivative spectra are transformed and do not have a regular Raman appearance.

After baseline correction, spectra may also require normalization to correct for sample and experimental variables, such as thickness and density. Vector normalization and min-max normalization are two popular methods that can be applied to spectra after any baseline correction algorithms without substantially affecting spectral features¹³⁴. Amide I peak normalization is also commonly used in IR and Raman studies⁷⁹. However, this technique is not appropriate after differentiation, because of the shift of the typical amide bands, or for experiments in which you are measuring changes in protein structure, as all values are scaled to 1.

Finally, an optional data reduction step can be included in the pre-processing procedure to optimize statistical analysis. As highlighted previously, large spectral data sets can often present a significant computational burden, because of the many absorbance intensities contained in a single spectrum. By truncating the spectrum to shorter wavenumber ranges, this burden can be reduced, especially if the range focuses on individual Raman peaks¹⁴³. Alternatively, data-reduction algorithms, such as partial least squares (PLS) or PCA, can be used to reduce individual spectra down to a few key factors, and they have been widely implemented as both pre-processing and feature-extraction steps¹³⁶.

The selection of pre-processing steps and the order in which they are conducted has been shown to have a major impact on the outcomes of spectral analysis, thus complicating the development of a universal approach¹⁴⁴. Wherever possible, we advise the use of derivative baseline correction and vector normalization; although this does require high-SNR data, it can be particularly effective in diagnostic studies. In addition, whenever necessary, the use of noise and data reduction tools can be applied.

Feature extraction. In both exploratory and diagnostic studies, it is important to transform individual spectra into appropriate variables that confer biological information. Feature-extraction methods (see Step 17) range from the very simple, such as defining a band area, to considerably more complicated computational functions. Feature extraction can broadly be split into two distinct approaches: feature construction and feature selection. These approaches are comprehensively reviewed by Trevisan *et al.*¹³⁶. Briefly, feature construction can be defined as the creation of new features in a data set that can infer otherwise obscured information: for example, the previously mentioned linear methods PCA and PLS. This can be exceptionally important for diagnostics, biomarker extraction and pattern recognition in otherwise homogeneous data sets, and it has an important role in hyperspectral imaging, as individual pixels can be reduced to single values relating to spectral intensity or variance⁷⁹. Feature selection approaches extrapolate existing features from the data set, such as specific wavenumbers, that can be used to determine spectral biomarkers and/or feed into diagnostic frameworks¹⁴⁵. Techniques such as genetic algorithm, multivariate curve resolution and successive projection algorithm have proven to be particularly popular as feature-extraction methods, as only informative variables are included in the resultant model¹⁴⁶.

Classification. Classification of samples based on their spectra is often desirable, in both imaging and diagnostic studies, as spectra can be categorized based on prior user input (supervised classification) or spectral variance alone (unsupervised; see Step 17). Unsupervised classification typically relies on a clustering technique, of which hierarchical cluster analysis, *k*-means clustering and fuzzy C-means clustering are three popular options⁸⁰. PCA is another unsupervised approach that is commonly used to extract key variables describing the largest variance within a data set. In imaging studies, this approach requires no prior knowledge of the sample in question, and it produces information-rich pseudo-spectral images that are ideal for exploratory studies¹⁴⁷. The loadings or spectral features used to calculate the scores or weight images can provide key information on molecular distributions in a sample.

For diagnostic analysis, supervised classification is most commonly used, as the desired outputs are dependent on class labels provided by the user. This could be gold-standard histopathology, cell type or an alternative measure of class. These class assignments are taken into consideration when implementing the classification technique, using a proportion of the data set, referred to as a 'training data set.' A classifier is then able to categorize a separate 'test data set' accordingly. It is a common approach to validate the classification outputs using an independent data set. Linear discriminant classifiers (LDCs), artificial neural networks and support vector machines (SVMs) are particularly common



PROTOCOL

machine-learning techniques that effectively classify spectral data, although other techniques are available¹⁴⁸. Semisupervised classification is an alternative option when some, but not all, data classes can be determined^{149,150}.

Sample size. Classifier performance and validity is highly influenced by sample size, and thus choosing how many samples to use and also how many spectra to acquire is an essential aspect of experimental design. The number of spectra within a data set can easily surpass millions, as a sufficient number of spectra per sample and class type is required to account for the inherent sample intra- and inter-class variability. However, it must be

remembered that the number of spectra is not representative of the sample size, and frequently the number of independent samples is much smaller and may, for example, be determined by the overall patient number in a given study. It has been shown that a sample size of 75–100 is sufficient to train a classification model with good precision and validation¹⁵¹. Cross-validation may be a suitable solution in smaller data sets, as resampling approaches can repeat or iterate different training and test data sets for a defined number of times, effectively using as much of the data set as possible^{136,152}. However, full independent testing of a previously developed classification algorithm is the ideal approach, if the sample numbers permit.

MATERIALS

REAGENTS

! CAUTION We note that most of the listed reagents are chemicals with potential hazards. Users should consult with the chemical's MSDS and the appropriate facility safety guidelines before handling chemicals.

Raman spectra for each reagent used may be provided by the reagent supplier or accessed via a Raman database provided by the instrument manufacturer.

▲ CRITICAL For all materials listed alternative suppliers can be used, unless otherwise stated.

- Sample acquisition: fixed tissue, fresh tissue, cryosectioned tissue, fixed cells, live cells, biofluids and powders from a variety of biological specimens
- ▲ **CRITICAL** Research carried out with human subjects must be compliant with the Declaration of Helsinki. Research carried out with animals must be approved by the local institutional review board or animal use ethical board. Approvals must be established before the experiment's start.
- Paraffin wax pelletized with added polymers, 57–58 °C (Fisher Scientific, cat. no. 12624077)
- Liquid nitrogen (BOC, CAS no. 7727-37-9)
- Isopentane (Fisher Scientific, cat. no. P/1030/08)
- Virkon disinfectant (Fisher Scientific, cat. no. NC0480633)

Fixative agents

- Formalin, 10% (vol/vol; Sigma-Aldrich, cat. no. HT5011128)
- Glutaraldehyde, 25% (vol/vol; Sigma-Aldrich, cat. no. G5882)
- Ethanol (Fisher Scientific, cat. no. E/0600DF/17)
- Methanol (Fisher Scientific, cat. no. A456-212)
- Acetone (Fisher Scientific, cat. no. A19-1)
- Osmium tetroxide, 2% (wt/vol; Sigma-Aldrich, cat. no. 75633)

SERS nanoparticles

- Gold, 150 nm (1.66 × 10⁹ particles per ml; BBI Solutions, cat. no. EM. GC150)
- Gold, 40 nm (9.00 × 10¹⁰ particles per ml; BBI Solutions, cat. no. EM. GC40)
- Silver, 40 nm (2.6 × 10⁹ particles per ml; BBI Solutions, cat. no. EM. SC40)

De-waxing agents

- Xylenes (Sigma-Aldrich, 534056)
- HistoChoice clearing agent (Sigma-Aldrich, cat. no. H2779)

EQUIPMENT

! CAUTION We note that the listed equipment has potential hazards. Users should consult with the equipment instruction manual and the appropriate facility safety guidelines before use.

- Microtome (Thermo Fisher Scientific, cat. no. 902100A)
- Wax dispenser (Electrothermal, cat. no. MH8523B)
- Sectioning bath (Electrothermal, cat. no. MH8517)
- Centrifuge (Thermo Fisher Scientific, cat. no. 75002410)
- Desicator (Thermo Fisher Scientific, cat. no. 5311-0250)

Substrates

- Glass slides (Fisher Scientific, cat. no. 12657956)
- CaF₂ slides (Crystran, cat. no. CAFPI0-10-1)
- Quartz slides (UQG Optics, cat. no. FQM-2521)
- Gold-coated slides (Platypus Technologies, cat. no. AU.0500.ASLI)
- Aluminum-coated slides (EMF, cat. no. AL134)
- Quartz vial (Starna Cells, cat. no. 1-Q-1)

Accessories

- Laser power meter (Coherent, cat. no. 1098293)
- Microtome blades (Leica Biosystems, cat. no. 14035843490)
- Desiccant (Sigma-Aldrich, cat. no. 13767)
- Embedding base molds (Leica Biosystems, cat. no. 38VSP58167)
- Magnets, weights or mounting putty

Electronic equipment

- Raman microspectrometer (Table 3 illustrates a number of commercially available systems)
- Computer system: a standard computer should be sufficient for basic spectral acquisition and basic data analysis. As computational demand increases in proportion to the complexity of the data processing, it is advised that a system with sufficient RAM access (upwards of 4 GB) and a high-speed processor be used

REAGENT SETUP

Fixatives Fixatives must be diluted to the appropriate concentration using PBS or saline H₂O solution. They can be refrigerated at 4 °C for several weeks before use.

SERS nanoparticles Dilute the nanoparticles to an appropriate concentration depending on the experimental parameters. These can be prepared in advance and refrigerated at 4 °C for several weeks before use.

Fixed tissue Generally, tissues are fixed using an appropriate concentration of chemical fixative, followed by alcohol dehydration. Tissues can then either be desiccated and stored at room temperature (20–22 °C) for a number of months or paraffin embedded. An embedding base mold should be filled with molten wax using a wax dispenser. The sample should be carefully placed into the wax at the desired orientation and allowed to cool. FFPE tissue blocks can be stored at room temperature indefinitely.

Fresh tissue *In vitro* studies, such as when tissue has been excised from the independent sample, will be prone to sample degradation, and thus should be analyzed as soon after excision as possible. Refrigeration at 4 °C may be sufficient for 2–3 d of storage. Tissues may be snap-frozen using liquid nitrogen and isopentane for up to 1 year with minimal effect on sample integrity.

Fixed cells Cells can be fixed using appropriate chemical fixative or a preservative buffer, and they can be stored at room temperature for 1 month, or for 3 months at 4 °C. Cells can be gently centrifuged at 1,000g for 5 min at room temperature to form a concentrated cell pellet, wherever necessary.

▲ CRITICAL Splitting cells at ~60% confluence greatly diminishes the number of lipid droplets per cell, which can be caused by cell 'stress'.

Live cells Depending on the desired experimental aims, live cells must be kept in optimum living conditions throughout the study, including the maintenance of nutrient requirements via media, as well as temperature, pH, light and gas conditions.

Biofluids Once obtained, biofluids can be stored at –80 °C for several years to prevent degradation. Before sample preparation, biofluids should be thawed at room temperature or by using a water bath at 35–37 °C.

EQUIPMENT SETUP

Software Table 3 describes the available software options that come standard with each specific commercial instrument. These software options are essential for spectral acquisition, and they may also provide data processing provisions. However, for specialized spectral analysis, we direct the user to Table 2, in which alternative software options are listed.

TABLE 3 | Commercially available instruments and corresponding operational software.

Manufacturer	Instruments	Format	Software
BaySpec	Agility	S	Spec 20/20
	RamSpec	S	
	RamSpec-HR	S	
	Nomadic	M	
	MovingLab	MP	
Bruker Optics	SENTERA	M	OPUS
	RamanScopeIII	M	
	MultiRAM	S	
	RAM II	S	
	BRAVO	SP	
Horiba Scientific	XploRA Series	M	LabSpec 6
	LabRAM HR Evolution	M	
	Triple Raman Spectrometers	S	
	OEM Miniature Raman	SP	
JASCO	NRS-5000 Series Raman	M	Spectra Manager II
	NRS-7000 Series Raman	M	
	RMP-10	SP	
Kaiser Optical Systems	RamanRXN1	M	iC Raman
	Raman WorkStation	M	HoloMap
Ocean Optics	Maya2000 Pro	S	OceanView
	QE Pro	S	
	Ventana Series	S	
Ondax	THz-Raman Spectroscopy Systems	M	NA
	TR-MICRO	M	
Renishaw	InVia confocal Raman microscope	M	WiRE
	RA100 portable Raman analyzer	SP	
SciAps	Inspector300	S	NuSpec
	Inspector500	S	NuSpec Pro
	Reporter	SP	
Thermo Fisher Scientific	DXR Series	M	ValPro System Qualification
	FirstDefender RM Chemical	SP	
	Identification System	SP	
	FirstDefender RMX Handheld	SP	
WITec	Chemical Identification	SP	
	Alpha300 Series	M	WITec Suite
	apylon ∞	SM	

M, microspectrometer; NA, not applicable; P, portable; S, spectrometer.



PROTOCOL

PROCEDURE

Sample preparation

1| Prepare the samples and mount them onto appropriate Raman substrates according to option A for *in vivo* plant analysis; option B for FFPE tissue samples; option C for SERS biofluid analysis; or option D for analysis of cultured mammalian cells.

(A) Plant tissue • **TIMING 5 min**

- (i) Remove the plant sample from the plant specimen (e.g., take a leaf or a section of root).
- (ii) Place the sample on a suitable Raman substrate (depending on the thickness of the tissue). We typically use gold-coated slides for plant tissues, as they are not adhered to the surface and the substrate can therefore be reused.
- ▲ **CRITICAL STEP** Leaf tissue in most plant species should be sufficiently thick to avoid background interference from the substrate. However, root tissues, for example, may require a high-quality substrate.
- (iii) Secure the sample using a weight, adhesive or magnet if using a magnetic stage accessory.

(B) FFPE tissue • **TIMING 30 min + de-waxing (1.5 h)**

- (i) Acquire FFPE tissue blocks from a pathology laboratory with appropriate ethical approval.
- (ii) Place an FFPE block on a cool (preferably frozen) surface for at least 10 min.
- ▲ **CRITICAL STEP** Cooling hardens the wax, which therefore facilitates smooth sectioning.
- (iii) Position the block in a microtome sample holder, and begin to trim using large sections (up to 25 μm) until the surface on the tissue is exposed.
- (iv) Alter the microtome sectioning thickness appropriately, 5–10 μm is common in histopathology, and begin to cut sample ribbons.
- (v) Float individual ribbons in a heated sectioning bath at 40–44 °C.
- ▲ **CRITICAL STEP** Gentle heat will help relax the wax and enable effective mounting. Heat must not surpass 45 °C, as the sample will begin to degenerate as the wax approaches its melting point.
- (vi) Carefully mount the samples onto an appropriate Raman substrate, by using the slide to lift the ribbon out of the water. We typically use Raman-grade CaF_2 slides.
- ▲ **CRITICAL STEP** If the sample requires de-waxing, proceed to Step 1B(vii), if not, proceed to Step 1B(ix).
- (vii) Allow the slide to dry for 30 min.
- ▲ **CRITICAL STEP** The sample must be adequately adhered to the slide surface before de-waxing or the sample can be lost.
- (viii) Immerse the tissue in xylene for 5 min. Repeat this step twice to ensure that wax is adequately removed.
- (ix) Clear xylene residues using a 15-min 100% ethanol wash, followed by a further 15-min wash with 90% (vol/vol) ethanol and a final wash for 15 min with 70% (vol/vol) ethanol.
- (x) Store the samples at room temperature in a dry environment until analysis.

■ **PAUSE POINT** Samples can be stored for up to 1 year without significant degradation.

(C) SERS biofluids • **TIMING 10 min + drying (24 h)**

- (i) Obtain biofluid specimens with suitable ethical approval.
- **PAUSE POINT** Samples can be stored at –80 °C for 1–2 years, depending on license constraints.
- (ii) Apply 200 μl of biofluids and 200 μl of colloidal nanoparticles onto appropriate Raman substrate (volumes and ratios can be altered depending on the experimental design).
- ▲ **CRITICAL STEP** The user has three distinct methods for nanoparticle and biofluid mixture: apply the nanoparticle solution to the substrate, allow it to dry and subsequently add the sample; carry out the reverse of the above process, in which the sample is added first followed by the nanoparticles; or combine the two solutions together and apply the mixture onto the substrate.
- (iii) Allow the samples to dry before analysis. Larger sample volumes require extended drying times, and thus we recommend overnight drying as a standard for continuity.
- ▲ **CRITICAL STEP** As water evaporates from the biofluid, biopolymers can concentrate at the extremities of the drop, thus creating a concentration gradient across the sample. This is known as the coffee ring phenomenon, and we advise the user to appreciate this inconsistency across the sample before sample acquisition.

(D) Cells • **TIMING 12 h for cell attachment + 15 min for sample preparation**

- (i) Seed a known number of cells onto the appropriate Raman substrate in supplemented cell culture medium, under sterile conditions, and incubate them overnight at 37 °C.
- (ii) After 12 h or more, allowing for sufficient cellular adhesion to the substrate, remove cells from the incubator and aspirate off the cell culture medium. Wash the samples with warmed sterile PBS. For live-cell imaging, samples can be imaged in this warmed sterile PBS solution or warmed sterile-filtered 0.9% (wt/vol) NaCl saline solution. Proceed to Step 2.
- ▲ **CRITICAL STEP** Ensure that all reagents are warmed to 37 °C. Warming reagents to 37 °C reduces the shock to the cells and helps maintain overall morphology.

(iii) For cell fixation, immerse the cells in warmed 10% (vol/vol) formalin for 10 min. Wash the cells three times in warmed sterile PBS to remove any trace of the fixative. Samples can be then measured either dry or in sterile-filtered 0.9% (wt/vol) NaCl saline solution.

▲ **CRITICAL STEP** Ensure that all reagents are warmed to 37 °C. Warming to 37 °C reduces the shock to the cells and helps maintain overall morphology.

■ **PAUSE POINT** Fixed cultured cells can be stored for up to 3 months at 4 °C in sterile NaCl saline solution.

Spectral acquisition

2| Switch on the Raman microspectrometer and open the instrument operating software.

▲ **CRITICAL STEP** Carefully read the instrument operating manual and become aware of the operating features, specifications and safety operating procedures.

3| Determine suitable instrumentation options, including laser wavelength, detector type and suitable optics. Please refer to the 'Experimental design: instrument options' section of the INTRODUCTION for further guidance on these options, and set up the microspectrometer accordingly.

4| Calibrate and align the spectrometer using a calibration source. See the 'Experimental design: spectral acquisition' section of the INTRODUCTION for more information on the calibration procedure and the range of sources available.

5| Mount the sample on the microscope stage for spectral acquisition.

6| Use the microscope at the chosen magnification to examine the sample and focus on a feature of interest.

? TROUBLESHOOTING

7| Determine the sampling area using the microscope and operating software using a point-mapping (option A) or image-mapping (option B) approach. Fewer spectra are acquired in point-mapping experiments. This means that spectral quality can, and should, be optimized in order to get meaningful results. In contrast, image mapping can generally acquire a high number of spectra. This means that the researcher has to find a balance between acquisition time and spectral quality (see 'Experimental design' for further guidance). Very long sampling periods may be impractical in terms of sample throughput, and it might be that the sample degrades during the acquisition. This problem can be reduced using multivariate approaches, which can extract much spectral detail from a large number of noisy data.

(A) Point mapping ● **TIMING 1–5 min**

(i) Selectively, or randomly, choose numerous points in the sampling area to interrogate (anywhere between 5 and 50 spectra would be typical).

▲ **CRITICAL STEP** In SERS studies, enhanced spectra are obtained from molecules in close proximity to nanoparticles. In a point-mapping approach, we advise that the user determine where the nanoparticles have aggregated and choose points from this region.

? TROUBLESHOOTING

(B) Image mapping ● **TIMING 1–5 min**

(i) Select a mapping area using a 'shape fill' option (usually rectangular filled).

(ii) Determine the number of spectra to be acquired within the mapping area by altering the step size.

▲ **CRITICAL STEP** Be aware of the step size in use (typically ~1 μm), as sizes above this will result in undersampling, and sizes below this will result in oversampling.

8| Input the optimum spectral parameters to ensure the best SNR and spectral quality within an appropriate acquisition time, depending on the sample suitability. Determination of the laser power at the sample using the designated spectral parameters may be conducted using a laser power meter. This is a useful thing to do, so that the precise amount of power applied to the sample can be defined.

9| Acquire the sample measurement (1 s to 5 min per spectrum).

? TROUBLESHOOTING

10| Save the measurements before data processing, and convert them to a universal format if appropriate.

■ **PAUSE POINT** Data sets can be stored until data processing.

PROTOCOL

Data pre-processing ● TIMING 10–60 min (depending on data set size)

▲ **CRITICAL** Steps 11–16 highlight possible pre-processing steps that can be performed on the spectral data set in an advised order. All these steps are optional and can be applied in multiple combinations with varying effects on visual output. We recommend that the user observe the spectral output at each stage to inspect any adverse effects on the data sets. For further information, we direct the reader to ‘Experimental design: data processing’ in the INTRODUCTION.

11| Load the data into the selected software (Table 2).

12| Screen the data for anomalies and poor-quality spectra using quality tests.

? TROUBLESHOOTING

13| Apply a noise-reduction technique on the data set, such as PCA, to improve SNR.

14| Conduct a baseline correction algorithm to account for fluorescence interference.

15| Perform a data-normalization approach to account for confounding sample variables.

16| If necessary, perform a data-reduction technique such as simple truncation or PCA to reduce the number of variables in the data set.

Data analysis

17| Choose an appropriate data analysis approach that will extract the required information from your point spectra or images, depending on the desired analysis goal. The options described here are exploratory analysis for pattern finding and biomarker extraction (option A), and diagnostic analysis for spectral classification (option B). For more information, please refer to ‘Experimental design: data processing’ in the INTRODUCTION.

▲ **CRITICAL STEP** All timings are estimated for typical data sets containing anywhere between 500 and 5,000 spectra. Any deviations from this range will alter these estimates accordingly.

(A) Exploratory ● TIMING 15–60 min (depending on the data set size)

(i) Input the pre-processed data set into a feature-extraction algorithm.

▲ **CRITICAL STEP** For imaging, continue to Step 17A(ii); for point spectra, move to Step 17A(iv).

(ii) For image analysis, use feature-extraction outputs to assign a scalar value to each spectrum (such as wavenumber intensities or PC score).

(iii) Use a color gradient or code for scalar values.

(iv) Visualize analysis output for biomarker and pattern extraction.

(B) Diagnostic ● TIMING 1–4 h (depending on the data set size)

▲ **CRITICAL** For supervised classification, the data set must be split into training and test data sets.

(i) Input the pre-processed data set into a feature-extraction algorithm, either construction or selection, in training mode.

(ii) Apply this trained feature-extraction model to a training data set.

(iii) Train a classification algorithm using this training data set.

(iv) Input the test data set into the trained feature-extraction model followed by the trained classification algorithm.

▲ **CRITICAL STEP** Cross-validation is recommended on small sample sizes.

(v) Obtain a class estimation per spectrum.

(vi) For imaging, this class estimation can be assigned a scalar value and visualized using a color code.

(C) Diagnosis (unsupervised) ● TIMING 15–60 min (depending on the data set size)

(i) Use a clustering classification algorithm to categorize spectra on the basis of spectral variance.

(ii) Assign each cluster a numerical value or color for visualization.

? TROUBLESHOOTING

Step 6: maintaining optical focus

It can be difficult to maintain optical focus if the sample is not secured sufficiently, or if the surface is not adequately flat. Good optical focus is essential for obtaining good-quality spectra; this can be ensured by observing the focus on the sample before and after spectral acquisition. To improve stability, bulky samples should be held in place using magnets or weights when possible, or they should be secured with adhesive materials such as tape. A small amount of mounting clay or putty on the underside of hard specimens may help secure them onto a substrate. This should also help flatten some samples, but it may be necessary to physically smooth sample surfaces, such as when analyzing powders. Increased stability stages are

available, and they are recommended in systems using high magnification (100 \times), as small stage movements can have more significant effects at high magnification.

Step 7A(i): obtaining enhanced spectra

As enhancement depends on direct sampling of an area in close proximity to a nanoparticle, the probability of acquiring enhanced spectra is particularly low. We recommend isolating nanoparticle aggregates, which, unlike monomers, may be visible under magnification. A good knowledge of the sample in question is needed, and we advise carefully studying subtle differences between control and SERS samples. The use of larger nanoparticles (>100 nm) may also aid in nanoparticle aggregate identification⁶². Otherwise, using an automatic mapping procedure may produce enhanced spectra without the need of substantial user input.

Step 9: insufficient spectral quality

As data are obtained, the user should look out for four key indicators of poor spectral quality: (i) low SNR, (ii) fluorescence baseline, (iii) saturation of the CCD and (iv) photoablation. If any of these are seen, troubleshooting intervention is required.

(i) Low SNR—this is indicated by a strong background signal in comparison with Raman peaks, and it is indicative of insufficient Raman signal as a consequence of the sample or the experimental parameters. First, check that the system is appropriately aligned, that the optical focus is optimized and that the laser illuminates the sample. If possible, increase the laser power, followed by the exposure time and then an increased number of coadditions. If this is not possible, consider system alterations, including an alternative laser wavelength or a Raman approach that is better suited to your sample (Table 1).

(ii) Fluorescence baseline—a range of fluorescence manifestations can be observed, depending on the excitation wavelength in use, but it is principally indicated by a strong, broad and featureless spectrum, similar to the fluorescence wavelength profile (Fig. 6a). Fluorescence is predominantly due to sample characteristics, although it can be influenced by background conditions, such as ambient lighting. We advise using a UV or NIR laser wavelength, or implementing an alternative Raman approach that can overcome fluorescence, such as SERS or SRS. Photobleaching may also reduce fluorescence contributions, with enhanced risk of photoablation.

(iii) Saturation of the CCD—each CCD will have a limit as to how many Raman-scattered photons it can measure. When exceeded, this limit can be observed on the spectrum by a feature such as a flat-line effect (Fig. 6b). As saturation is indicative of increased Raman scattering, this issue is usually found in strong-scattering materials, samples of a large volume and in SERS studies. This can be overcome by attenuating the laser power and/or exposure time on the sample. Saturation cannot be corrected in postacquisition processing.

(iv) Photoablation—some samples will be sensitive to high laser powers and can burn once exposed. Sometimes a burned sample will result in a saturated CCD, and some residue may be on the objective. If a burned sample is observed, inspect the microscope objective for residue and check the CCD signal for saturation. When this occurs, it can lead to visible damage of the sample and increased intensity of amorphous carbon peaks. To avoid photodamage, the laser power and exposure times should be decreased accordingly, or a different laser wavelength could be used. If these approaches are inadequate, the laser

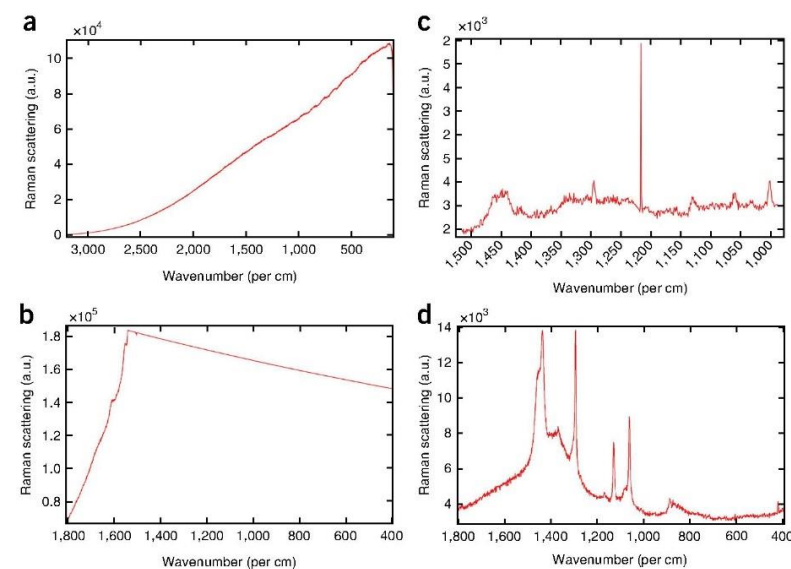


Figure 6 | Examples of common troubleshooting issues during spectral acquisition. (a) Typical fluorescence from a urine sample using a 785-nm laser. (b) Saturation of a CCD detector from a tomato leaf exposed to excessive laser power. (c) Cosmic ray at ~1,220 cm⁻¹ from a mapping experiment on endometrial tissue. (d) Paraffin contamination from an embedded prostate tissue sample. a.u., arbitrary units.

PROTOCOL

power can be attenuated at the sample surface by using a larger laser spot, which is achieved by using a lower-magnification setting or altering the laser focus.

Step 12: spectral contaminants

Cosmic rays or interference from sample contaminants can render spectra unusable unless they are removed. Cosmic rays can be identified as sharp spikes with narrow bandwidths that can often overshadow true Raman peaks (Fig. 6c). These should be removed using cosmic ray-removal algorithms, which are generally available in instrument operation software. Raman peaks associated with spectral contaminants such as paraffin (Fig. 6d) can occur because of inadequate sample preparation; however, these can also be removed with respective computational algorithms, or they can be simply ignored if you are studying spectral regions unaffected by their presence.

● TIMING

We provide approximate times for each of the steps. All timings will depend on the size of the data set, as sample processing and computational analysis are both proportional to the number of samples used.

Step 1A, plant tissue: 5 min

Step 1B, FFPE tissue: 30 min to 2 h

Step 1C, SERS biofluids: 10 min to 24 h

Step 1D, cells: 12 h for cell attachment + 15 min for sample preparation

Steps 2–8, spectral acquisition: 15–25 min

Step 9, point and map acquisition: 1 s to 5 min per spectrum (point mapping: average 15 spectra per sample, ~30 min; image mapping: average 1,000 spectra per sample, ~3 h)

Step 10, saving and converting measurements: 5 min

Steps 11–16, data pre-processing: 10 min to 1 h

Step 17A, exploratory: 15 min to 1 h

Step 17B, diagnostic: 1–4 h

Step 17C, diagnosis: 15 min to 1 h

Minimum experimental time of ~1 h per sample; maximum experimental time of ~32 h per sample

ANTICIPATED RESULTS

Pre-processing options

Figure 7 shows an example of the effects of pre-processing on spectra with strong fluorescence baseline interference (785-nm laser). Spectra were truncated to a defined spectral region (700–1,700 cm⁻¹) to account for Raman peaks present in this particular sample (tomato leaf). A WDN step was performed to smooth the appearance of the data and reduce unwanted noise. With first derivative baseline correction, the SG smoothing function is run simultaneously to account for loss of spectral quality using this approach. This example illustrates how effectively differentiation can account for baseline fluorescence; however, spectral noise is increased and interpretability is reduced because of the transformation of the spectrum. In contrast, polynomial baseline correction results in spectra with conventional appearance and sufficiently relieved of background interference. Vector normalization was used in both

Figure 7 | A brief overview of pre-processing options in Raman spectral data analysis and their contribution to spectral transformation using an example spectrum from a tomato plant leaflet. WDN is conducted as a smoothing process, before polynomial baseline correction and vector normalization. First-order differentiation and Savitzky-Golay smoothing are conducted simultaneously to account for noise introduction in the spectra.

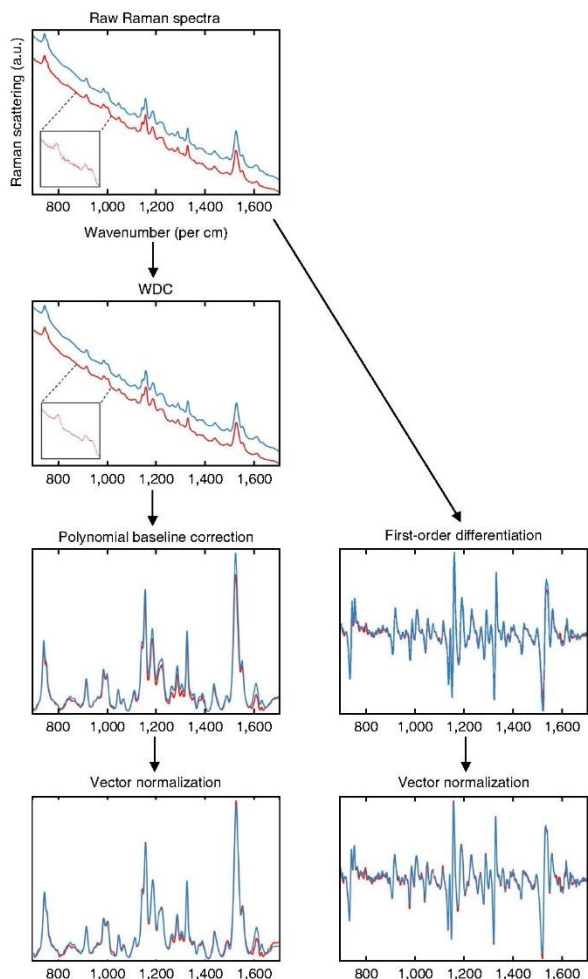


TABLE 4 | Sensitivity and specificity rates (% classification \pm s.d.) of control and endometrial cancer patients from blood serum and plasma samples.

Sample	Pre-processing	Classification approach (%)			
		SVM		PCA-LDC	
		Sensitivity	Specificity	Sensitivity	Specificity
Serum	Polynomial \rightarrow vector normalization	87.38 \pm 8.64	91.78 \pm 05.71	84.46 \pm 15.38	92.66 \pm 07.32
	First-order differentiation \rightarrow vector normalization	77.89 \pm 06.07	81.37 \pm 12.39	80.36 \pm 13.41	79.21 \pm 09.51
Plasma	Polynomial \rightarrow vector normalization	97.8 \pm 03.23	96.75 \pm 04.50	91.77 \pm 09.77	95.33 \pm 6.59
	First-order differentiation \rightarrow vector normalization	98.42 \pm 11.89	98.57 \pm 03.19	92.90 \pm 05.39	97.24 \pm 04.91

Two pre-processing approaches and two classification approaches are used to illustrate varied performances. Polynomial baseline correction was conducted with a polynomial order of five and first-order SG differentiation used nine filter coefficients with a polynomial order of two. A SVM (optimized C and γ parameters) classifier was implemented without a feature extraction step, whereas PCA (optimized number of PCs) was used before a LDC.

incidences to attribute for confounding sample features, such as thickness; the effect of this is a slight reduction in variance between classes.

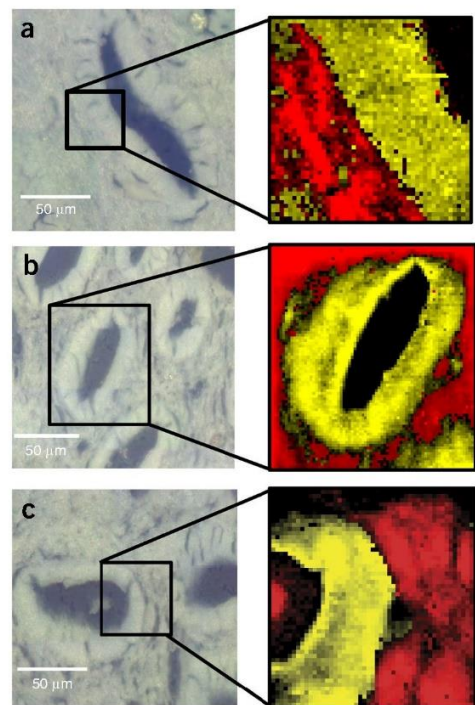
Classification of blood plasma and serum using SERS

Table 4 illustrates the effect of pre-processing, feature-extraction and classification approaches on blood plasma and serum in endometrial cancer patients⁶². From this study, plasma samples produced better classification rates compared with blood serum; this might be explained by the inclusion of clotting proteins in blood serum. The effect of pre-processing can be seen when comparing the classification rates in serum and plasma, with the former performing better with polynomial baseline correction and the latter performing best with differentiation correction. In this example, the classification approach used had a small effect on rates of classification, but this may not be the case in other circumstances. To assess diagnostic efficiency, a variety of pre-processing and classification approaches should be used and compared.

Mapping of endometrial tissue

Figure 8 depicts FFPE endometrial tissue in control patients in order to identify the epithelial lining of the endometrial crypts. These tissue structures seen throughout the three examples are found ubiquitously throughout endometrial tissue initiating at the lumen and spiraling toward the myometrium (not visible). Each map was acquired using an increasing exposure time (**Fig. 8a–c**), ultimately increasing the spectral quality at each pixel. The Raman data were analyzed using the multivariate technique PCA, with PC2 effectively identifying the connective tissue (red) largely due to protein alterations at 1,003 and 1,280 cm^{-1} , and PC3 depicting the epithelial layer (yellow) surrounding the crypt lumen, due to fatty acid and lipid differences at 1,060, 1,131 and 1,295 cm^{-1} . This was apparent across all three image maps, despite the range of laser exposure times used.

Figure 8 | Raman map of fixed endometrial tissue, focusing on uterine glands that spiral throughout the tissue. Samples are FFPE and were mounted on BaF_2 slides before de-waxing. (**a–c**) Left images are white-light images of the tissues, whereas right images show PCA maps. Epithelial tissue is depicted in yellow, whereas connective tissue is shown in red; these correspond to PC3 and PC2, respectively. Spectra were all obtained using a 785-nm laser with 25 mW of power at the sample, a 1,200 l/mm grating and a step size of 1 μm . Image acquisition parameters were as follows: 5-s exposure time, comprising 47 \times 48 pixels (**a**, right); 10 s, with 74 \times 81 pixels (**b**, right); and 15 s, with 55 \times 53 pixels (**c**, right).



PROTOCOL

ACKNOWLEDGMENTS H.J.B.'s project is mediated by the Centre for Global Eco-Innovation funding through the European Regional Development Fund (ERDF). Work in F.L.M.'s laboratories has been funded by the UK Engineering and Physical Sciences Research Council (EPSRC), the Rosemere Cancer Foundation and the UK Biotechnology and Biological Sciences Research Council (BBSRC). K.E.-W. acknowledges a Pilot and Feasibility grant from the Michigan Diabetes Research and Training (subsidiary of National Institutes of Health (NIH)/National Institute of Diabetes and Digestive and Kidney Diseases (NIDDK) 2P30 DK020572).

AUTHOR CONTRIBUTIONS F.L.M. is the principal investigator who conceived the idea for and finalized the manuscript; H.J.B. wrote and compiled the manuscript and figures. L.A., B.B., G.C., K.E.-W., B.G., M.J.W., M.R.M. and N.S. provided information and feedback throughout the article; and K.C., J.D., N.J.F. and P.L.M.-H. provided feedback on the manuscript.

COMPETING FINANCIAL INTERESTS The authors declare no competing financial interests.

Reprints and permissions information is available online at <http://www.nature.com/reprints/index.html>.

1. Clemens, G., Hands, J.R., Dorling, K.M. & Baker, M.J. Vibrational spectroscopic methods for cytology and cellular research. *Analyst* **139**, 4411–4444 (2014).
2. Ellis, D.I., Cowcher, D.P., Ashton, L., O'Hagan, S. & Goodacre, R. Illuminating disease and enlightening biomedicine: Raman spectroscopy as a diagnostic tool. *Analyst* **138**, 3871–3884 (2013).
3. Downes, A. & Elfick, A. Raman spectroscopy and related techniques in biomedicine. *Sensors* **10**, 1871–1889 (2010).
4. Krafft, C. & Popp, J. The many facets of Raman spectroscopy for biomedical analysis. *Anal. Bioanal. Chem.* **407**, 699–717 (2015).
5. Movasagh, Z., Rehman, S. & Rehman, I.U. Raman spectroscopy of biological tissues. *Appl. Spectrosc. Rev.* **42**, 493–541 (2007).
6. Chase, B. A new generation of Raman instrumentation. *Appl. Spectrosc.* **48**, 14–19 (1994).
7. Zhang, Y., Hong, H. & Cai, W. Imaging with Raman spectroscopy. *Curr. Pharm. Biotechnol.* **11**, 654–661 (2010).
8. Kneipp, K., Kneipp, H., Itzkan, I., Dasari, R.R. & Feld, M.S. Surface-enhanced Raman scattering and biophysics. *J. Phys. Condens. Matter* **14**, R597–R624 (2002).
9. Hartschuh, A., Sánchez, E.J., Xie, X.S. & Novotny, L. High-resolution near-field Raman microscopy of single-walled carbon nanotubes. *Phys. Rev. Lett.* **90**, 095503 (2003).
10. Cooper, J.B. Chemometric analysis of Raman spectroscopic data for process control applications. *Chemometr. Intell. Lab. Syst.* **46**, 231–247 (1999).
11. Widjaja, E., Zheng, W. & Huang, Z. Classification of colonic tissues using near-infrared Raman spectroscopy and support vector machines. *Int. J. Oncol.* **32**, 653–662 (2008).
12. Krafft, C., Steiner, G., Beleites, C. & Salzer, R. Disease recognition by infrared and Raman spectroscopy. *J. Biophotonics* **2**, 13–28 (2009).
13. Vankeirsbilck, T. *et al.* Applications of Raman spectroscopy in pharmaceutical analysis. *Trends Analys. Chem.* **21**, 869–877 (2002).
14. Ekins, S. & Sasic, S. *Pharmaceutical Applications of Raman Spectroscopy* (John Wiley & Sons, 2008).
15. Frosch, T., Yan, D. & Popp, J. Ultrasensitive fiber enhanced UV resonance Raman sensing of drugs. *Anal. Chem.* **85**, 6264–6271 (2013).
16. Jarvis, R.M. & Goodacre, R. Discrimination of bacteria using surface-enhanced Raman spectroscopy. *Anal. Chem.* **76**, 40–47 (2004).
17. Maquelin, K. *et al.* Identification of medically relevant microorganisms by vibrational spectroscopy. *J. Microbiol. Methods* **51**, 255–271 (2002).
18. Neugebauer, U. *et al.* On the way to nanometer-sized information of the bacterial surface by tip-enhanced Raman spectroscopy. *Chemphyschem* **7**, 1428–1430 (2006).
19. Pahlow, S., Meisel, S., Cialla-May, D., Weber, K. & Röschac, J.P.P. Isolation and identification of bacteria by means of Raman spectroscopy. *Adv. Drug Deliv. Rev.* **89**, 105–120 (2015).
20. Ashton, L., Lau, K., Winder, C.L. & Goodacre, R. Raman spectroscopy: lighting up the future of microbial identification. *Future Microbiol.* **6**, 991–997 (2011).
21. Owen, C.A. *et al.* *In vitro* toxicology evaluation of pharmaceuticals using Raman micro-spectroscopy. *J. Cell. Biochem.* **99**, 178–186 (2006).
22. Krief, P. *et al.* Raman spectroscopy—a potential platform for the rapid measurement of carbon nanotube-induced cytotoxicity. *Analyst* **134**, 1182–1191 (2009).
23. Mansfield, J.C. *et al.* Label-free chemically specific imaging *in planta* with stimulated Raman scattering microscopy. *Anal. Chem.* **85**, 5055–5063 (2013).
24. Baranska, M., Roman, M., Schulz, H. & Baranski, R. Recent advances in Raman analysis of plants: alkaloids, carotenoids, and polyacetylenes. *Curr. Anal. Chem.* **9**, 108–127 (2013).
25. Gierlinger, N. & Schwanninger, M. The potential of Raman microscopy and Raman imaging in plant research. *Spectroscopy* **21**, 69–89 (2007).
26. Kallaway, C. *et al.* Advances in the clinical application of Raman spectroscopy for cancer diagnostics. *Photodiagnosis Photodyn. Ther.* **10**, 207–219 (2013).
27. Byrne, H.J. *et al.* Spectropathology for the next generation: Quo vadis? *Analyst* **140**, 2066–2073 (2015).
28. Meyer, T. *et al.* Nonlinear microscopy, infrared, and Raman microspectroscopy for brain tumor analysis. *J. Biomed. Opt.* **16**, 021113 (2011).
29. Fullwood, L.M. *et al.* Investigating the use of Raman and immersion Raman spectroscopy for spectral histopathology of metastatic brain cancer and primary sites of origin. *Anal. Methods* **6**, 3948–3961 (2014).
30. Gajjar, K. *et al.* Diagnostic segregation of human brain tumours using Fourier-transform infrared and/or Raman spectroscopy coupled with discriminant analysis. *Anal. Methods* **5**, 89–102 (2013).
31. Krafft, C., Neudert, L., Simat, T. & Salzer, R. Near-infrared Raman spectra of human brain lipids. *Spectrochim. Acta A Mol. Biomol. Spectrosc.* **61**, 1529–1535 (2005).
32. Stone, N., Baker, R., Rogers, K., Parker, A.W. & Matousek, P. Subsurface probing of calcifications with spatially offset Raman spectroscopy (SORS): future possibilities for the diagnosis of breast cancer. *Analyst* **132**, 899–905 (2007).
33. Crow, P., Uff, J., Farmer, J., Wright, M. & Stone, N. The use of Raman spectroscopy to identify and characterize transitional cell carcinoma *in vitro*. *BJU Int.* **93**, 1232–1236 (2004).
34. Lin, D. *et al.* Colorectal cancer detection by gold nanoparticle based surface-enhanced Raman spectroscopy of blood serum and statistical analysis. *Opt. Express* **19**, 13565–13577 (2011).
35. Dekker, E. & Fockens, P. Advances in colonic imaging: new endoscopic imaging methods. *Eur. J. Gastroenterol. Hepatol.* **17**, 803–808 (2005).
36. Stone, N., Stavroulaki, P., Kendall, C., Birchall, M. & Barr, H. Raman spectroscopy for early detection of laryngeal malignancy: preliminary results. *Laryngoscope* **110**, 1756–1763 (2000).
37. Huang, Z. *et al.* Near-infrared Raman spectroscopy for optical diagnosis of lung cancer. *Int. J. Cancer* **107**, 1047–1052 (2003).
38. Horsnell, J.D. *et al.* Raman spectroscopy—a potential new method for the intra-operative assessment of axillary lymph nodes. *Surgeon* **10**, 123–127 (2012).
39. Lloyd, G.R. *et al.* Discrimination between benign, primary and secondary malignancies in lymph nodes from the head and neck utilising Raman spectroscopy and multivariate analysis. *Analyst* **138**, 3900–3908 (2013).
40. Stone, N., Kendall, C., Shepherd, N., Crow, P. & Barr, H. Near-infrared Raman spectroscopy for the classification of epithelial pre-cancers and cancers. *J. Raman Spectrosc.* **33**, 564–573 (2002).
41. Kendall, C. *et al.* Raman spectroscopy, a potential tool for the objective identification and classification of neoplasia in Barrett's oesophagus. *J. Pathol.* **200**, 602–609 (2003).
42. Bergholt, M.S. *et al.* *In vivo* diagnosis of esophageal cancer using image-guided Raman endoscopy and biomolecular modeling. *Technol. Cancer Res. Treat.* **10**, 103–112 (2011).
43. Crow, P. *et al.* Assessment of fiberoptic near-infrared Raman spectroscopy for diagnosis of bladder and prostate cancer. *Urology* **65**, 1126–1130 (2005).
44. Patel, I.I. & Martin, F.L. Discrimination of zone-specific spectral signatures in normal human prostate using Raman spectroscopy. *Analyst* **135**, 3060–3069 (2010).
45. Patel, I.I. *et al.* Segregation of human prostate tissues classified high-risk (UK) versus low-risk (India) for adenocarcinoma using Fourier-transform infrared or Raman microspectroscopy coupled with discriminant analysis. *Anal. Bioanal. Chem.* **401**, 969–982 (2011).
46. Crow, P. *et al.* The use of Raman spectroscopy to identify and grade prostatic adenocarcinoma *in vitro*. *Br. J. Cancer* **89**, 106–108 (2003).
47. Rashid, N. *et al.* Raman microspectroscopy for the early detection of pre-malignant changes in cervical tissue. *Exp. Mol. Pathol.* **97**, 554–564 (2014).
48. Patel, I.I. *et al.* High contrast images of uterine tissue derived using Raman microspectroscopy with the empty modelling approach of multivariate curve resolution-alternating least squares. *Analyst* **136**, 4950–4959 (2011).
49. Krishna, C.M. *et al.* Raman spectroscopy studies for diagnosis of cancers in human uterine cervix. *Vib. Spectrosc.* **41**, 136–141 (2006).
50. Lyng, F.M. *et al.* Vibrational spectroscopy for cervical cancer pathology, from biochemical analysis to diagnostic tool. *Exp. Mol. Pathol.* **82**, 121–129 (2007).
51. Mitchell, A.L., Gajjar, K.B., Theophilou, G., Martin, F.L. & Martin-Hirsch, P.L. Vibrational spectroscopy of biofluids for disease screening or diagnosis: translation from the laboratory to a clinical setting. *J. Biophotonics* **7**, 153–165 (2014).





PROTOCOL

52. Wood, B.R. *et al.* Raman imaging of hemozoin within the food vacuole of *Plasmodium falciparum* trophozoites. *FEBS Lett.* **554**, 247–252 (2003).
53. Wood, B.R. *et al.* Tip-enhanced Raman scattering (TERS) from hemozoin crystals within a sectioned erythrocyte. *Nano Lett.* **11**, 1868–1873 (2011).
54. Wood, B.R. & McNaughton, D. Resonance Raman spectroscopy in malaria research. *Expert Rev. Proteomics* **3**, 525–544 (2006).
55. Wood, B.R. *et al.* Resonance Raman spectroscopy reveals new insight into the electronic structure of β -hematin and malaria pigment. *J. Am. Chem. Soc.* **126**, 9233–9239 (2004).
56. Bonnier, F. *et al.* Imaging live cells grown on a three dimensional collagen matrix using Raman microspectroscopy. *Analyst* **135**, 3169–3177 (2010).
57. Notingher, I. & Hench, L.L. Raman microspectroscopy: a noninvasive tool for studies of individual living cells *in vitro*. *Expert Rev. Med. Devices* **3**, 215–234 (2006).
58. Zhang, X. *et al.* Label-free live-cell imaging of nucleic acids using stimulated Raman scattering microscopy. *Chemphyschem* **13**, 1054–1059 (2012).
59. Kneipp, J., Kneipp, H., Rajadurai, A., Redmond, R.W. & Kneipp, K. Optical probing and imaging of live cells using SERS labels. *J. Raman Spectrosc.* **40**, 1–5 (2009).
60. Farhane, Z., Bonnier, F., Casey, A. & Byrne, H. Raman micro spectroscopy for *in vitro* drug screening: subcellular localisation and interactions of doxorubicin. *Analyst* **140**, 4212–4223 (2015).
61. Meister, K. *et al.* Label-free imaging of metal–carbonyl complexes in live cells by Raman microspectroscopy. *Angew. Chem. Int. Ed.* **49**, 3310–3312 (2010).
62. Butler, H.J. *et al.* Gold nanoparticles as a substrate in bio-analytical near-infrared surface-enhanced Raman spectroscopy. *Analyst* **140**, 3090–3097 (2015).
63. Ackermann, K.R., Henkel, T. & Popp, J. Quantitative online detection of low-concentrated drugs via a SERS microfluidic system. *Chemphyschem* **8**, 2665–2670 (2007).
64. Harper, M.M., Dougan, J.A., Shand, N.C., Graham, D. & Faulds, K. Detection of SERS active labelled DNA based on surface affinity to silver nanoparticles. *Analyst* **137**, 2063–2068 (2012).
65. Barrett, L., Dougan, J.A., Faulds, K. & Graham, D. Stable dye-labelled oligonucleotide-nanoparticle conjugates for nucleic acid detection. *Nanoscale* **3**, 3221–3227 (2011).
66. Faulds, K., Smith, W., Graham, D. & Lacey, R. Assessment of silver and gold substrates for the detection of amphetamine sulfate by surface enhanced Raman scattering (SERS). *Analyst* **127**, 282–286 (2002).
67. Gill, D., Kilponen, R. & Rimai, L. Resonance Raman scattering of laser radiation by vibrational modes of carotenoid pigment molecules in intact plant tissues. *Nature* **227**, 743–744 (1970).
68. Greene, P.R. & Bain, C.D. Total internal reflection Raman spectroscopy of barley leaf epicuticular waxes *in vivo*. *Colloids Surf. B Biointerfaces* **45**, 174–180 (2005).
69. Schulz, H. & Baranska, M. Identification and quantification of valuable plant substances by IR and Raman spectroscopy. *Vib. Spectrosc.* **43**, 13–25 (2007).
70. Sene, C., McCann, M.C., Wilson, R.H. & Griner, R. Fourier-transform Raman and Fourier-transform infrared spectroscopy (an investigation of five higher plant cell walls and their components). *Plant Physiol.* **106**, 1623–1631 (1994).
71. Schulz, H., Baranska, M. & Baranski, R. Potential of NIR-FT-Raman spectroscopy in natural carotenoid analysis. *Biopolymers* **77**, 212–221 (2005).
72. Rösch, P., Popp, J. & Kiefer, W. Raman and surface enhanced Raman spectroscopic investigation on Lamiaceae plants. *J. Mol. Struct.* **480**–481, 121–124 (1999).
73. Schmidt, M. *et al.* Raman imaging of cell wall polymers in *Arabidopsis thaliana*. *Biochem. Biophys. Res. Commun.* **395**, 521–523 (2010).
74. Gierlinger, N. & Schwanninger, M. Chemical imaging of poplar wood cell walls by confocal Raman microscopy. *Plant Physiol.* **140**, 1246–1254 (2006).
75. Gierlinger, N., Keplinger, T. & Harrington, M. Imaging of plant cell walls by confocal Raman microscopy. *Nat. Protoc.* **7**, 1694–1708 (2012).
76. Asher, S.A. & Johnson, C.R. Raman spectroscopy of a coal liquid shows that fluorescence interference is minimized with ultraviolet excitation. *Science* **225**, 311–313 (1984).
77. Butler, H.J., McAinsh, M.R., Adams, S. & Martin, F.L. Application of vibrational spectroscopy techniques to non-destructively monitor plant health and development. *Anal. Methods* **7**, 4059–4070 (2015).
78. Baranski, R., Baranska, M. & Schulz, H. Changes in carotenoid content and distribution in living plant tissue can be observed and mapped *in situ* using NIR-FT-Raman spectroscopy. *Planta* **222**, 448–457 (2005).
79. Baker, M.J. *et al.* Using Fourier transform IR spectroscopy to analyze biological materials. *Nat. Protoc.* **9**, 1771–1791 (2014).
80. Diem, M., Romeo, M., Boydston-White, S., Miljković, M. & Matthäus, C. A decade of vibrational micro-spectroscopy of human cells and tissue (1994–2004). *Analyst* **129**, 880–885 (2004).
81. Dumas, P., Sockalingum, G.D. & Sule-Suso, J. Adding synchrotron radiation to infrared microspectroscopy: what's new in biomedical applications? *Trends Biotechnol.* **25**, 40–44 (2007).
82. Bhargava, R. Infrared spectroscopic imaging: the next generation. *Appl. Spectrosc.* **66**, 1091–1120 (2012).
83. Palonpon, A.F. *et al.* Raman and SERS microscopy for molecular imaging of live cells. *Nat. Protoc.* **8**, 677–692 (2013).
84. Felten, J. *et al.* Vibrational spectroscopic image analysis of biological material using multivariate curve resolution–alternating least squares (MCR-ALS). *Nat. Protoc.* **10**, 217–240 (2015).
85. Kong, L. *et al.* Characterization of bacterial spore germination using phase-contrast and fluorescence microscopy, Raman spectroscopy and optical tweezers. *Nat. Protoc.* **6**, 625–639 (2011).
86. Li, J.F. *et al.* Surface analysis using shell-isolated nanoparticle-enhanced Raman spectroscopy. *Nat. Protoc.* **8**, 52–65 (2013).
87. Martin, F.L. *et al.* Distinguishing cell types or populations based on the computational analysis of their infrared spectra. *Nat. Protoc.* **5**, 1748–1760 (2010).
88. Angel, S., Carrabba, M. & Cooney, T. The utilization of diode lasers for Raman spectroscopy. *Spectrochim. Acta A Mol. Biomol. Spectrosc.* **51**, 1779–1799 (1995).
89. Müller, A. *et al.* Diode laser based light sources for biomedical applications. *Laser Photonics Rev.* **7**, 605–627 (2013).
90. Yan, F. & Vo-Dinh, T. Surface-enhanced Raman scattering detection of chemical and biological agents using a portable Raman integrated tunable sensor. *Sensor. Actuat. B Chem.* **121**, 61–66 (2007).
91. Moore, D. & Scharff, R.J. Portable Raman explosives detection. *Anal. Bioanal. Chem.* **393**, 1571–1578 (2009).
92. Draux, F. *et al.* Raman spectral imaging of single living cancer cells: a preliminary study. *Analyst* **134**, 542–548 (2009).
93. Creely, C., Volpe, G., Singh, G., Soler, M. & Petrov, D. Raman imaging of floating cells. *Opt. Express* **13**, 6105–6110 (2005).
94. Swain, R. & Stevens, M. Raman microspectroscopy for non-invasive biochemical analysis of single cells. *Biochem. Soc. Trans.* **35**, 544–549 (2007).
95. Zoladek, A., Pascut, F.C., Patel, P. & Notingher, I. Non-invasive time-course imaging of apoptotic cells by confocal Raman micro-spectroscopy. *J. Raman Spectrosc.* **42**, 251–258 (2011).
96. Vo-Dinh, T. *Biomedical Photonics Handbook: Biomedical Diagnostics* Vol. 2 (CRC press, 2014).
97. Asher, S.A., Ludwig, M. & Johnson, C.R. UV resonance Raman excitation profiles of the aromatic amino acids. *J. Am. Chem. Soc.* **108**, 3186–3197 (1986).
98. Kumamoto, Y., Taguchi, A., Smith, N.I. & Kawata, S. Deep ultraviolet resonant Raman imaging of a cell. *J. Biomed. Opt.* **17**, 076001 (2012).
99. Ivanda, M. & Furić, K. Line focusing in micro-Raman spectroscopy. *Appl. Opt.* **31**, 6371–6375 (1992).
100. Okada, M. *et al.* Label-free Raman observation of cytochrome c dynamics during apoptosis. *Proc. Natl. Acad. Sci. USA* **109**, 28–32 (2012).
101. Schlücker, S., Schaeberle, M.D., Huffman, S.W. & Levin, I.W. Raman microspectroscopy: a comparison of point, line, and wide-field imaging methodologies. *Anal. Chem.* **75**, 4312–4318 (2003).
102. Minamikawa, T. *et al.* Label-free detection of peripheral nerve tissues against adjacent tissues by spontaneous Raman microspectroscopy. *Histochem. Cell Biol.* **139**, 181–193 (2013).
103. Markwort, L., Kip, B., Da Silva, E. & Roussel, B. Raman imaging of heterogeneous polymers: a comparison of global versus point illumination. *Appl. Spectrosc.* **49**, 1411–1430 (1995).
104. Ma, J. & Ben-Amotz, D. Rapid micro-Raman imaging using fiber-bundle image compression. *Appl. Spectrosc.* **51**, 1845–1848 (1997).
105. Cooper, J. *et al.* Raman spectroscopy with a low-cost imaging CCD array. *Spectrochim. Acta A Mol. Spectrosc.* **50**, 567–575 (1994).
106. LaPlant, F. in *Emerging Raman Applications and Techniques in Biomedical and Pharmaceutical Fields* Vol. 1 (eds. Matousek, P. & Morris, M.D.) 1–24 (Springer, 2010).
107. Dieing, T. & Hollricher, O. High-resolution, high-speed confocal Raman imaging. *Vib. Spectrosc.* **48**, 22–27 (2008).
108. Harnly, J.M. & Fields, R.E. Solid-state array detectors for analytical spectrometry. *Appl. Spectrosc.* **51**, 334A (1997).
109. Li, Z., Deen, M.J., Kumar, S. & Selvaganapathy, P.R. Raman spectroscopy for in-line water quality monitoring—instrumentation and potential. *Sensors* **14**, 17275–17303 (2014).
110. Carriere, J.T. & Havermeier, F. Ultra-low-frequency Stokes and anti-Stokes Raman spectroscopy at 785 nm with volume holographic grating filters. *SPIE BiOS Proceedings* (Biomedical Vibrational Spectroscopy V: Advances in Research and Industry, January 21, 2012, San Francisco) **8219**, 821905 (2012).

PROTOCOL

111. Pitt, G.D. *et al.* Engineering aspects and applications of the new Raman instrumentation. *IEE Proceedings: Science, Measurement and Technology* **152**, 241–218 (2005).

112. Tfayli, A. *et al.* Digital dewaxing of Raman signals: discrimination between nevi and melanoma spectra obtained from paraffin-embedded skin biopsies. *Appl. Spectrosc.* **63**, 564–570 (2009).

113. Ali, S.M. *et al.* Raman spectroscopic analysis of human skin tissue sections *ex vivo*: evaluation of the effects of tissue processing and dewaxing. *J. Biomed. Opt.* **18**, 61202 (2013).

114. Mariani, M.M., Lampen, P., Popp, J., Wood, B.R. & Deckert, V. Impact of fixation on *in vitro* cell culture lines monitored with Raman spectroscopy. *Analyst* **134**, 1154–1161 (2009).

115. Deegan, R.D. *et al.* Capillary flow as the cause of ring stains from dried liquid drops. *Nature* **389**, 827–829 (1997).

116. Filik, J. & Stone, N. Analysis of human tear fluid by Raman spectroscopy. *Anal. Chim. Acta* **616**, 177–184 (2008).

117. Filik, J. & Stone, N. Investigation into the protein composition of human tear fluid using centrifugal filters and drop coating deposition Raman spectroscopy. *J. Raman Spectrosc.* **40**, 218–224 (2009).

118. Bonnier, F., Petitjean, F., Baker, M.J. & Byrne, H.J. Improved protocols for vibrational spectroscopic analysis of body fluids. *J. Biophotonics* **7**, 167–179 (2014).

119. Esmonde-White, K.A., Esmonde-White, F.W., Morris, M.D. & Roessler, B.J. Characterization of biofluids prepared by sessile drop formation. *Analyst* **139**, 2734–2741 (2014).

120. Esmonde-White, K.A., Le Clair, S.V., Roessler, B.J. & Morris, M.D. Effect of conformation and drop properties on surface-enhanced Raman spectroscopy of dried biopolymer drops. *Appl. Spectrosc.* **62**, 503–511 (2008).

121. Byrne, H.J., Sockalingum, G. & Stone, N. in *Biomedical Applications of Synchrotron Infrared Microspectroscopy: A Practical Approach* (ed. Moss, D.) Ch. 4, 105–142 (Royal Society of Chemistry, 2011).

122. Fullwood, L.M. *et al.* Effect of substrate choice and tissue type on tissue preparation for spectral histopathology by Raman microspectroscopy. *Analyst* **139**, 446–454 (2014).

123. Wehbe, K., Filik, J., Frogley, M.D. & Cinque, G. The effect of optical substrates on micro-FTIR analysis of single mammalian cells. *Anal. Bioanal. Chem.* **405**, 1311–1324 (2013).

124. Cui, L., Butler, H.J., Martin-Hirsch, P.L. & Martin, F.L. Aluminium foil as a potential substrate for ATR-FTIR, transfection FTIR or Raman spectrochemical analysis of biological specimens. *Anal. Methods* **8**, 481–487 (2016).

125. Lee, K.-S. & El-Sayed, M.A. Gold and silver nanoparticles in sensing and imaging: sensitivity of plasmon response to size, shape, and metal composition. *J. Phys. Chem. B* **110**, 19220–19225 (2006).

126. Faulds, K., Littleford, R.E., Graham, D., Dent, G. & Smith, W.E. Comparison of surface-enhanced resonance Raman scattering from unaggregated and aggregated nanoparticles. *Anal. Chem.* **76**, 592–598 (2004).

127. Nehl, C.L. & Hafner, J.H. Shape-dependent plasmon resonances of gold nanoparticles. *J. Mater. Chem.* **18**, 2415–2419 (2008).

128. Lewis, I.R. & Edwards, H. *Handbook of Raman Spectroscopy: From the Research Laboratory to the Process Line* (CRC Press, 2001).

129. Liu, Z., Zhao, C., Han, L. & Mo, Y. Study on the configuration and applications of high spectral resolution Raman spectrometer. *Guang Pu Xue Yu Guang Pu Fen Xi* **30**, 567–570 (2010).

130. Wieboldt, D. *Understanding Raman Spectrometer Parameters* <http://www.spectroscopyonline.com/understanding-raman-spectrometer-parameters> (2010).

131. Wiberley, S.E., Colthup, N.B. & Daly, L.H. *Introduction to Infrared and Raman Spectroscopy* 3rd edn. (Elsevier, 2012).

132. Stone, N., Kendall, C., Smith, J., Crow, P. & Barr, H. Raman spectroscopy for identification of epithelial cancers. *Faraday Discuss.* **126**, 141–157 (2004).

133. Zhang, L. & Henson, M.J. A practical algorithm to remove cosmic spikes in Raman imaging data for pharmaceutical applications. *Appl. Spectrosc.* **61**, 1015–1020 (2007).

134. Lasch, P. Spectral pre-processing for biomedical vibrational spectroscopy and microspectroscopic imaging. *Chemometr. Intell. Lab. Syst.* **117**, 100–114 (2013).

135. Barman, I., Kong, C.-R., Singh, G.P. & Dasari, R.R. Effect of photobleaching on calibration model development in biological Raman spectroscopy. *J. Biomed. Opt.* **16**, 011004 (2011).

136. Trevisan, J., Angelov, P.P., Carmichael, P.L., Scott, A.D. & Martin, F.L. Extracting biological information with computational analysis of Fourier-transform infrared (FTIR) biospectroscopy datasets: current practices to future perspectives. *Analyst* **137**, 3202–3215 (2012).

137. Naumann, D. in *Biomedical Optical Spectroscopy, Proceedings of SPIE (Biomedical Optical Spectroscopy 68530G)* (International Society for Optics and Photonics, 2008).

138. Jolliffe, I. *Principal Component Analysis* (Wiley Online Library, 2002).

139. Chen, G. & Shen-En, Q. Denoising of hyperspectral imagery using principal component analysis and wavelet shrinkage. *IEEE Geosci. Remote Sens. Soc.* **49**, 973–980 (2011).

140. Lieber, C.A. & Mahadevan-Jansen, A. Automated method for subtraction of fluorescence from biological Raman spectra. *Appl. Spectrosc.* **57**, 1363–1367 (2003).

141. Mazet, V., Carteret, C., Brie, D., Idier, J. & Humbert, B. Background removal from spectra by designing and minimising a non-quadratic cost function. *Chemometr. Intell. Lab. Syst.* **76**, 121–133 (2005).

142. Savitzky, A. & Golay, M.J.E. Smoothing and differentiation of data by simplified least squares procedures. *Anal. Chem.* **36**, 1627–1639 (1964).

143. Bocklitz, T., Walter, A., Hartmann, K., Rösch, P. & Popp, J. How to pre-process Raman spectra for reliable and stable models? *Anal. Chim. Acta* **704**, 47–56 (2011).

144. Heraud, P., Wood, B.R., Beardall, J. & McNaughton, D. Effects of pre-processing of Raman spectra on *in vivo* classification of nutrient status of microalgal cells. *J. Chemometr.* **20**, 193–197 (2006).

145. Trevisan, J. *et al.* Measuring similarity and improving stability in biomarker identification methods applied to Fourier-transform infrared (FTIR) spectroscopy. *J. Biophotonics* **7**, 254–265 (2014).

146. de Sousa Marques, A., de Melo, M.C.N., Cidral, T.A. & de Lima, K.M.G. Feature selection strategies for identification of *Staphylococcus aureus* recovered in blood cultures using FT-IR spectroscopy successive projections algorithm for variable selection: a case study. *J. Microbiol. Methods* **98**, 26–30 (2014).

147. Lasch, P., Haensch, W., Naumann, D. & Diem, M. Imaging of colorectal adenocarcinoma using FT-IR microspectroscopy and cluster analysis. *Biochim. Biophys. Acta* **1688**, 176–186 (2004).

148. Ellis, D.I. & Goodacre, R. Metabolic fingerprinting in disease diagnosis: biomedical applications of infrared and Raman spectroscopy. *Analyst* **131**, 875–885 (2006).

149. Lloyd, G.R. *et al.* Utilising non-consensus pathology measurements to improve the diagnosis of oesophageal cancer using a Raman spectroscopic probe. *Analyst* **139**, 381–388 (2014).

150. Balabin, R.M., Safieva, R.Z. & Lomakina, E.I. Near-infrared (NIR) spectroscopy for motor oil classification: from discriminant analysis to support vector machines. *Microchem. J.* **98**, 121–128 (2011).

151. Beleites, C., Neugebauer, J., Bocklitz, T., Kraft, C. & Popp, J. Sample size planning for classification models. *Anal. Chim. Acta* **760**, 25–33 (2013).

152. Esbensen, K.H. & Geladi, P. Principles of proper validation: use and abuse of re-sampling for validation. *J. Chemometr.* **24**, 168–187 (2010).

153. Antonio, K.A. & Schultz, Z.D. Advances in biomedical Raman microscopy. *Anal. Chem.* **86**, 30–46 (2013).

154. Parekh, S.H., Lee, Y.J., Aamer, K.A. & Cicerone, M.T. Label-free cellular imaging by broadband coherent anti-Stokes Raman scattering microscopy. *Biophys. J.* **99**, 2695–2704 (2010).

155. Zumbusch, A., Holtom, G.R. & Xie, X.S. Three-dimensional vibrational imaging by coherent anti-Stokes Raman scattering. *Phys. Rev. Lett.* **82**, 4142–4145 (1999).

156. Kraft, C., Dietzek, B. & Popp, J. Raman and CARS microspectroscopy of cells and tissues. *Analyst* **134**, 1046–1057 (2009).

157. Evans, C.L. *et al.* Chemical imaging of tissue *in vivo* with video-rate coherent anti-Stokes Raman scattering microscopy. *Proc. Natl. Acad. Sci. USA* **102**, 16807–16812 (2005).

158. Le, T.T., Huff, T.B. & Cheng, J.-X. Coherent anti-Stokes Raman scattering imaging of lipids in cancer metastasis. *BMC Cancer* **9**, 42 (2009).

159. Gao, L. *et al.* Label-free high-resolution imaging of prostate glands and cavernous nerves using coherent anti-Stokes Raman scattering microscopy. *Biomed. Opt. Express* **2**, 915–926 (2011).

160. Garrett, N. *et al.* Label-free imaging of polymeric nanomedicines using coherent anti-Stokes Raman scattering microscopy. *J. Raman Spectrosc.* **43**, 681–688 (2012).

161. Windbergs, M. *et al.* Chemical imaging of oral solid dosage forms and changes upon dissolution using coherent anti-Stokes Raman scattering microscopy. *Anal. Chem.* **81**, 2085–2091 (2009).

162. Schuster, K.C., Reese, I., Urlaub, E., Gapes, J.R. & Lendl, B. Multidimensional information on the chemical composition of single bacterial cells by confocal Raman microspectroscopy. *Anal. Chem.* **72**, 5529–5534 (2000).

163. Majzner, K. *et al.* 3D confocal Raman imaging of endothelial cells and vascular wall: perspectives in analytical spectroscopy of biomedical research. *Analyst* **138**, 603–610 (2012).

164. Caspers, P.J., Lucassen, G.W. & Puppels, G.J. Combined *in vivo* confocal Raman spectroscopy and confocal microscopy of human skin. *Biophys. J.* **85**, 572–580 (2003).

165. Choi, J. *et al.* Direct observation of spectral differences between normal and basal cell carcinoma (BCC) tissues using confocal Raman microscopy. *Biopolymers* **77**, 264–272 (2005).

166. Yu, C., Gestl, E., Eckert, K., Alara, D. & Irudayaraj, J. Characterization of human breast epithelial cells by confocal Raman microspectroscopy. *Cancer Detect. Prev.* **30**, 515–522 (2006).

167. Haka, A.S. *et al.* Identifying microcalcifications in benign and malignant breast lesions by probing differences in their chemical composition using Raman spectroscopy. *Cancer Res.* **62**, 5375–5380 (2002).

168. Breitenbach, J., Schrof, W. & Neumann, J. Confocal Raman-spectroscopy: analytical approach to solid dispersions and mapping of drugs. *Pharm. Res.* **16**, 1109–1113 (1999).

169. Franzen, L., Selzer, D., Fluh, J.W., Schaefer, U.F. & Windbergs, M. Towards drug quantification in human skin with confocal Raman microscopy. *Eur. J. Pharm. Biopharm.* **84**, 437–444 (2013).

170. Skoulika, S.G. & Georgiou, C.A. Rapid quantitative determination of ciprofloxacin in pharmaceuticals by use of solid-state FT-Raman spectroscopy. *Appl. Spectrosc.* **55**, 1259–1265 (2001).

171. Edwards, H., Farwell, D. & Webster, D. FT Raman microscopy of untreated natural plant fibres. *Spectrochim. Acta A Mol. Biomol. Spectrosc.* **53A**, 2383–2392 (1997).

172. Morris, M.D. *et al.* Kerr-gated time-resolved Raman spectroscopy of equine cortical bone tissue. *J. Biomed. Opt.* **10**, 14014 (2005).

173. Prieto, M.C.H. *et al.* Use of picosecond Kerr-gated Raman spectroscopy to suppress signals from both surface and deep layers in bladder and prostate tissue. *J. Biomed. Opt.* **10**, 44006 (2005).

174. Baker, R. *et al.* Depth profiling of calcifications in breast tissue using picosecond Kerr-gated Raman spectroscopy. *Analyst* **132**, 48–53 (2007).

175. Galvis, L., Dunlop, J.W.C., Duda, G., Fratzl, P. & Masic, A. Polarized Raman anisotropic response of collagen in tendon: towards 3D orientation mapping of collagen in tissues. *PLoS ONE* **8**, e63518 (2013).

176. Brose, K., Zouni, A., Broser, M., Mühl, F. & Maultzsch, J. Polarised Raman measurements on the core complex of crystallised photosystem II. *Phys. Status Solidi* **246**, 2813–2816 (2009).

177. Blanch, E.W. *et al.* Is proline II helix the killer conformation? a Raman optical activity study of the amyloidogenic prefibrillar intermediate of human lysozyme. *J. Mol. Biol.* **301**, 553–563 (2000).

178. McColl, I.H. *et al.* A new perspective on β-sheet structures using vibrational Raman optical activity: from poly(l-lysine) to the prion protein. *J. Am. Chem. Soc.* **125**, 10019–10026 (2003).

179. Blanch, E.W., Hecht, L. & Barron, L.D. Vibrational Raman optical activity of proteins, nucleic acids, and viruses. *Methods* **29**, 196–209 (2003).

180. Nieto-Ortega, B. *et al.* Raman optical activity spectra and conformational elucidation of chiral drugs. The case of the antiangiogenic aeroplysinin-1. *J. Phys. Chem. A* **115**, 2752–2755 (2011).

181. Yamamoto, S., Watarai, H. & Bouř, P. Monitoring the backbone conformation of valinomycin by Raman optical activity. *Chemphyschem* **12**, 1509–1518 (2011).

182. Robert, B. Resonance Raman spectroscopy. *Photosynth. Res.* **101**, 147–155 (2009).

183. Wood, B.R., Caspers, P., Puppels, G.J., Pandiancherri, S. & McNaughton, D. Resonance Raman spectroscopy of red blood cells using near-infrared laser excitation. *Anal. Bioanal. Chem.* **387**, 1691–1703 (2007).

184. Darvin, M. *et al.* Non-invasive *in vivo* detection of the carotenoid antioxidant substance lycopene in the human skin using the resonance Raman spectroscopy. *Laser Phys. Lett.* **3**, 460–463 (2006).

185. Xie, C. & Li, Y.-q. Confocal micro-Raman spectroscopy of single biological cells using optical trapping and shifted excitation difference techniques. *J. Appl. Phys.* **93**, 2982–2986 (2003).

186. Sowoidnich, K. & Kronfeldt, H.-D. Fluorescence rejection by shifted excitation Raman difference spectroscopy at multiple wavelengths for the investigation of biological samples. *ISRN Spectrosc.* **2012**, 1–11 (2012).

187. da Silva Martins, M.A. *et al.* Shifted-excitation Raman difference spectroscopy for *in vitro* and *in vivo* biological samples analysis. *Biomed. Opt. Express* **1**, 617–626 (2010).

188. Matousek, P. & Stone, N. Prospects for the diagnosis of breast cancer by noninvasive probing of calcifications using transmission Raman spectroscopy. *J. Biomed. Opt.* **12**, 024008 (2007).

189. Keller, M.D. *et al.* Development of a spatially offset Raman spectroscopy probe for breast tumor surgical margin evaluation. *J. Biomed. Opt.* **16**, 077006 (2011).

190. Matousek, P. *et al.* Noninvasive Raman spectroscopy of human tissue *in vivo*. *Appl. Spectrosc.* **60**, 758–763 (2006).

191. Olds, W.J. *et al.* Spatially offset Raman spectroscopy (SORS) for the analysis and detection of packaged pharmaceuticals and concealed drugs. *Forensic Sci. Int.* **212**, 69–77 (2011).

192. Stone, N. *et al.* Surface enhanced spatially offset Raman spectroscopic (SESORS) imaging—the next dimension. *Chem. Sci.* **2**, 776–780 (2011).

193. Ma, K. *et al.* *In vivo*, transcutaneous glucose sensing using surface-enhanced spatially offset Raman spectroscopy: multiple rats, improved hypoglycemic accuracy, low incident power, and continuous monitoring for greater than 17 days. *Anal. Chem.* **83**, 9146–9152 (2011).

194. Yuen, J.M., Shah, N.C., Walsh, J.T. Jr., Glucksberg, M.R. & Van Duyne, R.P. Transcutaneous glucose sensing by surface-enhanced spatially offset Raman spectroscopy in a rat model. *Anal. Chem.* **82**, 8382–8385 (2010).

195. Xie, H.N. *et al.* Tracking bisphosphonates through a 20 mm thick porcine tissue by using surface-enhanced spatially offset Raman spectroscopy. *Angew. Chem.* **124**, 8637–8639 (2012).

196. Sharma, B., Ma, K., Glucksberg, M.R. & Van Duyne, R.P. Seeing through bone with surface-enhanced spatially offset Raman spectroscopy. *J. Am. Chem. Soc.* **135**, 17290–17293 (2013).

197. Saar, B.G. *et al.* Label-free, Real-time monitoring of biomass processing with stimulated Raman scattering microscopy. *Angew. Chem. Int. Ed.* **49**, 5476–5479 (2010).

198. Littlejohn, G.R. *et al.* *In vivo* chemical and structural analysis of plant cuticular waxes using stimulated Raman scattering (SRS) microscopy. *Plant Physiol.* **168**, 18–28 (2015).

199. Kneipp, K. *et al.* Single molecule detection using surface-enhanced Raman scattering (SERS). *Phys. Rev. Lett.* **78**, 1667–1670 (1997).

200. Nie, S. & Emory, S.R. Probing single molecules and single nanoparticles by surface-enhanced Raman scattering. *Science* **275**, 1102–1106 (1997).

201. Qian, X. *et al.* *In vivo* tumor targeting and spectroscopic detection with surface-enhanced Raman nanoparticle tags. *Nat. Biotechnol.* **26**, 83–90 (2008).

202. Kneipp, K., Kneipp, H. & Kneipp, J. Surface-enhanced Raman scattering in local optical fields of silver and gold nanoaggregates from single-molecule Raman spectroscopy to ultrasensitive probing in live cells. *Acc. Chem. Res.* **39**, 443–450 (2006).

203. Cintá Pinzaru, S., Pavel, I., Leopold, N. & Kiefer, W. Identification and characterization of pharmaceuticals using Raman and surface-enhanced Raman scattering. *J. Raman Spectrosc.* **35**, 338–346 (2004).

204. Huang, X., El-Sayed, I.H., Qian, W. & El-Sayed, M.A. Cancer cells assemble and align gold nanorods conjugated to antibodies to produce highly enhanced, sharp, and polarized surface Raman spectra: A potential cancer diagnostic marker. *Nano Lett.* **7**, 1591–1597 (2007).

205. Feng, S. *et al.* Nasopharyngeal cancer detection based on blood plasma surface-enhanced Raman spectroscopy and multivariate analysis. *Biosens. Bioelectron.* **25**, 2414–2419 (2010).

206. Premasiri, W. *et al.* Characterization of the surface enhanced Raman scattering (SERS) of bacteria. *J. Phys. Chem. B* **109**, 312–320 (2005).

207. Zeiri, I. L. SERS of plant material. *J. Raman Spectrosc.* **38**, 950–955 (2007).

208. McNay, G., Eustace, D., Smith, W.E., Faulds, K. & Graham, D. Surface-enhanced Raman scattering (SERS) and surface-enhanced resonance Raman scattering (SERRS): a review of applications. *Appl. Spectrosc.* **65**, 825–837 (2011).

209. Graham, D. *et al.* Selective detection of deoxyribonucleic acid at ultralow concentrations by SERRS. *Anal. Chem.* **69**, 4703–4707 (1997).

210. Murgida, D.H. & Hildebrandt, P. Electron-transfer processes of cytochrome c at interfaces. New insights by surface-enhanced resonance Raman spectroscopy. *Acc. Chem. Res.* **37**, 854–861 (2004).

211. Murgida, D.H. & Hildebrandt, P. Disentangling interfacial redox processes of proteins by SERR spectroscopy. *Chem. Soc. Rev.* **37**, 937–945 (2008).

212. Böhme, R. *et al.* Biochemical imaging below the diffraction limit—probing cellular membrane related structures by tip-enhanced Raman spectroscopy (TERS). *J. Biophotonics* **3**, 455–461 (2010).

213. Stone, N. & Matousek, P. Advanced transmission Raman spectroscopy: a promising tool for breast disease diagnosis. *Cancer Res.* **68**, 4424–4430 (2008).

214. Johansson, J., Sparén, A., Svensson, O., Folestad, S. & Claybourn, M. Quantitative transmission Raman spectroscopy of pharmaceutical tablets and capsules. *Appl. Spectrosc.* **61**, 1211–1218 (2007).

215. Buckley, K. & Matousek, P. Recent advances in the application of transmission Raman spectroscopy to pharmaceutical analysis. *J. Pharm. Biomed. Anal.* **55**, 645–652 (2011).

Chapter 4

Application of vibrational spectroscopy techniques to non-destructively monitor plant health and development

Holly J. Butler, Martin R. McAinsh, Steven Adams, and Francis L. Martin

Analytical Methods 7(10): 4015-4378 (2015)

Contribution:

I conducted all experimental work

I wrote and prepared the manuscript for publication

I produced the front cover image and all figures

Professor F. L Martin

Dr. Martin. R. McAinsh

H. J. Butler

Analytical Methods

www.rsc.org/methods



ISSN 1759-9660



PAPER

Martin R. McAinsh, Francis L. Martin *et al.*
Application of vibrational spectroscopy techniques to non-destructively
monitor plant health and development



Cite this: *Anal. Methods*, 2015, 7, 4059

Application of vibrational spectroscopy techniques to non-destructively monitor plant health and development[†]

Holly J. Butler,^{ab} Martin R. McAinsh,^{*c} Steven Adams^d and Francis L. Martin^{*a}

Vibrational spectroscopy is a powerful analytical tool that is yet to be fully developed in plant science. Previously, such tools have been primarily applied to fixed or *in vitro* biological materials, which do not effectively encapsulate real-time physiological conditions of whole organisms. Coupled with multivariate analysis, this study examines the potential application of ATR-FTIR or Raman spectroscopy to determine spectral alterations indicative of healthy plant growth in leaf samples of *Solanum lycopersicum*. This was achieved in the absence of destructive effects on leaf tissues locally or on plant health systemically; additionally, autofluorescence was not a confounder. Feature extraction techniques including PCA-LDA were employed to examine variance within spectral datasets. *In vivo* measurements are able to successfully characterise key constituents of the leaf cuticle and cell wall, whilst qualifying leaf growth. Major alterations in carbohydrate and protein content of leaves were observed, correlating with known processes within leaf development from cell wall expansion to leaf senescence. These findings show that vibrational spectroscopy is an ideal technique for *in vivo* investigations in plant tissues.

Received 9th February 2015
Accepted 2nd April 2015

DOI: 10.1039/c5ay00377f
www.rsc.org/methods

Introduction

With an increasing population anticipated to reach 9 billion by 2050, it is estimated that agricultural productivity will need to increase by 70% in order to meet global food demands.¹ For this reason, plant science and food security are prominent research topics that are fundamental to providing sustainable nutrition for the foreseeable future. There are powerful genomic, proteomic and physiological analysis tools available that have been widely implemented in plant research, yet many are invasive and destructive to the whole tissue. In particular, determination of the nutrient status of plant tissue is profoundly reliant upon chemical analyses, which often requires substantial sample preparation and training that can prove time-consuming and expensive.² Plant-focused research remains limited due to a lack of analytical methods that can be applied in a truly non-destructive manner, that can convey both chemical and structural information *in vivo* across all plant species.³

It is evident that a high-throughput, cost effective and non-destructive technique would benefit the field of plant science

and therefore food security. Vibrational spectroscopy in biological systems, or biospectroscopy, has been shown to be a valuable tool for exploratory analysis in the disciplines of eco-toxicology,^{4–6} food science^{7,8} and biomedical research.⁹ The latter of these fields has expanded markedly in the past decade with research spanning pharmaceuticals,¹⁰ cytology,^{11,12} histopathology^{13–15} and cancer diagnostics in cervical,¹⁶ prostate,¹⁷ breast¹⁸ and mucosal¹⁹ tissues. This is in part associated with advancements in biospectroscopy that allows for non-invasive analysis of live cells and tissues,²⁰ additional to biological fluids samples such as blood,²¹ serum²² and plasma²³ that translate into a clinical setting. In comparison, vibrational spectroscopy has only been tentatively implemented across fundamental plant biology and agronomy to provide an insight into the microscopic and subcellular properties of plant tissues.^{24–26} This could not only infer qualitative and quantitative information regarding the biological components of the tissues in question, but also any mechanical, environmental and nutritional stress that they are subjected to.^{27–29}

Infrared (IR) and Raman spectroscopy are two complementary vibrational spectroscopy methods that are commonly employed when investigating biological samples. Although based on distinctly different physical processes, both observe the excitation of a molecule to higher energy levels due to chemical bond absorption of radiation. IR spectroscopy uses polychromatic light in the IR region that causes molecules within a sample to vibrate due to their chemical composition.³⁰ Coupled with the Fourier-transform (FT) algorithm conversion of an interferogram, a spectrum is rapidly obtained as

^aCentre for Biophotonics, Lancaster University, Lancaster LA1 4YQ, UK. E-mail: f.martin@lancaster.ac.uk; Tel: +44 (0)1524 510206

^bCentre for Global Eco-Innovation, Lancaster University, Lancaster LA1 4YQ, UK

^cLancaster Environment Centre, Lancaster University, Lancaster LA1 4YQ, UK. E-mail: m.mcainsh@lancaster.ac.uk; Tel: +44 (0)1524 510553

^dPlant Impact Plc, Rothamsted, West Common, Harpenden, Hertfordshire AL5 2JQ, UK

[†] Electronic supplementary information (ESI) available. See DOI: 10.1039/c5ay00377f

transmittance or absorption of energy plotted against energy in wavenumbers. The consequent spectrum derived is indicative of the chemical bonds present and therefore provides an insight into biochemical 'fingerprint' of the sample.³¹ FTIR spectroscopy in plant research has been limited due to the strong dipole moment of water and thus investigations have been predominantly conducted in non-aqueous and dried material.³² This has been beneficial in the quantification of plant substances^{32–34} and deriving information regarding cell wall architecture.^{35–38} FTIR spectroscopy has also contributed to our understanding of key biotic and abiotic stresses such as plant–pathogen interactions and salinity respectively.^{28,35,39–41} Furthermore, the imaging capabilities of FTIR spectroscopy, particularly when utilised in conjunction with synchrotron radiation, have allowed the development of high resolution chemical imaging for plant tissues including leaf,⁴² seed^{43,44} and vascular tissues,⁴⁵ that accurately portray biochemical distributions of the intrinsic structure. However, the necessity of dried samples inhibits the use of FTIR for *in vivo* studies and also results in substantial preparation time for *in situ* studies. This issue has in part been overcome by the development of attenuated total reflection (ATR)-FTIR that utilises an internal reflective element (IRE), commonly made of diamond, Ge or ZnSe, to produce an

evanescent wave that interrogates the sample in contact with the ATR attachment.²⁸ Consequently, analysis of fresh plant tissue *in situ* is possible and has so far been implemented in plant leaves to observe cell wall expansion,⁴⁶ monitor temporal variations,^{5,47} identify indicators of senescence,⁴⁸ and also to characterise components of the epicuticular waxes.^{49,50}

In comparison, Raman spectroscopy uses monochromatic light in the near-IR region in order to excite molecules to higher virtual energy states. The technique exploits the phenomena of inelastic, or Raman scattering, when a chemical bond is excited by an incidence ray to a virtual energy state but does not return to the original ground energy state, therefore resulting in an energy shift represented in spectra.⁵¹ Although the occurrence of Raman scattering is a low probability process, the technique is highly sensitive with potential resolution approaching the nanometer scale.⁵² Unlike IR spectroscopy, Raman spectroscopy is not inhibited by aqueous samples, as water molecules do not exhibit strong Raman scattering features, making the technique ideal for analysis of live material. However, progress in plant research has been impeded due to interference from auto-fluorescence of plant enzymes, which can completely suppress the Raman signal.⁵³ The use of radiation in the near-IR (NIR) like that emitted from a Nd:YAG laser at 1064 nm, has been

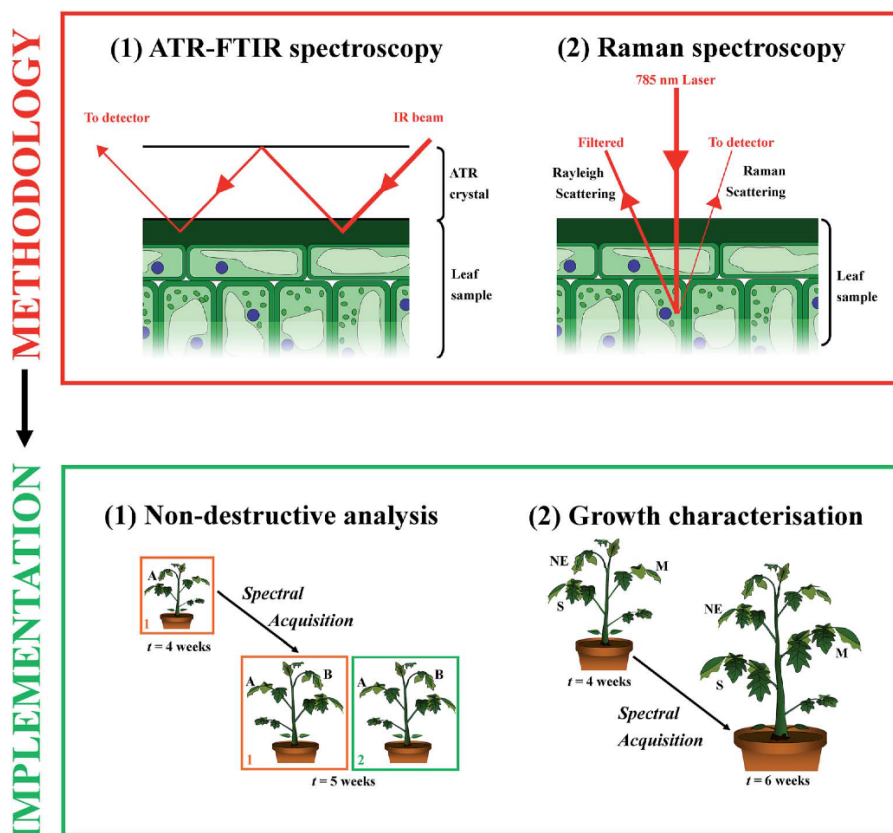


Fig. 1 An overview of the experimental principles and procedure. ATR-FTIR and Raman spectroscopy rely on distinctly different physical processes and therefore have discrete targets in the leaf tissue, with the cuticle being interrogated by both techniques and the epidermis and palisade parenchyma by Raman alone.

shown to reduce the influence of fluorescence on the Raman spectrum; however, this can also reduce spatial resolution and produce thermal emissions and absorption bands from hydrogen bonding.^{54,55} Further development of the Raman technique has increased our ability to obtain stronger Raman signals free from autofluorescence. Surface-enhanced Raman scattering (SERS),^{55,56,57} resonance Raman,^{26,58} coherent anti-Stokes Raman scattering (CARS),^{59,60} and stimulated Raman scattering (SRS)³ have all contributed to improved resolution and the advancement of imaging capabilities in plant and crop science.⁶¹ In particular, the use of metallic nanoparticles in SERS approaches have successfully quenched fluorescence that occurs in the presence of chlorophyll and pheophytin, two key chromophores constituents of photosystems situated on the thylakoid membrane of chloroplasts.^{62,63}

IR spectroscopy is dependent on molecules being IR-active, therefore having a dipole moment; however, Raman spectroscopy is reliant on molecules having polarisability. Thus in combination the techniques are complementary and information that could be otherwise lost, is regained by employing both techniques.⁶⁴ Both systems are regarded as non-destructive due to the use of relatively low energy lasers that are sufficient to vibrate but not damage chemical bonds. In this study, ATR-FTIR and Raman spectroscopy are critically assessed as analytical tools for non-destructive monitoring of plant health and development in *Solanum lycopersicum* (tomato) leaves. An experimental overview can be seen in Fig. 1. We demonstrate that biochemical information regarding cell wall expansion during development can be characterised *in vivo* without concerns from water and autofluorescence interference.

Materials & methods

Plant growth conditions

Solanum lycopersicum cv. Moneymaker (Moles Seeds, Colchester, UK) were germinated and cultivated individually in M3 compost (Levington Horticulture Ltd, Ipswich, UK) in a controlled environment growth room and watered daily up to water-holding capacity. Artificial light was generated by 600 W metal halide lamp (Osram Ltd, UK) for 16 hours per day at an intensity of $150 \pm 25 \mu\text{mol m}^{-2} \text{ s}^{-1}$. The temperature was maintained at $25 \pm 2^\circ\text{C}$ and $20 \pm 2^\circ\text{C}$ for photophase and scotophase respectively. All plants were analysed in the middle of the light period (12–4 pm) in order to maintain continuity. Prior and during spectral acquisition in the lab, a portable light system was used to maintain optimum light levels.

Review of non-destructive analysis

Tomato plants ($t = 4$ weeks) were observed over a four week period in response to analysis by ATR-FTIR spectroscopy. Initially one set of plants ($n = 3$) was analysed by ATR-FTIR spectroscopy on a mature leaflet (A) for at least three time points across a seven day period. The following week another set of plants ($n = 3$) was introduced to the experiment, with all plants ($n = 6$) analysed on the same or equivalent leaflet three times across another seven day period. Additionally during this

second week of analysis ($t = 5$ weeks) newly-expanded leaflets (B) from all plants in both sets were analysed to determine any systemic effects of the ATR-FTIR technique. This process was repeated for the following two weeks ($t = 6$ and 7 weeks), each time introducing a new set of previously unanalysed plants, comparing leaflets that had been previously analysed and newly expanded leaflets for systemic effects ($n = 12$, leaflets C and D respectively). Furthermore this methodology was repeated on separate tomato plants ($n = 9$) over a period of three weeks ($t = 4$ –6 weeks) using Raman spectroscopy, to compare the destructive effects both locally and systemically on living tissue. A full overview of this process can be seen in the ESI Fig. S1.† Simultaneously to all spectral acquisitions, measurements for rate of CO_2 assimilation, H_2O assimilation, internal CO_2 and stomatal conductance were obtained using a CIRAS-2 Portable Photosynthesis System (PP Systems, MA, USA) to determine any physiological indication of damage to the samples. Cuvette conditions corresponded to ambient CO_2 (390 ppm) light ($200 \mu\text{mol m}^{-2} \text{ s}^{-1}$), temperature (22°C) and humidity (50%) conditions within the controlled environment room.

Characterisation of healthy plant growth and development

Two time-course experiments over the course of three weeks were conducted in a total of nine tomato plants ($t = 4$ weeks), which were analysed using ATR-FTIR and Raman spectroscopy at 12 and 11 different time points respectively. Three plants were analysed at each time point to allow for sample rotation and high-throughput analysis. Each plant was analysed on 3 separate leaves; a newly expanded (NE), a fully-expanded mature (M) and a fully expanded senescing (S) leaf, to illustrate spectral alterations in leaves at distinct morphological and developmental stages.

ATR-FTIR spectroscopy

IR spectra were derived using a Bruker TENSOR 27 FTIR spectrometer with Helios ATR attachment (Bruker Optics, Coventry, UK). The approximate sampling area was $250 \mu\text{m} \times 250 \mu\text{m}$ as defined by the IRE, diamond crystal. Spectra were obtained at a spectral resolution of 8 cm^{-1} , resulting in 3.84 cm^{-1} data spacing, with 32 co-additions and a mirror velocity of 2.2 kHz for optimum signal to noise ratio.^{9,28} Five spectra were obtained from separate locations on each sample leaf with the diamond crystal cleaned using distilled water and dried between each measurement. Additionally, a background measurement was taken before each new sample to account for any changes in atmospheric conditions. Whole plant samples were positioned carefully around the spectrometer, with individual leaflets rested upon MirrIR Low-E glass slides (Kevley Technologies, OH, USA) on the sample stage. Raw spectra were cut at the spectral fingerprint region between 1800 – 900 cm^{-1} where biological molecules are known to absorb, second order differentiated for baseline correction and vector normalised using Matlab 2013a software (The Maths Works, MA, USA) with open-source IRootLab graphical interface (<https://code.google.com/p/irootlab/>).^{65,66} The penetration depth (d_p) of the ATR-FTIR evanescent wave varies between 0.5 – $2.9 \mu\text{m}$ at 4000 – 700 cm^{-1} wavenumbers.^{9,47}

This infers that this technique can derive information predominantly from the plant leaf cuticle (0.1–10 μm), the extracellular matrix of epidermal cells walls that is an essential barrier for water loss and protection.^{67,68}

Raman spectroscopy

An InVia Renishaw Raman spectrometer with a 785 nm excitation laser (Renishaw Plc, Gloucestershire, UK), with charged couple detector (CCD) and microscope attachment (Leica Microsystems, Milton Keynes, UK) was employed to acquire Raman spectra. The system was calibrated using a silicon source prior to any sample analysis. Plants were positioned around the microscope stage and individual leaflets were rested upon gold-coated glass slides (Platypus Technologies, WI, USA). Ten spectra per sample were obtained at using a 1200 l mm^{-1} grating, $\times 50$ objective (0.75 numerical aperture), 50% laser power (13 mW at sample), 10 seconds exposure time and one accumulation within the spectral range 500–2000 cm^{-1} for optimum resolution ($\sim 1 \mu\text{m}$). The zap function in Renishaw Wire 3.1 software was used to remove any cosmic ray artefacts from spectra, and the IRootLab Matlab interface was employed to truncate spectra between 1750–700 cm^{-1} , baseline correct (1st order differentiation), vector normalise and wavelet denoise.⁶⁹ The d_p of Raman spectroscopy can be up to several hundred micrometres in living tissues, therefore spectral analysis of leaf tissue could interrogate both the cuticle and the underlying adaxial epidermal cells and potentially the palisade parenchyma.⁷⁰ However in this investigation, focus is placed upon examination of the cuticle and epidermal cell wall.

Computational analysis

Dataset analysis was conducted using the IRootLab toolbox for Matlab, unless otherwise stated. Spectral datasets are often complex, with each spectrum containing around 235 and up to 900 data points for ATR-FTIR and Raman spectra, respectively. Subsequently any underlying variance within these datasets can be difficult to unearth and feature extraction is essential.⁷¹ Exploratory principal component analysis (PCA), following spectral standardisation, is an unsupervised technique that effectively reduces the dataset into principal components (PCs), which encapsulate variance throughout data classes.⁷² Coupled with supervised linear discriminant analysis (LDA), a technique to attain inter-class separation and minimize intra-class differences, a critical insight into spectral variance can be ascertained.⁷³ The number of PCs used was optimised using the PCA Pareto function within the IRootLab toolbox, in order to prevent noise introduction, and K-fold, leave-one-out, cross-validation was conducted to prevent over-fitting.⁷¹

For biomarker identification, three main approaches were conducted in order to visualise developmental differences in leaves over time. Difference between mean spectra (DBM) is an unsophisticated approach where mean spectra from two classes are subtracted, creating a curve of fundamental wavenumber differences between them.⁷⁴ The cluster vector (CV) approach takes input from data reduction by PCA and consequent linear combination of variables from LDA, to create a loadings vector

for each class that passes through respective data points.⁷⁵ The pseudo-spectra that are created allow one to identify which variables, or wavenumbers, are responsible for variance in the data set in direct relation to the original absorbance/intensity spectrum.⁷³ Forward feature selection (FFS) periodically incorporates sub-sets of wavenumbers into a data set and ranks them based on their contribution to improved classification, producing a feature selection histogram that visualises the number of times each wavenumber was selected.^{71,74} A Gaussian fit classifier was used with random sub-sampling, repeated 100 times to randomise training and test data (90% training, 10% data), and 10 variables were employed to improve stability of biomarker identification.⁷⁶ Wavenumbers were extracted using a peak detection algorithm as described by Coombes *et al.* 2003.⁷⁷ Following biomarker extraction, linear regression was conducted on mean absorbance/intensity values between leaves at distinct developmental stages, to characterise heterogeneity between leaves.

Potential anomalies were identified using the Grubb's test and one-way analysis of variance (ANOVA) with Tukey's multiple comparison tests were conducted in GraphPad Prism 4 software (GraphPad Software Inc, CA, USA) to determine significant differences between classes. Statistical tests were conducted using mean data from each sample, as opposed to individual scores.

Results and discussion

Review of non-destructive analysis

In order to identify any destructive effects of either ATR-FTIR or Raman spectroscopy on living plant samples, a number of comparisons between leaflet observations were made. Initially, physical damage to the leaf was assessed visually to detect any signs of tissue damage and stress. Raman spectroscopy did not contribute to any visual alterations in leaf tissue viability in comparison to control leaves; however, ATR-FTIR spectroscopy resulted in clear indentation of the tissue (Fig. 2). This occurs as the technique requires contact between the diamond crystal and the sample, resulting in pressure being applied to the adaxial leaf surface and therefore causing damage to the cuticle and epidermis. Although local damage can be seen at the analysis site, no differences can be seen at other leaflets and systemic leaves, indicating that any damage is confined to the defined leaflet. Interestingly, no significant alterations can be observed when rates of CO_2 assimilation were compared between leaflet samples (Table 1) following interrogation by ATR-FTIR spectroscopy in both local and systemic leaves, despite compromises to the leaf surface. No significant alterations were apparent in additional gas exchanges measurements either (ESI Table S1†). It can be assumed that there is no significant effect on CO_2 assimilation as a consequence of analysis using ATR-FTIR and therefore no apparent impact on leaf functionality.

Vibrational spectroscopy is a valuable tool for analysis of plant material and can infer subtle alterations in structure and biochemical composition that can be indicative of environmental stress.^{5,78} Minimal variations can be seen in pre-

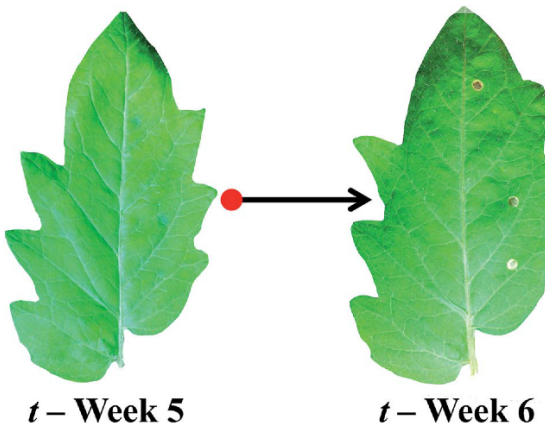


Fig. 2 Visible effect of ATR-FTIR spectroscopy on leaf tissue. (A) depicts leaflet sample immediately following analysis at three distinct points ($t = 4$ weeks) and (B) shows the same leaflet one week later ($t = 5$ weeks).

processed mean spectra from both ATR-FTIR and Raman spectra (ESI Fig. S2 and S3†) when comparing the effects of both analysis techniques in previously analysed and systemic leaves. This displays similarity in leaf stage of development, but also indicates the necessity of a feature extraction technique to identify subtle variation between samples that reveal biomarkers of damage. One-dimensional (1D) scores plots produced by cross-validated PCA-LDA of IR spectral data across the course of three weeks are shown (Fig. 3). Fig. 3A shows variance between equivalent leaflets at week 5 of plant development in two plant sets, one of which had been previously analysed using the ATR-FTIR technique. Spectra are plotted as points against the first linear discriminant (LD1), where separation in the y -axis suggests difference between the individual classes and consequently the samples. In this scores plot, initially no separation can be identified between 'plant set 1' and 'plant set 2' in either leaflet A (full square), which is a direct comparison between an interrogated leaflet and an equivalent non-interrogated leaflet. This suggests that there is no spectral alteration between the two that can be associated with continued analysis with ATR-FTIR spectroscopy, which is also confirmed by a one-way ANOVA test with Tukey's post-hoc test on each average sample score (ESI Table S2A†). Similarly in a

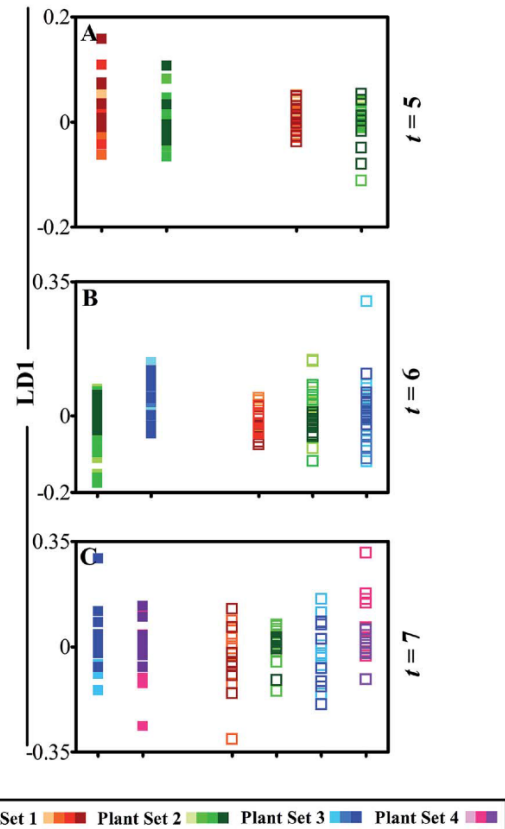


Fig. 3 Cross-validated PCA-LDA 1D scores plot of ATR-FTIR spectra obtained over a three week period ($t = \text{weeks } 5, 6 \text{ and } 7$ of development) to distinguish spectral effects of the technique. Each square corresponds to an individual spectrum, and colour variation indicates advancing time points through the respective time frame. Full squares (■) represent a comparison between leaflets specifically analysed the previous week with equivalent leaflets from a newly introduced plant set, and empty squares (□) compare a newly expanded leaflet to observe any systemic effects as well as local effects of the technique. (A) Compares previously analysed leaflet A and systemic leaflet B in plant sets 1 and 2; (B) leaflets B and C and (C) leaflets C and D.

systemic leaf, leaflet B in both plant sets, no differences can be seen showing that the technique is not causing any distinguishable damage to the overall plant health. Individual time

Table 1 Average rate of CO_2 assimilation ($\mu\text{mol CO}_2 \text{ m}^{-2} \text{ s}^{-1} \pm \text{standard error}$) for equivalent leaflets (A–D) in four plant sets over a time course of three weeks ($t = 5\text{--}7$) to determine any detrimental effects of ATR-FTIR spectroscopy interrogation. An ANOVA test was performed to determine any significant differences between values, however no significance was depicted ($P > 0.05$). Leaflets previously analysed using the technique are shown in italic

Leaflet	$t = 5$ weeks		$t = 6$ weeks		$t = 7$ weeks		
	A	B	B	C	C	D	
Plant set	1	<i>8.03 ± 0.61</i>	10.54 ± 0.99	—	11.39 ± 1.72	—	10.65 ± 0.44
	2	6.44 ± 0.40	12.26 ± 0.59	6.97 ± 0.97	12.70 ± 1.22	—	11.86 ± 0.79
	3			8.66 ± 1.59	10.36 ± 1.73	12.28 ± 1.84	10.63 ± 1.49
	4					6.70 ± 1.78	6.82 ± 1.25

points are identified using colour shading of individual spectra in order to identify any time related patterns; however, none are apparent.

During the following week of analysis (Fig. 3B), small alterations can be observed between leaflet B in both 'plant set 2', which had been analysed since week 5 of development, and the newly introduced 'plant set 3'. This alteration may be due to the effect of the ATR-FTIR technique on the integrity of the leaf. However, a degree of overlap occurs and following statistical analysis, this spectral feature is in fact not significant (ESI Table S2B†). Interestingly, no statistically significant shifts in LD1 are present in leaflet C across all three plant sets, notwithstanding a potential outlier that could be associated with analysis at the beginning of the time period (ESI Table S2C†). In Fig. 3C, the final week of analysis is shown ($t = 7$) and a comparison between 'plant set 3' and 'plant set 4' in leaflet C indicates no movement in LD1, demonstrating no spectral effects due to previous analysis using ATR-FTIR spectroscopy. This is replicated in leaflet D across all four plant sets, which highlight the

lack of systemic effects on overall plant health. Deterioration of leaf integrity would be identifiable *via* IR spectroscopy as key biochemical alterations occur during senescence including higher absorption at $1650\text{--}1500\text{ cm}^{-1}$ corresponding to phenolic and proteinaceous compounds.⁴⁸ Therefore any indication of leaf degradation or senescence induced by the technique would be observable using the multivariate method of analysis shown in Fig. 3.

Following cross-validated PCA-LDA manipulation of Raman spectra, 1D scores plots comparing leaflets against LD1 display little separation or variance between data classes (Fig. 4). This observation corresponds with the lack of visual damage to the leaf surface, unlike the clear physical effects of the ATR-FTIR technique (Fig. 2). It is for this reason that analysis was conducted using the Raman across three weeks of development ($t = 4\text{--}6$) as such minimal effects were perceived. Fig. 4A compares spectral differences between leaflet A in 'plant set 1', analysed during week 4 of plant development, and in 'plant set 2' newly introduced at week 5. The scores plot shows almost identical spectral responses between the equivalent leaflets, depicting heterogeneity between both classes (ESI Table S3†). This pattern is also replicated in leaflet B, representing the systemic health of the plant away from the site of interrogation. Following an additional week of analysis, further alterations between leaflet B in 'plant sets 2' and '3' cannot be distinguished (Fig. 4B). Furthermore, systemic effects on plant health shown by comparison of leaflet C in 'plant sets 1', '2' and '3', indicate no spectral separation in LD1 and therefore display no observable effect of interrogation using Raman spectroscopy.

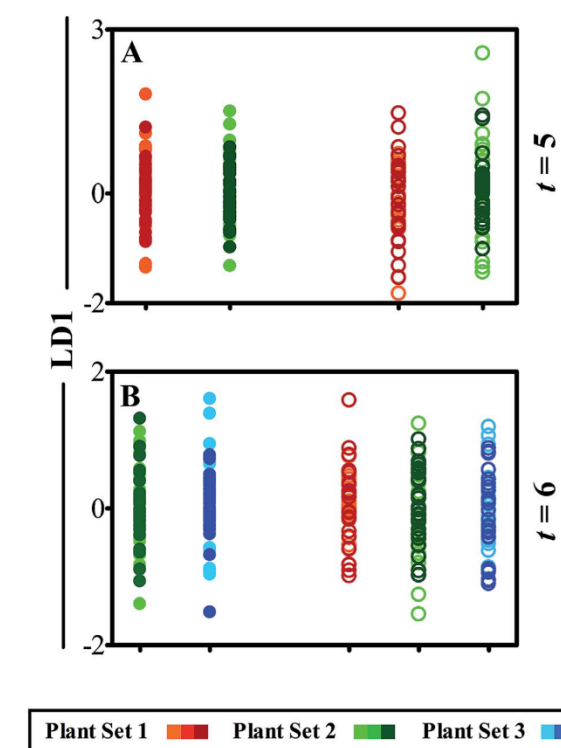


Fig. 4 Cross-validated PCA-LDA 1D scores plot of Raman spectra obtained over a two week period ($t = \text{weeks 5 and 6 of development}$) to distinguish spectral effects of the technique. Each point corresponds to an individual spectrum, and colour variation indicates advancing time points through the respective time frame. Full circles (●) represent a comparison between leaflets specifically analysed the previous week with equivalent leaflets from a newly introduced plant set, and empty circles (○) compare a newly expanded leaflet to observe any systemic and local effects of the technique. (A) Compares previously analysed leaflet A and systemic leaflet B in plant sets 1 and 2 and (B) leaflets B and C.

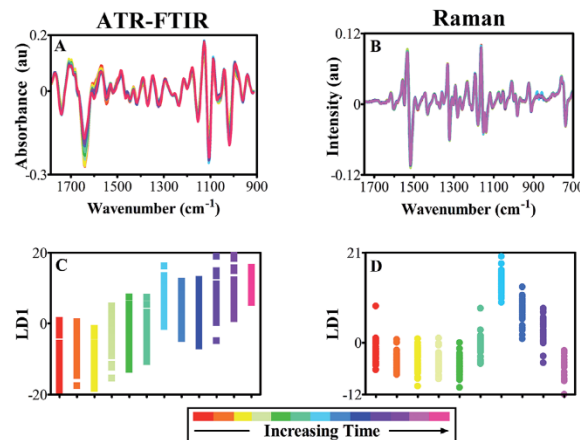


Fig. 5 Spectral data derived from ATR-FTIR (A and C) and Raman (B and D) spectroscopy over time points spanning a three week period in order to identify alterations indicative of healthy growth. (A) ATR-FTIR class means spectra of pre-processed data, cut to $1800\text{--}900\text{ cm}^{-1}$ wavenumbers, 2nd order differentiation baseline correction and vector normalisation; (B) Raman class means spectra cut to $1750\text{--}700\text{ cm}^{-1}$ wavenumbers, 1st order differentiated, vector normalised and wavelet de-noised; (C) cross-validated PCA-LDA 1D scores plot of ATR-FTIR spectra in regards to LD1 (D) cross-validated PCA-LDA 1D scores plot of Raman spectra across LD1.

Characterisation of healthy plant growth and development

Establishment of both ATR-FTIR and Raman spectroscopy as entirely non-destructive, non-invasive techniques with high throughput and resolution capabilities, indicates huge potential in the research fields of plant science. Firstly, it is important to typify healthy plant growth and identify key spectral biomarkers that are indicative of normal leaf development in an *in vivo* system. Pre-processed FTIR spectra shown in Fig. 5A, depict well-defined time dependent alterations across two distinct spectral regions: the polysaccharide fingerprint region from 1000–1150 cm^{-1} (ref. 41) and the protein absorbance region between 1500–1700 cm^{-1} wavenumbers.⁴² Interestingly, there is an opposite response at each of these regions, with a reduction in absorbance over time apparent at 1570, 1639 and 1709 cm^{-1} , associated with protein absorbance and an increase observed at 1018, 1107 and 1125 cm^{-1} in the polysaccharides region. During leaf development, it has been shown that plant cell walls undergo secondary cell wall formation, mediated by expansion proteins that allow for expansion of the cell wall by introduction of matrix polysaccharides such as cellulose, pectin and hemicelluloses.⁷⁹ This correlates to the increased absorbance over time, with cellulose alterations identified primarily at 1125 cm^{-1} ,³² as well as 1107 and 1018 cm^{-1} with additional contributions from pectin and hemicelluloses.^{34,80} At the higher end of the spectrum, a decrease in overall protein contribution can be seen at the amide I and amide II peaks, 1639 and 1570 cm^{-1} respectively, which could be tentatively associated with progression towards leaf senescence during the analysis period.⁴⁸ In comparison, class mean spectra obtained using Raman spectroscopy do not reveal any obvious spectral differences due to growth and development of the leaves (Fig. 5B) and

therefore further multivariate analysis is necessary to distinguish biochemical features. It is important to note, that the Raman spectra derived from *in vivo* analysis of plant samples has good signal to noise ratio and good spectral resolution, despite potential issues surrounding autofluorescence. Any minimal effect of this phenomenon has been alleviated or removed by baseline correction.

Cross-validated PCA-LDA with optimised PC factors was conducted on both FTIR absorbance (Fig. 5C) and Raman scattering (Fig. 5D) spectra in order to elucidate variance patterns within the data that correspond to the time progression. Fig. 5C shows a 1D scores plot that illustrates a gradual migration in LD1, indicating an additive effect of subtle spectral alterations between data classes. These differences are highly

Table 2 Key wavenumber features determined by difference between mean (DBM), cluster vector (CV) and forward feature selection (FFS) biomarker extraction methods, as identified in Fig. 7. Wavenumbers are displayed in descending order of significance and bold type represents wavenumbers identified in two or more extraction methods

		Top six discriminating biomarkers (cm^{-1})		
		DBM	CV	FFS
ATR-FTIR	Days 1–3 <i>versus</i> Days 4–7	1107^a	968	1192
		1547	1057	1408
		1643	1705	1327
		1018	1408	1508
		1126	1254	1076
	Days 1–3 <i>versus</i> Days 8–11	1593	1512	1666
		1103^a	1331	1408
		1639	968	1508
		1018	1057	1470
		1126	1466	1358
Raman	Days 1–3 <i>versus</i> Days 12–17	1547	1308	1296
		1593	1254	1666
		1639	1327	1647
		1015	1636	1751
		1103	1308	1574
	Days 1–3 <i>versus</i> Days 4–7	1123	1466	1431
		991	1597	1099
		1038	1011	990
		704	1318	1464
		723	1173	1191
	Days 1–3 <i>versus</i> Days 8–11	1229	1130	1654
		1173	1217	1321
		1103	1423	911
		1513	718	1628
		1158	1328	1527
	Days 1–3 <i>versus</i> Days 12–17	1327	1157	1328
		1526	1526	1157
		1513	1287	1689
		744	1186	1669
		1186	1169	1643

^a Derived from one feature extraction technique.

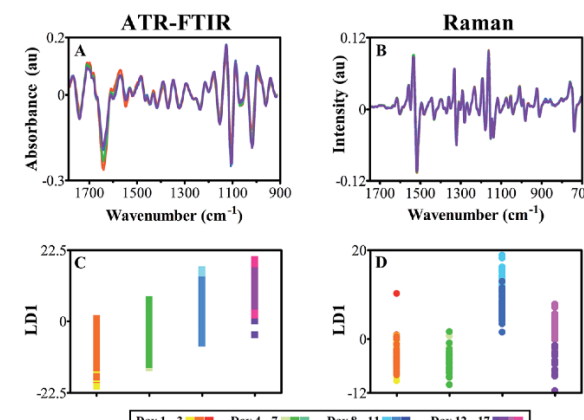


Fig. 6 Spectra derived from ATR-FTIR (A and C) and Raman (B and D) spectroscopy with grouped time points in order to depict clear spectral differences symptomatic of leaf development. (A) ATR-FTIR pre-processed class means spectra, cut to 1800–900 cm^{-1} , 2nd order differentiation and vector normalised; (B) Raman class means spectra cut to 1750–700 cm^{-1} , 1st order differentiation base line correction, vector normalised and wavelet de-noised; (C) cross-validated PCA-LDA 1D scores plot of ATR-FTIR spectra against LD and (D) cross-validated PCA-LDA scores plot of Raman spectra across LD1.

significant between relatively equal time periods of around 7 days, effectively splitting the classes into two, which potentially allows for grouping of different time points that would aid spectral analysis by reducing class size (ESI Table S4†). PCA-LDA of Raman spectra displays few significant alterations between classes initially, indicating lack of change within the plant leaf samples (Fig. 5D). However, a clear shift is seen mid-way through the study shown in blue (Day 9), followed by a steady progression back to the starting baseline. This feature is likely to be attributed to the spectral variation shown in Fig. 5B, which has increased absorbance between $890\text{--}850\text{ cm}^{-1}$, tentatively associated with cellulose.⁶¹ The reason for this artefact could be tentatively associated with secondary cell wall expansion, resulting in sampling at a different region of the leaf tissue, from initially the epidermal cell layer itself, to the then thickened cell wall.

As both data sets depict overlap between adjacent time points on 1D cross-validated PCA-LDA scores plots, classes were merged to reduce number of classes and aid in visualisation of spectral alterations. *P*-values relating to 1D scores plots, ATR-FTIR classes effectively split the data set into two halves,

which were then split again to produce four classes, each ranging from 3–5 days of acquisition (ESI Table S4†). This grouping was simulated in Raman data, despite more varied significance patterns between classes. In doing so, the deviations in protein and polysaccharide intensity seen previously in FTIR data are emphasised further and optimised for biomarker extraction (Fig. 6A and C). Although few differences were visible in class means spectra of leaf samples using Raman spectroscopy, by grouping the individual time point classes these subtle changes are accentuated and simplified (Fig. 8B). Upon closer inspection, it is possible to see a reduction in Raman scattering at 1233 cm^{-1} which is conventionally associated with the amide III peak, mirroring the decline in protein content and structure found in ATR-FTIR spectra.⁵⁵ Furthermore, a decline in chlorophyll content is observed at 1534 cm^{-1} representing a well-characterised indication of senescence as chloroplasts are degenerated.^{81,82} This is a particularly good example of the complementary nature of both the ATR-FTIR and Raman techniques. Additional spectral differences are visible in the Raman polysaccharide region, between $1160\text{--}970\text{ cm}^{-1}$ associated predominantly with cellulose.⁵⁵ At this stage no overall change

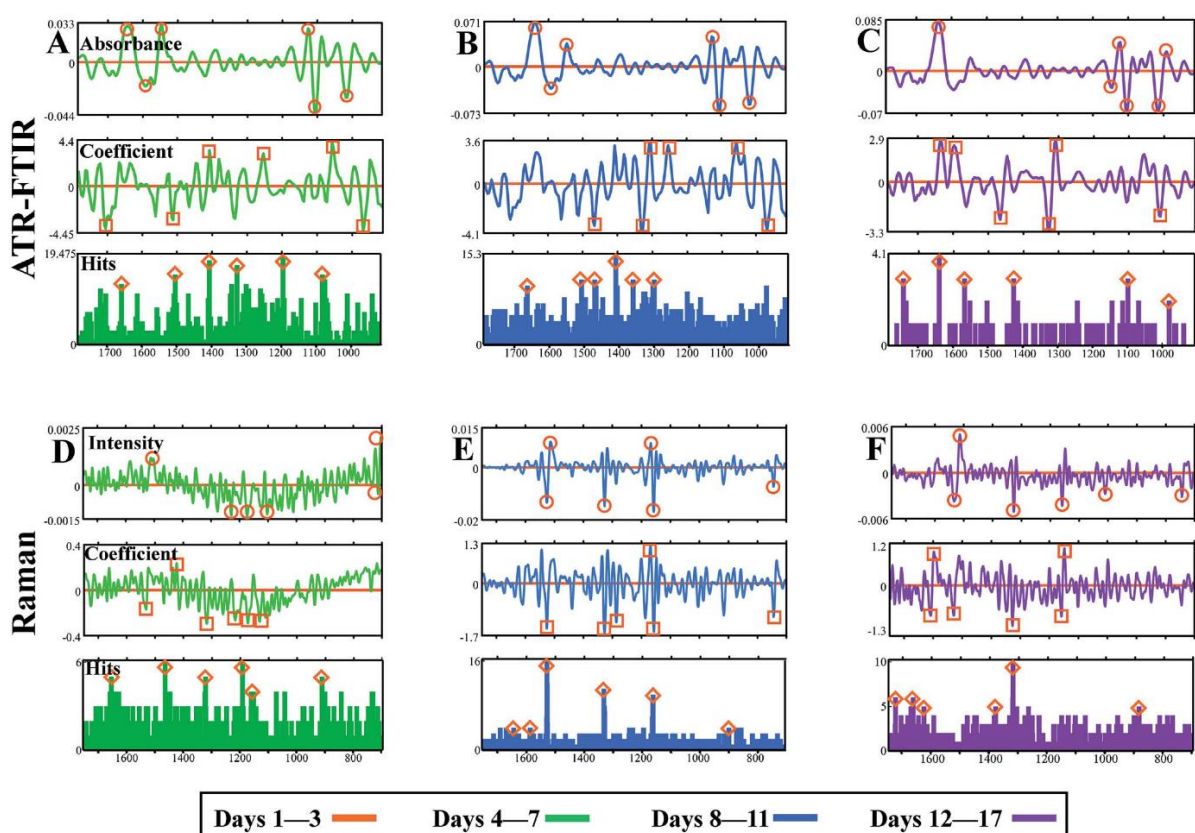


Fig. 7 Three biomarker extraction approaches, difference between mean spectra (top panels), PCA-LDA cluster vector (middle panels) and forward feature selection histograms (bottom panels) to establish spectral biomarkers indicative of plant development in both ATR-FTIR and Raman data. 'Days 1–3' represent the initial spectral characterisation of the leaf and therefore 'Days 4–7' (A and D); 'Days 8–11' (B and E); and 'Days 12–17' (C and F) are all compared to this data class. The top six biomarkers identified in each approach are highlighted with symbols. All units are arbitrary.

in cellulose can be identified; conflicting intensity patterns at 1054 cm^{-1} , which displays a reduction over time, and 1139 cm^{-1} that depicts an increase over time, provide unclear evidence for cellulose alterations. By grouping together equivalent classes, 1D scores plots following PCA-LDA show that group 'Days 8–11' significantly deviates from the other data classes (Fig. 6D).

A number of feature extraction methods are available to feed into biomarker determination and classification models.⁷¹ In this study, three approaches are explored to ascertain robust biomarkers suggestive of standard leaf development: DBM (top panels, \circ), CV approach (middle panel, \square) and FFS histograms (bottom panels, Δ). In each instance, the first data group 'Days 1–3' was used as a reference class and any consequent changes along the biological spectrum would be indicative of developmental alterations from this starting point of spectral acquisition. The top six biomarkers for each approach were identified using a peak detection algorithm and are listed in Table 2.

Initially, by comparing 'Days 1–3' with 'Days 4–7' from ATR-FTIR analysis it is clear to see a number of potential wavenumbers emerging from all three feature extraction methods (Fig. 7A). The DBM approach identifies wavenumbers principally from the protein and polysaccharide regions, emulating patterns identified in class means spectra. This is also replicated in CV and FFS analysis, additional to a number of wavenumbers across the spectrum that are also classified. Table 3 describes the top three biomarkers from each comparison, derived from wavenumbers uncovered by two or more biomarker extraction approaches, with a tentative band assignment. As shown previously, the main alterations in Fig. 7A are found at 1107 and 1408 cm^{-1} accounting for pectin found in the plant cell wall, as well as at $\sim 1510\text{ cm}^{-1}$, tentatively assigned to lignin or protein.⁸⁰ Lignin is present in vascular bundles within a tomato leaf and so may be noticeable due to spectral acquisition on the leaf midrib or because of damage to

the leaf surface during analysis. When comparing 'Days 1–3' with 'Days 8–11' alterations in the protein regions manifests across all three approaches with the amide III peak at 1302 cm^{-1} being the most discriminating (Fig. 7B). The DBM and CV methodology also show similarities in polysaccharide alterations, particularly at 1103 cm^{-1} associated with ester and pectins, although this is not selected by the FFS histogram. Ester bonds crosslink cutin in the leaf cuticle and thus this peak infers information about this upper leaf surface layer.⁸³ Fig. 7C illustrates parity between the DBM, CV and FFS extraction methods with each approach consistently identifying protein alterations at 1642 cm^{-1} the amide I peak, and carbohydrate markers at 1101 and 1014 cm^{-1} assigned to cellulose and pectin respectively. As this is a comparison between the two extreme time classes, the differences are expected to be more identifiable by all approaches.

Raman data compared between 'Days 1–3' and 'Days 4–7' show very little variation, indicated by relatively noisy curves in both DBM and CV analysis and a featureless FFS histogram (Fig. 7D). As shown in ATR-FTIR data, these two data classes are most similar and therefore spectral differences would be minimal. In contrast, Fig. 7E consistently locates three distinct wavenumbers associated principally with carotenoid at 1158 and 1527 cm^{-1} , as well as chlorophyll at 1328 cm^{-1} . The latter of these observations may be expected as a leaf develops towards senescence, due to a breakdown of chloroplasts and therefore a decrease in chlorophyll content.⁸⁴ The same wavenumbers are again deduced when comparing 'Days 1–3' with 'Days 12–17', although surprisingly these are not picked out as robustly in the FFS histogram (Fig. 7F). Alterations at the 1158 and 1526 cm^{-1} band begins to infer that there is a variance in carotenoid content between classes, attributed to leaf development. It is well established that carotenoid content remains constant whilst chlorophyll reduces through development of the leaf, evidenced by colour transition from green to brown in young

Table 3 Top discriminating biomarkers as derived from feature extraction techniques, with tentative wavenumbers assignments derived

		Wavenumber (cm^{-1})	Tentative assignment	Reference
ATR-FTIR	Days 1–3 versus Days 4–7	1408	CH_3 deformation, $\nu_s(\text{COO}^-)$ in pectin	88
		1512–1508	$\nu(\text{C}=\text{C})$ in lignin, carotenoid or protein	43
		1107	$\nu(\text{CO})$, $\nu(\text{CC})$, pectin	32
	Days 1–3 versus Days 8–11	1470–1466	CH_2 bending in lipid	47
		1308–1296	Amide III	80
		1103	$\nu(\text{C}=\text{O})$ in ester	89
	Days 1–3 versus Days 12–17	1647–1636	Amide I	61
		1103–1099	$\nu(\text{CO})$ in cellulose	36
		1015–1013	$\nu(\text{CO})$, $\nu(\text{CC})$, $\delta(\text{OCH})$, ring in pectin	34
Raman	Days 1–3 versus Days 4–7	1229–1217	Amide III	55
		1191–1173	$\text{as}(\text{PO}_4^{3-})$ in DNA	40
		1462	$\delta(\text{CH}_2)$ in hemicellulose	61
	Days 1–3 versus Days 8–11	1158–1157	$\nu(\text{CC})$ in carotenoid	90
		1328–1327	Chlorophyll	56
		1526–1527	$\nu(\text{C}=\text{C})$ in carotenoid	91
	Days 1–3 versus Days 12–17	1327–1326	Chlorophyll	56
		1159–1148	$\nu(\text{CC})$ in carotenoid	90
		1533–1529	$\nu(\text{C}=\text{C})$ in carotenoid, chlorophyll	56

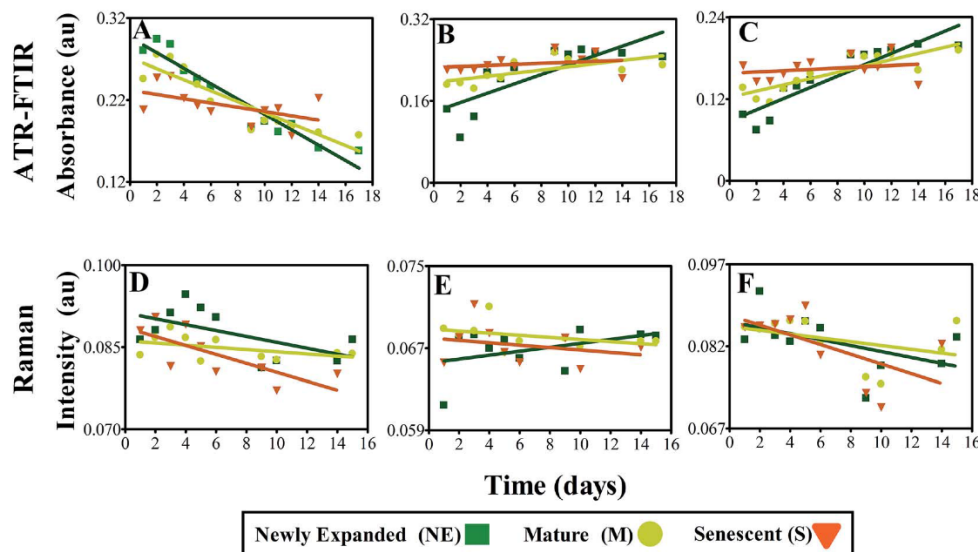


Fig. 8 Linear regression analysis at key biomarker wavenumbers 1639 cm^{-1} (A), 1103 cm^{-1} (B), 1015 cm^{-1} (C) from mean IR spectra and 1529 cm^{-1} (D), 1327 cm^{-1} (E), 1158 cm^{-1} (F) from mean Raman spectra of leaves at different developmental stages.

and senescent leaves.⁸⁵ Thus any alteration in carotenoids pigments is unexpected in regards to development of the leaf.

Linear regression analysis was conducted on the most distinguishing biomarkers previously determined, to ascertain any patterns in absorbance between leaves at different morphological stages (Fig. 8). In general, a negative relationship can be seen between protein absorbance over time, particularly NE leaves, typified by IR absorbance values at 1639 cm^{-1} , representing progression from young towards senescent leaf (Fig. 8A). This is also replicated to a lesser extent in M leaves, which is attributed to the leaf being closer to senescence and therefore not experiencing as severe protein reduction in the acquisition time frame. No significant decrease in protein can be identified in S leaves over the course of the study due to already having undergone substantial protein degradation (ESI Table S5†). Fig. 8B and C highlight positive variations in absorbance bands at 1107 and 1015 cm^{-1} corresponding to polysaccharides cellulose and pectin, respectively. NE leaves again depict the greatest alterations at these wavenumbers corresponding to cell wall expansion. This pattern is less visible in M leaves and even less so in S leaves, mirroring the response shown in protein. A diminution of protein and increase of carbohydrate are simple characteristics of leaf development and have been effectively characterised here by ATR-FTIR in different leaf stages.

Fig. 8D shows linear regression analysis of scattering intensity at 1529 cm^{-1} resultant from Raman analysis of NE, M and S leaves. Although only minimal significance can be seen in M leaves, there is a slight negative trend in the data, showing a reduction in chlorophyll and carotenoid intensity. This acknowledged indicator of leaf senescence appears to occur more significantly in M leaves, highlighting that chlorophyll degradation in this case appears to be a late on-set process

within leaf senescence.⁸⁶ In contrast, at peak 1328 cm^{-1} corresponding primarily with chlorophyll, no significant patterns can be identified with NE expanded leaves showing slight increases compared with small reductions in M and S leaves (Fig. 8E). Overlap with DNA and protein can be observed around this region and may contribute to masking any chlorophyll scattering effect.⁸⁷ Carotenoid alterations are portrayed in Fig. 8F relative to intensity at 1158 cm^{-1} and do not show any significant differences between leaf samples.

Conclusion

ATR-FTIR and Raman spectroscopy are highly informative, non-destructive and robust techniques that have been limitedly employed in the field of plant science.³² Whilst many studies demonstrate the successful use of vibrational spectroscopy to characterise plant tissues in fixed and *in vitro* samples, thus far research has been hindered by water interference and auto-fluorescence.³ In this investigation, *in vivo* spectral measurements are obtained with no destructive effect on systemic plant health. Although ATR-FTIR appears to cause minor local damage, this had no significant effect on the leaf and therefore does not necessarily rule out non-destructive analysis. The technique may not be suitable for direct analysis of fruit or yieldable products, however in future field studies, a single leaf is more easily sacrificed in a plant or crop system, with no detriment to crop yield or quality. Raman spectroscopy in particular had little visible effect on plant health and viability and may prove to be a crucial tool for live plant analysis. Additionally, both complementary methods coupled with multivariate analysis, provide data that can accurately depict known plant developmental processes, providing groundwork for characterisation of complex stress responses, such as

nutrient deficiency, that could be used in the field. A prerequisite for future studies would be to characterise a stress response and locate spectral biomarkers indicative of this given stress. This presents a novel method of fingerprinting plant health in a high-throughput manner, which can be effectively employed in agricultural and environmental studies.

Acknowledgements

HJB is a member of the Centre for Global Eco-Innovation with ERDF funding.

References

- 1 H. C. J. Godfray, J. R. Beddington, I. R. Crute, L. Haddad, D. Lawrence, J. F. Muir, J. Pretty, S. Robinson, S. M. Thomas and C. Toulmin, *Science*, 2010, **327**(5967), 812–818.
- 2 I. Domínguez-Martínez, O. G. Meza-Márquez, G. Osorio-Revilla, J. Proal-Nájera and T. Gallardo-Velázquez, *J. Korean Soc. Appl. Biol. Chem.*, 2014, **57**(1), 133–142.
- 3 J. C. Mansfield, G. R. Littlejohn, M. P. Seymour, R. J. Lind, S. Perfect and J. Moger, *Anal. Chem.*, 2013, **85**(10), 5055–5063.
- 4 V. Llabjani, R. N. Malik, J. Trevisan, V. Hoti, J. Ukpobor, Z. K. Shinwari, C. Moeckel, K. C. Jones, R. F. Shore and F. L. Martin, *Environ. Int.*, 2012, **48**, 39–46.
- 5 B. E. Obinaju, A. Alaoma and F. L. Martin, *Environ. Pollut.*, 2014, **192**, 222–231.
- 6 M. Mecozzi, M. Pietroletti and R. Di Mento, *Vib. Spectrosc.*, 2007, **44**(2), 228–235.
- 7 L. G. Thygesen, M. M. Løkke, E. Micklander and S. B. Engelsen, *Trends Food Sci. Technol.*, 2003, **14**(1), 50–57.
- 8 D.-W. Sun, *Infrared spectroscopy for food quality analysis and control*, Academic Press, 2009.
- 9 M. J. Baker, J. Trevisan, P. Bassan, R. Bhargava, H. J. Butler, K. M. Dorling, P. R. Fielden, S. W. Fogarty, N. J. Fullwood, K. A. Heys, C. Hughes, P. Lasch, P. L. Martin-Hirsch, B. Obinaju, G. D. Sockalingum, J. Sulé-Suso, R. J. Strong, M. J. Walsh, B. R. Wood, P. Gardner and F. L. Martin, *Nat. Protoc.*, 2014, **9**(8), 1771–1791.
- 10 J. M. Chalmers, P. R. Griffiths, D. E. Pivonka, J. Chalmers and P. Griffiths, *Applications of vibrational spectroscopy in pharmaceutical research and development*, ed. D. E. Pivonka, J. M. Chalmers and P. R. Griffiths, 2007.
- 11 G. Clemens, J. R. Hands, K. M. Dorling and M. J. Baker, *Analyst*, 2014, **139**(18), 4411–4444.
- 12 P. Lasch, A. Pacifico and M. Diem, *Biopolymers*, 2002, **67**(4–5), 335–338.
- 13 M. Diem, A. Mazur, K. Lenau, J. Schubert, J. Fore, B. Bird, M. Miljković and C. Krafft, in *Ex-vivo and In-vivo Optical Molecular Pathology*, ed. J. Popp, 2014, ch. 3, pp. 45–102.
- 14 F. M. Lyng, E. Ó. Faoláin, J. Conroy, A. D. Meade, P. Krief, B. Duffy, M. Hunter, J. Byrne, P. Kelehan and H. J. Byrne, *Exp. Mol. Pathol.*, 2007, **82**(2), 121–129.
- 15 D. C. Fernandez, R. Bhargava, S. M. Hewitt and I. W. Levin, *Nat. Biotechnol.*, 2005, **23**(4), 469–474.
- 16 B. R. Wood, M. A. Quinn, F. R. Burden and D. McNaughton, *Biospectroscopy*, 1996, **2**(3), 143–153.
- 17 P. Crow, A. Molekovsky, N. Stone, J. Uff, B. Wilson and L. Wongkeesong, *Urology*, 2005, **65**(6), 1126–1130.
- 18 N. Stone and P. Matousek, *Cancer Res.*, 2008, **68**(11), 4424–4430.
- 19 P. Lasch, W. Haensch, D. Naumann and M. Diem, *Biochim. Biophys. Acta, Mol. Basis Dis.*, 2004, **1688**(2), 176–186.
- 20 M. K. Kuimova, K. Chan and S. G. Kazarian, *Appl. Spectrosc.*, 2009, **63**(2), 164–171.
- 21 J. Ollesch, M. Heinze, H. M. Heise, T. Behrens, T. Brüning and K. Gerwert, *J. Biophotonics*, 2014, **7**(3–4), 210–221.
- 22 K. M. Dorling and M. J. Baker, *Trends Biotechnol.*, 2013, **31**(6), 327–328.
- 23 D. Lin, S. Feng, J. Pan, Y. Chen, J. Lin, G. Chen, S. Xie, H. Zeng and R. Chen, *Opt. Express*, 2011, **19**(14), 13565–13577.
- 24 J. W. Allwood, J. Heald, A. J. Lloyd, R. Goodacre and L. A. Mur, in *Plant Metabolomics*, Springer, 2012, vol. 860, pp. 31–49.
- 25 M. Baranska, W. Schütze and H. Schulz, *Anal. Chem.*, 2006, **78**(24), 8456–8461.
- 26 D. Gill, R. Kilponen and L. Rimai, *Nature*, 1970, **227**(5259), 743–744.
- 27 R. H. Wilson, A. C. Smith, M. Kačuráková, P. K. Saunders, N. Wellner and K. W. Waldron, *Plant Physiol.*, 2000, **124**(1), 397–406.
- 28 H. E. Johnson, D. Broadhurst, R. Goodacre and A. R. Smith, *Phytochemistry*, 2003, **62**(6), 919–928.
- 29 Z. Wei, L. Dong and Z. Tian, *Pak. J. Bot.*, 2009, **41**(4), 1743–1750.
- 30 P. Griffiths and J. A. De Haseth, *Fourier transform infrared spectrometry*, Wiley-Interscience, 2007.
- 31 F. L. Martin, *Nat. Methods*, 2011, **8**(5), 385–387.
- 32 H. Schulz and M. Baranska, *Vib. Spectrosc.*, 2007, **43**(1), 13–25.
- 33 Y. Li, D. Kong and H. Wu, *Ind. Crops Prod.*, 2013, **41**(1), 269–278.
- 34 M. Kacurakova, P. Capek, V. Sasinkova, N. Wellner and A. Ebringerova, *Carbohydr. Polym.*, 2000, **43**(2), 195–203.
- 35 P. Rösch, W. Kiefer and J. Popp, *Biopolymers*, 2002, **67**(4–5), 358–361.
- 36 M. C. McCann, M. Defernez, B. R. Urbanowicz, J. C. Tewari, T. Langewisch, A. Olek, B. Wells, R. H. Wilson and N. C. Carptita, *Plant Physiol.*, 2007, **143**(3), 1314–1326.
- 37 M. McCann, L. Chen, K. Roberts, E. Kemsley, C. Sene, N. Carptita, N. Stacey and R. Wilson, *Physiol. Plant.*, 1997, **100**(3), 729–738.
- 38 D. Harris, V. Bulone, S.-Y. Ding and S. DeBolt, *Plant Physiol.*, 2010, **153**(2), 420–426.
- 39 R. Gessner, P. Rösch, R. Petry, M. Schmitt, M. Strehle, W. Kiefer and J. Popp, *Analyst*, 2004, **129**(12), 1193–1199.
- 40 E. Gidman, R. Goodacre, B. Emmett, A. R. Smith and D. Gwynn-Jones, *Phytochemistry*, 2003, **63**(6), 705–710.
- 41 J. W. Allwood, D. I. Ellis and R. Goodacre, *Physiol. Plant.*, 2008, **132**(2), 117–135.

42 P. Heraud, S. Caine, G. Sanson, R. Gleadow, B. R. Wood and D. McNaughton, *New Phytol.*, 2007, **173**(1), 216–225.

43 P. Yu, J. J. McKinnon, C. R. Christensen, D. A. Christensen, N. S. Marinkovic and L. M. Miller, *J. Agric. Food Chem.*, 2003, **51**(20), 6062–6067.

44 B. O. Budevska, S. T. Sum and T. J. Jones, *Appl. Spectrosc.*, 2003, **57**(2), 124–131.

45 D. S. Himmelsbach, S. Khalili and D. E. Akin, *J. Sci. Food Agric.*, 2002, **82**(7), 685–696.

46 F. Monti, R. Dell'Anna, A. Sanson, M. Fasoli, M. Pezzotti and S. Zenoni, *Vib. Spectrosc.*, 2012, **65**, 36–43.

47 B. Ribeiro da Luz, *New Phytol.*, 2006, **172**(2), 305–318.

48 D. G. Ivanova and B. R. Singh, *Biopolymers*, 2003, **72**(2), 79–85.

49 E. Dubis, A. Dubis and J. Morzycki, *J. Mol. Struct.*, 1999, **511**, 173–179.

50 E. N. Dubis, A. T. Dubis and J. Poplawski, *J. Mol. Struct.*, 2001, **596**(1), 83–88.

51 E. B. Wilson, *Molecular vibrations: the theory of infrared and Raman vibrational spectra*, Courier Dover Publications, 1955.

52 E. Smith and G. Dent, *Modern Raman spectroscopy: a practical approach*, John Wiley & Sons, 2005.

53 M. Baranska, M. Roman, H. Schulz and R. Baranski, *Curr. Anal. Chem.*, 2013, **9**(1), 108–127.

54 B. Schrader, A. Hoffmann and S. Keller, *Spectrochim. Acta, Part A*, 1991, **47**(9), 1135–1148.

55 C. Sene, M. C. McCann, R. H. Wilson and R. Grinter, *Plant Physiol.*, 1994, **106**(4), 1623–1631.

56 L. Zeiri, *J. Raman Spectrosc.*, 2007, **38**(7), 950–955.

57 P. Rösch, J. Popp and W. Kiefer, *J. Mol. Struct.*, 1999, **480–481**, 121–124.

58 J. C. Merlin, *Pure Appl. Chem.*, 1985, **57**(5), 785–792.

59 Y. Zeng, M. E. Himmel and S.-Y. Ding, in *Biomass Conversion*, Springer, Methods in Molecular Biology, 2012, vol. 908, pp. 49–60.

60 Y. Zeng, B. G. Saar, M. G. Friedrich, F. Chen, Y.-S. Liu, R. A. Dixon, M. E. Himmel, X. S. Xie and S.-Y. Ding, *BioEnergy Res.*, 2010, **3**(3), 272–277.

61 M. Chylinska, M. Szymanska-Chargot and A. Zdunek, *Plant Methods*, 2014, **10**(1), 14.

62 R. Picorel, G. Chumanov, E. Torrado, T. M. Cotton and M. Seibert, *J. Phys. Chem. B*, 1998, **102**(15), 2609–2613.

63 M. Seibert, R. Picorel, J.-H. Kim and T. M. Cotton, *Methods Enzymol.*, 1992, **213**, 31–42.

64 B. Schrader, *Infrared and Raman spectroscopy: methods and applications*, John Wiley & Sons, 2008.

65 F. L. Martin, J. G. Kelly, V. Llabjani, P. L. Martin-Hirsch, I. I. Patel, J. Trevisan, N. J. Fullwood and M. J. Walsh, *Nat. Protoc.*, 2010, **5**(11), 1748–1760.

66 J. Trevisan, P. P. Angelov, A. D. Scott, P. L. Carmichael and F. L. Martin, *Bioinformatics*, 2013, **29**(8), 1095–1097.

67 E. Domínguez, J. A. Heredia-Guerrero and A. Heredia, *New Phytol.*, 2011, **189**(4), 938–949.

68 M. Riederer and L. Schreiber, *J. Exp. Bot.*, 2001, **52**(363), 2023–2032.

69 G. Strang and T. Nguyen, *Wavelets and filter banks*, SIAM, 1996.

70 P. Matousek, *Chem. Soc. Rev.*, 2007, **36**(8), 1292–1304.

71 J. Trevisan, P. P. Angelov, P. L. Carmichael, A. D. Scott and F. L. Martin, *Analyst*, 2012, **137**(14), 3202–3215.

72 I. I. Patel, W. J. Harrison, J. G. Kerns, J. Filik, K. Wehbe, P. L. Carmichael, A. D. Scott, M. P. Philpott, M. D. Frogley, G. Cinque and F. L. Martin, *Anal. Bioanal. Chem.*, 2012, **404**(6–7), 1745–1758.

73 F. L. Martin, M. J. German, E. Wit, T. Fearn, N. Ragavan and H. M. Pollock, *J. Comput. Biol.*, 2007, **14**(9), 1176–1184.

74 J. Trevisan, P. P. Angelov, I. I. Patel, G. M. Najand, K. T. Cheung, V. Llabjani, H. M. Pollock, S. W. Bruce, K. Pant and P. L. Carmichael, *Analyst*, 2010, **135**(12), 3266–3272.

75 J. G. Kelly, J. I. Trevisan, A. D. Scott, P. L. Carmichael, H. M. Pollock, P. L. Martin-Hirsch and F. L. Martin, *J. Proteome Res.*, 2011, **10**(4), 1437–1448.

76 J. Trevisan, J. Park, P. P. Angelov, A. A. Ahmadzai, K. Gajjar, A. D. Scott, P. L. Carmichael and F. L. Martin, *J. Biophotonics*, 2014, **7**(3–4), 254–265.

77 K. R. Coombes, H. A. Fritsche, C. Clarke, J.-N. Chen, K. A. Baggerly, J. S. Morris, L.-C. Xiao, M.-C. Hung and H. M. Kuerer, *Clin. Chem.*, 2003, **49**(10), 1615–1623.

78 I. Weissflog, N. Vogler, D. Akimov, A. Dellith, D. Schachtschabel, A. Svatos, W. Boland, B. Dietzek and J. Popp, *Plant Physiol.*, 2010, **154**(2), 604–610.

79 D. J. Cosgrove, *Nat. Rev. Mol. Cell Biol.*, 2005, **6**(11), 850–861.

80 Z. Movasaghi, S. Rehman and D. I. ur Rehman, *Appl. Spectrosc. Rev.*, 2008, **43**(2), 134–179.

81 C. M. Smart, *New Phytol.*, 1994, **126**(3), 419–448.

82 V. Buchanan-Wollaston, *J. Exp. Bot.*, 1997, **48**(2), 181–199.

83 P. Kolattukudy, K. Espelie and C. Soliday, in *Plant Carbohydrates II*, Springer, 1981, pp. 225–254.

84 B. Schrader, B. Dippel, I. Erb, S. Keller, T. Löchte, H. Schulz, E. Tatsch and S. Wessel, *J. Mol. Struct.*, 1999, **480–481**, 21–32.

85 R. Baranski, M. Baranska and H. Schulz, *Planta*, 2005, **222**(3), 448–457.

86 L. Guyer, S. S. Hofstetter, B. Christ, B. S. Lira, M. Rossi and S. Hörtener, *Plant Physiol.*, 2014, **166**(1), 44–56.

87 Z. Movasaghi, S. Rehman and I. U. Rehman, *Appl. Spectrosc. Rev.*, 2007, **42**(5), 493–541.

88 L. Chen, N. C. Carpita, W.-D. Reiter, R. H. Wilson, C. Jeffries and M. C. McCann, *Plant J.*, 1998, **16**(3), 385–392.

89 R. Hunt, *Basic growth analysis*, Unwin Hyman Ltd, 1990.

90 H. Schulz, M. Baranska and R. Baranski, *Biopolymers*, 2005, **77**(4), 212–221.

91 J. J. Jansen, J. W. Allwood, E. Marsden-Edwards, W. H. van der Putten, R. Goodacre and N. M. van Dam, *Metabolomics*, 2009, **5**(1), 150–161.

Electronic Supplementary Information

A critical analysis of vibrational spectroscopy to non-destructively monitor plant health and development.

Holly J. Butler ^{ab}, Martin R. McAinsh ^c, Steve Adams ^d, Francis L. Martin ^a

^a *Centre for Biophotonics, ^c Lancaster Environment Centre, Lancaster University, Lancaster LA1 4YQ, UK*

^b *Centre for Global Eco-Innovation, Lancaster Environment Centre, Lancaster University, LA1 4YQ, UK*

^d *Plant Impact Plc, Rothamsted, West Common, Harpenden, Hertfordshire, AL5 2JQ, UK*

***Correspondence to:** Prof Francis L Martin, Centre for Biophotonics, LEC, Lancaster University, Lancaster LA1 4YQ, UK; Email: f.martin@lancaster.ac.uk; Tel.: +44(0)1524 51020

Number of Pages: 9

Number of Figures: 3

Number of Tables: 5

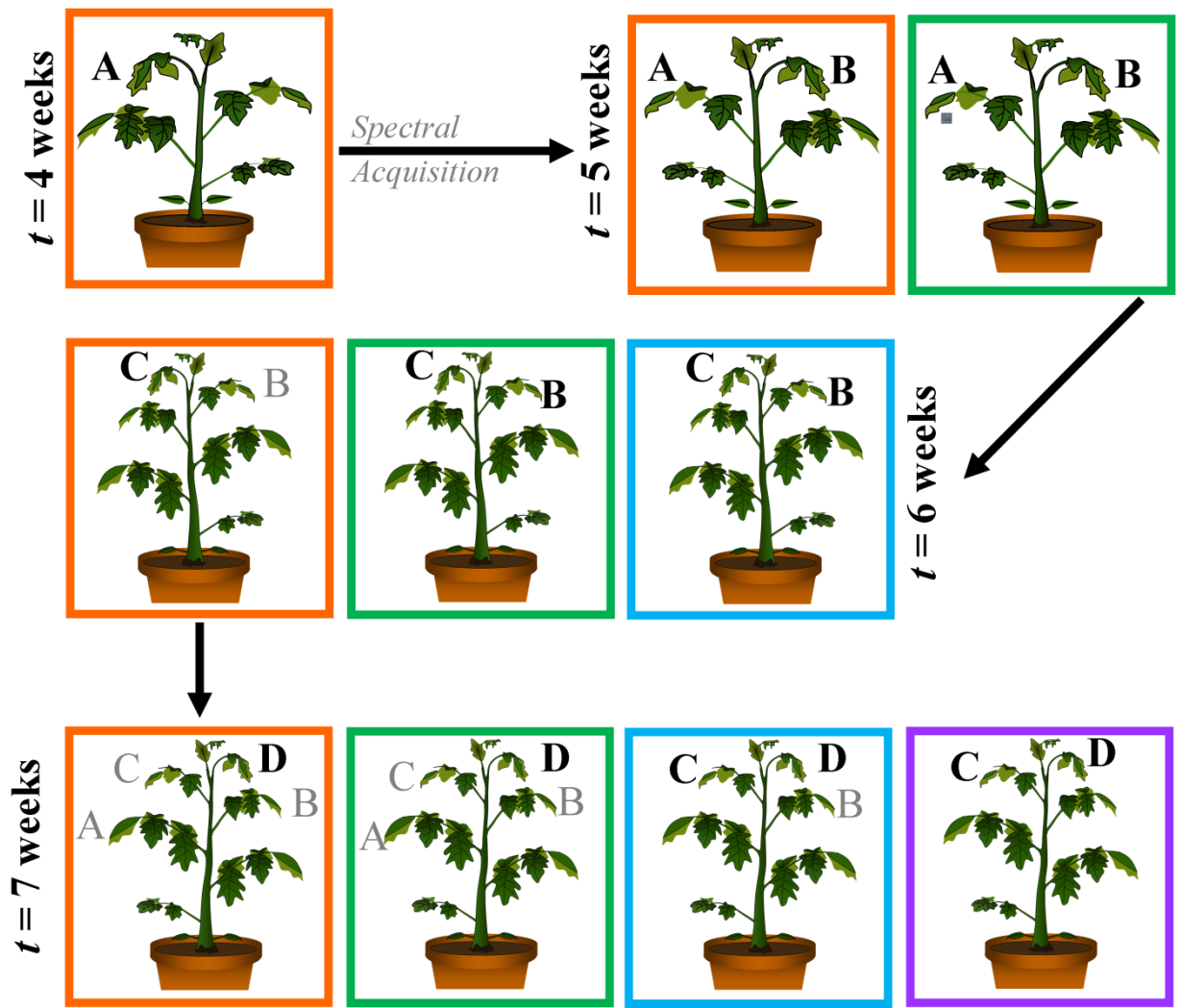


Figure S1. An overview schematic of the experimental procedure for the review of non-destructive analysis. A new set of plants was introduced each week and is symbolised by coloured boxes ('Plant Set 1' orange, 'Plant Set 2' green, 'Plant Set 3' blue and 'Plant Set 4' purple). Individual leaflets are labelled and represent equivalent leaflets between plant sets. Greyed out labels show previously analysed leaflet, which are no longer being interrogated at that particular week of analysis.

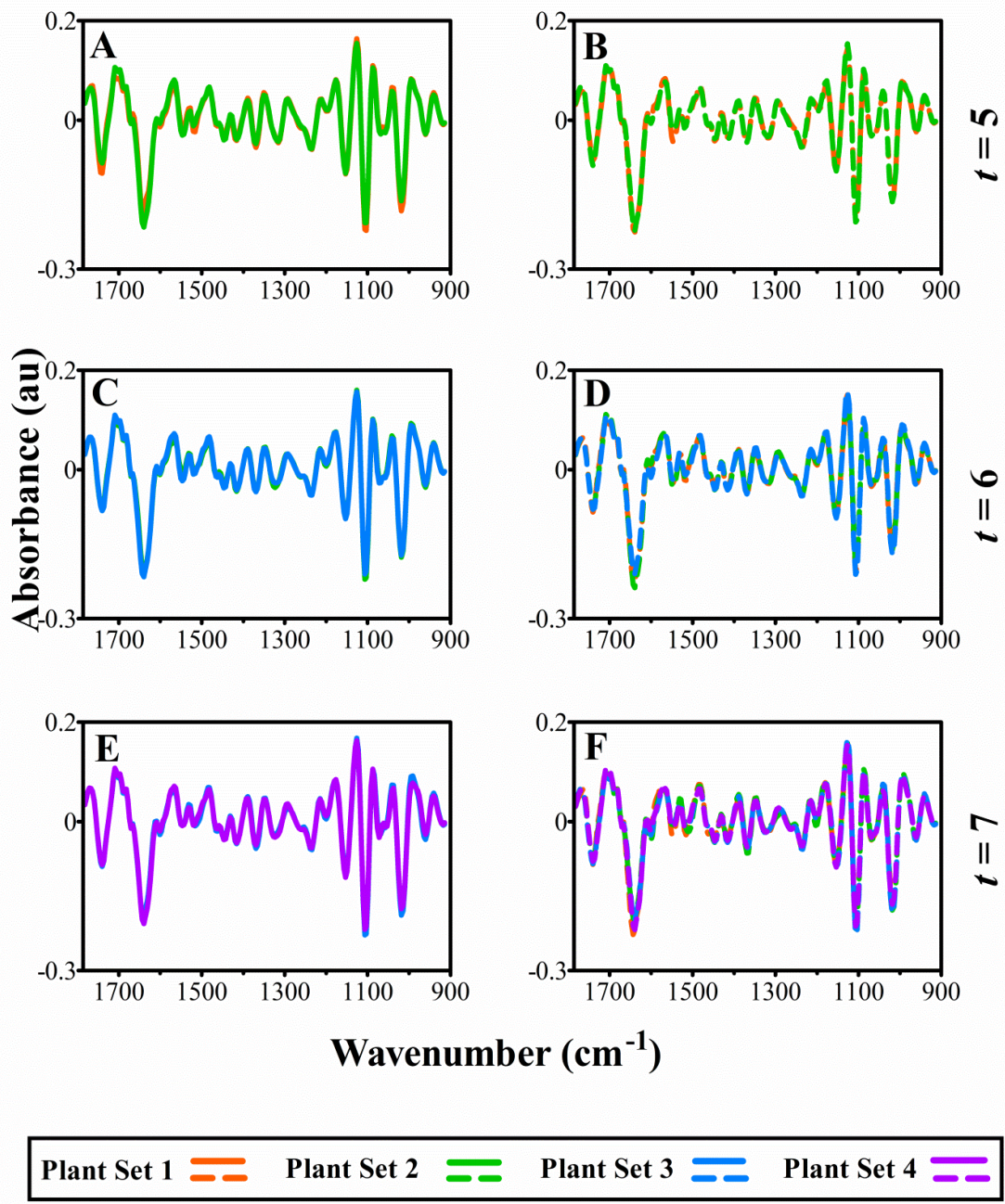


Figure S2. ATR-FTIR class means spectra to compare previously analysed and equivalent leaflets (full line), as well as differences in systemic leaflets (dashed line). At week 5 ($t = 5$) of development, plants were compared at mature leaflet A (**A**) and newly expanded leaflet B (**B**); at week 6 ($t = 6$), plants were compared at leaflet B (**C**) and newly expanded C (**D**); and finally at week 7 ($t = 7$), leaflet C (**E**) and D (**F**) were compared. Spectra were processed with second order differentiation baseline correction and vector normalisation.

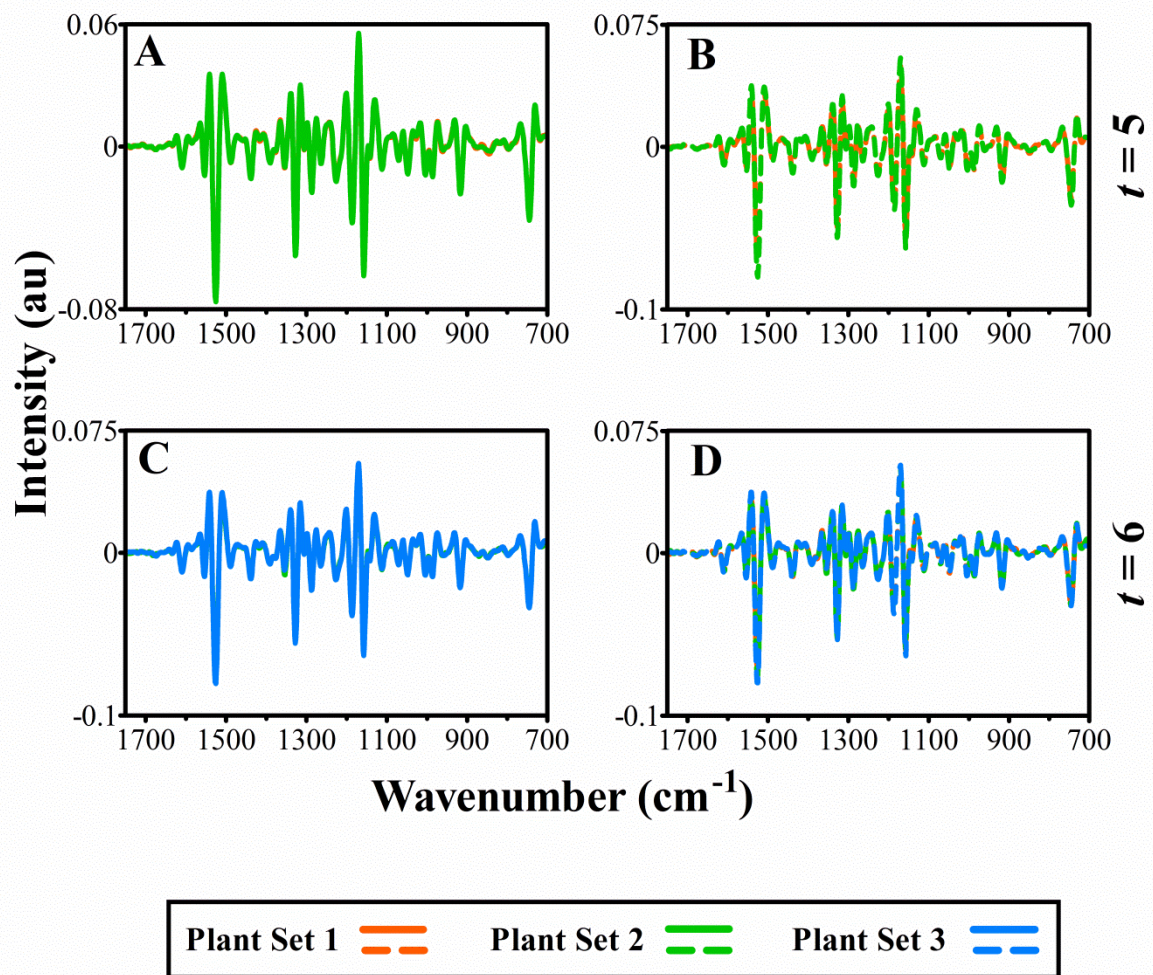


Figure S3. Raman class means spectra to compare previously analysed and equivalent leaflets (full line), as well as differences in systemic leaflets (dashed line). At week 5 ($t = 5$) of development, plants were compared at mature leaflet A (**A**) and newly expanded leaflet B (**B**); at week 6 ($t = 6$), plants were compared at leaflet B (**C**) and newly expanded C (**D**). Spectra were processed with first order differentiation baseline correction and vector normalisation.

Table S1.A. Average rate of H_2O assimilation ($\text{mmol H}_2\text{O m}^{-2} \text{s}^{-1} \pm$ standard error) for equivalent leaflets (A-D) in four plant sets over a time course of three weeks ($t = 5-7$) to determine any detrimental effects of ATR-FTIR spectroscopy interrogation. Leaflets previously analysed using the technique are shown in italic. No significant responses were determined by statistical analyses.

Leaflet	<i>t = 5 weeks</i>		<i>t = 6 weeks</i>		<i>t = 7 weeks</i>	
	A	B	B	C	C	D
Plant Set 1	0.84 ± 0.12	1.92 ± 0.18		2.04 ± 0.23		1.58 ± 0.16
	2.08 ± 0.40	2.40 ± 0.62	1.09 ± 0.23	1.31 ± 0.18		2.02 ± 0.32
			3 2.32 ± 0.30	1.47 ± 0.26	1.32 ± 0.25	1.63 ± 0.29
					4 0.77 ± 0.27	1.18 ± 0.21

Table S1.B. Average rate of stomatal conductance ($\text{mmol m}^{-2} \text{s}^{-1} \pm$ standard error)

	<i>t = 5 weeks</i>		<i>t = 6 weeks</i>		<i>t = 7 weeks</i>	
	A	B	B	C	C	D
1	89.25 ± 27.16	106.50 ± 19.37		47.56 ± 8.45		73.83 ± 8.49
	64.50 ± 16.59	70.83 ± 13.59	120.67 ± 20.59	70.56 ± 14.73		101.83 ± 20.23
			3 93.67 ± 18.49	42.78 ± 8.50	62.33 ± 15.83	80.67 ± 17.95
					4 33.33 ± 13.14	50.83 ± 10.54

Table S1.C. Average rate of internal CO_2 ($\mu\text{mol mol}^{-1} \pm$ standard error)

	<i>t = 5 weeks</i>		<i>t = 6 weeks</i>		<i>t = 7 weeks</i>	
	A	B	B	C	C	D
1	206.36 ± 30.66	108.22 ± 9.30		135.00 ± 29.00		122.33 ± 23.98
	133.11 ± 19.57	187.25 ± 37.30	155.71 ± 24.78	214.75 ± 43.17		293.33 ± 132.29
			3 208.57 ± 42.27	267.67 ± 38.40	77.75 ± 9.26	191.75 ± 39.32
					4 372.33 ± 99.15	289.17 ± 64.62

Table S1.D. Average rate of vapour pressure deficit ($\text{mPa Pa}^{-1} \pm$ standard error)

	<i>t = 5 weeks</i>		<i>t = 6 weeks</i>		<i>t = 7 weeks</i>	
	A	B	B	C	C	D
1	25.27 ± 0.73	23.22 ± 0.99		24.09 ± 0.42		23.08 ± 0.32
	26.87 ± 0.63	23.67 ± 0.87	25.67 ± 0.57	23.24 ± 0.63		22.13 ± 1.03
			3 23.29 ± 0.59	21.99 ± 1.01	23.17 ± 1.03	22.45 ± 0.72
					4 25.57 ± 0.77	24.38 ± 0.68

Table S2. *P*-values corresponding to cross validated PCA-LDA scores plots in Figure 3 derived by one-way ANOVA with Tukey's multiple comparison test. (A) week 5; (B) week 6; (C) week 7 of plant development. Significant values are highlighted in bold type and colours correspond to

specific plants sets highlighted in Figure 3 (red = ‘Plant Set 1’, green ‘Plant Set 2’, blue = ‘Plant Set 3’, purple = ‘Plant Set 4’). Columns and rows in full colour represent comparison of leaves previously analysed and bordered cells represent comparisons of systemic leaves.

Leaflets						
(A) Week 5		A	A	B	-	
		A	$P > 0.05$	—	—	—
		B	$P > 0.05$	$P > 0.05$	—	—
(B) Week 6		C	$P > 0.05$	$P > 0.05$	$P > 0.05$	—
		B	B	C	C	—
		B	$P > 0.05$	—	—	—
		C	$P > 0.05$	$P > 0.05$	$P > 0.05$	—
(C) Week 7		C	C	D	D	D
		C	$P > 0.05$	—	—	—
		D	$P > 0.05$	$P > 0.05$	—	—
		D	$P > 0.05$	$P > 0.05$	$P > 0.05$	—
		D	$P > 0.05$	$P > 0.05$	$P > 0.05$	$P > 0.05$

Table S3. *P*-values corresponding to cross validated PCA-LDA scores plots in Figure 4 derived by one-way ANOVA with Tukey's multiple comparison test. Table (A) week 5; (B) week 4 of plant development. Significant values are highlighted in bold type and colours correspond to specific plants sets highlighted in Figure 3 (red = 'Plant Set 1', green 'Plant Set 2', blue = 'Plant Set 3', purple = 'Plant Set 4'). Columns and rows in full colour represent comparison of leaves previously analysed and bordered cells represent comparisons of systemic leaves.

Leaflets				
(A) Week 5		A	A	B
A	P >0.05	–	–	–
	P >0.05	P >0.05	–	–
	P >0.05	P >0.05	P >0.05	–
(B) Week 6		B	B	C
B	P >0.05	–	–	–
	P >0.05	P >0.05	–	–
	P >0.05	P >0.05	P >0.05	–
	P >0.05	P >0.05	P >0.05	P >0.05

Table S4. *P*-values corresponding to cross validated PCA-LDA scores plots of Figure 5C (A) and Figure 5D (B) deduced by one-way ANOVA with Tukey's multiple comparison test. Significant values are highlighted in bold type and colours correspond to classes (days) as shown in Figure 5.

		Days										
(A) ATR-FTIR		1	2	3	4	5	7	9	10	11	13	14
2	P > 0.05	—	—	—	—	—	—	—	—	—	—	—
3	P > 0.05	P > 0.05	—	—	—	—	—	—	—	—	—	—
4	P < 0.05	P > 0.05	P > 0.05	—	—	—	—	—	—	—	—	—
5	P < 0.05	P > 0.05	P > 0.05	P > 0.05	—	—	—	—	—	—	—	—
7	P > 0.05	—	—	—	—	—	—	—				
9	P < 0.001	P < 0.001	P < 0.001	P < 0.05	P < 0.05	P < 0.05	P < 0.001	—	—	—	—	—
10	P < 0.001	P < 0.001	P < 0.001	P < 0.05	P < 0.05	P < 0.05	P < 0.001	0.05	—	—	—	—
11	P < 0.001	P < 0.001	P < 0.001	P < 0.01	P < 0.01	P < 0.01	P < 0.001	0.05	0.05	—	—	—
13	P < 0.001	0.05	0.05	0.05	—	—						
14	P < 0.001	0.05	0.05	0.05	0.05	—						
17	P < 0.001	0.05	0.05	0.05	0.05	0.05						
(B) Raman		1	2	3	4	5	7	9	10	13		
2	P < 0.01	—	—	—	—	—	—	—	—	—	—	—
3	P > 0.05	P > 0.05	—	—	—	—	—	—	—	—	—	—
4	P < 0.01	P > 0.05	P > 0.05	—	—	—	—	—	—	—	—	—
5	P < 0.001	P > 0.05	P > 0.05	P > 0.05	—	—	—	—	—	—	—	—
7	P > 0.05	P < 0.001	—	—	—	—	—	—				
9	P < 0.001	—	—	—	—	—						
10	P < 0.001	—	—	—	—							
13	P < 0.001	—	—	—								
15	P < 0.001	0.05	0.05	0.05	0.05	0.05	P < 0.001					

Table S5. *P*-values for linear regression curve analysis in most discriminating wavenumbers, calculated at 95% confidence rates, with significant values highlighted in bold, derived from Figure 10. Colours correspond to Figure 8.

	Wavenumber (cm ⁻¹)	NE	M	S
ATR-FTIR	1107	<i>P</i> <0.01	<i>P</i> <0.05	<i>P</i> >0.05
	1639	<i>P</i> <0.0001	<i>P</i> <0.0001	<i>P</i> >0.05
	1015	<i>P</i> <0.0001	<i>P</i> <0.001	<i>P</i> >0.05
Raman	1328	<i>P</i> >0.05	<i>P</i> >0.05	<i>P</i> >0.05
	1158	<i>P</i> >0.05	<i>P</i> >0.05	<i>P</i> >0.05
	1529	<i>P</i> >0.05	<i>P</i> >0.05	<i>P</i> <0.05

Chapter 5

Observation and quantification of Calcium uptake at the adaxial surface of leaves of tomato (*Solanum lycopersicum*) using Raman spectroscopy

Holly J. Butler, Steve Adams, Martin R. McAinsh, and Francis L. Martin

Submitted for publication: Analyst August 2016

Contribution:

I conducted all experimental work

I wrote and prepared the manuscript for publication

I produced all figures

Professor F. L Martin

Dr. Martin. R. McAinsh

H. J. Butler

Observation and quantification of Calcium uptake at the adaxial surface of leaves of tomato (*Solanum lycopersicum*) using Raman spectroscopy

Holly J. Butler^{abc}, Francis L. Martin^{ad*}, Steve Adams^e, Martin R. McAinsh^{a*}

^a *Lancaster Environment Centre, Lancaster University, Lancaster LA1 4YQ, UK*

^b *Centre for Global Eco-Innovation, Lancaster Environment Centre, Lancaster University, Lancaster LA1 4YQ, UK*

^c *WESTChem, Department of Pure and Applied Chemistry, Technology and Innovation Centre, University of Strathclyde, Glasgow G1 1RD, UK*

^d *School of Pharmacy and Biomedical Sciences, University of Central Lancashire, Preston PR1 2HE, UK*

^e *Plant Impact Plc, Rothamsted, West Common, Harpenden, Hertfordshire AL5 2JQ, UK*

***Correspondence to:** Prof Francis L. Martin, School of Pharmacy and Biomedical Sciences, University of Central Lancashire, Preston, PR1 2HE, UK; Email: flmartin@uclan.ac.uk

Dr Martin R. McAinsh, Lancaster Environment Centre, Lancaster University, Lancaster, LA1 4YQ; Email: m.mcainsh@lancaster.ac.uk; Tel.: +44(0)1524 510553

Abstract

Foliar application of nutrient fertilisers is standard practice in agricultural environments, and has been shown to increase crop yield and quality more efficiently and economically than soil-based fertilisers. The adsorption of macro- and micro-nutrients through the upper epidermis of leaves is largely species dependent; reliant upon penetration through the cuticle and stomata, and also upon the plant's ability to translocate the nutrient. Herein we describe a method to observe calcium (Ca) uptake at the adaxial leaf surface to determine the efficacy of foliar fertilisers. We use Raman microspectroscopy as a sensitive approach to indirectly monitor Ca, through the use of nitrate (NO_3^-) associated vibrational modes, complemented by ion probe measurements and measurements of leaf nutrient status using flame atomic absorption spectroscopy. Our results show that Ca uptake can be observed down to concentrations as low as 15 mM using Raman microspectroscopy over a defined surface area, and that the rate of Ca uptake can also be quantified using this approach. We believe that Raman microspectroscopy provides a novel method for monitoring nutrient movement throughout plant tissue, and provides a potential tool for nutrient screening.

Introduction

In order to produce optimum yield and quality, it is essential that crops receive adequate levels of macro- (N, P, K, Ca, Mg and S) and micro- (B, Cl, Cu, Fe, Mn, Mo, N and Zn) nutrients during cultivation. The application of nutrient fertilisers is a practice well-exercised through time, traditionally centred around the three primary macronutrients, N, P and K, which have the greatest immediate effect on crop yield¹. This is in accordance with Liebig's Law of the Minimum, where nitrogen can be considered the most limiting nutrient for crop growth². In 2013, as much as 140 kg of nitrogen-based fertiliser was applied to each hectare of arable land in the UK as a prerequisite for cultivation³. Whilst this process has been shown to have positive impacts on overall crop yield, quality and shelf life; this is by no means an efficient process. Over-application of these nutrients does not meet the additional nutrient requirements of the crop, which can result in equally detrimental nutrient deficiencies of other macro- and micro-nutrients. Furthermore, as well as the considerable carbon footprint that is associated with fertiliser production, N losses through leaching and denitrification present a significant environmental impact to the land surrounding agricultural sites and the human water supply^{4, 5}. Due to the threat of continued population growth, the maintenance of global food security demands a drastic increase in agricultural productivity and thus a movement away from such agricultural customs⁶.

An alternative approach is application of fertilisers *via* a foliar spray; where a single or mixture of solutions (as well as pesticides and herbicides) can be applied directly onto the leaf and fruit tissue⁷. In providing nutrients directly to the crop rather than the growth medium, a reduced volume of fertiliser is required, presenting a more efficient process that has been shown to increase the nutrient recovery rate in crops^{8, 9}. Foliar fertiliser application also has the added benefit of reduced lag time between application and uptake by the plant, as well as overcoming issues surrounding poor absorption from nutrient complex in the soil^{10, 11}. As the majority of fertiliser application protocols are soil-based, the analysis of nutrients in the soil has been particularly valuable to determine the nutrient availability in different environments¹². However, this is not always reflective of the uptake into the plant, as some nutrients are fixed within the soil and therefore not available for uptake, whilst some are only partially utilised, and some are readily lost within the environment¹. By focusing upon foliar applications of

nutrient fertiliser, it is possible to directly observe the effect of product formulation on net elemental uptake.

Foliar sprays do not however provide a magic bullet for the application of nutrients. The efficiency of foliar sprays is variable depending upon environmental conditions, the crop species and fertiliser formulations; all of which have substantial impact on nutrient penetration through the cuticle surface and subsequent translocation, see Fernàndes and Eichert¹³. As with soil application of fertilisers, environmental conditions such as humidity, temperature and light availability all can prevent the efficient uptake of nutrient at the leaf surface, due to the effect these conditions have on rates of transpiration and photosynthesis, as well as the effects upon stomatal aperture¹⁴,¹⁵.

The exact composition of the fertiliser applied will also have distinct effects on nutrient uptake at the leaf surface, primarily dependent upon the exact nutrient that is being provided. Whilst all essential elements should be able to pass through the leaf cuticle, the movement to systemic regions of the plant may be inhibited¹⁶. Translocation in the leaf is predominantly through the apoplastic or symplastic pathway; either through the extracellular material and the cell wall, or through the cell cytoplasm *via* plasmodesmata, respectively¹⁴. It has been shown that the rate of translocation within plant tissues differs between each essential nutrient, with Cl, Na, K and N being considered more mobile than Fe, and Ca being relatively immobile¹⁷. This may be associated with the charge associated with the ionic form of the nutrient in solution, due to accumulations of negative charges within the plant apoplast. Foliar fertilisers often contain a number of complementary components in addition to the nutrient content, that are added to aid the absorption process. Wetting agents, or surfactants, reduce the surface tension of the solution and allow maximum dispersal across the foliage, thus utilising the entire surface area of the crop wherever possible¹⁸. Furthermore, penetrants can be applied to improve uptake through the waxy cuticle, pH modifiers can be used to alter the ionic composition of specific nutrient and thus aid uptake, humectants are used to prolong the drying process, and adjuvants are utilised to extend the time the fertiliser remains on the leaf surface, preventing run off in wet conditions¹⁹.

The cuticle is the primary site of nutrient uptake via foliar sprays and therefore its composition is a significant factor in the rate of nutrient uptake²⁰. The purpose of the

cuticle is to prevent water loss, and thus the composition of the epicuticular wax is variable between crop species, dependent upon the natural environment of the plant. As such, the efficiency of a foliar fertiliser is variable across different crop species. Moreover, the total leaf surface area of a crop will also impact the overall efficacy of a foliar fertiliser, as a lesser surface area will result in reduced application. The presence of leaf trichomes, hair-like projections on the leaf surface, will increase the surface available for uptake and may result in enhanced absorption²¹. In addition, the stage of leaf development, will play a role in uptake, as will the general tissue and plant health.

Due to the contribution of these factors to the variable efficacy of foliar fertilisers, this method of nutrient supplementation is not yet considered a direct replacement of soil-based fertilisers²². However, a step change in fertiliser technology, or the development of rapid screening methods to assess the potency of foliar fertiliser may increase the adoption of this approach. One such method that may be able to contribute to nutrient uptake studies is Raman microspectroscopy. Based on the phenomena of inelastic light scattering, Raman microspectroscopy is a highly sensitive technique that can be used to detect and monitor single molecules by observing the interaction of light with the chemical bonds within a sample²³. The occurrence of Raman scatter is an inherently low probability process, which can be problematic in samples with intrinsic fluorescence, such as plants, where Raman information can be swamped by stronger fluorescence signals²⁴. The development of alternative Raman modes such as stimulated Raman spectroscopy has helped overcome some of these restrictions to plant based applications. In addition, it has recently been shown that spontaneous Raman can be applied *in vivo* to derive spectral information from leaves, due to the quenching effect of water found ubiquitously through the plant²⁵⁻²⁷.

In this study, we employ Raman microspectroscopy as a novel method of monitoring Ca at the adaxial leaf surface using tomato (*Solanum lycopersicum*) as a model plant, complemented by ion probe and flame atomic absorption spectroscopy (FAAS) measurements conventionally used as alternatives. Ca is an essential macronutrient required for successful plant growth, and low availabilities can result in deficiencies that are known to manifest across a range of crop species and cause significant yield losses²⁸. Foliar nutrient supplementation is one way in which such deficiencies have been combatted, with frequent applications of Ca fertilisers preventing the incidence of deficiency and also increasing overall Ca content in fruits²⁹⁻³¹. However,

as mentioned previously, Ca has been shown to be relatively immobile within plant tissues following absorption through the leaf cuticle, and it is thought that Ca transportation is solely unidirectional in the flow of the transpiration stream *via* the xylem^{32, 33}. The lack of mobility is associated with the toxicity of Ca at high concentrations in the cell, and the tightly linked signalling pathways that have developed as a consequence of this active control of Ca in biological systems³⁴. Currently, the mechanism by which foliar Ca sprays are able to improve a crops tolerance to nutrient stress is not therefore fully understood given translocation to affected tissues is not possible.

Our aim is to use the three-pronged Raman microspectroscopy, ion probe and FAAS approach in order to observe and quantify Ca uptake at the leaf surface. This will present a novel assay for assessing the efficacy of a foliar fertiliser, by observing its rate of uptake and subsequent mobility within the plant.

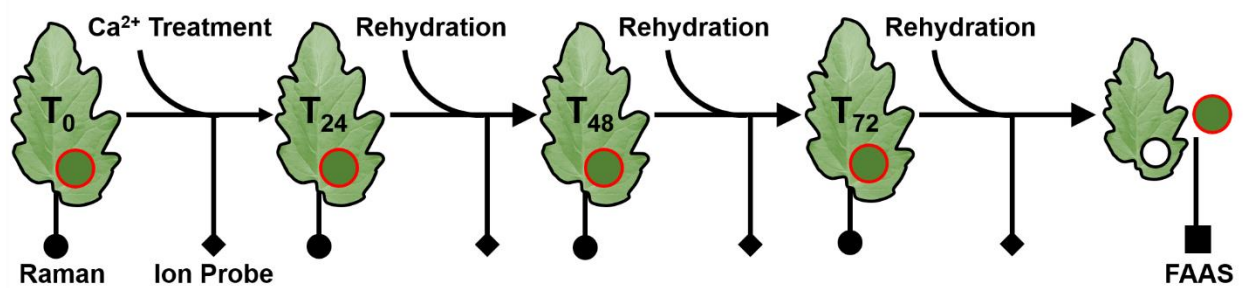


Figure 1. A schematic overview of the experimental procedure described in this study to measure uptake of supplementary Ca at the adaxial leaf surface of *Solanum lycopersicum* samples. Measurements using Raman microspectroscopy (●) were conducted upon dry leaves in order to detect residual traces of $\text{Ca}(\text{NO}_3)_2$ on the surface. Upon application of $\text{Ca}(\text{NO}_3)_2$ solution, and subsequent rehydration with H_2O , ion probe measurements (◆) were made by aspirating the solution directly from the leaf. This process was repeated over a 72-hour period (T_0 , T_{24} , T_{48} , T_{72}) before finally harvesting the remaining leaflets, separating the ‘banded area’ (outlined in red) and the ‘remaining leaflet’ (outlined in black), and analysing both separating using flame atomic absorption spectroscopy (FAAS) to determine overall Ca content.

Materials & Methods

Calcium compound characterisation

Ca can be delivered to the crop via a range of compounds such as calcium nitrate $[\text{Ca}(\text{NO}_3)_2]$, calcium chloride (CaCl_2), calcium sulphate ('Gypsum'; CaSO_4), calcium oxide (CaO) and calcium carbonate (CaCO_3). In order to investigate the uptake of Ca at the leaf surface, $\text{Ca}(\text{NO}_3)_2$ was chosen as a model compound due to its widespread use in agriculture as both a Ca and nitrate fertiliser, and as well as its distinct Raman vibrational modes.

$\text{Ca}(\text{NO}_3)_2 \bullet 4\text{H}_2\text{O}$ at 99% reagent grade (Sigma-Aldrich Ltd, Dorset, UK) was characterised using an InVia Raman spectrometer with a 785 nm excitation laser and charge coupled device (CCD) detector (Renishaw Plc, Gloucestershire, UK) with a microscope attachment (Leica Microsystems, Buckinghamshire, UK). Spectral calibration was conducted using a silicon source prior to spectral acquisition. 500 mg of solid $\text{Ca}(\text{NO}_3)_2 \bullet 4\text{H}_2\text{O}$ was applied onto an Au-coated slide (Platypus Technologies, WI, USA); even pressure was applied to produce a flattened surface for analysis. This was repeated three times for each sample, with 10 spectra obtained per repeat. A 1 M $\text{Ca}(\text{NO}_3)_2 \bullet 4\text{H}_2\text{O}$ solution was prepared using Milli-Q filtered water up to a volume of 500 mL for increased accuracy. To investigate the effects of Ca chelation, ethylenediaminetetraacetic acid (EDTA) was prepared at 1, 0.5 and 0.25 M using filtered water, and this was mixed 1:1 with 1 M $\text{Ca}(\text{NO}_3)_2 \bullet 4\text{H}_2\text{O}$, resulting in 0.5 M $\text{Ca}(\text{NO}_3)_2 \bullet 4\text{H}_2\text{O}$ -EDTA solution. For each solution, 50 μl was applied onto an Au-coated slide and 10 spectra were obtained per solution, with each solution repeated three times. Spectra were obtained using a $50\times$ magnification (0.75 numerical aperture), 1200 mm^{-1} grating, 50% laser power (13 mW at the sample) and a 10 second exposure time. Spectra were visualised across the 2000 - 500 cm^{-1} region, accounting for regions of overlap with plant associated vibrational modes, using Matlab 2016a software (The Math Works, MA, USA).

Plant growth conditions

The tomato plant, *Solanum lycopersicum* cv. Moneymaker (Moles Seeds, Essex, UK), was chosen as a model species to observe Ca uptake at the leaf surface due to its susceptibility to Ca deficiencies in the form of 'blossom end rot', as well as the presence of trichomes

on the leaf surface and relatively fast growth rate. This crop variety had been previously used in spectroscopic studies and had been shown to display no signs of damage following Raman interrogation²⁷. Seeds were germinated in M3 compost (Levington Horticulture, Suffolk, UK) and watered daily in a controlled environment growth room with relative light intensity of $150 \pm \mu\text{mol m}^{-2} \text{ s}^{-1}$ provided by 600 W metal halide lamps (Osram Ltd, Merseyside, UK) with a 16 h / $25 \pm 2^\circ\text{C}$ day, 8 h / $20 \pm 2^\circ\text{C}$ night cycle. To account for time dependent alterations in rates of CO_2 and H_2O assimilation that may affect nutrient translocation, all experimentation was conducted during the middle of light period where the plants were assumed to be in a stabilise state. Plants were grown for 8 weeks following germination, before being selected for this study.

Raman Microspectroscopy and Ion Probe measurements

An overview of the experimental procedure is illustrated in **Figure 1**. In brief, the uptake of six $\text{Ca}(\text{NO}_3)_2$ solutions at defined concentrations of 0, 5, 10, 15, 20 and 25 mM were monitored using parallel Raman microspectroscopy and ion probe measurements. A circular banded area, 1.77 cm^2 ($r = 0.75 \text{ cm}$), was isolated using silicone grease and all treatments were applied to this defined area throughout. A total of 60 plants were used for this study; 10 per Ca treatment. On each plant, five leaflets were banded and used for this study. Only mature leaflets of a similar morphological stage were chosen, as these were fully expanded and less prone to movement resulting in treatment run-off. Throughout this study, live plant systems were analysed and no leaflets were removed at any point.

All solutions were prepared using filtered water, a calibrated balance and made up to volumes of 500 mL. All solutions contained 0.01% Silwet L-77 wetting agent (de Sangosse Ltd, Cambridgeshire, UK), to optimise spread of the nutrient solution across the banded area, which was shown in preliminary studies to reduce variability with uptake across the leaf surface. An InVia Raman spectrometer with Leica microscope attachment was used to obtain Raman spectra, using a $50\times$ objective, 1200 mm^{-1} grating, 50% laser power, and a 15 second exposure time. A minimum of 5 spectra was obtained per sample, spanning across the whole of the banded area. LAQUAtwin compact Ca^{2+} and a NO_3^- meters (Horiba Instruments Ltd, Northamptonshire, UK; models B-751 and B-741 respectively) were used as ion-selective electrodes, to monitor alterations in these ions. Each probe was washed with deionised water between all measurements.

Initially, a control Raman measurement was taken from four randomly chosen leaflets at T_0 to derive the plant biochemical fingerprint prior to Ca application. Immediately following this, the 30- μ L Ca treatment was applied onto the leaf surface within the banded area. This volume was chosen as it sufficiently covered the banded area, whilst not affecting leaf stabilisation and therefore preventing run-off. On four randomly selected leaflets, this solution was aspirated off the leaflet after 30 seconds and analysed using the ion-selective probes. Once a leaflet had been analysed, it was excluded from the study. The solutions were then allowed to dry overnight. The following day (T_{24}), 24-hours post the initial Raman measurement, a second Raman measurement was obtained from a further four randomly selected leaflets. In order to re-suspend any remaining $\text{Ca}(\text{NO}_3)_2$ upon the leaflet, 30 μ L of distilled water was applied and gently dispersed across the banded area. The contribution of specific gravity at such small volumes of dilute solution was deemed to be too small to quantify accurately, and so rehydration of the remaining $\text{Ca}(\text{NO}_3)_2$ was maintained at 30 μ L and compared against measurements made from reference materials, glass and plastic, that were conducted in parallel. Again, the solution on four leaflets was aspirated from the surface 30 seconds following H_2O application, and analysed using the ion probes. This process of Raman interrogation followed by rehydration of the banded area and subsequent ion probe measurement, was repeated at T_{48} and T_{72} .

At each time point, four leaflets were chosen at random across the sample cohort for Raman analysis, and a further four were used for ion probe measurements. Therefore, of the total 50 leaflets initially selected for study (10 plants \times 5 leaflets) in each treatment group, a minimum of 36 leaflets were analysed per treatment across the 72-hour period. This resulted in a dataset containing over 1080 spectra (36 leaflets \times 6 treatments \times 5 spectra).

Tissue digestion and FAAS

Following analysis across the four time points using Raman microspectroscopy and ion probe measurements, a selection of the remaining leaflets were analysed using FAAS in order to determine the overall Ca content of the tissue. FAAS is a common analytical method of determining elemental content of plant tissue, and has been used routinely to monitor crop nutrient status³⁵. Leaflets were excised from the plant and washed thoroughly using deionised water to ensure any residual treatment was adequately

removed. The ‘banded area’ from each leaflet was isolated from the ‘remaining’ area using a scalpel, and both tissues were dried at 80°C in a drying oven for 3 days in order to remove all water content. This tissue was then homogenised into a fine powder, and the total mass was recorded. Each sample was digested in 10 mL concentrated, trace metal grade HNO₃ (Sigma-Aldrich Ltd, Dorset, UK) at 200°C on a digital hot plate (Bibby Scientific Ltd, Staffordshire, UK; SD500), in a volumetric flask sealed with a ‘bubble top’, to allow reflux of the acid for a minimum of 2 h and to guarantee complete digestion. When digestion was complete, the tops were removed and the HNO₃ was allowed to evaporate until near dryness, when the samples were then removed from heat. The residual material was re-dissolved in <5 mL of 5% HNO₃ and 0.5 mL of 1% LaCl₃ was added to ensure full Ca release from the material. This solution was then filtered using a Whatman® 541 hardened, ashless filter paper (Fisher Scientific, Leicestershire, UK), and made up to standard volumes of 25 mL.

These digested samples were then analysed using a AAnalyst 200 flame atomic absorption spectrometer (Perkin Elmer, MA, USA) with acetylene gas, compressed air and a Ca-Mg lamp (422.7 nm) to provide an absorbance value corresponding to a Ca concentration, as determined by a calibration curve obtained prior to acquisition. Absorbance above 0.4 arbitrary units (au) is considered outside of the linear range of detection for the spectrometer, and thus any samples reading above this value were diluted accordingly; as a result, the majority of samples were diluted 1 in 50. Three replicates were taken per sample, with a read delay of three seconds. Absorbance values were converted to ppm using a calibration curve, and subsequently % Ca values were derived by multiplying by the dilution factor, and the total volume, and dividing this by the mass of homogenised sample initially used.

Data Analysis

Unless otherwise stated, Raman spectra were processed using the IRootLab toolbox for Matlab³⁶. All spectra were initially cut to 1700-500 cm⁻¹ as this region encompassed all biological information from the leaf samples as well as any overlapping Ca(NO₃)₂ vibrational modes. For the purpose of comparison between these two samples, a polynomial baseline correction was conducted in order to maintain the conventional morphology of a Raman spectrum, whilst reducing any residual background fluorescence that can commonly occur when analysing plant materials with intrinsic

fluorescence²⁴. It is worth noting, that live plant tissues have been shown to have reduced susceptibility to fluorescence, associated with the high water content and potential quenching effect²⁷. To characterise the vibrational modes of $\text{Ca}(\text{NO}_3)_2$ spectra, a second order derivative (with Savitzky-Golay noise reduction) was conducted followed by vector normalisation and a wavelet denoising, in order to effectively highlight subtle differences in the scattering intensity of each solution at the $780 - 680 \text{ cm}^{-1}$. Spectra obtained during the Ca treatments were second order differentiated, with vector normalisation and wavelet denoising. A second order derivative was chosen so that the peak centroid could be obtained, and a Raman scattering intensity value at a specific wavenumber could be derived that was reflective of the original spectrum, whilst still benefitting from background elimination.

One-way analysis of variance (ANOVA) with Tukey's multiple comparison tests were conducted in GraphPad Prism 4 software (GraphPad Software Inc, CA, USA). All figures were also produced using Prism 4 software.

Results & Discussions

Effects of surfactant on treatment dispersal

The addition of surfactants to foliar fertiliser sprays, reduces the surface tension of the solution and consequently increases the surface area exposed to the solution³⁷. The evidence of this can be seen in **Figure 2.**, which displays distinct droplets of solution upon the leaflet surface of a *S. lycopersicum* without the addition of Silwet L-77 (**B**), and the homogenous spread within the banded area as a consequence of Silwet use (**C**). In regards to Ca uptake, an even spread across the adaxial leaf surface means a larger surface area for Ca absorption. Upon drying, any residual Ca that remains on the leaf surface is also evenly dispersed, preventing concentrated areas of Ca that would make consequent Raman measurements highly variable. Due to this, 0.01% Silwet was applied in all Ca treatments to ensure reproducibility.

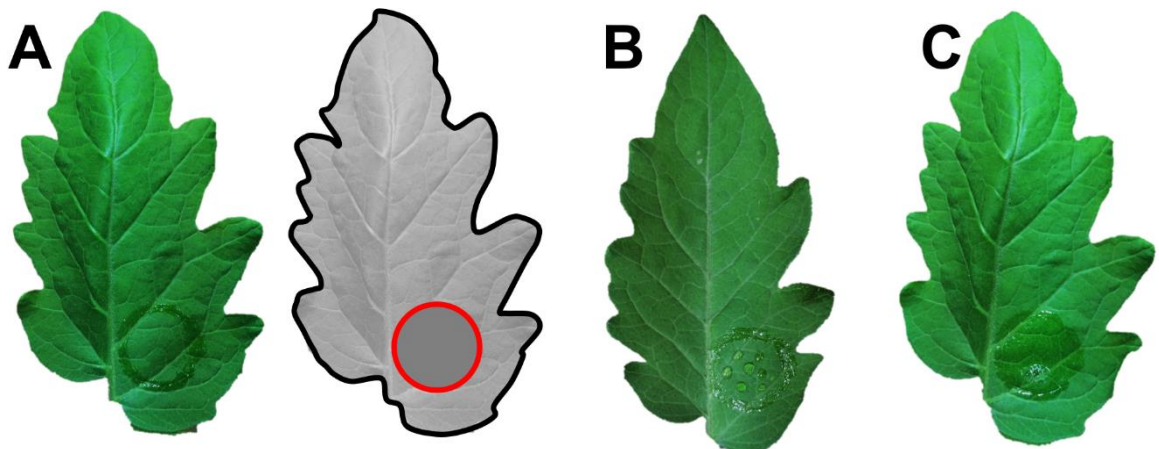


Figure 2. Example of the effects of surfactant use in Ca solution dispersal in a defined area. (**A**) displays the ‘banded area’ defined by silicone grease (photograph versus diagram for emphasis), the radius of which is 0.75 cm resulting in an overall area of 1.77 cm^2 ; (**B**) dispersal of $30 \mu\text{L}$ Ca treatment without a surfactant and; (**C**) the spread of $30 \mu\text{L}$ Ca with the use of surfactant on a *S. lycopersicum* leaflet.

Ca(NO₃)₂ characterisation

Numerous studies have been conducted to characterise solid and aqueous forms of Ca(NO₃)₂ using Raman spectroscopy, of which four distinct vibrational modes have been deduced: a double degenerate mode at 1400 cm⁻¹, a symmetric stretch at 1050 cm⁻¹, a double degenerate mode at 720 cm⁻¹, as well as a Raman inactive band at 830 cm⁻¹³⁸⁻⁴¹. These same modes were visible in this study, in both solid and aqueous forms (Figure 3). The peak at 1050 cm⁻¹ is synonymous with NO₃⁻ stretching and show a clear concentration effect when observing a varying range of Ca(NO₃)₂. The subtle peak at the 720 cm⁻¹ region is intriguing as it may provide further details towards the physical state of the compound and its related ions. In solution, this peak is known to split into 743 and 719 cm⁻¹, associated with 'bound' and 'free' NO₃⁻ respectively⁴⁰. Bound NO₃⁻ refers to the [CaNO₃]⁺ complex, whilst free is related to NO₃⁻ interaction with H₂O³⁹.

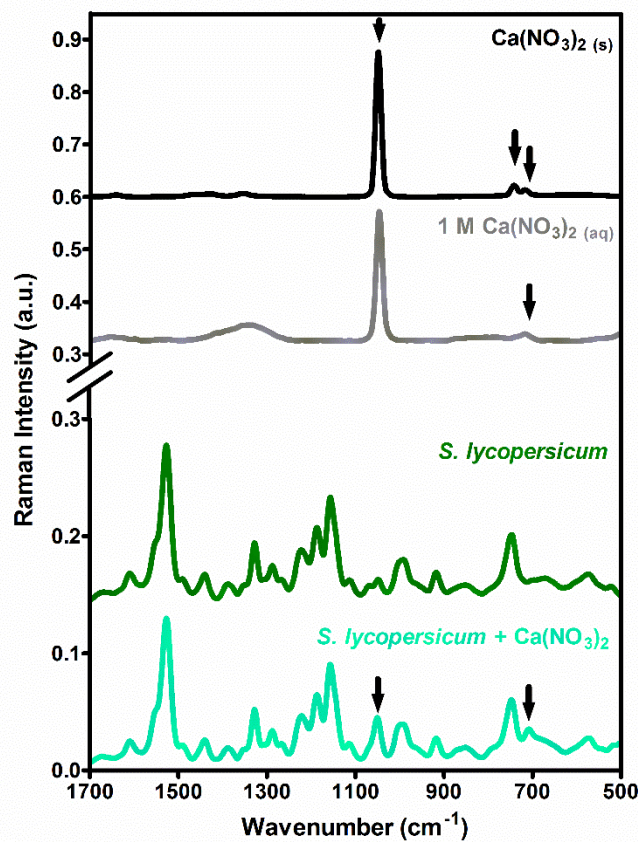


Figure 3. Proof of concept study observing spectra derived from solid (s) Ca(NO₃)₂, 1 M Ca(NO₃)₂ solution (aq) and the subsequent effect of this upon the standard spectrum derived from a *Solanum lycopersicum* leaf. The symmetric stretch of NO₃⁻ at 1050 cm⁻¹ appears strongly in the presence of Ca(NO₃)₂, as well as the subtle mode at 743 cm⁻¹.

The Raman spectrum of a *S. lycopersicum* leaf is also shown, as well as the consequent spectra following application of 1 M $\text{Ca}(\text{NO}_3)_2$ solution upon the adaxial surface. The $\nu_{\text{sym}}(\text{NO}_3^-)$ can be seen strongly additional to the underlying plant spectrum, where there would be potential overlap with $\nu(\text{CO})$ and $\delta(\text{CO})$ modes of leaf polysaccharides⁴²; however, no specific Raman band within plant tissues is known to be present at this specific wavenumber^{43, 44}. There is also evidence of a $\text{Ca}(\text{NO}_3)_2$ peak at around 740 cm^{-1} , although there is thought to be some overlap in this region with chlorophyll scattering⁴⁵.

As a consequence of this investigation, it is clear that there is the capability to detect trace residues of $\text{Ca}(\text{NO}_3)_2$ upon the leaf surface, through monitoring scattering associated predominantly with the NO_3^- component of the compound. However, Ca^{2+} ions would not have a Raman signature, therefore we investigated the possibility that NO_3^- may be an indirect indicator of the presence of Ca. To this end, we investigated the effect of the Ca chelator, ethylenediaminetetraacetic acid (EDTA), at this lower wavenumber region in order to determine whether Ca can be monitored *via* NO_3^- peaks. EDTA will essentially sequester Ca^{2+} ions and thus it was predicted that in its presence there should be a higher proportion of free NO_3^- in solution. **Figure 4** illustrates $\text{Ca}(\text{NO}_3)_2$ solutions in the presence of varying concentrations of EDTA in the $780 - 690 \text{ cm}^{-1}$ region, encompassing the bound and free NO_3^- bands. In the absence of EDTA, the peak at 743 cm^{-1} is slightly lower than the peak at 719 cm^{-1} , highlighting that NO_3^- is found both in complex with Ca^{2+} ions and as a free ion. As EDTA is added, the relationship between these two peaks alters, with a reduction in bound NO_3^- peak and an increase in the free peak at 719 cm^{-1} . The effect of this is markedly larger in the more concentrated EDTA solution. This indicates that the theoretical loss of Ca^{2+} ions mimicked by the addition of EDTA, can be monitored indirectly by observing NO_3^- associated Raman bands. Therefore, all subsequent in all subsequent experiments, Ca was monitored *via* indirect measurements as described above.

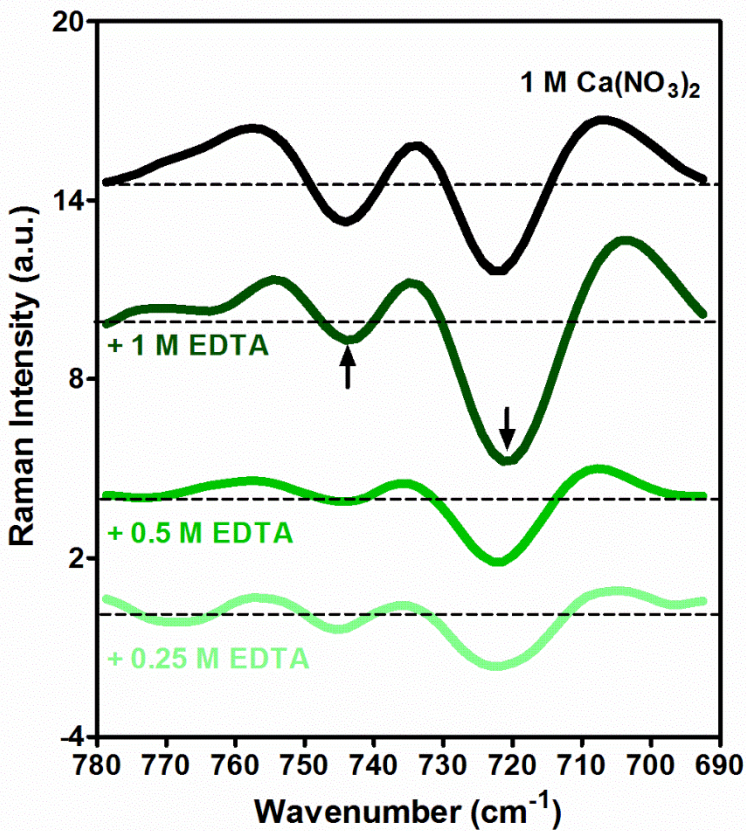


Figure 4. Second derivative Raman spectra of aqueous $\text{Ca}(\text{NO}_3)_2$ with and without varying concentrations of ethylenediaminetetraacetic acid (EDTA), a known calcium chelator, in the $780 - 690 \text{ cm}^{-1}$ region. The fourth vibrational mode of $\text{Ca}(\text{NO}_3)_2$ can be found in this region, and this double degenerate is known to appear in concentrated solutions, associated with ‘bound’ nitrate at 743 cm^{-1} and ‘free’ nitrate at 719 cm^{-1} . Spectra have been off-set for clarity.

Raman spectroscopy as a monitor of Ca uptake

The ability of Raman spectroscopy to determine the presence of Ca on the leaf surface was initially demonstrated using a 1 M solution of $\text{Ca}(\text{NO}_3)_2$; a relatively high concentration in regards to standard nutrient fertiliser compositions. Determining an agriculturally relevant concentration range is challenging as application levels are dependent upon the manufacturer of choice, as well as the growers own preference. Commercially available Ca fertilisers are sold as stock solutions, often containing between 5-30% Ca w/v, and have varied recommended dilution levels (1 in 50-500)⁴⁶. The concentration range used in this study was based upon recommended values and previous studies into fertiliser efficacy⁴⁷⁻⁵⁰.

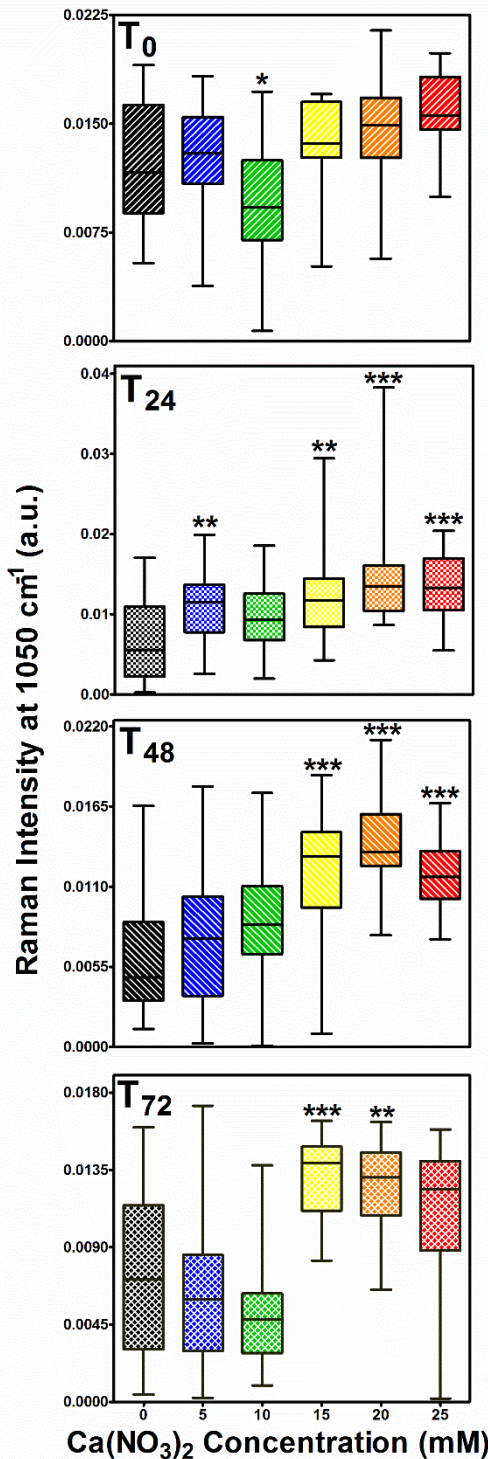


Figure 5. Raman intensity at 1050 cm^{-1} representative of $\text{V}_{\text{sym}}(\text{NO}_3^-)$ at four individual time points (T_0 , T_{24} , T_{48} , T_{72} hours), displaying spectral alterations as a consequence of increasing $\text{Ca}(\text{NO}_3)_2$ concentration. Intensity values were obtained from second derivative, vector normalised and wavelet smoothed data in order to standardise comparisons between individual leaf samples. $*P<0.05$, $**P<0.01$, $***P<0.001$.

Following the experimental procedures previously defined, Raman spectral measurements were obtained from the adaxial leaf surface, following treatment with six $\text{Ca}(\text{NO}_3)_2$ treatments (0, 5, 10, 15, 20, 25 mM) over a 72-hour time course (T_0 , T_{24} , T_{48} , T_{72}). **Figure 5** represents the Raman scattering intensity at the $\text{V}_{\text{sym}}(\text{NO}_3^-)$ region (1050 cm^{-1}) at each time point, in order to compare each Ca treatment and determine a concentration dependent effect. At T_0 , no treatment has been applied and is therefore an indicator of generic variance between each sample. Some slight differences are apparent between each of the samples that may be due to slight differences in leaf age, but importantly no treatment pattern is observed at this time point. Raman spectra obtained at T_{24} depict the leaf surface following application of each treatment and subsequent drying, and should therefore represent the time point when the concentration gradient should be most evident.

The Raman intensity at 1050 cm^{-1} overall show an upward trend with increasing Ca concentration, with the two highest treatments, 20 and 25 mM, displaying the most significant differences. Although the 10 mM treatment is not statistically significant, there is an overall increase in the mean that obeys the concentration gradient. The interquartile

range between treatments is relatively consistent, whereas the upper extremes are considerably more variable, indicating that there are numerous intensity values that are higher than the mean of each data point. Such variability between data points may indicate that residual $\text{Ca}(\text{NO}_3)_2$ upon the leaf surface is not spread evenly across the leaf surface. At T_{48} , this concentration gradient is still visible, however at a lower intensity than the previous time point, and only statistically significant at 15, 20 and 25 mM treatments. This suggests that there is still Ca remaining upon the leaf surface, but that some has been absorbed through the cuticle into the underlying tissue.

The data range within each treatment also supports this there are fewer extreme data points associated with areas of high Ca content. The final time point, T_{72} , displays some indication of a concentration effect, although at lower levels of significance, and with much variability between treatments. In contrast to T_{24} , the upper extremes for all treatments are almost equivalent, whereas lower extremes depict the greatest differences, possibly the reason for the statistical difference between 15 and 20 mM treatments.

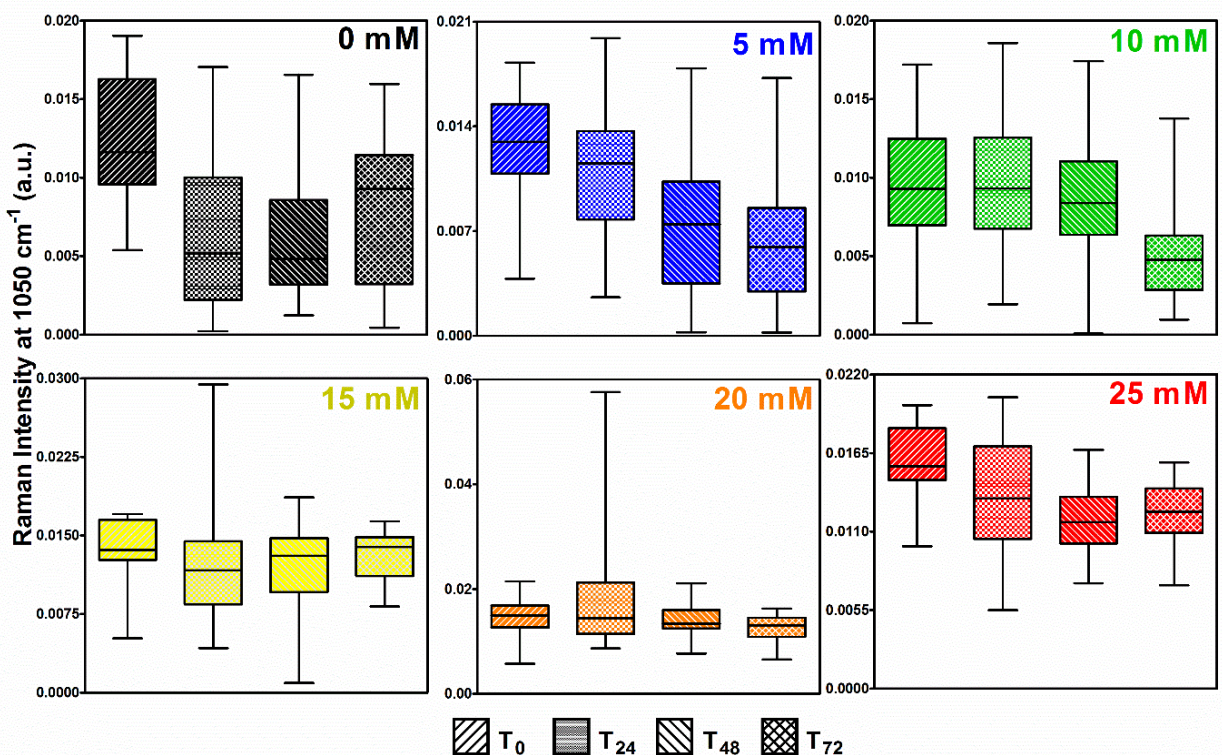


Figure 6. Alterations of the Raman intensity at 1050 cm^{-1} , representative of $\text{V}_{\text{sym}}(\text{NO}_3^-)$, over a 72-hour period (T_0 , T_{24} , T_{48} , T_{72} hours) at a range of $\text{Ca}(\text{NO}_3)_2$ treatments. Intensity values were obtained from second derivative, vector normalised and wavelet smoothed data in order to standardise comparisons between individual leaf samples.

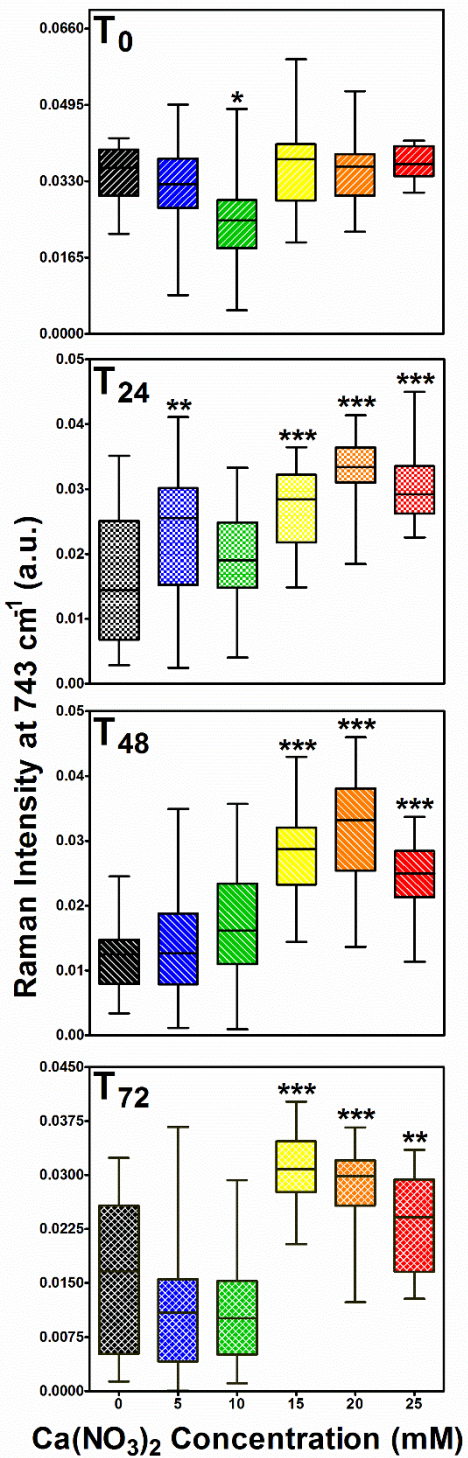


Figure 7. Raman intensity at 743 cm^{-1} , representative of bound NO_3^- , at four individual time points (T_0 , T_{24} , T_{48} , T_{72} hours), displaying spectral alterations as a consequence of increasing $\text{Ca}(\text{NO}_3)_2$ concentration. Intensity values were obtained from second derivative, vector normalised and wavelet smoothed data in order to standardise comparisons between individual leaf samples.
 $*P<0.05$, $**P<0.01$, $***P<0.001$.

As there is some overlap at the 1050 cm^{-1} peak with plant polysaccharides, this lower limit may be indicative of slight differences in the leaf age, as older leaves are known to have increased levels of cellulose due to secondary cell wall expansion^{27, 51}. The spectral intensity values are parallel with T_0 measurements, showing a reduction in the Raman scattering over time, indicating that the majority of the remaining Ca on the leaf surface 72 hours post application.

As alternative view through the data, **Figure 6** displays each individual Ca treatment monitored over the 72-hour period, in order to show a rise in Ca on the leaf surface following application and a sequential decline, indicative of uptake. The control treatment, 0 mM presents some distinct variance between each time point, which consequently shows the typical range of Raman scattering intensity at 1050 cm^{-1} . 5 and 10 mM treatments, display very small increases in scattering range at T_{24} , post-Ca application, but not to an extent significantly different to that of the overall variance shown in the 0 mM treatment. At the higher concentrations, 15, 20 and 25 mM however, there is a much more marked increase from T_{0-24} , when focusing on the range of intensity values derived, a successive decrease over the remainder of the time course. Although, the higher of these treatments does not depict this pattern to the same extend as 15 and 20 mM,

there is still some subtle time dependent alterations, showing potential uptake of Ca at the leaf surface.

When observing purely the mean of all the data points, the time related pattern of an increase in absorbance between T_0 and T_{24} and then a progressive reduction at T_{48} and T_{72} , is not shown significantly and suggests that the information specific to Ca uptake is relatively inconsistent. This may be due uneven drying on the leaf surface of $\text{Ca}(\text{NO}_3)_2$ despite the addition of a wetting agent, that is subsequently resulting in salt deposits at distinct locations. Additionally, the overlap of the 1050 cm^{-1} with underlying plant cell components, such as cellulose, may influence the reproducibility of the spectra derived. Although leaflets of a similar morphological stage were chosen, small differences in growth rate, position and general health would have significant impacts on the spectral baseline of this study. There is also the possibility that by providing increased $\text{Ca}(\text{NO}_3)_2$ to the area, there may be some stimulatory effects on cell growth; however, the relatively short time frame makes this suggestion unlikely.

The Raman peak at 743 cm^{-1} , corresponding to bound NO_3^- , are apparent within the leaf spectral fingerprint following foliar application of $\text{Ca}(\text{NO}_3)_2$ in a region where only broad underlying Raman bands were visible. Therefore, to observe Ca uptake spectral intensities from this band were extracted and analysed using the same approach as shown previously with the $\nu_{\text{sym}}(\text{NO}_3^-)$ region. Initially, it is evident that a concentration dependent relationship can be seen at T_{24} , highlighting that following application of the nutrient treatment the residual $\text{Ca}(\text{NO}_3)_2$ salt can be monitored on the leaf surface (**Figure 7**). Interestingly, the range of values is noticeably less than portrayed in 1050 cm^{-1} values, potentially inferring that this peak is less prone to reproducibility issues.

Mean values of these data further support this relationship, which show a clear upwards trend. This could be attributed to the lack of overlap with other scattering bands, particularly those which are sensitive to morphological differences, such as the 1050 cm^{-1} peak. The control time point T_0 , shows the expected variance from the 743 cm^{-1} band and as anticipated, no concentration effects are evident. At T_{48} , the scattering intensity increases in a concentration dependent manner, to an extent not dissimilar to that of T_{24} , suggesting that Ca absorption is low between these two time points. It is more likely in reality that this artefact is due to inconsistency in the Raman spectra,

rather than a reduced absorption rate, which is later clarified by data from ion selective probes. At T_{72} , there is also residual evidence of the Ca treatment indicated by significant differences in the intensity of values for 15, 20 and 25 cm^{-1} , although closer to the intensities displayed at T_0 . A distinctly higher lower limit for the data points may be responsible for the significant differences shown, which again may occur due to the spectral baseline from the leaf itself. This spectral region is where DNA associated bond vibrations occur, as well as contributions from chlorophyll⁴². The latter of these molecules could be found at differing levels within tissues of varying ages, morphologies and growth status in relation to their photosynthetic capability⁵². The application of fertiliser could also have a direct effect on chlorophyll content in plant cells, corresponding to elevated scattering intensities seen in higher treatments⁵³.

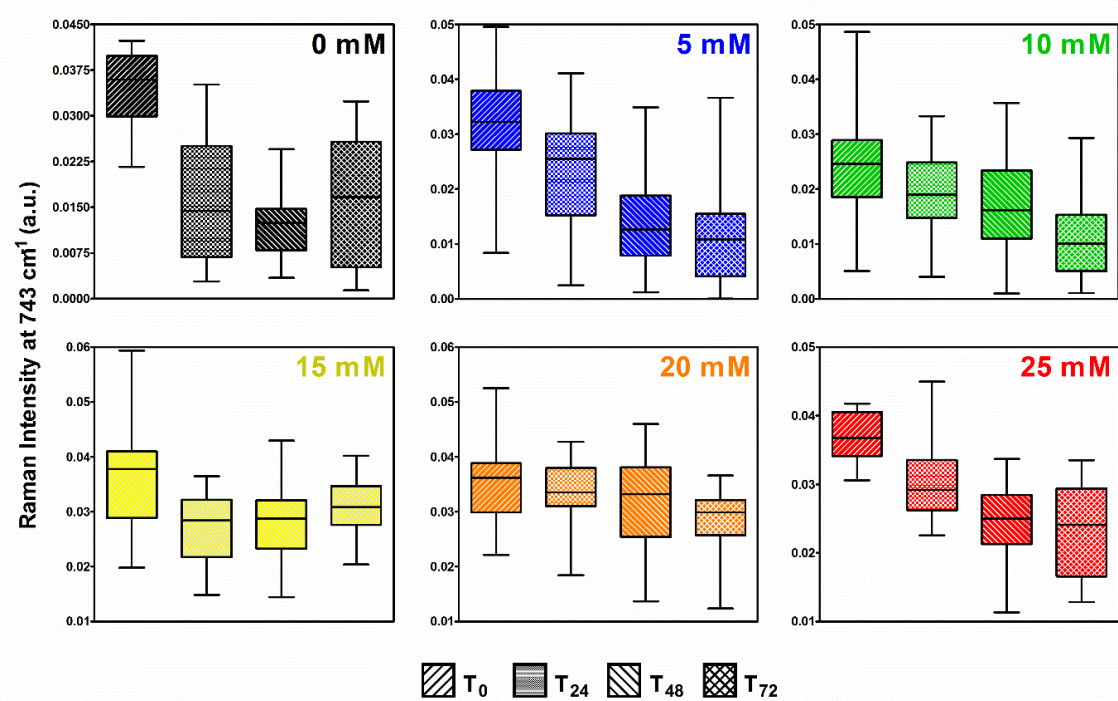


Figure 8. Alterations of the Raman intensity at 743 cm^{-1} , representative of bound NO_3^- , over a 72-hour period (T_0 , T_{24} , T_{48} , T_{72} hours) at a range of $\text{Ca}(\text{NO}_3)_2$ treatments. Intensity values were obtained from second derivative, vector normalised and wavelet smoothed data in order to standardise comparisons between individual leaf samples.

In contrast, when comparing individual treatments over the 72-hour time course, the pattern of Ca uptake is not as clear as earlier observations, even at higher concentrations (Figure 8). The first slight indication of an increase in scattering intensity from T_0 to T_{24} is only evident in the 25 mM treatment, and even so, this effect is not

significant across the four time points. This could be largely attributed to the relatively high intensity of the T_0 measurements, which is mimicked across nearly all of the different treatments, including the control. This suggests at this particular time point, regardless of foliar $\text{Ca}(\text{NO}_3)_2$ application, the starting Raman intensity at 743 cm^{-1} was higher than at the end of the study. As this peak can be associated with chlorophyll, this may be due to a heightened rate of photosynthesis on this particular date, despite the environmental conditions within the glasshouse being actively controlled ⁵⁴.

Ion selective probes to monitor Ca^{2+} and NO_3^-

In parallel to Raman microspectroscopy measurements, Ca^{2+} and NO_3^- selective probes were used to elucidate the relative quantities of each ion remaining on the leaf surface over the course of the study. Ion selective electrodes have proven useful tools within plant research, allowing the accurate measurement of ionic fluxes within plant tissues, as well as to determine ionic content of xylem sap⁵⁵⁻⁵⁷. These standard commercial probes were utilised to measure differences in ionic content of the nutrient solution remaining upon the leaf surface in aqueous format.

Figure 9 depicts Ca^{2+} -selective probe measurements derived from the adaxial leaf surface (**A**) and also from control surfaces; plastic (**B**) and glass (**C**). At T_0 , immediately following application upon the leaf surface, the concentration determined by the probe correlated to the known concentrations of the treatment solutions (0 – 1000 ppm). After drying, and subsequent Raman measurements, the banded area of the leaflet was rehydrated and reanalysed at T_{24} . Here, there is a clear reduction in the levels of Ca^{2+} in the eluate from the leaf surface, implying that there is less Ca on the leaf surface as a consequence of uptake of the foliar treatment. In comparison to this time point in both the glass and plastic controls, no alteration in the ionic content is displayed showing that this effect is specific to absorption upon the leaf surface. The rate of Ca uptake was determined to be at its highest during this initial 24-hour period, with the highest concentrations showing the fastest rate of uptake (**Table 1**). Interestingly, 20 and 25 mM treatments display an almost identical rate of Ca uptake that infers the maximum absorption across the leaf surface had been achieved at this concentration. After this initial time period, the levels of Ca remaining on the leaf continues to diminish at T_{48} , at a much reduced rate, and again at T_{72} , where almost all treatments are at similar resting

level. This indicates that across the 72-hour time period, the majority of the applied $\text{Ca}(\text{NO}_3)_2$ has been actively absorbed into the leaf tissue and is no longer present upon the adaxial leaf surface.

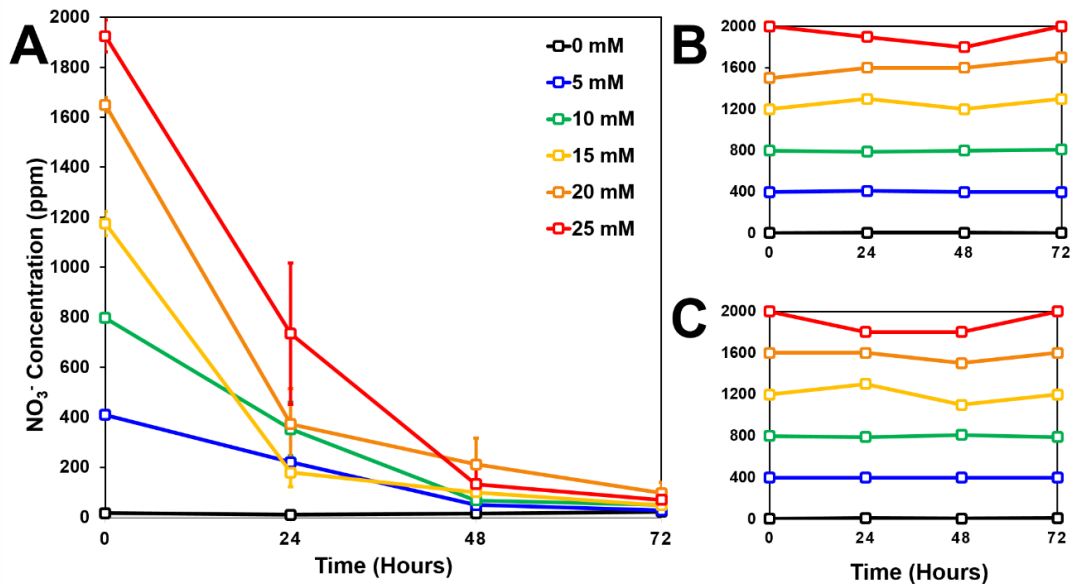


Figure 9. Ca^{2+} ion concentration (ppm) on; (A) the adaxial leaf surface; (B) a plastic surface; and (C) a glass surface, across a 72-hour period determined by the use of a Ca^{2+} ion probe (Horiba Scientific, UK) as consequence of $\text{Ca}(\text{NO}_3)_2$ treatment. Standard error bars are shown to present the variation within acquisitions.

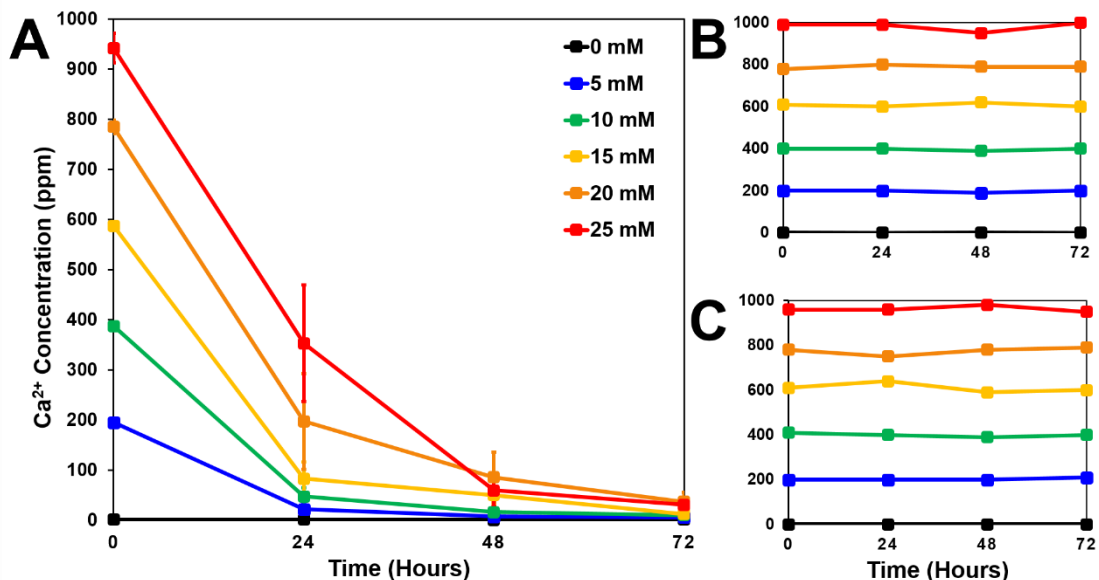


Figure 10. NO_3^- ion concentration (ppm) on; (A) the adaxial leaf surface; (B) a plastic surface; and (C) a glass surface, across a 72-hour period determined by the use of a Ca^{2+} ion probe (Horiba Scientific, UK) as consequence of $\text{Ca}(\text{NO}_3)_2$ treatment. Standard error bars are shown to present the variation within acquisitions.

Table 1. The overall rate of ion uptake at the adaxial leaf surface of *S. lycopersicum* samples determined using an ion probe following foliar application of $\text{Ca}(\text{NO}_3)_2 \bullet 4\text{H}_2\text{O}$ solutions.

Ca Treatment	(mM)	Rate of Ca^{2+} uptake (ppm $\text{cm}^{-1} \text{h}^{-1}$)				Rate of NO_3^- uptake (ppm $\text{cm}^{-1} \text{h}^{-1}$)			
		0-24 h	24-48 h	48-72 h	Overall	0-24 h	24-48 h	48-72 h	Overall
0	0	0.000 \pm 0.000	0.003 \pm 0.000	0.000 \pm 0.002	0.000 \pm 0.005	0.037 \pm 0.000	0.000 \pm 0.000	0.000 \pm 0.000	0.000 \pm 0.000
5	5	1.023 \pm 0.038	0.084 \pm 0.056	0.009 \pm 0.009	1.116 \pm 0.024	1.12 \pm 0.002	1.011 \pm 0.002	0.127 \pm 0.001	2.258 \pm 0.001
10	10	2.007 \pm 0.015	0.183 \pm 0.106	0.037 \pm 0.049	2.227 \pm 0.028	2.623 \pm 0.001	1.678 \pm 0.004	0.103 \pm 0.002	4.405 \pm 0.001
15	15	2.975 \pm 0.044	0.193 \pm 0.192	0.223 \pm 0.109	3.391 \pm 0.018	5.871 \pm 0.002	0.467 \pm 0.008	0.308 \pm 0.005	6.646 \pm 0.001
20	20	3.465 \pm 0.078	0.659 \pm 0.564	0.287 \pm 0.284	4.411 \pm 0.112	7.530 \pm 0.003	1.039 \pm 0.024	0.965 \pm 0.012	9.159 \pm 0.005
25	25	3.475 \pm 0.174	1.730 \pm 0.683	0.171 \pm 0.171	5.376 \pm 0.045	7.019 \pm 0.007	3.547 \pm 0.028	0.450 \pm 0.008	10.94 \pm 0.002

This notion is further supported when studying results from the NO_3^- selective probe, which illustrates an almost identical pattern to the Ca^{2+} results obtained (Figure 10). The concentration values derived from the probe again correlate with the known concentration of the foliar treatments, displaying double the ppm value of Ca^{2+} due to two molecules of NO_3^- being present in the compound. As such, the variability within this dataset is marginally higher than previously seen, due to a larger concentration range being observed. However, the overall trend of decreasing levels of NO_3^- in the eluate from the leaf surface over time is still evident. The rate of uptake also correlates with the Ca uptake data, with the initial 24-hour time period being the point where highest rates

of uptake are seen, with some evidence of a saturation point being reached at the 20 and 25 mM concentration. This rate also reduces over time and is often found to be twice as efficient as Ca uptake.

FAAS to monitor Ca uptake

In preliminary investigations, spectroscopic measurements were taken outside of the banded area, in order to determine if Ca supplementation resulted in an increased Ca content of the surrounding tissues. Raman spectroscopy was unable to infer any information regarding potential Ca translocation, as spectroscopic measurements in the banded area were focused upon the leaf surface, rather than penetration into the leaf tissue. The same is also true with the ion selective probe approach, which is absolutely defined to the leaf surface.

In order to determine whether foliar application of $\text{Ca}(\text{NO}_3)_2$ resulted in an increase in Ca within the leaf tissue, FAAS was employed to analyse the banded area, as well as tissue from the remaining leaflet. Increases in total Ca in the banded area would substantiate that applied nutrient were in fact absorbed into the plant tissue, whereas increases in the surrounding tissue would provide evidence of translocation to regions isolated from the area of foliar application. Previous literature suggests that Ca is immobile in plant tissues and any increases in this tissue would be unexpected^{34, 58}.

Figure 11 compares the % Ca content of both tissue samples across the range of Ca treatments applied in this study. In tissue derived from the banded area, a net gradual increase can be seen across the concentration range, as well as an over increase in variability within the data; an observation that has been highlighted by all analytical techniques used in this study. Although there are no statistically significant differences between each treatment group, this pattern in the data may still suggest that some applied Ca has been taken into the plant tissue. In the remaining area of the leaflet however, very little difference can be observed between the Ca content of each treatment group. This supports the notion that Ca is immobile in plant tissue and is unable to translocate following foliar nutrient application. However, it is worth noting that the remaining leaflet surface area was distinctly larger than that of the banded area, with as much as ten

times more dried plant material available for FAAS. Such differences may dilute the already subtle Ca content alterations, if they had occurred in the tissue.

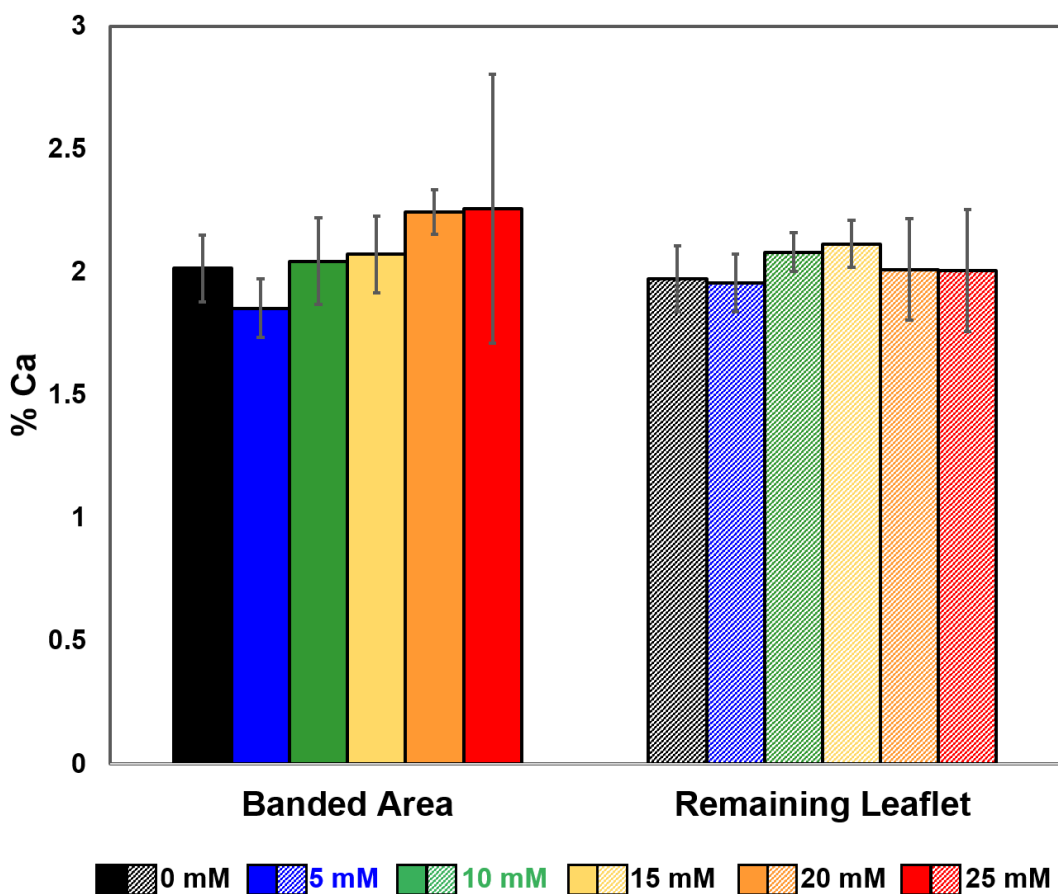


Figure 11. % Ca content within the ‘banded area’ and ‘remaining’ area of the leaflet as determined using flame atomic absorption spectroscopy across a range of Ca(NO₃)₂ concentrations. Standard error bars representative of variance within the dataset are shown.

Conclusions

By better understanding nutrient uptake and translocation in crop species, we can begin to alter agricultural practises to achieve an optimum level of efficiency that will allow a sustainable supply of food for the growing population¹. Current fertiliser procedures do not directly address the specific nutrient requirements of the plant, particularly the secondary macro-nutrients, and the micronutrient needs, which are known to be common

and detrimental to crop quality in deficient conditions. In order to understand the efficacy and mechanistic action of novel bio-enhancement fertilisers, which move away from traditional NPK fertilisers, there is a need for a rapid screening tool to observe nutrient movement within plant tissues as well as to determine the effectiveness of fertiliser formulations. Current methods require monitoring plant or soil nutrient content post-treatment, which often require extended trials and extensive sample preparation¹².

The purpose of this study was to observe and quantify Ca uptake at the adaxial leaf surface in *S. lycopersicum* as a model crop using Raman spectroscopy, ion-selective probes and FAAS. By employing these methods, we were able to identify time dependent uptake of Ca at the leaf surface at different levels of efficiency. Initially, Raman spectroscopy was utilised as a rapid, sensitive and non-destructive approach to detect foliar applied Ca(NO₃)₂ on the leaf surface of live plant samples. The presence of this compound could be established using this technique at concentrations as low as 5mM in isolated experiments. Overall uptake of Ca over time was indirectly measured through NO₃⁻ associated vibrational modes, and consequently was able to observe a gradual depletion in Ca on the leaf surface over time, indicative of uptake. One limitation of this approach however, is that data are extremely variable due to the uneven drying of the compound across the surface area, which resulted in 15 mM Ca(NO₃)₂ being the detection threshold for repeatable uptake observations over time. One potential method to overcome the issues of reproducibility with Raman measurements, is to use an imaging approach to observe Ca(NO₃)₂ deposits within the banded area that the treatment was applied. By image mapping a smaller banded region, areas containing residual salt deposits can be identified rapidly and in a highly interpretable false colour image²⁴. This may a useful approach to not only assess the efficiency of nutrient uptake in live plant systems, but also to assess the efficiency of fertiliser compositions. Despite this, single measurements could be acquired in as little as 15 seconds and whole screening studies in a few short hours. With the additional benefit of being ideal for in situ analysis, Raman spectroscopy could prove a valuable tool for fertiliser screening and general crop monitoring in the research and field studies²⁷. Potentially, this technique could also be used as a non-destructive analysis method to determine the total nutrient status of the plant, as shown previously using near infrared reflectance (NIR) spectroscopy⁵⁹⁻⁶¹.

The use of ion-selective probes for direct quantification of $\text{Ca}(\text{NO}_3)_2$ demonstrated that the concentration of a given compound could be accurately and rapidly determined on the leaf surface over time. This simple methodology proved to be a powerful adaption of these common instruments and could be readily implemented for fertiliser screening purposes, as rates of uptake can be determined and thus the efficiency of different formulations can be interrogated.

Analytical techniques such as FAAS and inductively coupled plasma mass spectrometry (ICP-MS), are two of many approaches that are able to quantify total elemental content in plant and soil tissue³⁵. Tests such as these could be considered the most informative tools available to growers and fertiliser producers, as valuable information regarding total nutrient content of crops can be determined that⁶². This can reflect the efficiency of the nutrient supply system and help to optimise growing practises. However, there is a substantial sample preparation burden with such approaches, with tissue digestion steps required prior to analysis^{63, 64}. In this study we were able to illustrate the net movement of $\text{Ca}(\text{NO}_3)_2$ from the leaf surface into the leaf tissue as a consequence of foliar fertiliser application using this technique. These data were complementary to the previously acquired Raman spectroscopy and ion selective probe measurements and clarified that Ca was effectively being absorbed into the leaf tissue. However, the sensitivity of this approach compared to Raman spectroscopy and probe techniques was considerably less, and was unable to statistically depict differences between treatments. This suggests that FAAS is less effective for fertiliser screening studies, than the two novels approaches presented in this investigation.

Our studies show that the approaches discussed in this article provide a novel alternative for the observation and quantification of Ca uptake at the adaxial surface of plant leaves, although there are still opportunity for improvements, particularly in regards to reproducibility and the detection limit of Raman spectroscopy. The efficiency of foliar fertiliser formulation could be assessed using this approach, and in doing so, this raises the possibility of elucidating the elusive mechanisms by which Ca is absorbed at the leaf surface. Furthermore, we envisage that this methodology could be used to detect nutrient deficiencies by *in vivo* leaf analysis, at a higher sensitivity than current techniques, and without the requirement of extensive preparation steps. Taken together, the advances we report here will contribute towards the more efficient production of

crops that is desperately required to meet the need for increased agricultural productivity in order to maintain global food security.

Acknowledgements

Holly J. Butler is a member of the Centre for Global Eco-Innovation, who are funded by the European Union Regional Development Fund and mediate the collaboration between Lancaster University and Plant Impact Plc.

References

1. Roy R, Finck A, Blair G, Tandon H. Plant nutrition for food security. A guide for integrated nutrient management FAO Fertilizer and Plant Nutrition Bulletin. 2006;16:368.
2. van der Ploeg RR, Böhm W, Kirkham MB. On the origin of the theory of mineral nutrition of plants and the law of the minimum. *Soil Sci Soc Am* 1999;63(5):1055-62.
3. The British survey of fertiliser practice: Fertiliser use on farm crops for crop year 2013. In: Department for Environment FaRA, editor.: The United Kingdom Statistics Authority; 2014.
4. Gooding MJ, Davies WP. Foliar urea fertilization of cereals: A review. *Fert Res.* 1992;32(2):209-22.
5. Hillier J, Hawes C, Squire G, Hilton A, Wale S, Smith P. The carbon footprints of food crop production. *Int J Agr Sust.* 2009;7(2):107-18.
6. Parry MAJ, Hawkesford MJ. Food security: increasing yield and improving resource use efficiency. *Pro Nutr Soc.* 2010;69(04):592-600.
7. Swietlik D, Faust M. Foliar nutrition of fruit crops. *Hortic Rev.* 1984.
8. Dixon RC. Foliar fertilization improves nutrient use efficiency. *Fluid Journal.* 2003;11:22-3.
9. Saleem I, Javid S, Sial RA, Ehsan S, Ahmad ZA. Substitution of soil application of urea with foliar application to minimize the wheat yield losses. *Soil Environ.* 2013;32(2).
10. Alexander A. Optimum timing of foliar nutrient sprays. *Foliar fertilization:* Springer; 1986. p. 44-60.
11. Fageria N, Filho MB, Moreira A, Guimaraes C. Foliar fertilization of crop plants. *J Plant Nutr.* 2009;32(6):1044-64.
12. Jones Jr JB. Laboratory guide for conducting soil tests and plant analysis: CRC press; 2001.
13. Fernández V, Eichert T. Uptake of hydrophilic solutes through plant leaves: current state of knowledge and perspectives of foliar fertilization. *Crit Rev Plant Sci.* 2009;28(1-2):36-68.
14. Fernández V, Brown PH. From plant surface to plant metabolism: the uncertain fate of foliar-applied nutrients. *Front Plant Sci.* 2013;4:289.

15. Schönherr J, Luber M. Cuticular penetration of potassium salts: Effects of humidity, anions, and temperature. *Plant Soil*. 2001;236(1):117-22.
16. Wittwer SH, Bukovac M. The uptake of nutrients through leaf surfaces. *Z Pflanz*: Springer; 1969. p. 235-61.
17. Bukovac MJ, Wittwer SH. Absorption and Mobility of Foliar Applied Nutrients. *Plant Physiol*. 1957;32(5):428-35.
18. Tanq M, Sharif M, Shah Z, Khan R. Effect of foliar application of micronutrients on the yield and quality of sweet orange (*Citrus sinensis* L.). *Pak J Biol Sci*. 2007;10(11):1823-8.
19. Stevens P. Formulation of sprays to improve the efficacy of foliar fertilisers. *N Z J For Sci*. 1994;24(1):27-34.
20. Riederer M, Schreiber L. Waxes: the transport barriers of plant cuticles. *The Oily Press*: Dundee, Scotland; 1995. p. 131-56.
21. Kannan S. Physiology of foliar uptake of inorganic nutrients. *Proceedings: Plant Sciences*. 1986;96(6):457-70.
22. Mengel K, editor *Alternative or complementary role of foliar supply in mineral nutrition*. International Symposium on Foliar Nutrition of Perennial Fruit Plants 594; 2001.
23. Kneipp K, Kneipp H, Itzkan I, Dasari RR, Feld MS. Ultrasensitive chemical analysis by Raman spectroscopy. *Chem Rev*. 1999;99(10):2957-76.
24. Butler HJ, Ashton L, Bird B, Cinque G, Curtis K, Dorney J, et al. Using Raman spectroscopy to characterize biological materials. *Nat Protoc*. 2016;11(4):664-87.
25. Mansfield JC, Littlejohn GR, Seymour MP, Lind RJ, Perfect S, Moger J. Label-free chemically specific imaging in planta with stimulated Raman scattering microscopy. *Anal Chem*. 2013;85(10):5055-63.
26. Littlejohn GR, Mansfield JC, Parker D, Lind R, Perfect S, Seymour M, et al. In vivo chemical and structural analysis of plant cuticular waxes using stimulated Raman scattering microscopy. *Plant Physiol*. 2015;168(1):18-28.
27. Butler HJ, McAinsh MR, Adams S, Martin FL. Application of vibrational spectroscopy techniques to non-destructively monitor plant health and development. *Anal Methods*. 2015;7(10):4059-70.
28. Simon E. The symptoms of calcium deficiency in plants. *New Phytol*. 1978;80(1):1-15.

29. Van Goor B. The effect of frequent spraying with calcium nitrate solutions on the mineral composition and the occurrence of bitter pit of the apple Cox's Orange Pippin. *J Hortic Sci.* 1971;46(4):347-64.
30. Wada T, Ikeda H, Ikeda M, Furukawa H. Effects of Foliar Application of Calcium Solutions on the Incidence of Blossom-end Rot of Tomato Fruit. *J Jpn Soc Hortic Sci.* 1996;65(3):553-8.
31. Geraldson C. Factors affecting calcium nutrition of celery, tomato, and pepper. *Soil Sci Soc Am J.* 1957;21(6):621-5.
32. Taylor MD, Locascio SJ. Blossom-end rot: A calcium deficiency. *J Plant Nutr.* 2004;27(1):123-39.
33. Kirkby E, Pilbeam D. Calcium as a plant nutrient. *Plant Cell Environ.* 1984;7(6):397-405.
34. White PJ, Broadley MR. Calcium in Plants. *Ann Bot.* 2003;92(4):487-511.
35. Harborne A. *Phytochemical methods a guide to modern techniques of plant analysis*: Springer Science & Business Media; 1998.
36. Trevisan J, Angelov PP, Scott AD, Carmichael PL, Martin FL. IRootLab: a free and open-source MATLAB toolbox for vibrational biospectroscopy data analysis. *Bioinformatics.* 2013;btt084.
37. Stevens PJ. Organosilicone surfactants as adjuvants for agrochemicals. *Pestic Sci.* 1993;38(2-3):103-22.
38. Irish D, Walrafen G. Raman and infrared spectral studies of aqueous calcium nitrate solutions. *J Chem Phys.* 1967;46(1):378-84.
39. Hester RE, Plane RA. Raman spectrophotometric study of complex formation in aqueous solutions of calcium nitrate. *J Chem Phys.* 1964;40(2):411-4.
40. Balshaw B, Smedley SI. Raman spectroscopy of concentrated calcium nitrate solutions at high pressure. *J Phys Chem.* 1975;79(13):1323-5.
41. Nyquist RA, Kagel RO. *Handbook of infrared and raman spectra of inorganic compounds and organic salts: infrared spectra of inorganic compounds*: Academic press; 2012.
42. Movasaghi Z, Rehman S, Rehman IU. Raman spectroscopy of biological tissues. *Appl Spectrosc Rev.* 2007;42(5):493-541.
43. Sene CF, McCann MC, Wilson RH, Grinter R. Fourier-transform Raman and Fourier-transform infrared spectroscopy (an investigation of five higher plant cell walls and their components). *Plant Physiol.* 1994;106(4):1623-31.

44. Schulz H, Baranska M. Identification and quantification of valuable plant substances by IR and Raman spectroscopy. *Vib Spectrosc.* 2007;43(1):13-25.
45. Schrader B, Klump H, Schenzel K, Schulz H. Non-destructive NIR FT Raman analysis of plants. *J Mol Struct.* 1999;509(1):201-12.
46. Ochiman ID. The impact of foliar application of calcium fertilizers on the quality of highbush blueberry fruits belonging to the 'Duke' cultivar. *Not Bot Horti Agrobo.* 2012;40(2):163-9.
47. Domagała-Świątkiewicz I, Błaszczyk J. Effect of calcium nitrate spraying on mineral contents and storability of 'Elise' apples. *Pol J Environ Stud.* 2009;18(5):971-6.
48. Peyvast G, Olfati J, Ramezani-Kharazi P, Kamari-Shahmaleki S. Uptake of calcium nitrate and potassium phosphate from foliar fertilization by tomato. *J Hortic For.* 2009;1(1):7-13.
49. Syahren AM, Wong N, Mahamud S. The efficacy of calcium formulation for treatment of tomato blossom-end rot. *J Trop Agric and Fd Sc.* 2012;40(1):89-98.
50. Murillo-Amador B, Jones HG, Kaya C, Aguilar RL, García-Hernández JL, Troyo-Diéguéz E, et al. Effects of foliar application of calcium nitrate on growth and physiological attributes of cowpea (*Vigna unguiculata* L. Walp.) grown under salt stress. *Environ Exp Bot.* 2006;58(1):188-96.
51. Monti F, Dell'Anna R, Sanson A, Fasoli M, Pezzotti M, Zenoni S. A multivariate statistical analysis approach to highlight molecular processes in plant cell walls through ATR FT-IR microspectroscopy: The role of the α -expansin PhEXPA1 in *Petunia hybrida*. *Vib Spectrosc.* 2013;65:36-43.
52. Antoniaa L, Tompetrini S, Svetlanab P. Quantification of pigments in tomato leaves using reflectance spectroscopy. *P Int Symp Rem S Environ.* 2005;31:39-42.
53. Jianfeng W, Dongxian H, Jinxiu S, Haijie D, Weifen D. Non-destructive measurement of chlorophyll in tomato leaves using spectral transmittance. *Int J Agr Biol Eng.* 2015;8(5):73.
54. Zeiri L. SERS of plant material. *J Raman Spectrosc.* 2007;38(7):950-5.
55. Newman I. Ion transport in roots: measurement of fluxes using ion-selective microelectrodes to characterize transporter function. *Plant, cell & environment.* 2001;24(1):1-14.
56. Rothwell SA, Dodd IC. Xylem sap calcium concentrations do not explain liming-induced inhibition of legume gas exchange. *Plant Soil.* 2014;382(1-2):17-30.

57. Boyle RK, McAinsh M, Dodd IC. Stomatal closure of *Pelargonium* × *hortorum* in response to soil water deficit is associated with decreased leaf water potential only under rapid soil drying. *Physiol Plantarum*. 2016;156(1):84-96.
58. Hanger B. The movement of calcium in plants. *Commun Soil Sci Plan*. 1979;10(1-2):171-93.
59. Bruno-Soares AM, Murray I, Paterson RM, Abreu JM. Use of near infrared reflectance spectroscopy (NIRS) for the prediction of the chemical composition and nutritional attributes of green crop cereals. *Anim Feed Sci Tech*. 1998;75(1):15-25.
60. Foley WJ, McIlwee A, Lawler I, Aragones L, Woolnough AP, Berding N. Ecological applications of near infrared reflectance spectroscopy—a tool for rapid, cost-effective prediction of the composition of plant and animal tissues and aspects of animal performance. *Oecologia*. 1998;116(3):293-305.
61. Cozzolino D, Fassio A, Gimenez A. The use of near-infrared reflectance spectroscopy (NIRS) to predict the composition of whole maize plants. *J Sci Food Agr*. 2001;81(1):142-6.
62. Oliveira SR, Neto JAG, Nobrega JA, Jones BT. Determination of macro-and micronutrients in plant leaves by high-resolution continuum source flame atomic absorption spectrometry combining instrumental and sample preparation strategies. *Spectrochim Acta B*. 2010;65(4):316-20.
63. Huang CYL, Schulte E. Digestion of plant tissue for analysis by ICP emission spectroscopy. *Commun Soil Sci Plan*. 1985;16(9):943-58.
64. Zarcinas B, Cartwright B, Spouncer L. Nitric acid digestion and multi-element analysis of plant material by inductively coupled plasma spectrometry. *Commun Soil Sci Plan*. 1987;18(1):131-46.

Chapter 6

Detecting nutrient deficiency in plant systems using synchrotron FTIR microspectroscopy

Holly J. Butler, Steve Adams, Martin R. McAinsh, and Francis L. Martin

Submitted for publication: Vibrational Spectroscopy

Invite for special issue 'Prominent Young Spectroscopists'

Contribution:

I conducted all experimental work

I wrote and prepared the manuscript for publication

I produce all figures

Professor F. L Martin

Dr. Martin. R. McAinsh

H. J. Butler

Detecting nutrient deficiency in plant systems using synchrotron Fourier-transform infrared microspectroscopy

Holly J. Butler ^{abc}, Steve Adams ^d, Martin R. McAinsh ^{e*}, Francis L. Martin ^{af*}

^a *Centre for Biophotonics, Lancaster Environment Centre, Lancaster University, Lancaster LA1 4YQ, UK*

^b *Centre for Global Eco-Innovation, Lancaster Environment Centre, Lancaster University, Lancaster LA1 4YQ, UK*

^c *WESTChem, Department of Pure and Applied Chemistry, Technology and Innovation Centre, University of Strathclyde, Glasgow G1 1RD, UK*

^d *Plant Impact Plc, Rothamsted, West Common, Harpenden, Hertfordshire, AL5 2JQ, UK*

^e *Lancaster Environment Centre, Lancaster University, Lancaster LA1 4YQ, UK*

^f *Division of Biosciences, School of Pharmacy and Biomedical Sciences, University of Central Lancashire, Preston PR1 2HE, UK*

***Correspondence to:** Holly Butler, WESTChem, Department of Pure and Applied Chemistry, Technology and Innovation Centre, University of Strathclyde, Glasgow G1 1RD, UK; Email: holly.butler@strath.ac.uk;

Prof Francis L. Martin, Division of Biosciences, School of Pharmacy and Biomedical Sciences, University of Central Lancashire, Preston PR1 2HE, UK; Email: f.martin@lancaster.ac.uk; Tel.: +44(0)1524 510206

Dr Martin R. McAinsh, Lancaster Environment Centre, Lancaster University, Lancaster LA1 4YQ, UK; Email: m.mcainsh@lancaster.ac.uk; Tel.: +44(0)1524 510553

Abstract

By 2050, it is estimated that the global population will have surpassed 9 billion people, presenting a significant challenge with regards to food security. In order to provide sufficient quantities of nutritious food in the future, it is necessary to improve agricultural productivity by several orders of magnitude. Nutrient deficiencies are one particular threat to food security that can have a negative impact on crop yield and quality. Currently the standard agricultural approach to prevention is to supply an excess macronutrient fertiliser, such as nitrate or phosphate, during crop production. However, the efficiency of this approach is poor as deficiencies of specific nutrients, such as Ca, are not prevented in this circumstance, and fertiliser use is associated with a host of adverse environmental impacts. Herein, we describe a novel method to detect Ca deficiency using synchrotron radiation-based Fourier-transform infrared (FTIR) microspectroscopy in live and fixed tissue of the model plant *Commelina communis*, as a precursor to targeted nutrient remediation in the field.

Keywords: Calcium, Deficiency, Fourier-transform infrared (FTIR) microspectroscopy, Nutrient, Plant, Synchrotron radiation

1. Introduction

Food security can be defined as providing a constant supply of nutrition for all, in order to live a healthy lifestyle, regardless of social, economic and physical circumstances [1]. The expanding global population has increased demand for food of sufficient quality, and has further emphasised the challenge of maintaining food security in the modern era [2]. Climate change, competition for arable land, and agricultural productivity are significant factors affecting global food production [3]. Improving efficiency during crop production is an area where small alterations to farming practices, may result in large-scale yield and quality increases. The difference between the attainable yield and the observed yield is known as a yield gap, and it is by reducing this deficit that agricultural productivity can be improved [4].

Plants require fourteen essential nutrients in order to grow optimally and produce the maximum attainable yield; these can be split into macro- (N, P, K, Ca, Mg and S) and micro- nutrients (B, Cl, Cu, Fe, Mn, Mo, N and Zn) [5]. Poor availability of one or more of these nutrients, can not only reduce the quantity of produce per hectare of land, but can also decrease food quality and shelf life. The use of nutrient fertilisers is a traditional practice of agricultural intensification that has been shown to increase yield (and thus reduce the yield gap) in crop species by between 30-50% [6]. Fertilisers containing primary macronutrients (N, P and K) are most commonly applied, as deficiencies in these elements are more commonplace in agricultural environments. However, it has been shown that use of such fertilisers is relatively inefficient and less than 50% of the nutrient applied is recovered in the produce output [7]. Furthermore, the use of fertilisers, such as NH_4 , has a number of detrimental effects on the environment, such as eutrophication from nitrate leaching, and also enormous carbon footprints associated with their production and application [8]. It is estimated that crop production, including farm operations, equates to the generation of around 769.4 kg of CO_2 , and its equivalents (such as N_2O), per hectare of farmland each year; of this total, over 90% is associated with fertiliser use [9]. It is also important to note that deficiencies in all nutrients can occur, with a diverse array of physiological symptoms and severities, which would not be remediated by the use of a generic N, P or K containing fertiliser [10].

Reduced Ca availability can have a significant impact on crop yield, due to the pivotal role this element has in structural stability within the plant tissues[11]. Ca pectate is a key component of plant cells walls and thus reduced availability of Ca can often result in degradation of the cell walls, particularly in developing and enclosed tissues, and those that are supplied predominantly by the phloem [12]. Ca is absorbed into the plant via the root system and is transported unidirectionally in the xylem and transport is therefore dependent on the rate of transpiration [13, 14]. Consequently, rapidly growing tissues and fruit, are particularly susceptible to reduced Ca availability and therefore degradation. Ca deficiencies manifest in a range of crop species, from blossom end rot in tomatoes, tip burn in lettuce and bitter pit in apples and in some instances can result in up to a 50% loss of yield [15, 16]. Although relatively uncommon in nature, due to intensive farming practices, Ca deficiencies are increasingly widespread in agricultural settings [17]. Due to the detrimental effect of this deficiency, as well as the role that Ca plays in fruit ripening, maintaining fruit firmness and reducing postharvest decay, Ca supplementation in agriculture is becoming an emerging section of the crop enhancement market [18]. This approach not only directly targets the nutrient status of the crop, but also reduces environmental impacts associated with N-based fertilisers.

It has been proposed that accurate determination of the nutrient status of plants can be used to better understand and target the specific nutritional needs of crops [19, 20]. In doing so, nutrient use efficiency would be vastly improved as the appropriate nutrient can be applied as and when required, improving the agricultural productivity whilst also reducing financial and environmental burdens. Currently, crop nutrient status is determined by foliar and soil analyses using analytical techniques such as flame photometry and flame atomic absorption spectroscopy [21, 22]. Although these approaches derive elemental information to a high degree of sensitivity, they require a nutrient extraction step, usually via acid digestion, which can often be time-limiting and also removes any information regarding spatial origin and distribution [23]. It is evident that there is a need for a novel crop screening approach that is able to detect the effects of nutrient deficiency before any detrimental effects are observed, which can be rapidly acquired in the field without any detrimental effects on plants, and without extensive sample preparation requirements.

Vibrational spectroscopy may be such a tool to fill this gap. It has been widely shown that infrared (IR) or Raman microspectroscopy can be used to characterise

valuable plant substances, but can also be implemented to analyse *in vivo* and fixed plant tissues samples in order to monitor plant health [24-27]. The application of Raman microspectroscopy in plant research had been relatively limited due to intrinsic fluorescence issues found within tissues. However, analysis of live samples has recently been shown to effectively quench fluorescence due to the presence of water allowing the acquisition of high quality point spectra and spectral maps [24, 28]. Conversely, Fourier-transform IR (FTIR) microspectroscopy has been largely restricted to the interrogation of fixed plant samples, as water has a detrimental effect on the IR spectrum due to its strong dipole moment. This has been overcome by the use of attenuated total reflection (ATR) acquisition mode FTIR, which uses a refractive prism to attenuate the IR beam into the sample and has recently allowed the investigation of foliar tissues [29, 30].

The combination of FTIR microspectroscopy with synchrotron radiation (SR) can improve the spatial resolution and signal-to-noise ratio (SNR) achievable in comparison to conventional benchtop instruments that employ globar IR sources [31, 32]. This is because SR is up to 1000 times brighter than thermally produced IR radiation, and thus is delivered to the sample at high flux density [33]. SR-based FTIR (SR-FTIR) microspectroscopy may therefore shed light upon molecular changes at spatial resolutions $<10\text{ }\mu\text{m}$, providing subcellular detail unachievable with traditional FTIR microspectroscopy [23, 34]. In plant research, SR-FTIR microspectroscopy has been employed to interrogate the molecular composition in a range of tissues including kernels, roots, and leaves [35-38]. The imaging capabilities of SR-FTIR have also been exploited to image the spatial distribution of cell wall components, and tissue microstructures [39-42]. However, in contrast to the biomedical and material science fields, SR-FTIR has not been widely in plant-based studies due largely to the aforementioned limitations of FTIR with water containing samples, which restricts *in vivo* analyses [35]. Nevertheless, it has been suggested that the high brilliance of a synchrotron light source, may overcome interference from water, thus allowing improved measurements in fresh or even live plant tissue [43].

Herein we investigate the effects of Ca depletion on the model plant species *Commelina communis* using SR-FTIR microspectroscopy for pre-symptomatic detection of Ca deficiency. *C. communis* is commonly used to study intracellular signalling in stomatal guard cells due to the ease with which the abaxial epidermis in which the stomata are primarily located can be isolated from the leaves of this species [44]. In this

investigation, this characteristic is exploited in order to examine the effects of sample preparation on deficiency detection by comparing freshly isolated tissue (unfixed) with chemically fixed tissue that is conventionally interrogated using FTIR and SR-FTIR microspectroscopy.

2. Material and Methods

2.1 Plant growth conditions

C. communis seeds were sown into rock wool cubes and supplied with distilled water until germination (~10 days). Seedlings were then transferred to purpose built hydroponic nutrient supply systems containing three distinct Ca concentrations (optimal Ca, 200; low Ca, 100, Ca deficient, 0 ppm), supplied using a modified Hoagland's solution for 21 days [45]. These treatments were chosen to mimic common nutrient requirements of agriculturally relevant crops such as *Solanum lycopersicum*. Each Ca treatment was replicated in three separate systems, each of which contained 16 L of nutrient solution and housed 6 seedlings from which three were randomly selected for analysis. Dissolved oxygen levels were maintained at 5.5 ± 0.5 mg/L using aquatic air pumps (Boyu, China); conductivity at 2 ± 0.1 mS; and pH 6.1 ± 0.1 . Plants were grown $25 \pm 2^\circ\text{C}$ / $20 \pm 2^\circ\text{C}$, day / night; 16 h photoperiod; $150 \pm 25 \mu\text{mol m}^{-2} \text{ s}^{-1}$ using 600W metal halide lamps (Osram Ltd, UK) and transferred to the laboratory immediately prior to acquisition where they were maintained under similar conditions. The youngest, fully expanded leaves were excised from each four-week-old plant and were prepared for SR-FTIR microspectroscopy or fixation immediately post-excision.

2.2 Epidermis isolation for unfixed samples

Isolated epidermis was prepared according to Weyers and Travis [46]. In short, a rectangular strip around 8 mm in width was cut from the lamina on either side of the major leaf vein using a sharp blade. A small incision was then placed onto the adaxial surface, without damaging the lower epidermal surface, creating a tab that can be carefully peeled backwards using forceps. The epidermal strip was then trimmed to an appropriate size before being mounted on a BaF₂ slide (Crystran Ltd, UK), with 50 µL of 50 mM KCL, 10 mM Mes/KOH, pH 6.15 (KCl-Mes) buffer. Samples were then immediately analysed using SR-FTIR microspectroscopy.

2.3 Sample fixation and embedding

Formalin fixation followed by paraffin embedding was chosen as a model approach for sample preparation prior to SR-FTIR microspectroscopy, as this technique has been well implemented in plant and biomedical studies [41]. Rectangular leaf sections were first excised and immediately fixed in 10% formalin for 24 h, dehydrated in an ethanol series

(70, 90 and 100%) for 6 h, and placed into xylene for 1 h. At each stage of fixation, the solution was changed twice.

To begin the embedding process, samples were transferred to molten paraffin wax at 60°C for 24 h to allow for sufficient wax infiltration. Samples were then orientated longitudinally in wax moulds in order to isolate the epidermis, and left to cool on ice for 30 min. Sections were cut at a thickness of 5 μm using a microtome, and placed into a warm water bath to allow expansion of the paraffin wax, before being floated onto a BaF₂ slide. Samples were dewaxed using xylene for 1 h, and hydrated using an ethanol series (100, 90 and 70%) for 6 h. Fixed samples were stored at room temperature (20 °C) until analysis.

2.4 Synchrotron radiation- based FTIR microspectroscopy

Spectra were obtained using a Bruker Vertex 80 V FTIR spectrometer coupled to a Hyperion 3000 microscope ($\times 36$ objective and condenser), a LN₂ cooled MCT detector, and the SR IR source, at the Multimode IR Imaging and Microspectroscopy (MIRIAM) beamline at Diamond Light Source, UK. An aperture size of 10 $\mu\text{m} \times 10 \mu\text{m}$ was used to collect spectra at a spectral resolution of 4 cm^{-1} with 256 co-additions across the mid-IR region (4000 - 600 cm^{-1}). Measurements were acquired in transmission mode as recent literature has identified its advantages over reflection measurements [47]. On average, 10 spectra were obtained per sample each live and fixed sample. A background measurement was taken from the substrate for every ten sample spectra to account for atmospheric conditions. Spectra were converted to absorbance units using OPUS 8 software (Bruker, UK).

2.5 Globar-based FTIR microspectroscopy

A Thermo Nicolet 6700 FTIR spectrometer coupled to a Nicolet Continuum microscope (Thermo Fisher Scientific, UK) and a LN₂ cooled mercury cadmium telluride (MCT) detector was employed to acquire transmission IR measurements (4000 - 650 cm^{-1}). Spectra were acquired using a 36 \times objective at a spectral resolution of 4 cm^{-1} , with 256 co-additions, whilst background spectra were taken after every ten sample spectra. Spectra were converted to absorbance units using Omnic spectra software (Thermo Fisher Scientific, UK).

2.6 Spectral pre-processing

Spectral analysis was conducted using the IRootLab Matlab toolbox (<https://github.com/trevisanj/irootlab>) unless otherwise stated [48]. Initially, spectra were quality tested using in-house written scripts to identify spectra with low SNR and potential outliers. The number of features within each spectrum was then reduced by focusing on the fingerprint region ($1800 - 900 \text{ cm}^{-1}$) as this is where biological molecules are known to absorb IR [49]. Spectra were first order differentiated (1st order polynomial) with Savitzky-Golay smoothing, and vector normalised to account for confounding sample characteristics such as thickness. For biomarker extraction using first derivative data, the point at which the spectra cross the zero line will represent the peak maxima from the original spectra and thus these values are used throughout.

2.6 *Multivariate analysis*

Exploratory principal component analysis (PCA) was conducted on the mean centred data in order to reduce the dataset down to factors that accounted for underlying variance in the spectra. This output was then fed in linear discriminant analysis (LDA), to minimize intra-class differences and maximises inter-class separation, and therefore give optimum separation of the dataset classes. The number of principal components used were optimized using the PCA pareto tool in IRootLab; this was determined as the ‘elbow’ point of the cumulative variance plot and always accounting for >95% of the variance in the dataset [50]. This process was cross validated using 10 k-folds and a leave-one-out approach, to prevent overfitting of the data. Classification of spectral classes was conducted using a PCA-linear discriminant classifier (LDC) with the same validation parameters.

2.7 *Statistical Analysis*

A Mann-Whitney ‘U’-test per wavenumber was conducted to compare spectral differences in pre-processed data at a confidence interval of 0.01.

3 Results & Discussion

3.1 Synchrotron radiation- versus globar-based FTIR microspectroscopy

Due to the high flux of photons in a synchrotron produced light beam, it is possible to generate high quality spectra with a superior SNR and spatial resolution than in comparison to traditional thermal based approaches [51]. **Fig. 1** depicts raw mean data from a SR and a globar-based FTIR system taken from unfixed abaxial epidermis of *C. communis*, and compares the spectral information and quality between the two instrument configurations. Whilst spectra derived from the conventional benchtop system are far from featureless, it is evident that SR-FTIR data are acquired at a substantially higher signal intensity, which consequently reveals further detail in the spectrum. This can be seen consistently across the fingerprint region where subtle shoulders of broader absorbance regions can be identified, particularly around the peak at $\sim 1335\text{ cm}^{-1}$ corresponding to plant cell wall polysaccharides such as cellulose and pectin [52]. As more information is derived using SR-FTIR at a cellular level, the technique represents a powerful tool for plant research and can be exploited in a range of stress determination studies, including biotic stresses such as pest and disease and abiotic stresses such as nutrient deficiency [53].

Additional to the overall improvement in spectral quality and spatial resolution of the data obtainable when employing SR radiation, there is also the benefit that samples with a high water content can also be interrogated to a higher capability than with a traditional benchtop FTIR. Water absorbs strongly at $\sim 1650\text{ cm}^{-1}$ and thus can result in a loss of spectral information in this important spectral region, often associated with the amide I of protein structure and composition. It is therefore possible to obtain good quality spectra from live samples or samples in aqueous environments, when employing SR [54]. **Figure 1** clearly shows that the interference of water is negligible when investigating monolayers of plant cells, such as found in isolated epidermis.

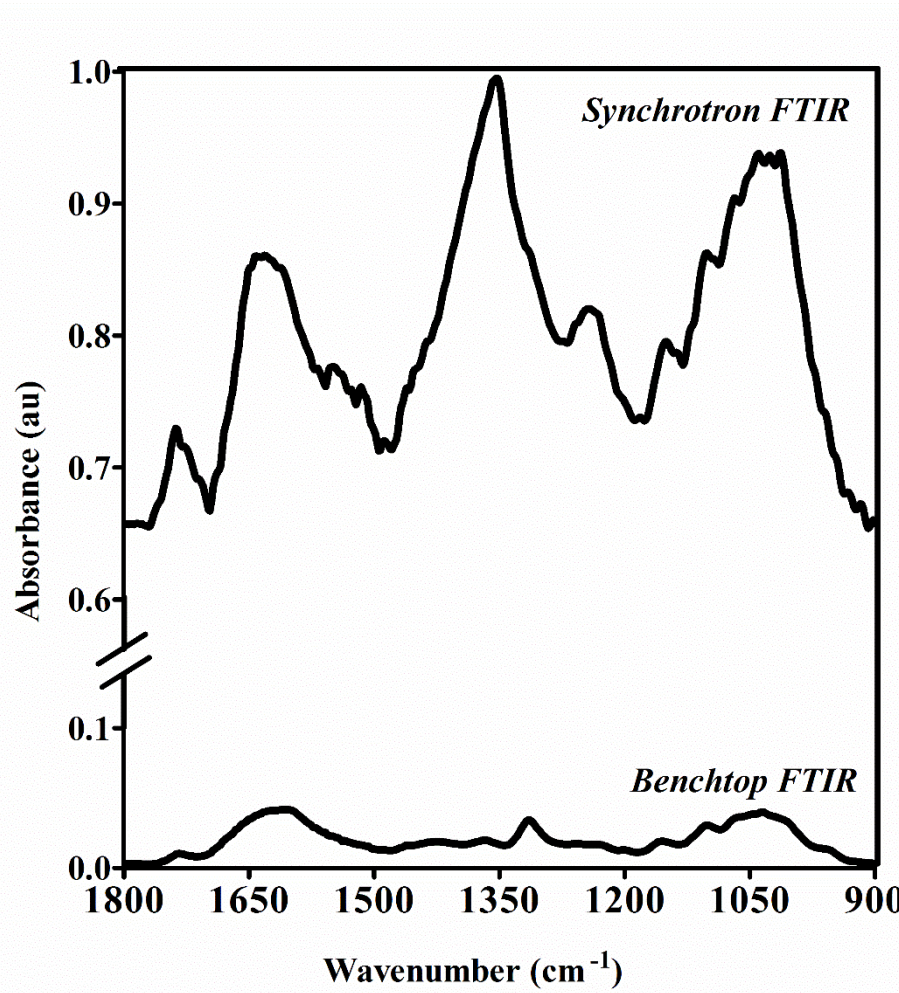


Figure 1. Unprocessed spectra from the fingerprint region ($1800 - 900 \text{ cm}^{-1}$) derived from unfixed abaxial epidermis of *C. communis* grown at optimal (200 ppm) Ca, using a benchtop FTIR instrument with a globar source (Thermo Fisher, UK), in comparison to a FTIR with a synchrotron radiation source (Bruker, UK; Diamond Light Source, UK). The superior signal to noise ratio can be observed when employing synchrotron radiation whilst also uncovering more spectral information from the sample.

3.2 Unfixed and fixed tissue

As it is possible to derive meaningful spectra from water containing samples, we look to compare the reproducibility and suitability of both fixed and unfixed (*ex vivo*) plant tissue samples for identifying Ca nutrient deficiency. **Figure 2A** presents representative bright field image of freshly prepared isolated abaxial epidermal in which the stomatal pores, surrounded by a pair of guard cells (GCs; identified with an arrow), and subsidiary and epidermal cells (ECs) are clearly visible. This contrasts markedly with the representative sample from fixed leaf tissue shown in **Figure 2B**. In order to produce a

sample appropriate for transmission FTIR measurements, paraffin embedded tissue must be sectioned at a thickness no larger than 12 μm [55]. During this process it is challenging to construct a sample that contains both epidermal and guard cells. The GCs surrounding the open stomatal pore are clearly visible in **Figure 2B**; the surrounding material is likely to be derived from the spongy mesophyll, which can be recognised by the irregular cell architecture of this tissue that is necessary to allow the movement of gas within the internal airspaces of the leaf. As a consequence of this, only stomatal GCs are probed in fixed leaf tissue samples for the remainder of this study, whilst both guard and epidermal cells are investigated in fixed tissue.

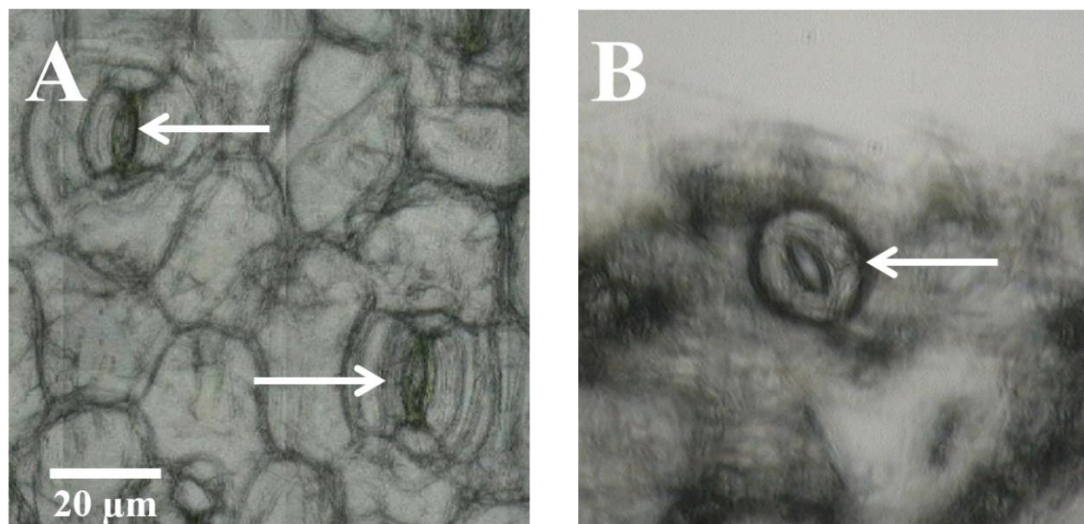


Figure 2. Brightfield images obtained from an unfixed abaxial epidermis (A), and a fixed sample (B), of *C. communis* grown at optimal (200 ppm) Ca. Stomatal guard cells (GCs) can be identified in both samples, although at a higher frequency in isolated epidermis, due to the simplicity of this approach for their isolation.

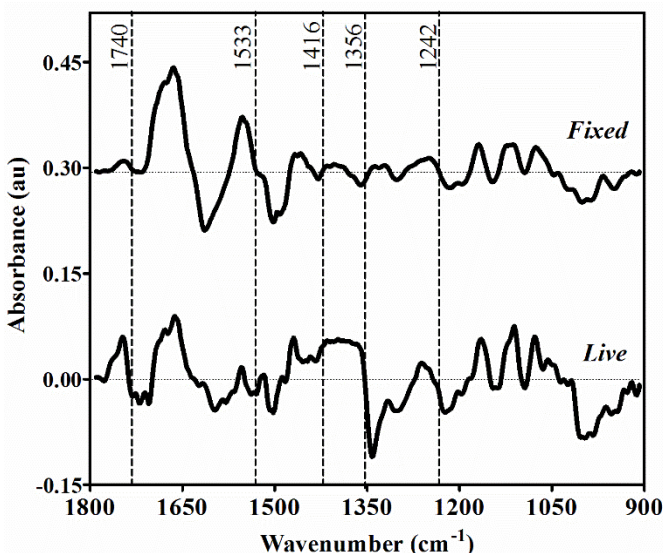


Figure 3. A comparison of pre-processed spectra from unfixed isolated abaxial epidermis and formalin-fixed paraffin embedded tissue from *C. communis*. Spectra were cut to the fingerprint region ($1800 - 900 \text{ cm}^{-1}$), first order differentiated, vector normalised and offset for clarity. Dashed markers indicate the top five statistically significant wavenumbers where the gradient is maximum ($y=0$).

In regards to the biochemical alterations that occur due to chemical fixation, clear differences can be observed between unfixed and fixed samples (Fig. 3, Table 1). It is preferable to remove any paraffin wax from samples prior to spectral acquisition due to the strong absorbance of the wax in the fingerprint. However, many dewaxing protocols have been shown to have significant effects on the resultant spectra obtained, particularly in regard to lipids [56]. This is evident when comparing fixed and unfixed plant tissue, where a decrease in lipid absorbance at 1740 cm^{-1} can be seen following fixation and dewaxing. The absorbance profiles of key cell wall polysaccharides are also stronger in live tissues, shown predominantly at 1416 and 1356 cm^{-1} . GC cell walls characteristically contain more phenolic esters of pectins than the surrounding cells, which is more effectively differentiated when using unfixed samples [57]. Fixed tissues displayed an increased absorbance at the amide II region, whilst live tissues depicted a higher absorbance at 1533 cm^{-1} , showing widespread protein alterations in the spectra. This effect may be tentatively associated with protein cross-linkages as a consequence of formalin fixation [58]. Overall, a slight reduction in signal strength can be observed in live tissues, which may be due to underlying water interference and a lower concentration of biological material compared to fixed samples which are dehydrated.

Table 1. Discriminating spectral regions derived from **Figure 3, 4 and 5** with tentative molecular assignments, and description of the direction of change in regards to the data class.

Wavenumber (cm ⁻¹)	Tentative Band Assignment	Ref.	Description
1740	v(C=O) polysaccharide, esterified pectin, lipids	[59, 60]	↑ Live ↑ GC
1728	v(C=O) lipid, polysaccharide, esterified pectin, cutin	[29, 60]	↑ Deficient*
1637	Amide I	[60]	↑ GC
1635	β-sheet of amide I	[41, 60]	↓ Deficient*
1630	v(C=O) and ring breathing, β-sheet of amide I	[41, 61]	↓ Deficient
1533	Amide II, C=N	[62]	↓ Live
1522	Amide II, C=N, C=C	[60]	↓ Deficient
1487	v(C=C), δ(C-H), Amide II	[26, 60]	↓ Deficient
1416	δ(NH), δ(CH), v(C-N) polysaccharides, unesterified pectin	[57, 60]	↑ Live
1356	δ(C-OH) polysaccharide	[63]	↑ Live ↓ GC
1354	v(C-O), δ(C-H), δ(C-OH), pectin, cellulose	[26, 63]	↑ Deficient
1246	v(C-O) cellulose and hemicellulose, asymmetric v(PO ₂ ⁻),	[40, 60]	↑ GC ↓ Deficient
1242	Asymmetric v(PO ₂ ⁻), Amide III	[60]	↑ Live
1097	v(C-O) carbohydrate, asymmetric v(PO ₂ ⁻),	[60, 64]	↑ Deficient*
1049	v(C-O), δ(C-OH) carbohydrate	[60, 65]	↑ GC
1020	v(C-O), v(C-C), δ(C-OH) polysaccharides, pectin,	[26, 60]	↓ Deficient*

* in fixed tissue

3.3 Guard cells versus epidermal cells

GCs are crucial for the regulation of gas exchange (uptake of CO₂ for photosynthesis and loss of water via transpiration) in plants [66]. This is mediated by rapid alterations in the water content of the GC in response to external stimuli, driven by fluxes of osmotically active anion and cations and controlled by a well characterised signalling network [67]. An increase in GC turgor pressure results in the opening of the stomatal pore, thus promoting gas and water exchange, whilst a reduction in turgor pressure closes the stomatal pore[68]. These cells are therefore key indicators of stress and have been studied in response to a range of biotic and abiotic stresses [44, 69-71]. The surrounding ECs act as a barrier to internal and external environments and thus have a relatively simple function in comparison to GCs and consequently, the biochemical composition of stomatal GCs are distinctly different from the surrounding ECs [57]. Here we investigate the suitability of GCs as a target in plant monitoring studies using vibrational spectroscopy by observing the effects of Ca deficiencies on these tissues.

When comparing derivative spectra obtained from GCs and ECs in unfixed tissue, distinct difference in cell wall materials can be seen, particularly regarding cellulosic polysaccharides (**Fig. 4A**). Increased absorbance at 1740, 1246, and 1049 cm⁻¹ corresponding to celluloses and lignins in GCs corresponding the differentially thickened cell walls in these cells, up to 5 um across compared to the 1-2 um typical of ECs, that is essential to GC function (**Table 1**) [68]. Increased absorbance at the amide I band at 1637 cm⁻¹, also indicates a markedly different protein structure in GCs compared to ECs which may be due to the varying functions of each cell, with GCs responding dynamically to changes environmental conditions, whereas epidermal cells require a constant protein conformation to maintain overall leaf structure. Interestingly, the levels of unesterified pectins, another crucial cell wall component, are considerably higher in the epidermis, which has also been observed in other studies [57]. This could be indicative of the ordered structure of epidermal tissues, which are maintained by Ca-pectin cross-linking that provides structural support to the leaf.

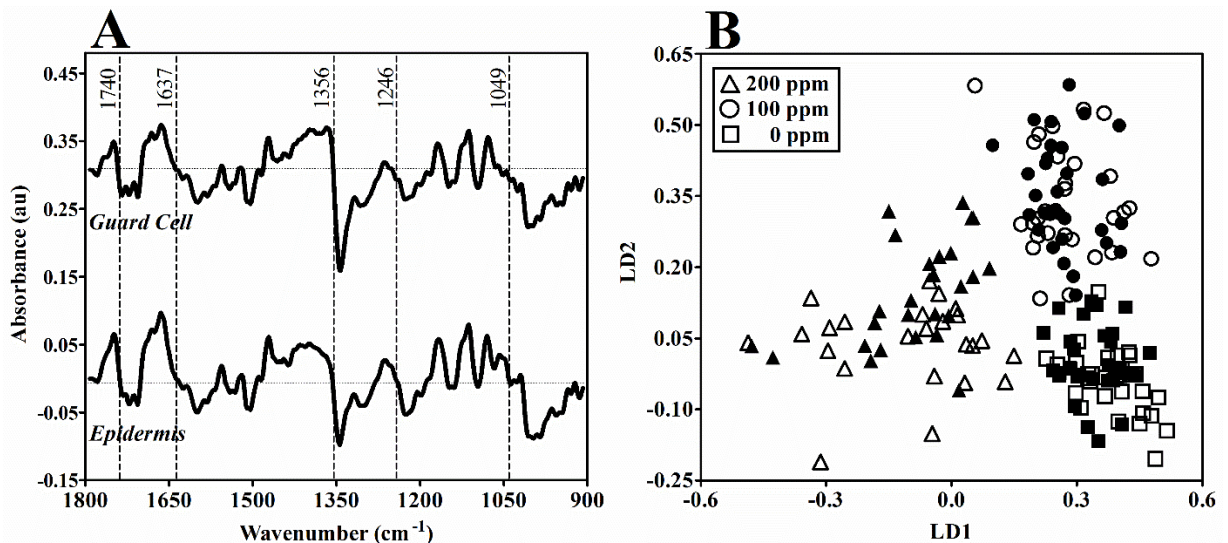


Figure 4. SR-FTIR spectral analysis of unfixed abaxial epidermis from *C. communis*. **(A)** Pre-processed spectra from guard cells (GCs) that surround the stomatal pore are compared with surrounding ECs to identify differences in biomolecular composition. Spectra were cut to the fingerprint region ($1800 - 900 \text{ cm}^{-1}$), first order differentiated, vector normalised and offset for clarity, whilst dashed markers indicate the wavenumber regions that most discriminate between the two classes. **(B)** A 2-dimension scores plot of cross validated PCA-LDA (leave-one-out) to compare the suitability GCs (\blacktriangle \bullet \blacksquare) and ECs (\triangle \circ \square) as screening targets for detection of Ca deficiencies. 200 ppm is defined as optimal conditions, whereas 0 ppm is defined as Ca deficient.

As a preliminary step to compare the suitability of GCs versus ECs as targets for monitoring nutrient deficiencies, exploratory multivariate analysis was conducted on the data (Fig. 4B). The 2D PCA-LDA scores plot examines the differences between the three Ca treatments, and whether any effects are more apparent in GCs or ECs. It is clear that Ca treatments effectively split the classes, showing that there is an observable alteration in the spectra as a consequence of Ca depletion, which is further investigated later in this study. With regards to the two target tissues, both GC and the epidermis tend to separate almost identically with the Ca stress, indicating that both tissues are potentially suitable targets for nutrient screening. An optimum level of Ca in this study is defined as 200 ppm, and this class of data significantly ($P < 0.001$) separates from depleted treatments in LD1, whereas differences between depleted samples separate in LD2. Within the control treatment cluster, there are some subtle differences between GC and the epidermis although this separation is not visible in lower Ca treatments. This may be due to fundamental alterations associated with Ca stress overhauling the sensitive variance differences between guard and epidermal cells.

3.4 Ca deficiency

The effects of Ca availability in the growth environment (optimal Ca, 200 ppm; low Ca, 100 ppm; Ca deficient, 0 ppm) on the SR-FTIR spectra obtained from living and fixed tissues from *C. communis* was examined to determine the spectral alterations indicative of nutrient deficiency, and whether this spectral information is sufficient to accurately identify plants undergoing nutrient stress.

The processed spectra from each of the tissues exposed to three Ca environments, depict clear absorbance alterations throughout the fingerprint region (**Fig. 5; Table 1**). In both *ex vivo* tissues and fixed tissue samples, absorbance bands associated with proteins are shown to decrease consistently in response to Ca deficiency, specifically around the Amide I region (1635 and 1630 cm^{-1}) and Amide II (1522 and 1487 cm^{-1}) regions. This observation is more apparent in spectra acquired from unfixed tissues (**Fig. 5A and 5B**), in comparison to fixed tissue (**Fig. 5C**), which in this case is associated with the formalin fixation process. As mentioned previously, this sample preparation step can result in protein cross linkages and may therefore increase protein stability at the point of spectral acquisition. An overall reduction in protein absorbance may be indicative of a compromised structure, and possibly be an earlier indicator of senescence [24].

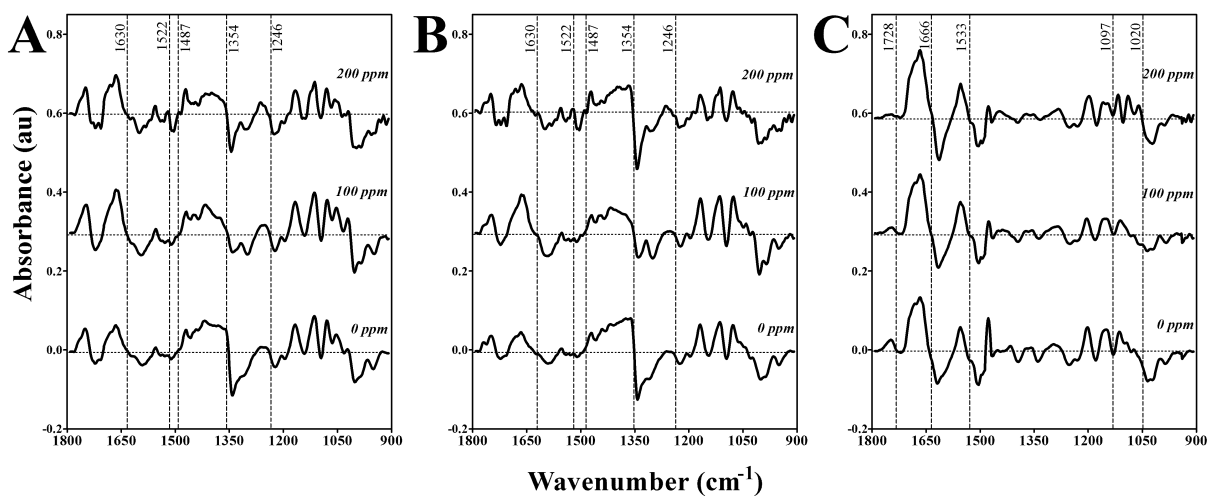


Figure 5. Pre-processed spectra comparing the effects of varying Ca availabilities in guard cells (GCs) (**A**) and epidermal cells (ECs) (**B**) from unfixed epidermal peels; additional to fixed tissue samples (**C**) samples. Spectra were cut to the fingerprint region ($1800 - 900\text{ cm}^{-1}$), first order differentiated, vector normalised and offset for clarity, whilst dashed markers indicate the wavenumber regions that most discriminate between the two classes.

Furthermore, widespread polysaccharide absorbance differences can be seen across all samples as a consequence of Ca stress. Interestingly, in fixed samples, these differences are limited to the lower wavenumber region between 1200 - 1050 cm^{-1} , whereas in unfixed tissues, both GCs and the epidermis, these alterations manifest around 1550 - 1250 cm^{-1} . Many valuable plant substances have characteristic IR bond vibrations across the whole spectrum and there are few regions specific to a given biomolecule, showing that this unlikely to be due to a single molecule. However, this difference may again infer details about the chemical fixation process on plant tissue prior to IR spectroscopic analysis, as fixation has had a substantial impact on bond vibrations in the lower wavenumber region, where simple bending vibrations are found [72]. It is evident from Figure 5, that the absorbance of pectin-related IR bands (1728, 1354 and 1097 cm^{-1}) increase due to Ca deficiency, and may indicate an increased production of structural polymers to accommodate the reduction in structural Ca pectate. In contrast, absorbance bands associated with cellulosic compounds (1246 and 1020 cm^{-1}) illustrate a clear decline due to Ca deficit. Similar to protein absorbance, this may be symptomatic of a decrease in tissue viability, as cell wall growth and expansion is hampered due to lack of Ca.

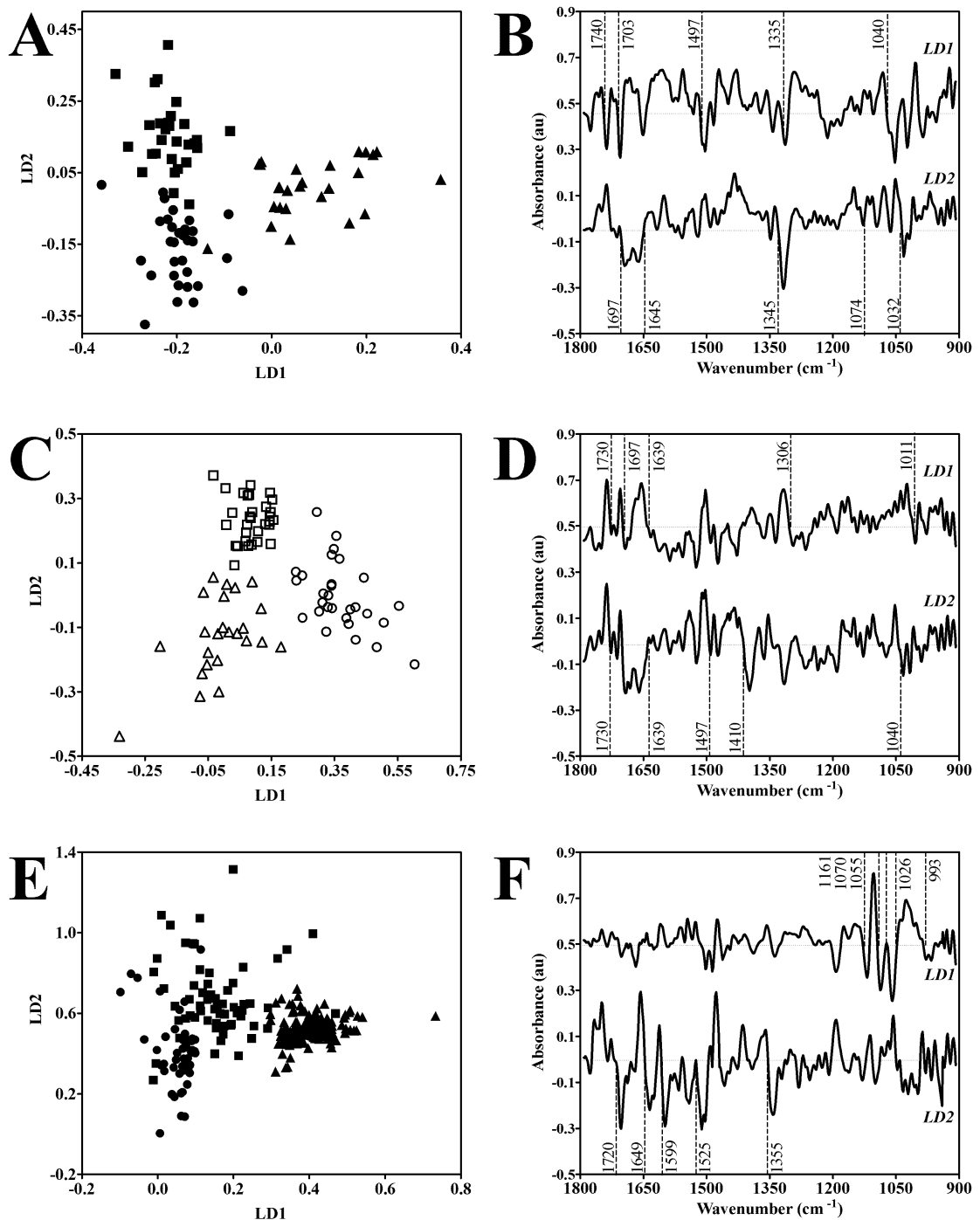


Figure 6. Leave-one-out cross validated PCA-LDA analysis of both fixed and unfixed *C. communis* samples. (A), (C) and (E) display the 2-dimensional scores plots from guard cells (GCs), epidermal cells (ECs) and fixed tissue, whilst (B), (D) and (F) show the corresponding first and second linear discriminant loadings from GCs, ECs and fixed tissue, respectively. The most discriminating wavenumbers are indicated with a dashed line for each individual loading.

Table 2. Discriminating biomarkers of Ca deficiency as derived from PCA-LDA analysis of SR-FTIR spectra of unfixed and fixed *C. communis* samples exposed to low Ca availabilities.

Wavenumber (cm ⁻¹)	Tentative Band Assignment	Ref.
1740	v(C=O) polysaccharide, esterified pectin, lipids	[59, 60]
1730	v(C=O) ester, lipid, lignin	[41, 60]
1720	v(C=O) unsaturated ester, pectin	[27]
1703	v(C=O)	[73]
1697	v(C=O)	[60]
1649	v(C=O), v(C=N) Amide I	[40, 62, 74]
1645	Amide I	[60]
1639	Amide I	[60]
1599	v(COO-) pectin, carboxylic acids, v(C=C) lignin	[41, 75, 76]
1525	Amide II, C=N, C=C	[27, 60]
1497	δ(C-H) Amide II	[26]
1410	δ(NH), δ(CH), v(C-N) polysaccharides	[57, 60]
1355	δ(C-OH) polysaccharide	[63]
1345	Carbohydrate	[77]
1335	δ(CH) polysaccharides, pectin, cellulose	[60]
1306	Amide III	[60]
1161	v(C-OH), v(C-O-C) polysaccharide, cellulose	[53, 64, 75]
1074	v(CO), v(CC)	[60]
1070	v(CO), v(CC) cellulose	[78]
1055	v(CO), v(CC), δ(C-OH), pectin	[78]
1040	v(CO), v(CC), cellulose	[78]
1032	v(O-CH ₃) cellulose	[29, 60]
1026	v(CO), v(CC) cellulose	[76]
1011	v(CO), v(CC), δ(C-OH), pectin	[26, 60]
933	Carotenoid, carbohydrate	[60, 79]

Cross-validated PCA-LDA, using a leave-one-out approach, was conducted on the spectral data in order to maximise the interclass differences, and separate data based upon the nutrient availability [80]. **Fig. 6** depicts the 2D scores plots from this data reduction step, and the consequent loadings plots transformed from this data, indicating spectral regions where variance is apparent in the dataset, as described by Martin et al. [81]. Tentative bond assignments for spectral peaks described as accountable for variance in the dataset can be seen in Table 2. Initially, spectra obtained from GCs of unfixed epidermal peels, separate strongly with regards to Ca depletion (**Fig. 6A**). The control treatment of 200 ppm is almost entirely separated from low Ca treatments in LD1, whilst low Ca treatments are distinguishable in LD2. This may indicate that the general response of the plant to Ca deficiency is readily observable compared to optimum Ca conditions, whereas a subtle, yet still discernible, difference may be found in the response to different levels of Ca deficiency. With regards to exact wavenumber regions where variance can be found between Ca treatments, observations in the loadings of LD1 and LD2 may shed light on these subtle differences. LD1 indicates major differences around the polysaccharide region at 1055 cm^{-1} , likely to be correlated to pectin absorbance (**Fig. 6B**). A decrease in Ca, would substantially affect the Ca pectate levels in the plant tissues, and thus this response is as expected between the optimal and Ca deficient treatments. Alterations in $\nu(\text{C=O})$ are also evident in the loadings, which can be assigned to both lignin and protein contributions to the spectrum, possibly highlighting a structural compensation as a consequence of integrity loss. The same response can be seen in LD2; however, the most discriminatory spectral region in this curve is attributed to polysaccharides. This could potentially infer that this region may be used to discriminate between levels of Ca deficiency, in this targeted group of cells. In order to determine the diagnostic potential of this study, a PCA-LDC was conducted on the sample data, which was shown to positively classify Ca deficient, low Ca and optimal Ca samples at a rate of 100, 93.75, and 96.15% respectively (**Table 3**). This is promising in regards to future studies on large datasets taken from field data, which will likely be highly variable in comparison to a laboratory based investigation. It is important to note that the use of SR-FTIR for studies *in planta* in the field would be impossible, and so the use of a less powerful technique, such as standard globar-based FTIR microspectroscopy, may not provide such high levels of accuracy. As such it is

encouraging that near perfect classification is possible with the highly sensitive SR-FTIR approach. Additionally, one difficulty with detection and consequent remediation of nutrient deficiencies is that they are often co-dependent upon the availability of other nutrients, yet such a high accuracy rate even for intermediate deficiency samples is promising [82, 83]. As such, it may be possible to identify nutrient deficiencies in the field and instigate a targeted nutrient remediation process.

Table. 3 Classification rates of each tissue sample and Ca treatment (%) as derived from principal component analysis (PCA) fed linear discriminant classifiers, using a leave-one-out approach and 10 *k*-folds

	Classification Rate (%) \pm SE		
	0 ppm	100 ppm	200 ppm
Unfixed Guard Cell	100.0 \pm 0.0	93.75 \pm 4.49	96.15 \pm 3.92
Unfixed Epidermis	100.0 \pm 0.0	93.10 \pm 4.96	95.83 \pm 4.26
Fixed Tissue	75.84 \pm 6.30	91.49 \pm 4.30	99.43 \pm 0.06

Spectra obtained from living epidermal tissues exhibit a similar degree of separation within a 2D PCA-LDA scores plot, although it is the low (100 ppm) Ca treatment that separates on LD1, and the optimal (200 ppm Ca) and deficient (0 ppm Ca) treatments that separate effectively in LD2 (**Fig. 6C & 6D**). Loadings derived from this dataset correlate with findings in analysis of live GCs, that depict that the low Ca treatment is identifiable by protein differences, specifically at the Amide III region, shown in LD1. Additionally, deficient and optimal Ca treatments can be primarily isolated due to Amide I protein alterations. As shown earlier in this study, epidermal tissue has distinctly less polysaccharide content, and thus spectral alterations as a consequence of Ca depletion are less likely to be visible in the absorbance of these molecules. Despite this, the rate of classification in this dataset remains high at 100, 93.10 and 95.83% for deficient, low and optimal Ca treatments (**Table 3**). This indicates that epidermal tissue is marginally less efficient at identifying Ca deficiencies than GCs; however, this is a minimal reduction in efficiency and is likely insignificant.

In fixed tissue, 2D PCA-LDA scores plots indicate an almost identical separation pattern to that seen in multivariate analysis of spectra from live GCs, with the optimal Ca

treatment effectively separating in LD1 (**Fig. 6E**). There is a larger degree of overlap between Ca treatment groups in fixed tissue, and may indicate enhanced difficulty at detecting subtle biological changes as a consequence of Ca depletion. This is further highlighted in looking at the classification accuracy within this dataset in **Table 3**, which depicts reduced identification of samples grown in Ca deficient conditions, at a rate of 75.84%. This class is particularly spread in the scatterplot, indicating increased variability in these samples which may suggest that the fixation process had a greater detrimental effect upon the Ca deficient samples. The optimal Ca treatment groups together relatively tightly in comparison, reflected by a high classification rate of 99.43%.

Interestingly, loading plots derived from this dataset exhibit a striking response in LD1 and 2, with the former highlighting spectral alterations solely below 1200 cm^{-1} , and the latter exclusively above 1300 cm^{-1} (**Fig. 6F**). As a consequence, the optimal Ca treatment that is clearly distinguishable in LD1, is primarily segregated due to variance in polysaccharides, particularly cellulose. The differences between the Ca deficient and low Ca treatments shown in LD2, can be correlated predominantly with protein alterations, and also pectin and lignin molecules. The pattern displayed here in fixed tissue correlates with the differences observable in spectra derived from *in vivo* measurements of GCs, that show that the major differences in spectra explained by LD1, are largely attributed to polysaccharide alterations. This is intuitive due to the known effect of Ca deficiency on tissue structure; that as the Ca availability reduces, less Ca pectate is found in tissues, which may be responsible for the large polysaccharide changes we observe here. Also, alterations in cellulose and other cell wall carbohydrates such as arabinose and galactose levels may be an indicator of increased production to account for weaknesses in tissue structure as a consequence of Ca depletion [84].

4 Conclusions

The use of SR-FTIR for plant-based studies has, to date, been relatively underdeveloped as the strong absorption of water in the fingerprint region can often conceal spectral information, particularly in live tissue samples. In this study, we investigated the ability of such an approach to identify Ca deficiencies in both living and fixed tissue, to determine how accurately this can be determined prior to the appearance of nutrient deficiency symptoms. Due to the high flux density of SR, the interference from water

can be minimised, allowing sampling from isolated epidermal tissues. The ability to sample from living tissues, is promising for further investigations using SR-FTIR *in planta*, and also prevents the need to fix tissue samples, which is both time consuming and detrimental to the spectral output, including the ability to detect Ca deficiencies.

Using this approach, it is possible to differentiate between specific cell types on the abaxial leaf surface of leaves by observing increased levels of absorbance in cellulosic compounds in GCs compared to ECs. In order to determine a standard approach for crop screening in the field, it is first important to establish an ideal target for spectroscopic analysis. Initially, leaves are an ideal focus as they are relatively disposable, and readily exhibit symptoms of stress; however, the heterogeneity of such tissues indicates the need to identify a sole target for screening. Using the highly specific approach of SR-FTIR, both GCs and ECs performed equally well in detection of Ca deficiency prior to symptom onset, and were able to identify both low Ca and Ca deficient treatments at above 90% classification accuracy. As both cell types were uniform in their suitability, it could indicate that the whole epidermis of a leaf could be an ideal target for field trials observing nutrient deficiencies. As a prerequisite for such trials, the proficiency at which a globar based FTIR study is able to accurately detect Ca deficiencies is needed.

In this study, we show that SR-FTIR as a crop screening tool, is able to accurately determine the Ca nutrient status of *C. communis* leaf samples grown at a range of Ca availabilities. Such a technique would not only be highly beneficial for wider nutrient screening applications, but also for identifying other abiotic stresses such as ozone damage, and biotic stresses including pest infestations [30]. In doing so, the overall efficiency of our agricultural practises can be improved with targeted remediation, that will increase yield and contribute towards the global food security.

5 Acknowledgements

HJB is a member of the Centre for Global Eco-Innovation funded by the European Union Regional Development Fund. This project is in collaboration with Plant Impact Plc. Special thanks to Dionysios Touliatos for his guidance with hydroponic plant cultivation.

7 Bibliography

- [1.] Mechlem K, European Law Journal 10 (2004) 631-648.
- [2.] Godfray HCJ, Beddington JR, Crute IR, Haddad L, Lawrence D, Muir JF, et al., science 327 (2010) 812-818.
- [3.] Rosegrant MW, Cline SA, Science 302 (2003) 1917-1919.
- [4.] Licker R, Johnston M, Foley JA, Barford C, Kucharik CJ, Monfreda C, et al., Global ecology and biogeography 19 (2010) 769-782.
- [5.] Roy R, Finck A, Blair G, Tandon H, A guide for integrated nutrient management FAO Fertilizer and Plant Nutrition Bulletin 16 (2006) 368.
- [6.] Stewart W, Dibb D, Johnston A, Smyth T, Agronomy Journal 97 (2005) 1-6.
- [7.] Fageria N, Baligar V, Advances in agronomy 88 (2005) 97-185.
- [8.] Snyder C, Bruulsema T, Jensen T, Fixen P, Agriculture, Ecosystems & Environment 133 (2009) 247-266.
- [9.] Hillier J, Hawes C, Squire G, Hilton A, Wale S, Smith P, International Journal of Agricultural Sustainability 7 (2009) 107-118.
- [10.] Graham RD. Micronutrient deficiencies in crops and their global significance. *Micronutrient deficiencies in global crop production*: Springer; 2008. p. 41-61.
- [11.] Jones RW, Lunt O, The Botanical Review 33 (1967) 407-426.
- [12.] White PJ, Broadley MR, Annals of botany 92 (2003) 487-511.
- [13.] White PJ, Journal of Experimental Botany 52 (2001) 891-899.
- [14.] Clarkson DT, Plant, Cell & Environment 7 (1984) 449-456.
- [15.] Simon E, New phytologist 80 (1978) 1-15.
- [16.] Taylor MD, Locascio SJ, Journal of plant nutrition 27 (2004) 123-139.
- [17.] Kirkby E, Pilbeam D, Plant, Cell & Environment 7 (1984) 397-405.
- [18.] Raese JT, Drake SR, Journal of plant nutrition 16 (1993) 1807-1819.
- [19.] Auernhammer H, Computers and electronics in agriculture 30 (2001) 31-43.
- [20.] Robert P, Plant and soil 247 (2002) 143-149.
- [21.] Bradfield E, Spincer D, Journal of the Science of Food and Agriculture 16 (1965) 33-38.
- [22.] Wolf B, Communications in Soil Science and Plant Analysis 13 (1982) 1035-1059.
- [23.] Yu P, British journal of nutrition 92 (2004) 869-885.
- [24.] Butler HJ, McAinsh MR, Adams S, Martin FL, Analytical Methods 7 (2015) 4059-4070.
- [25.] Butler HJ, Ashton L, Bird B, Cinque G, Curtis K, Dorney J, et al., Nature protocols 11 (2016) 664-687.
- [26.] Schulz H, Baranska M, Vibrational Spectroscopy 43 (2007) 13-25.
- [27.] Schulz H, Özkan G, Baranska M, Krüger H, Özcan M, Vibrational Spectroscopy 39 (2005) 249-256.

[28.] Baranski R, Baranska M, Schulz H, *Planta* 222 (2005) 448-457.

[29.] Ribeiro da Luz B, *New Phytologist* 172 (2006) 305-318.

[30.] Ord J, Butler HJ, McAinsh MR, Martin FL, *Analyst* (2016).

[31.] Martin FL, *Nat Meth* 8 (2011) 385-387.

[32.] Miller L, Carr G, Jackson M, Dumas P, Williams G, *Synchrotron Radiation News* 13 (2000) 31-38.

[33.] Duncan W, Williams GP, *Applied optics* 22 (1983) 2914-2923.

[34.] Dumas P, Sockalingum GD, Sulé-Suso J, *Trends in Biotechnology* 25 (2007) 40-44.

[35.] Vijayan P, Willick IR, Lahlali R, Karunakaran C, Tanino KK, *Plant and Cell Physiology* (2015) pcv080.

[36.] Bonwell ES, Fisher TL, Fritz AK, Wetzel DL, *Vibrational Spectroscopy* 48 (2008) 76-81.

[37.] Raab TK, Martin MC, *Planta* 213 (2001) 881-887.

[38.] Thumanu K, Sompong M, Phansak P, Nontapot K, Buensanteai N, *Journal of Plant Interactions* 10 (2015) 270-279.

[39.] Kumar S, Lahlali R, Liu X, Karunakaran C, *Applied Spectroscopy Reviews* 51 (2016) 466-483.

[40.] Yu P, McKinnon JJ, Christensen CR, Christensen DA, Marinkovic NS, Miller LM, *Journal of agricultural and food chemistry* 51 (2003) 6062-6067.

[41.] Heraud P, Caine S, Sanson G, Gleadow R, Wood BR, McNaughton D, *New Phytologist* 173 (2007) 216-225.

[42.] Dokken KM, Davis LC, *Journal of Agricultural and Food Chemistry* 55 (2007) 10517-10530.

[43.] Bonnier F, Petitjean F, Baker MJ, Byrne HJ, *Journal of biophotonics* 7 (2014) 167-179.

[44.] McAinsh MR, Clayton H, Mansfield TA, Hetherington AM, *Plant Physiology* 111 (1996) 1031-1042.

[45.] Hoagland DR, Arnon DI, *Circular California Agricultural Experiment Station* 347 (1950).

[46.] WEYERS JDB, TRAVIS AJ, *Journal of Experimental Botany* 32 (1981) 837-850.

[47.] Wehbe K, Filik J, Frogley MD, Cinque G, *Analytical and bioanalytical chemistry* 405 (2013) 1311-1324.

[48.] Trevisan J, Angelov PP, Scott AD, Carmichael PL, Martin FL, *Bioinformatics* (2013) btt084.

[49.] Martin FL, Kelly JG, Llabjani V, Martin-Hirsch PL, Patel II, Trevisan J, et al., *Nature protocols* 5 (2010) 1748-1760.

[50.] Daley CM, (2008).

[51.] Miller LM, Dumas P, *Biochimica et Biophysica Acta (BBA) - Biomembranes* 1758 (2006) 846-857.

[52.] Himmelsbach D, Khalili S, Akin D, *Cellular and molecular biology* 44 (1998) 99-108.

[53.] Dokken KM, Davis LC, Marinkovic NS, *Applied Spectroscopy Reviews* 40 (2005) 301-326.

[54.] Tobin MJ, Puskar L, Barber RL, Harvey EC, Heraud P, Wood BR, et al., *Vibrational Spectroscopy* 53 (2010) 34-38.

[55.] Baker MJ, Trevisan J, Bassan P, Bhargava R, Butler HJ, Dorling KM, et al., *Nature protocols* 9 (2014) 1771-1791.

[56.] Hughes C, Gaunt L, Brown M, Clarke NW, Gardner P, *Analytical Methods* 6 (2014) 1028-1035.

[57.] Jones L, Milne JL, Ashford D, McCann MC, McQueen-Mason SJ, *Planta* 221 (2005) 255-264.

[58.] Faolain EO, Hunter MB, Byrne JM, Kelehan P, McNamara M, Byrne HJ, et al., *Vibrational Spectroscopy* 38 (2005) 121-127.

[59.] Chatjigakis AK, Pappas C, N.Proxenia, O.Kalantzi, P.Rodis, Polissiou M, *Carbohydrate Polymers* 37 (1998) 395-408.

[60.] Movasaghi Z, Rehman S, ur Rehman DI, *Applied Spectroscopy Reviews* 43 (2008) 134-179.

[61.] Shih M-D, Hsieh T-Y, Jian W-T, Wu M-T, Yang S-J, Hoekstra FA, et al., *Plant Science* 196 (2012) 152-159.

[62.] Gidman E, Goodacre R, Emmett B, Smith AR, Gwynn-Jones D, *Phytochemistry* 63 (2003) 705-710.

[63.] Geun Goo B, Baek G, Jin Choi D, Il Park Y, Synytsya A, Bleha R, et al., *Bioresource Technology* 129 (2013) 343-350.

[64.] Brown DM, Zeef LA, Ellis J, Goodacre R, Turner SR, *The Plant Cell* 17 (2005) 2281-2295.

[65.] Kacurakova M, Capek P, Sasinkova V, Wellner N, Ebringerova A, *Carbohydrate Polymers* 43 (2000) 195-203.

[66.] Schroeder JI, Allen GJ, Hugouvieux V, Kwak JM, Waner D, *Annual review of plant biology* 52 (2001) 627-658.

[67.] McAinsh MR, Brownlee C, Hetherington AM, *Physiologia Plantarum* 100 (1997) 16-29.

[68.] McAinsh M. Water relations of plants: Stomata. In: B. Thomas DM, B. Murray, editor. *Plant Encyclopedia of Applied Plant Science*. Academic Press, London: Academic Press, London; 2003. p. 1459-1466.

[69.] Ng CK-Y, Carr K, McAinsh MR, Powell B, Hetherington AM, *Nature* 410 (2001) 596-599.

[70.] McAinsh MR, Evans NH, Montgomery LT, North KA, *New Phytologist* 153 (2002) 441-447.

[71.] Shen L, Sun P, Bonnell VC, Edwards KJ, Hetherington AM, McAinsh MR, et al., *Frontiers in plant science* 6 (2015).

[72.] Coates J, *Encyclopedia of analytical chemistry* (2000).

[73.] Ashokkumar R, Ramaswamy M, *Int J Curr Microbiol Appl Sci* 3 (2014) 395-396.

[74.] Sene C, McCann MC, Wilson RH, Grinter R, *Plant Physiology* 106 (1994) 1623-1631.

[75.] Chen L, Carpita NC, Reiter WD, Wilson RH, Jeffries C, McCann MC, *The Plant journal : for cell and molecular biology* 16 (1998) 385-392.

[76.] Monti F, Dell'Anna R, Sanson A, Fasoli M, Pezzotti M, Zenoni S, *Vib Spectrosc* 65 (2013) 36-43.

[77.] Allwood JW, Ellis DI, Goodacre R, *Physiologia plantarum* 132 (2008) 117-135.

[78.] Wilson RH, Smith AC, Kačuráková M, Saunders PK, Wellner N, Waldron KW, *Plant Physiology* 124 (2000) 397-406.

[79.] Erukhimovitch V, Hazanovsky M, Huleihel M, *Spectroscopy* 24 (2010) 609-619.

[80.] Trevisan J, Angelov PP, Carmichael PL, Scott AD, Martin FL, *Analyst* 137 (2012) 3202-3215.

[81.] Martin FL, German MJ, Wit E, Fearn T, Ragavan N, Pollock HM, *Journal of Computational Biology* 14 (2007) 1176-1184.

[82.] Maas E, Grieve C, *Plant, Cell & Environment* 10 (1987) 559-564.

[83.] Geraldson C, *Soil Science Society of America Journal* 21 (1957) 621-625.

[84.] Konno H, Nakashima S, Maitani T, Katoh K, *Physiologia Plantarum* 107 (1999) 287-293.

Chapter 7

Pre-symptomatic detection of Ca stress in tomato using vibrational spectroscopy and next generation sequencing

Holly J. Butler, Steve Adams, Martin R. McAinsh, and Francis L. Martin

Submitted for publication: Nature Communications

Contribution:

I conducted all experimental work

I wrote and prepared the manuscript for publication

I produced all figures

Professor F. L Martin

Dr. Martin. R. McAinsh

H. J. Butler

Pre-symptomatic detection of calcium deficiency *in tomato* using vibrational spectroscopy and RNA-sequencing

Holly J. Butler ^{abc*}, Steve Adams ^d, Martin R. McAinsh ^e, Francis L. Martin ^{af*}

^a *Centre for Biophotonics, Lancaster Environment Centre, Lancaster University, Lancaster LA1 4YQ, UK*

^b *Centre for Global Eco-Innovation, Lancaster Environment Centre, Lancaster University, Lancaster LA1 4YQ, UK*

^c *WestCHEM, Pure and Applied Chemistry, Technology & Innovation Centre, University of Strathclyde, Glasgow, UK, G1 1RD*

^d *Plant Impact Plc, Rothamsted, West Common, Harpenden, Hertfordshire, AL5 2JQ, UKs*

^e *Lancaster Environment Centre, Lancaster University, Lancaster LA1 4YQ, UK*

^f *School of Pharmacy and Biomedical Sciences, University of Central Lancashire, Preston PR1 2HE, UK*

***Correspondence to:**

Miss Holly J. Butler, WESTChem, Pure and Applied Chemistry, Technology & Innovation Centre, University of Strathclyde, Glasgow, G1 1RD, UK; Email: holly.butler@strath.ac.uk; Tel.: +44 (0) 7837 244214

Prof Francis L. Martin, Centre for Biophotonics, LEC, Lancaster University, Lancaster LA1 4YQ, UK; Email: f.martin@lancaster.ac.uk; Tel.: +44(0)1524 510206

Dr Martin R. McAinsh, Lancaster Environment Centre, Lancaster University, Lancaster, LA1 4YQ; Email: m.mcainsh@lancaster.ac.uk; Tel.: +44(0)1524 510553

Abstract

Precision farming relies upon the supply of required macro- and micro-nutrients only, thus preventing excessive fertiliser application, nutrient specific deficiencies and environmental impacts, whilst also improving crop efficiency, with increased produce yield and quality. This requires the rapid determination of crop nutrient requirements to allow targeted nutrient supplementation in agricultural environments, whilst avoiding symptoms of nutrient deficiency, thereby contributing towards global food security. In this study, Raman and Attenuated total reflectance Fourier-transform infrared spectroscopy (ATR-FTIR) were used to detect calcium (Ca) deficiency in *Solanum lycopersicum* prior to the onset of symptoms of 'blossom-end rot' (BER) associated with Ca deficiency. *In vivo* Raman microspectroscopy was able to detect severe Ca deficiency following 4-week exposure to deficient environments, whilst ATR-FTIR spectroscopy of dried plant material could distinguish even subtle deficiency in this time frame. The effect of nutrient remediation was also discernible using these approaches, as well as alterations to the overall Ca content (%) in the plant tissues as determined by flame atomic absorption spectroscopy (FAAS). Analysis of differential expression of genes between Ca deficient and Ca remediated plants revealed novel insights into the transcriptional response to Ca deficiency in plants further increasing understanding crop-nutrient relationships.

This study highlights Raman and ATR-FTIR spectroscopy as a system to pre-sympotomatically detect nutrient deficiencies, such as BER in tomato, allowing the crop specific nutrient status to be determined, fuelling the drive towards targeted nutrient supplementation and overall improvements in agricultural productivity.

Introduction

Crops require a nutrient supply that delivers sufficient levels of essential macro- and micro-nutrients for optimal growth, defined as nitrogen (N), Potassium (K), calcium (Ca), sulphur (S), magnesium (Mg), and zinc (Z), copper (Cu), iron (Fe), manganese (Mn), boron (B), chlorine (Cl), molybdenum (Mo) and cobalt (Co)¹. Nutrient deficiencies can arise when there is an inadequate supply of any of these key elements; a frequent occurrence in agricultural environments, where intense farming practises and inefficient fertiliser use are commonplace due to the limited availability of arable land². The onset of nutrient deficiency is dependent upon the limiting nutrient, crop species, genotype, co-dependence with other nutrients and light, as well as water and CO₂ availability³. Due to the diversity of deficiency symptoms between crop species, as well as delayed, non-specific symptoms, the management of an efficient nutrient supply is challenging. However, there is an increasing pressure to manage crop nutrient availability efficiently in order to achieve the increases in agricultural productivity necessary to meet the food demands of the growing global population, estimated to reach 9 billion people by 2050^{4,5}.

Ca is a secondary macronutrient crucial for plant growth, development and nutrition due to its function in a plethora of fundamental biological processes⁶. These can be broadly divided into signalling and structural roles⁷. Ca is also ubiquitous second messenger in plant signal transduction, thought to be an evolutionary development coupled to maintaining sub-toxic intracellular Ca levels, where it plays an essential role in a variety of plant responses to environmental and developmental stimuli^{8,9}. The resting cytosolic Ca²⁺ concentration within plants cells is 100 – 200 nM, which can be a significant difference compared to the surrounding extracellular material^{7,8}. Ca is also an essential component of the plant cell wall where it forms complexes with pectin polysaccharides, that provide structural stability to the cell and tissue¹⁰. Specifically, Ca ions are able to cross-link the negatively charged carboxyl groups of pectins and consequently provide increased rigidity of the cell wall at high Ca availabilities, particularly in low-ester pectins¹¹. Conversely at low levels of Ca, the cell wall can become weakened and permeable, due to insufficient Ca-pectate interactions¹⁰.

In newly formed tissues, the majority of deposited pectins are in low-ester form and therefore require Ca more readily than highly esterified tissues. Symptoms of Ca

deficiency can be often visible in these tissues, with ‘tip burn’ in lettuce a prime example, where insufficient Ca results in a degradation of the cell wall shown by areas of necrosis at the tip of leaf tissue ¹². Ca deficiencies can also arise in tissues with low rates of transpiration, often resulting in the necrosis of fruit, such as BER in tomatoes^{13,14}. This essential nutrient is considered immobile in the phloem and thus dependent upon the unidirectional flow of the transpiration stream in the xylem⁶. Rapidly transpiring tissues such as mature leaves, can be found to accumulate high levels of Ca, whereas tissues and fruits with low rates of transpiration, can develop Ca gradients and thus display symptoms of deficiency¹⁵. Furthermore, as transport is only possible with the flow of transpiration, Ca cannot be translocated, resulting in differential Ca concentrations throughout the plant ¹⁶. In line with these fundamental roles of Ca in plants, Ca deficiencies are significantly detrimental to crop yields and can manifest in across a range of crop species ¹⁵.

One major issue with the prevention of Ca deficiency disorders in crops, is that visual symptoms often do not become apparent until the deficiency has already had a detrimental effect upon crop quality and yield ¹⁷. In the case of BER, the first truss does not appear until around 6 weeks post-germination, dependent upon the cultivar and environmental conditions, by which point a significant amount of time and resources have been inputted¹⁸. Additionally, visual symptoms are not always unique to deficiency of a specific nutrient and therefore it is not always possible to determine the crop’s nutrient requirements by visual inspection alone ¹⁹.

Analyses of soil and tissue nutrient content, and crop growth responses, provide an alternative to the use of visual symptoms to diagnose nutrient deficiencies ²⁰. The soil, or other growth medium, is the primary source of nutrients, therefore the elemental content can be used infer the levels of nutrients available to the plant ²¹⁻²³. A number of analytical techniques are available to identify the relative abundancies of key nutrients from soil samples, such as flame atomic absorption photometry and spectroscopy, as well as highly sensitive inductively coupled plasma (ICP) based approaches, like ICP – mass spectrometry (ICP-MS) ^{24,25}. Whilst these provide vital information regarding the nutrient status of the environment, this does not necessarily infer the nutrient status of the crop, as uptake is also affected by additional environmental factors ²⁶. Alternatively, these approaches can be applied to plant tissues providing an insight into the specific nutrient content of the crop ^{22,27}. Nutrient deficiencies can also be monitored through

their impact on plant tissue structure using histochemical and microscopic methods ²⁸. In addition, biochemical methods can be used to determine crop nutrient status, based largely around measuring enzymatic activity of key biological processes in both soil and plant tissues ^{1,29}. Furthermore, whole genome transcriptome analysis can be employed to study the molecular impacts of environmental factors, such as nutrient deficiency in crops ^{30,31,32,33}. However, although highly informative, the RNA sequencing approaches used require extensively sample preparation protocols, additional to a substantially high cost-burden.

Despite the availability of the aforementioned approaches for determining plant nutrient status, crop-specific nutritional information is not however routine in the field due to technical limitations inherent in these approaches including their destructive nature, substantial sample preparation time, and confinement to a laboratory setting, which contributes to extended delays in analysis ³⁴. Therefore, non-destructive and high throughput approaches are urgently required for the accurate and rapid determination of plant nutrient status ³⁵.

Light based methodologies are potential non-destructive alternatives to traditional chemical analyses. In particular near infrared (NIR) and visible-NIR reflectance spectroscopy has been widely implemented as a tool for plant composition studies ³⁶. Although this technique has been used to elucidate the nutrient status of crops, and also as a presymptomatic detection method ³⁷⁻³⁹, the derived spectral data are limited and do not provide high enough resolution to infer specific biochemical alterations ⁴⁰. In contrast, application of mid-IR based spectroscopies such as Fourier transform IR (FTIR) and Raman spectroscopy may provide this additional detail, whilst still delivering non-destructive, rapid and *in situ* measurements to be obtained ^{41,42}. Both spectroscopic approaches are based upon the principle that chemical bonds have discrete vibrational modes which can be observed when biological samples are irradiated with IR light ⁴³. FTIR spectroscopy is dependent a change in the dipole moment of a chemical bond and monitors the absorption of energy as electrons are elevated to vibrational energy modes ^{44,45}. This energy absorption is equivalent to the transition energy of the bond, allowing specific bond identification via absorbance spectra ⁴⁶. In contrast, Raman spectroscopy is based upon the principle of inelastic light scattering, where the molecule of interest is excited to a virtual energy state via the incoming photon, but returns to a higher (Stokes)

or a lower (Anti-Stokes) energy level ^{47,48}. Whereas FTIR is dependent upon the dipole of a chemical bond, Raman spectroscopy is reliant upon the change in polarisability ⁴⁹. As such, some bonds that are considered IR inactive are often distinguishable using Raman spectroscopy and vice versa, resulting in two complementary techniques ⁵⁰.

Fourier transform infrared (FTIR) spectroscopy has been used previously to observe plant cell structure and fruit quality, as well as to identify and quantify valuable plant constituents, including polysaccharides and essential oils ⁵¹⁻⁵⁵. Due to the dipole moment of water, FTIR analysis of plant tissue has been largely restricted to fixed sample analysis ⁵⁶⁻⁵⁹. However, the development of attenuated total reflectance (ATR)-FTIR has facilitated the interrogation of plant tissues without the interference of water, thus allowing *in vivo* measurements to be acquired ⁶⁰⁻⁶². In contrast to IR, water has a relatively weak Raman scattering effect and consequently the analysis of *in vivo* plant tissues that contain large amounts of water is possible ⁶³. Nevertheless, the application of Raman spectroscopy in plant research is limited by the issue of autofluorescence that is prominent in plant tissues that contain intrinsic fluorophores ⁶⁴. This issue has been shown to be overcome by the use of NIR laser sources, but is also shown to be less apparent in *in vivo* samples due to the fluorescence quenching effects of water ^{61,65,66}. Consequently Raman spectroscopy has been a powerful technique for investigation of plant cell walls and monitoring plant metabolites ⁶⁷.

Here we describe a study employing ATR-FTIR and Raman spectroscopy to presymptomatically detect Ca deficiency in *Solanum lycopersicum*, prior to the onset of BER. Specifically, the use of Raman spectroscopy for *in vivo* spectroscopic analysis of plant material is investigated, in comparison to the efficiency of ATR-FTIR for fixed sample analysis of nutrient status. Complementary elemental analysis by flame atomic absorption spectroscopy (FAAS) is used to compare to the exact Ca content of the tissue. The effects of Ca deficiency, and subsequent Ca remediation, on gene expression has also been investigated using RNA sequencing technology in order to understand the transcriptional changes underpinning the growth and spectral responses to the differing Ca nutrition of plants.

Materials & Methods

Cultivation conditions

S. lycopersicum cv. Moneymaker (Moles Seeds, Essex, UK) were sown into rock wool cubes and grown for 10 days with a distilled water supply. Once germinated, these seedlings were transferred to purpose-built hydroponic systems, containing 16 L of four modified Hoagland's solutions ⁶⁸. Full-strength Hoagland's solution provided a Ca concentration of 200 ppm, determined as optimum for tomato growth, and sub-optimal levels of 100, 50 and 0 ppm were also used. Dissolved oxygen levels were maintained at 5.5 ± 0.5 mg/L using aquatic air pumps (Boyu, China) with an electrical conductivity at 2 ± 0.1 mS; and pH 6.1 ± 0.1 . The solution was refreshed every 3-7 days, when the levels of conductivity were reduced. Plants were grown at $25 \pm 2^\circ\text{C}$ / $20 \pm 2^\circ\text{C}$, day / night; 16 h photoperiod; $150 \pm 25 \mu\text{mol m}^{-2} \text{ s}^{-1}$ using 600W metal halide lamps (Osram Ltd, UK).

The investigation was separated into two approaches; a 4-week full Ca depletion study, and a 4-week remediation study. For the former, plants were exposed to the different Ca conditions for the full 4-week period, with interrogation at both 2- and 4-week time points with ATR-FTIR, Raman spectroscopy and FAAS to monitor the progress of deficiency. For the latter, plants were exposed to Ca conditions for the initial 2-week period and then provided with optimum levels of Ca for the final 2-week time period, to mimic the remediation process of fertiliser application. Plants were again interrogated using the aforementioned techniques at the 2- and 4-week time points.

Each Ca treatment was replicated in 3 separate hydroponic systems, each containing 4 seedlings, resulting in a total of 48 plants for the full depletion study, and a further 48 plants for the remediation study.

In vivo Raman microspectroscopy

Raman spectroscopic measurements were obtained using a InVia Raman spectrometer (Renishaw Plc, Gloucestershire, UK) with a 785 nm excitation laser and charge coupled device (CCD) detector and a microscope attachment (Leica Microsystems, Buckinghamshire, UK). A x 50 magnification (0.75 numerical aperture), 1200 mm^{-1}

grating, 50% laser power (13 mW at the sample) and a 15 second exposure time were utilised for optimal spectral acquisition across the $2000 - 400\text{ cm}^{-1}$ region. Wavenumber spectral calibration was conducted using a silicon source prior to spectral acquisition.

S. lycopersicum plants were carefully positioned adjacent to the microspectrometer and leaves were held in positon above a gold-coated glass slide; the penetration depth of the laser was not expected to fully transmit through the leaflet and therefore the use of a substrate was precautionary⁶⁹. 10 spectra were acquired at both the 2- and 4-week time point from newly expanded leaflets at the same developmental stage in each live *S. lycopersicum* sample. Outliers were removed using in house developed quality tests that detected insufficient spectral quality (signal-to-noise<10) and any evidence of saturation. Cosmic rays were removed using the ‘Zap’ function in-built into the Wire 4.0 software (Renishaw Plc, Gloucestershire, UK).

ATR-FTIR spectroscopy

Although proven to be a non-destructive technique in principle, the effects of ATR-FTIR interrogation can be seen upon the surface of a living plant leaf, due to the pressure that is required to bring the sample into contact with the internal reflection element (IRE), which can cause localised necrosis⁶¹. For this reason, ATR-FTIR was used only for fixed measurements of fixed plant samples, and compared to the efficiency of *in vivo* Raman spectroscopic measurements which have been shown to have no localised or systemic effects⁶¹.

Prior to ATR-FTIR spectroscopic interrogation, the mass of fresh tissue was measured using a calibrated balance, before being dried at 80° for 48 hours and the mass was further measured to account for dry material weight. Leaf tissue was then isolated and homogenised using a mortar and pestle until a homogenous powder was created. This sample was then carefully deposited upon a low-E mirrIR reflective slide (Kevley Technologies, OH, USA) before spectral analysis. A Bruker TENSOR 27 FTIR spectrometer with Helios ATR attachment (Bruker Optics, Coventry, UK) containing a diamond crystal with approximately a $250 \times 250\text{ }\mu\text{m}$ sampling area was employed to acquired IR spectra. Spectra were obtained at a spectral resolution of 8 cm^{-1} , and a zero-filing option resulting in 3.84 cm^{-1} data spacing, with 32 co-additions and a mirror velocity of 2.2 kHz for optimum signal to noise ratio⁴⁵. A background spectra was acquired prior to each sample measurement. Five spectra were obtained from separate

locations of each sample with the diamond crystal cleaned using distilled water and dried between each measurement.

As ATR-FTIR spectral acquisition was conducted upon dried samples, a number of plant samples were required to be excluded from the remaining experiment at the 2-week time point. As such, only one single plant was analysed from each hydroponic system, resulting in 3 samples per treatment at this time point (rather than 9 at 4-weeks). This did not affect Raman interrogation as this step did not require sample exclusion.

Spectral pre-processing

Spectral processing was conducted within the IRootLab Toolbox (<https://github.com/trevisanj/irootlab>) developed for MATLAB (The Math Works, MA, USA), unless otherwise stated⁷⁰. For Raman data, spectra were cut to 1700 – 500 cm⁻¹ wavenumbers to account for the scattering regions of known biological constituents of plant material. A polynomial baseline correction (fifth order) was applied to remove any baseline features associated with background fluorescence. This was followed by a vector normalisation step to account for any technical variation between samples, and a wavelet denoising step to smooth any residual noise in the spectra⁷¹.

For IR data, spectra were cut to the 1800 – 900 cm⁻¹ fingerprint region where biological bonds are known to vibrate⁷². A second order differentiation step, with a polynomial order of two and 9 filter coefficients, was applied to deconvolute spectral regions from the numerous overlapping bands of this complex spectrum. This was then followed by a vector normalisation step.

Multivariate Analysis

The complexity of IR and Raman spectra can often require additional processing steps in order to extract discriminatory information, whilst simultaneously reducing the computational burden associated with such large datasets. Principal component analysis (PCA) was implemented technique to unearth underlying spectral variance between test classes, by reducing each spectrum down to a defined number of principal components (PCs), each of which accounting for a decreasing proportional of variance in the dataset⁷³. This unsupervised technique was coupled to a supervised technique called linear discriminant analysis (LDA), that takes into account class information as well as spectral covariance as derived from PCA⁷⁴. The result of this multi-stage analysis process is

between-class (inter) differences are maximised, whilst within-class (intra) differences are minimised, producing more efficient spectral classification.

In this approach, the optimum number of PCs was determined for each dataset using a Pareto function to account for the point at which the percentage variance explained reached a plateau. This was found to be between 12-13 PCs for each dataset and accounted for 94 – 99% of the spectral variance in each dataset. A leave-one-out cross validation step with 10 k-folds was then conducted using the optimum PC number in conjunction with LDA ⁷⁵. The output of this was visualised as a 1-dimensional (1D) scores plot, to illustrate separation between Ca treatments solely down to variance within the spectra.

To quantify the capabilities of both Raman and ATR-FTIR spectroscopy for detection of nutrient status, a support vector machine (SVM) classification algorithm was implemented. The c and gamma values were optimised during this process, and a leave-one-out cross validation system was used; the output of this was visualised as sensitivity and specificity (%) between the Ca treatment class and the control. Binary classifiers were chosen as the control treatment of 200 ppm, can be considered the baseline prior to deficiency and consequently moderate to severe deficiency were compared against this value.

Flame Atomic Absorption Spectroscopy

Around 500 mg of dried tissue from each Ca treatment and time point was initially digested in 10 cm³ of concentrated HNO₃ (Sigma-Aldrich Ltd, Dorset, UK) at 200°C on a digital hot plate (Bibby Scientific Ltd, Staffordshire, UK; SD500). This was allowed to reflux in the sealed volumetric flask for around 2 h, or until full digestion had been completed, visualised by no coloured fumes. Once complete, the remaining HNO₃ was allowed to evaporate, and the residual material was re-dissolved in 24.5 cm³ of 5% HNO₃ and 0.5 cm³ of 1% LaCl₃ to ensure full Ca extraction, and filtered using a Whatman® 541 hardened, ashless filter paper (Fisher Scientific, Leicestershire, UK). An AAnalyst 200 flame atomic absorption spectrometer (Perkin Elmer, MA, USA) with acetylene gas, compressed air and a Ca-Mg lamp (422.7 nm) was employed to determine the Ca concentration in each digested sample. Samples were digested accordingly to fulfil the linear range of the spectrometer. Three replicates were taken per sample, with a

read delay of three seconds, and each absorbance value was converted to ppm using a calibration curve, and subsequently % Ca values were derived.

RNA-sequencing

Whole transcriptome sequencing was conducted at the 4-week time point, upon 3 control (200 ppm), 3 full-deficiency (0 ppm) and 3 remediated treatments (0 ppm for two weeks, followed by 200 ppm for remaining two weeks) *S. lycopersicum* samples. Newly expanded leaflets were excised and immediately freeze dried using liquid N and homogenised into a powder. RNA was extracted using the RNeasy Plant Mini Kit (Qiagen, Manchester, UK), following the Qiagen protocol with input from previous literature⁷⁶. The RNA quantity per sample was determined using spectrophotometry, with the absorbance at 260 nm (A₂₆₀) used for quantification and the ratio between A₂₆₀ and A₂₈₀ used to establish adequate RNA purity.

Samples were analysed at The Genome Analysis Centre (TGAC), Norwich, UK for RNA-sequencing using the Illumina HiSeq 2000 (Illumina, CA, USA), with a 50 base pair (bp) single end read metric, with a minimum yield of 100 million reads. Quality control was conducted using FastQC (Babraham Bioinformatics, Cambridgeshire, UK) to check for the basic metric of quality control in the raw data, and the TGAC in-house contamination screening ‘Kontaminant’ was run to identify any adulterated samples. RNA samples were mapped to a reference sequence, provided by The International Tomato Genome Sequencing Consortium, using TopHat (Centre for Computational Biology, John Hopkin University, MD, USA) and differential expression levels across the three experimental treatments were constructed using Cufflinks 2.2.1 (Trapnell Lab, University of Washington, WA, USA). The outputs of this was visualised using the CummeRbund package (Bioconductor, USA).

The mapped sequence tool SeqMonk (Babraham Bioinformatics, Cambridgeshire, UK) was also used to visualise gene expression between Ca treatments. Initially data store trees were used to visualise the clustering of biological replicates as an additional form of quality control. Hierarchical clustering was then used to generate heat maps of differentially expressed genes based on the intensity differences. These gene clusters were then annotated using the PANTHER Classification System to determine specific gene function^{77,78}.

Results & Discussion

Fresh and dry weight analysis

Determination of nutrient status of crops is currently reliant upon visual symptoms of deficiency, or chemical analyses of crop or soil samples^{19,22}. Although visual symptoms may take time to manifest, such as the rotting of fruit in BER, the effects of nutrient deficiency may be observable in simple growth parameters which may indicate underlying stress. **Figure 1** shows the effects of Ca Treatments and Ca remediation on plant fresh and dry weight. The effect of Ca deficiency should be most evident in plants exposed to reduced Ca levels for 4 weeks ('Full Treatment'), particularly by the week 4 and to a lesser extent at 2-weeks. It is clear that after 2 weeks of reduced Ca availability, there is a distinct difference in weights between the 0 and 200 ppm Ca, representing fully deficient and optimum Ca (control), respectively, although this is not statistically significant. This pattern is almost identical for both fresh and dry weight, suggesting that the water content in each sample was not affected by the reduced Ca level.

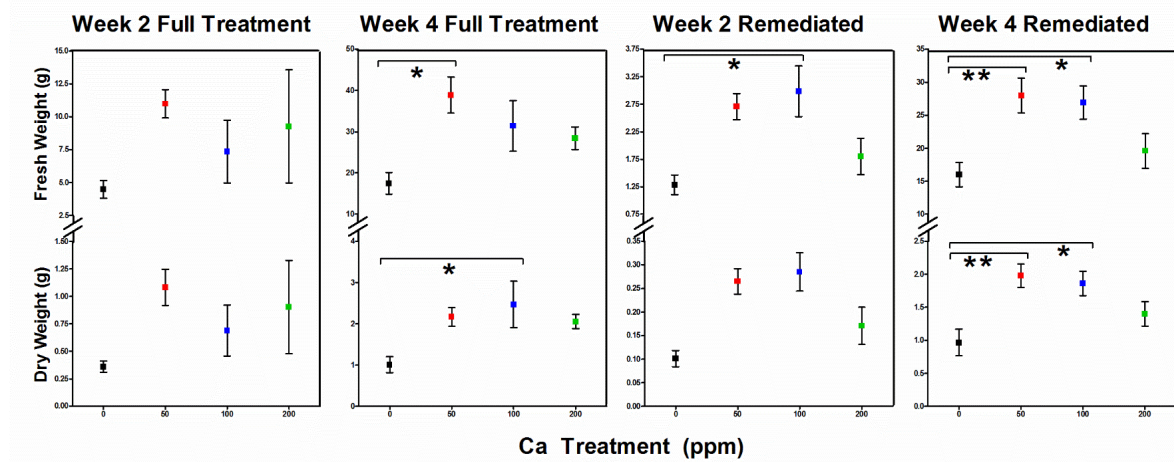


Figure 1. Fresh and dry weights of *S. lycopersicum* plants grown in modified Hoagland's solution containing 0, 50, 100 and 200 ppm Ca for 4 weeks (Full Treatment) or for 2 weeks followed by a further 2 weeks growth at 200 ppm Ca (Remediated Treatment). Values are mean +/- with standard deviation. A one-way analysis of variance (ANOVA) with Tukey's post-hoc test were implemented to determine statistical difference between treatment groups. *P<0.05, **P<0.01

A similar response is evident after 4-weeks exposure to reduced Ca levels, with the fully deficient treatment (0 ppm) displaying much lower weights in comparison to the other Ca treatments. Interestingly, the dry weight of this extreme deficiency is only significantly different from the 50 and 100 ppm Ca treatments suggesting these intermediate Ca treatments have increased growth compared to the control treatment. Comparison between fresh and dried material indicates that this could be due to increase water content in the tissues, as this effect is reduced following drying. This may be a stress response due to Ca depletion, as the plant begins to increase rates of transpiration to transport Ca from the nutrient solution. Again however, no statistical significance can be extracted from the control and intermediate treatments, showing how inefficient this approach is for detecting the onset of nutrient deficiencies.

It was envisaged that by exposing *S. lycopersicum* samples to reduced Ca treatments for two weeks and subsequently resupplying the Ca supply for an additional two weeks, plants may be able to recover from nutrient stress and return to a healthy state. Although the growth of the 2-week Full Treatment and 2-week Remediated Treatment should be comparable, there was a marked reduction in both the fresh and dry weights in the remediation investigation in comparison to the full treatment investigation, which depicts the highly variable growth rate due to the Ca depleted environments despite identical growth environments. However, in the Remediated Treatment after 4-weeks, both the fresh and dry weights of the 0 ppm treatment were again significantly different from the reduced Ca treatments, but not from the 200 ppm control treatment. Considering these samples had been supplemented with optimum levels of Ca for 2 weeks, surprisingly the differences between the treatments were more significant than in the Full Treatment plants after 4 weeks. This may be associated with the fact that Ca depletion may be having a more complex effect on plant growth, that is not simply observable by physiological measurements such as fresh and dry weight.

FAAS Analysis

In order to correlate the physiological effects observed on overall plant mass, in terms of fresh and dry weights, and the subsequent spectral and sequencing data with a known depletion in Ca at the tissue level, FAAS was conducted to derive exact Ca concentrations from sample leaves (**Figure 2**). During the full deficiency investigation, it is evident that at the 2-week time point the effects of Ca depletion are already reflected

in the overall Ca content in the tissues, with a significant drop of around 2% between control and extreme deficiency. This effect is further exaggerated at the 4-week time point where all reduced Ca treatments display a highly significant diminution in overall Ca content compared to the 200 ppm plants. FAAS is considered one of the most sensitive measures available to determine overall crop nutrient status and this result provides evidence for its sensitivity ⁷⁹.

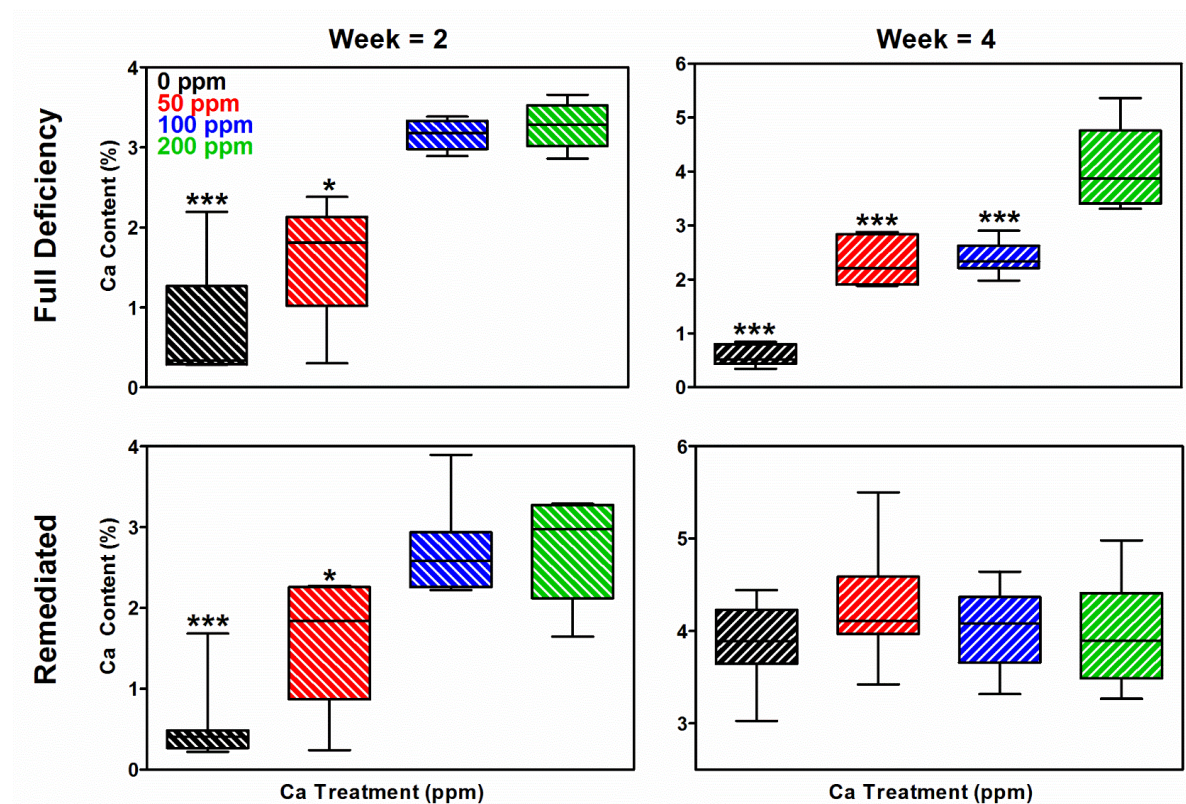


Figure 2. Ca content (%) as determined by flame atomic absorption spectroscopy (FAAS) from acid digested leaf samples of *S. lycopersicum* plants grown in modified Hoagland's solution containing 0, 50, 100 and 200 ppm Ca for 4 weeks (Full Treatment) or for 2 weeks followed by a further 2 weeks growth at 200ppm Ca (Remediated Treatment). A one-way analysis of variance (ANOVA) with Tukey's post-hoc tests were implemented to determined statistical difference between 0, 50 and 100 ppm treatment groups with the 200 ppm control group. (*P<0.05, **P<0.01)

In the remediation investigation, at the 2-week time point, an almost identical response is seen in overall Ca content of leaf samples as in the full deficiency experiment. The Ca content of plants exposed to extreme Ca deficiency (0 ppm) is significantly different from the control (200 ppm) plants, and 50 ppm plants are also discernible using this approach. Following remediation for the remaining 2-week period, the overall Ca content between each treatment becomes equivalent, with no significant differences identifiable. This indicates that remediation has effectively re-supplied Ca in the plant tissues in over this time period.

It is clear from this approach that FAAS can effectively determine the overall Ca content of a plant and observe when supplementation, such as by a nutrient fertiliser, has been effective. However, when comparing to our measurements for fresh and dry weights, there appears to be residual effects of Ca deficiency that are not sufficiently addressed using this approach. Additionally, the sample preparation involved in this analysis is time-consuming and not easily implemented by growers who would benefit from such an approach.

Ca deficiency detection with Raman spectroscopy

Raman spectroscopy was applied as an *in vivo* screening tool to determine the nutrient status of *S. lycopersicum* plants exposed to the aforementioned concentrations of Ca. The effects of a 4-week exposure to deficient conditions are shown in **Figure 3**. The processed mean spectra at both the 2- and 4-week time point all show very little variation between the four treatments. At 2-weeks it is evident that there is a variable region that can be seen at 876 and 852 cm^{-1} . These alterations do not follow a Ca concentration dependent pattern, potentially indicating that they are not severity linked.

However, 852 cm^{-1} is a characteristic Raman band identified in pectin studies, and is noticeably lower in the 0 ppm treatment, compared to the 200 ppm treatment which displays the highest level of scattering at this peak ⁸⁰. Reduced scattering of a pectin related Raman band, may be indicative of a reduction in Ca pectate levels in the tissue, which would be expected in Ca deficient environments ⁸¹. At the end of the 4-week treatment, the Raman spectra display less band specific differences, but do depict a spectrum wide difference in scattering intensity, particularly between 0 and 50 ppm treatments. As seen previously in the fresh weight measurements, it appears as though 50 ppm treatment may have accumulated water in the tissue which may begin to explain,

the increased scattering intensity. Due to intrinsic fluorescence, it is challenging to derive Raman spectra from dried tissue and it is thought that increased water content can contribute to fluorescence quenching in these tissues^{48,61,66}. With this in mind, increased water content could influence the spectra between Ca treatments.

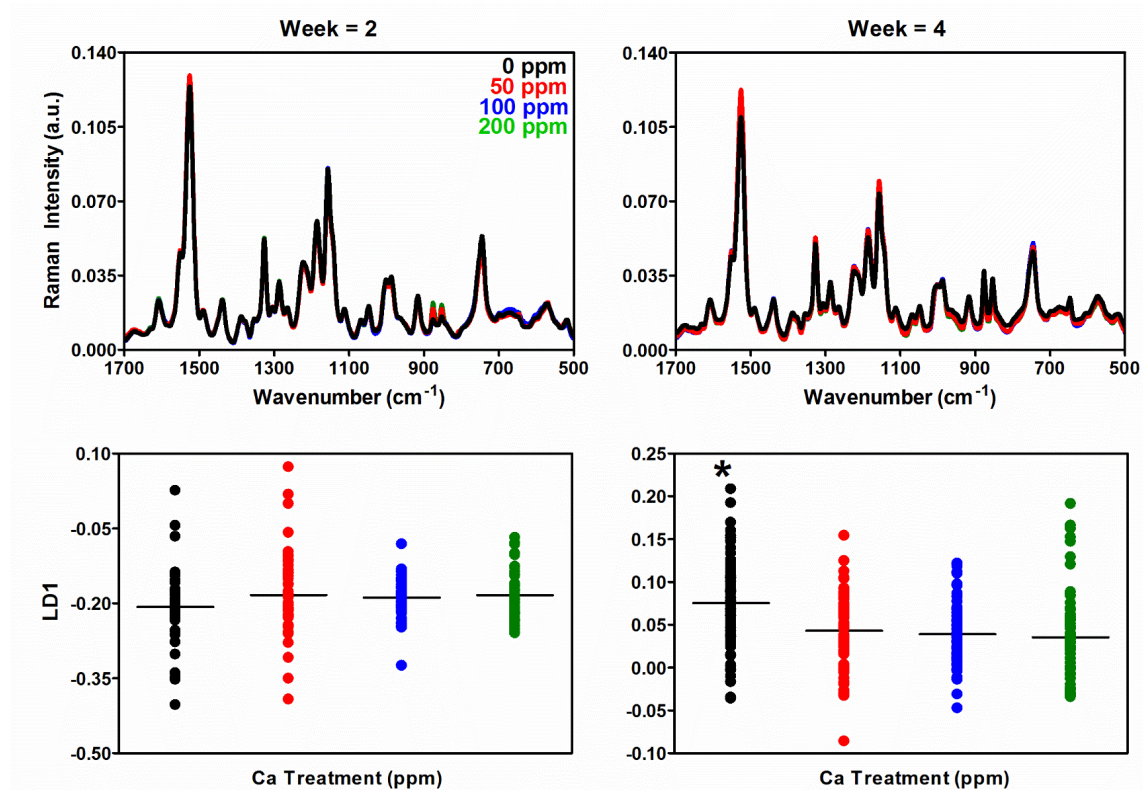


Figure 3. Processed Raman mean spectra (top panels) and corresponding 1D PCA-LDA scatterplots (bottom panels) for *S. lycopersicum* samples exposed to Ca deficient environments (0, 50, 100 and 200 ppm Ca) for 4-week time period. Left panels depict the 2-week time point, and right panels show the 4-week time point. (a.u., arbitrary units; LD, linear discriminant)

As no single spectral feature can be immediately identified by eye or by simple univariate techniques, it is warranted to conduct multivariate analyses to try and extract only the discriminatory variables in the dataset. PCA-LDA was conducted on each dataset to observe separation of each Ca of the treatments as a consequence of their inherent variance (**Figure 3**). In these 1D scatterplots, separation in the y-axis infers

difference between the Ca treatments. At the 2-week time point, there is very little difference discernible between 0, 50, 100 and 200 ppm Ca availabilities, demonstrating that after a 2-week exposure, Raman spectroscopy is unable to effectively detect any indicators of Ca deficiency. This is reflected in the sensitivity and specificity values derived by a validated SVM classifier, which indicate highly variable classification performances (**Table 1 and 2**).

Table 1. Sensitivity and specificity values of binary SVM classifiers, distinguishing Ca treatments from control *Solanum lycopersicum* samples grown at 200 ppm.

		Sensitivity (%)			Specificity (%)		
		100	50	0	100	50	0
Raman	Full	2	64.81	92.59	100.00	60.42	54.17
		4	57.38	63.93	68.85	67.12	66.67
	Remediated	2	84.31	62.75	66.67	29.79	58.70
		4	50.94	45.28	79.25	72.73	95.74
ATR-FTIR	Full	2	75.00	80.00	90.00	36.25	83.33
		4	56.19	81.90	100.00	71.48	87.50
	Remediated	2	0.00	40.00	100.00	100.00	66.67
		4	44.44	44.44	48.89	40.00	40.00

Table 2. Standard deviation of sensitivity and specificity values of binary SVM classifiers, distinguishing Ca treatments from control *Solanum lycopersicum* samples grown at 200 ppm.

		Sensitivity (%)			Specificity (%)		
		100	50	0	100	50	0
Raman	Full	2	48.20	26.44	0.00	49.42	50.35
		4	49.86	48.42	46.69	47.30	47.45
	Remediated	2	50.47	50.25	40.94	44.95	20.40
		4	36.73	48.83	47.61	46.23	49.78
ATR-FTIR	Full	2	46.31	15.82	0.00	20.49	23.75
		4	50.00	28.28	20.00	33.50	28.87
	Remediated	2	0.00	28.28	0.00	0.00	30.55
		4	26.03	26.03	38.87	41.40	41.40

Although a sensitivity of 100% is achieved between 0 and 200 ppm treatments, the corresponding specificity is 0%, displaying that the classification was able to consistently detect the extreme deficiency, but not the control, which is an unreliable model. However, after the full 4-week Ca treatment, it is evident that the 0 ppm treatment becomes significantly more separated in LD1, showing that it may be possible to differentiate this data group as a consequence of the Ca treatment. The classification

performance is markedly more stable in this instance, with a rate of 68.85% and 72% sensitivity and specificity respectively between the control and 0 ppm treatments.

Moderate Ca depletion treatments, 50 and 100 ppm are also detected by this classification process, although to lesser efficiencies dependent upon the severity of the treatment.

The effects of the Remediation Treatment are shown in **Figure 4**, first comparing processed spectra at week 2 and 4 and the corresponding PCA-LDA 1D scatterplots. In this instance, spectra again display little variation by eye at each time point. Interestingly, in the 4-week dataset, there is again alteration around the 876 and 852 cm^{-1} bands, previously associated with pectic compound, and this observation does follow a concentration dependent reduction in scattering from the 200 ppm Ca control. At this time point, the plants have been re-supplied with optimum Ca levels and should thus return to a healthy state, mirroring the normalised Ca content determined by FAAS. These spectral alterations, although small, indicate that further biochemical changes may have occurred due to deficiency and may represent residual effects of Ca depletion.

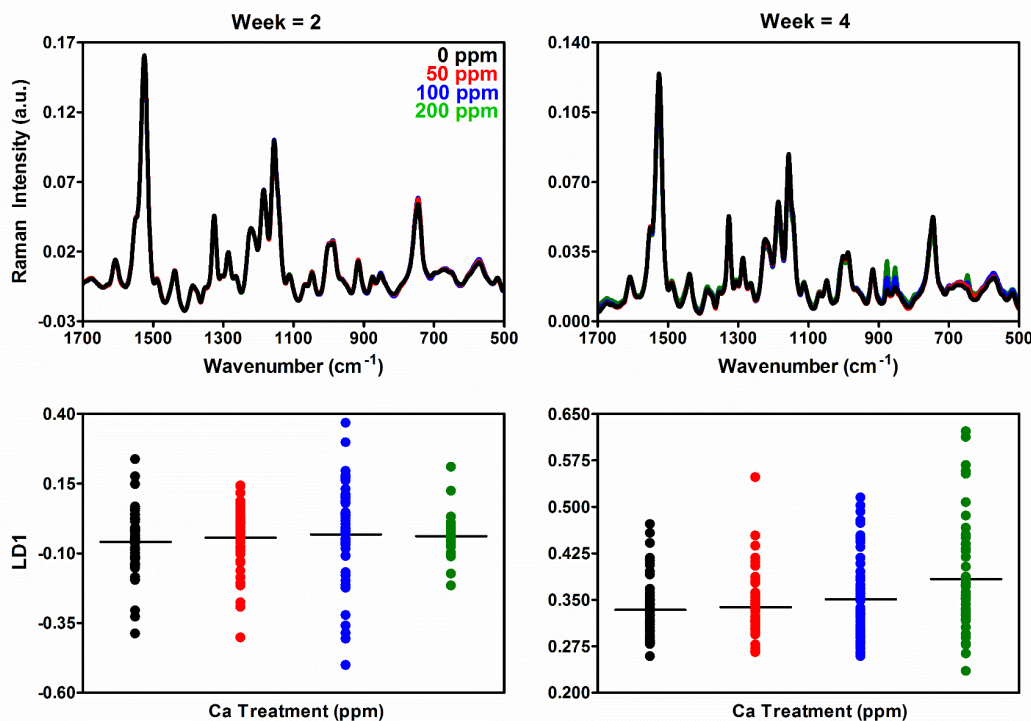


Figure 4. Processed Raman mean spectra (top panels) and corresponding 1D PCA-LDA scatterplots (bottom panels) for *S. lycopersicum* samples exposed to Ca deficient environments (0, 50, 100 and 200 ppm Ca) for a 2-week time period, followed by 2-weeks in a remediated environment. Left panels depict the 2-week time point, and right panels show the 4-week time point. (a.u., arbitrary units; LD, linear discriminant)

However, PCA-LDA scatterplots show no significant separation between Ca treatments following nutrient remediation, illustrating that these spectral alterations, may in fact be artefacts that do not contribute to the overall variance in the dataset. By comparing the sensitivity and specificity of this dataset, it is evident that following nutrient remediation SVM classifiers are able to distinguish between control and 2-week deficient plants prior to remediation at levels as high as 68.89% for 0 ppm plants. Across other Ca treatments the sensitivity and specificity vary markedly and are less consistent; for example, an 84.31% sensitivity rate versus a 29.79% specificity rate for distinguishing 100 and 200 ppm treatments. This may be indicative of the similarity between these spectra, as likely the effects of Ca stress will be moderate at this time point and between these two treatments. At week 4, this large variability across sensitivity and specificity values is again visible, although larger values can be seen. This infers that despite remediation, there are residual biochemical alterations present in the plant tissues that are distinguishable between spectral classes.

Ca deficiency detection with ATR-FTIR spectroscopy

The effect of Ca stress on *S. lycopersicum* plants was also investigated using ATR-FTIR spectroscopy on dried, fixed, leaf tissues. Due to the use of homogenised samples and the larger sampling area provided by the ATR diamond crystal, larger macro measurements are provided using this approach and an overall indicator of biochemical changes can be derived. From looking at the processed IR spectra, a plethora of spectral alterations can be seen between all Ca treatment during the progression of deficiency, from analysis at 2- to 4-weeks. (**Figure 5**). Between these two time points, the spectral differences occur in the same absorbance band regions, although to a larger extent at the 4-week time point, associated with the increased exposure to deficient conditions.

Using the 4-week spectra, the majority of spectral alterations can be seen around the Amide I region between $1600 - 1700 \text{ cm}^{-1}$, related to the absorption of protein content. Previous literature suggests that protein differences can be identified in plant leaves following Ca stress environments, specifically reduction in protein structure pointing towards leaf senescence, but also through the increased expression of pathogenesis-related proteins ^{61,82}. Control treatment samples display lower absorbance values at the Amide I and Amide II peaks that are assigned to $\nu(\text{CN})$ and $\delta(\text{NH})$, when compared to the intermediate and extreme Ca deficient samples. This effect was also

visible in in cadmium stress of clover leaves and may be associated with increased protein production due to provide additional stability to the tissue, due to the reduction on available Ca pectate⁸³.

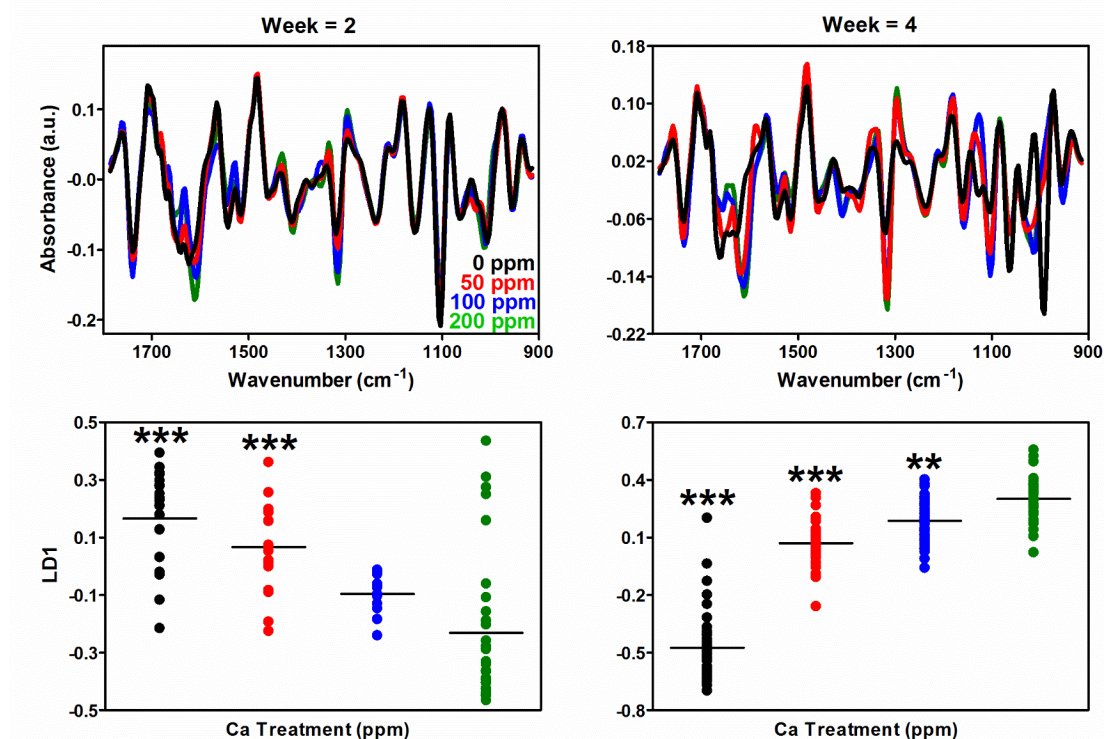


Figure 5. Processed ATR-FTIR mean spectra (top panels) and corresponding 1D PCA-LDA scatterplots (bottom panels) for *S. lycopersicum* samples exposed to Ca deficient environments (0, 50, 100 and 200 ppm Ca) for 4-week time period. Left panels depict the 2-week time point, and right panels show the 4-week time point. (a.u., arbitrary units; LD, linear discriminant)

A reduction in Ca pectate is visible at the absorbance bands at 1609 and 1408 cm⁻¹, which have been characterised in Ca pectate studies as $\nu_{\text{asy}}(\text{COO}^-)$ and $\nu_{\text{sy}}(\text{COO}^-)$ stretches of phenolic compounds respectively^{63,65,84}. This shows a direct observation of the known effects of Ca deficiency in tomato leaves, prior to the onset of visual symptoms⁶. Increased absorbance of singular pectin molecules at 1103 cm⁻¹ in samples exposed to Ca stress, also complement this observation, as increased levels of non-Ca associated pectin are present in the tissue^{62,85}. As the symptoms of BER manifest in the fruit tissue because of the Ca gradient that is developed in the tissue, the detection of this Ca stress effect in the leaves is useful as a potential presymptomatic screening technique.

Figure 5 presents the 1D PCA-LDA scatterplots of this dataset and also illustrates the efficiency of the technique to identify the onset of Ca deficiency. After 2 weeks exposure to Ca deficient conditions, 0 and 50 ppm treatments are significantly separated from the control treatment. After 4 weeks, this separation can also be extended to the moderate deficiency treatment of 100 ppm. This performance is also represented in the sensitivity and specificity values from binary SVM classifiers (**Table 1**). At the 2-week time point, extreme (0 ppm Ca) deficiency can be diagnosed at rates of 90 – 93% sensitivity and specificity, whilst the 50 ppm can be distinguished at levels of 80 – 83%. This is further exemplified at the 4-week time point, where the full deficiency had a prolonged effect on the samples and subsequently classification levels reached highs of 100%. Although values of this level should always be treated tentatively, the high performance of all treatment shows the potential of this technique for crop nutrient screening.

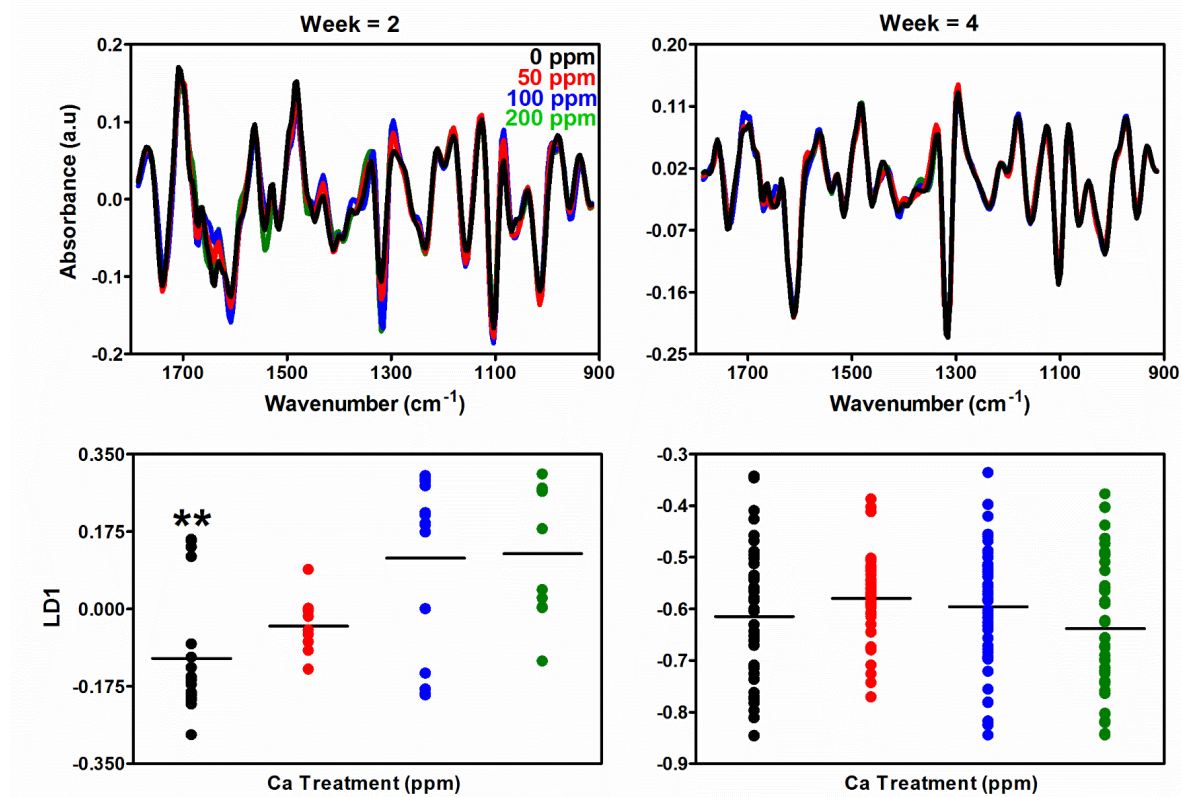


Figure 6. Processed ATR-FTIR mean spectra (top panels) and corresponding 1D PCA-LDA scatterplots (bottom panels) for *S. lycopersicum* samples exposed to Ca deficient environments (0, 50, 100 and 200 ppm Ca) for a 2-week time period, followed by 2-weeks in a remediated environment (200 ppm Ca). Left panels depict the 2-week time point, and right panels show the 4-week time point. (a.u., arbitrary units; LD, linear discriminant)

Observing the effects of nutrient remediation with optimum Ca levels, also shows the sensitivity of this approach. The effects of 2-week exposure to reduce Ca availabilities, can be seen in the processed IR spectra from this study and mimic the previously identified spectral differences of the full deficiency study (**Figure 6**). In overview, this is a reduction in the absorbance of Ca pectate residues at 1609 cm^{-1} as a consequence of reduced Ca availability, and widespread variation in protein related peaks. Following 2-weeks of remediation however, the effects of Ca deficiency become undefinable in the IR spectra, with hardly any spectral differences noticeable by eye. This is reflected in PCA-LDA scatterplots of this data, as no significant separation can be identified. Furthermore, the performance of SVM classification between each treatment falls away markedly, with sensitivity and specificity generally falling below 50% (**Table 1**).

Although, this approach required a drying step, and therefore had increased sample preparation times, this is still a much simpler approach in comparison to analytical techniques such as FAAS. Whilst the drying process in this instance was conducted over a 48-hour period, this process is still less labour intensive than approaches that require acid digestion of samples, that would require specialist users. With the advancement towards hand-held and portable devices, the use of ATR-FTIR for nutrient status screening is inexpensive and rapid, whilst the ease of use allows widespread implementation⁸⁶.

RNA-Sequencing analysis

Whole genome sequencing has provided insight into plant stress pathways in crops in response to nutrient deficiency, including Ca^{31-33,87}. For this study, a comparison was made between plants grown at optimum Ca (200 ppm Ca), extreme Ca deficiency (0 ppm), and Ca remediated conditions (0 ppm for two weeks, 200 ppm subsequently) for four weeks, in order to establish alterations in gene expression due to Ca stress. Initially, the mapped genomic data was visualised as a data store tree in order to cluster together known biological replicates (**Figure 7A**). In this example, the first branch on this tree effectively separates deficient treatments apart from control and remediated treatments, suggesting that the greatest gene differences can be identified by these two groupings. Unfortunately, one deficient replicate was not differentiated in this process, which has been related back to reduced RNA quality prior to sequencing

analysis. Despite this, all control and remediated replicates separate at the next branch of the decision tree, indicating a distinct difference in gene expression.

PCA analysis of differentially expressed genes between treatments reveals a separation between the Ca treatments, with deficiency showing greatest variance compared to the control and remediated treatments (**Figure 7B**). Again, the ‘Deficient 3’ sample does not follow this pattern and clusters more centrally in the plot with some control replicates due to the aforementioned quality insufficiency. As one may expect, there is overlap between control and remediated replicates which may represent a return to normal gene expression as a consequence of returned Ca levels. In regards to presymptomatic detection of deficiency, this approach appears to be highly sensitive to the effects of nutrient stress, with a plethora of gene-specific changes observable.

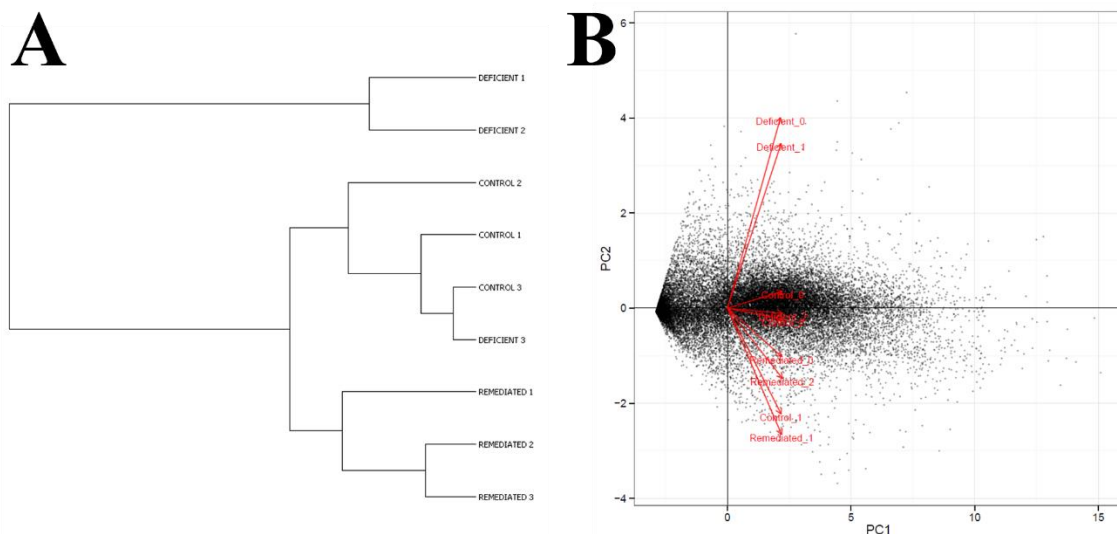


Figure 7. Separation of replicate control, deficient and remediated Ca treatment replicates based upon gene expression values derived from RNA-sequencing analysis. (A) Data store tree to observe biological clustering of Ca treatments; (B) PCA plot displaying the expression of all gene probes in the genome with sample distribution illustrated.

In order to compare differential expression between each Ca treatment, hierarchical clustering was conducted on genes displaying intensity differences and was visualised using a heat map. This approach clusters together genes that are expressed at differing levels between treatments and often identifies genes with similar functionalities, resulting in aided biological interpretation ⁸⁸. The heat map portrayed in **Figure 8** depicts 6 distinct clusters of genes that are differentially expressed between control, deficient and remediated. Clusters 1 and 4 are representative of genes that are up

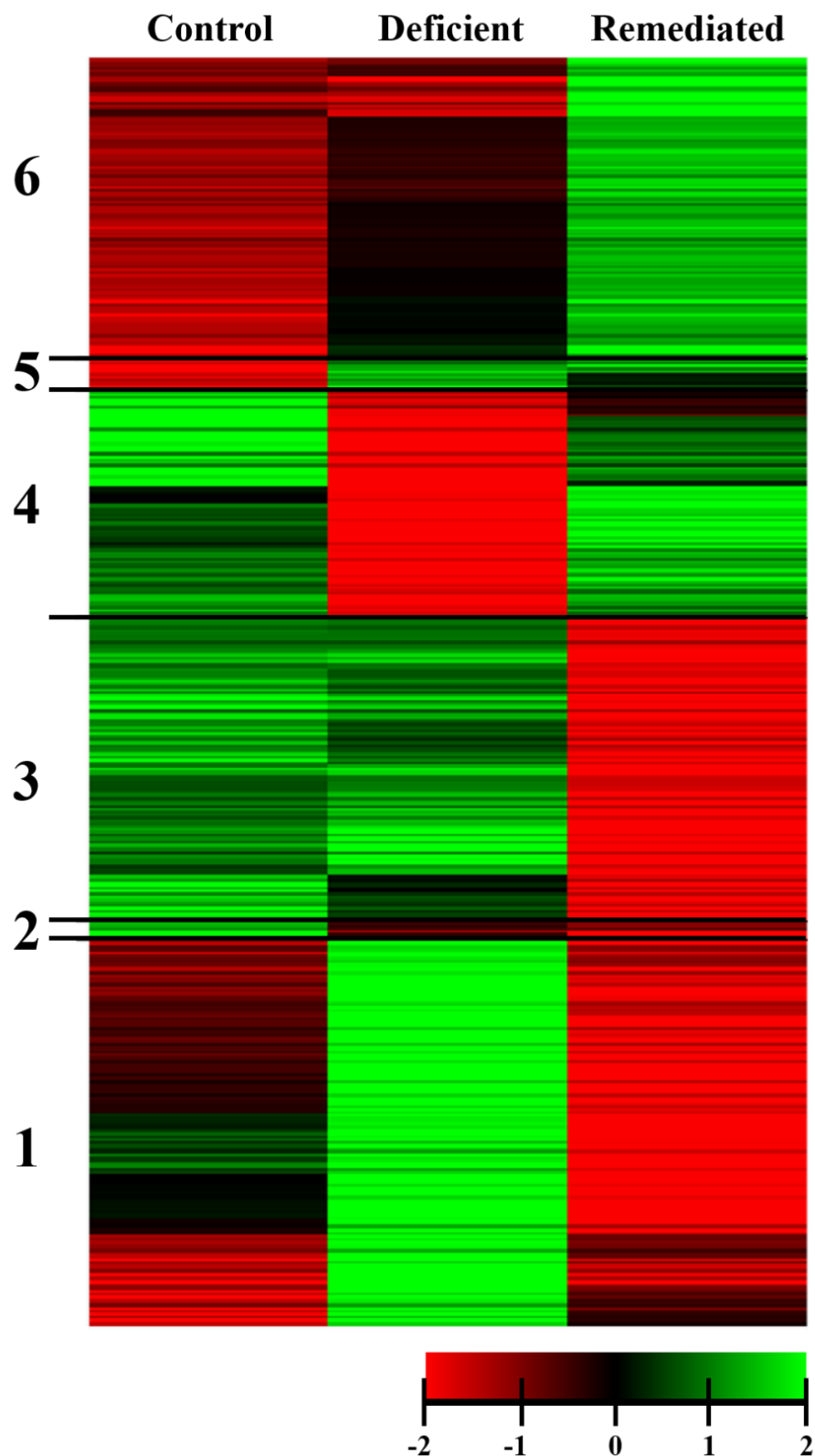


Figure 8. Hierarchical cluster map of gene probes displaying intensity differences in expression between Ca treatments at a P value > 0.05 . Clusters have been numerically identified and relate to **Tables 3 and 4**.

and downregulated respectively between deficient and control samples sets, whereas Clusters 3 and 6 highlight down and upregulation respectively as a consequence of remediation. The two smallest clusters of genes, Cluster 2 and 5, are indicative of up- and downregulation that is evident across both deficient and remediated treatments. This suggests that alterations to the plant transcriptome as a consequence of deficiency and remediation are distinctly processes, that results in separate genome responses.

A breakdown of gene functionality within each cluster can be seen in **Table 3**, primarily indicating that catalytic pathways and binding proteins are targeted in response to Ca deficiency. Each gene contained within each cluster and its respective protein annotation is identified in the supplementary information (**SI**). An overview of the five genes exhibiting the largest expression differences within each cluster is presented in

Table 4.

Table 3. Functional overview of genes identified within each cluster identified using hierarchical cluster analysis of all genes presenting an intensity difference between Ca treatments

Hierarchical Cluster	% of Genes	General Function
Cluster 1	63.2%	Catalytic Activity
	21.1%	Binding
	14.0%	Transporter Activity
	1.8%	Receptor Activity
Cluster 2	100%	Catalytic Activity
Cluster 3	77.1%	Catalytic Activity
	12.5%	Transporter Activity
	8.3%	Binding
	2.1%	Antioxidant Activity
Cluster 4	48.8%	Catalytic Activity
	39.0%	Binding
	7.3%	Transporter Activity
	2.4%	Receptor Activity
Cluster 5	2.4%	Structural Molecule Activity
	80.0%	Catalytic Activity
	20.0%	Binding
Cluster 6	58.1%	Binding
	27.9%	Catalytic Activity
	9.3%	Structural Molecule Activity
	4.7%	Transporter Activity

Table 4. Top 5 differentially expressed genes with known gene function from each hierarchical cluster derived from probes displaying intensity differences between control, deficient and remediated Ca treated *S. lycopersicum* samples. Cluster 2 only yielded 3 genes with known protein functions and thus only contains 3 genes.

Cluster	Expression	Gene ID	Gene Family	Gene Function
1	Upregulated in Deficient	Solyc12g098540.1	NTPASE, ISOFORM F	Transcription regulation ⁹⁸
		Solyc04g007760.2	MLP-LIKE PROTEIN 165-RELATED	Plant defence ⁹⁹
		Solyc04g016470.2	BETA-1,3-GLUCANASE 4-RELATED	Control of plasmodesmatal transport ⁹⁰
		Solyc06g005310.2	TRANSCRIPTION FACTOR MYB48-RELATED	Transcription factor involved in abiotic stress regulation ⁸⁹
		Solyc03g005980.2	AQUAPORIN NIP1 RELATED	Cell water uptake ¹⁰⁰
2	Downregulated in Deficient and Remediated	Solyc02g094040.2	TRIACYLGLYCEROL LIPASE 2	Lipid breakdown ¹⁰¹
		Solyc06g048410.2	SUPEROXIDE DISMUTASE 1	Antioxidant ⁹⁷
		Solyc03g119540.2	CCT MOTIF FAMILY PROTEIN-RELATED	Transcription regulation ¹⁰²
3	Downregulated in Remediated	Solyc11g022590.1	DR4 PROTEIN-RELATED	Auxin sensitive transcription factor in fruit development ¹⁰³
		Solyc03g095650.2	MLO-LIKE PROTEIN 12-RELATED	Plant defence ¹⁰⁴
		Solyc12g099780.1	RPM1-INTERACTING PROTEIN 4 (RIN4)	Plant defence regulator ¹⁰⁵
		Solyc11g021060.1	PROTEINASE INHIBITOR TYPE-2 TR*	Plant defence due to wounding ¹⁰⁶
		Solyc01g096320.2	HOMEobox-LEUCINE ZIPPER PROTEIN ATHB-12-RELATED	Plant defence, symptom development ¹⁰⁷
4	Downregulated in Deficient	Solyc03g005280.2	ASPARTYL PROTEASE	Negative regulator of defence mechanisms ¹⁰⁸
		Solyc02g080210.2	PECTINESTERASE/PECTINESTERASE INHIBITOR 18-RELATED	Promotion of cell wall degradation ⁹¹
		Solyc05g009270.2	3-KETOACYL-COA SYNTHASE 5-RELATED	Cuticular wax biosynthesis ¹⁰⁹
		Solyc05g053850.2	PROTEIN FLOWERING LOCUS T-RELATED	Promotion of flowering ⁹²
		Solyc02g071000.1	CHLOROPHYLL A-B BINDING PROTEIN BINDING FAMILY	ABA sensitivity ¹¹⁰

5	Upregulated in Deficient and Remediated	Solyc07g064380.2	AMINOTRANSFERASE-LIKE	Protein biosynthesis ¹¹¹
		Solyc05g047680.2	CYTOCHROME P450-RELATED	Involvement in biosynthetic and detoxification pathways ¹¹²
		Solyc08g074620.1	OSMOTIN-LIKE PROTEIN	Abiotic stress response ⁹⁵
		Solyc10g045240.1	BETA-GLUCOSIDASE 33	Cellulosic breakdown ⁹³
		Solyc09g008380.2	PECTATE LYASE 12-RELATED	Pectate cleavage ¹¹³
6	Upregulated in Remediated	Solyc02g070180.1	BERBERINE BRIDGE ENZYME-LIKE	Wound response ¹¹⁴
		Solyc01g109670.2	KINESIN-LIKE PROTEIN KIF15	Cell wall development ⁹⁴
		Solyc09g072770.1	POLLEN OLE E 1 ALLERGEN AND EXTENSIN FAMILY	Developmental regulators ¹¹⁵
		Solyc01g107370.2	GIBBERELLIN-REGULATED GASA/GAST/SNAKIN FAMILY	Hormone mediated stress tolerance ¹¹⁶
		Solyc12g011030.1	GLYCOSYL HYDROLASE FAMILY	Cell wall breakdown ¹¹⁷

Cluster 1 contains genes that are upregulated in deficient treatment and the increased expression of transcription factors specifically relating to plant defence and stress mechanisms, portray the response of the plant to Ca stress. MYB transcription factors have been shown to mediate plant responses to abiotic stresses, such as the Ca deficiency presented here ⁸⁹. Increased expression of plant defence proteins has been isolated in Ca deficiency and here upregulation of MLP-like proteins mirrors this ⁸². Furthermore, upregulation of proteins involved in plasmodesmatal transport and water uptake reveal that plants in deficient conditions are actively attempting to increase Ca transport, as Ca transport is predominantly through the transpiration stream ⁶. The plasmodesmata span adjacent cells control symplastic transport through the plant and β -1,3-glucanase activity is known to increase permeability of this transport pathway ⁹⁰. As such, increased activity in this protein family indicate increase symplastic transport to aid Ca transportation in deficient plants.

Genes downregulated in the deficient treatment are encompassed in Cluster 3. Cell wall degradation is reduced by under expression of pectinesterase inhibitors and is a clear response to reduced Ca availability ⁹¹. As structural integrity is compromised due to reduced Ca, and therefore Ca-pectate, the maintenance of the existing cell wall is crucial to survival. Additionally, decreased expression of proteins that promote flowering suggest that onset of flowering, and subsequently fruit set, is delayed as a consequence of Ca deficiency ⁹². As Ca specifically manifests in tomato fruit, this response prevents the immediate onset of BER.

Remediated Ca treatments exhibit increased expression of proteins largely involved in cell wall development and maintenance as well as a continued expression of stress response proteins (Cluster 6). Contrastingly, both hydrolase proteins that are involved with cell wall breakdown, and kinesin-like proteins that are involved with cell wall generation are over expressed in this treatment ^{93,94}. However, this may be an indicator of degradation of compromised tissues versus synthesis of healthy tissues, due to the resumed availability of Ca. Cluster 3 depicts proteins related to plant defence mechanisms are the principal targets of downregulation in this Ca treatment and illustrates that the plant is no longer in a nutrient stressed state.

Fewer genes are shown to be upregulated in both deficient and remediated Ca treatment, yet there is a distinct overlap in binding and catalytic activity genes (Cluster 4). Osmotin-like proteins are expressed in response to abiotic stress, specifically water and pathogens, and their expression in both treatments here indicate that both immediate and long-term Ca stress responses are regulated by this pathway ⁹⁵. Increased expression of protein biosynthesis genes, such as aminotransferases, correlate to ATR-FTIR data shown in this investigation, as Ca deficiency results in increased protein absorbance in leaves. As there is reduced stability in the leaf tissue, this may be an attempt by the plant to restore structural rigidity. In regards to downregulation between both Ca treatments, only three genes could be isolated that exhibited the same response. Somewhat surprisingly, superoxide dismutase is shown to be downregulated by both Ca treatments, despite role in the breakdown of reactive oxygen species produced as consequence of Ca stress ⁹⁶. However, a similar response was also observed by Schmitz-Eiberger *et al.* although this may be due expression of difference splice isoforms ⁹⁷.

Conclusions

The purpose of this study was to determine if spectroscopic methodology was able to presymptomatically detect Ca deficiency in *S. lycopersicum* prior to the onset of BER. Specifically, Raman spectroscopy and ATR-FTIR spectroscopy were compared with standard approaches of determining crop nutrient status. FAAS is one such example where sensitive measures of single elemental content can be derived, however require extensive sample preparation to yield univariate values of deficiency.

Raman spectroscopy is a potentially powerful tool for *in vivo* diagnostics in an agricultural setting, as a novel method for nutrient status determination. Using this approach, biochemical information can be derived without the need for extensive sample preparation. In this study, we show that Ca deficiency can be identified in *S. lycopersicum* leaf samples, prior to the production of fruit and thus providing presymptomatic detection. For *in vivo* measurements, severe deficiency can be isolated at reasonable levels between 72-69% sensitivity and specificity. However, there is further development required to develop a sensitive classifier suitable for this application, as variability between comparisons is high. Despite this, Raman spectroscopy is able to not only differentiation between treatments, but also simultaneously provides biochemical information.

ATR-FTIR spectroscopy provides a sensitive approach to nutrient screening that is able to identify severe and moderate Ca stress after as little as two weeks' exposure to deficient conditions. Although a sample preparation step was used in this instance to compare fixed tissue analysis to *in vivo* analysis with Raman spectroscopy, this technique could potentially be employed as an *in vivo* monitoring tool^{60,62}. It is important to note that ATR-FTIR analysis of plant tissue can lead to localised damage of tissue, which may not be preferably for fruit analysis, but may be acceptable for leaf tissue⁶¹.

The differential expression of genes involved in nutrient stress response pathways are analysed and compared between deficient and remediated crops. This approach was able to complement spectroscopic information, whilst also effectively isolating deficient samples. In regards to a nutrient status screening tool, the precise sample preparation and high-cost of such an approach may not be readily translatable.

However, the wealth of information that is extracted using this approach is highly beneficial in a research setting for further understanding crop-nutrient relationships.

In conclusion, vibrational spectroscopic measurements are able to detect nutrient deficiencies rapidly, without extensive sample preparation steps and damage to the crop under investigation. This approach could contribute to precision farming, where the only the exact nutrient requirements of the crop are provided, reducing the environmental impacts of excessive fertiliser use. Movement towards more efficient crop production will increase agricultural productivity and help to tackle the threat of global food security.

References

- 1 Marschner, H. *Marschner's mineral nutrition of higher plants*. (Academic press, 2011).
- 2 Cakmak, I. in *Progress in Plant Nutrition: Plenary Lectures of the XIV International Plant Nutrition Colloquium*. 3-24 (Springer).
- 3 van der Ploeg, R. R. & Kirkham, M. On the origin of the theory of mineral nutrition of plants and the law of the minimum. (1999).
- 4 Godfray, H. C. J. *et al.* Food security: the challenge of feeding 9 billion people. *science* **327**, 812-818 (2010).
- 5 Tilman, D., Cassman, K. G., Matson, P. A., Naylor, R. & Polasky, S. Agricultural sustainability and intensive production practices. *Nature* **418**, 671-677 (2002).
- 6 White, P. J. & Broadley, M. R. Calcium in Plants. *Annals of Botany* **92**, 487-511 (2003).
- 7 Hirschi, K. D. The calcium conundrum. Both versatile nutrient and specific signal. *Plant physiology* **136**, 2438-2442 (2004).
- 8 Clapham, D. E. Calcium signaling. *Cell* **80**, 259-268 (1995).
- 9 Rudd, J. & Franklin-Tong, V. Calcium signaling in plants. *Cellular and Molecular Life Sciences CMLS* **55**, 214-232 (1999).
- 10 Hepler, P. K. Calcium: a central regulator of plant growth and development. *The Plant Cell* **17**, 2142-2155 (2005).
- 11 Hepler, P. K. & Winship, L. J. Calcium at the Cell Wall-Cytoplasm Interface. *Journal of integrative plant biology* **52**, 147-160 (2010).
- 12 Collier, G. F. & Tibbitts, T. W. in *Horticultural Reviews* 49-65 (Springer, 1982).
- 13 Ho, L., Belda, R., Brown, M., Andrews, J. & Adams, P. Uptake and transport of calcium and the possible causes of blossom-end rot in tomato. *Journal of Experimental Botany* **44**, 509-518 (1993).
- 14 Simon, E. The symptoms of calcium deficiency in plants. *New phytologist* **80**, 1-15 (1978).
- 15 Bangerth, F. Calcium-related physiological disorders of plants. *Annual review of phytopathology* **17**, 97-122 (1979).
- 16 Malone, M., White, P. & Morales, M. A. Mobilization of calcium in glasshouse tomato plants by localized scorching. *Journal of Experimental Botany* **53**, 83-88 (2002).
- 17 Lucena, J. in *III International Symposium on Mineral Nutrition of Deciduous Fruit Trees* 448. 179-192.
- 18 Hatirli, S. A., Ozkan, B. & Fert, C. Energy inputs and crop yield relationship in greenhouse tomato production. *Renewable Energy* **31**, 427-438 (2006).
- 19 Reuter, D. *Plant analysis: an interpretation manual*. (CSIRO publishing, 1997).

20 Fageria, N., Filho, M. B., Moreira, A. & Guimaraes, C. Foliar fertilization of crop plants. *Journal of plant nutrition* **32**, 1044-1064 (2009).

21 Jones Jr, J. B. *Laboratory guide for conducting soil tests and plant analysis*. (CRC press, 2001).

22 Wolf, B. A comprehensive system of leaf analyses and its use for diagnosing crop nutrient status. *Communications in Soil Science and Plant Analysis* **13**, 1035-1059 (1982).

23 Bray, R. H. A nutrient mobility concept of soil-plant relationships. *Soil Science* **78**, 9-22 (1954).

24 White, J. G. & Zasoski, R. J. Mapping soil micronutrients. *Field crops research* **60**, 11-26 (1999).

25 Tan, K. H. *Soil sampling, preparation, and analysis*. (CRC press, 2005).

26 Fried, M. & Dean, L. A concept concerning the measurement of available soil nutrients. *Soil Science* **73**, 263-272 (1952).

27 Oliveira, S. R., Neto, J. A. G., Nobrega, J. A. & Jones, B. T. Determination of macro- and micronutrients in plant leaves by high-resolution continuum source flame atomic absorption spectrometry combining instrumental and sample preparation strategies. *Spectrochimica Acta Part B: Atomic Spectroscopy* **65**, 316-320 (2010).

28 Vesk, M., Possingham, J. & Mercer, F. The effect of mineral nutrient deficiencies on the structure of the leaf cells of tomato, spinach, and maize. *Australian Journal of Botany* **14**, 1-18 (1966).

29 Bouma, D. in *Inorganic plant nutrition* 120-146 (Springer, 1983).

30 Zeng, H. *et al.* Role of microRNAs in plant responses to nutrient stress. *Plant and soil* **374**, 1005-1021 (2014).

31 Zhao, W. *et al.* RNA-Seq-based transcriptome profiling of early nitrogen deficiency response in cucumber seedlings provides new insight into the putative nitrogen regulatory network. *Plant and Cell Physiology*, pcu172 (2014).

32 Hsieh, L.-C. *et al.* Uncovering Small RNA-Mediated Responses to Phosphate Deficiency in Arabidopsis by Deep Sequencing. *Plant Physiology* **151**, 2120-2132 (2009).

33 Shankar, A. *et al.* Whole genome transcriptome analysis of rice seedling reveals alterations in Ca 2+ ion signaling and homeostasis in response to Ca 2+ deficiency. *Cell calcium* **55**, 155-165 (2014).

34 Macy, P. The quantitative mineral nutrient requirements of plants. *Plant physiology* **11**, 749 (1936).

35 Besford, R. A rapid tissue test for diagnosing phosphorus deficiency in the tomato plant. *Annals of Botany* **45**, 225-227 (1980).

36 Batten, G. D. Plant analysis using near infrared reflectance spectroscopy: the potential and the limitations. *Australian Journal of Experimental Agriculture* **38**, 697-706 (1998).

37 Foley, W. J. *et al.* Ecological applications of near infrared reflectance spectroscopy—a tool for rapid, cost-effective prediction of the composition of plant and animal tissues and aspects of animal performance. *Oecologia* **116**, 293-305 (1998).

38 Menesatti, P. *et al.* Estimation of plant nutritional status by Vis–NIR spectrophotometric analysis on orange leaves [Citrus sinensis (L) Osbeck cv Tarocco]. *Biosystems engineering* **105**, 448-454 (2010).

39 Shi, J. *et al.* Pre-visual diagnostics of phosphorus deficiency in mini-cucumber plants using near-infrared reflectance spectroscopy. *Applied spectroscopy* **66**, 1426-1432 (2012).

40 Yang, H., Irudayaraj, J. & Paradkar, M. M. Discriminant analysis of edible oils and fats by FTIR, FT-NIR and FT-Raman spectroscopy. *Food Chemistry* **93**, 25-32 (2005).

41 Sene, C. F., McCann, M. C., Wilson, R. H. & Grinter, R. Fourier-transform Raman and Fourier-transform infrared spectroscopy (an investigation of five higher plant cell walls and their components). *Plant Physiology* **106**, 1623-1631 (1994).

42 Kačuráková, M. & Wilson, R. Developments in mid-infrared FT-IR spectroscopy of selected carbohydrates. *Carbohydrate Polymers* **44**, 291-303 (2001).

43 Sathyaranayana, D. N. *Vibrational spectroscopy: theory and applications*. (New Age International, 2015).

44 Griffiths, P. R. & De Haseth, J. A. *Fourier transform infrared spectrometry*. Vol. 171 (John Wiley & Sons, 2007).

45 Baker, M. J. *et al.* Using Fourier transform IR spectroscopy to analyze biological materials. *Nature protocols* **9**, 1771-1791 (2014).

46 Stuart, B. *Infrared spectroscopy*. (Wiley Online Library, 2005).

47 Kereszty, G. Raman spectroscopy: theory. *Handbook of vibrational spectroscopy* (2002).

48 Butler, H. J. *et al.* Using Raman spectroscopy to characterize biological materials. *Nature protocols* **11**, 664-687 (2016).

49 Larkin, P. *Infrared and Raman spectroscopy; principles and spectral interpretation*. (Elsevier, 2011).

50 Schrader, B. *Infrared and Raman spectroscopy: methods and applications*. (John Wiley & Sons, 2008).

51 Harborne, A. *Phytochemical methods a guide to modern techniques of plant analysis*. (Springer Science & Business Media, 1998).

52 McCann, M. C., Hammouri, M., Wilson, R., Belton, P. & Roberts, K. Fourier transform infrared microspectroscopy is a new way to look at plant cell walls. *Plant Physiology* **100**, 1940-1947 (1992).

53 Kacurakova, M., Capek, P., Sasinkova, V., Wellner, N. & Ebringerova, A. FT-IR study of plant cell wall model compounds: pectic polysaccharides and hemicelluloses. *Carbohydrate polymers* **43**, 195-203 (2000).

54 Pandey, K. A study of chemical structure of soft and hardwood and wood polymers by FTIR spectroscopy. *Journal of Applied Polymer Science* **71**, 1969-1975 (1999).

55 Mohamed, G. F., Shaheen, M. S., Khalil, S. K., Hussein, A. & Kamil, M. Application of FTIR spectroscopy for rapid and simultaneous quality determination of some fruit products. *Nat Sci* **9**, 21-31 (2011).

56 Heraud, P. *et al.* Focal plane array infrared imaging: a new way to analyse leaf tissue. *New Phytologist* **173**, 216-225 (2007).

57 Naumann, A. & Polle, A. FTIR imaging as a new tool for cell wall analysis of wood. *New Zealand Journal of Forestry Science* **36**, 54 (2006).

58 Brown, D. M., Zeef, L. A., Ellis, J., Goodacre, R. & Turner, S. R. Identification of novel genes in *Arabidopsis* involved in secondary cell wall formation using expression profiling and reverse genetics. *The Plant Cell* **17**, 2281-2295 (2005).

59 Kim, S. *et al.* Taxonomic discrimination of flowering plants by multivariate analysis of Fourier transform infrared spectroscopy data. *Plant cell reports* **23**, 246-250 (2004).

60 Ivanova, D. G. & Singh, B. R. Nondestructive FTIR monitoring of leaf senescence and elicitin-induced changes in plant leaves. *Biopolymers* **72**, 79-85 (2003).

61 Butler, H. J., McAinsh, M. R., Adams, S. & Martin, F. L. Application of vibrational spectroscopy techniques to non-destructively monitor plant health and development. *Analytical Methods* **7**, 4059-4070 (2015).

62 Ribeiro da Luz, B. Attenuated total reflectance spectroscopy of plant leaves: a tool for ecological and botanical studies. *New Phytologist* **172**, 305-318 (2006).

63 Schulz, H. & Baranska, M. Identification and quantification of valuable plant substances by IR and Raman spectroscopy. *Vibrational Spectroscopy* **43**, 13-25 (2007).

64 Baranska, M., Roman, M., Schulz, H. & Baranski, R. Recent advances in Raman analysis of plants: alkaloids, carotenoids, and polyacetylenes. *Current Analytical Chemistry* **9**, 108-127 (2013).

65 Schulz, H., Baranska, M. & Baranski, R. Potential of NIR-FT-Raman spectroscopy in natural carotenoid analysis. *Biopolymers* **77**, 212-221 (2005).

66 Baranski, R., Baranska, M. & Schulz, H. Changes in carotenoid content and distribution in living plant tissue can be observed and mapped *in situ* using NIR-FT-Raman spectroscopy. *Planta* **222**, 448-457 (2005).

67 Gierlinger, N. & Schwanninger, M. The potential of Raman microscopy and Raman imaging in plant research. *Spectroscopy* **21**, 69-89 (2007).

68 Hoagland, D. R. & Arnon, D. I. The water-culture method for growing plants without soil. *Circular. California Agricultural Experiment Station* **347** (1950).

69 Butler, H. J., McAinsh, M. R., Adams, S. & Martin, F. L. Application of vibrational spectroscopy techniques to non-destructively monitor plant health and development. *Anal. Methods* **7**, 4059-4070 (2015).

70 Trevisan, J., Angelov, P. P., Scott, A. D., Carmichael, P. L. & Martin, F. L. IRootLab: a free and open-source MATLAB toolbox for vibrational biospectroscopy data analysis. *Bioinformatics*, btt084 (2013).

71 Butler, H. J. *et al.* Using Raman spectroscopy to characterize biological materials. *Nat. Protoc.* **11**, 664-687 (2016).

72 Martin, F. L. *et al.* Distinguishing cell types or populations based on the computational analysis of their infrared spectra. *Nature protocols* **5**, 1748-1760 (2010).

73 Lasch, P. Spectral pre-processing for biomedical vibrational spectroscopy and microspectroscopic imaging. *Chemometrics and Intelligent Laboratory Systems* **117**, 100-114 (2012).

74 Trevisan, J., Angelov, P. P., Carmichael, P. L., Scott, A. D. & Martin, F. L. Extracting biological information with computational analysis of Fourier-transform infrared (FTIR) biospectroscopy datasets: current practices to future perspectives. *Analyst* **137**, 3202-3215 (2012).

75 Chen, L. *et al.* A rapid method to screen for cell-wall mutants using discriminant analysis of Fourier transform infrared spectra. *The Plant Journal* **16**, 385-392 (1998).

76 MacRae, E. Extraction of plant RNA. *Protocols for Nucleic Acid Analysis by Nonradioactive Probes*, 15-24 (2007).

77 Mi, H., Poudel, S., Muruganujan, A., Casagrande, J. T. & Thomas, P. D. PANTHER version 10: expanded protein families and functions, and analysis tools. *Nucleic acids research* **44**, D336-342 (2016).

78 Mi, H., Muruganujan, A., Casagrande, J. T. & Thomas, P. D. Large-scale gene function analysis with the PANTHER classification system. *Nat. Protocols* **8**, 1551-1566 (2013).

79 Bradfield, E. & Spencer, D. Leaf analysis as a guide to the nutrition of fruit crops. VI—Determination of magnesium, zinc and copper by atomic absorption spectroscopy. *Journal of the Science of Food and Agriculture* **16**, 33-38 (1965).

80 Syntysya, A., Čopíková, J., Matějka, P. & Machovič, V. Fourier transform Raman and infrared spectroscopy of pectins. *Carbohydrate Polymers* **54**, 97-106 (2003).

81 Nightingale, G., Addoms, R. M., Robbins, W. & Schermerhorn, L. Effects of calcium deficiency on nitrate absorption and on metabolism in tomato. *Plant physiology* **6**, 605 (1931).

82 Baboulène, L., Silvestre, J., Pinelli, E. & Morard, P. Effect of Ca deficiency on growth and leaf acid soluble proteins of tomato. *Journal of plant nutrition* **30**, 497-515 (2007).

83 Wei, Z., Dong, L. & Tian, Z. Fourier transform infrared spectrometry study on early stage of cadmium stress in clover leaves. *Pak J Bot* **41**, 1743-1750 (2009).

84 Mimmo, T., Marzadori, C., Montecchio, D. & Gessa, C. Characterisation of Ca- and Al-pectate gels by thermal analysis and FT-IR spectroscopy. *Carbohydrate Research* **340**, 2510-2519 (2005).

85 McCann, M. C. *et al.* Neural network analyses of infrared spectra for classifying cell wall architectures. *Plant Physiology* **143**, 1314-1326 (2007).

86 Kazarian, S. G. & Chan, K. A. ATR-FTIR spectroscopic imaging: recent advances and applications to biological systems. *Analyst* **138**, 1940-1951 (2013).

87 Lu, Y.-B. *et al.* Identification of boron-deficiency-responsive microRNAs in Citrus sinensis roots by Illumina sequencing. *BMC plant biology* **14**, 1 (2014).

88 Liu, P. & Si, Y. in *Statistical Analysis of Next Generation Sequencing Data* 191-217 (Springer, 2014).

89 Roy, S. Function of MYB domain transcription factors in abiotic stress and epigenetic control of stress response in plant genome. *Plant Signaling & Behavior* **11**, e1117723 (2016).

90 Levy, A., Guenoune-Gelbart, D. & Epel, B. L. β -1,3-Glucanases: Plasmodesmal Gate Keepers for Intercellular Communication. *Plant Signaling & Behavior* **2**, 404-407 (2007).

91 Tucker, G. A., Robertson, N. G. & Grierson, D. Purification and changes in activities of tomato pectinesterase isoenzymes. *Journal of the Science of Food and Agriculture* **33**, 396-400 (1982).

92 Cao, K. *et al.* Four Tomato FLOWERING LOCUS T-Like Proteins Act Antagonistically to Regulate Floral Initiation. *Frontiers in plant science* **6**, 1213 (2015).

93 Minic, Z. & Jouanin, L. Plant glycoside hydrolases involved in cell wall polysaccharide degradation. *Plant physiology and Biochemistry* **44**, 435-449 (2006).

94 Zhong, R., Burk, D. H., Morrison, W. H. & Ye, Z.-H. A kinesin-like protein is essential for oriented deposition of cellulose microfibrils and cell wall strength. *The plant cell* **14**, 3101-3117 (2002).

95 Zhu, B., Chen, T. H. & Li, P. H. Activation of two osmotin-like protein genes by abiotic stimuli and fungal pathogen in transgenic potato plants. *Plant Physiology* **108**, 929-937 (1995).

96 Tewari, R. K., Kumar, P., Tewari, N., Srivastava, S. & Sharma, P. N. Macronutrient deficiencies and differential antioxidant responses—fluence on the activity and expression of superoxide dismutase in maize. *Plant Science* **166**, 687-694 (2004).

97 Schmitz-Eiberger, M., Haefs, R. & Noga, G. Calcium deficiency-Influence on the antioxidative defense system in tomato plants. *Journal of Plant Physiology* **159**, 733-742 (2002).

98 Borowski, P. *et al.* NTPase/helicase of Flaviviridae: inhibitors and inhibition of the enzyme. *ACTA BIOCHIMICA POLONICA-ENGLISH EDITION* **49**, 597-614 (2002).

99 Selvakumar, P., Gahlot, D., Tomar, P. P., Sharma, N. & Sharma, A. K. Molecular evolution of miraculin-like proteins in soybean Kunitz super-family. *Journal of molecular evolution* **73**, 369-379 (2011).

100 Kamiya, T. *et al.* NIP1;1, an aquaporin homolog, determines the arsenite sensitivity of *Arabidopsis thaliana*. *The Journal of biological chemistry* **284**, 2114-2120 (2009).

101 El-Kouhen, K. *et al.* Identification and characterization of a triacylglycerol lipase in *Arabidopsis* homologous to mammalian acid lipases. *FEBS letters* **579**, 6067-6073 (2005).

102 Sun, C.-W., Chen, L.-J., Lin, L.-C. & Li, H.-m. Leaf-specific upregulation of chloroplast translocon genes by a cct motif-containing protein, cia 2. *The Plant Cell* **13**, 2053-2061 (2001).

103 Wang, H. *et al.* Characterisation of a ux/iaa like genes expressed in tomato fruit. *Biology and Biotechnology of the Plant Hormone Ethylene III* **349**, 309 (2003).

104 Büschges, R. *et al.* The barley Mlo gene: a novel control element of plant pathogen resistance. *Cell* **88**, 695-705 (1997).

105 Liu, J., Elmore, J. M. & Coaker, G. Investigating the functions of the RIN4 protein complex during plant innate immune responses. *Plant Signaling & Behavior* **4**, 1107-1110 (2009).

106 Pēna-Cortés, H., Sánchez-Serrano, J. J., Mertens, R., Willmitzer, L. & Prat, S. Abscisic acid is involved in the wound-induced expression of the proteinase inhibitor II gene in potato and tomato. *Proceedings of the National Academy of Sciences* **86**, 9851-9855 (1989).

107 Park, J. *et al.* The *Arabidopsis thaliana* homeobox gene ATHB12 is involved in symptom development caused by geminivirus infection. *PloS one* **6**, e20054 (2011).

108 Simões, I. & Faro, C. Structure and function of plant aspartic proteinases. *European journal of biochemistry* **271**, 2067-2075 (2004).

109 Schnurr, J. & Shockley, J. The acyl-CoA synthetase encoded by LACS2 is essential for normal cuticle development in *Arabidopsis*. *The Plant Cell* **16**, 629-642 (2004).

110 Xu, Y.-H. *et al.* Light-harvesting chlorophyll a/b-binding proteins are required for stomatal response to abscisic acid in *Arabidopsis*. *Journal of experimental botany* **63**, 1095-1106 (2012).

111 Maloney, G. S. *et al.* Characterization of the Branched-Chain Amino Acid Aminotransferase Enzyme Family in Tomato. *Plant Physiology* **153**, 925-936 (2010).

112 Bolwell, G. P., Bozak, K. & Zimmerlin, A. Plant cytochrome P450. *Phytochemistry* **37**, 1491-1506 (1994).

113 Marín-Rodríguez, M. C., Orchard, J. & Seymour, G. B. Pectate lyases, cell wall degradation and fruit softening. *Journal of Experimental Botany* **53**, 2115-2119 (2002).

114 Cheong, Y. H. *et al.* Transcriptional profiling reveals novel interactions between wounding, pathogen, abiotic stress, and hormonal responses in *Arabidopsis*. *Plant Physiology* **129**, 661-677 (2002).

115 Hu, B. *et al.* Epigenetic control of Pollen Ole e 1 allergen and extensin family gene expression in *Arabidopsis thaliana*. *Acta physiologiae plantarum* **36**, 2203-2209 (2014).

116 Nahirñak, V., Almasia, N. I., Hopp, H. E. & Vazquez-Rovere, C. Snakin/GASA proteins: Involvement in hormone crosstalk and redox homeostasis. *Plant Signaling & Behavior* **7**, 1004-1008 (2012).

117 Saladié, M., Rose, J. K., Cosgrove, D. J. & Catalá, C. Characterization of a new xyloglucan endotransglucosylase/hydrolase (XTH) from ripening tomato fruit and implications for the diverse modes of enzymic action. *The Plant Journal* **47**, 282-295 (2006).

Chapter 8

General Discussion

Holly J. Butler

8. General Discussion

Currently available methods to derive informative data on plant health and function are limited to specialised approaches that require extensive sample preparation steps and are thus not readily implemented in the field. Consequently, there is a need for a robust analytical technique that is able to rapidly provide equivalent information. In this series of studies, the viability of vibrational spectroscopy as a method to elucidate valuable chemical information from plant samples is addressed.

Initially, the application of ATR-FTIR and Raman spectroscopy as non-destructive methods to monitor plant health was investigated. In order to obtain information that was specific to the physiological condition of the plant at a specific time point, measurements were acquired from *S. lycopersicum* leaflets whilst still attached to the whole plant. This is contrary to previous studies that have employed ATR-FTIR for *in situ* analysis¹⁻³. Primarily, it was evident that Raman spectra could be obtained from *in vivo* plant leaves, despite contributions from autofluorescence and Raman background. This affect was attributed to the fluorescence quenching effect of water contained within the leaves, and also the ability of water to facilitate light penetration through the sample. Water content had no negative impacts on the signal obtained from ATR-FTIR spectroscopy.

By monitoring the IR and Raman spectral signature of samples over time, the non-destructive nature of these approaches was interrogated. Due to the necessity of the IRE being placed in contact with the sample, localised damage can be seen when used upon the adaxial leaf surface. Using chemometric feature extraction, this was shown to have a detrimental effect on the leaf tissue over time, although had no effect upon systemic tissues. No effect of Raman sampling could be observed both locally and systemically to the area of analysis. To further investigate the validity of the data obtained, spectral alterations indicative of healthy plant growth were inspected. These changes were known to correlate with known biochemical changes that occur during plant growth, including cell wall expansion and leaf senescence. This indicates that both techniques could be employed for *in vivo* crop monitoring.

With the capabilities of these methods for plant-based analysis established, vibrational spectroscopy techniques were employed in several crop screening investigations. Due to the negative impacts of traditional fertiliser use, the use of foliar fertiliser sprays for nutrient supplementation was investigated as a novel system for crop screening. Primarily, Raman microspectroscopy was employed to monitor the uptake of Ca from the leaf surface, complementary to ion specific measurements. The uptake of Ca solutions down to 15 mM concentrations could be monitored using this spectroscopic approach, whilst ion probe measurements yielded specific information regarding the rate of uptake. A combination of these approaches thus could be used a method of monitoring the effects of fertiliser composition on rate of uptake and may be of use in the agrochemical and bio-enhancement industry ⁴. Furthermore, this approach could be used to better understand the mechanisms of nutrient uptake and translocation, by observing alterations in nutrient uptake in transgenic species ^{5,6}.

An additional application of vibrational spectroscopy screening of crops is for the determination of crop nutrient status. Nutrient deficiencies are a primary cause of reduced crop yields, crop quality and shelf life; all of which are substantially the efficiency of the food production line ⁷. The use of NIR reflectance technologies have shown that a method of rapidly determining the nutrient requirements of a crop is useful in agricultural settings ⁸. IR and Raman spectroscopy can similarly provide detection of nutrient stress, whilst also exposing further spectral, and therefore biochemical, detail. The result of this is the potential to presymptomatically detect nutrient deficiencies from crops, by interrogation of the spectral fingerprint. Ca deficiency was employed as model nutrient stress due to the element's fundamental role in plant structure and function ⁹. The symptoms of Ca deficiency are analogous with other immobile plant nutrient deficiencies and often do not manifest until fruit set in species such as BER in tomato ¹⁰.

The effects of Ca deficiency were first typified in *C. communis* plants using SR-FTIR microspectroscopy. The purpose of this was two pronged; firstly, to extract information regarding the deficiency, but also to assess if SR could overcome the issues of water interference in IR measurements. SR-FTIR microspectroscopy was also able to distinguish between cell types in fresh tissue that had a significant water content, showing that plant-based investigations should not always be confined to fixed samples, where biochemical differences due to the fixation process can be seen. Using chemometrics, Ca deficiency could be detected in freshly prepared, Ca stressed tissues at

a classification accuracy above 90%, without the need of considerable sample preparation steps. This showed that presymptomatic detection of Ca deficiencies could be determined using FTIR microspectroscopy, albeit an extremely powerful SR-based approach.

To further interrogate this finding, the use of benchtop ATR-FTIR spectroscopy and spontaneous Raman microspectroscopy were employed to presymptomatic detect Ca deficiency in the model system *S. lycopersicum*. *In vivo* measurements using Raman microspectroscopy were able to distinguish extreme levels of deficiency without the need for sample preparation, such as required for alternative elemental analyses¹¹. Complementary ATR-FTIR of dried plant tissues was able to further distinguish these biochemical symptoms at high rates of sensitivity and specificity. Both of these approaches were also able to characterise the successful remediate of deficiency by the addition of an optimum Ca level. The addition of RNA-sequencing analysis to this biochemical information provides a compelling insight into plant stress mechanisms.

From these studies, it is evident that there is much potential for all of the techniques discussed to have a significant role in the field of plant and agricultural sciences. Whilst Raman microspectroscopy has been substantially limited in such plant based samples, here it is shown that biological information can be extracted simply and robustly, without the need for extensive preparation steps. The performance of the Raman approach however, is observably lower than alternative techniques employed in these studies, particularly in comparison to ATR-FTIR. Utilising powerful light sources in a SR-FTIR approach, also showed the potential of overcoming water absorption in aqueous samples. Despite this, a significant limitation of this technique in plant research is the dependency on large facilities which often do not have plant growth amenities. Furthermore, from an agricultural and crop screening viewpoint, synchrotron facilities are not readily accessible.

With all this in mind, this study shows that the most powerful technique, that is readily available for plant investigations on the macroscale, is ATR-FTIR. This approach is able to distinguish plant growth characteristics as well as sensitively and presymptomatically detect nutrient deficiency, whilst having no systemic effects on the crop. Although some local damage can be seen, due to the reliance upon crystal-to-sample contact, this is often not significant in the field as leaves and even single fruit

could be easily sacrificed for the purpose of crop screening. As the sampling area is limited to 250 x 250 µm, an overall spectrum from the leaf rather than from specific tissues can be obtained, which may prove more useful in real-world analyses. FTIR and Raman microspectroscopy would be suitable for when tissue specific information is required, and also for the latter, when a greater penetration depth is needed.

8.1 Future Perspectives

The results of these investigations show promise towards implementation in the field, where the efficiency of the techniques can be truly assessed on a real-world sample set. Thanks to the collaboration between Lancaster University and Plant Impact Plc., this has already begun, with fertiliser compositions being assessed based on the rate of uptake at the leaf surface. However, for the applications of nutrient status screening, there are a number of key considerations and studies required prior to this happening.

In a controlled environment such as in a research greenhouse, the effects of humidity, temperature and nutrient availability can be readily manipulated, whereas this is not the case in the field. The relationship between Ca and other essential plant nutrients must be considered before field trials could be conducted ^{12,13}. Furthermore, for use as a generic screening tool, there would be a requirement to investigate additional crop species additional to *S. lycopersicum*, as well as the other nutrient deficiencies.

More widely, these investigations highlight the capabilities of vibrational spectroscopies for plant-based research. Although sophisticated techniques have been developed to overcome some of the well characterised issues with FTIR and Raman spectroscopy for fresh plant tissue analysis, here it is shown that informative biochemical data can be produced from simple, rapid and non-destructive approaches. As such, it is hoped that further studies continue to apply these approaches for plant biology and contribute towards our understanding of crop responses in the fight for food security.

References

- 1 Ivanova, D. G. & Singh, B. R. Nondestructive FTIR monitoring of leaf senescence and elicitin-induced changes in plant leaves. *Biopolymers* **72**, 79-85 (2003).
- 2 Monti, F. *et al.* A multivariate statistical analysis approach to highlight molecular processes in plant cell walls through ATR FT-IR microspectroscopy: The role of the α -expansin PhEXPA1 in Petunia hybrida. *Vibrational Spectroscopy* **65**, 36-43 (2013).
- 3 Ribeiro da Luz, B. Attenuated total reflectance spectroscopy of plant leaves: a tool for ecological and botanical studies. *New Phytologist* **172**, 305-318 (2006).
- 4 Dixon, R. C. Foliar fertilization improves nutrient use efficiency. *Fluid Journal* **11**, 22-23 (2003).
- 5 Fernández, V. & Brown, P. H. From plant surface to plant metabolism: the uncertain fate of foliar-applied nutrients. *Front. Plant Sci.* **4**, 289 (2013).
- 6 Bukovac, M. J. & Wittwer, S. H. Absorption and Mobility of Foliar Applied Nutrients. *Plant Physiol.* **32**, 428-435 (1957).
- 7 Mueller, N. D. *et al.* Closing yield gaps through nutrient and water management. *Nature* **490**, 254-257 (2012).
- 8 Foley, W. J. *et al.* Ecological applications of near infrared reflectance spectroscopy—a tool for rapid, cost-effective prediction of the composition of plant and animal tissues and aspects of animal performance. *Oecologia* **116**, 293-305 (1998).
- 9 White, P. J. & Broadley, M. R. Calcium in Plants. *Annals of Botany* **92**, 487-511 (2003).
- 10 Simon, E. W. The symptoms of calcium deficiency in plants. *New Phytologist* **80**, 1-15 (1978).
- 11 Reuter, D. *Plant analysis: an interpretation manual.* (CSIRO publishing, 1997).
- 12 Sonneveld, C. & Voogt, W. in *II Symposium on Horticultural Substrates and their Analysis, XXIII IHC* 294. 81-88.
- 13 Nonami, H., Fukuyama, T., Yamamoto, M., Yang, L. & Hashimoto, Y. Blossom-end rot of tomato plants may not be directly caused by calcium deficiency. *Hydroponics and Transplant Production* **396**, 107-114 (1994).

References

Abidi, N., Cabrales, L. & Haigler, C. H. Changes in the cell wall and cellulose content of developing cotton fibers investigated by FTIR spectroscopy. *Carbohydrate Polymers* **100**, 9-16 (2014).

Ackermann, K. R., Henkel, T. & Popp, J. Quantitative Online Detection of Low-Concentrated Drugs via a SERS Microfluidic System. *ChemPhysChem* **8**, 2665-2670 (2007).

Agarwal, U. P. Raman imaging to investigate ultrastructure and composition of plant cell walls: distribution of lignin and cellulose in black spruce wood (*Picea mariana*). *Planta* **224**, 1141-1153 (2006).

Aghdam, M. S., Hassanpouraghdam, M. B., Paliyath, G. & Farmani, B. The language of calcium in postharvest life of fruits, vegetables and flowers. *Scientia Horticulturae* **144**, 102-115 (2012).

Ahmadzai, A. A. *et al.* The Syrian hamster embryo (SHE) assay (pH 6.7): mechanisms of cell transformation and application of vibrational spectroscopy to objectively score endpoint alterations. *Mutagenesis* **27**, 257-266 (2012).

Alexander, A. in *Foliar fertilization* 44-60 (Springer, 1986).

Ali, S. M. *et al.* Raman spectroscopic analysis of human skin tissue sections ex-vivo: evaluation of the effects of tissue processing and dewaxing. *J. Biomed. Opt.* **18**, 61202 (2013).

Alloway, B. J. *Micronutrient deficiencies in global crop production*. (Springer Science & Business Media, 2008).

Allwood, J. W., Ellis, D. I. & Goodacre, R. Metabolomic technologies and their application to the study of plants and plant–host interactions. *Physiologia plantarum* **132**, 117-135 (2008).

Allwood, J. W., Heald, J., Lloyd, A. J., Goodacre, R. & Mur, L. A. in *Plant Metabolomics* Vol. 860 31-49 (Springer, 2012).

Ami, D., Natalello, A., Zullini, A. & Doglia, S. M. Fourier transform infrared microspectroscopy as a new tool for nematode studies. *FEBS Lett.* **576**, 297-300 (2004).

Angel, S., Carrabba, M. & Cooney, T. The utilization of diode lasers for Raman spectroscopy. *Spectrochim. Acta A* **51**, 1779-1799 (1995).

Antoniaa, L., Tompetrini, S. & Svetlanab, P. Quantification of pigments in tomato leaves using reflectance spectroscopy. *P. Int. Symp. Rem. S. Environ.* **31**, 39-42 (2005).

Antonio, K. A. & Schultz, Z. D. Advances in biomedical Raman microscopy. *Anal. Chem.* **86**, 30-46 (2013).

Asher, S. A. & Johnson, C. R. Raman spectroscopy of a coal liquid shows that fluorescence interference is minimized with ultraviolet excitation. *Science* **225**, 311-313 (1984).

Asher, S. A., Ludwig, M. & Johnson, C. R. UV resonance Raman excitation profiles of the aromatic amino acids. *J. Am. Chem. Soc.* **108**, 3186-3197 (1986).

Ashokkumar, R. & Ramaswamy, M. Phytochemical screening by FTIR spectroscopic analysis of leaf extracts of selected Indian medicinal plants. *Int J Curr Microbiol Appl Sci* **3**, 395-396 (2014).

Ashton, L., Lau, K., Winder, C. L. & Goodacre, R. Raman spectroscopy: lighting up the future of microbial identification. *Future Microbiol.* **6**, 991-997 (2011).

Auerhammer, H. Precision farming—the environmental challenge. *Computers and electronics in agriculture* **30**, 31-43 (2001).

Baboulène, L., Silvestre, J., Pinelli, E. & Morard, P. Effect of Ca deficiency on growth and leaf acid soluble proteins of tomato. *Journal of plant nutrition* **30**, 497-515 (2007).

Baker, M. *et al.* An investigation of the RWPE prostate derived family of cell lines using FTIR spectroscopy. *Analyst* **135**, 887-894 (2010).

Baker, M. J. *et al.* Investigating FTIR based histopathology for the diagnosis of prostate cancer. *J. Biophotonics* **2**, 104-113 (2009).

Baker, M. J. *et al.* FTIR-based spectroscopic analysis in the identification of clinically aggressive prostate cancer. *Br. J. Cancer* **99**, 1859-1866 (2008).

Baker, M. J., Hughes, C. S. & Hollywood, K. A. in *Biophotonics: Vibrational Spectroscopic Diagnostics* 3-1-3-13 (Morgan & Claypool Publishers, 2016).

Baker, M. J., Hughes, C. S. & Hollywood, K. A. in *Biophotonics: Vibrational Spectroscopic Diagnostics* 2-1-2-14 (Morgan & Claypool Publishers, 2016).

Baker, M. J. *et al.* Developing and understanding biofluid vibrational spectroscopy: a critical review. *Chemical Society Reviews* **45**, 1803-1818 (2016).

Baker, M. J. *et al.* Using Fourier transform IR spectroscopy to analyze biological materials. *Nature protocols* **9**, 1771-1791 (2014).

Balabin, R. M., Safieva, R. Z. & Lomakina, E. I. Near-infrared (NIR) spectroscopy for motor oil classification: From discriminant analysis to support vector machines. *Microchem. J.* **98**, 121-128 (2011).

Baligar, V., Fageria, N. & He, Z. Nutrient use efficiency in plants. *Communications in Soil Science and Plant Analysis* **32**, 921-950 (2001).

Balshaw, B. & Smedley, S. I. Raman spectroscopy of concentrated calcium nitrate solutions at high pressure. *J. Phys. Chem.* **79**, 1323-1325 (1975).

Bangerth, F. Calcium-related physiological disorders of plants. *Annual review of phytopathology* **17**, 97-122 (1979).

Baranska, M., Roman, M., Schulz, H. & Baranski, R. Recent advances in Raman analysis of plants: alkaloids, carotenoids, and polyacetylenes. *Current Analytical Chemistry* **9**, 108-127 (2013).

Baranska, M., Schütze, W. & Schulz, H. Determination of lycopene and β -carotene content in tomato fruits and related products: comparison of FT-Raman, ATR-IR, and NIR spectroscopy. *Anal. Chem.* **78**, 8456-8461 (2006).

Baranski, R., Baranska, M. & Schulz, H. Changes in carotenoid content and distribution in living plant tissue can be observed and mapped in situ using NIR-FT-Raman spectroscopy. *Planta* **222**, 448-457 (2005).

Barman, I., Kong, C.-R., Singh, G. P. & Dasari, R. R. Effect of photobleaching on calibration model development in biological Raman spectroscopy. *J. Biomed. Opt.* **16**, 011004 (2011).

Barrett, L., Dougan, J. A., Faulds, K. & Graham, D. Stable dye-labelled oligonucleotide-nanoparticle conjugates for nucleic acid detection. *Nanoscale* **3**, 3221-3227 (2011).

Barth, A. Infrared spectroscopy of proteins. *Biochimica et Biophysica Acta (BBA) - Bioenergetics* **1767**, 1073-1101 (2007).

Bassan, P. *et al.* Resonant Mie scattering in infrared spectroscopy of biological materials - understanding the 'dispersion artefact'. *Analyst* **134**, 1586-1593 (2009).

Bassan, P. *et al.* Resonant Mie Scattering (RMieS) correction of infrared spectra from highly scattering biological samples. *Analyst* **135**, 268-277 (2010).

Bassan, P. *et al.* RMieS-EMSC correction for infrared spectra of biological cells: Extension using full Mie theory and GPU computing. *J. Biophotonics* **3**, 609-620 (2010).

Bassan, P. *et al.* The inherent problem of transfection-mode infrared spectroscopic microscopy and the ramifications for biomedical single point and imaging applications. *Analyst* **138**, 144-157 (2013).

Bassan, P. *et al.* FTIR microscopy of biological cells and tissue: data analysis using resonant Mie scattering (RMieS) EMSC algorithm. *Analyst* **137**, 1370-1377 (2012).

Bassan, P., Sachdeva, A., Lee, J. & Gardner, P. Substrate contributions in micro ATR of thin samples: Implications for analysis of cells, tissue and biological fluids. *Analyst* **38**, 4139-4146 (2013).

Bassan, P. *et al.* Whole organ cross-section chemical imaging using label-free mega-mosaic FTIR microscopy. *Analyst* **138**, 7066-7069 (2013).

Batten, G. D. Plant analysis using near infrared reflectance spectroscopy: the potential and the limitations. *Australian Journal of Experimental Agriculture* **38**, 697-706 (1998).

Baulcombe, D. *et al.* *Reaping the benefits: science and the sustainable intensification of global agriculture.* (The Royal Society, 2009).

Beddington, J. Food security: contributions from science to a new and greener revolution. *Philosophical Transactions of the Royal Society of London B: Biological Sciences* **365**, 61-71 (2010).

Beer, A. Bestimmung der Absorption des rothen Lichts in farbigen Flüssigkeiten. *Annalen der Physik* **162**, 78-88 (1852).

Beier, B. D. & Berger, A. J. Method for automated background subtraction from Raman spectra containing

known contaminants. *Analyst* **134**, 1198-1202 (2009).

Beleites, C., Neugebauer, U., Bocklitz, T., Krafft, C. & Popp, J. Sample size planning for classification models. *Analytica chimica acta* **760**, 25-33 (2013).

Beleites, C. & Salzer, R. Assessing and improving the stability of chemometric models in small sample size situations. *Analytical and bioanalytical chemistry* **390**, 1261-1271 (2008).

Bellisola, G. & Sorio, C. Infrared spectroscopy and microscopy in cancer research and diagnosis. *Am. J. Cancer Res.* **2**, 1-21 (2012).

Berenbaum, M. C. The Histochemistry of Bound Lipids. *Q. J. Microsc. Sci.* **s3-99**, 231-242 (1958).

Bergholt, M. S. *et al.* In vivo diagnosis of esophageal cancer using image-guided Raman endoscopy and biomolecular modeling. *Technol. Cancer Res. T.* **10**, 103-112 (2011).

Berridge, M. J., Lipp, P. & Bootman, M. D. The versatility and universality of calcium signalling. *Nature Reviews Molecular Cell Biology* **1**, 11-21 (2000).

Besford, R. A rapid tissue test for diagnosing phosphorus deficiency in the tomato plant. *Annals of Botany* **45**, 225-227 (1980).

Bhargava, R. Towards a practical Fourier transform infrared chemical imaging protocol for cancer histopathology. *Anal Bioanal Chem* **389**, 1155-1169 (2007).

Bhargava, R. Infrared spectroscopic imaging: the next generation. *Appl. Spectrosc.* **66**, 1091-1120 (2012).

Bhargava, R., Fernandez, D. C., Hewitt, S. M. & Levin, I. W. High throughput assessment of cells and tissues: Bayesian classification of spectral metrics from infrared vibrational spectroscopic imaging data. *Biochimica et Biophysica Acta (BBA)-Biomembranes* **1758**, 830-845 (2006).

Bhargava, R., Fernandez, D. C., Schaeberle, M. D. & Levin, I. W. Effect of focal plane array cold shield aperture size on Fourier transform infrared micro-imaging spectrometer performance. *Appl. Spectrosc.* **54**, 1743-1750 (2000).

Bhargava, R. & Levin, I. W. Fourier transform infrared imaging: theory and practice. *Anal. Chem.* **73**, 5157-5167 (2001).

Bhargava, R. & Levin, I. W. Effective time averaging of multiplexed measurements: A critical analysis. *Anal. Chem.* **74**, 1429-1435 (2002).

Bhargava, R. & Levin, I. W. *Spectrochemical Analysis Using Infrared Multichannel Detectors*. (Wiley-Blackwell, Oxford, UK, 2005).

Bhargava, R., Ribar, T. & Koenig, J. L. Towards faster FT-IR imaging by reducing noise. *Appl. Spectrosc.* **53**, 1313-1322 (1999).

Bhargava, R., Schaeberle, M. D., Fernandez, D. C. & Levin, I. W. Novel route to faster Fourier transform infrared spectroscopic imaging. *Appl. Spectrosc.* **55**, 1079-1084 (2001).

Bhargava, R., Wall, B. G. & Koenig, J. L. Comparison of the FT-IR mapping and imaging techniques applied to polymeric systems. *Appl. Spectrosc.* **54**, 470-479 (2000).

Bhargava, R., Wang, S.-Q. & Koenig, J. L. Route to higher fidelity FT-IR imaging. *Appl. Spectrosc.* **54**, 486-495 (2000).

Birch, A. N. E., Begg, G. S. & Squire, G. R. How agro-ecological research helps to address food security issues under new IPM and pesticide reduction policies for global crop production systems. *Journal of Experimental Botany* **62**, 3251-3261 (2011).

Bird, B. *et al.* Detection of breast micro-metastases in axillary lymph nodes by infrared micro-spectral imaging. *Analyst* **134**, 1067-1076 (2009).

Bird, B. *et al.* Infrared spectral histopathology (SHP): a novel diagnostic tool for the accurate classification of lung cancer. *Lab. Invest.* **92**, 1358-1373 (2012).

Bird, B. *et al.* Infrared micro-spectral imaging: distinction of tissue types in axillary lymph node histology. *BMC Clin. Pathol.* **8**, 8-8 (2008).

Bird, B. *et al.* Cytology by infrared micro-spectroscopy: Automatic distinction of cell types in urinary cytology. *Vib. Spectrosc.* **48**, 101-106 (2008).

Blanch, E. W., Hecht, L. & Barron, L. D. Vibrational Raman optical activity of proteins, nucleic acids, and viruses. *Methods* **29**, 196-209 (2003).

Blanch, E. W. *et al.* Is polyproline II helix the killer conformation? a raman optical activity study of the amyloidogenic prefibrillar intermediate of human lysozyme. *J. Mol. Biol.* **301**, 553-563 (2000).

Bocklitz, T., Walter, A., Hartmann, K., Rösch, P. & Popp, J. How to pre-process Raman spectra for reliable and stable models? *Analytica chimica acta* **704**, 47-56 (2011).

Böhme, R. *et al.* Biochemical imaging below the diffraction limit—probing cellular membrane related structures by tip-enhanced Raman spectroscopy (TERS). *J. Biophotonics* **3**, 455-461 (2010).

Bolwell, G. P., Bozak, K. & Zimmerlin, A. Plant cytochrome P450. *Phytochemistry* **37**, 1491-1506 (1994).

Bonnier, F. *et al.* Imaging live cells grown on a three dimensional collagen matrix using Raman microspectroscopy. *Analyst* **135**, 3169-3177 (2010).

Bonnier, F., Petitjean, F., Baker, M. J. & Byrne, H. J. Improved protocols for vibrational spectroscopic analysis of body fluids. *Journal of biophotonics* **7**, 167-179 (2014).

Bonwell, E. S., Fisher, T. L., Fritz, A. K. & Wetzel, D. L. Determination of endosperm protein secondary structure in hard wheat breeding lines using synchrotron infrared microspectroscopy. *Vibrational Spectroscopy* **48**, 76-81 (2008).

Borowski, P. *et al.* NTPase/helicase of Flaviviridae: inhibitors and inhibition of the enzyme. *ACTA BIOCHIMICA POLONICA-ENGLISH EDITION* **49**, 597-614 (2002).

Bouma, D. in *Inorganic plant nutrition* 120-146 (Springer, 1983).

Boyle, R. K., McAinsh, M. & Dodd, I. C. Stomatal closure of *Pelargonium* × *hortorum* in response to soil water deficit is associated with decreased leaf water potential only under rapid soil drying. *Physiol. Plantarum* **156**, 84-96 (2016).

Bradfield, E. & Spincer, D. Leaf analysis as a guide to the nutrition of fruit crops. VI—Determination of magnesium, zinc and copper by atomic absorption spectroscopy. *Journal of the Science of Food and Agriculture* **16**, 33-38 (1965).

Bradley, P. & Marulanda, C. in *World Congress on Soilless Culture: Agriculture in the Coming Millennium* 554. 289-296.

Bray, R. H. A nutrient mobility concept of soil-plant relationships. *Soil Science* **78**, 9-22 (1954).

Breitenbach, J., Schröf, W. & Neumann, J. Confocal Raman-spectroscopy: analytical approach to solid dispersions and mapping of drugs. *Pharm. Res.* **16**, 1109-1113 (1999).

Bretzloff, R. & Bahder, T. Apodization effects in Fourier transform infrared difference spectra. *Rev. Phys. Appl.* **21**, 833-844 (1986).

Brose, K., Zouni, A., Broser, M., Müh, F. & Maultzsch, J. Polarised Raman measurements on the core complex of crystallised photosystem II. *Phys. Status Solidi* **246**, 2813-2816 (2009).

Brown, D. M., Zeef, L. A., Ellis, J., Goodacre, R. & Turner, S. R. Identification of novel genes in *Arabidopsis* involved in secondary cell wall formation using expression profiling and reverse genetics. *The Plant Cell* **17**, 2281-2295 (2005).

Brown, P. H. in *IV International Symposium on Mineral Nutrition of Deciduous Fruit Crops* 564. 217-223.

Bruno-Soares, A. M., Murray, I., Paterson, R. M. & Abreu, J. M. Use of near infrared reflectance spectroscopy (NIRS) for the prediction of the chemical composition and nutritional attributes of green crop cereals. *Anim. Feed Sci. Tech.* **75**, 15-25 (1998).

Bruun, S. W. *et al.* Correcting Attenuated Total Reflection—Fourier Transform Infrared Spectra for Water Vapor and Carbon Dioxide. *Appl. Spectrosc.* **60**, 1029-1039 (2006).

Buchanan-Wollaston, V. The molecular biology of leaf senescence. *J. Exp. Bot.* **48**, 181-199 (1997).

Buckley, K. & Matousek, P. Recent advances in the application of transmission Raman spectroscopy to pharmaceutical analysis. *J. Pharm. Biomed. Anal.* **55**, 645-652 (2011).

Budevska, B. O., Sum, S. T. & Jones, T. J. Application of multivariate curve resolution for analysis of FT-IR microspectroscopic images of *in Situ* plant tissue. *Appl. Spectrosc.* **57**, 124-131 (2003).

Bukovac, M. J. & Wittwer, S. H. Absorption and Mobility of Foliar Applied Nutrients. *Plant Physiol.* **32**, 428-435 (1957).

Bula, R. *et al.* Light-emitting diodes as a radiation source for plants. *HortScience* **26**, 203-205 (1991).

Büschges, R. *et al.* The barley *Mlo* gene: a novel control element of plant pathogen resistance. *Cell* **88**, 695-705 (1997).

Butler, H. J. *et al.* Using Raman spectroscopy to characterize biological materials. *Nature protocols* **11**, 664-687 (2016).

Butler, H. J. *et al.* Gold nanoparticles as a substrate in bio-analytical near-infrared surface-enhanced Raman spectroscopy. *Analyst* **140**, 3090-3097 (2015).

Butler, H. J., McAinsh, M. R., Adams, S. & Martin, F. L. Application of vibrational spectroscopy techniques to non-destructively monitor plant health and development. *Analytical Methods* **7**, 4059-4070 (2015).

Byrne, H., Sockalingum, G. & Stone, N. Raman microscopy: complement or competitor. (2011).

Byrne, H. J. *et al.* Spectropathology for the next generation: Quo vadis? *Analyst* **140**, 2066-2073 (2015).

Byrne, H. J., Sockalingum, G. & Stone, N. in *Biomedical applications of synchrotron infrared microspectroscopy: a practical approach* (ed David Moss) Ch. 4, 105-142 (Royal Society of Chemistry, 2011).

Cakmak, G., Togan, I. & Severcan, F. 17 β -Estradiol induced compositional, structural and functional changes in rainbow trout liver, revealed by FT-IR spectroscopy: a comparative study with nonylphenol. *Aquat. Toxicol.* **77**, 53-63 (2006).

Cakmak, I. in *Progress in Plant Nutrition: Plenary Lectures of the XIV International Plant Nutrition Colloquium*. 3-24 (Springer).

Cao, J. *et al.* Fourier transform infrared microspectroscopy reveals that tissue culture conditions affect the macromolecular phenotype of human embryonic stem cells. *Analyst* **38**, 4147-4160 (2013).

Cao, K. *et al.* Four Tomato FLOWERING LOCUS T-Like Proteins Act Antagonistically to Regulate Floral Initiation. *Front Plant Sci* **6**, 1213 (2015).

Carr, G. Resolution limits for infrared microspectroscopy explored with synchrotron radiation. *Review of Scientific Instruments* **72**, 1613-1619 (2001).

Carriere, J. T. & Havermeyer, F. in *SPIE BiOS*. 821905 (International Society for Optics and Photonics).

Carter, E. A., Tam, K. K., Armstrong, R. S. & Lay, P. A. Vibrational spectroscopic mapping and imaging of tissues and cells. *Biophys. Rev.* **1**, 95-103 (2009).

Carter, M. & Cutcliffe, J. Effects of gypsum on growth and mineral content of Brussels sprouts, and soil properties of Orthic Podzols. *Fertilizer research* **24**, 77-84 (1990).

Case, R. M. *et al.* Evolution of calcium homeostasis: From birth of the first cell to an omnipresent signalling system. *Cell Calcium* **42**, 345-350 (2007).

Caspers, P. J., Lucassen, G. W. & Puppels, G. J. Combined in vivo confocal Raman spectroscopy and confocal microscopy of human skin. *Biophys. J.* **85**, 572-580 (2003).

Chalmers, J. M., Griffiths, P. R., Pivonka, D. E., Chalmers, J. & Griffiths, P. *Applications of vibrational spectroscopy in pharmaceutical research and development*. (Edited by: Pivonka, DE, Chalmers, JM and Griffiths, PR, 2007).

Chan, K. & Kazarian, S. New opportunities in micro-and macro-attenuated total reflection infrared spectroscopic imaging: spatial resolution and sampling versatility. *Appl. Spectrosc.* **57**, 381-389 (2003).

Chan, K. L. A. & Kazarian, S. G. FT-IR spectroscopic imaging of reactions in multiphase flow in microfluidic channels. *Anal. Chem.* **84**, 4052-4056 (2012).

Chan, K. L. A. & Kazarian, S. G. Aberration-free FTIR spectroscopic imaging of live cells in microfluidic devices. *Analyst* **138**, 4040-4047 (2013).

Chang, C.-C. & Lin, C.-J. LIBSVM: a library for support vector machines. *ACM TIST* **2**, 27 (2011).

Chase, B. A new generation of Raman instrumentation. *Appl. Spectrosc.* **48**, 14-19 (1994).

Chasman, R., Green, G. K. & Rowe, E. Preliminary design of a dedicated synchrotron radiation facility. *IEEE Transactions on Nuclear Science* **22**, 1765-1767 (1975).

Chatjigakis, A. K. *et al.* FT-IR spectroscopic determination of the degree of esterification of cell wall pectins from stored peaches and correlation to textural changes. *Carbohydrate Polymers* **37**, 395-408 (1998).

Chen, G. & Shen-En, Q. Denoising of hyperspectral imagery using principal component analysis and wavelet shrinkage. *IEEE Geosci. Remote Sens. Mag.* **49**, 973-980 (2011).

Chen, L. *et al.* A rapid method to screen for cell-wall mutants using discriminant analysis of Fourier transform infrared spectra. *The Plant journal : for cell and molecular biology* **16**, 385-392 (1998).

Cheng, J.-X. & Xie, X. S. Coherent anti-Stokes Raman scattering microscopy: instrumentation, theory,

and applications. *The Journal of Physical Chemistry B* **108**, 827-840 (2004).

Cheong, Y. H. *et al.* Transcriptional profiling reveals novel interactions between wounding, pathogen, abiotic stress, and hormonal responses in *Arabidopsis*. *Plant Physiology* **129**, 661-677 (2002).

Choi, J. *et al.* Direct observation of spectral differences between normal and basal cell carcinoma (BCC) tissues using confocal Raman microscopy. *Biopolymers* **77**, 264-272 (2005).

Chylinska, M., Szymanska-Chargot, M. & Zdunek, A. Imaging of polysaccharides in the tomato cell wall with Raman microspectroscopy. *Plant Methods* **10**, 14 (2014).

Cîntă Pînzaru, S., Pavel, I., Leopold, N. & Kiefer, W. Identification and characterization of pharmaceuticals using Raman and surface-enhanced Raman scattering. *J. Raman Spectrosc.* **35**, 338-346 (2004).

Clapham, D. E. Calcium signaling. *Cell* **80**, 259-268 (1995).

Clapham, D. E. Calcium signaling. *Cell* **131**, 1047-1058 (2007).

Clarkson, D. T. Calcium transport between tissues and its distribution in the plant. *Plant, Cell & Environment* **7**, 449-456 (1984).

Clemens, G., Bird, B., Weida, M., Rowlette, J. & Baker, M. J. Quantum cascade laser-based mid-infrared spectrochemical imaging of tissue and biofluids. *Spectroscopy Europe* **26**, 14-19 (2014).

Clemens, G., Hands, J. R., Dorling, K. M. & Baker, M. J. Vibrational spectroscopic methods for cytology and cellular research. *Analyst* **139**, 4411-4444 (2014).

Coates, J. Interpretation of infrared spectra, a practical approach. *Encyclopedia of analytical chemistry* (2000).

Colarusso, P. *et al.* Infrared spectroscopic imaging: from planetary to cellular systems. *Appl. Spectrosc.* **52**, 106-120 (1998).

Collier, G. F. & Tibbitts, T. W. in *Horticultural Reviews* 49-65 (Springer, 1982).

Colthup, N. *Introduction to infrared and Raman spectroscopy*. (Elsevier, 2012).

Coombes, K. R. *et al.* Quality control and peak finding for proteomics data collected from nipple aspirate fluid by surface-enhanced laser desorption and ionization. *Clin. Chem.* **49**, 1615-1623 (2003).

Cooper, J. *et al.* Raman spectroscopy with a low-cost imaging CCD array. *Spectrochim. Acta A* **50**, 567-575 (1994).

Cooper, J. B. Chemometric analysis of Raman spectroscopic data for process control applications. *Chemometr. Intell. Lab.* **46**, 231-247 (1999).

Cosgrove, D. J. Growth of the plant cell wall. *Nat. Rev. Mol. Cell Biol.* **6**, 850-861 (2005).

Cowe, I. A. & McNicol, J. W. The Use of Principal Components in the Analysis of Near-Infrared Spectra. *Applied Spectroscopy* **39**, 257-266 (1985).

Cozzolino, D., Fassio, A. & Gimenez, A. The use of near-infrared reflectance spectroscopy (NIRS) to predict the composition of whole maize plants. *J. Sci. Food Agr.* **81**, 142-146 (2001).

Craswell, E. & Godwin, D. The efficiency of nitrogen fertilizers applied to cereals grown in different climates. (1984).

Creely, C., Volpe, G., Singh, G., Soler, M. & Petrov, D. Raman imaging of floating cells. *Optics express* **13**, 6105-6110 (2005).

Crow, P. *et al.* Assessment of fiberoptic near-infrared Raman spectroscopy for diagnosis of bladder and prostate cancer. *Urology* **65**, 1126-1130 (2005).

Crow, P. *et al.* The use of Raman spectroscopy to identify and grade prostatic adenocarcinoma in vitro. *Br. J. Cancer* **89**, 106-108 (2004).

Cui, L., Butler, H. J., Martin-Hirsch, P. L. & Martin, F. L. Aluminium foil as a potential substrate for ATR-FTIR, transfection FTIR or Raman spectrochemical analysis of biological specimens. *Anal. Methods* (2015).

Daley, C. M. Application of data mining tools for exploring data: Yarn quality case study. (2008).

Darvin, M. *et al.* Non-invasive in vivo detection of the carotenoid antioxidant substance lycopene in the human skin using the resonance Raman spectroscopy. *Laser Phys. Lett.* **3**, 460 (2006).

Davis, B. J., Carney, P. S. & Bhargava, R. Theory of mid-infrared absorption microspectroscopy: II. Heterogeneous samples. *Anal. Chem.* **82**, 3487-3499 (2010).

Davis, B. J., Carney, P. S. & Bhargava, R. Theory of mid-infrared absorption microspectroscopy: I.

Homogeneous samples. *Anal. Chem.* **82**, 3474-3486 (2010).

Davis, W., Erickson, C., Johnston, C., Delfino, J. & Porter, J. Quantitative Fourier Transform Infrared spectroscopic investigation humic substance functional group composition. *Chemosphere* **38**, 2913-2928 (1999).

de Sousa Marques, A., de Melo, M. C. N., Cidral, T. A. & de Lima, K. M. G. Feature selection strategies for identification of *Staphylococcus aureus* recovered in blood cultures using FT-IR spectroscopy successive projections algorithm for variable selection: A case study. *J. Microbiol. Meth.* **98**, 26-30 (2014).

Deegan, R. D. *et al.* Capillary flow as the cause of ring stains from dried liquid drops. *Nature* **389**, 827-829 (1997).

Dekker, E. & Fockens, P. Advances in colonic imaging: new endoscopic imaging methods. *Euro. J. Gastroen. Hepat.* **17**, 803-808 (2005).

Delmer, D. P. Agriculture in the developing world: connecting innovations in plant research to downstream applications. *Proceedings of the National Academy of Sciences of the United States of America* **102**, 15739-15746 (2005).

Demidchik, V. & Maathuis, F. J. M. Physiological roles of nonselective cation channels in plants: from salt stress to signalling and development. *New Phytologist* **175**, 387-404 (2007).

Despommier, D. The vertical farm: controlled environment agriculture carried out in tall buildings would create greater food safety and security for large urban populations. *Journal für Verbraucherschutz und Lebensmittelsicherheit* **6**, 233-236 (2011).

Dibden, J., Gibbs, D. & Cocklin, C. Framing GM crops as a food security solution. *Journal of Rural Studies* **29**, 59-70 (2013).

Dieing, T. & Hollricher, O. High-resolution, high-speed confocal Raman imaging. *Vib. Spectrosc.* **48**, 22-27 (2008).

Diem, M. *et al.* in *Ex-vivo and In-vivo Optical Molecular Pathology* (ed Jürgen Popp) Ch. 3, 45-102 (2014).

Diem, M., Romeo, M., Boydston-White, S., Miljkovic, M. & Matthaus, C. A decade of vibrational micro-spectroscopy of human cells and tissue (1994-2004). *Analyst* **129**, 880-885 (2004).

Diem, M., Romeo, M., Boydston-White, S., Miljković, M. & Matthäus, C. A decade of vibrational micro-spectroscopy of human cells and tissue (1994-2004). *Analyst* **129**, 880-885 (2004).

Diem, M. *et al.* Comparison of Fourier transform infrared (FTIR) spectra of individual cells acquired using synchrotron and conventional sources. *Infrared Phys. Techn.* **45**, 331-338 (2004).

Dixon, R. C. Foliar fertilization improves nutrient use efficiency. *Fluid Journal* **11**, 22-23 (2003).

Dodd, A. N., Kudla, J. & Sanders, D. The language of calcium signaling. *Annual review of plant biology* **61**, 593-620 (2010).

Dokken, K. M. & Davis, L. C. Infrared Imaging of Sunflower and Maize Root Anatomy. *Journal of Agricultural and Food Chemistry* **55**, 10517-10530 (2007).

Dokken, K. M., Davis, L. C. & Marinkovic, N. S. Use of infrared microspectroscopy in plant growth and development. *Applied Spectroscopy Reviews* **40**, 301-326 (2005).

Domagała-Świątkiewicz, I. & Błaszczyk, J. Effect of calcium nitrate spraying on mineral contents and storability of 'Elise' apples. *Pol. J. Environ. Stud.* **18**, 971-976 (2009).

Domínguez, E., Heredia-Guerrero, J. A. & Heredia, A. The biophysical design of plant cuticles: an overview. *New Phytol.* **189**, 938-949 (2011).

Domínguez-Martínez, I., Meza-Márquez, O. G., Osorio-Revilla, G., Proal-Nájera, J. & Gallardo-Velázquez, T. Determination of capsaicin, ascorbic acid, total phenolic compounds and antioxidant activity of *Capsicum annuum* L. var. serrano by mid infrared spectroscopy (Mid-FTIR) and chemometric analysis. *J. Korean Soc. Appl. Biol. Chem.* **57**, 133-142 (2014).

Dong, A., Huang, P. & Caughey, W. S. Protein secondary structures in water from second-derivative amide I infrared spectra. *Biochemistry* **29**, 3303-3308 (1990).

Dorling, K. M. & Baker, M. J. Highlighting attenuated total reflection Fourier transform infrared spectroscopy for rapid serum analysis. *Trends Biotechnol.* **31**, 327-328 (2013).

Downes, A. & Elfick, A. Raman spectroscopy and related techniques in biomedicine. *Sensors* **10**, 1871-

1889 (2010).

Draux, F. *et al.* Raman spectral imaging of single living cancer cells: a preliminary study. *Analyst* **134**, 542-548 (2009).

Du, Q., Superfine, R., Freysz, E. & Shen, Y. Vibrational spectroscopy of water at the vapor/water interface. *Physical Review Letters* **70**, 2313 (1993).

Dubis, E., Dubis, A. & Morzycki, J. Comparative analysis of plant cuticular waxes using HATR FT-IR reflection technique. *J. Mol. Struct.* **511**, 173-179 (1999).

Dubis, E. N., Dubis, A. T. & Popławski, J. Determination of the aromatic compounds in plant cuticular waxes using FT-IR spectroscopy. *J. Mol. Struct.* **596**, 83-88 (2001).

Duda, R. O., Hart, P. E. & Stork, D. G. *Pattern Classification*. 2nd edn, (Wiley Interscience, Hoboken, USA, 2001).

Dumas, P., Sockalingum, G. D. & Sule-Suso, J. Adding synchrotron radiation to infrared microspectroscopy: what's new in biomedical applications? *Trends Biotechnol.* **25**, 40-44 (2007).

Duncan, W. & Williams, G. P. Infrared synchrotron radiation from electron storage rings. *Applied optics* **22**, 2914-2923 (1983).

Edwards, H., Farwell, D. & Webster, D. FT Raman microscopy of untreated natural plant fibres. *Spectrochimica Acta Part A: Molecular and Biomolecular Spectroscopy* **53**, 2383-2392 (1997).

Ekins, S. & Sasic, S. *Pharmaceutical applications of Raman spectroscopy*. (John Wiley & Sons, 2008).

El-Kouhen, K. *et al.* Identification and characterization of a triacylglycerol lipase in *Arabidopsis* homologous to mammalian acid lipases. *FEBS letters* **579**, 6067-6073 (2005).

Ellis, D. I., Cowcher, D. P., Ashton, L., O'Hagan, S. & Goodacre, R. Illuminating disease and enlightening biomedicine: Raman spectroscopy as a diagnostic tool. *Analyst* **138**, 3871-3884 (2013).

Ellis, D. I. & Goodacre, R. Metabolic fingerprinting in disease diagnosis: biomedical applications of infrared and Raman spectroscopy. *Analyst* **131**, 875-885 (2006).

Erukhimovitch, V., Hazanovsky, M. & Huleihel, M. Direct identification of potato's fungal phytopathogens by Fourier-transform infrared (FTIR) microscopy. *Spectroscopy* **24**, 609-619 (2010).

Esbensen, K. H. & Geladi, P. Principles of proper validation: use and abuse of re-sampling for validation. *J. Chemometr.* **24**, 168-187 (2010).

Esmonde-White, K. A., Esmonde-White, F. W., Morris, M. D. & Roessler, B. J. Characterization of biofluids prepared by sessile drop formation. *Analyst* **139**, 2734-2741 (2014).

Esmonde-White, K. A., Le Clair, S. V., Roessler, B. J. & Morris, M. D. Effect of Conformation and Drop Properties on Surface-Enhanced Raman Spectroscopy of Dried Biopolymer Drops. *Applied spectroscopy* **62**, 503-511 (2008).

Evans, C. L. *et al.* Chemical imaging of tissue *in vivo* with video-rate coherent anti-Stokes Raman scattering microscopy. *PNAS. USA* **102**, 16807-16812 (2005).

Evenson, R. E. & Gollin, D. Assessing the impact of the Green Revolution, 1960 to 2000. *Science* **300**, 758-762 (2003).

Fageria, N. & Baligar, V. Enhancing nitrogen use efficiency in crop plants. *Advances in agronomy* **88**, 97-185 (2005).

Fageria, N., Filho, M. B., Moreira, A. & Guimaraes, C. Foliar fertilization of crop plants. *J. Plant Nutr.* **32**, 1044-1064 (2009).

Fageria, N. K., Baligar, V. C. & Jones, C. A. *Growth and mineral nutrition of field crops*. (CRC Press, 2010).

FAO. in *World Food Summit*. (FAO).

FAO. How to feed the world in 2050. (2009).

FAO. Current world fertilizer trends and outlook to 2016. (Rome, 2012).

FAO. Food Wastage Footprint: Impacts on natural resources. (FAO Regional Conference for Europe 2014).

FAO. World Population Prospects: The 2015 Revision - Key Findings and Advance Tables. (United Nations, 2015).

FAO. The FAO Hunger Map 2015. (The State of Food Security in the World 2015, 2015).

FAO. Yield gap analysis of field crops: methods and case studies. (UN, Rome, 2015).

Faolain, E. O. *et al.* A study examining the effects of tissue processing on human tissue sections using vibrational spectroscopy. *Vibrational Spectroscopy* **38**, 121-127 (2005).

Farhane, Z., Bonnier, F., Casey, A. & Byrne, H. Raman micro spectroscopy for in vitro drug screening: subcellular localisation and interactions of Doxorubicin. *Analyst* **140**, 4212-4223 (2015).

Faulds, K., Littleford, R. E., Graham, D., Dent, G. & Smith, W. E. Comparison of surface-enhanced resonance Raman scattering from unaggregated and aggregated nanoparticles. *Anal. Chem.* **76**, 592-598 (2004).

Faulds, K., Smith, W., Graham, D. & Lacey, R. Assessment of silver and gold substrates for the detection of amphetamine sulfate by surface enhanced Raman scattering (SERS). *Analyst* **127**, 282-286 (2002).

Felten, J. *et al.* Vibrational spectroscopic image analysis of biological material using multivariate curve resolution-alternating least squares (MCR-ALS). *Nat. Protoc.* **10**, 217-240 (2015).

Feng, S. *et al.* Nasopharyngeal cancer detection based on blood plasma surface-enhanced Raman spectroscopy and multivariate analysis. *Biosens. Bioelectron.* **25**, 2414-2419 (2010).

Fernandez, D. C., Bhargava, R., Hewitt, S. M. & Levin, I. W. Infrared spectroscopic imaging for histopathologic recognition. *Nature biotechnology* **23**, 469-474 (2005).

Fernández, V. & Brown, P. H. From plant surface to plant metabolism: the uncertain fate of foliar-applied nutrients. *Front. Plant Sci.* **4**, 289 (2013).

Fernández, V. & Eichert, T. Uptake of hydrophilic solutes through plant leaves: current state of knowledge and perspectives of foliar fertilization. *Crit. Rev. Plant Sci.* **28**, 36-68 (2009).

Fernández, V. *et al.* New insights into the properties of pubescent surfaces: Peach fruit as a model. *Plant Physiology* **156**, 2098-2108 (2011).

Filik, J., Frogley, M. D., Pijanka, J. K., Wehbe, K. & Cinque, G. Electric field standing wave artefacts in FTIR micro-spectroscopy of biological materials. *Analyst* **137**, 853-861 (2012).

Filik, J. & Stone, N. Analysis of human tear fluid by Raman spectroscopy. *Anal. Chim. Acta* **616**, 177-184 (2008).

Filik, J. & Stone, N. Investigation into the protein composition of human tear fluid using centrifugal filters and drop coating deposition Raman spectroscopy. *J. Raman Spectrosc.* **40**, 218-224 (2009).

Foley, W. J. *et al.* Ecological applications of near infrared reflectance spectroscopy—a tool for rapid, cost-effective prediction of the composition of plant and animal tissues and aspects of animal performance. *Oecologia* **116**, 293-305 (1998).

Franzen, L., Selzer, D., Fluhr, J. W., Schaefer, U. F. & Windbergs, M. Towards drug quantification in human skin with confocal Raman microscopy. *Euro. J. Pharm. Biopharm.* **84**, 437-444 (2013).

Fried, M. & Dean, L. A concept concerning the measurement of available soil nutrients. *Soil Science* **73**, 263-272 (1952).

Frosch, T., Yan, D. & Popp, J. r. Ultrasensitive fiber enhanced UV resonance Raman sensing of drugs. *Anal. Chem.* **85**, 6264-6271 (2013).

Fullwood, L. M. *et al.* Investigating the use of Raman and immersion Raman spectroscopy for spectral histopathology of metastatic brain cancer and primary sites of origin. *Anal. Methods* **6**, 3948-3961 (2014).

Fullwood, L. M. *et al.* Effect of substrate choice and tissue type on tissue preparation for spectral histopathology by Raman microspectroscopy. *Analyst* **139**, 446-454 (2014).

Gajjar, K. *et al.* Diagnostic segregation of human brain tumours using Fourier-transform infrared and/or Raman spectroscopy coupled with discriminant analysis. *Anal. Methods* **5**, 89-102 (2013).

Gajjar, K. *et al.* Fourier-transform infrared spectroscopy coupled with a classification machine for the analysis of blood plasma or serum: a novel diagnostic approach for ovarian cancer. *Analyst* **138**, 3917-3926 (2013).

Galvis, L., Dunlop, J. W. C., Duda, G., Fratzl, P. & Masic, A. Polarized Raman anisotropic response of collagen in tendon: towards 3D orientation mapping of collagen in tissues. *PLoS. One* **8**, e63518 (2013).

Gao, L. *et al.* Label-free high-resolution imaging of prostate glands and cavernous nerves using coherent anti-Stokes Raman scattering microscopy. *Biomed. Opt. Express* **2**, 915-926 (2011).

García-González, D. L., Baeten, V., Pierna, J. A. F. & Tena, N. in *Handbook of Olive Oil* 335-393 (Springer, 2013).

Garrett, N. *et al.* Label-free imaging of polymeric nanomedicines using coherent anti-stokes Raman scattering microscopy. *J. Raman Spectrosc.* **43**, 681-688 (2012).

Gazi, E. *et al.* A correlation of FTIR spectra derived from prostate cancer biopsies with gleason grade and tumour stage. *Eur. Urol.* **50**, 750-761 (2006).

Gazi, E. *et al.* The combined application of FTIR microspectroscopy and ToF-SIMS imaging in the study of prostate cancer. *Faraday Discuss.* **126**, 41-59 (2004).

Gazi, E. *et al.* Fixation protocols for subcellular imaging by synchrotron-based Fourier transform infrared microspectroscopy. *Biopolymers* **77**, 18-30 (2005).

Gazi, E. *et al.* Fixation protocols for subcellular imaging by synchrotron-based Fourier transform infrared microspectroscopy. *Biopolymers* **77**, 18-30 (2005).

Geraldson, C. Factors affecting calcium nutrition of celery, tomato, and pepper. *Soil Science Society of America Journal* **21**, 621-625 (1957).

German, M. J. *et al.* Infrared spectroscopy with multivariate analysis potentially facilitates the segregation of different types of prostate cell. *Biophys. J.* **90**, 3783-3795 (2006).

Gessner, R. *et al.* The application of a SERS fiber probe for the investigation of sensitive biological samples. *Analyst* **129**, 1193-1199 (2004).

Geun Goo, B. *et al.* Characterization of a renewable extracellular polysaccharide from defatted microalgae *Dunaliella tertiolecta*. *Bioresource Technology* **129**, 343-350 (2013).

Gidman, E., Goodacre, R., Emmett, B., Smith, A. R. & Gwynn-Jones, D. Investigating plant-plant interference by metabolic fingerprinting. *Phytochemistry* **63**, 705-710 (2003).

Gierlinger, N., Keplinger, T. & Harrington, M. Imaging of plant cell walls by confocal Raman microscopy. *Nature protocols* **7**, 1694-1708 (2012).

Gierlinger, N. *et al.* Cellulose microfibril orientation of *Picea abies* and its variability at the micron-level determined by Raman imaging. *Journal of experimental botany* **61**, 587-595 (2010).

Gierlinger, N. & Schwanninger, M. Chemical imaging of poplar wood cell walls by confocal Raman microscopy. *Plant Physiology* **140**, 1246-1254 (2006).

Gierlinger, N. & Schwanninger, M. The potential of Raman microscopy and Raman imaging in plant research. *Spectroscopy* **21**, 69-89 (2007).

Gill, D., Kilponen, R. & Rimai, L. Resonance Raman scattering of laser radiation by vibrational modes of carotenoid pigment molecules in intact plant tissues. *Nature* **227**, 743-744 (1970).

Gilliam, M. *et al.* Calcium delivery and storage in plant leaves: exploring the link with water flow. *Journal of experimental botany* **62**, 2233-2250 (2011).

Glassford, S. E., Byrne, B. & Kazarian, S. G. Recent applications of ATR FTIR spectroscopy and imaging to proteins. *Biochimica et Biophysica Acta (BBA)-Proteins and Proteomics* **1834**, 2849-2858 (2013).

Godfray, H. C. J. *et al.* Food security: the challenge of feeding 9 billion people. *science* **327**, 812-818 (2010).

Gómez-De-Anda, F. *et al.* Determination of *Trichinella spiralis* in pig muscles using Mid-Fourier Transform Infrared Spectroscopy (MID-FTIR) with Attenuated Total Reflectance (ATR) and Soft Independent Modeling of Class Analogy (SIMCA). *Meat Sci.* **91**, 240-246 (2012).

Goodacre, R. Explanatory analysis of spectroscopic data using machine learning of simple, interpretable rules. *Vibrational Spectroscopy* **32**, 33-45 (2003).

Gooding, M. J. & Davies, W. P. Foliar urea fertilization of cereals: A review. *Fert. Res.* **32**, 209-222 (1992).

Goormaghtigh, E., Raussens, V. & Ruysschaert, J. M. Attenuated total reflection infrared spectroscopy of proteins and lipids in biological membranes. *BBA-Rev. Biomembranes* **1422**, 105-185 (1999).

Graham, D. *et al.* Selective detection of deoxyribonucleic acid at ultralow concentrations by SERRS. *Anal. Chem.* **69**, 4703-4707 (1997).

Graham, R. D. in *Micronutrient deficiencies in global crop production* 41-61 (Springer, 2008).

Greene, P. R. & Bain, C. D. Total internal reflection Raman spectroscopy of barley leaf epicuticular waxes

in vivo. *Colloid. Surface. B* **45**, 174-180 (2005).

Gremlich, H. U. The use of optical spectroscopy in combinatorial chemistry. *Biotechnology and bioengineering* **61**, 179-187 (1999).

Griffiths, P. & De Haseth, J. A. *Fourier transform infrared spectrometry*. Vol. 171 (Wiley-Interscience, 2007).

Gromski, P. S. *et al.* A tutorial review: Metabolomics and partial least squares-discriminant analysis--a marriage of convenience or a shotgun wedding. *Anal Chim Acta* **879**, 10-23 (2015).

Guyer, L. *et al.* Different mechanisms are responsible for chlorophyll dephytylation during fruit ripening and leaf senescence in tomato. *Plant Physiol.* **166**, 44-56 (2014).

Guyon, I., Gunn, S., Nikravesh, M. & Zadeh, L. *Feature Extraction, Foundations and Applications*. (Springer, New York City, USA, 2006).

Haka, A. S. *et al.* Identifying microcalcifications in benign and malignant breast lesions by probing differences in their chemical composition using Raman spectroscopy. *Cancer Res.* **62**, 5375-5380 (2002).

Hammiche, A., German, M. J., Hewitt, R., Pollock, H. M. & Martin, F. L. Monitoring cell cycle distributions in MCF-7 cells using near-field photothermal microspectroscopy. *Biophys. J.* **88**, 3699-3706 (2005).

Hands, J. *et al.* Investigating the rapid diagnosis of gliomas from serum samples using infrared spectroscopy and cytokine and angiogenesis factors. *Anal Bioanal Chem* **405**, 7347-7355 (2013).

Hanger, B. The movement of calcium in plants. *Commun. Soil Sci. Plan.* **10**, 171-193 (1979).

Harborne, A. *Phytochemical methods a guide to modern techniques of plant analysis*. (Springer Science & Business Media, 1998).

Harnly, J. M. & Fields, R. E. Solid-state array detectors for analytical spectrometry. *Appl. Spectrosc.* **51**, 334A (1997).

Harper, M. M., Dougan, J. A., Shand, N. C., Graham, D. & Faulds, K. Detection of SERS active labelled DNA based on surface affinity to silver nanoparticles. *Analyst* **137**, 2063-2068 (2012).

Harris, D., Bulone, V., Ding, S.-Y. & DeBolt, S. Tools for cellulose analysis in plant cell walls. *Plant Physiol.* **153**, 420-426 (2010).

Hartschuh, A., Sánchez, E. J., Xie, X. S. & Novotny, L. High-resolution near-field Raman microscopy of single-walled carbon nanotubes. *Phys. Rev. Lett.* **90**, 095503 (2003).

Harvey, T. *et al.* Factors influencing the discrimination and classification of prostate cancer cell lines by FTIR microspectroscopy. *Analyst* **134**, 1083-1091 (2009).

Hastie, T., Tibshirani, R. & Friedman, J. *The Elements of Statistical Learning: Data Mining, Inference and Prediction*. 2nd edn, (Springer, New York, 2009).

Hatirli, S. A., Ozkan, B. & Fert, C. Energy inputs and crop yield relationship in greenhouse tomato production. *Renewable Energy* **31**, 427-438 (2006).

Heller, E. J., Sundberg, R. & Tannor, D. Simple aspects of Raman scattering. *The Journal of Physical Chemistry* **86**, 1822-1833 (1982).

Hepler, P. K. Calcium: a central regulator of plant growth and development. *The Plant Cell* **17**, 2142-2155 (2005).

Hepler, P. K. & Winship, L. J. Calcium at the Cell Wall-Cytoplasm Interface. *Journal of integrative plant biology* **52**, 147-160 (2010).

Heraud, P. *et al.* Focal plane array infrared imaging: a new way to analyse leaf tissue. *New Phytologist* **173**, 216-225 (2007).

Heraud, P., Wood, B. R., Beardall, J. & McNaughton, D. Effects of pre-processing of Raman spectra on in vivo classification of nutrient status of microalgal cells. *J. Chemometr.* **20**, 193-197 (2006).

Heredia-Guerrero, J. A. *et al.* Infrared and Raman spectroscopic features of plant cuticles: a review. *Frontiers in plant science* **5**, 305 (2014).

Hester, R. E. & Plane, R. A. Raman spectrophotometric study of complex formation in aqueous solutions of calcium nitrate. *J. Chem. Phys.* **40**, 411-414 (1964).

Hill, J. The remobilization of nutrients from leaves. *Journal of Plant Nutrition* **2**, 407-444 (1980).

Hillier, J. *et al.* The carbon footprints of food crop production. *International Journal of Agricultural*

Sustainability **7**, 107-118 (2009).

Himmelsbach, D., Khalili, S. & Akin, D. FT-IR microspectroscopic imaging of flax (*Linum usitatissimum* L.) stems. *Cellular and molecular biology* **44**, 99-108 (1998).

Himmelsbach, D. S., Khalili, S. & Akin, D. E. The use of FT-IR microspectroscopic mapping to study the effects of enzymatic retting of flax (*Linum usitatissimum* L) stems. *J. Sci. Food Agr.* **82**, 685-696 (2002).

Hirschi, K. D. The calcium conundrum. Both versatile nutrient and specific signal. *Plant physiology* **136**, 2438-2442 (2004).

Hirschmugl, C. J. & Gough, K. M. Fourier transform infrared spectrochemical imaging: review of design and applications with a focal plane array and multiple beam synchrotron radiation source. *Applied spectroscopy* **66**, 475-491 (2012).

Ho, L., Belda, R., Brown, M., Andrews, J. & Adams, P. Uptake and transport of calcium and the possible causes of blossom-end rot in tomato. *Journal of Experimental Botany* **44**, 509-518 (1993).

Hoagland, D. R. & Arnon, D. I. The water-culture method for growing plants without soil. *Circular. California Agricultural Experiment Station* **347** (1950).

Hobro, A. J. & Lendl, B. Fourier-transform mid-infrared FPA imaging of a complex multicellular nematode. *Vib. Spectrosc.* **57**, 213-219 (2011).

Holman, H.-Y. N., Bechtel, H. A., Hao, Z. & Martin, M. C. Synchrotron IR spectromicroscopy: chemistry of living cells. *Anal. Chem.* **82**, 8757-8765 (2010).

Holton, S. E., Walsh, M. J. & Bhargava, R. Subcellular localization of early biochemical transformations in cancer-activated fibroblasts using infrared spectroscopic imaging. *Analyst* **136**, 2953-2958 (2011).

Horsnell, J. D. *et al.* Raman spectroscopy—a potential new method for the intra-operative assessment of axillary lymph nodes. *Surgeon* **10**, 123-127 (2012).

Hsieh, L.-C. *et al.* Uncovering Small RNA-Mediated Responses to Phosphate Deficiency in *Arabidopsis* by Deep Sequencing. *Plant Physiology* **151**, 2120-2132 (2009).

Hu, B. *et al.* Epigenetic control of Pollen Ole e 1 allergen and extensin family gene expression in *Arabidopsis thaliana*. *Acta physiologiae plantarum* **36**, 2203-2209 (2014).

Huang, C. Y. L. & Schulte, E. Digestion of plant tissue for analysis by ICP emission spectroscopy. *Commun. Soil Sci. Plan.* **16**, 943-958 (1985).

Huang, X., El-Sayed, I. H., Qian, W. & El-Sayed, M. A. Cancer cells assemble and align gold nanorods conjugated to antibodies to produce highly enhanced, sharp, and polarized surface Raman spectra: A potential cancer diagnostic marker. *Nano Lett.* **7**, 1591-1597 (2007).

Huang, Z. *et al.* Near-infrared Raman spectroscopy for optical diagnosis of lung cancer. *Int. J. Cancer* **107**, 1047-1052 (2003).

Hughes, C., Gaunt, L., Brown, M., Clarke, N. W. & Gardner, P. Assessment of paraffin removal from prostate FFPE sections using transmission mode FTIR-FPA imaging. *Analytical Methods* **6**, 1028-1035 (2014).

Hughes, C. *et al.* FTIR microspectroscopy of selected rare diverse sub-variants of carcinoma of the urinary bladder. *J. Biophotonics* **6**, 73-87 (2013).

Hunt, R. *Basic growth analysis*. (Unwin Hyman Ltd, 1990).

Irish, D. & Walrafen, G. Raman and infrared spectral studies of aqueous calcium nitrate solutions. *J. Chem. Phys.* **46**, 378-384 (1967).

Ivanda, M. & Furić, K. Line focusing in micro-Raman spectroscopy. *Appl. Opt.* **31**, 6371-6375 (1992).

Ivanova, D. G. & Singh, B. R. Nondestructive FTIR monitoring of leaf senescence and elicitin-induced changes in plant leaves. *Biopolymers* **72**, 79-85 (2003).

Jacobsen, S.-E., Sørensen, M., Pedersen, S. M. & Weiner, J. Feeding the world: genetically modified crops versus agricultural biodiversity. *Agronomy for sustainable development* **33**, 651-662 (2013).

Jaiswal, J. Calcium—how and why? *Journal of biosciences* **26**, 357-363 (2001).

Jansen, J. J. *et al.* Metabolomic analysis of the interaction between plants and herbivores. *Metabolomics* **5**, 150-161 (2009).

Jarvis, R. M. & Goodacre, R. Discrimination of bacteria using surface-enhanced Raman spectroscopy.

Anal. Chem. **76**, 40-47 (2004).

Jarvis, R. M. & Goodacre, R. Genetic algorithm optimization for pre-processing and variable selection of spectroscopic data. *Bioinformatics* **21**, 860-868 (2005).

Jianfeng, W., Dongxian, H., Jinxiu, S., Haijie, D. & Weifen, D. Non-destructive measurement of chlorophyll in tomato leaves using spectral transmittance. *Int. J. Agr. Biol. Eng.* **8**, 73 (2015).

Johansson, J., Sparén, A., Svensson, O., Folestad, S. & Claybourn, M. Quantitative transmission Raman spectroscopy of pharmaceutical tablets and capsules. *Appl. Spectrosc.* **61**, 1211-1218 (2007).

Johnson, H. E., Broadhurst, D., Goodacre, R. & Smith, A. R. Metabolic fingerprinting of salt-stressed tomatoes. *Phytochemistry* **62**, 919-928 (2003).

Jolliffe, I. in *Wiley StatsRef: Statistics Reference Online* (John Wiley & Sons, Ltd, 2014).

Jones Jr, J. B. *Laboratory guide for conducting soil tests and plant analysis*. (CRC press, 2001).

Jones, L., Milne, J. L., Ashford, D., McCann, M. C. & McQueen-Mason, S. J. A conserved functional role of pectic polymers in stomatal guard cells from a range of plant species. *Planta* **221**, 255-264 (2005).

Jones, R. W. & Lunt, O. The function of calcium in plants. *The Botanical Review* **33**, 407-426 (1967).

Kacurakova, M., Capek, P., Sasinkova, V., Wellner, N. & Ebringerova, A. FT-IR study of plant cell wall model compounds: pectic polysaccharides and hemicelluloses. *Carbohydrate Polymers* **43**, 195-203 (2000).

Kačuráková, M. & Wilson, R. Developments in mid-infrared FT-IR spectroscopy of selected carbohydrates. *Carbohydrate Polymers* **44**, 291-303 (2001).

Kallaway, C. *et al.* Advances in the clinical application of Raman spectroscopy for cancer diagnostics. *Photodiagnosis Photodyn. Ther.* **10**, 207-219 (2013).

Kallenbach-Thielges, A. *et al.* Immunohistochemistry, histopathology and infrared spectral histopathology of colon cancer tissue sections. *J. Biophotonics* **6**, 88-100 (2013).

Kamiya, T. *et al.* NIP1;1, an aquaporin homolog, determines the arsenite sensitivity of *Arabidopsis thaliana*. *The Journal of biological chemistry* **284**, 2114-2120 (2009).

Kannan, S. Physiology of foliar uptake of inorganic nutrients. *Proceedings: Plant Sciences* **96**, 457-470 (1986).

Kastyak-Ibrahim, M. *et al.* Biochemical label-free tissue imaging with subcellular-resolution synchrotron FTIR with focal plane array detector. *NeuroImage* **60**, 376-383 (2012).

Kazarian, S. & Chan, K. Applications of ATR-FTIR spectroscopic imaging to biomedical samples. *Biochimica et Biophysica Acta (BBA)-Biomembranes* **1758**, 858-867 (2006).

Kazarian, S. G. & Chan, K. A. ATR-FTIR spectroscopic imaging: recent advances and applications to biological systems. *Analyst* **138**, 1940-1951 (2013).

Keller, M. D. *et al.* Development of a spatially offset Raman spectroscopy probe for breast tumor surgical margin evaluation. *J. Biomed. Opt.* **16**, 077006-077006-077008 (2011).

Kelly, J. G., Martin-Hirsch, P. L. & Martin, F. L. Discrimination of base differences in oligonucleotides using mid-infrared spectroscopy and multivariate analysis. *Anal. Chem.* **81**, 5314-5319 (2009).

Kelly, J. G. *et al.* Derivation of a subtype-specific biochemical signature of endometrial carcinoma using synchrotron-based Fourier-transform infrared microspectroscopy. *Cancer Lett.* **274**, 208-217 (2009).

Kelly, J. G. *et al.* Biospectroscopy to metabolically profile biomolecular structure: a multistage approach linking computational analysis with biomarkers. *J. Prot. Res.* **10**, 1437-1448 (2011).

Kendall, C. *et al.* Raman spectroscopy, a potential tool for the objective identification and classification of neoplasia in Barrett's oesophagus. *J. Pathol.* **200**, 602-609 (2003).

Kereszty, G. Raman spectroscopy: theory. *Handbook of vibrational spectroscopy* (2002).

Kerr, L. T., Byrne, H. J. & Hennelly, B. M. Optimal choice of sample substrate and laser wavelength for Raman spectroscopic analysis of biological specimen. *Analytical Methods* **7**, 5041-5052 (2015).

Khush, G. S. Challenges for meeting the global food and nutrient needs in the new millennium. *Proceedings of the Nutrition Society* **60**, 15-26 (2001).

Kim, S. *et al.* Taxonomic discrimination of flowering plants by multivariate analysis of Fourier transform infrared spectroscopy data. *Plant cell reports* **23**, 246-250 (2004).

Kirkby, E. & Pilbeam, D. Calcium as a plant nutrient. *Plant, Cell & Environment* **7**, 397-405 (1984).

Kneipp, J., Kneipp, H., Rajadurai, A., Redmond, R. W. & Kneipp, K. Optical probing and imaging of live cells using SERS labels. *J. Raman Spectrosc.* **40**, 1-5 (2009).

Kneipp, K., Kneipp, H., Itzkan, I., Dasari, R. R. & Feld, M. S. Ultrasensitive chemical analysis by Raman spectroscopy. *Chem. Rev.* **99**, 2957-2976 (1999).

Kneipp, K., Kneipp, H., Itzkan, I., Dasari, R. R. & Feld, M. S. Surface-enhanced Raman scattering and biophysics. *J. Phys: Condens. Mat.* **14**, R597-R624 (2002).

Kneipp, K., Kneipp, H. & Kneipp, J. Surface-enhanced Raman scattering in local optical fields of silver and gold nanoaggregates from single-molecule Raman spectroscopy to ultrasensitive probing in live cells. *Accounts Chem. Res.* **39**, 443-450 (2006).

Kneipp, K. *et al.* Single molecule detection using surface-enhanced Raman scattering (SERS). *Phys. Rev. Lett.* **78**, 1667-1670 (1997).

Knief, P. *et al.* Raman spectroscopy—a potential platform for the rapid measurement of carbon nanotube-induced cytotoxicity. *Analyst* **134**, 1182-1191 (2009).

Kohler, A. *et al.* Estimating and correcting Mie scattering in synchrotron-based microscopic Fourier transform infrared spectra by extended multiplicative signal correction. *Applied spectroscopy* **62**, 259-266 (2008).

Kolattukudy, P., Espelie, K. & Soliday, C. in *Plant Carbohydrates II* 225-254 (Springer, 1981).

Kole, M. R., Reddy, R. K., Schulmerich, M. V., Gelber, M. K. & Bhargava, R. Discrete frequency infrared microspectroscopy and imaging with a tunable quantum cascade laser. *Anal. Chem.* **84**, 10366-10372 (2012).

Kong, L. *et al.* Characterization of bacterial spore germination using phase-contrast and fluorescence microscopy, Raman spectroscopy and optical tweezers. *Nat. Protoc.* **6**, 625-639 (2011).

Konno, H., Nakashima, S., Maitani, T. & Katoh, K. Alteration of pectic polysaccharides in cell walls, extracellular polysaccharides, and glycan-hydrolytic enzymes of growth-restricted carrot cells under calcium deficiency. *Physiologia Plantarum* **107**, 287-293 (1999).

Krafft, C., Dietzek, B. & Popp, J. Raman and CARS microspectroscopy of cells and tissues. *Analyst* **134**, 1046-1057 (2009).

Krafft, C., Neudert, L., Simat, T. & Salzer, R. Near infrared Raman spectra of human brain lipids. *Spectrochim. Acta A* **61**, 1529-1535 (2005).

Krafft, C. & Popp, J. The many facets of Raman spectroscopy for biomedical analysis. *Anal Bioanal Chem* **407**, 699-717 (2015).

Krafft, C., Steiner, G., Beleites, C. & Salzer, R. Disease recognition by infrared and Raman spectroscopy. *Journal of biophotonics* **2**, 13-28 (2009).

Krishna, C. M. *et al.* Raman spectroscopy studies for diagnosis of cancers in human uterine cervix. *Vib. Spectrosc.* **41**, 136-141 (2006).

Kristensen, J. B., Thygesen, L. G., Felby, C., Jørgensen, H. & Elder, T. Cell-wall structural changes in wheat straw pretreated for bioethanol production. *Biotechnology for biofuels* **1**, 1 (2008).

Krupa, Z., Siedlecka, A., Skorzynska-Polit, E. & Maksymiec, W. in *Physiology and biochemistry of metal toxicity and tolerance in plants* 287-301 (Springer, 2002).

Kuimova, M. K., Chan, K. & Kazarian, S. G. Chemical imaging of live cancer cells in the natural aqueous environment. *Appl. Spectrosc.* **63**, 164-171 (2009).

Kumamoto, Y., Taguchi, A., Smith, N. I. & Kawata, S. Deep ultraviolet resonant Raman imaging of a cell. *J. Biomed. Opt.* **17**, 076001(076001)-076001(076004) (2012).

Kumar, J. K. & Prasad, A. D. Identification and comparison of biomolecules in medicinal plants of *Tephrosia tinctoria* and *Atylosia albicans* by using FTIR. *Romanian J Biophys* **21**, 63-71 (2011).

Kumar, S., Lahlali, R., Liu, X. & Karunakaran, C. Infrared spectroscopy combined with imaging: A new developing analytical tool in health and plant science. *Applied Spectroscopy Reviews* **51**, 466-483 (2016).

Kumar, S. *et al.* Raman and infra-red microspectroscopy: towards quantitative evaluation for clinical research by ratiometric analysis. *Chemical Society Reviews* **45**, 1879-1900 (2016).

Kwak, J. T., Reddy, R., Sinha, S. & Bhargava, R. Analysis of variance in spectroscopic imaging data from

human tissues. *Anal. Chem.* **84**, 1063-1069 (2011).

L'Annunziata, M. F. *Handbook of radioactivity analysis*. (Academic Press, 2012).

LaPlant, F. in *Emerging Raman applications and techniques in biomedical and pharmaceutical fields* Vol. 1 (eds Pavel Matousek & Michael D. Morris) 1-24 (Springer, 2010).

Larkin, P. *Infrared and Raman spectroscopy; principles and spectral interpretation*. (Elsevier, 2011).

Lasch, P. Spectral pre-processing for biomedical vibrational spectroscopy and microspectroscopic imaging. *Chemometr. Intell. Lab.* **117**, 100-114 (2013).

Lasch, P., Boese, M., Pacifico, A. & Diem, M. FT-IR spectroscopic investigations of single cells on the subcellular level. *Vib. Spectrosc.* **28**, 147-157 (2002).

Lasch, P., Haensch, W., Naumann, D. & Diem, M. Imaging of colorectal adenocarcinoma using FT-IR microspectroscopy and cluster analysis. *Biochimica et Biophysica Acta (BBA) - Molecular Basis of Disease* **1688**, 176-186 (2004).

Lasch, P. & Kneipp, J. *Biomedical vibrational spectroscopy*. (John Wiley & Sons, 2008).

Lasch, P. & Naumann, D. Spatial resolution in infrared microspectroscopic imaging of tissues. *BBA - Biomembranes* **1758**, 814-829 (2006).

Lasch, P., Pacifico, A. & Diem, M. Spatially resolved IR microspectroscopy of single cells. *Biopolymers* **67**, 335-338 (2002).

Lasch, P. & Petrich, W. Data acquisition and analysis in biomedical vibrational spectroscopy. *Biomedical Applications of Synchrotron Infrared Microspectroscopy: a Practical Approach, RSC Analytical Spectroscopy Series* **11**, 192-225 (2011).

Lasch, P. & Petrich, W. in *Biomedical Applications of Synchrotron Infrared Microspectroscopy: a Practical Approach, RSC Analytical Spectroscopy Series* Vol. 11 (ed D. Moss) 192-225 (RSC Analytical Spectroscopy Series, 2011).

Le, T. T., Huff, T. B. & Cheng, J.-X. Coherent anti-Stokes Raman scattering imaging of lipids in cancer metastasis. *BMC Cancer* **9**, 42 (2009).

Lee, K.-S. & El-Sayed, M. A. Gold and silver nanoparticles in sensing and imaging: sensitivity of plasmon response to size, shape, and metal composition. *J. Phys. Chem. B* **110**, 19220-19225 (2006).

Leeds, S., Davis, T., May, P., Pickard, C. & Ashfold, M. Use of different excitation wavelengths for the analysis of CVD diamond by laser Raman spectroscopy. *Diamond and Related Materials* **7**, 233-237 (1998).

Leger, M. N. & Ryder, A. G. Comparison of derivative preprocessing and automated polynomial baseline correction method for classification and quantification of narcotics in solid mixtures. *Applied spectroscopy* **60**, 182-193 (2006).

Levy, A., Guenoune-Gelbart, D. & Epel, B. L. β -1,3-Glucanases: Plasmodesmal Gate Keepers for Intercellular Communication. *Plant Signaling & Behavior* **2**, 404-407 (2007).

Lewis, A. T. *et al.* Mirrored stainless steel substrate provides improved signal for Raman spectroscopy of tissue and cells. *Journal of Raman Spectroscopy* (2016).

Lewis, E. N. *et al.* Fourier transform spectroscopic imaging using an infrared focal-plane array detector. *Analytical chemistry* **67**, 3377-3381 (1995).

Lewis, I. R. & Edwards, H. *Handbook of Raman spectroscopy: from the research laboratory to the process line*. (CRC Press, 2001).

Li, J. F. *et al.* Surface analysis using shell-isolated nanoparticle-enhanced Raman spectroscopy. *Nat. Protoc.* **8**, 52-65 (2013).

Li, Y., Kong, D. & Wu, H. Analysis and evaluation of essential oil components of cinnamon barks using GC-MS and FTIR spectroscopy. *Ind. Crop. Prod.* **41**, 269-278 (2013).

Li, Z., Deen, M. J., Kumar, S. & Selvaganapathy, P. R. Raman Spectroscopy for In-Line Water Quality Monitoring—Instrumentation and Potential. *Sensors* **14**, 17275-17303 (2014).

Licker, R. *et al.* Mind the gap: how do climate and agricultural management explain the 'yield gap' of croplands around the world? *Global ecology and biogeography* **19**, 769-782 (2010).

Lieber, C. A. & Mahadevan-Jansen, A. Automated method for subtraction of fluorescence from biological Raman spectra. *Appl. Spectrosc.* **57**, 1363-1367 (2003).

Lin, D. *et al.* Colorectal cancer detection by gold nanoparticle based surface-enhanced Raman spectroscopy of blood serum and statistical analysis. *Opt. Express* **19**, 13565-13577 (2011).

Littlejohn, G. R. *et al.* In vivo chemical and structural analysis of plant cuticular waxes using stimulated Raman scattering microscopy. *Plant Physiol.* **168**, 18-28 (2015).

Liu, J., Elmore, J. M. & Coaker, G. Investigating the functions of the RIN4 protein complex during plant innate immune responses. *Plant Signaling & Behavior* **4**, 1107-1110 (2009).

Liu, J.-N., Schulmerich, M. V., Bhargava, R. & Cunningham, B. T. Optimally designed narrowband guided-mode resonance reflectance filters for mid-infrared spectroscopy. *Opt. Express* **19**, 24182-24197 (2011).

Liu, P. & Si, Y. in *Statistical Analysis of Next Generation Sequencing Data* 191-217 (Springer, 2014).

Liu, Z., Zhao, C., Han, L. & Mo, Y. Study on the configuration and applications of high spectral resolution Raman spectrometer. *Guang Pu Xue Yu Guang Pu Fen Xi* **30**, 567-570 (2010).

Llabjani, V. *et al.* Differential Effects in Mammalian Cells Induced by Chemical Mixtures in Environmental Biota As Profiled Using Infrared Spectroscopy. *Environ. Sci. Technol.* **45**, 10706-10712 (2011).

Llabjani, V. *et al.* Polybrominated diphenyl ether-associated alterations in cell biochemistry as determined by attenuated total reflection fourier-transform infrared spectroscopy: a comparison with DNA-reactive and/or endocrine-disrupting agents. *Environ. Sci. Technol.* **43**, 3356-3364 (2009).

Llabjani, V. *et al.* Alterations in the infrared spectral signature of avian feathers reflect potential chemical exposure: A pilot study comparing two sites in Pakistan. *Environ. Int.* **48**, 39-46 (2012).

Lloyd, G. R. *et al.* Utilising non-consensus pathology measurements to improve the diagnosis of oesophageal cancer using a Raman spectroscopic probe. *Analyst* **139**, 381-388 (2014).

Lloyd, G. R. *et al.* Discrimination between benign, primary and secondary malignancies in lymph nodes from the head and neck utilising Raman spectroscopy and multivariate analysis. *Analyst* **138**, 3900-3908 (2013).

Lonergan, J., Snowball, K., Robson, A. & Wardlaw, I. Remobilization of nutrients and its significance in plant nutrition. *Transport and transfer processes in plants*, 463-469 (1976).

Long, D. A. Raman spectroscopy. *New York*, 1-12 (1977).

LouiseáRonayne, K. & WilliamáParker, A. Depth profiling of calcifications in breast tissue using picosecond Kerr-gated Raman spectroscopy. *Analyst* **132**, 48-53 (2007).

Lu, Y.-B. *et al.* Identification of boron-deficiency-responsive microRNAs in Citrus sinensis roots by Illumina sequencing. *BMC plant biology* **14**, 1 (2014).

Lucena, J. in *III International Symposium on Mineral Nutrition of Deciduous Fruit Trees* 448. 179-192.

Ly, E. *et al.* Combination of FTIR spectral imaging and chemometrics for tumour detection from paraffin-embedded biopsies. *Analyst* **133**, 197-205 (2008).

Lyng, F., Gazi, E. & Gardner, P. Preparation of tissues and cells for infrared and Raman spectroscopy and imaging. (2011).

Lyng, F. M. *et al.* Vibrational spectroscopy for cervical cancer pathology, from biochemical analysis to diagnostic tool. *Exp. Mol. Pathol.* **82**, 121-129 (2007).

Ma, J. & Ben-Amotz, D. Rapid micro-Raman imaging using fiber-bundle image compression. *Appl. Spectrosc.* **51**, 1845-1848 (1997).

Ma, K. *et al.* In vivo, transcutaneous glucose sensing using surface-enhanced spatially offset Raman spectroscopy: multiple rats, improved hypoglycemic accuracy, low incident power, and continuous monitoring for greater than 17 days. *Anal. Chem.* **83**, 9146-9152 (2011).

Maas, E. & Grieve, C. Sodium-induced calcium deficiency in salt-stressed corn. *Plant, Cell & Environment* **10**, 559-564 (1987).

MacRae, E. Extraction of plant RNA. *Protocols for Nucleic Acid Analysis by Nonradioactive Probes*, 15-24 (2007).

Macy, P. The quantitative mineral nutrient requirements of plants. *Plant physiology* **11**, 749 (1936).

Majzner, K. *et al.* 3D confocal Raman imaging of endothelial cells and vascular wall: perspectives in analytical spectroscopy of biomedical research. *Analyst* **138**, 603-610 (2012).

Malins, D. C. *et al.* Biomarkers signal contaminant effects on the organs of English sole (Parophrys

vetulus) from Puget Sound. *Environ. Health Perspect.* **114**, 823-829 (2006).

Malone, M., White, P. & Morales, M. A. Mobilization of calcium in glasshouse tomato plants by localized scorching. *Journal of Experimental Botany* **53**, 83-88 (2002).

Maloney, G. S. *et al.* Characterization of the Branched-Chain Amino Acid Aminotransferase Enzyme Family in Tomato. *Plant Physiology* **153**, 925-936 (2010).

Mansfield, J. C. *et al.* Label-free chemically specific imaging in planta with stimulated Raman scattering microscopy. *Anal. Chem.* **85**, 5055-5063 (2013).

Mantsch, H. H. & Chapman, D. *Infrared Spectroscopy of Biomolecules*. (Wiley-Liss, Hoboken, New Jersey, USA, 1996).

Maquelin, K. *et al.* Identification of medically relevant microorganisms by vibrational spectroscopy. *J. Microbiol. Meth.* **51**, 255-271 (2002).

Marcisin, E. J., Uttero, C. M., Miljkovic, M. & Diem, M. Infrared microspectroscopy of live cells in aqueous media. *Analyst* **135**, 3227-3232 (2010).

Mariani, M. M., Lampen, P., Popp, J., Wood, B. R. & Deckert, V. Impact of fixation on in vitro cell culture lines monitored with Raman spectroscopy. *Analyst* **134**, 1154-1161 (2009).

Mariey, L., Signolle, J. P., Amiel, C. & Travert, J. Discrimination, classification, identification of microorganisms using FTIR spectroscopy and chemometrics. *Vib. Spectrosc.* **26**, 151-159 (2001).

Marín-Rodríguez, M. C., Orchard, J. & Seymour, G. B. Pectate lyases, cell wall degradation and fruit softening. *Journal of Experimental Botany* **53**, 2115-2119 (2002).

Markwort, L., Kip, B., Da Silva, E. & Roussel, B. Raman imaging of heterogeneous polymers: a comparison of global versus point illumination. *Appl. Spectrosc.* **49**, 1411-1430 (1995).

Marschner, H. *Marschner's mineral nutrition of higher plants*. (Academic press, 2011).

Martens, H., Nielsen, J. P. & Engelsen, S. B. Light scattering and light absorbance separated by extended multiplicative signal correction. Application to near-infrared transmission analysis of powder mixtures. *Analytical Chemistry* **75**, 394-404 (2003).

Martens, H. & Stark, E. Extended multiplicative signal correction and spectral interference subtraction - new preprocessing methods for near-infrared spectroscopy. *J. Pharmaceut. Biomed.* **9**, 625-635 (1991).

Martin, F. L. Shining a new light into molecular workings. *Nat Meth* **8**, 385-387 (2011).

Martin, F. L. *et al.* Identifying variables responsible for clustering in discriminant analysis of data from infrared microspectroscopy of a biological sample. *Journal of Computational Biology* **14**, 1176-1184 (2007).

Martin, F. L. *et al.* Distinguishing cell types or populations based on the computational analysis of their infrared spectra. *Nature protocols* **5**, 1748-1760 (2010).

Martins, M. A. d. S. *et al.* Shifted-excitation Raman difference spectroscopy for in vitro and in vivo biological samples analysis. *Biomed. Opt. Express* **1**, 617-626 (2010).

Matousek, P. Deep non-invasive Raman spectroscopy of living tissue and powders. *Chem. Soc. Rev.* **36**, 1292-1304 (2007).

Matousek, P. *et al.* Noninvasive Raman spectroscopy of human tissue in vivo. *Appl. Spectrosc.* **60**, 758-763 (2006).

Matousek, P. & Stone, N. Prospects for the diagnosis of breast cancer by noninvasive probing of calcifications using transmission Raman spectroscopy. *J. Biomed. Opt.* **12**, 024008(024001)-024008(024008) (2007).

Mazet, V., Carteret, C., Brie, D., Idier, J. & Humbert, B. Background removal from spectra by designing and minimising a non-quadratic cost function. *Chemometr. Intell. Lab.* **76**, 121-133 (2005).

McAinsh, M. in *Plant Encyclopedia of Applied Plant Science* (ed D. Murphy B. Thomas, B. Murray) 1459-1466 (Academic Press, London, 2003).

McAinsh, M. R., Brownlee, C. & Hetherington, A. M. Calcium ions as second messengers in guard cell signal transduction. *Physiologia Plantarum* **100**, 16-29 (1997).

McAinsh, M. R., Clayton, H., Mansfield, T. A. & Hetherington, A. M. Changes in stomatal behavior and guard cell cytosolic free calcium in response to oxidative stress. *Plant Physiology* **111**, 1031-1042 (1996).

McAinsh, M. R., Evans, N. H., Montgomery, L. T. & North, K. A. Calcium signalling in stomatal responses to pollutants. *New Phytologist* **153**, 441-447 (2002).

McAinsh, M. R. & Ng, C. K.-Y. Vol. 312 289-302 (2005).

McAinsh, M. R. & Pittman, J. K. Shaping the calcium signature. *New Phytologist* **181**, 275-294 (2009).

McCann, M. *et al.* Infrared microspectroscopy: sampling heterogeneity in plant cell wall composition and architecture. *Physiol. Plant.* **100**, 729-738 (1997).

McCann, M. C. *et al.* Neural network analyses of infrared spectra for classifying cell wall architectures. *Plant Physiology* **143**, 1314-1326 (2007).

McCann, M. C., Hammouri, M., Wilson, R., Belton, P. & Roberts, K. Fourier transform infrared microspectroscopy is a new way to look at plant cell walls. *Plant Physiology* **100**, 1940-1947 (1992).

McColl, I. H. *et al.* A new perspective on β -sheet structures using vibrational Raman optical activity: from poly(l-lysine) to the prion protein. *J. Am. Chem. Soc.* **125**, 10019-10026 (2003).

McGuire, S. FAO, IFAD, and WFP. The State of Food Insecurity in the World 2015: Meeting the 2015 International Hunger Targets: Taking Stock of Uneven Progress. Rome: FAO, 2015. *Advances in Nutrition: An International Review Journal* **6**, 623-624 (2015).

McNay, G., Eustace, D., Smith, W. E., Faulds, K. & Graham, D. Surface-enhanced Raman scattering (SERS) and surface-enhanced resonance Raman scattering (SERRS): a review of applications. *Appl. Spectrosc.* **65**, 825-837 (2011).

Mechlem, K. Food Security and the Right to Food in the Discourse of the United Nations. *European Law Journal* **10**, 631-648 (2004).

Mecozzi, M., Pietroletti, M. & Di Mento, R. Application of FTIR spectroscopy in ecotoxicological studies supported by multivariate analysis and 2D correlation spectroscopy. *Vib. Spectrosc.* **44**, 228-235 (2007).

Meinke, D. W., Cherry, J. M., Dean, C., Rounsley, S. D. & Koornneef, M. *Arabidopsis thaliana*: a model plant for genome analysis. *Science* **282**, 662-682 (1998).

Meister, K. *et al.* Label-free imaging of metal-carbonyl complexes in live cells by Raman microspectroscopy. *Angew. Chem. Int.* **49**, 3310-3312 (2010).

Menesatti, P. *et al.* Estimation of plant nutritional status by Vis-NIR spectrophotometric analysis on orange leaves [*Citrus sinensis* (L) Osbeck cv Tarocco]. *Biosystems engineering* **105**, 448-454 (2010).

Mengel, K. in *International Symposium on Foliar Nutrition of Perennial Fruit Plants* 594. 33-47.

Menzel, L. *et al.* Spectroscopic detection of biological NO with a quantum cascade laser. *Appl. Phys. B* **72**, 859-863 (2001).

Merk, S., Blume, A. & Riederer, M. Phase behaviour and crystallinity of plant cuticular waxes studied by Fourier transform infrared spectroscopy. *Planta* **204**, 44-53 (1997).

Merlin, J. C. Resonance Raman spectroscopy of carotenoids and carotenoid-containing systems. *Pure Appl. Chem.* **57**, 785-792 (1985).

Meyer, T. *et al.* Nonlinear microscopy, infrared, and Raman microspectroscopy for brain tumor analysis. *J. Biomed. Opt.* **16**, 021113(021111)-021113(021110) (2011).

Mi, H., Muruganujan, A., Casagrande, J. T. & Thomas, P. D. Large-scale gene function analysis with the PANTHER classification system. *Nat. Protocols* **8**, 1551-1566 (2013).

Mi, H., Poudel, S., Muruganujan, A., Casagrande, J. T. & Thomas, P. D. PANTHER version 10: expanded protein families and functions, and analysis tools. *Nucleic acids research* **44**, D336-342 (2016).

Michelson, A. A. & Morley, E. W. On the Relative Motion of the Earth and of the Luminiferous Ether. *Sidereal Messenger*, vol. 6, pp. 306-310 **6**, 306-310 (1887).

Miljković, M., Bird, B., Lenau, K., Mazur, A. I. & Diem, M. Spectral cytopathology: new aspects of data collection, manipulation and confounding effects. *Analyst* **138**, 3975-3982 (2013).

Miller, L., Carr, G., Jackson, M., Dumas, P. & Williams, G. The impact of infrared synchrotron radiation in biology: Past, present and future. *Synchrotron Radiation News* **13**, 31-38 (2000).

Miller, L. M. & Dumas, P. Chemical imaging of biological tissue with synchrotron infrared light. *Biochimica et Biophysica Acta (BBA) - Biomembranes* **1758**, 846-857 (2006).

Miller, L. M. & Smith, R. J. Synchrotrons versus globars, point-detectors versus focal plane arrays: Selecting the best source and detector for specific infrared microspectroscopy and imaging applications. *Vibrational spectroscopy* **38**, 237-240 (2005).

Mimmo, T., Marzadori, C., Montecchio, D. & Gessa, C. Characterisation of Ca- and Al-pectate gels by thermal analysis and FT-IR spectroscopy. *Carbohydrate Research* **340**, 2510-2519 (2005).

Minamikawa, T. *et al.* Label-free detection of peripheral nerve tissues against adjacent tissues by spontaneous Raman microspectroscopy. *Histochem. Cell Biol.* **139**, 181-193 (2013).

Minic, Z. & Jouanin, L. Plant glycoside hydrolases involved in cell wall polysaccharide degradation. *Plant physiology and Biochemistry* **44**, 435-449 (2006).

Mitchell, A. L., Gajjar, K. B., Theophilou, G., Martin, F. L. & Martin-Hirsch, P. L. Vibrational spectroscopy of biofluids for disease screening or diagnosis: translation from the laboratory to a clinical setting. *J. Biophotonics* **7**, 153-165 (2014).

Mohamed, G. F., Shaheen, M. S., Khalil, S. K., Hussein, A. & Kamil, M. Application of FTIR spectroscopy for rapid and simultaneous quality determination of some fruit products. *Nat Sci* **9**, 21-31 (2011).

Monti, F. *et al.* A multivariate statistical analysis approach to highlight molecular processes in plant cell walls through ATR FT-IR microspectroscopy: the role of the α -expansin *PhEXP1* in *Petunia hybrida*. *Vib. Spectrosc.* **65**, 36-43 (2012).

Moore, D. & Scharff, R. J. Portable Raman explosives detection. *Anal Bioanal Chem* **393**, 1571-1578 (2009).

Morris, M. D. *et al.* Kerr-gated time-resolved Raman spectroscopy of equine cortical bone tissue. *J. Biomed. Opt.* **10**, 14014(14011)-14014(14017) (2005).

Movagagh, Z., Rehman, S. & Rehman, I. U. Raman spectroscopy of biological tissues. *Applied Spectroscopy Reviews* **42**, 493-541 (2007).

Movagagh, Z., Rehman, S. & ur Rehman, D. I. Fourier transform infrared (FTIR) spectroscopy of biological tissues. *Applied Spectroscopy Reviews* **43**, 134-179 (2008).

Mueller, N. D. *et al.* Closing yield gaps through nutrient and water management. *Nature* **490**, 254-257 (2012).

Müller, A. *et al.* Diode laser based light sources for biomedical applications. *Laser Photon. Rev.* **7**, 605-627 (2013).

Munro, K. L. *et al.* Synchrotron radiation infrared microspectroscopy of arsenic-induced changes to intracellular biomolecules in live leukemia cells. *Vib. Spectrosc.* **53**, 39-44 (2010).

Murgida, D. H. & Hildebrandt, P. Electron-transfer processes of cytochrome c at interfaces. New insights by surface-enhanced resonance Raman spectroscopy. *Accounts Chem. Res.* **37**, 854-861 (2004).

Murgida, D. H. & Hildebrandt, P. Disentangling interfacial redox processes of proteins by SERR spectroscopy. *Chem. Soc. Rev.* **37**, 937-945 (2008).

Murillo-Amador, B. *et al.* Effects of foliar application of calcium nitrate on growth and physiological attributes of cowpea (*Vigna unguiculata* L. Walp.) grown under salt stress. *Environ. Exp. Bot.* **58**, 188-196 (2006).

Nahirñák, V., Almasia, N. I., Hopp, H. E. & Vazquez-Rovere, C. Snakin/GASA proteins: Involvement in hormone crosstalk and redox homeostasis. *Plant Signaling & Behavior* **7**, 1004-1008 (2012).

Nakamura, T. *et al.* Microspectroscopy of spectral biomarkers associated with human corneal stem cells. *Mol. Vis.* **16**, 359-368 (2010).

Nallala, J. *et al.* Infrared imaging as a cancer diagnostic tool: Introducing a new concept of spectral barcodes for identifying molecular changes in colon tumors. *Cytometry Part A* **83**, 294-300 (2013).

Nasse, M., Ratti, S., Giordano, M. & Hirschmugl, C. Demountable Liquid/Flow Cell for in Vivo Infrared Microspectroscopy of Biological Specimens. *Appl. Spectrosc.* **63**, 1181-1186 (2009).

Nasse, M. J. *et al.* High-resolution Fourier-transform infrared chemical imaging with multiple synchrotron beams. *Nature methods* **8**, 413-416 (2011).

Naumann, A. & Polle, A. FTIR imaging as a new tool for cell wall analysis of wood. *New Zealand Journal of Forestry Science* **36**, 54 (2006).

Naumann, D. in *Encyclopedia of Analytical Chemistry* (John Wiley & Sons, Chichester, UK, 2000).

Naumann, D. in *Biomedical Optical Spectroscopy, Proceedings of SPIE*. (International Society for Optics and Photonics).

Naumann, D., Lasch, P. & Fabian, H. in *Biomedical Optics 2006*. (International Society for Optics and Photonics).

Nehl, C. L. & Hafner, J. H. Shape-dependent plasmon resonances of gold nanoparticles. *J. Mater. Chem.* **18**, 2415-2419 (2008).

Neugebauer, U. *et al.* On the way to nanometer-sized information of the bacterial surface by tip-enhanced Raman spectroscopy. *ChemPhysChem* **7**, 1428-1430 (2006).

Newman, I. Ion transport in roots: measurement of fluxes using ion-selective microelectrodes to characterize transporter function. *Plant, cell & environment* **24**, 1-14 (2001).

Ng, C. K. Y. *et al.* Calcium-based signalling systems in guard cells. *New Phytologist* **151**, 109-120 (2001).

Ng, C. K.-Y., Carr, K., McAinsh, M. R., Powell, B. & Hetherington, A. M. Drought-induced guard cell signal transduction involves sphingosine-1-phosphate. *Nature* **410**, 596-599 (2001).

Nie, S. & Emory, S. R. Probing single molecules and single nanoparticles by surface-enhanced Raman scattering. *Science* **275**, 1102-1106 (1997).

Nieto-Ortega, B. *et al.* Raman optical activity spectra and conformational elucidation of chiral drugs. The case of the antiangiogenic aeroplysinin-1. *J. Phys. Chem. A* **115**, 2752-2755 (2011).

Nightingale, G., Addoms, R. M., Robbins, W. & Schermerhorn, L. Effects of calcium deficiency on nitrate absorption and on metabolism in tomato. *Plant physiology* **6**, 605 (1931).

Nonami, H., Fukuyama, T., Yamamoto, M., Yang, L. & Hashimoto, Y. Blossom-end rot of tomato plants may not be directly caused by calcium deficiency. *Hydroponics and Transplant Production* **396**, 107-114 (1994).

Notingher, I. & Hench, L. L. Raman microspectroscopy: a noninvasive tool for studies of individual living cells in vitro. *Expert Rev. Med. Devices* **3**, 215-234 (2006).

Nyquist, R. A. & Kagel, R. O. *Handbook of infrared and raman spectra of inorganic compounds and organic salts: infrared spectra of inorganic compounds*. Vol. 4 (Academic press, 2012).

Obinaju, B. E., Alaoma, A. & Martin, F. L. Novel sensor technologies towards environmental health monitoring in urban environments: A case study in the Niger Delta (Nigeria). *Environ. Pollut.* **192**, 222-231 (2014).

Ochiman, I. D. The impact of foliar application of calcium fertilizers on the quality of highbush blueberry fruits belonging to the 'Duke' cultivar. *Not. Bot. Horti. Agrobo.* **40**, 163-169 (2012).

Okada, M. *et al.* Label-free Raman observation of cytochrome c dynamics during apoptosis. *PNAS. USA* **109**, 28-32 (2012).

Olds, W. J. *et al.* Spatially offset Raman spectroscopy (SORS) for the analysis and detection of packaged pharmaceuticals and concealed drugs. *Forensic Sci. Int.* **212**, 69-77 (2011).

Oliveira, S. R., Neto, J. A. G., Nobrega, J. A. & Jones, B. T. Determination of macro-and micronutrients in plant leaves by high-resolution continuum source flame atomic absorption spectrometry combining instrumental and sample preparation strategies. *Spectrochimica Acta Part B: Atomic Spectroscopy* **65**, 316-320 (2010).

Ollesch, J. *et al.* FTIR spectroscopy of biofluids revisited: an automated approach to spectral biomarker identification. *Analyst* **138**, 4092-4102 (2013).

Ollesch, J. *et al.* It's in your blood: spectral biomarker candidates for urinary bladder cancer from automated FTIR spectroscopy. *J. Biophotonics* **7**, 210-221 (2014).

Ooi, G. J. *et al.* Fourier transform infrared imaging and small angle x-ray scattering as a combined biomolecular approach to diagnosis of breast cancer. *Med. Phys.* **35**, 2151-2161 (2008).

Ord, J., Butler, H. J., McAinsh, M. R. & Martin, F. L. Spectrochemical analysis of sycamore (*Acer pseudoplatanus*) leaves for environmental health monitoring. *Analyst* (2016).

Owen, C. A. *et al.* In vitro toxicology evaluation of pharmaceuticals using Raman micro-spectroscopy. *J. Cell. Biochem.* **99**, 178-186 (2006).

Pahlow, S., Meisel, S., Cialla-May, D., Weber, K. & Röschac, J. P. P. Isolation and identification of bacteria by means of Raman spectroscopy. *Adv. Drug Deliv. Rev.* **Forthcoming** (2015).

Palonpon, A. F. *et al.* Raman and SERS microscopy for molecular imaging of live cells. *Nat. Protoc.* **8**, 677-692 (2013).

Pandey, K. A study of chemical structure of soft and hardwood and wood polymers by FTIR spectroscopy. *Journal of Applied Polymer Science* **71**, 1969-1975 (1999).

Parekh, S. H., Lee, Y. J., Aamer, K. A. & Cicerone, M. T. Label-free cellular imaging by broadband coherent anti-Stokes Raman scattering microscopy. *Biophys. J.* **99**, 2695-2704 (2010).

Park, J. *et al.* The *Arabidopsis thaliana* homeobox gene ATHB12 is involved in symptom development caused by geminivirus infection. *PLoS One* **6**, e20054 (2011).

Parry, M. A. J. & Hawkesford, M. J. Food security: increasing yield and improving resource use efficiency. *Pro. Nutr. Soc.* **69**, 592-600 (2010).

Patel, II *et al.* Isolating stem cells in the inter-follicular epidermis employing synchrotron radiation-based Fourier-transform infrared microspectroscopy and focal plane array imaging. *Anal Bioanal Chem* **404**, 1745-1758 (2012).

Patel, I. I. & Martin, F. L. Discrimination of zone-specific spectral signatures in normal human prostate using Raman spectroscopy. *Analyst* **135**, 3060-3069 (2010).

Patel, I. I. *et al.* High contrast images of uterine tissue derived using Raman microspectroscopy with the empty modelling approach of multivariate curve resolution-alternating least squares. *Analyst* **136**, 4950-4959 (2011).

Patel, I. I. *et al.* Segregation of human prostate tissues classified high-risk (UK) versus low-risk (India) for adenocarcinoma using Fourier-transform infrared or Raman microspectroscopy coupled with discriminant analysis. *Anal Bioanal Chem* **401**, 969-982 (2011).

Péna-Cortés, H., Sánchez-Serrano, J. J., Mertens, R., Willmitzer, L. & Prat, S. Abscisic acid is involved in the wound-induced expression of the proteinase inhibitor II gene in potato and tomato. *Proceedings of the National Academy of Sciences* **86**, 9851-9855 (1989).

Petibois, C. & Deleris, G. Chemical mapping of tumor progression by FT-IR imaging: towards molecular histopathology. *Trends in biotechnology* **24**, 455-462 (2006).

Peyvast, G., Olfati, J., Ramezani-Kharazi, P. & Kamari-Shahmaleki, S. Uptake of calcium nitrate and potassium phosphate from foliar fertilization by tomato. *J. Hortic. For.* **1**, 7-13 (2009).

Picorel, R., Chumanov, G., Torrado, E., Cotton, T. M. & Seibert, M. Surface-enhanced resonance Raman scattering spectroscopy of plant photosystem II reaction centers excited on the red-edge of the Q_y band. *J. Phys. Chem. B* **102**, 2609-2613 (1998).

Pijanka, J. K. *et al.* Spectroscopic signatures of single, isolated cancer cell nuclei using synchrotron infrared microscopy. *Analyst* **134**, 1176-1181 (2009).

Pinstrup-Andersen, P. Food security: definition and measurement. *Food security* **1**, 5-7 (2009).

Pitt, G. *et al.* in *Science, Measurement and Technology, IEE Proceedings-*. 241-318 (IET).

Pitts, D. G. & Kleinstein, R. The electromagnetic spectrum. *Environmental Vision*. Boston, Butterworth-Heinemann, 87-135 (1993).

Planck, M. Ueber das gesetz der energieverteilung im normalspectrum. *Annalen der physik* **309**, 553-563 (1901).

Popp, J., Pető, K. & Nagy, J. Pesticide productivity and food security. A review. *Agronomy for sustainable development* **33**, 243-255 (2013).

Premanandh, J. Factors affecting food security and contribution of modern technologies in food sustainability. *Journal of the Science of Food and Agriculture* **91**, 2707-2714 (2011).

Premasiri, W. *et al.* Characterization of the surface enhanced Raman scattering (SERS) of bacteria. *J. Phys. Chem. B* **109**, 312-320 (2005).

Prieto, M. C. H. *et al.* Use of picosecond Kerr-gated Raman spectroscopy to suppress signals from both surface and deep layers in bladder and prostate tissue. *J. Biomed. Opt.* **10**, 44006(44001)-44006(44006) (2005).

Qaim, M. & Kouwer, S. Genetically modified crops and food security. *PLoS one* **8**, e64879 (2013).

Qian, X. *et al.* In vivo tumor targeting and spectroscopic detection with surface-enhanced Raman nanoparticle tags. *Nat. Biotechnol.* **26**, 83-90 (2008).

Raab, T. K. & Martin, M. C. Visualizing rhizosphere chemistry of legumes with mid-infrared synchrotron

radiation. *Planta* **213**, 881-887 (2001).

Raese, J. T. & Drake, S. R. Effects of preharvest calcium sprays on apple and pear quality. *Journal of plant nutrition* **16**, 1807-1819 (1993).

Rahmelow, K. & Hubner, W. Phase correction in Fourier transform spectroscopy: Subsequent displacement correction and error limit. *Appl. Optics* **36**, 6678-6686 (1997).

Raman, C. V. & Krishnan, K. S. A new type of secondary radiation. *Nature* **121**, 501-502 (1928).

Ramirez, F., Luque, P., Heredia, A. & Bukovac, M. Fourier transform IR study of enzymatically isolated tomato fruit cuticular membrane. *Biopolymers* **32**, 1425-1429 (1992).

Rashid, N. *et al.* Raman microspectroscopy for the early detection of pre-malignant changes in cervical tissue. *Exp. Mol. Path.* **97**, 554-564 (2014).

Reddy, R. K. & Bhargava, R. Accurate histopathology from low signal-to-noise ratio spectroscopic imaging data. *Analyst* **135**, 2818-2825 (2010).

Reichenbächer, M. & Popp, J. *Challenges in molecular structure determination*. (Springer Science & Business Media, 2012).

Reuter, D. *Plant analysis: an interpretation manual*. (CSIRO publishing, 1997).

Ribeiro da Luz, B. Attenuated total reflectance spectroscopy of plant leaves: a tool for ecological and botanical studies. *New Phytologist* **172**, 305-318 (2006).

Ricci, A., Olejar, K. J., Parpinello, G. P., Kilmartin, P. A. & Versari, A. Application of Fourier Transform Infrared (FTIR) Spectroscopy in the Characterization of Tannins. *Applied Spectroscopy Reviews* **50**, 407-442 (2015).

Riederer, M. & Schreiber, L. Vol. 6 131-156 (The Oily Press: Dundee, Scotland, 1995).

Riederer, M. & Schreiber, L. Protecting against water loss: analysis of the barrier properties of plant cuticles. *J. Exp. Bot.* **52**, 2023-2032 (2001).

Robert, B. Resonance Raman spectroscopy. *Photosynth. Res.* **101**, 147-155 (2009).

Robert, P. Precision agriculture: a challenge for crop nutrition management. *Plant and soil* **247**, 143-149 (2002).

Rodriguez-Saona, L. & Allendorf, M. Use of FTIR for rapid authentication and detection of adulteration of food. *Annual review of food science and technology* **2**, 467-483 (2011).

Romeo, M. J. *et al.* in *Vibrational Spectroscopy for Medical Diagnosis* (eds M. Diem, P. Lasch, & J. Chalmers) (John Wiley & Sons, Hoboken, New Jersey, USA, 2008).

Rösch, P., Kiefer, W. & Popp, J. Chemotaxonomy of mints of genus *Mentha* by applying Raman spectroscopy. *Biopolymers* **67**, 358-361 (2002).

Rösch, P., Popp, J. & Kiefer, W. Raman and surface enhanced Raman spectroscopic investigation on Lamiaceae plants. *Journal of molecular structure* **480**, 121-124 (1999).

Rosegrant, M. W. & Cline, S. A. Global food security: challenges and policies. *Science* **302**, 1917-1919 (2003).

Rothwell, S. A. & Dodd, I. C. Xylem sap calcium concentrations do not explain liming-induced inhibition of legume gas exchange. *Plant Soil* **382**, 17-30 (2014).

Roy, R., Finck, A., Blair, G. & Tandon, H. Plant nutrition for food security. *A guide for integrated nutrient management. FAO Fertilizer and Plant Nutrition Bulletin* **16**, 368 (2006).

Roy, S. Function of MYB domain transcription factors in abiotic stress and epigenetic control of stress response in plant genome. *Plant Signaling & Behavior* **11**, e1117723 (2016).

Rudd, J. & Franklin-Tong, V. Calcium signaling in plants. *CMLS, Cell. Mol. Life Sci.* **55**, 214-232 (1999).

Saar, B. G. *et al.* Label-free, Real-time monitoring of biomass processing with stimulated Raman scattering microscopy. *Angew. Chem. Int.* **49**, 5476-5479 (2010).

Saladié, M., Rose, J. K., Cosgrove, D. J. & Catalá, C. Characterization of a new xyloglucan endotransglucosylase/hydrolase (XTH) from ripening tomato fruit and implications for the diverse modes of enzymic action. *The Plant Journal* **47**, 282-295 (2006).

Saleem, I., Javid, S., Sial, R. A., Ehsan, S. & Ahmad, Z. A. Substitution of soil application of urea with foliar application to minimize the wheat yield losses. *Soil Environ.* **32** (2013).

Sanders, D., Pelloux, J., Brownlee, C. & Harper, J. F. Calcium at the crossroads of signaling. *The Plant Cell Online* **14**, S401-S417 (2002).

Sathyanarayana, D. N. *Vibrational spectroscopy: theory and applications*. (New Age International, 2015).

Sauerbeck, D. & Helal, H. in *Genetic aspects of plant mineral nutrition* 11-17 (Springer, 1990).

Saure, M. Causes of the tipburn disorder in leaves of vegetables. *Scientia Horticulturae* **76**, 131-147 (1998).

Savitzky, A. & Golay, M. J. E. Smoothing and differentiation of data by simplified least squares procedures. *Anal. Chem.* **36**, 1627-1639 (1964).

Scaglia, E. et al. Noninvasive assessment of hepatic fibrosis in patients with chronic hepatitis C using serum Fourier transform infrared spectroscopy. *Anal Bioanal Chem* **401**, 2919-2925 (2011).

Schlücker, S., Schaeberle, M. D., Huffman, S. W. & Levin, I. W. Raman microspectroscopy: a comparison of point, line, and wide-field imaging methodologies. *Anal. Chem.* **75**, 4312-4318 (2003).

Schmidhuber, J. & Tubiello, F. N. Global food security under climate change. *Proceedings of the National Academy of Sciences* **104**, 19703-19708 (2007).

Schmidt, M. et al. Raman imaging of cell wall polymers in *Arabidopsis thaliana*. *Biochem. Biophys. Res. Comm.* **395**, 521-523 (2010).

Schmitz-Eiberger, M., Haefs, R. & Noga, G. Calcium deficiency-Influence on the antioxidative defense system in tomato plants. *Journal of Plant Physiology* **159**, 733-742 (2002).

Schnitkey, G., Hopkins, J. & Tweeten, L. An economic evaluation of precision fertilizer applications on corn-soybean fields. *Precision Agriculture*, 977-987 (1996).

Schnurr, J. & Shockey, J. The acyl-CoA synthetase encoded by LACS2 is essential for normal cuticle development in *Arabidopsis*. *The Plant Cell* **16**, 629-642 (2004).

Schönherr, J. & Luber, M. Cuticular penetration of potassium salts: Effects of humidity, anions, and temperature. *Plant Soil* **236**, 117-122 (2001).

Schrader, B. *Infrared and Raman spectroscopy: methods and applications*. (John Wiley & Sons, 2008).

Schrader, B. et al. NIR Raman spectroscopy in medicine and biology: results and aspects. *J. Mol. Struct.* **480-481**, 21-32 (1999).

Schrader, B., Hoffmann, A. & Keller, S. Near-infrared fourier transform raman spectroscopy: facing absorption and background. *Spectrochim. Acta A - Molecular Spectroscopy* **47**, 1135-1148 (1991).

Schrader, B., Klump, H., Schenzel, K. & Schulz, H. Non-destructive NIR FT Raman analysis of plants. *J. Mol. Struct.* **509**, 201-212 (1999).

Schroeder, J. I., Allen, G. J., Hugouvieux, V., Kwak, J. M. & Waner, D. Guard cell signal transduction. *Annual review of plant biology* **52**, 627-658 (2001).

Schubert, J. M., Mazur, A. I., Bird, B., Miljković, M. & Diem, M. Single point vs. mapping approach for spectral cytopathology (SCP). *J. Biophotonics* **3**, 588-596 (2010).

Schulz, H. & Baranska, M. Identification and quantification of valuable plant substances by IR and Raman spectroscopy. *Vibrational Spectroscopy* **43**, 13-25 (2007).

Schulz, H., Baranska, M. & Baranski, R. Potential of NIR-FT-Raman spectroscopy in natural carotenoid analysis. *Biopolymers* **77**, 212-221 (2005).

Schulz, H., Özkan, G., Baranska, M., Krüger, H. & Özcan, M. Characterisation of essential oil plants from Turkey by IR and Raman spectroscopy. *Vibrational Spectroscopy* **39**, 249-256 (2005).

Schuster, K. C., Reese, I., Urlaub, E., Gapes, J. R. & Lendl, B. Multidimensional information on the chemical composition of single bacterial cells by confocal Raman microspectroscopy. *Anal. Chem.* **72**, 5529-5534 (2000).

Seibert, M., Picorel, R., Kim, J.-H. & Cotton, T. M. Surface-enhanced Raman scattering spectroscopy of photosynthetic membranes and complexes. *Method. Enzymology* **213**, 31-42 (1992).

Selvakumar, P., Gahlot, D., Tomar, P. P., Sharma, N. & Sharma, A. K. Molecular evolution of miraculin-like proteins in soybean Kunitz super-family. *Journal of molecular evolution* **73**, 369-379 (2011).

Sene, C., McCann, M. C., Wilson, R. H. & Grinter, R. Fourier-Transform Raman and Fourier-Transform Infrared Spectroscopy (An Investigation of Five Higher Plant Cell Walls and Their Components). *Plant Physiology* **106**, 1623-1631 (1994).

Sene, C. F., McCann, M. C., Wilson, R. H. & Grinter, R. Fourier-transform Raman and Fourier-transform

infrared spectroscopy (an investigation of five higher plant cell walls and their components). *Plant Physiology* **106**, 1623-1631 (1994).

Shankar, A. *et al.* Whole genome transcriptome analysis of rice seedling reveals alterations in Ca 2+ ion signaling and homeostasis in response to Ca 2+ deficiency. *Cell calcium* **55**, 155-165 (2014).

Sharma, B., Ma, K., Glucksberg, M. R. & Van Duyne, R. P. Seeing through bone with surface-enhanced spatially offset Raman spectroscopy. *J. Am. Chem. Soc.* **135**, 17290-17293 (2013).

Shaw, R. A. & Mantsch, H. H. Vibrational biospectroscopy: from plants to animals to humans. A historical perspective. *Journal of Molecular Structure* **480-481**, 1-13 (1999).

Shen, L. *et al.* Measuring stress signaling responses of stomata in isolated epidermis of graminaceous species. *Frontiers in plant science* **6** (2015).

Sheppard, N. in *Handbook of Vibrational Spectroscopy* (John Wiley & Sons, Ltd, 2006).

Shi, J. *et al.* Pre-visual diagnostics of phosphorus deficiency in mini-cucumber plants using near-infrared reflectance spectroscopy. *Applied spectroscopy* **66**, 1426-1432 (2012).

Shih, M.-D. *et al.* Functional studies of soybean (*Glycine max* L.) seed LEA proteins GmPM6, GmPM11, and GmPM30 by CD and FTIR spectroscopy. *Plant Science* **196**, 152-159 (2012).

Siebert, F. & Hildebrandt, P. *Vibrational spectroscopy in life science*. (John Wiley & Sons, 2008).

Simões, I. & Faro, C. Structure and function of plant aspartic proteinases. *European journal of biochemistry* **271**, 2067-2075 (2004).

Simon, E. The symptoms of calcium deficiency in plants. *New phytologist* **80**, 1-15 (1978).

Simon, E. W. The symptoms of calcium deficiency in plants. *New Phytologist* **80**, 1-15 (1978).

Skinner, J. *et al.* An overview of the environmental impact of agriculture in the UK. *Journal of environmental Management* **50**, 111-128 (1997).

Skoulika, S. G. & Georgiou, C. A. Rapid quantitative determination of ciprofloxacin in pharmaceuticals by use of solid-state FT-Raman spectroscopy. *Appl. Spectrosc.* **55**, 1259-1265 (2001).

Smart, C. M. Gene expression during leaf senescence. *New Phytol.* **126**, 419-448 (1994).

Smith, B. C. *Fundamentals of Fourier transform infrared spectroscopy*. (CRC press, 2011).

Smith, E. & Dent, G. *Modern Raman spectroscopy: a practical approach*. (John Wiley & Sons, 2005).

Smith, E. & Dent, G. *Modern Raman spectroscopy: a practical approach*. (John Wiley & Sons, 2013).

Smith, P. Delivering food security without increasing pressure on land. *Global Food Security* **2**, 18-23 (2013).

Smith, V. H., Tilman, G. D. & Nekola, J. C. Eutrophication: impacts of excess nutrient inputs on freshwater, marine, and terrestrial ecosystems. *Environmental pollution* **100**, 179-196 (1999).

Snook, R. D., Harvey, T. J., Faria, E. C. & Gardner, P. Raman tweezers and their application to the study of singly trapped eukaryotic cells. *Integr. Biol.* **1**, 43-52 (2009).

Snyder, C., Bruulsema, T., Jensen, T. & Fixen, P. Review of greenhouse gas emissions from crop production systems and fertilizer management effects. *Agriculture, Ecosystems & Environment* **133**, 247-266 (2009).

Socrates, G. *Infrared and Raman characteristic group frequencies: tables and charts*. (John Wiley & Sons, 2004).

Sonneveld, C. & Voogt, W. in *II Symposium on Horticultural Substrates and their Analysis, XXIII IHC* 294. 81-88.

Sowoidnich, K. & Kronfeldt, H.-D. Fluorescence rejection by shifted excitation Raman difference spectroscopy at multiple wavelengths for the investigation of biological samples. *Int. Sch. Res. Net.* **2012**, 1-11 (2012).

Stevens, P. Formulation of sprays to improve the efficacy of foliar fertilisers. *N. Z. J. For. Sci.* **24**, 27-34 (1994).

Stevens, P. J. Organosilicone surfactants as adjuvants for agrochemicals. *Pestic. Sci.* **38**, 103-122 (1993).

Stewart, D. Fourier transform infrared microspectroscopy of plant tissues. *Applied Spectroscopy* **50**, 357-365 (1996).

Stewart, D., McDougall, G. J. & Baty, A. Fourier-transform infrared microspectroscopy of anatomically different cells of flax (*Linum usitatissimum*) stems during development. *Journal of agricultural and food chemistry* **43**, 1853-1858 (1995).

Stewart, W., Dibb, D., Johnston, A. & Smyth, T. The contribution of commercial fertilizer nutrients to food production. *Agronomy Journal* **97**, 1-6 (2005).

Stitt, D. M. *et al.* Tissue acquisition and storage associated oxidation considerations for FTIR microspectroscopic imaging of polyunsaturated fatty acids. *Vib. Spectrosc.* **60**, 16-22 (2012).

Stone, N., Baker, R., Rogers, K., Parker, A. W. & Matousek, P. Subsurface probing of calcifications with spatially offset Raman spectroscopy (SORS): future possibilities for the diagnosis of breast cancer. *Analyst* **132**, 899-905 (2007).

Stone, N., Kendall, C., Shepherd, N., Crow, P. & Barr, H. Near-infrared Raman spectroscopy for the classification of epithelial pre-cancers and cancers. *J. Raman Spectrosc.* **33**, 564-573 (2002).

Stone, N., Kendall, C., Smith, J., Crow, P. & Barr, H. Raman spectroscopy for identification of epithelial cancers. *Faraday discussions* **126**, 141-157 (2004).

Stone, N. *et al.* Surface enhanced spatially offset Raman spectroscopic (SESORS) imaging—the next dimension. *Chem. Sci.* **2**, 776-780 (2011).

Stone, N. & Matousek, P. Advanced transmission Raman spectroscopy: a promising tool for breast disease diagnosis. *Cancer Res.* **68**, 4424-4430 (2008).

Stone, N., Stavroulaki, P., Kendall, C., Birchall, M. & Barr, H. Raman spectroscopy for early detection of laryngeal malignancy: preliminary results. *Laryngoscope* **110**, 1756-1763 (2000).

Strang, G. & Nguyen, T. *Wavelets and filter banks*. (SIAM, 1996).

Stuart, B. *Infrared spectroscopy*. (Wiley Online Library, 2005).

Stuart, B. *Infrared Spectroscopy: Fundamentals and Applications* (John Wiley and Sons Inc. Hoboken, New Jersey, USA, 2005).

Sun, C.-W., Chen, L.-J., Lin, L.-C. & Li, H.-m. Leaf-specific upregulation of chloroplast translocon genes by a cct motif-containing protein, cia 2. *The Plant Cell* **13**, 2053-2061 (2001).

Sun, D.-W. *Infrared spectroscopy for food quality analysis and control*. (Academic Press, 2009).

Swain, R. & Stevens, M. Raman microspectroscopy for non-invasive biochemical analysis of single cells. *Biochem. Soc. T.* **35**, 544-550 (2007).

Swietlik, D. & Faust, M. Foliar nutrition of fruit crops. *Hortic. Rev.* (1984).

Syahren, A. M., Wong, N. & Mahamud, S. The efficacy of calcium formulation for treatment of tomato blossom-end rot. *J. Trop. Agric. and Fd. Sc* **40**, 89-98 (2012).

Synytsya, A., Čopíková, J., Matějka, P. & Machovič, V. Fourier transform Raman and infrared spectroscopy of pectins. *Carbohydrate Polymers* **54**, 97-106 (2003).

Tahtouh, M., Despland, P., Shimmon, R., Kalman, J. R. & Reedy, B. J. The application of infrared chemical imaging to the detection and enhancement of latent fingerprints: method optimization and further findings. *J. Forensic Sci.* **52**, 1089-1096 (2007).

Tan, K. H. *Soil sampling, preparation, and analysis*. (CRC press, 2005).

Tanq, M., Sharif, M., Shah, Z. & Khan, R. Effect of foliar application of micronutrients on the yield and quality of sweet orange (*Citrus sinensis* L.). *Pak. J. Biol. Sci.* **10**, 1823-1828 (2007).

Tapp, H. S., Defernez, M. & Kemsley, E. K. FTIR spectroscopy and multivariate analysis can distinguish the geographic origin of extra virgin olive oils. *Journal of agricultural and food chemistry* **51**, 6110-6115 (2003).

Taylor, M. D. & Locascio, S. J. Blossom-end rot: a calcium deficiency. *Journal of plant nutrition* **27**, 123-139 (2004).

Tewari, R. K., Kumar, P., Tewari, N., Srivastava, S. & Sharma, P. N. Macronutrient deficiencies and differential antioxidant responses—fluence on the activity and expression of superoxide dismutase in maize. *Plant Science* **166**, 687-694 (2004).

Tfayli, A. *et al.* Digital dewaxing of Raman signals: discrimination between nevi and melanoma spectra obtained from paraffin-embedded skin biopsies. *Appl. Spectrosc.* **63**, 564-570 (2009).

Thumanu, K., Sompong, M., Phansak, P., Nontapot, K. & Buensanteai, N. Use of infrared microspectroscopy to determine leaf biochemical composition of cassava in response to *Bacillus subtilis* CaSUT007. *Journal of Plant Interactions* **10**, 270-279 (2015).

Thygesen, L. G., Løkke, M. M., Micklander, E. & Engelsen, S. B. Vibrational microspectroscopy of food. Raman vs. FT-IR. *Trends Food Sci. Tech.* **14**, 50-57 (2003).

Tilman, D., Balzer, C., Hill, J. & Befort, B. L. Global food demand and the sustainable intensification of agriculture. *Proceedings of the National Academy of Sciences* **108**, 20260-20264 (2011).

Tilman, D., Cassman, K. G., Matson, P. A., Naylor, R. & Polasky, S. Agricultural sustainability and intensive production practices. *Nature* **418**, 671-677 (2002).

Tobin, M. J. *et al.* FTIR spectroscopy of single live cells in aqueous media by synchrotron IR microscopy using microfabricated sample holders. *Vibrational Spectroscopy* **53**, 34-38 (2010).

Trevisan, J., Angelov, P. P., Carmichael, P. L., Scott, A. D. & Martin, F. L. Extracting biological information with computational analysis of Fourier-transform infrared (FTIR) biospectroscopy datasets: current practices to future perspectives. *Analyst* **137**, 3202-3215 (2012).

Trevisan, J. *et al.* Syrian hamster embryo (SHE) assay (pH 6.7) coupled with infrared spectroscopy and chemometrics towards toxicological assessment. *Analyst* **135**, 3266-3272 (2010).

Trevisan, J., Angelov, P. P., Scott, A. D., Carmichael, P. L. & Martin, F. L. IRootLab: a free and open-source MATLAB toolbox for vibrational biospectroscopy data analysis. *Bioinformatics*, btt084 (2013).

Trevisan, J. *et al.* Measuring similarity and improving stability in biomarker identification methods applied to Fourier-transform infrared (FTIR) spectroscopy. *J. Biophotonics* **7**, 254-265 (2014).

Tscharntke, T. *et al.* Global food security, biodiversity conservation and the future of agricultural intensification. *Biological conservation* **151**, 53-59 (2012).

Tucker, G. A., Robertson, N. G. & Grierson, D. Purification and changes in activities of tomato pectinesterase isoenzymes. *Journal of the Science of Food and Agriculture* **33**, 396-400 (1982).

Udelhoven, T., Novozhilov, M. & Schmitt, J. The NeuroDeveloper (R): a tool for modular neural classification of spectroscopic data. *Chemometr. Intell. Lab.* **66**, 219-226 (2003).

Vaccari, L. *et al.* Synchrotron radiation infrared microspectroscopy of single living cells in microfluidic devices: advantages, disadvantages and future perspectives. *J. Phys.: Conf. Ser.* **359**, 012007 (2012).

Valle, J. J. *et al.* Free electron laser-Fourier transform ion cyclotron resonance mass spectrometry facility for obtaining infrared multiphoton dissociation spectra of gaseous ions. *Rev. Sci. Instrum.* **76**, 023103-023103 (2005).

Van De Weert, M., Hering, J. A. & Haris, P. I. Fourier Transform Infrared. *Methods for structural analysis of protein pharmaceuticals* **3**, 131 (2005).

van der Ploeg, R. R., Böhm, W. & Kirkham, M. B. On the origin of the theory of mineral nutrition of plants and the law of the minimum. *Soil Sci. Soc. Am.* **63**, 1055-1062 (1999).

van Dijk, T., Mayerich, D., Bhargava, R. & Carney, P. S. Rapid spectral-domain localization. *Opt. Express.* **21**, 12822-12830 (2013).

van Dijk, T., Mayerich, D., Carney, P. S. & Bhargava, R. Recovery of Absorption Spectra from Fourier Transform Infrared (FT-IR) Microspectroscopic Measurements of Intact Spheres. *Appl. Spectrosc.* **67**, 546-552 (2013).

Van Goor, B. The effect of frequent spraying with calcium nitrate solutions on the mineral composition and the occurrence of bitter pit of the apple Cox's Orange Pippin. *J. Hortic. Sci.* **46**, 347-364 (1971).

Vankeirsbilck, T. *et al.* Applications of Raman spectroscopy in pharmaceutical analysis. *TrAC*. **21**, 869-877 (2002).

Vesk, M., Possingham, J. & Mercer, F. The effect of mineral nutrient deficiencies on the structure of the leaf cells of tomato, spinach, and maize. *Australian Journal of Botany* **14**, 1-18 (1966).

Vijayan, P., Willick, I. R., Lahlali, R., Karunakaran, C. & Tanino, K. K. Synchrotron Radiation Sheds Fresh Light on Plant Research: The Use of Powerful Techniques to Probe Structure and Composition of Plants. *Plant and Cell Physiology*, pcv080 (2015).

Vo-Dinh, T. *Biomedical Photonics Handbook: Biomedical Diagnostics*. Vol. 2 (CRC press, 2014).

Wada, T., Ikeda, H., Ikeda, M. & Furukawa, H. Effects of Foliar Application of Calcium Solutions on the Incidence of Blossom-end Rot of Tomato Fruit. *J. Jpn. Soc. Hortic. Sci.* **65**, 553-558 (1996).

Walsh, M. J. *et al.* Fourier transform infrared microspectroscopy identifies symmetric PO(2)(-) modifications as a marker of the putative stem cell region of human intestinal crypts. *Stem Cells*

26, 108-118 (2008).

Walsh, M. J. *et al.* IR microspectroscopy: potential applications in cervical cancer screening. *Cancer Lett.* **246**, 1-11 (2007).

Walsh, M. J. *et al.* Tracking the cell hierarchy in the human intestine using biochemical signatures derived by mid-infrared microspectroscopy. *Stem Cell Res.* **3**, 15-27 (2009).

Walsh, M. J., Holton, S. E., Kajdacsy-Balla, A. & Bhargava, R. Attenuated total reflectance Fourier-transform infrared spectroscopic imaging for breast histopathology. *Vib. Spectrosc.* **60**, 23-28 (2012).

Walsh, M. J. *et al.* FTIR microspectroscopy coupled with two-class discrimination segregates markers responsible for inter-and intra-category variance in exfoliative cervical cytology. *Biomark. insights* **3**, 179-189 (2008).

Wang, H. *et al.* Characterisation of a ux/iaa like genes expressed in tomato fruit. *Biology and Biotechnology of the Plant Hormone Ethylene III* **349**, 309 (2003).

Warren, F. J. *et al.* Infrared microspectroscopic imaging of plant tissues: spectral visualization of *Triticum aestivum* kernel and *Arabidopsis* leaf microstructure. *The Plant Journal* **84**, 634-646 (2015).

Waste, L. F. H., (2016).

Wehbe, K., Filik, J., Frogley, M. D. & Cinque, G. The effect of optical substrates on micro-FTIR analysis of single mammalian cells. *Analytical and bioanalytical chemistry* **405**, 1311-1324 (2013).

Wei, Z., Dong, L. & Tian, Z. Fourier transform infrared spectrometry study on early stage of cadmium stress in clover leaves. *Pak J Bot* **41**, 1743-1750 (2009).

Weissflog, I. *et al.* Toward in vivo chemical imaging of epicuticular waxes. *Plant Physiol.* **154**, 604-610 (2010).

WEYERS, J. D. B. & TRAVIS, A. J. Selection and Preparation of Leaf Epidermis for Experiments on Stomatal Physiology. *Journal of Experimental Botany* **32**, 837-850 (1981).

Whelan D.R., Bamberg K.R., Puskar L., McNaughton D. & B.R., W. Quantification of DNA in simple eukaryotic cells using Fourier transform infrared spectroscopy. *J. Biophotonics* **6**, 775-784 (2013).

Whelan, D. R. *et al.* Monitoring the reversible B to A-like transition of DNA in eukaryotic cells using Fourier transform infrared spectroscopy. *Nucleic Acids Res.* **39**, 5439-5448 (2011).

Whelan, D. R., Bamberg, K. R., Puskar, L., McNaughton, D. & Wood, B. R. Synchrotron Fourier Transform Infrared (FTIR) analysis of single living cells progressing through the cell cycle. *Analyst*, 3891-3899 (2013).

White, J. G. & Zasoski, R. J. Mapping soil micronutrients. *Field crops research* **60**, 11-26 (1999).

White, P. J. The pathways of calcium movement to the xylem. *Journal of Experimental Botany* **52**, 891-899 (2001).

White, P. J. & Broadley, M. R. Calcium in plants. *Annals of botany* **92**, 487-511 (2003).

Wiberley, S. E., Colthup, N. B. & Daly, L. H. *Introduction to infrared and Raman spectroscopy*. 3rd edn, (Elsevier, 2012).

Widjaja, E., Zheng, W. & Huang, Z. Classification of colonic tissues using near-infrared Raman spectroscopy and support vector machines. *Int. J. Oncol.* **32**, 653-662 (2008).

Wieboldt, D. Understanding Raman Spectrometer Parameters. (2010).

Wigglesworth, V. B. Bound lipid in the tissues of mammal and insect: a new histochemical method. *J. Cell Sci.* **8**, 709-725 (1971).

Wilson, E. B. *Molecular vibrations: the theory of infrared and Raman vibrational spectra*. (Courier Dover Publications, 1955).

Wilson, R. H. *et al.* The mechanical properties and molecular dynamics of plant cell wall polysaccharides studied by Fourier-transform infrared spectroscopy. *Plant Physiology* **124**, 397-406 (2000).

Windbergs, M. *et al.* Chemical imaging of oral solid dosage forms and changes upon dissolution using coherent anti-Stokes Raman scattering microscopy. *Anal. Chem.* **81**, 2085-2091 (2009).

Wittwer, S. H. & Bukovac, M. in *Z. Pflanz.* 235-261 (Springer, 1969).

Wolf, B. A comprehensive system of leaf analyses and its use for diagnosing crop nutrient status. *Communications in Soil Science and Plant Analysis* **13**, 1035-1059 (1982).

Wood, B. R. *et al.* Tip-enhanced Raman scattering (TERS) from hemozoin crystals within a sectioned erythrocyte. *Nano Lett.* **11**, 1868-1873 (2011).

Wood, B. R., Bamberg, K. R., Evans, C. J., Quinn, M. A. & McNaughton, D. A three-dimensional multivariate image processing technique for the analysis of FTIR spectroscopic images of multiple tissue sections. *BMC Med. Imaging* **6**, 12 (2006).

Wood, B. R., Caspers, P., Puppels, G. J., Pandiancherri, S. & McNaughton, D. Resonance Raman spectroscopy of red blood cells using near-infrared laser excitation. *Anal Bioanal Chem* **387**, 1691-1703 (2007).

Wood, B. R. *et al.* Raman imaging of hemozoin within the food vacuole of *Plasmodium falciparum* trophozoites. *FEBS Lett.* **554**, 247-252 (2003).

Wood, B. R. *et al.* Resonance Raman spectroscopy reveals new insight into the electronic structure of β -hematin and malaria pigment. *J. Am. Chem. Soc.* **126**, 9233-9239 (2004).

Wood, B. R. & McNaughton, D. Resonance Raman spectroscopy in malaria research. *Expert Rev. Proteomic.* **3**, 525-544 (2006).

Wood, B. R., Quinn, M. A., Burden, F. R. & McNaughton, D. An investigation into FTIR spectroscopy as a biodiagnostic tool for cervical cancer. *Biospectroscopy* **2**, 143-153 (1996).

Wrobel, T. P., Wajnhold, B., Byrne, H. J. & Baranska, M. Electric field standing wave effects in FT-IR transfection spectra of biological tissue sections: Simulated models of experimental variability. *Vibrational Spectroscopy* **69**, 84-92 (2013).

Wynne, B. Creating public alienation: expert cultures of risk and ethics on GMOs. *Science as culture* **10**, 445-481 (2001).

Xie, C. & Li, Y.-q. Confocal micro-Raman spectroscopy of single biological cells using optical trapping and shifted excitation difference techniques. *J. Appl. Phys.* **93**, 2982-2986 (2003).

Xie, H. n. *et al.* Tracking bisphosphonates through a 20 mm thick porcine tissue by using surface-enhanced spatially offset Raman spectroscopy. *Angew. Chem.* **124**, 8637-8639 (2012).

Xu, Y.-H. *et al.* Light-harvesting chlorophyll a/b-binding proteins are required for stomatal response to abscisic acid in *Arabidopsis*. *Journal of experimental botany* **63**, 1095-1106 (2012).

Yamamoto, S., Watarai, H. & Bouř, P. Monitoring the backbone conformation of valinomycin by Raman optical activity. *ChemPhysChem* **12**, 1509-1518 (2011).

Yan, F. & Vo-Dinh, T. Surface-enhanced Raman scattering detection of chemical and biological agents using a portable Raman integrated tunable sensor. *Sensor. Actuat. B-Chem.* **121**, 61-66 (2007).

Yang, H., Irudayaraj, J. & Paradkar, M. M. Discriminant analysis of edible oils and fats by FTIR, FT-NIR and FT-Raman spectroscopy. *Food Chemistry* **93**, 25-32 (2005).

Yeh, K., Kenkel, S., Liu, J.-N. & Bhargava, R. Fast infrared chemical imaging with a quantum cascade laser. *Analytical chemistry* **87**, 485-493 (2014).

Yu, C., Gestl, E., Eckert, K., Allara, D. & Irudayaraj, J. Characterization of human breast epithelial cells by confocal Raman microspectroscopy. *Cancer Detect. Prev.* **30**, 515-522 (2006).

Yu, P. Application of advanced synchrotron radiation-based Fourier transform infrared (SR-FTIR) microspectroscopy to animal nutrition and feed science: a novel approach. *British journal of nutrition* **92**, 869-885 (2004).

Yu, P. Molecular chemistry imaging to reveal structural features of various plant feed tissues. *Journal of Structural Biology* **150**, 81-89 (2005).

Yu, P. *et al.* Use of synchrotron FTIR microspectroscopy to identify chemical differences in barley endosperm tissue in relation to rumen degradation characteristics. *Canadian journal of animal science* **84**, 523-527 (2004).

Yu, P., McKinnon, J. J., Christensen, C. R. & Christensen, D. A. Using synchrotron transmission FTIR microspectroscopy as a rapid, direct, and nondestructive analytical technique to reveal molecular microstructural-chemical features within tissue in grain barley. *Journal of agricultural and food chemistry* **52**, 1484-1494 (2004).

Yu, P., McKinnon, J. J., Christensen, C. R. & Christensen, D. A. Using synchrotron-based FTIR microspectroscopy to reveal chemical features of feather protein secondary structure: comparison with other feed protein sources. *Journal of agricultural and food chemistry* **52**, 7353-7361

(2004).

Yu, P. *et al.* Chemical imaging of microstructures of plant tissues within cellular dimension using synchrotron infrared microspectroscopy. *Journal of agricultural and food chemistry* **51**, 6062-6067 (2003).

Yuen, J. M., Shah, N. C., Walsh Jr, J. T., Glucksberg, M. R. & Van Duyne, R. P. Transcutaneous glucose sensing by surface-enhanced spatially offset Raman spectroscopy in a rat model. *Anal. Chem.* **82**, 8382-8385 (2010).

Zarcinas, B., Cartwright, B. & Spouncer, L. Nitric acid digestion and multi-element analysis of plant material by inductively coupled plasma spectrometry. *Commun. Soil Sci. Plan.* **18**, 131-146 (1987).

Zeiri, L. SERS of plant material. *Journal of Raman Spectroscopy* **38**, 950-955 (2007).

Zeng, H. *et al.* Role of microRNAs in plant responses to nutrient stress. *Plant and soil* **374**, 1005-1021 (2014).

Zeng, Y., Himmel, M. E. & Ding, S.-Y. in *Biomass Conversion* Vol. 908 49-60 (Springer, 2012).

Zeng, Y. *et al.* Imaging lignin-downregulated alfalfa using coherent anti-Stokes Raman scattering microscopy. *Bioenerg. Res.* **3**, 272-277 (2010).

Zhang, L. & Henson, M. J. A practical algorithm to remove cosmic spikes in Raman imaging data for pharmaceutical applications. *Appl. Spectrosc.* **61**, 1015-1020 (2007).

Zhang, X. *et al.* Label-free live-cell imaging of nucleic acids using stimulated Raman scattering microscopy. *ChemPhysChem* **13**, 1054-1059 (2012).

Zhang, Y., Hong, H. & Cai, W. Imaging with Raman spectroscopy. *Curr. Pharm. Biotechno.* **11**, 654-661 (2010).

Zhao, J., Lui, H., McLean, D. I. & Zeng, H. Automated autofluorescence background subtraction algorithm for biomedical Raman spectroscopy. *Applied spectroscopy* **61**, 1225-1232 (2007).

Zhao, W. *et al.* RNA-Seq-based transcriptome profiling of early nitrogen deficiency response in cucumber seedlings provides new insight into the putative nitrogen regulatory network. *Plant and Cell Physiology*, pcu172 (2014).

Zhong, R., Burk, D. H., Morrison, W. H. & Ye, Z.-H. A kinesin-like protein is essential for oriented deposition of cellulose microfibrils and cell wall strength. *The plant cell* **14**, 3101-3117 (2002).

Zhu, B., Chen, T. H. & Li, P. H. Activation of two osmotin-like protein genes by abiotic stimuli and fungal pathogen in transgenic potato plants. *Plant Physiology* **108**, 929-937 (1995).

Zoladek, A., Pascut, F. C., Patel, P. & Notingher, I. Non-invasive time-course imaging of apoptotic cells by confocal Raman micro-spectroscopy. *J. Raman Spectrosc.* **42**, 251-258 (2011).

Zumbusch, A., Holtom, G. R. & Xie, X. S. Three-dimensional vibrational imaging by coherent anti-Stokes Raman scattering. *Phys. Rev. Lett.* **82**, 4142-4145 (1999).

Appendix 1 – Other Publications



Analyst

PAPER

[View Article Online](#)

[View Journal](#) | [View Issue](#)



Cite this: *Analyst*, 2016, **141**, 2896

Open Access Article. Published on 06 April 2016. Downloaded on 18/09/2016 23:20:55.
This article is licensed under a Creative Commons Attribution 3.0 Unported Licence.



Received 16th February 2016,
Accepted 6th April 2016
DOI: 10.1039/c6an00392c
www.rsc.org/analyst

Spectrochemical analysis of sycamore (*Acer pseudoplatanus*) leaves for environmental health monitoring†

James Ord,^{a,b} Holly J. Butler,^b Martin R. McAinsh*^b and Francis L. Martin^{b,c}

Terrestrial plants are ideal sentinels of environmental pollution, due to their sedentary nature, abundance and sensitivity to atmospheric changes. However, reliable and sensitive biomarkers of exposure have hitherto been difficult to characterise. Biospectroscopy offers a novel approach to the derivation of biomarkers in the form of discrete molecular alterations detectable within a biochemical fingerprint. We investigated the application of this approach for the identification of biomarkers for pollution exposure using the common sycamore (*Acer pseudoplatanus*) as a sentinel species. Attenuated total reflection Fourier-transform infrared (ATR-FTIR) spectroscopy was used to interrogate leaf tissue collected from three sites exposed to different levels of vehicle exhaust emissions. Following multivariate analysis of acquired spectra, significant biochemical alterations were detected between comparable leaves from different sites that may constitute putative biomarkers for pollution-induced stress. These included differences in carbohydrate and nucleic acid conformations, which may be indicative of sub-lethal exposure effects. We also observed several corresponding spectral alterations in both the leaves of *A. pseudoplatanus* exposed to ozone pollution under controlled environmental conditions and in leaves infected with the fungal pathogen *Rhytisma acerinum*, indicating that some stress-induced changes are conserved between different stress signatures. These similarities may be indicative of stress-induced reactive oxygen species (ROS) generation, although further work is needed to verify the precise identity of infrared biomarkers and to identify those that are specific to pollution exposure. Taken together, our data clearly demonstrate that biospectroscopy presents an effective toolkit for the utilisation of higher plants, such as *A. pseudoplatanus*, as sentinels of environmental pollution.

1. Introduction

Exposure to complex mixtures of anthropogenic emissions in the environment is currently a major concern for human health. Air pollution from industrial and vehicular sources has been linked with respiratory illness, cardiovascular disease, cancer, and mortality.¹ Although gaseous pollutants (e.g., SO₂) have been of major concern throughout the last century,² attention has since shifted to other potentially dangerous pollutants, notably particulate matter (PM₁₀ and PM_{2.5}),³ nano-

particles,⁴ and polycyclic aromatic hydrocarbons (PAHs).⁵ While the adverse effects of individual agents are well-studied, the effects of exposure to mixtures may be difficult to predict, and thus there is an urgent need to monitor environmental exposures in sentinel organisms.^{6,7}

The advantages of using higher plants as sentinels for environmental pollution are well known.^{8,9} Firstly, as sedentary organisms, they allow easy comparison between set geographical locations. Furthermore, plant biochemistry is fundamentally similar to that of animals in aspects relevant to toxic exposure, including DNA organisation and repair mechanisms, and antioxidant activity.¹⁰ Plant cells can be exposed to air pollutants either directly *via* leaf stomata, or indirectly *via* root uptake of pollutants deposited in the soil. Adverse effects on plants can be induced by a variety of air pollutants, among which ozone (O₃) is considered to be the most damaging. O₃ causes oxidative damage to cell components *via* the formation of reactive oxygen species (ROS),¹¹ which are also generated by exposure to heavy metals.¹² Other adverse effects of air

^aDepartment of Animal and Plant Sciences, University of Sheffield, Sheffield S10 2TN, UK

^bCentre for Biophotonics, Lancaster Environment Centre, Lancaster University, Lancaster LA1 4YQ, UK. E-mail: f.martin@lancaster.ac.uk, m.mcainsh@lancaster.ac.uk

^cSchool of Pharmacy and Biomedical Sciences, University of Central Lancashire, Preston PR1 2HE, UK

†Electronic supplementary information (ESI) available. See DOI: 10.1039/c6an00392c

pollutants on plant cells may include acidification of the intracellular space by SO_2 ,¹¹ and genotoxicity of nanoparticles¹³ and PAHs.¹⁴

For a plant species to be utilised as a sentinel requires that it is present in areas of both high and low pollution exposure, and that it also exhibits quantifiable biomarkers for the adverse effects of pollution. The deciduous tree *Acer pseudoplatanus* (common sycamore) represents an ideal sentinel species, due to its widespread European distribution, and frequent occurrence in urban and rural areas. Previous attempts to utilise *A. pseudoplatanus* as a sentinel have relied on the abundance of tar spot (*Rhytisma acerinum*) fungal lesions (stromata) on leaf surfaces, as the fungus was perceived to be sensitive to SO_2 exposure.¹⁵ However, this has since been refuted, due to evidence that the prevalence of the fungus in urban areas is reduced by leaf litter clearance.¹⁶

A range of approaches have been used for the detection of environmental stress biomarkers in higher plants, including chlorophyll fluorescence measurement for effects on photosynthetic efficiency,¹⁷ and gas chromatography for examining changes in leaf fatty acid composition in response to metal exposure.¹⁸ The *Tradescantia* micronucleus (Trad-MCN) assay, which uses the appearance of micronuclei in tetrad phase pollen cells of *Tradescantia* spp. as a biomarker of chromosomal anomalies, has also been widely used to study genotoxicity.¹⁹ There are disadvantages inherent in many of the existing biomarker systems used in plant toxicology: (i) they rely on a single endpoint, and do not account for the wide range of biochemical effects that may be exerted by pollutants; and, (ii) they may require extensive sample preparation.¹⁸ Hence, development of informative, non-destructive, and high-throughput approaches for the identification of robust biomarkers for environmental stress is essential.

Biospectroscopy refers to the application of vibrational spectroscopy techniques to address biological questions.^{20,21} As such, it offers a novel approach to biomarker derivation which is both sensitive and high-throughput, and which can be used to deduce a wide range of effects within a biochemical 'fingerprint'.²² Infrared (IR) spectroscopy relies upon the absorption of IR at different wavelengths by the principle functional groups, which constitute molecular components of cells depending on the vibrations generated by their chemical bonds.²³ Attenuated total reflection Fourier-transform infrared (ATR-FTIR) spectroscopy employs a diamond crystal, through which an IR beam is transmitted and penetrates a few microns into the sample. Consequently, the reflected beam delivers an absorbance spectrum with distinct wavenumber peaks corresponding to biological molecules present including amides, nucleic acids, and polysaccharides.²⁴ The resulting datasets are complex, requiring computational analyses of the spectra in order to determine the distinguishing features between experimental treatments.^{20,25} Multivariate techniques such as principal component analysis-linear discriminant analysis (PCA-LDA) are typically performed to achieve this.

Biochemical fingerprints derived from ATR-FTIR have strong potential to reflect changes induced by exposure to

xenobiotics and therefore biospectroscopy is increasingly being utilised in ecotoxicology, with toxic effects having been characterised *in vitro*,^{26,27} and in sentinel organisms such as birds,²⁸ earthworms,²⁹ catfish, and water spinach.³⁰ Given the advantages of plants as sentinels, biospectroscopy offers the potential of a convenient plant-based monitoring system for pollution exposure over time and space. This technique is ideal for analysing plant tissue, as it requires little-to-no sample preparation, allowing specimens to be collected from the field and analysed rapidly.^{21,31}

Plants are exposed to a range of environmental stresses, both abiotic and biotic, that will act together to affect their biochemical fingerprint and which may confound attempts to study pollution-induced alterations. Most notably, plant pathogens represent a ubiquitous biotic stress in the environment. Pathogens of *A. pseudoplatanus* include the tar spot leaf fungus (*Rhytisma acerinum*),¹⁶ and leaf galls induced by the mite *Artacris macrorhynchus*.³² The presence of these pathogens or the plant's defensive response may substantially alter leaf biochemistry, and therefore it is essential to assess their impacts on the biochemical fingerprint of *A. pseudoplatanus* if it is to be considered as a candidate as a sentinel species for environmental pollution monitoring.

Herein, the potential of *A. pseudoplatanus* as a sentinel for environmental exposure was assessed using biospectroscopy. Specifically, the effects of different pollution scenarios on the biochemical fingerprints of field-derived leaf samples were examined, with the aim of identifying spectral biomarkers associated with pollution exposure. Additionally, we examined the effects of O_3 fumigation on leaves of *A. pseudoplatanus* under controlled environment conditions and *R. acerinum* infection on the derived biochemical fingerprints. We show that there are key spectral differences between of *A. pseudoplatanus* leaves sampled from environments with different pollution exposures, which are indicative of plant stress and which, importantly, could not be detected using changes in chlorophyll fluorescence (Fv/Fm). If these alterations can be established to provide definitive and robust biomarkers of pollution-induced stress this will confirm *A. pseudoplatanus* as a sentinel plant system providing an effective approach to environmental health monitoring.

2. Materials and methods

Field sites

Three field sites were selected, representing a range of exposure levels to environmental pollutants (Table 1). All three sites featured an abundance of mature *A. pseudoplatanus*. Site 1 comprised an area of rural woodland within the Fairfield Nature Reserve, Lancaster (UK). The site is 1.2 km from the nearest busy road, and is further shielded from busy roads by rows of trees and a canal. Site 2 is an area of mixed vegetation located immediately adjacent to a busy 6-lane highway. Site 3 is an urban site located on a busy city centre roundabout. In addition, a fourth site (Site 4) was used to study the

Table 1 Descriptions of the three main study sites from which *A. pseudoplatanus* samples were taken for the comparison of different pollution scenarios

Site	Pollution exposure	Site description
Site 1	Rural (reference site)	A woodland area in the Fairfield Nature Reserve, Lancaster. The site is not immediately exposed to pollution sources such as busy roads. The <i>A. pseudoplatanus</i> trees at the site were planted in the 1830s.
Site 2	Highway	A woodland area at the edge of Lancaster University campus, and next to a busy 6-lane highway. This was the most densely vegetated site, featuring a very high abundance of <i>A. pseudoplatanus</i> .
Site 3	Urban	A busy roundabout near Lancaster's urban centre, frequently used by vehicles. Several mature <i>A. pseudoplatanus</i> trees were identified at the site, including three on the roundabout itself.

effects of *R. acerinum* infection. This was comprised of abundant *A. pseudoplatanus* vegetation in hedges bordering a rural road only infrequently used by light road vehicles.

Sample collection and storage

A pilot study was undertaken to determine the method for sample storage. We compared the spectral signatures of leaves maintained in a moist condition³¹ and leaves fixed in 70% ethanol (three immersion times: 10 min, 30 min, and 60 min) after 24 h, with the spectral signature of moist leaves on the day of collection. Ethanol fixation induced a significant shift in LD1 scores, which increased with immersion time, whereas there was no significant effect of the moist condition after 24 h [see ESI Fig. S1†].

Leaves (physiological age \leq 3 months) were removed from mature *A. pseudoplatanus* trees (age unknown) by cutting the petiole no less than 1 cm from the leaf and placing them in zip-lock bags containing 3x damp cotton wool balls to prevent desiccation.³¹ For Sites 1–3, three leaves were collected from each of five trees (15 total leaves) from low in the canopy, approximately 1–3 m from the ground. We selected young leaves which fell within 5–10 cm in width, and did not display any obvious signs of foliar disease (e.g., herbivory, tar spots) or senescence (e.g., chlorosis, desiccation). After transport to the laboratory, leaves were rinsed in reverse osmosis water to remove insects and mites, and placed on dry paper towels to remove excess water. Spectral acquisition followed immediately, with five spectra taken per leaf sample. The entire study was carried out over three days, one site per day.

Chlorophyll fluorescence measurements

In situ measurements of the ratio of variable to maximal fluorescence of photosystem II (Fv/Fm) were taken using a Hansatech Pocket PEA Chlorophyll fluorometer (Hansatech Instruments, Norfolk, UK); Fv/Fm values less than 0.83 are indicative of stress.¹⁷ Three leaves on at least five trees at each

site were dark acclimatised for 30–40 min before Fv/Fm values were recorded.

O₃ fumigation

Six cuttings of *A. pseudoplatanus* approximately 20 cm in length comprising of 3–4 healthy leaves were obtained from an additional urban site. In contrast to Site 3, this was located away from busy roads and sheltered from any potential sources of vehicle-derived pollution by high walls. Cuttings were incubated in 500 ml plastic bottles wrapped in aluminium foil to exclude light containing 250 ml of 1:1 Hoagland's nutrient solution³³ for 2 days prior to fumigation treatments. Two cuttings each were fumigated with either O₃-free air filtered through Purafil (control) or a modulated episodic ozone treatment (150 ppb or 300 ppb O₃) under the same conditions for a period of three days to simulate a summer O₃ 'episode'.³⁴ In all experiments fumigations were performed at midday although the duration of the fumigation treatment (approximately 6 hours into the photoperiod) varied: day-1 – 2 h, day-2 – 3 h, day-3 – 2 h. Cuttings were then incubated for a further 1-day under the same conditions following fumigation before analysis with ATR-FTIR spectroscopy.

Characterisation of *R. acerinum* infection levels

The severity of *R. acerinum* infection was assessed through the occurrence of characteristic large black lesions, called stromata or tar spots on the adaxial leaf surface. Leaves, 7–9 cm in width, collected from Site 4 were categorised according to the number of tar spots present: category 1 – leaves with no obvious tar spots (control), category 2 – leaves displaying 1–5 obvious tar spots, and Category 3 – leaves displaying \geq 10 obvious tar spots. For each category, five leaves were taken from different plants. For each leaf, three spectra were taken from areas of healthy-looking tissue in close proximity to the afflicted area. A second biotic stress, galls induced by the mite, *Artacris macrorhynchus* (protruding red lesions on the adaxial leaf surface) was also examined. In this instance, five leaves displaying prominent galls were collected from the rural Site 1, and were compared with leaves displaying no obvious signs of *A. macrorhynchus*-induced damage taken from the same site as a control. Three spectra were acquired from each leaf, from areas of healthy tissue in close proximity to the affected area or from an equivalent area in the control leaves.

ATR-FTIR spectroscopy

Spectra were acquired from adaxial leaf surfaces using a Bruker Tensor 27 FTIR spectrometer with Helios ATR attachment (Bruker Optics Ltd, Coventry, UK), controlled using the software 'OPUS'. Leaf samples were placed on Low-E slides on the sampling platform, and 1 kg of force was applied for even contact between the crystal and the sample. In between sample spectra, the crystal was cleaned with dH₂O, and background spectra were taken to compensate for atmospheric changes.





Pre-processing and computational analyses

Spectral datasets were classed in Microsoft Excel, and were processed using the IRootLab toolbox (<http://irootlab.googlecode.com>) running on MATLAB r2013a (The Maths Works Inc., USA). Spectra were pre-processed by cutting to the bio-fingerprint region ($1800\text{--}900\text{ cm}^{-1}$), rubberband baseline-corrected, and vector normalised. Pre-processed spectral datasets were analysed by principal component analysis-linear discriminant analysis (PCA-LDA). PCA-LDA is a composite technique whereby PCA is applied to a dataset to reduce the number of variables, then LDA derives orthogonal variables from which between-class variance is maximised over within-class variance.²⁰ The PCA-LDA models were then used to derive cluster vector plots, derived by pointing from the mean of the control class towards the mean of each treatments class, deriving a separate vector or 'pseudospectrum' for each treatment class, representing biochemical alterations in relation to the control (expressed as coefficient).²⁵ For more detailed overviews of the computational methods applied in biospectroscopy, readers are directed to the literature.^{20,25}

Statistical analyses

All statistical tests were carried out in 'R' version 3.2.3 (R Foundation for Statistical Computing, Austria). To derive values of statistical significance between sites, the first two linear discriminant (LD) scores derived from PCA-LDA were compared using a nested linear mixed effects model fit by REML (Residual Maximum Likelihood) using the (nlme) package (<http://CRAN.R-project.org/package=nlme>), with 'Tree' and 'Leaf' included as nested random factors to account for variation between individual trees and leaves. Linear mixed effects models with 'Leaf' as a random factor were carried out to assess the significance of shifts in LD scores as a function of O_3 concentration or tar spot number. One-way ANOVA with type-1 sums of squares was used to compare Fv/Fm values between sites. A P -value of <0.05 was considered statistically significant.

3. Results and discussion

Site location has a marked impact on the spectral signature of *A. pseudoplatanus*

Spectral datasets from *A. pseudoplatanus* leaves derived from Sites 1–3 were compared using multivariate analyses in order to derive biomarkers of inter-site differences. Following PCA-LDA transformation of pre-processed datasets, the corresponding 2-D LDA scores plot (Fig. 1a) showed a degree of segregation of data from the sites into three clusters, although complete segregation was not observed. A nested linear mixed effects model fit by REML revealed an overall significant effect of site on LD scores ($P = 0.003$), with a significant difference in overall LD scores between the urban-located Site 3 and the rural-located Site 1 ($P = 0.015$). There was no significant difference in overall LD scores between Site 1 and the highway-

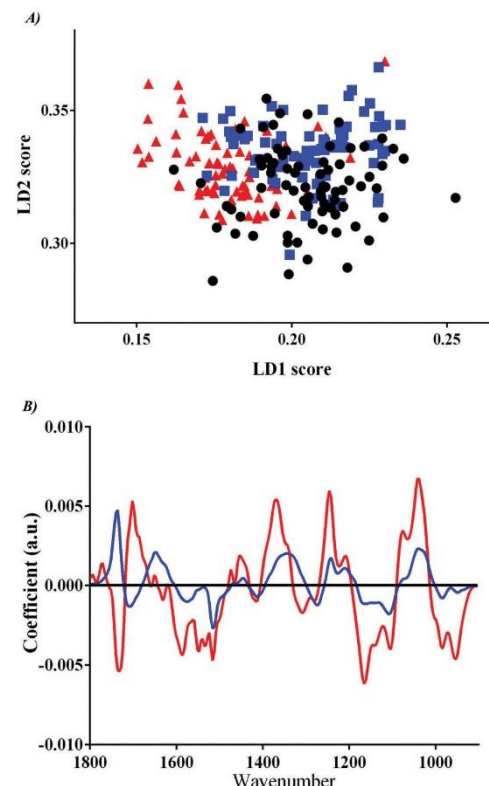


Fig. 1 (A) PCA-LDA scores plot in two dimensions derived from *A. pseudoplatanus* leaf tissue collected from three field sites (black, Site 1; blue, Site 2; red, Site 3) characteristic of different environmental exposures. (B) Cluster vectors plot by PCA-LDA indicating wavenumber basis for segregation between *A. pseudoplatanus* leaf tissue samples collected from three field sites. The two sites exposed to vehicular pollution (blue, Site 2; red, Site 3) were compared to the rural control site (black, Site 1), with the magnitude of the cluster vector peak or trough proportional to the extent of biochemical alteration compared to Site 1.

located Site 2 ($P = 0.158$), but a highly significant difference in LD2 scores ($P = 0.006$).

The pseudospectra shown in the cluster vectors plot (Fig. 1b) displayed substantial changes between sites across the biochemical fingerprint region. Site 2 and Site 3 leaves exhibited several common areas of segregation from Site 1 leaves, suggesting pollution-associated alterations stemming from their different exposures to vehicle exhaust emissions. Several alterations were linked with specific molecular features (Table 2). Notably, alterations in the carbohydrate region (e.g., 1107 cm^{-1} in Site 2, 1165 cm^{-1} in Site 3) may imply alterations to cell wall conformation, reduced photosynthetic capacity, or increased energy expenditure. Alterations were also observed in the DNA/RNA region ($\sim 950\text{ cm}^{-1}$) at both sites, which may suggest exposure to genotoxic agents.^{14,35} In addition, peaks

Table 2 ATR-FTIR spectroscopy distinguishing wavenumbers as shown in cluster vectors plot for *A. pseudoplatanus* leaf tissue collected from three field sites characteristic of different environmental exposures to vehicular pollution. For Site 2 and Site 3 leaves, the most important wavenumbers responsible for segregation from control (Site 1) leaves are shown, along with their tentative chemical assignments

Site	Wavenumber (cm ⁻¹)	Tentative assignment(s)	Reference (s)
Site 2	1736	Lipid; fatty acid esters	(1)
	1647	Amide I; pectin	(1), (3)
	1574	Amide I	
	1516 ^b	Amide II	(1)
	1447 ^a	Protein; $\delta(\text{CH}_2)$ of sesquiterpenes	(1), (2)
	1412 ^a	Protein	
	1346	COO-symmetric stretching vibrations of fatty acids and amino acid	(1)
	1242 ^a	Asymmetric phosphate; amide III (C-N stretching of α -helical proteins)	(1)
	1161 ^a	Carbohydrate; stretching vibrations of hydrogen-bonding C-OH groups (found in serine, threonine and tyrosine residues of cellular proteins); cellulose	(1), (3)
	1107 ^a	Symmetric phosphate; $\nu(\text{CO})$, $\nu(\text{CC})$ ring (polysaccharides, pectin)	(1)
	1038 ^a	$\nu(\text{CC})$ skeletal <i>cis</i> conformation, $\nu(\text{CH}_2\text{OH})$; Galactan(CO) stretching coupled with C-O bending;	(1), (2)
	984	Protein phosphorylation; $\omega(\text{CH}_2)$ of monoterpenes	(1), (2)
	949 ^a	Protein phosphorylation	(1), (3)
	1771	Lipid; fatty acid esters	(1)
Site 3	1732	Lipid; fatty acid esters; hemicellulose	(1), (3)
	1701	Lipid; fatty acid esters	(1)
	1632	Amide I; pectin	(1), (3)
	1585	Amide I	(1)
	1516 ^b	Amide II	(1)
	1454 ^a	Protein; $\delta(\text{CH}_2)$ of tetraterpenes	(1), (2)
	1416 ^a	Protein	(1)
	1369	COO-symmetric stretching vibrations of fatty acids and amino acid; $\delta_{\text{sym}}(\text{CH}_3)$ sesquiterpenes	(1), (3)
	1308	Amide III	(1)
	1246 ^a	Amide III (C-N stretching of α -helical proteins)	(1)
	1207	Asymmetric phosphate	(1)
	1165 ^a	Carbohydrate; cellulose	(1), (3)
	1103 ^a	Symmetric phosphate	(1)
	1042 ^a	Symmetric PO_2 stretching in RNA and DNA;	(1)
	953 ^a	Protein phosphorylation	(1)

ν : stretching, δ : deformation. ^a Loose correlation with other polluted site. ^b Exact correlation with other polluted site. References: (1) Movasagh *et al.*, 2008;⁴⁷ (2) Schulz and Baranska, 2007;³⁶ (3) Stuart, 2004.²³

associated with terpenes³⁶ were discovered at both sites (1447 cm⁻¹ in Site 2 leaves, 1369 and 1454 cm⁻¹ in Site 3 leaves). Several terpenes, particularly carotenoids are known to

function as scavengers of ROS,³⁷ implying that leaves from polluted sites may have been exposed to higher ROS levels, possibly as a result of increased pollution exposure. Segregation from the rural control site (Site 1) was markedly greater for Site 3 leaves, implying a stronger effect of the urban exposure (Site 3) on leaf biochemistry than highway exposure (Site 2). Interestingly, there was no significant difference using one-way ANOVA (see ESI Table S1†) between the average Fv/Fm values from the three field sites ($P = 0.287$), indicating no discernible differences in the levels of stress experienced by plants at the different sites using this technique.

O₃ fumigation induces dose-dependent change in the spectral signature

Spectral datasets from O₃-free air- and O₃-fumigated (150 ppb and 300 ppb O₃) *A. pseudoplatanus* leaves were compared using multivariate analyses in order to derive biomarkers of controlled O₃ exposure. Following PCA-LDA transformation of pre-processed datasets, the three treatments segregated completely into distinct clusters (Fig. 2a). Segregation appeared to be predominantly in LD1, in concentration-dependent manner. A linear mixed effects model fit by REML revealed a significant effect of O₃ on LD1 values ($P = 0.003$). The cluster vectors plot (Fig. 2b) revealed substantial spectral segregation between the O₃ treatments and the control O₃-free air treatment across the biochemical fingerprint region. Similar changes were observed in both O₃ treatments and were generally more substantial in 300 ppb O₃-fumigated leaves this being indicative of a concentration-dependent response to O₃. Alterations were detected in several molecules (Table 3), and were highly prominent in lipid, amides, and proteins (1701, 1520, and 1458 cm⁻¹, respectively) suggesting possible damage to cell membranes and protein structures resulting from the generation of ROS by O₃. This is consistent with oxidative damage as the primary mode of O₃ toxicity in plants.¹¹

Biotic stresses induce similar changes in the spectral signature

Spectral datasets from healthy (control) leaves of *A. pseudoplatanus* and those exhibiting two levels of *R. acerinum* infection (1–5 spots, and ≥ 10 spots) were compared using multivariate analyses. Following PCA-LDA transformation of pre-processed datasets, the three categories segregated completely into distinct clusters (Fig. 3a). As with O₃ treatment, segregation was predominantly in LD1, in a dose-dependent manner. A linear mixed effects model fit by REML revealed a significant effect of *R. acerinum* infection on LD1 values ($P < 0.001$). The cluster vectors plot (Fig. 3b) reveals substantial spectral segregation between the two infection levels and the uninfected control leaves across the biochemical fingerprint region. Strong alterations were detected in several molecules (Table 3), including amides, lipids, and proteins. Alterations to lipid may reflect ROS damage to cell membranes, which are generated in defence against pathogens *via* the oxidative burst mechanism.³⁸ In this case, ROS may be employed by the immune system as executioners of either the pathogen or the host cell.³⁹ Interestingly, leaf galls also

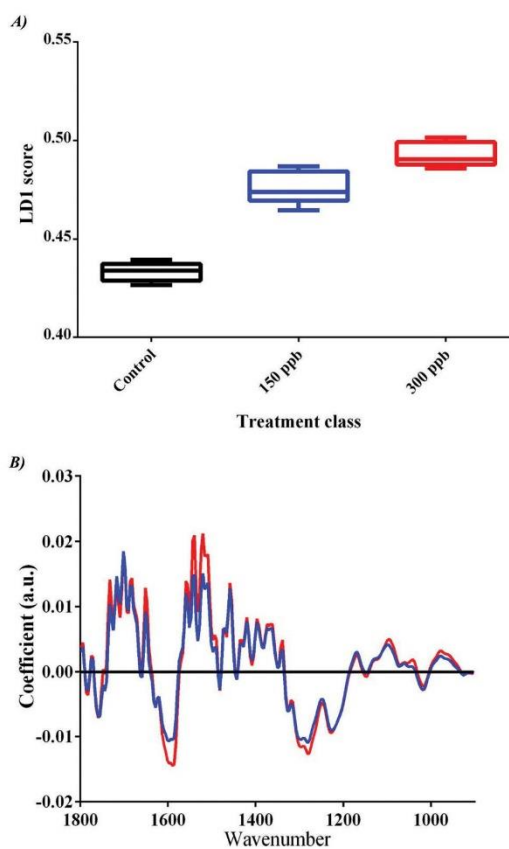


Fig. 2 (A) Box plot of PCA-LDA scores plot in one dimension derived from *A. pseudoplatanus* leaf tissue fumigated with either O₃-free air (black) or O₃ (blue, 150 ppb; red, 300 ppb) for seven hours over three days at two treatment concentrations, in addition to a control. (B) Cluster vectors plot by PCA-LDA indicating wavenumber basis for segregation following fumigation of *A. pseudoplatanus* leaf tissue with O₃. Each treatment (blue, 150 ppb; red, 300 ppb) was compared to the control (black, O₃-free air). The magnitude of the cluster vector peak or trough is proportional to the extent of biochemical alteration compared to the air control.

induced a highly significant effect on LD1 values (Welch two-sample *T*-test, *P* < 0.001), and the signature of alterations was almost identical to *R. acerinum* across the biochemical fingerprint region (see ESI Fig. S2, Table S2†), implying that the patterns observed are representative of a non-specific immune response.

Conserved changes in spectral signature between sampling sites, O₃, and biotic stresses

While it is important to note that our proposed mechanistic explanations for spectral alterations are largely speculative, conserved changes between different sites and stressors imply similar modes of action. The pseudospectra of the leaves

Table 3 ATR-FTIR spectroscopy distinguishing wavenumbers as shown in cluster vectors plot for *A. pseudoplatanus* leaf tissue exposed to abiotic (O₃ fumigation) and biotic stressors (tar spot infection). The most important wavenumbers responsible for segregation from the respective control leaves are shown, along with their tentative chemical assignments

Stressor	Wavenumber (cm ⁻¹)	Tentative assignment(s)	Reference(s)
Ozone	1759	Lipid	(1)
	1755	Lipid	(1)
	1701	Lipid; bases; fatty acid esters	(1)
	1651	Amide I; pectin	(1), (3)
	1597	Amide I; C=N, NH ₂ adenine	(1)
	1589	Amide I; ring C-C stretch of phenyl	(1)
	1558	Amide II; ring base	(1)
	1520	Amide II	(1)
	1458	Proteins; δ _{as} CH ₃	(1)
	1373	COO-symmetric stretching vibrations of fatty acids and amino acid	(1)
	1366	COO-symmetric stretching vibrations of fatty acids and amino acid	(1)
	1281	Amide III	(1)
	1227	Asymmetric phosphate; ν _{as} (C-O-C) of geranyl acetate (acyclic monoterpene)	(1), (2)
	1099	Symmetric phosphate	(1)
Tar spot	1169	Carbohydrate	(1)
	1096	Symmetric phosphate	(1)
	976	Protein phosphorylation	(1)
	1724	Lipid; fatty acid esters	(1)
	1701	Lipid; fatty acid esters	(1)
	1686	Amide I	(1)
	1632	Amide I; C=C uracil, C=O; pectin	(1), (3)
	1628	Amide I	(1)
	1597	Amide I; C=N, NH ₂ of adenine	(1)
	1593	Amide I	(1)
	1539	Amide II	(1)
1458	1458	Proteins; δ _{as} CH ₃	(1)
	1373	COO-symmetric stretching vibrations of fatty acids and amino acid	(1)
	1308	Amide III	(1)
	1304	Amide III	(1)
	1246	Amide III; PO ₂ asymmetric	(1)
	1107	Symmetric phosphate; ν(CO), ν(CC) ring (polysaccharides, pectin)	(1)
	1011	Glycogen; CH _{α,α'} out-of-plane bending and C _α =C _{α'} torsion	(1)

ν: stretching, δ: deformation. References: (1) Movasaghi *et al.*, 2008;⁴⁷ (2) Schulz and Baranska, 2007;³⁶ (3) Stuart, 2004.²³

exposed to the model abiotic and biotic stresses (O₃ and pathogen-infection, respectively) appear to be strikingly similar, particularly in the upper half of the spectrum (lipid, amide and protein regions). Many of these common elements also appear in the comparison between sites exposed to different vehicular

References

- P. H. Fischer, M. Marra, C. B. Ameling, G. Hoek, R. Beelen, K. de Hoogh, O. Breugelmans, H. Kruize, N. A. Janssen and D. Houthuijs, *Environ. Health Perspect.*, 2015, **123**, 697–704.
- R. M. Harrison, *Pollution: Causes, Effects and Control*, Royal Society of Chemistry, 2001.
- D. W. Dockery and P. H. Stone, *N. Engl. J. Med.*, 2007, **356**, 511–513.
- G. Oberdörster, E. Oberdörster and J. Oberdörster, *Environ. Health Perspect.*, 2005, **1**, 823–839.
- P. Georgiadis, J. Topinka, M. Stoikidou, S. Kaila, M. Gioka, K. Katsouyanni, R. Sram, H. Autrup and S. A. Kyrtopoulos, *Carcinogenesis*, 2001, **22**, 1447–1457.
- A. Klumpp, W. Ansel, G. Klumpp, V. Calatayud, J. P. Garrec, S. He, J. Penuelas, A. Ribas, H. Ro-Poulsen, S. Rasmussen and M. J. Sanz, *Environ. Pollut.*, 2006, **139**, 515–522.
- F. L. Martin, *Nat. Methods*, 2011, **8**, 385–387.
- D. J. Nowak, D. E. Crane and J. C. Stevens, *Urban For. Urban Green.*, 2006, **4**, 115–123.
- D. J. Nowak, S. Hirabayashi, A. Bodine and E. Greenfield, *Environ. Pollut.*, 2014, **193**, 119–129.
- L. D. Claxton and G. M. Woodall, *Mutat. Res., Rev. Mutat. Res.*, 2007, **636**, 36–94.
- J. N. Bell and M. Treshow, *Air Pollution and Plant Life*, John Wiley & Sons, Ltd, 2002.
- A. Nadgórska-Socha, B. Ptasiński and A. Kita, *Ecotoxicology*, 2013, **22**, 1422–1434.
- E. Navarro, A. Baun, R. Behra, N. B. Hartmann, J. Filser, A. J. Miao, A. Quigg, P. H. Santschi and L. Sigg, *Ecotoxicology*, 2008, **17**, 372–386.
- R. Aina, L. Palin and S. Citterio, *Chemosphere*, 2006, **65**, 666–673.
- A. S. Heagle, *Annu. Rev. Phytopathol.*, 1973, **11**, 365–388.
- I. D. Leith and D. Fowler, *New Phytol.*, 1988, **108**, 175–181.
- K. Maxwell and G. N. Johnson, *J. Exp. Bot.*, 2000, **51**, 659–668.
- E. Schreck, C. Laplanche, M. Le Guédard, J. J. Bessoule, A. Austruy, T. Xiong, Y. Foucault and C. Dumat, *Environ. Pollut.*, 2013, **179**, 242–249.
- J. Meireles, R. Rocha, A. C. Neto and E. Cerqueira, *Mutat. Res., Genet. Toxicol. Environ. Mutagen.*, 2009, **675**, 46–50.
- J. Trevisan, P. P. Angelov, P. L. Carmichael, A. D. Scott and F. L. Martin, *Analyst*, 2012, **137**, 3202–3215.
- B. E. Obinaju and F. L. Martin, *Environ. Pollut.*, 2013, **183**, 46–53.
- J. G. Kelly, J. Trevisan, A. D. Scott, P. L. Carmichael, H. M. Pollock, P. L. Martin-Hirsch and F. L. Martin, *J. Proteome Res.*, 2011, **10**, 1437–1448.
- B. H. Stuart, *Infrared Spectroscopy: Fundamentals and Applications*, John Wiley & Sons, Ltd, 2004.
- M. S. Braiman and K. J. Rothschild, *Annu. Rev. Biophys. Biophys. Chem.*, 1988, **17**, 541–570.
- M. J. Baker, J. Trevisan, P. Bassan, R. Bhargava, H. J. Butler, K. M. Dorling, P. R. Fielden, S. W. Fogarty, N. J. Fullwood, K. A. Heys, C. Hughes, P. Lasch, P. L. Martin-Hirsch, B. Obinaju, G. D. Sockalingum, J. Sulé-Suso, R. J. Strong, M. J. Walsh, B. R. Wood, P. Gardner and F. L. Martin, *Nat. Protoc.*, 2014, **9**, 1771–1791.
- X. Li, J. B. Zhang, B. Song, H. P. Li, H. Q. Xu, B. Qu, F. J. Dang and Y. C. Liao, *Phytopathology*, 2010, **100**, 183–191.
- K. A. Heys, M. J. Riding, R. J. Strong, R. F. Shore, M. G. Pereira, K. C. Jones, K. T. Semple and F. L. Martin, *Analyst*, 2014, **139**, 896–905.
- V. Llabjani, R. N. Malik, J. Trevisan, V. Hoti, J. Ulkpebor, Z. K. Shinwari, C. Moeckel, K. C. Jones, R. F. Shore and F. L. Martin, *Environ. Int.*, 2012, **48**, 39–46.
- M. Aja, M. Jaya, K. V. Nair and I. H. Joe, *Spectrochim. Acta Part A*, 2014, **120**, 534–541.
- B. E. Obinaju, A. Alaoma and F. L. Martin, *Environ. Pollut.*, 2014, **192**, 222–231.
- B. Ribeiro da Luz, *New Phytol.*, 2006, **172**, 305–318.
- J. P. O'Connor, M. A. O'Connor, P. Ashe and S. Wistow, *J. Nat. J.*, 1999, **26**, 241–248.
- D. R. Hoagland and D. I. Arnon, *The Water-culture Method for Growing Plants Without Soil*, Circular, California Agricultural Experiment Station, 2nd edn, 1950.
- L. Delle Monache and R. B. Stull, *Atmos. Environ.*, 2003, **37**, 3469–3474.
- C. M. Rico, J. R. Peralta-Videa and J. L. Gardea-Torresdey, *Appl. Spectrosc.*, 2015, **69**, 287–295.
- H. Schulz and M. Baranska, *Vib. Spectrosc.*, 2007, **43**, 13–25.
- L. Pérez-Rodríguez, *BioEssays*, 2009, **31**, 1116–1126.
- P. Wojtaszek, *Biochem. J.*, 1997, **322**, 681–692.
- M. A. Torres, J. D. Jones and J. L. Dangl, *Plant Physiol.*, 2006, **141**, 373–378.
- M. J. Riding, J. Trevisan, C. J. Hirschmugl, K. C. Jones, K. T. Semple and F. L. Martin, *Environ. Int.*, 2012, **50**, 56–65.
- R. A. Fuller, K. N. Irvine, P. Devine-Wright, P. H. Warren and K. J. Gaston, *Biol. Lett.*, 2007, **3**, 390–394.
- E. Ceretti, C. Zani, I. Zerbini, G. Viola, M. Moretti, M. Villarini, L. Dominici, S. Monarea and D. Feretti, *Chemosphere*, 2015, **120**, 221–229.
- A. H. Chappelka and L. J. Samuelson, *New Phytol.*, 1998, **139**, 91–108.
- S. Warrington, D. A. Cottam and J. B. Whittaker, *Oecologia*, 1989, **80**, 136–139.
- B. E. Obinaju, C. Graf, C. Halsall and F. L. Martin, *Environ. Pollut.*, 2015, **192**, 222–231.
- H. J. Butler, M. R. McAinsh, S. Adams and F. L. Martin, *Anal. Methods*, 2015, **7**, 4059–4070.
- Z. Mouasaghi, S. Rehman and D. I. ur Rehman, *Appl. Spectrosc. Rev.*, 2008, **43**, 134–179.

Electronic Supporting Information

Spectrochemical analysis of sycamore (*Acer pseudoplatanus*) leaves for environmental health monitoring

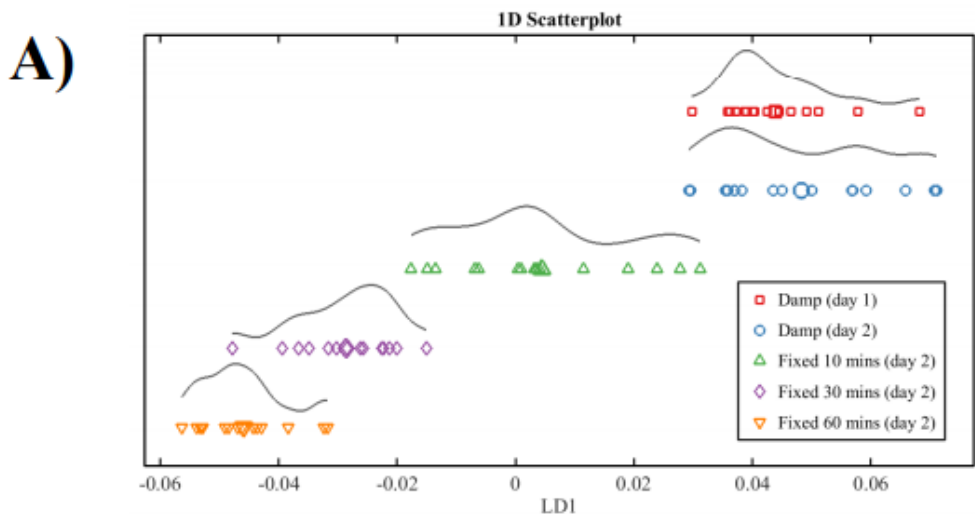
James Ord^{a,b}, Holly J. Butler^b, Martin R. McAinsh^b, and
Francis L. Martin^{b,c}**

^aDepartment of Animal and Plant Science, University of Sheffield, Sheffield S10 2TN, UK; ^bCentre for Biophotonics, Lancaster Environment Centre, Lancaster University, Lancaster LA1 4YQ, UK; ^cSchool of Pharmacy and Biomedical Sciences, University of Central Lancashire, Preston PR1 2HE, UK

*Corresponding authors: Prof Francis L Martin / Dr Martin R McAinsh; *Email:* f.martin@lancaster.ac.uk; m.mcainsh@lancaster.ac.uk

Summary

- **Number of pages: 4**
- **Number of Figures: 2**
- **Number of Tables: 2**



One-way ANOVA	LD1
Damp (day 1) vs. Damp (day 2)	$P > 0.05$
Damp (day 1) vs. Fixed, 10 mins (day 2)	$P < 0.001$
Damp (day 1) vs. Fixed, 30 mins (day 2)	$P < 0.001$
Damp (day 1) vs. Fixed, 60 mins (day 2)	$P < 0.001$

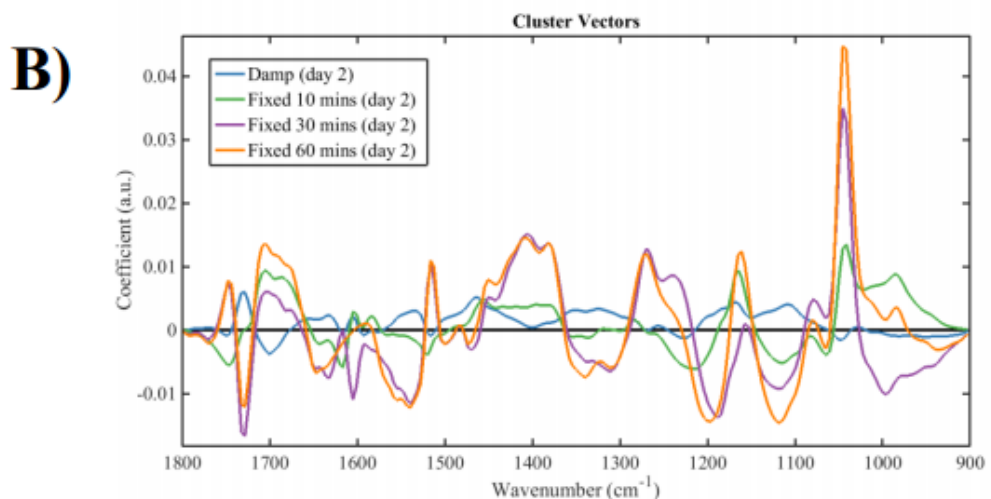


Figure S1 (A) One-D PCA-LDA scores plot derived from *A. pseudoplatanus* leaf tissue under different fixation conditions. Leaves (5×) were fixed in 70% ethanol for 10, 30 or 60 min, left to dry for 2 h and wrapped in aluminium foil. A further 5× leaves were not fixed and instead stored in zip-lock bags containing damp cotton wool. Spectra were acquired from fixed leaves ≈24 h after collection. Spectra were acquired from damp leaves on the day of collection, and ≈24 h after collection. Spectra (3×) were acquired per leaf. The damp condition had no significant effect on LD1 after 24 h, but ethanol at all three immersion times had a highly significant effect on LD1 as determined by one-way ANOVA ($P < 0.001$). **(B)** Cluster vectors plot by PCA-LDA indicating wavenumber basis for segregation after fixation of *A. pseudoplatanus* leaf tissue with 70% ethanol, plus non-fixed leaves, 24 h after collection. Each class is compared with non-fixed leaves on the day of collection. The magnitude of the cluster vector peak or trough is proportional to the extent of biochemical alteration compared to non-fixed leaves on the day of collection.

Table S1 Average Fv/Fm readings taken from the leaves of mature *A. pseudoplatanus* trees at the three main field sites. Student's T-tests revealed no significant difference between polluted sites and Reference.

Site	Average Fv/Fm	Number of readings	Significance (vs. ref. site)
Site 1	0.81	20	
Site 2	0.82	25	N/S
Site 3	0.81	18	N/S

(N/S) No significance ($p > 0.05$)

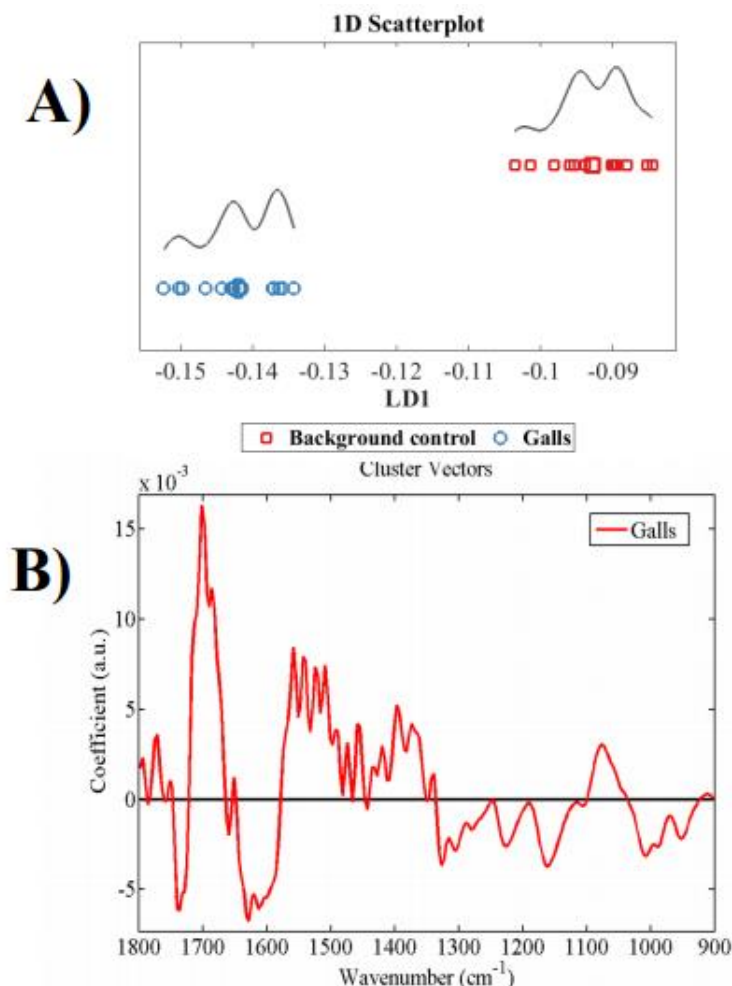


Figure S2 (A) One-D PCA-LDA scores plot of spectra derived from *A. pseudoplatanus* leaf tissue afflicted by galls of the mite *Artacris macrorhynchus*, compared to the background control leaf tissue (displaying no obvious affliction). Segregation in LD1 space was highly significant ($P < 0.001$) as determined by Student's T-test. (B) Cluster vectors plot by PCA-LDA indicating wavenumber basis for segregation in *A. pseudoplatanus* leaf tissue afflicted by galls, compared with the background control leaf tissue (origin).

Table S2 Top six discriminating wavenumbers (in descending order) identified by cluster vectors, associated with differences in *A. pseudoplatanus* leaves afflicted by leaf galls of the mite *Artacris macrorhynchus*, in relation to background control leaves. Tentative chemical assignments from Movasagh *et al* (2008), Schulz and Baranska (2006), and Stuart (2004).

Wavenumber (cm^{-1})	Tentative assignment(s)	Response (relative B.C.)
1701	Lipid; fatty acid esters	Increase
1585	Amide I	Decline
1520	Amide II	Increase
1632	Amide I; Pectin	Decline
1458	Protein; $\delta_{\text{as}}\text{CH}_3$	Increase
1169	Carbohydrate	Decline



Gold nanoparticles as a substrate in bio-analytical near-infrared surface-enhanced Raman spectroscopy†

Holly J. Butler,^a Simon W. Fogarty,^{a,b} Jemma G. Kerns,^c Pierre L. Martin-Hirsch,^a Nigel J. Fullwood*^b and Francis L. Martin*^a

As biospectroscopy techniques continue to be developed for screening or diagnosis within a point-of-care setting, an important development for this field will be high-throughput optimization. For many of these techniques, it is therefore necessary to adapt and develop parameters to generate a robust yet simple approach delivering high-quality spectra from biological samples. Specifically, this is important for surface-enhanced Raman spectroscopy (SERS) wherein there are multiple variables that can be optimised to achieve an enhancement of the Raman signal from a sample. One hypothesis is that "large" diameter (>100 nm) gold nanoparticles provide a greater enhancement at near-infrared (NIR) and infrared (IR) wavelengths than those <100 nm in diameter. Herein, we examine this notion using examples in which SERS spectra were acquired from MCF-7 breast cancer cells incubated with 150 nm gold nanoparticles. It was found that 150 nm gold nanoparticles are an excellent material for NIR/IR SERS. Larger gold nanoparticles may better satisfy the theoretical restraints for SERS enhancement at NIR/IR wavelengths compared to smaller nanoparticles. Also, larger nanoparticles or their aggregates are more readily observed *via* optical microscopy (and especially electron microscopy) compared to smaller ones. This allows rapid and straightforward identification of target areas containing a high concentration of nanoparticles and facilitating SERS spectral acquisition. To some extent, these observations appear to extend to biofluids such as blood plasma or (especially) serum; SERS spectra of such biological samples often exhibit a low signal-to-noise ratio in the absence of nanoparticles. With protein-rich biofluids such as serum, a dramatic SERS effect can be observed; although this might facilitate improved spectral biomarker identification in the future, it may not always improve classification between control vs. cancer. Thus, use of "large" gold nanoparticles are a good starting point in order to derive informative NIR/IR SERS analysis of biological samples.

Introduction

Biospectroscopy techniques are gaining more widespread usage in the bio-analytical field due to their ability to interrogate samples across a wide range of biomolecules, providing detailed and specific (sub-)cellular information. The specific vibrational nature of chemical bonds facilitates the acquisition of spectra in the "biochemical fingerprint" region. Near-infrared (NIR) and infrared (IR) spectroscopies are beneficial for

bioanalysis as biological molecules absorb radiation in these regions, unlike many non-biological samples.

Raman spectroscopy is a technique which has been employed extensively in the analysis of a variety of different biological samples,¹ including different tissue types,² individual cells,³ isolated cell components⁴ and biofluids.⁵ A key advantage of Raman over other IR spectroscopy techniques, such as Fourier-transform IR (FTIR), is the lack of interference from water. An absence of water interference is particularly advantageous for live-cell studies⁶ and for use *in vivo*.¹ Raman spectroscopy measures inelastic scattering caused by energy transfer between incident excitation photons and chemical bonds in a sample, which result in a change in the vibrational mode of the chemical bond and the energy, and thus the wavelength, of the scattered photon. This shift in wavelength is specific to particular molecular bonds, and readily interpreted from the output Raman spectrum.

^aCentre for Biophotonics, Lancaster Environment Centre, Lancaster University, Bailrigg, Lancaster LA1 4YQ, UK. E-mail: f.martin@lancaster.ac.uk;
Tel: +44 (0)1524 510206

^bDivision of Biomedical and Life Sciences, Faculty of Health and Medicine, Lancaster University, UK. E-mail: n.fullwood@lancaster.ac.uk; Tel: +44 (0)1524 593474

^cLancaster Medical School, Faculty of Health and Medicine, Lancaster University, UK
† Electronic supplementary information (ESI) available. See DOI: 10.1039/c4an01899k

However, there are significant limitations in the current usage of Raman scattering for biological purposes. It is much weaker than other scattering techniques, such as Rayleigh scattering or fluorescence, and thus biological samples which are typically weak Raman scatterers, may not give rise to an information-rich spectrum. The influence of fluorescence on Raman spectra is also problematic and can confound the biochemical signature; this influence can be reduced by using lasers at IR wavelengths. Additionally, cellular material is typically quite fragile and thus samples can be easily damaged by higher laser energies, introducing spectral artefacts into obtained data.

In order to overcome the limitations of conventional Raman scattering, it is possible to use surface-enhanced Raman spectroscopy (SERS). This is a phenomenon whereby the Raman signal of a target sample is greatly enhanced when placed into close proximity to a metal nanostructure.^{7,8} The nanoscale roughness necessary for SERS is present in many different types of metal nanostructures, including roughened electrodes, metal films and nanoparticles. In recent years, with the wide-scale production of metal nanoparticles, more novel forms of nanostructures have been identified as capable of generating a SERS effect. Nanostructure design for SERS experiments is important as the enhancement varies. The level of enhancement has been shown to reach up to 10^{14} times allowing the potential of SERS in single molecule detection.⁹⁻¹²

Nanoparticles potentially have a myriad of uses for SERS being able to specifically label sub-cellular regions both on the cell surface and within the intracellular environment.¹³ The dimensions of nanoparticles allow high localization of the SERS enhancement effect, permitting interrogation of a sample at the specific sub-cellular regions labelled.¹⁴ However, the degree of enhancement is dependent upon the physical parameters of the nanoparticles used and how they interact with the chosen excitation wavelength. Therefore, not all nanoparticle types will facilitate a large enhancement effect from the NIR or IR excitation wavelengths commonly used in bioanalysis. This means that optimization of the nanoparticle structure is required to gain sufficient enhancement from samples at these specific wavelengths. There are many influential factors including size, shape and composition that need to be considered for optimization of nanoparticle structure for different experimental Raman parameters;^{15,16} these have been elegantly represented previously.^{17,18}

Optimal experimental parameters are dependent upon the sample, such as tissue type, individual cells or isolated cell components, *e.g.*, nuclei. Additionally, a particular analytical target, such as a specific protein target, may require specific labelling of metal nanoparticles to the target location, such as antibody binding.¹⁹ However, there are many samples with unknown targets for which the above labelling parameters are not relevant, *e.g.*, biofluids such as blood samples. Non-specific labelling of metal nanoparticles has been demonstrated using cationic gold labeling.²⁰ Therefore, it is possible to use nanoparticles without any type of targeting molecules and to rely upon spontaneous associations of nanoparticles to biomolecules within/on the sample.

Many studies have used gold and silver nanoparticles that are 10 to 100 nm in diameter for SERS; however, theoretically these small gold and silver nanoparticles may not be optimal for use for NIR/IR SERS as their resonance wavelengths are within the visible or ultraviolet regions.²¹ It is important to consider that different metals have distinct responses under NIR/IR excitation. Gold and silver are good nanoparticle materials because they are unreactive and stable in solution compared to other metal nanoparticle types. Furthermore, they are easy to acquire, either commercially or through chemical preparation.^{22,23} There is a need to expand on SERS theory in order to find optimized metal nanostructures as SERS substrates for these excitation wavelengths. It is important to note that small nanoparticles have been shown experimentally to provide surface enhancement at IR wavelengths.²⁴

An increase in the diameter of gold or silver nanostructures leads to a red shift in the resonance excitation wavelength, therefore moving the resonance wavelength towards the NIR/IR region.²¹ By increasing the size of the nanoparticles beyond the electrostatic approximation (typically a diameter >100 nm), more parameters become relevant, changing how the nanoparticle reacts with the incident excitation light.²⁵⁻²⁷ This has led to the theory that increasing the diameter of the metal nanoparticles used may be preferential for biological NIR SERS, thus increasing its potential as a novel diagnostic tool.

Routine point-of-care bioanalysis requires a simple but robust sample preparation procedure. In this study, we examine whether SERS using 150 nm *vs.* 40 nm gold nanoparticles could be applied robustly yet simply for bioanalysis. To this end, we examine if large gold nanoparticles (150 nm in diameter) give a strong SERS signal from MCF-7 cell samples. Secondly, we investigate the potential of non-specific labelling of nanoparticles (not attached to any targeting ligands) for the development of a strong SERS signal in samples without known or relevant targets for labelling, *e.g.*, biofluids. Such a protocol would be applicable for routine cancer screening or diagnostics.

Experimental approach

Gold nanoparticles

Gold nanoparticles [150 (designated "large") and 40 nm (designated "small")] were obtained from British Biocell International (UK) at a stock concentration containing 2.9×10^{-4} moles of gold per litre.

MCF-7 cell analysis

MCF-7 cells were cultured in Dulbecco's Modified Eagle Medium (DMEM) (Lonza) with added foetal bovine serum (FBS) (Lonza) and penicillin/streptomycin mixture (10%). Cells were seeded in T25 flasks and cultured at 37 °C in 5% CO₂ for 24 h. Once confluent, cells were disaggregated from each flask using trypsinisation. They were then fixed with 70% ethanol and 400 μ l cell aliquots were placed on MIRR IR Low-E slides (Kevley Technologies, USA) and allowed to air-dry overnight.

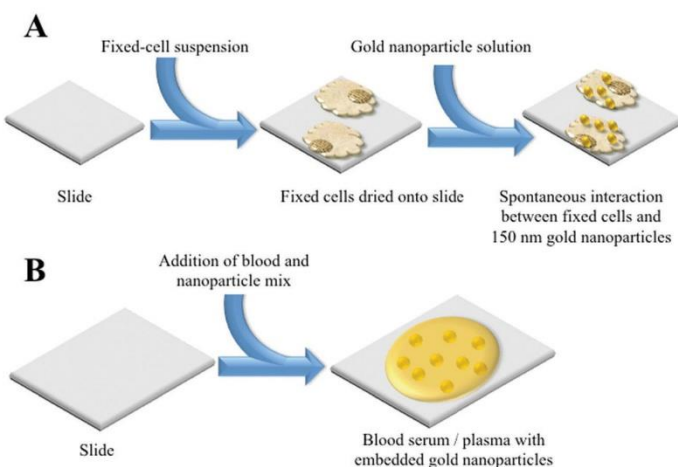


Fig. 1 Schematic detailing the NIR SERS of sample preparations; (A) cellular sample, and, (B) biofluid sample.

Nanoparticle solution (400 μ l of 150 nm) was then applied to the dried cells and slides were again left to air-dry, before being placed in a desiccator (Fig. 1A).

Raman spectra were acquired using an InVia Raman microscope (Renishaw plc, Gloucestershire, UK) equipped with a 100 mW 785 nm excitation laser, which was calibrated to 520.5 cm^{-1} using a silicon calibration source. Spectral maps of MCF-7 cells were acquired in a step-wise manner from the target area at 1 μm step sizes (Fig. 2). Spectra were acquired at 0.1% laser power at 50 \times magnification for 1 second and 1 accumulation. Analysis of an MCF-7 cell clump was acquired using StreamLineTM Raman analysis (Fig. 3) with an InVia Raman microscope equipped with a 150 mW 785 nm excitation laser, an exposure time of 10 seconds and 1 accumulation. Laser powers of 0.05% (0.075 mW) and 0.1% (0.15 mW) at source were used.

Post-SERS analysis, slides on which cells were deposited were processed for scanning electron microscopy (SEM) (Fig. 4). This involved mounting the slides onto aluminium stubs and gold-coating in a 150A Edwards sputter coater before examination at 15 KV in a JEOL 5600 digital scanning electron microscope.

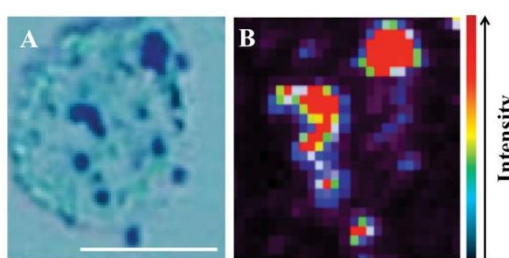


Fig. 2 Fixed MCF-7 cells on MIRR IR Low-E glass slides with 150 nm gold nanoparticles subsequently added. A light micrograph image in (A) shows labelling of MCF-7 cell with 150 nm nanoparticles (dark regions), which co-localize with areas of high Raman signal intensity in (B) (red areas). Scale bar = 10 μm .

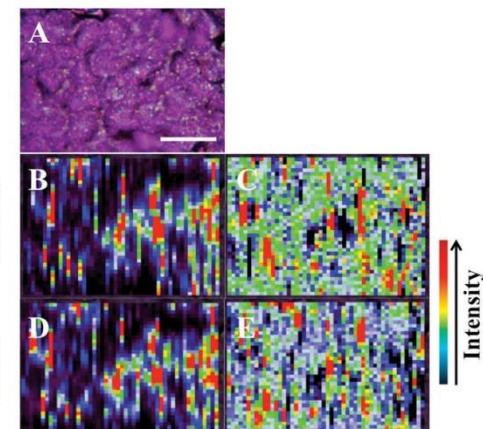


Fig. 3 The presence of large nanoparticles allows analysis of large target areas rapidly using StreamLineTM Raman. A large cell clump seen by light microscopy (A) was analysed to quickly give false colour image maps; (B + D) = intensity at 1295 cm^{-1} (CH_2 deformations); and, (C + E) = signal to baseline at 1194–1228 cm^{-1} (Amide III).³⁵ Areas of high intensity (red) appear to correspond to areas of high nanoparticle localisation. Also, by increasing laser power, regions of relevant high SERS expression become easier to determine (B + C = 0.05% laser power; D + E = 0.1% laser power). Scale bar = 20 μm .

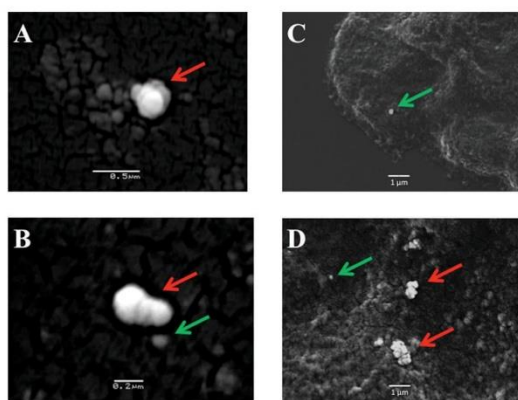


Fig. 4 Scanning electron micrographs of the gold nanoparticles on the surface of the MCF-7 cells. (A) Shows an aggregated clump of 40 nm nanoparticles (red arrow); (B) shows an aggregated clump of 40 nm nanoparticles (red arrow) with a single 40 nm nanoparticle adjacent to it (green arrow); (C) shows a single 150 nm nanoparticle on the cell surface (green arrow); and, (D) shows at least two aggregated clumps of nanoparticles (red arrows) as well as a single isolated 150 nm nanoparticle (green arrow).

Blood plasma and serum analysis

Samples were obtained from the Genitourinary Tissue Biobank at Lancashire Teaching Hospitals NHS Foundation Trust

(Preston, UK) with ethical approval [Research and Ethics Committee (REC) approval no.: 10/H0308/75]. From age-matched cohorts of patients ($n = 5$ endometrial cancer, $n = 5$ non-cancer control), plasma and serum samples were taken from storage at -80°C and thawed in a water bath at 37°C for approximately 1 h. In order to compare the enhancement effect of nanoparticles at two distinct sizes, 200 μl aliquots of blood plasma or serum were mixed with 200 μl of stock 150 nm or 40 nm gold nanoparticle solution (Fig. 1B). The resultant mixture (total volume 400 μl) was applied to MIRR IR Low-E slides and left to air-dry. Control slides without nanoparticles were also prepared using 200 μl of blood plasma or serum sample and allowed to air-dry. Blood SERS spectra were taken at 10% laser power (2.4 mW at sample) at 50 \times magnification across the 500–2000 cm^{-1} spectral range for 10 seconds and 1 accumulation; a minimum of 25 spectra per sample slide were acquired. These air-dried samples could be examined under optical brightfield microscopy to demonstrate the presence or absence of nanoparticles (Fig. 5A). For transmission electron microscopy (TEM), gold nanoparticles (40 or 150 nm) were mixed 50 : 50 with blood serum and then 10 μl were pipetted onto carbon-/formvar-coated electron microscope grids (Agar Scientific, UK), blotted and allowed to dry before examination with a 10–10 JEOL TEM.

Computational analysis was performed using MATLAB (Mathworks, Natick, USA) with an in-house developed toolkit (<https://code.google.com/p/irootlab/>), unless stated otherwise.²⁸ The resultant Raman spectra were cut to 450–1700 cm^{-1} wave-

Open Access Article. Published on 17 March 2015. Downloaded on 18/08/2015 15:15:35.
This article is licensed under a Creative Commons Attribution 3.0 Unported Licence.

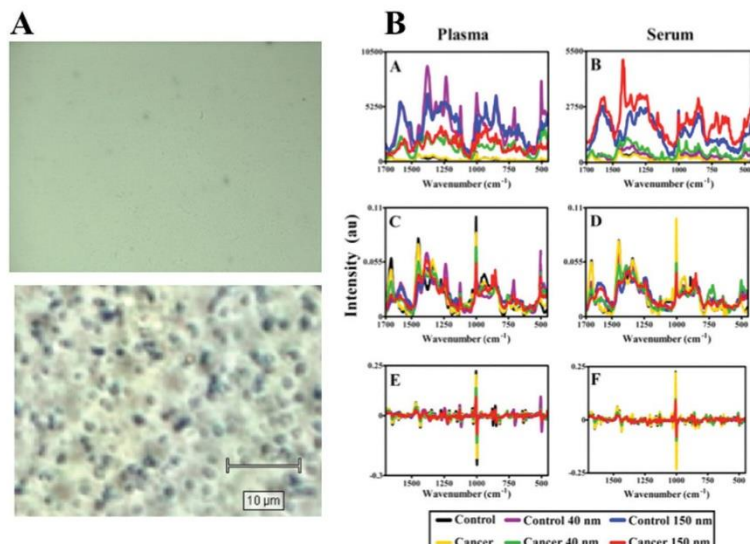


Fig. 5 Influence of nanoparticles on SERS effect in blood plasma or serum samples. (A) Optical brightfield microscopy images of blood plasma samples with or without large (150 nm) gold nanoparticles. (B) Raman spectra (class means) of blood plasma (A, C, E) or serum samples (B, D, F) with or without gold nanoparticles following polynomial baseline correction to show raw enhancement (A, B), polynomial baseline correction followed by vector normalisation (C, D) and 1st order differentiation followed by vector normalisation (E, F).

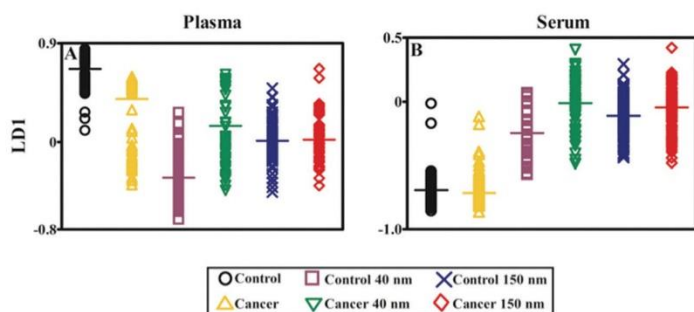


Fig. 6 Classification of control vs. cancer Raman spectra following principal component analysis-linear discriminant analysis (PCA-LDA). Following 1st order differentiation followed by vector normalisation, each spectrum is reduced to a single point in a PCA-LDA scores plot. For each class, the horizontal line represents the class mean.

Table 1 Classification (control vs. cancer) of blood plasma or serum samples with or without SERS^a

Class comparison	P-value	Significant
Plasma		
Control vs. cancer	<0.001	Yes
Control vs. cancer (40 nm)	<0.001	Yes
Control vs. cancer (150 nm)	>0.05	No
Serum		
Control vs. cancer	>0.05	No
Control vs. cancer (40 nm)	<0.001	Yes
Control vs. cancer (150 nm)	>0.05	No

^a Following acquisition of Raman spectra, one-way analysis of variance (ANOVA) with Bonferroni *post-hoc* tests were conducted on class means per sample to determine *P*-values for separation between cancer vs. non-cancer.

numbers inclusive of spectral peaks present in the sample and wavelet de-noised. In order to display raw spectral enhancement, spectra were polynomial baseline corrected maintaining Raman intensity units (counts) (Fig. 5B-A, and B-B). For computational analysis, spectra were pre-processed using 1st order differentiation followed by vector normalisation. Cross-validated principal component analysis (PCA) with optimised principal components (PC) factors followed by linear discriminant analysis (LDA) was conducted in order to discriminate between cancer vs. non-cancer patients (Fig. 6). Graphs were generated in GraphPad Prism 4.0 software (GraphPad Software Inc, CA, USA) and one-way analysis of variance (ANOVA) with Bonferroni *post-hoc* tests was conducted to determine *P*-values for separation between cancer vs. non-cancer (Table 1).

Results and discussion

The potential for 150 nm gold nanoparticles to generate good SERS enhancement is demonstrated; these larger nanoparticles allow for ready visualisation using optical microscopy (Fig. 2A). Fig. 2 shows an isolated MCF-7 cell labelled with

150 nm nanoparticles, which clearly demonstrates that regions of high Raman signal co-localize with the presence of the nanoparticles. Also, in Fig. 2B the signal appears to be highly localized to the regions surrounding the nanoparticles rather than being spread across the whole of the cell surface, supporting theoretical explanations of the SERS effect. As the cells were fixed prior to nanoparticles being added, one would expect that they would be adhered to the outer cell surface rather than having penetrated into the intracellular environment; therefore, the enhancement will be predominantly from the cell membrane nearest the nanoparticles. Post-SERS analysis using SEM (Fig. 4) shows that this is clearly the case. The nanoparticles adhere to the surface either as single entities or in aggregates. Compared to the smaller (40 nm) nanoparticles (Fig. 4A and B), the larger (150 nm) nanoparticles are much more readily detectable.

In Fig. 3, the application of rapid Raman scanning is tested on similar MCF-7 cell samples to those analysed in Fig. 2. Here, due to the capability of the StreamLine™ system to rapidly scan across a sample, a large clump of cells with 150 nm nanoparticle coverage was chosen for analysis. In the light microscope image of the sample (Fig. 3A), aggregates of nanoparticles this time appear as white spots across the cell surfaces. In false-colour image maps (Fig. 3B and D), areas of high nanoparticle expression show enhancement of the Raman signal. Also, Fig. 3C and E show that the enhancement is not just an increase in background signal but that relevant biological Raman signatures are present, calculated from the high signal-to-baseline intensity. These images show that, even despite the limiting factors of very rapid acquisition time and low laser power, enhanced biological spectra can be generated from large samples quickly using "large" nanoparticles. This allows for the potential of rapid SERS analysis of large tissue sections for diagnostics. Tissue sections parallel to conventional H&E staining may be mapped using SERS to facilitate high-throughput diagnosis.

The target area was analysed at two different laser powers, 0.05% (0.075 mW) and 0.1% (0.15 mW) in order to assess the sample with different laser exposures. It is more desirable to

have very low laser powers to demonstrate the effectiveness of the SERS enhancement process. Previous studies have used similar laser powers to generate large signal enhancements from SERS samples.^{19,20} As the laser power is increased, it appears that areas of SERS expression became more evident with greater spatial resolution, and can still be clearly defined from those without SERS enhancement. Another advantage of large nanoparticles is that they can be observed optically (Fig. 2A, 3A and 5A), where they appear as black or white dots. The ability to see small aggregates of nanoparticles or individual nanoparticles allows areas where they are abundant to be manually targeted for analysis. This leads to highly enhanced spectra being acquired more easily from a sample.

Fig. 5B shows the analysis of blood plasma or serum samples with or without SERS in order to investigate its potential to differentiate between control vs. endometrial cancer samples. The search for blood-based cancer biomarkers is a very important area for bioanalysis and a novel use for biospectroscopy. Previous studies have investigated the possibility of biospectroscopy as a blood-based diagnostic tool.^{29–31} Fig. 5B-A and B-B show that either 40 nm or 150 nm nanoparticles generate a SERS effect, with the larger nanoparticles giving rise to the more pronounced enhancement in the protein-rich serum biofluid. Marked variation in the level of SERS effect even in the biofluids tested was noted (see ESI Fig. S1–S3†). As one would expect, when these spectra are normalised the SERS effect is less apparent (Fig. 5B-C and B-D); however, surprisingly many of the main peak intensities are higher in control compared to cancer. The ready observation of a SERS effect in such biofluids lends promise towards deriving and identifying novel spectrochemical biomarkers. However, the immediate objective of biospectroscopy is likely to be towards classification and diagnosis/screening of disease. To facilitate this, the Raman spectra were pre-processed using 1st order differentiation followed by vector normalization prior to classification using PCA-LDA. Interestingly here, the use of smaller nanoparticles appears to give the best classification in both blood plasma and serum whereas the application of larger nanoparticles resulted in no between-class significance (Fig. 6). One explanation could be that aggregation of nanoparticles, even smaller ones, in a biofluid may be sufficient to give rise to an optimal SERS effect. Following TEM of 150 nm nanoparticles post-mixing with serum, it is noted that they form clusters, dimers and singlets (Fig. 7A). In this instance, the 150 nm nanoparticles in the clusters are in contact with each other and there is some variation in their shape; one is clearly pentagonal rather than spherical. In the case of 40 nm nanoparticles after mixing with serum, it is also observed that they form clusters with what are probably protein clumps (Fig. 7B). There are instances of the nanoparticles being in small groups of two to four, which are in contact. After mixing with serum, TEM shows 150 nm nanoparticles associated with what are probably serum proteins (Fig. 7B). Likewise, TEM shows 40 nm nanoparticles after mixing with serum; again, they appear to be associated with what are probably proteins (Fig. 7D).

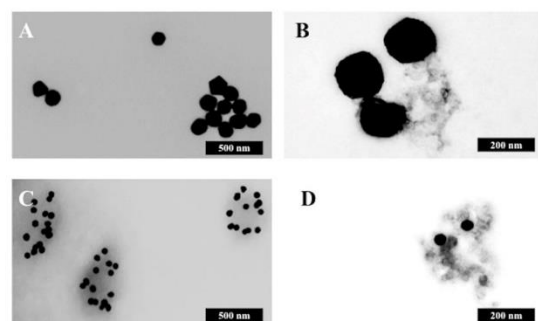


Fig. 7 Transmission electron micrographs of the gold nanoparticles following mixing with blood serum. (A) Shows 150 nm nanoparticles mixed with serum; (B) shows 40 nm nanoparticles mixed with serum; (C) shows 150 nm nanoparticles mixed with serum; and, (D) shows 40 nm mixed with serum. Scale bar = 500 nm (A + C) or 200 nm (B + D).

An important point to make for the use of nanoparticles for larger studies, such as those for diagnostic development of NIR-SERS, is that the preparation process can be made incredibly rapid. Coupled with the rapid acquisition of SERS spectra, it is possible to quickly analyse multiple samples to potentially high sensitivity rates. The preparation is simple, allowing it to be utilized without specialized expertise. Whilst nanoparticles are suitable substrates, they do have some limitations for biological NIR-SERS. They are not very amenable to live-cell imaging due to the difficulty of cells to endocytose large nanoparticles through simple incubation.³² Approaches such as electroporation may facilitate this but this may lead to artefacts affecting any resultant spectra, distorting their reflection of underlying cellular biochemical structure. Through investigating differing nanostructures,^{33,34} other sensitive NIR or IR SERS nanostructures can be elucidated for use in bioanalytical research.³⁵ Gold nanoparticles appear to be an optimal substrate for use in NIR or IR SERS. Ready enhancement of Raman spectra coupled with the rapid sample preparation and analysis increase the utility of large nanoparticles for biological NIR-SERS. This methodology greatly enhances the applicability of SERS as a high-throughput technology for disease diagnosis.

Acknowledgements

SWF was supported by a BBSRC doctoral training grant (BB/F017111/1). FLM is supported by Rosemere Cancer Foundation. We thank Renishaw PLC (UK) for access to their equipment.

References

- 1 E. B. Hanlon, R. Manoharan, T.-W. Koo, K. E. Shafer, J. T. Motz, M. Fitzmaurice, J. R. Kramer, I. Itzkan,

R. R. Dasari and M. S. Feld, Prospects for in vivo Raman spectroscopy, *Phys. Med. Biol.*, 2000, **45**(1), R1–59.

2 A. S. Haka, K. E. Shafer-Peltier, M. Fitzmaurice, J. Crowe, R. R. Dasari and M. S. Feld, Diagnosing breast cancer by using Raman spectroscopy, *Proc. Natl. Acad. Sci. U. S. A.*, 2005, **102**(35), 12371–12376.

3 I. Notinger, S. Verrier, H. Romanska, A. E. Bishop, J. M. Polak and L. L. Hench, In situ characterisation of living cells by Raman spectroscopy, *Spectroscopy*, 2002, **16**(2), 43–51.

4 K. W. Short, S. Carpenter, F. P. Freyer and J. R. Mourant, Raman spectroscopy detects biochemical changes due to proliferation in mammalian cell cultures, *Biophys. J.*, 2005, **88**(6), 4274–4288.

5 A. M. K. Enejder, T.-W. Koo, J. Oh, M. Hunter, S. Sasic and M. S. Feld, Blood analysis by Raman spectroscopy, *Opt. Lett.*, 2002, **27**(22), 2004–2006.

6 A. F. Palonpon, M. Sodeoka and K. Fujita, Molecular imaging of live cells by Raman microscopy, *Curr. Opin. Chem. Biol.*, 2013, **17**(4), 708–715.

7 M. Moskovits, Surface-enhanced Raman spectroscopy: a brief retrospective, *J. Raman Spectrosc.*, 2005, **36**(6–7), 485–496.

8 Z. Q. Tian, Surface-enhanced Raman spectroscopy: advancements and applications, *J. Raman Spectrosc.*, 2005, **36**(6–7), 466–470.

9 K. Kneipp, Y. Wang, H. Kneipp, L. T. Perelman, I. Itzkan, R. R. Dasari and M. S. Feld, Single molecule detection using surface-enhanced Raman scattering (SERS), *Phys. Rev. Lett.*, 1997, **78**(9), 1667–1670.

10 K. Kneipp and H. Kneipp, Single molecule Raman scattering, *Appl. Spectrosc.*, 2006, **60**(12), 322A–334A.

11 B. Vlckova, I. Pavel, M. Sladkova, K. Siskova and M. Slouf, Single molecule SERS: perspectives of analytical applications, *J. Mol. Struct.*, 2007, **834–836**, 42–47.

12 Y. Wang and J. Irudayaraj, Surface-enhanced Raman spectroscopy at single-molecule scale and its implications in biology, *Philos. Trans. R. Soc., B*, 2013, **368**(1161), 20120026.

13 D. Graham and R. Goodacre, Chemical and bioanalytical applications of surface enhanced Raman scattering spectroscopy, *Chem. Soc. Rev.*, 2008, **37**(5), 883–884.

14 K. Kneipp, H. Kneipp, I. Itzkan, R. R. Dasari and M. S. Feld, Surface-enhanced Raman scattering and biophysics, *J. Phys.: Condens. Matter*, 2002, **14**(18), R597–R624.

15 F. Tian, F. Bonnier, A. Casey, A. E. Shanahan and H. J. Byrne, Surface enhanced Raman scattering with gold nanoparticles: effect of particle shape, *Anal. Methods*, 2014, **6**(22), 9116–9123.

16 R. N. Cassar, D. Graham, I. Larmour, A. W. Wark and K. Faulds, Synthesis of size tunable monodispersed silver nanoparticles and the effect of size on SERS enhancement, *Vib. Spectrosc.*, 2014, **71**, 41–46.

17 I. A. Larmour and D. Graham, Surface enhanced optical spectroscopies for bioanalysis, *Analyst*, 2011, **136**(19), 3831–3853.

18 L. Y. T. Chou, K. Ming and W. C. W. Chan, Strategies for the intracellular delivery of nanoparticles, *Chem. Soc. Rev.*, 2011, **40**(1), 233–245.

19 M. D. Hodges, J. G. Kelly, A. J. Bentley, S. Fogarty, I. I. Patel, F. L. Martin and N. J. Fullwood, Combining immunolabeling and surface enhanced Raman spectroscopy on cell membranes, *ACS Nano*, 2011, **5**(12), 9535–9541.

20 S. W. Fogarty, I. I. Patel, F. L. Martin and N. J. Fullwood, Surface-enhanced Raman spectroscopy of the plasma membrane using cationic gold nanoparticles, *PLoS One*, 2014, **9**(9), e106283.

21 C. Sönnichsen, T. Franzl, T. Wilk, G. von Plessen and J. Feldmann, Plasmon resonances in large noble-metal clusters, *New J. Phys.*, 2002, **4**, 93.1–93.8.

22 Y. Sun and Y. Xia, Shape-controlled synthesis of gold and silver nanoparticles, *Science*, 2002, **298**(5601), 2176–2179.

23 P. Alexandridis, Gold nanoparticle synthesis, morphology control and stabilization facilitated by functional polymers, *Chem. Eng. Technol.*, 2011, **34**(1), 15–28.

24 V. Joseph, A. Matschulat, J. Polte, S. Rolf, F. Emmerling and J. Kneipp, SERS enhancement of gold nanospheres of defined size, *J. Raman Spectrosc.*, 2011, **42**(9), 1736–1742.

25 H. Kuwata, H. Tamaru, K. Esumi and K. Miyano, Resonant light scattering from metal nanoparticles: practical analysis beyond Rayleigh approximation, *Appl. Phys. Lett.*, 2003, **83**, 4625–4627.

26 S. A. Maier, *Plasmonics: fundamentals and applications*, Springer, 2007.

27 C. F. Bohren and D. R. Huffman, *Absorption and scattering of light by small particles*, John Wiley and Sons, 2008.

28 J. Trevisan, P. P. Angelov, A. D. Scott, P. L. Charmichael and F. L. Martin, IRootLab: a free and open-source MATLAB toolbox for vibrational biospectroscopy data analysis, *Bioinformatics*, 2013, **29**(8), 1095–1097.

29 K. Gajjar, J. Trevisan, G. Owens, P. J. Keating, N. J. Wood, H. F. Stringfellow, P. L. Martin-Hirsch and F. L. Martin, Fourier-transform infrared spectroscopy coupled with a classification machine for the analysis of blood plasma or serum: a novel diagnostic approach for ovarian cancer, *Analyst*, 2013, **138**(14), 3917–3926.

30 A. L. Mitchell, K. B. Gajjar, G. Theophilou, F. L. Martin and P. L. Martin-Hirsch, Vibrational spectroscopy of biofluids for disease screening or diagnosis: translation from the laboratory to a clinical setting, *J. Biophotonics*, 2014, **7**(3–4), 153–165.

31 G. L. Owens, K. Gajjar, J. Trevisan, S. W. Fogarty, S. E. Taylor, B. Da Gama-Rose, P. L. Martin-Hirsch and F. L. Martin, Vibrational biospectroscopy coupled with multivariate analysis extracts potentially diagnostic features in blood plasma/serum of ovarian cancer patients, *J. Biophotonics*, 2014, **7**(3–4), 200–209.



32 B. D. Chithran, A. A. Ghazani and W. C. W. Chan, Determining the size and shape dependence of gold nanoparticle uptake into mammalian cells, *Nano Lett.*, 2006, **6**(4), 662–668.

33 R. H. Lahr and P. J. Vikesland, Surface-enhanced Raman spectroscopy (SERS) cellular imaging of intracellularly biosynthesized gold nanoparticles, *ACS Sustainable Chem. Eng.*, 2014, **2**(7), 1599–1608.

34 L. Rodríguez-Lorenzo, Z. Krpetic, S. Barbosa, R. A. Alvarez-Puebla, L. M. Liz-Marzán, I. A. Prior and M. Brust, Intracellular mapping with SERS-encoded gold nanostars, *Integr. Biol.*, 2011, **3**(9), 922–926.

35 Z. Movasaghi, S. Rehman and I. U. Rehman, Raman spectroscopy of biological tissues, *Appl. Spectrosc. Rev.*, 2007, **42**(5), 493–541.

Open Access Article. Published on 17 March 2015. Downloaded on 18/08/2015 15:15:35.
This article is licensed under a Creative Commons Attribution 3.0 Unported Licence.


Electronic Supporting Information

Gold nanoparticles as a substrate in bio-analytical near-infrared surface-enhanced Raman scattering

Holly J. Butler¹, Simon W. Fogarty^{1,2}, Jemma G. Kerns³, Pierre L. Martin-Hirsch¹, Nigel J. Fullwood^{2,}, Francis L. Martin^{1,*}*

¹Centre for Biophotonics, Lancaster Environment Centre, Lancaster University, Bailrigg, Lancaster LA1 4YQ, UK; ²Division of Biomedical and Life Sciences, Faculty of Health and Medicine, Lancaster University, UK; ³Lancaster Medical School, Faculty of Health and Medicine, Lancaster University, UK

***Corresponding authors:** Dr Nigel J. Fullwood / Prof Francis L. Martin PhD;
Email: n.fullwood@lancaster.ac.uk / f.martin@lancaster.ac.uk; *Tel.:*
+44(0)1524 593474 / +44 (0)1524 510206

Summary

Number of Pages: 4

Number of Figures: 3

Number of Tables: 0

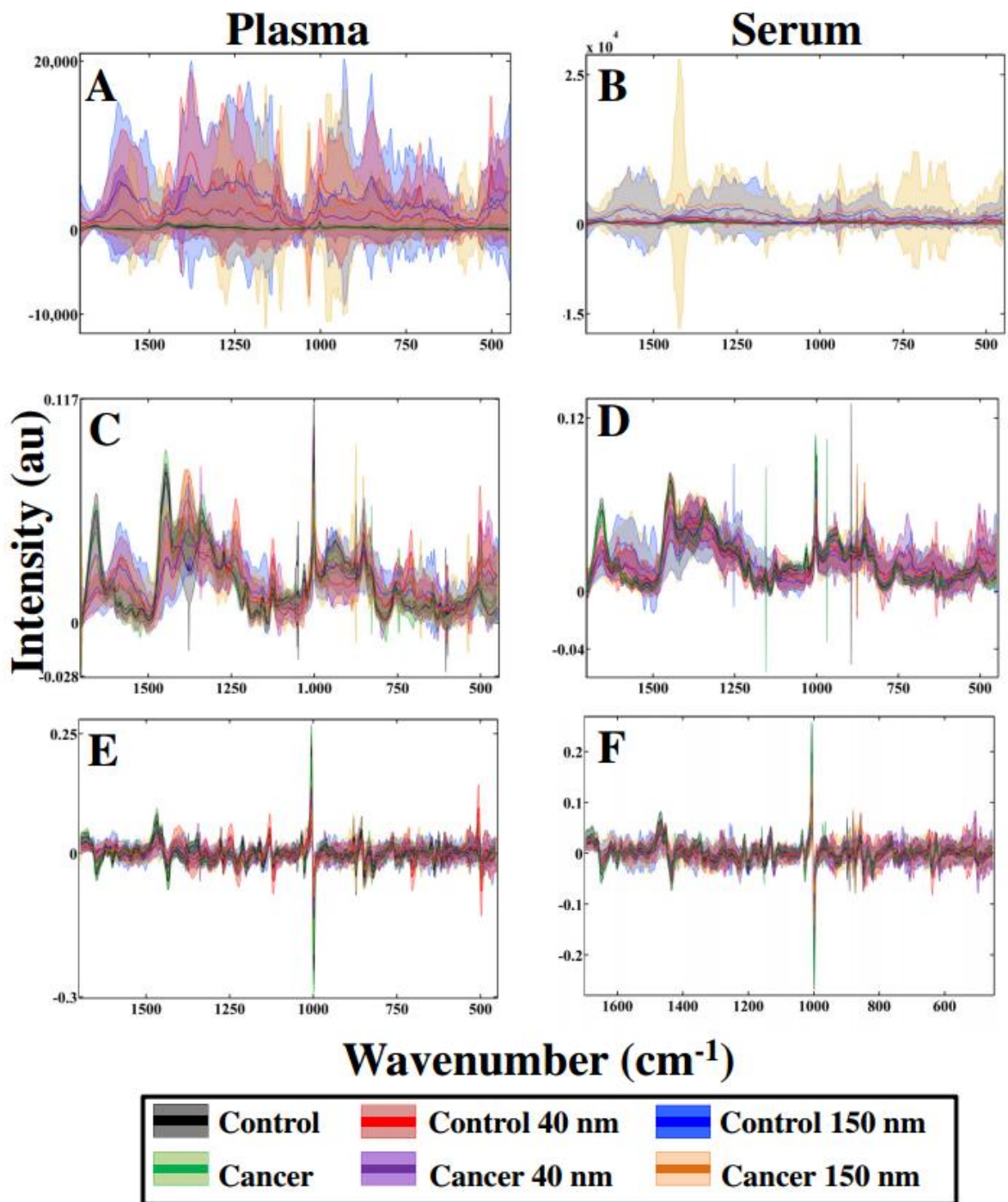
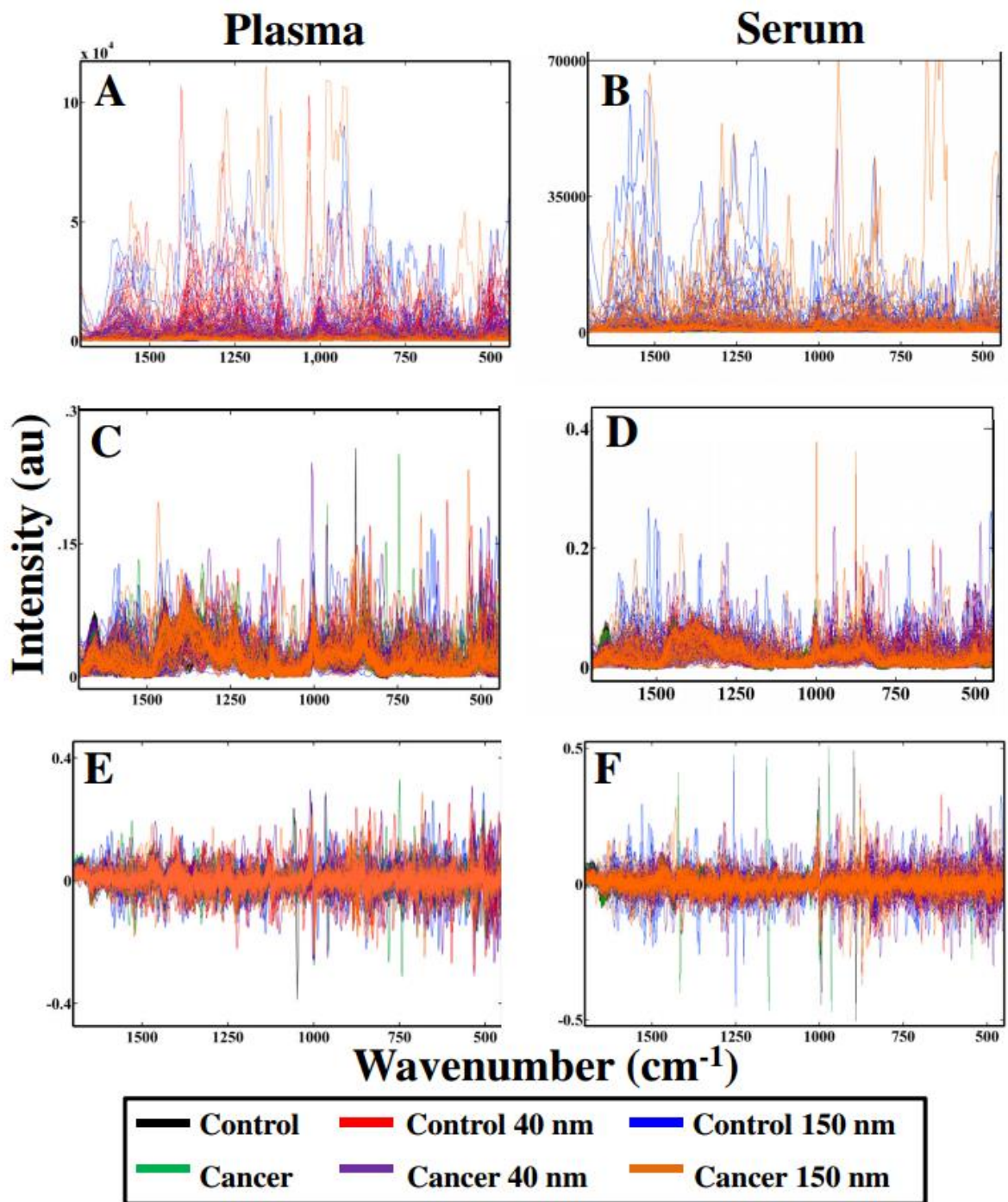


Figure S1. Influence of nanoparticles on SERS effect in blood plasma or serum samples. Raman spectra (class means with standard deviation) of blood plasma (A, C, E) or serum samples (B, D, F) with or without gold nanoparticles: following polynomial baseline correction to show raw enhancement (A, B), polynomial baseline correction followed by vector normalisation (C, D) or 1st order differentiation followed by vector normalisation (E, F).



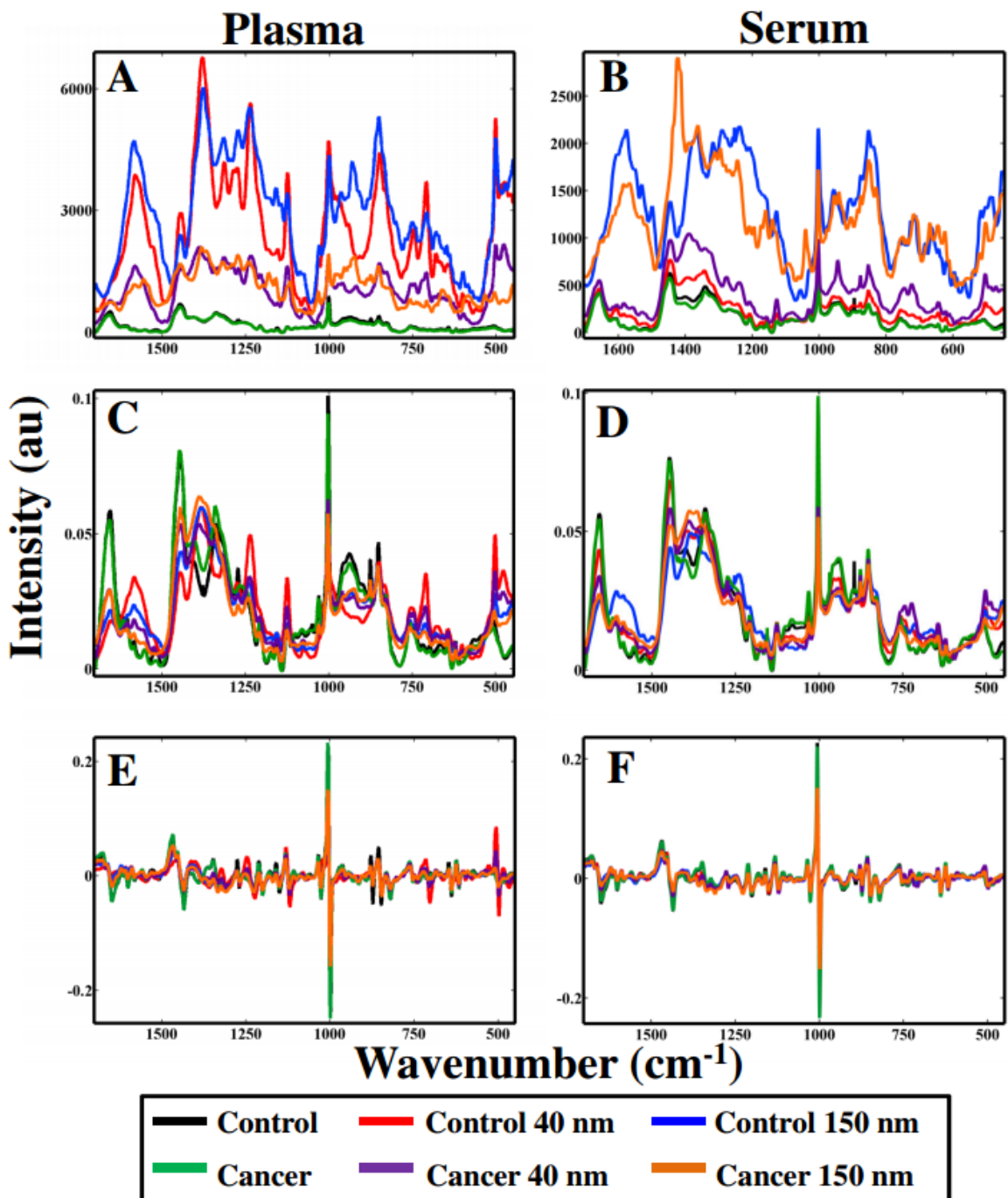
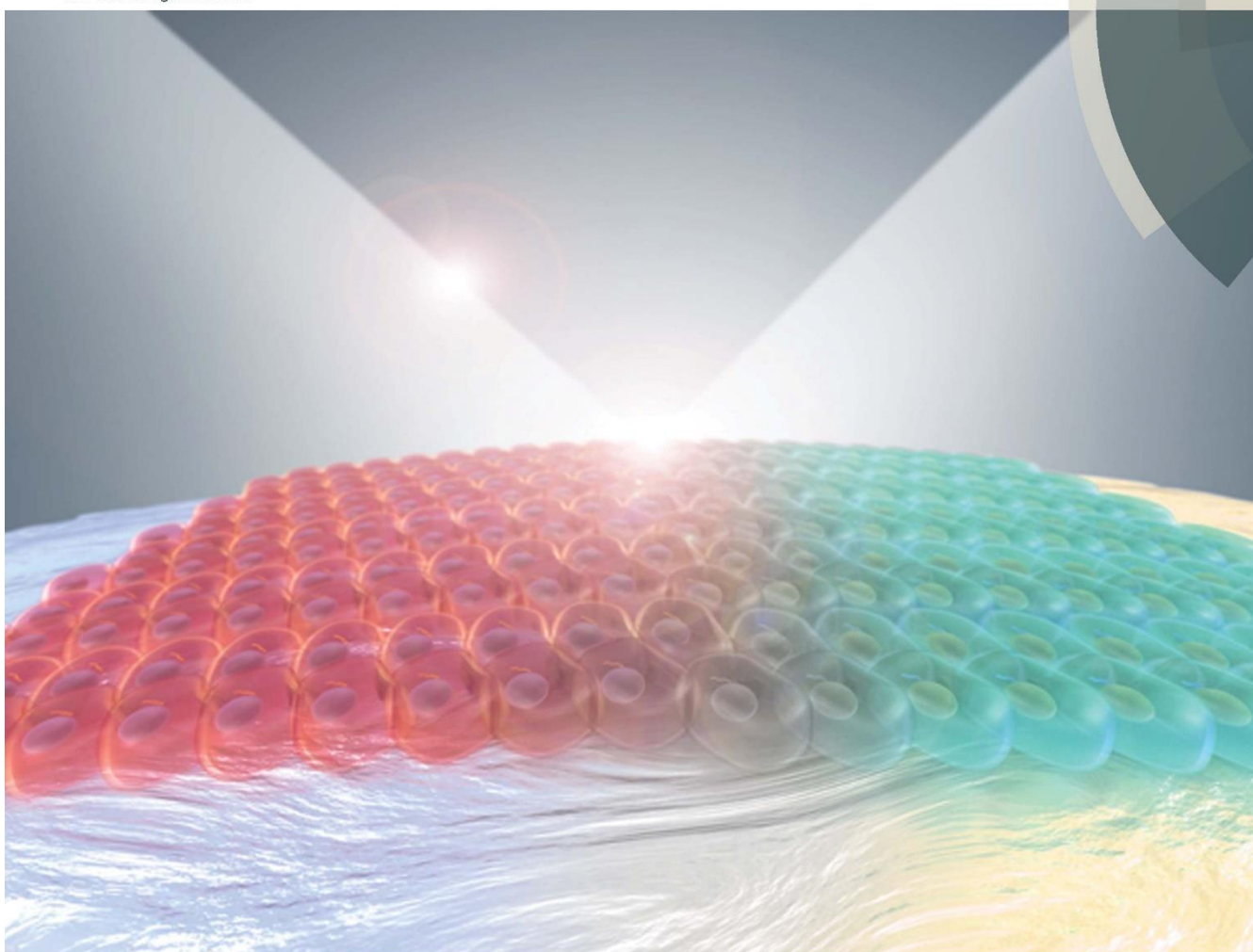


Figure S3. Influence of nanoparticles on SERS effect in blood plasma or serum samples. Class means spectra of all data acquired in this study, including non-enhanced spectra. Blood plasma (A, C, E) or serum samples (B, D, F) with or without gold nanoparticles: following polynomial baseline correction to show raw enhancement (A, B), polynomial baseline correction followed by vector normalisation (C, D) or 1st order differentiation followed by vector normalisation (E, F).

Analytical Methods

www.rsc.org/methods



ISSN 1759-9660



COMMUNICATION

Francis L. Martin, Matthew Briggs *et al.*
Aluminium foil as a potential substrate for ATR-FTIR, transfection FTIR or
Raman spectrochemical analysis of biological specimens

175 YEARS



Cite this: *Anal. Methods*, 2016, 8, 481

Received 4th October 2015
Accepted 30th October 2015

DOI: 10.1039/c5ay02638e

www.rsc.org/methods

Aluminium foil as a potential substrate for ATR-FTIR, transfection FTIR or Raman spectrochemical analysis of biological specimens

Li Cui,^{*ab} Holly J. Butler,^b Pierre L. Martin-Hirsch^b and Francis L. Martin^{*b}

The substantial cost of substrates is an enormous obstacle in the successful translation of biospectroscopy (IR or Raman) into routine clinical/laboratory practice (screening or diagnosis). As a cheap and versatile substrate, we compared the performance of readily available aluminium (Al) foil with low-E, Au-coated and glass slides for cytological and histological specimen analysis by attenuated total reflection Fourier-transform infrared (ATR-FTIR), transfection FTIR or Raman spectroscopy. The low and almost featureless background signal of Al foil enables the acquisition of IR or Raman spectra without substrate interference or sacrificing important fingerprint biochemical information of the specimen, even for very thin samples with thicknesses down to 2 μ m. Al foil is shown to perform as well as, if not better than, low-E or Au-coated slide, irrespective of its relatively rough surface. Although transmission FTIR is not possible on Al foil, this work demonstrates Al foil is an inexpensive, readily available and versatile substrate suitable for ATR-FTIR, transfection FTIR or Raman spectrochemical measurements of diverse biological specimens. The features of Al foil demonstrated here could promote a transition towards accessible substrates that can be readily implemented in either research or clinical settings.

Introduction

Vibrational spectroscopies including infrared (IR) or Raman have become highly regarded techniques for biological/biomedical applications through many proof-of-concept studies. Due to their fingerprinting capability, they could play a significant role in histopathology, cytology, targeting biopsies, determining surgical margins, treatment, monitoring and drug studies.^{1–12} However, successful translation and implementation of such techniques into routine clinical or laboratory practice has been slow, as recurrent costs of substrates represent a significant challenge.

Many proof-of-concept studies have been conducted under optimal experimental conditions, using spectral-optimized but costly substrates to minimize substrate interference and maximize signal.^{3,13} In transmission Fourier-transform IR (FTIR) measurements, IR transparent materials including CaF₂, BaF₂ and ZnSe slides are commonly used,^{14,15} but have the disadvantages that they are both expensive and fragile, and thus unsuitable for routine applications. Transfection FTIR and attenuated total reflection (ATR)-FTIR configurations using highly IR reflective low-E or Au (Ag)-coated slides may give a relatively low-cost alternative, but these still greatly exceed the current costs for glass slides alone.^{1,14,16,17} For Raman measurements, CaF₂ or Au (Al)-coated slide substrates without obvious background fluorescence and Raman signal are frequently used.^{1,7,18–20}

In the routine clinical/laboratory environment that requires a high throughput procedure for enormous numbers of specimens, such as cervical screening, standard glass microscope slides are used as a substrate. However, glass slides are generally unsuitable for either IR or Raman spectral measurement, since one then needs to sacrifice the most important fingerprint region required for spectral discrimination and disease diagnosis, due to the strong IR absorption or fluorescence bands of glass.⁷ This means that access to a broader spectrum can only be provided by more costly substrates. Additionally, the requirement for sample archiving in clinical practice implies that substrates are not reusable. Thus, for translation of biospectroscopy techniques for routine screening and/or diagnosis, a substrate without background signal interference and as inexpensive as glass is a major requirement.²¹

Ideally, spectroscopic diagnostic techniques should add in technical/medical value without compromising cost and/or efficiency. It is important to note that cost is not the single limiting factor for clinical/biological implementation, as a technique proven to improve quality of biological interpretation may justify increased expenditure. However, any substantial increase in running cost will not aid in the drive for clinical translation. To promote the translation of biospectroscopy to

^aKey Laboratory of Urban Pollutant Conversion, Institute of Urban Environment, Chinese Academy of Sciences, Xiamen 361021, China

^bCentre for Biophotonics, Lancaster Environment Centre, Lancaster University, Lancaster LA1 4YQ, UK. E-mail: lcui@iue.ac.cn; f.martin@lancaster.ac.uk

practical clinical diagnosis, the search for a cheap, easily available, and robust substrate suitable for both IR or Raman measurement is an urgent consideration. In this regard, aluminium (Al) foil could be a potential alternative. Similar to other pure metals-based substrates such as Au (Ag, Al)-coated slides, low spectral background and lack of spectral features can be anticipated on Al foil. More importantly, Al foil has substantially low cost. For instance, an annual cost of only £4900 is estimated for cervical smear, biopsies and histology specimens in UK, which is only 1/350 that of glass slides in terms of cost (Table 1). To demonstrate the feasibility of Al foil, its performance in ATR-FTIR, transfection FTIR or Raman spectrochemical analysis of cytology and histology specimen was compared with other well-recognized substrates, *i.e.*, Au-coated, low-E and glass slides.

Materials and methods

Substrates

Four types of substrates were used herein, including Al foil (Kitchen quality, Terinex Limited, UK), Au-coated slides (Item no. AU. 0500. ALSI, Platypus Technologies), low-E slides (Kevley Technologies, USA) and glass slides (Thermo Scientific). Al foil was placed onto glass slides and fixed by some tape to facilitate ease of handling and archiving.

Cell culture

An amphibian (A6) cell line was grown in modified L-15 medium supplemented with 70% Leibovitz's media (Gibco, Life Technologies Ltd, UK), 10% foetal bovine serum (Gibco), 1% penicillin (100 U mL⁻¹) and streptomycin (100 µg mL⁻¹) (Cat no. DE17-603 E, Lonza group Ltd., Belgium) and 19% autoclaved MilliQ water in air at room temperature. A6 cells were routinely cultured in T75 flasks and harvested when confluent by disaggregating cells using 3 mL trypsin (170 U mL⁻¹)/EDTA (0.02%) solution (Cat no. BE17-161E, Lonza group Ltd., Belgium) followed by neutralization using 7 mL modified L-15 medium.

To prepare fixed cell pellets on substrates, harvested A6 cells were centrifuged at 1000 rpm for 5 min to remove medium and then fixed in 70% ethanol (EtOH) for 1 h. After centrifugation and washing two more times using 70% EtOH, the final concentrated cells were applied to different substrates and air-dried.

To grow cells directly on substrates, substrates were initially sterilized by immersing in 70% EtOH and rinsed with autoclaved MilliQ water; then 2 mL harvested cells were seeded in

six-well plates containing substrates and to each an additional 4 mL modified L-15 medium was added. After two days of culture to allow cells to reach confluence, medium was removed and 70% EtOH was added for 1 h to fix, followed by washing in 70% EtOH twice more, whereupon substrates were left to air-dry.

Tissue

A formalin-fixed, paraffin-embedded (FFPE) prostate tissue block was obtained. All experimental protocols for the use of archival tissue retrieved from the Royal Preston Hospital Research Tissue Bank were approved by the UK National Research Ethics Service (<http://www.hra.nhs.uk/about-the-hra/our-committees/nres/>; Research Ethics Committee reference: 10/H0308/75). A ribbon of 20 µm-thick sections was cut by a microtome (Surgipath Medical Industries Inc), floated into a heated water bath at 40–50 °C, and finally picked up on substrates. After drying overnight, tissue slides were de-waxed by immersing in fresh xylene (histological grade, Sigma-Aldrich) for 2 min at room temperature; this process was repeated twice more. Subsequently, tissue slides were immersed in 100% fresh EtOH for 15 min twice and then to 70% fresh EtOH for 15 min twice. Fresh EtOH was used each time. Finally, tissue slides were allowed to air-dry prior to analysis.⁵

ATR-FTIR spectroscopy

ATR-FTIR spectral measurements were performed using a Bruker TENSOR 27 FTIR spectrometer (Bruker Optics Ltd., Coventry, UK) with Helios ATR attachment containing a diamond crystal internal reflective element and a 45° incidence angle of IR beam. The ATR crystal was cleaned using MilliQ water and a new background spectrum was collected prior to analysis of a new sample. The instrument was set up to perform a total of 32 scans with 8 cm⁻¹ spectral resolution on both background and sample. The sampling aperture of the system was 250 µm × 250 µm, and the mirror velocity was 2.2 kHz; it is a single signal bounce instrument and uses a diamond waveguide.

Transfection FTIR spectroscopy

Transfection FTIR spectroscopy was conducted using a Nicolet Continuum FTIR Microscope (Thermo Scientific) with IR beam provided by a Nicolet 6700 FTIR spectrometer. A 15 × infinity reflachromat objective with numerical aperture of 0.58 was used to illuminate sample and collect signal from a sample aperture

Table 1 Comparison of substrates price and estimated total annual cost of substrates in biomedical specimen screening in UK^{27–30}

Substrates	Price per piece (£)	Annual cost of cervical smear (million £)	Annual cost of biopsies (million £)	Annual cost of histology (million £)	Total (million £)
CaF ₂ (76.0 × 26.0 × 1.0 mm)	73.08	711.04	189.61	101.12	1001.78
Au-coated slide (75.0 × 25.0 × 0.7 mm)	42.08	409.46	109.19	58.23	576.88
Low-E (75.0 × 25.0 × 1.0 mm)	1.51	14.71	3.92	2.09	20.72
Glass (76.0 × 26.0 × 1.0 mm)	0.12	1.22	0.32	0.17	1.73
Aluminum foil (76.0 × 26.0 mm)	0.0004	0.0035	0.0009	0.0005	0.0049

of $100 \times 100 \mu\text{m}$. A total of 256 scans with spectral resolution of 8 cm^{-1} was setup for both background and sample collection.

Raman spectroscopy

Raman spectroscopy was acquired using a Renishaw InVia confocal micro-Raman system (Renishaw, Gloucestershire, UK) equipped with a 100 mW 785 nm laser and 1200 g mm^{-1} grating. A $100\times$ objective with numerical aperture of 0.85 was used to focus laser beam and collect Raman signal with an acquisition time of 30 s.

Results and discussion

Three typical biological specimens were prepared, *i.e.*, EtOH-fixed cell pellet applied to substrates, cells grown directly on substrates and de-waxed prostate tissue section floated on substrates. Fig. 1 shows the optical images of different sample preparations. Fixed-cell pellets were more spherical and smaller than cells grown directly on substrates (Fig. 1a), which exhibited a more expansive shape, thus looking bigger but being much thinner than the fixed-cell pellet (Fig. 1b). In addition, compared with the smooth surface of Au-coated, low-E or glass slides, the shiny side of Al foil used herein is rougher. The non-shiny side of foil was even rougher and thus not used, considering its low reflectivity. The thin layers of cells grown directly on the rough foil were not as discernible as those on smooth Au-coated or low-E substrates (Fig. 1b). However, after ATR-FTIR diamond pressure, the foil became smoother due to its ductility and cells can be clearly observed on it. This also indicates a simple way to obtain a smooth foil, which may be needed for some samples requiring an optimal focus and thus a better signal. Tissue sections with a thickness of $20 \mu\text{m}$ picked on substrates required de-waxing before measurement. De-waxing was performed by immersing and transferring tissue sections to different organic solvents of xylene, 100% EtOH, and 70% EtOH.⁵ This process may cause tissue section detaching from substrates. Fig. 1c indicates that the rough surface of foil can hold and stick such tissue sections as well as on the smooth low-E slide.

ATR-FTIR spectra were first obtained from four blank substrates (Fig. 2). In the fingerprint region, from 900 to 1800

cm^{-1} that is often most important for spectral discrimination and disease diagnosis, the Au-coated slide was cleanest without any obvious characteristic IR absorption band, followed by Al foil, which only showed a small band at 950 cm^{-1} . In comparison, a low-E slide displayed a moderately intense IR band at 1120 cm^{-1} whilst the glass slide spectrum exhibited multiple strong IR bands at 960 cm^{-1} and 1400 cm^{-1} . From ATR-FTIR spectra of a fixed-cell pellet, directly-grown cells and tissue section, only directly-grown cells consisting of a very thin layer exhibited spectral artefacts from the background signal of low-E (1120 cm^{-1}) and glass slides (960 cm^{-1}) (Fig. 2c), while the fixed-cell pellet and tissue section samples that were composed of a relatively thick layer displayed the same spectral features on all four substrates, indicating no interference from substrate background (Fig. 2b and d). This can be explained by the working principle of ATR-FTIR spectra. To generate ATR-FTIR spectra, the IR beam is directed through an internal reflection element (IRE) with a high refractive index (*e.g.*, diamond used here); the evanescent wave extending beyond the IRE surface penetrates the sample in direct contact with the IRE. The penetration depth of this wave typically ranges from 1 to $2 \mu\text{m}$ within the $1800\text{--}900 \text{ cm}^{-1}$ region but still with $\sim 5\%$ intensity at a depth of $3 \mu\text{m}$.⁵ So substrate interference can be avoided for samples thicker than $2\text{--}3 \mu\text{m}$, but for those $< 2 \mu\text{m}$, spectral artefacts from the underlying low-E or glass slide may become apparent, indicating that these substrates are unsuitable for thin samples. Bassan *et al.* also confirmed the interference of glass slide at sample thicknesses $< 2 \mu\text{m}$ *via* both theoretical calculations and experimental ATR-FTIR measurements.²² In comparison, the thin layer of cells grown directly on Al foil displayed similar spectral features to that on Au-coated slide. No obvious spectral artefacts were observed. This indicates the suitability of Al foil for preparations of very thin samples (*e.g.*, $< 2 \mu\text{m}$) towards ATR-FTIR measurements; more importantly, foil is available at a much-reduced cost compared to Au-coated slides.

For the transfection FTIR sampling mode, measurements were conducted with an IR beam passing through the sample and reflecting back from the substrate (*i.e.*, the reflective surface) through the sample a second time.⁵ Low-E slides are typical substrates used in transfection mode due to their high

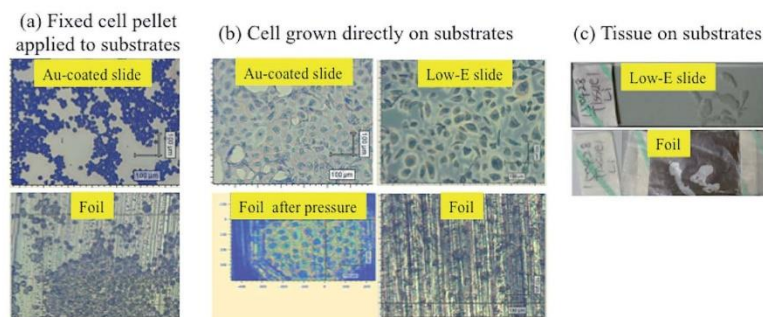


Fig. 1 Optical images of (a) fixed cell pellet; (b) directly-grown cells; and, (c) prostate tissue section on substrates.

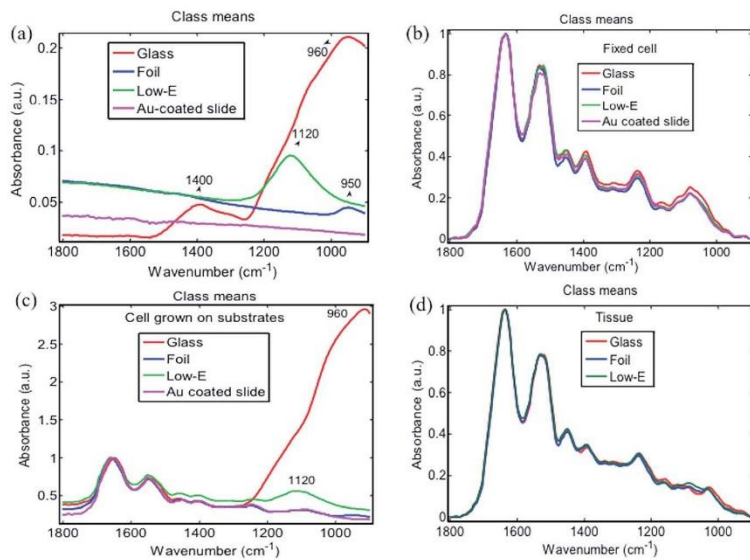


Fig. 2 ATR-FTIR spectra of (a) blank substrates; (b) fixed cell pellet; (c) cells directly grown on substrate; and, (d) prostate tissue section on substrate.

reflection towards IR beam combined with robustness and relatively low cost.¹⁴ Background spectra from low-E, Au-coated slide and Al foil were similar (Fig. 3a), whereas glass displayed a very strong IR absorption from 800 to 1200 cm⁻¹ region due to the penetration of IR beam into glass lacking an IR-reflective coating. The strong absorption of glass severely influenced the sample spectra irrespective of whether the sample was a thick

fixed-cell pellet or thin layer of cells grown on glass (Fig. 3b). In contrast, spectra of fixed-cell pellets on low-E slides, Au-coated slides or Al foil displayed the same typical fingerprint features of cells without substrate interference (Fig. 3c). For the thin layer of cells grown on substrates, transfection FTIR spectra of cells were also obtained, but with a markedly lower signal-to-noise ratio (SNR) than fixed-cell pellets due to the sample thinness

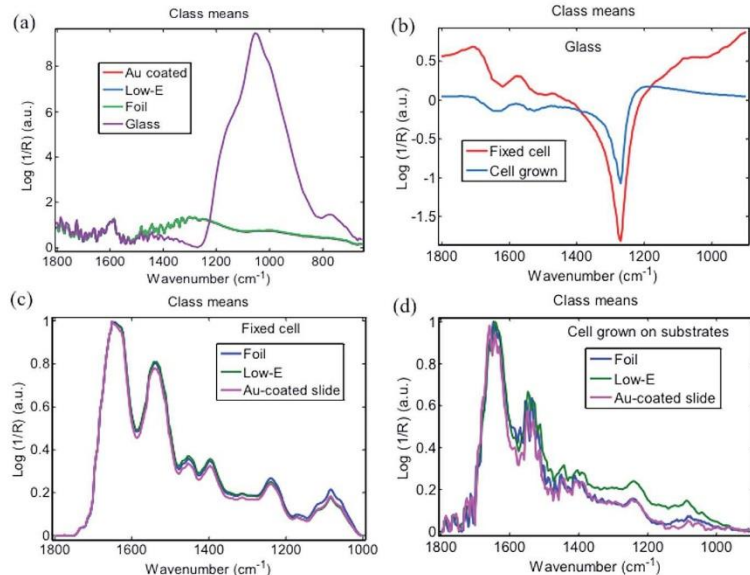


Fig. 3 Transfection FTIR spectra of (a) blank substrates; (b) fixed cell pellet or cells grown directly on glass; (c) fixed cell pellets on other substrates; and, (d) cells grown directly onto other substrates.

(Fig. 3d). This SNR was also lower than ATR-FTIR analysis of the same thin layer of cells grown on substrates (Fig. 2c), which should be related to the working principle of transfection and ATR mode.⁵ These results indicate that IR beam reflection on Al foil is enough to obtain similar-quality transfection FTIR spectra as from low-E or Au-coated slides, despite the rougher surface than the latter. Therefore, Al foil is applicable for transfection FTIR mode with a lower cost than low-E slides. A comparison of the relative reflectivity of these substrates will be interesting.

Many recent publications demonstrate a non-linear spectral distortion in transfection FTIR spectroscopy caused by the electric field standing wave (EFSW).^{14,15,23-25} This may result in spectral variation due to sample thickness rather than any biochemical differences. EFSW is suggested to be present on reflective metallic surfaces due to the interference of incident and reflected light. Smooth IR reflective low-E slides have been almost exclusively used to demonstrate the effect of EFSW; however, there is as yet no report studying the effect of substrate roughness on EFSW. On a rough surface like Al foil, reflected light may be emitted in many various directions different from the incident light. If this were the case, the probability of incident and reflected light interference, and how EFSW affects transfection FTIR spectra for samples mounted on a rough Al foil requires further study.

The performance of Al foil on Raman measurements was also investigated. Fig. 4a shows the raw Raman spectra of four blank substrates. Both low-E and glass display a strong and broad fluorescence band at 1382 cm^{-1} .^{7,26} In comparison, Al foil and Au-coated slide yield a very low and featureless spectral background. Raman spectra of three types of biomedical specimen on these substrates were also obtained. Unlike ATR- and transfection FTIR, all Raman spectra of the three biomedical specimens on low-E or glass slides exhibited interference from

the strong and broad glass band at 1382 cm^{-1} , which severely masked the important fingerprint bands at 1244 , 1325 , 1455 cm^{-1} , and even 1650 cm^{-1} at the tail region of 1382 cm^{-1} . This interference is more severe for the thin layer of cells grown directly on substrates, where no visible cell Raman bands can be observed over the strong background fluorescence of low-E or glass slides (Fig. 4c). This severe interference also makes it impossible to obtain biomedical specimen spectra by mathematically subtracting the glass band. Meanwhile, Raman spectra with all the well-defined bands constituting spectral fingerprints of cells or tissue are clearly distinguishable on Al foil or Au-coated slides, even for the thin layer of cells grown on substrates (Fig. 4b-d). Although the spectra of cells on Al foil were slightly tilting due to foil background compared with the rather flat spectra on Au-coated slide (Fig. 4c), it can be easily baseline subtracted without compromising any spectral features of cells (see inset of baseline-subtracted Raman spectra). Kamemoto *et al.* obtained high-quality near-IR Raman spectroscopy of cervical cancer tissue mounted on an Al-coated slides.⁷ Athamneh *et al.* obtained Raman spectra of bacteria on Al foil.¹¹ These studies further confirm the wide applicability of Al substrate in various Raman analyses. In comparison, despite the relatively rougher surface of Al foil compared to Au-coated slides, advantages of low cost and minimal interference on spectral acquisition could make it a first choice for high throughput analyses.

Table 2 summarizes the performance of Al foil and conventional substrates. Al foil performs as well as Au-coated slides in all ATR-FTIR, transfection FTIR or Raman spectrochemical measurements of very thin (cells grown directly on substrates) and thick specimens (fixed-cell pellet or tissue), but with a much reduced cost. In comparison, low-E is more suitable for ATR-FTIR measurement of samples thicker than $3\text{ }\mu\text{m}$, but not for

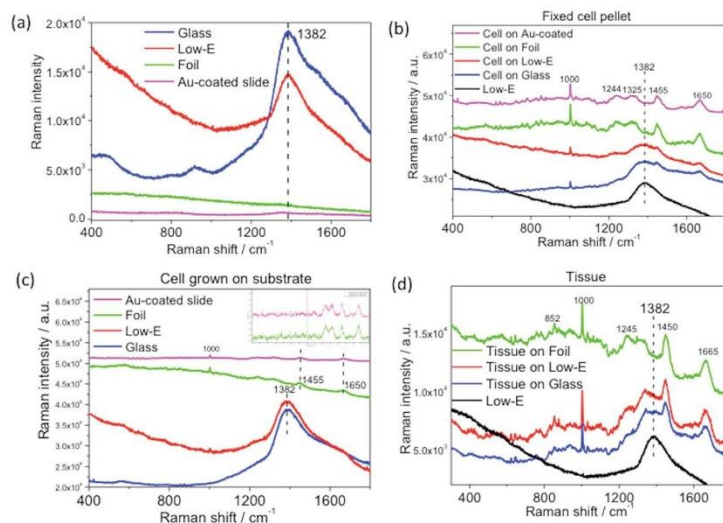


Fig. 4 Raman spectra of (a) blank substrates; (b) fixed cell pellet on substrates; (c) cells grown directly on substrates (inset represents baseline-subtracted Raman spectra on Au-coated slides or Al foil); and, (d) prostate tissue section on substrates.

Table 2 Performance and cost comparison of different substrates

Substrate	ATR-FTIR spectroscopy	Transflection FTIR spectroscopy	Raman spectroscopy	Cost
Au-coated slide	✓	✓	✓	High
Low-E	✓ (except for sample thinner than 2–3 µm)	✓	✗	Medium
Glass	✗	✗	✗	Lower
Aluminum foil	✓	✓	✓	Lowest

thinner specimens. Glass is cheap but unsuitable for either IR or Raman measurements because its strong background band will sacrifice the most important fingerprint biochemical information used for clinical diagnosis. Unfortunately, Al foil cannot be used in transmission FTIR because of its IR opacity.

Biocompatibility is an important consideration for future applications. A careful comparison indicates that ATR-FTIR spectral features of cells grown on Al foil are very close to other substrates including glass, low-E and Au-coated slide (Fig. 2c). Moreover, Raman spectra of cell grown on Al foil and Au-coated slide after baseline subtraction were almost identical (inset of Fig. 4c). These results may indicate that the biocompatibility of Al foil is comparable with conventional substrates. However, this will need to be assessed by conducting a comparison of survival rates of cells grown on such substrates.

Conclusion

This study demonstrates that readily available and inexpensive Al foil can be used as a versatile and suitable substrate for preparing diverse cytology and histology specimens for ATR-FTIR, transflection FTIR or Raman spectroscopic measurements. The low and almost featureless background spectra of Al foil enable the acquisition of high-quality IR and Raman spectra without substrate interference or sacrificing important fingerprint biochemical information of biomedical specimen. It is also suitable for diverse specimens with a broader thickness ranging from less than 2 µm to above. These features together with its much lower cost and availability make Al foil a potential substrate for the future application of IR and Raman spectroscopy in biomedical diagnosis. Although there are still many things to consider towards achieving final implementation, such as clinical trials and adaptation to current instruments, the use of Al foil makes this process a step forward by providing an additional low-cost substrate option. With little additional cost, a slightly thicker Al foil could replicate typical slide dimensions to better allow for handling and archiving.

Acknowledgements

This work was supported by China Scholarship Council, the National Natural Science Foundation of China (21173208), Natural Science Foundation of Ningbo (2014A610107) and Fujian Province (2015J01067).

References

- 1 M. Diem, A. Mazur, K. Lenau, J. Schubert, B. Bird, M. Miljkovic, C. Krafft and J. Popp, *J. Biophotonics*, 2013, **6**, 855–886.
- 2 D. I. Ellis, D. P. Cowcher, L. Ashton, S. O'Hagan and R. Goodacre, *Analyst*, 2013, **138**, 3871–3884.
- 3 C. Kendall, M. Isabelle, F. Bazant-Hegemark, J. Hutchings, L. Orr, J. Babrah, R. Baker and N. Stone, *Analyst*, 2009, **134**, 1029–1045.
- 4 A. Nijssen, K. Maquelin, L. F. Santos, P. J. Caspers, T. C. B. Schut, J. C. D. Hollander, M. H. A. Neumann and G. J. Puppels, *J. Biomed. Opt.*, 2007, **12**, 034004.
- 5 M. J. Baker, J. Trevisan, P. Bassan, R. Bhargava, H. J. Butler, K. M. Dorling, P. R. Fielden, S. W. Fogarty, N. J. Fullwood, K. A. Heys, C. Hughes, P. Lasch, P. L. Martin-Hirsch, B. Obinaju, G. D. Sockalingum, J. Sule-Suso, R. J. Strong, M. J. Walsh, B. R. Wood, P. Gardner and F. L. Martin, *Nat. Protoc.*, 2014, **9**, 1771–1791.
- 6 F. L. Martin, J. G. Kelly, V. Llabjani, P. L. Martin-Hirsch, I. I. Patel, J. Trevisan, N. J. Fullwood and M. J. Walsh, *Nat. Protoc.*, 2010, **5**, 1748–1760.
- 7 L. E. Kamemoto, A. K. Misra, S. K. Sharma, M. T. Goodman, H. Luk, A. C. Dykes and T. Acosta, *Appl. Spectrosc.*, 2010, **64**, 255–261.
- 8 K. Kong, C. Kendall, N. Stone and I. Notingher, *Adv. Drug Delivery Rev.*, 2015, **89**, 121–134.
- 9 J. Horsnell, C. Kallaway, C. Chan, J. Bristol and N. Stone, *Br. J. Surg.*, 2012, **99**, 5–6.
- 10 K. Gajjar, L. D. Heppenstall, W. Y. Pang, K. M. Ashton, J. Trevisan, I. I. Patel, V. Llabjani, H. F. Stringfellow, P. L. Martin-Hirsch, T. Dawson and F. L. Martin, *Anal. Methods*, 2013, **5**, 89–102.
- 11 A. I. M. Athamneh, R. A. Alajlouni, R. S. Wallace, M. N. Seleem and R. S. Senger, *Antimicrob. Agents Chemother.*, 2014, **58**, 1302–1314.
- 12 L. Cui, P. Y. Chen, S. D. Chen, Z. H. Yuan, C. P. Yu, B. Ren and K. S. Zhang, *Anal. Chem.*, 2013, **85**, 5436–5443.
- 13 L. T. Kerr, H. J. Byrne and B. M. Hennelly, *Anal. Methods*, 2015, **7**, 5041–5052.
- 14 M. J. Pilling, P. Bassan and P. Gardner, *Analyst*, 2015, **140**, 2383–2392.
- 15 D. Perez-Guaita, P. Heraud, K. M. Marzec, M. de la Guardia, M. Kiupel and B. R. Wood, *Analyst*, 2015, **140**, 2376–2382.
- 16 I. Amenabar, S. Poly, W. Nuansing, E. H. Hubrich, A. A. Govyadinov, F. Huth, R. Krutokhrostov, L. B. Zhang, M. Knez, J. Heberle, A. M. Bittner and R. Hillenbrand, *Nat. Commun.*, 2013, **4**, 2890.
- 17 J. Y. Li, R. Strong, J. Trevisan, S. W. Fogarty, N. J. Fullwood, K. C. Jones and F. L. Martin, *Environ. Sci. Technol.*, 2013, **47**, 10005–10011.
- 18 D. Berry, E. Mader, T. K. Lee, D. Woebken, Y. Wang, D. Zhu, M. Palatinszky, A. Schintmeister, M. C. Schmid,

B. T. Hanson, N. Shterzer, I. Mizrahi, I. Rauch, T. Decker, T. Bocklitz, J. Popp, C. M. Gibson, P. W. Fowler, W. E. Huang and M. Wagner, *Proc. Natl. Acad. Sci. U. S. A.*, 2015, **112**, E194–E203.

19 M. Q. Li, D. P. Canniffe, P. J. Jackson, P. A. Davison, S. FitzGerald, M. J. Dickman, J. G. Burgess, C. N. Hunter and W. E. Huang, *ISME J.*, 2012, **6**, 875–885.

20 S. A. Wang, J. H. Zhao, H. Lui, Q. L. He and H. S. Zeng, *Int. J. Spectrosc.*, 2010, **24**, 577–583.

21 [http://countymeters.info/en/United_Kingdom_\(UK\)](http://countymeters.info/en/United_Kingdom_(UK)), accessed 16 July 2015.

22 P. Bassan, A. Sachdeva, J. Lee and P. Gardner, *Analyst*, 2013, **138**, 4139–4146.

23 E. Staniszewska-Slezak, A. Rygula, K. Malek and M. Baranska, *Analyst*, 2015, **140**, 2412–2421.

24 J. Filik, M. D. Frogley, J. K. Pijanka, K. Wehbe and G. Cinque, *Analyst*, 2012, **137**, 853–861.

25 K. Kochan, P. Heraud, M. Kiupel, V. Yuzbasiyan-Gurkan, D. McNaughton, M. Baranska and B. R. Wood, *Analyst*, 2015, **140**, 2402–2411.

26 L. M. Fullwood, D. Griffiths, K. Ashton, T. Dawson, R. W. Lea, C. Davis, F. Bonnier, H. J. Byrne and M. J. Baker, *Analyst*, 2014, **139**, 446–454.

27 <http://www.crystran.co.uk/windows/calcium-fluoride-windows/calcium-fluoride-rectangular-windows>, accessed 16 July 2015.

28 <http://www.platypustech.com/glassslides.html>, accessed 16 July 2015.

29 <http://www.kevley.com/dnn/Ordering.aspx>, accessed 16 July 2015.

30 <http://www.scientificlabs.co.uk/product/MIC3022>, accessed 16 July 2015.

Appendix II – Conference Abstracts

Spec2014, Krakow, PL – August 2014 – Poster Presentation

IR and Raman spectroscopy to detect presymptomatic biomarkers of nutrient deficiency during crop production.

Holly J. Butler^{1,2}, Martin R. McAinsh², and Francis L. Martin^{2*}

¹*Centre for Global Eco-Innovation, Lancaster University, Lancaster, LA1 4YQ UK*

²*Lancaster Environment Centre, Lancaster University, Lancaster, LA1 4YQ, UK*

*f.martin@lancaster.ac.uk

With an increasing population, anticipated to reach 9 billion by 2050, it is estimated that agricultural productivity will need to increase by 70% in order to meet food demands¹. Nutrient deficiencies can result in up to 50% loss of yield and significantly decreased shelf life and therefore present a substantial threat to global food security. Foliar applications of calcium (Ca^{2+}) containing solutions upon crops have been shown to prevent the incidence of Ca^{2+} deficiencies such as 'blossom end rot' in fruiting vegetables. Deficiencies such as this often do not manifest until fruit set and therefore prevention methods are non-selective and can prove ineffective and costly to the grower.

The common tomato plant, *Solanum lycopersicum*, was used a model system to presymptomatically detect Ca^{2+} deficiency by using hydroponic systems with varying levels of Ca^{2+} availability. The plants were interrogated using IR and Raman spectroscopy over a course of several weeks to monitor any structural or chemical alterations due to the nutrient deficiency². Coupled with multivariate analysis, subtle biomarkers can be found that could potentially be used to discriminate between crops advancing into a deficient state. This study aims to employ vibrational spectroscopy as a non-destructive, high-throughput and cost effective tool for *in vivo* screening of crops in agricultural environments.

References

- ¹. Godfray H.C.J. *et al.* (2010) Food security: The challenge of feeding 9 billion people. *Science*. **372**:812-818
- ²Mansfield J.C. *et al.* (2013) Label-free chemically specific imaging in plants with stimulated Raman scattering microscopy. *Anal. Chem.* **85**: 5055-63

Acknowledgements

Holly Butler is part of the Centre for Global Eco-Innovation and works in collaboration with Plant Impact Plc. The project is ERDF funded.

Infrared and Raman Discussion Group (IRDG) Student Meeting

August 2015 – Oral Presentation

Pre-symptomatic detection of nutrient deficiencies in crop production using vibrational spectroscopy.

Holly J Butler^{ab}, Francis L Martin^b, Martin R McAinsh^c

^a*Centre for Global Eco-Innovation*, ^b*Centre for Biophotonics*, ^c*Lancaster Environment Centre, Lancaster University, LA1 4YQ, UK*

Nutrient deficiencies can result in up to 50% loss of yield and significantly decreased shelf life and therefore present a substantial threat to global food security¹. Deficiencies such as this often do not manifest until fruit set and therefore prevention methods are non-selective and can prove ineffective and costly to the grower. The common tomato plant, *Solanum lycopersicum*, was used a model system to presymptomatically detect Ca²⁺ deficiency by using hydroponic systems with varying levels of Ca²⁺ availability. The plants were interrogated using IR and Raman spectroscopy over a course of several weeks to monitor any structural or chemical alterations due to the nutrient deficiency². Coupled with multivariate analysis, subtle biomarkers can be found that could potentially be used to discriminate between crops advancing into a deficient state. This study aims to employ vibrational spectroscopy as a non-destructive³, high-throughput and cost effective tool for *in vivo* screening of crops in agricultural environments.

¹Godfray H.C.J. *et al.* (2010) *Science*, **372**:812:818

²White P.J. and Broadley M.R. (2003) *Annals of Botany*, **92**:487-511

³Butler H.J *et al.* (2015) *Analytical Methods*, **7**:4059-4070

Pacifichem 2015, Honolulu, USA – December 2015 – Oral Presentation
Faraday Discussions, Cambridge, UK – March 2016 – Poster
Presentation

Gold nanoparticles as a substrate in bio-analytical near-infrared surface-enhanced Raman spectroscopy

HJ Butler¹, SW Fogarty, AL Mitchell, FL Martin

1. Centre for Biophotonics, Lancaster University, Lancaster, LA1 4YT

As biospectroscopy techniques continue to be developed for screening or diagnosis within a point-of care setting, an important development for this field will be high-throughput optimization. For many of these techniques, it is therefore necessary to adapt and develop parameters to generate a robust yet simple approach delivering high-quality spectra from biological samples. Specifically, this is important for surface-enhanced Raman spectroscopy (SERS) wherein there are multiple variables that can be optimised to achieve an enhancement of the Raman signal from a sample. One hypothesis is that “large” diameter (>100 nm) gold nanoparticles provide a greater enhancement at near-infrared (NIR) and infrared (IR) wavelengths than those <100 nm in diameter. Larger gold nanoparticles may better satisfy the theoretical restraints for SERS enhancement at NIR/IR wavelengths compared to smaller nanoparticles. Also, larger nanoparticles or their aggregates are more readily observed via optical microscopy (and especially electron microscopy) compared to smaller ones. This allows rapid and straightforward identification of target areas containing a high concentration of nanoparticles and facilitating SERS spectral acquisition. However, the potential nanotoxicity of metallic nanoparticles may have a significant effect on the sample and consequently the derived SERS spectra. Herein, we examine this notion using examples in which SERS spectra were acquired from MCF-7 breast cancer cells incubated with 150 nm gold nanoparticles. It was found that 150 nm gold nanoparticles are an excellent material for NIR/IR SERS, with little evidence of toxic effects. These observations appear to extend to biofluids such as blood plasma and serum; SERS spectra of such biological samples often exhibit a low signal-to-noise ratio in the absence of nanoparticles. With protein-rich biofluids such as serum, a dramatic SERS effect can be observed; although this might facilitate improved spectral biomarker identification in the future, it may not always improve classification between control vs. cancer. Thus, use of “large” gold nanoparticles are a good starting point in order to derive informative NIR/IR SERS analysis of biological samples

Spec 2016, Montreal, Canada – July 2016 – Poster Presentation

Aluminium foil as a potential substrate for ATR-FTIR, transfection FTIR or Raman spectrochemical analysis of biological specimens

Li Cui ^{ab}, Holly J. Butler ^b, Pierre L. Martin-Hirsch ^b, and Francis L. Martin ^{*b}

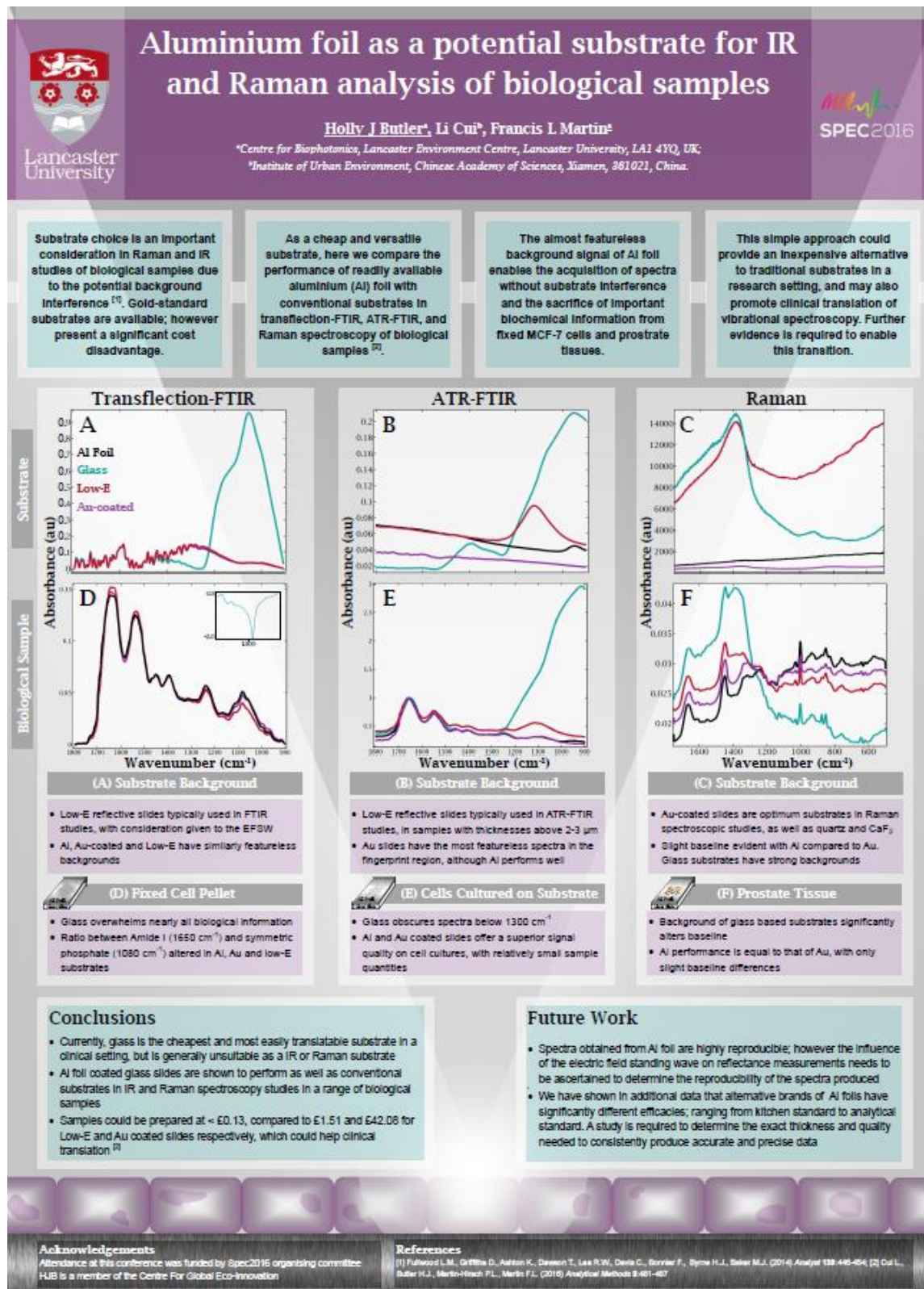
^a Key Laboratory of Urban Pollutant Conversion, Institute of Urban Environment, Chinese Academy of Sciences, Xiamen 361021, China

^b Centre for Biophotonics, Lancaster Environment Centre, Lancaster University, Lancaster LA1 4YQ, UK.

The substantial cost of substrates is an enormous obstacle in the successful translation of biospectroscopy into routine clinical/laboratory practice (screening or diagnosis). As a cheap and versatile substrate, we compared the performance of readily available aluminium (Al) foil with low-E, calcium fluoride, barium fluoride, Au-coated and glass slides for cytological and histological specimen analysis by attenuated total reflection Fourier-transform infrared (ATR-FTIR), transfection FTIR and Raman spectroscopy. The low and almost featureless background signal of Al foil enables the acquisition of IR or Raman spectra without substrate interference or sacrificing important fingerprint biochemical information of the specimen, even for particularly thin samples (<2 μ m). Al foil is shown to perform as well as, if not better than, low-E or Au-coated slide, irrespective of its relatively rough surface. Although transmission FTIR is not possible on Al foil, this work demonstrates Al foil is an inexpensive, readily available and versatile substrate suitable for ATR-FTIR, transfection FTIR or Raman spectrochemical measurements of diverse biological specimens. The features of Al foil demonstrated here could promote a transition towards accessible substrates that can be readily implemented in either research or clinical settings.

Appendix III – Conference Posters

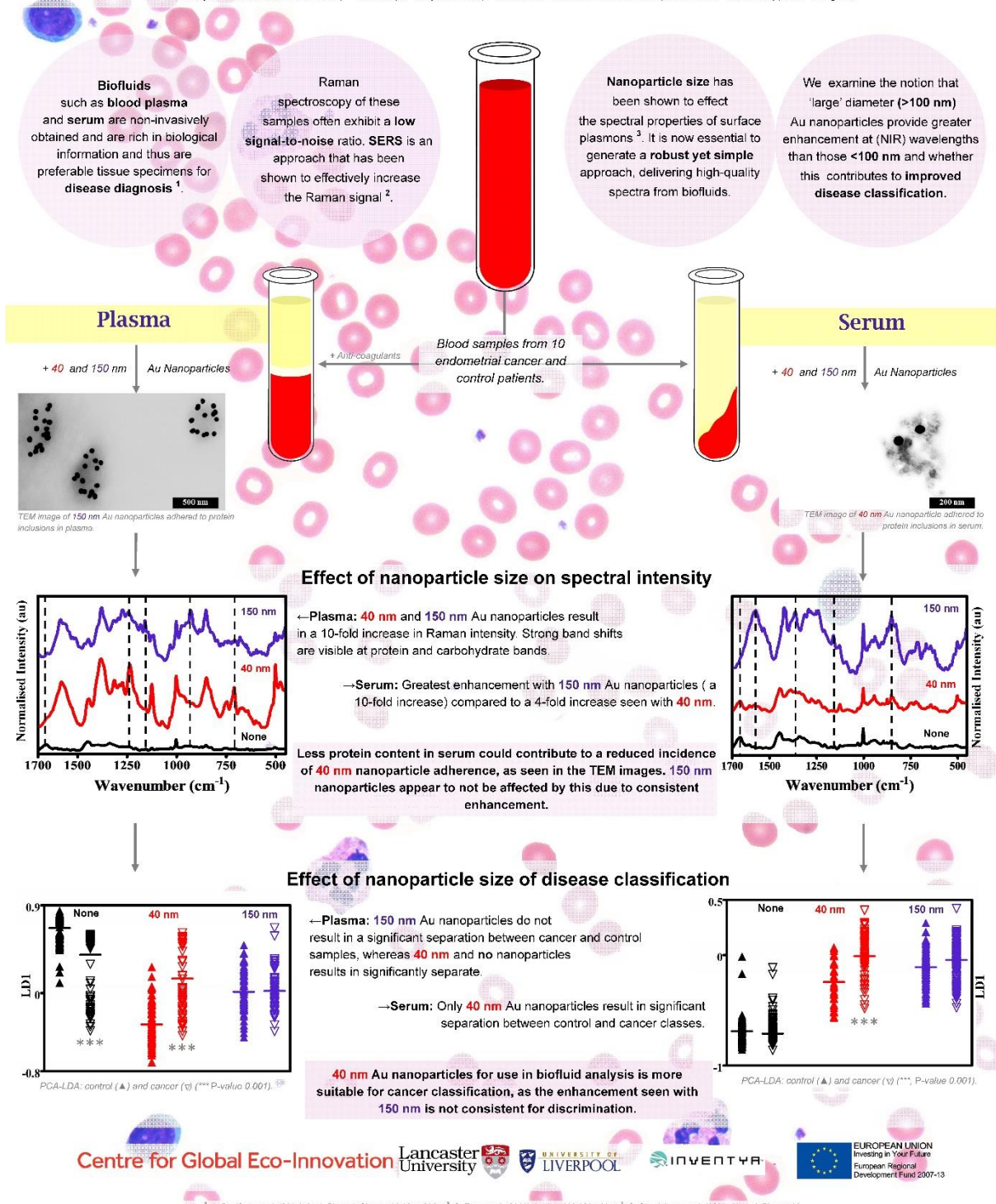
Spec2016, Montreal, Canada, 2016



Gold nanoparticles as a substrate in bio-analytical surface-enhanced Raman spectroscopy of biofluids

Holly J. Butler ^a, Simon W. Fogarty ^b, Nigel J. Fullwood ^c, Francis L. Martin ^b

^a Centre for Global Eco-Innovation, ^b Centre for Biophotonics, ^c Lancaster Environment Centre, Lancaster University, LA1 4YQ, UK



Pre-symptomatic detection of nutrient deficiency during crop production using vibrational spectroscopy

Holly J Butler^{a,b}, Francis L Martin^b, Martin R McAinsh^c^aCentre for Global Eco-Innovation, ^bCentre for Biophotonics, ^cLancaster Environment Centre, Lancaster University, LA1 4YQ, UK